UNCLASSIFIED

AD NUMBER

ADB232172

NEW LIMITATION CHANGE

TO

Approved for public release, distribution unlimited

FROM

Distribution authorized to U.S. Gov't. agencies and their contractors; Critical Technology; Aug 97. Other requests shall be referred to WL/FIGC, 2210 Eight St., Ste. 11, WPAFB, OH 45433

AUTHORITY

AFRL Ltr., 14 Sep 99

THIS PAGE IS UNCLASSIFIED

DEPARTMENT OF THE AIR FORCE
AIR FORCE RESEARCH LABORATORY
WRIGHT-PATTERSON AIR FORCE BASE OHIO 45433

9-14-99

MEMORANDUM FOR: Defense Technical Information Center/OMI
8725 John J. Kingman Rd, Suite 0944
Ft Belvoir, VA 22060-6218

FROM: Det 1 AFRL/WST
Bldg 640 Rm 60
2331 12th Street
Wright-Patterson AFB OH 45433-7950

SUBJECT: Notice of Changes in Technical Report(s) (see below)

Please change subject report(s) as follows:

The following have all been approved for public release; distribution is unlimited:

AFWAL-TR-83-3072,
WRDC-TR-90-3081,
WL-TR-96-3043,
WL-TR-96-3094,
WL-TR-97-3059,

AD B955 265
AD B166 585
AD B212 813 - OK ST-A
AD B212 361 ~~STA~~
AD B232 172 ~~OK~~

B212361

Joseph A. Burke
JOSEPH A. BURKE, Team Leader
STINFO and Technical Editing
Technical Information Division

WL-TR-97-3059

INNOVATIVE CONTROL EFFECTORS (ICE) PHASE II

Kenneth M. Dorsett
Scott P. Fears

Lockheed Martin Tactical Aircraft Systems
P.O. Box 748
Fort Worth TX 76101

Heather P. Houlden

Bihrle Applied Research, Inc.
18 Research Drive
Hampton VA 23666

AUGUST 1997

FINAL REPORT FOR MARCH 1996 - JULY 1997

Distribution: Approved for public Release; Distribution Unlimited.

DESTRUCTION NOTICE: **Destroy by any method that will prevent disclosure of contents or reconstruction of the document.**

FLIGHT DYNAMICS DIRECTORATE
WRIGHT LABORATORY
AIR FORCE MATERIEL COMMAND
WRIGHT-PATTERSON AIR FORCE BASE, OHIO 45433-7562

DTIC QUALITY INSPECTED 4

19971223 100

NOTICE

WHEN GOVERNMENT DRAWINGS, SPECIFICATIONS, OR OTHER DATA ARE USED FOR ANY PURPOSE OTHER THAN IN CONNECTION WITH A DEFINITE GOVERNMENT-RELATED PROCUREMENT, THE UNITED STATES GOVERNMENT INCURS NO RESPONSIBILITY OR ANY OBLIGATION WHATSOEVER. THE FACT THAT THE GOVERNMENT MAY HAVE FORMULATED OR IN ANY WAY SUPPLIED THE SAID DRAWINGS, SPECIFICATIONS, OR OTHER DATA, IS NOT TO BE REGARDED BY IMPLICATION, OR OTHERWISE IN ANY MANNER CONSTRUED, AS LICENSING THE HOLDER, OR ANY OTHER PERSON OR CORPORATION; OR AS CONVEYING ANY RIGHTS OR PERMISSION TO MANUFACTURE, USE, OR SELL ANY PATENTED INVENTION THAT MAY IN ANY WAY BE RELATED THERETO.

This technical report has been reviewed and is accepted for publication.

William J. Gillard

WILLIAM J. GILLARD
Project Engineer
Control Dynamics Branch

Stanley F. Lash

STANLEY F. LASH, Acting Chief
Control Dynamics Branch
Flight Control Division

David P. LeMaster

DAVID P. LEMASTER, Chief
Flight Control Division
Flight Dynamics Directorate

If your address has changed, if you wish to be removed from our mailing list, or if the addressee is no longer employed by your organization, please notify WL/FIGC, 2210 Eighth St. Suite 11, WPAFB OH 45433-7521 to help maintain a current mailing list.

Copies of this report should not be returned unless return is required by security considerations, contractual obligations, or notice on a specific document.

REPORT DOCUMENTATION PAGE

Form Approved
OMB No. 0704-0188

Public reporting burden for this collection of information is estimated to average 1 hour per response, including the time for reviewing instructions, searching existing data sources, gathering and maintaining the data needed, and completing and reviewing the collection of information. Send comments regarding this burden estimate or any other aspect of this collection of information, including suggestions for reducing this burden, to Washington Headquarters Services, Directorate for Information Operations and Reports, 1215 Jefferson Davis Highway, Suite 1204, Arlington, VA 22202-4302, and to the Office of Management and Budget, Paperwork Reduction Project (0704-0188), Washington, DC 20503.

1. AGENCY USE ONLY *(Leave blank)*	2. REPORT DATE	3. REPORT TYPE AND DATES COVERED
	August 1997	FINAL 03/01/96 - 07/31/97

4. TITLE AND SUBTITLE

INNOVATIVE CONTROL EFFECTORS (ICE) PHASE II

5. FUNDING NUMBERS

C F33615-94-C-3610
PE 62201F
PR 2403
TA 05
WU 9B

6. AUTHOR(S)

Kenneth M. Dorsett (LMTAS)
Scott P. Fears (LMTAS)
Heather P. Houlden (BAR)

7. PERFORMING ORGANIZATION NAME(S) AND ADDRESS(ES)

Lockheed Martin Tactical Aircraft Systems
P. O. Box 748
Fort Worth TX 76101

Bihrle Applied Research, Inc
18 Research Drive
Hampton VA 23666

8. PERFORMING ORGANIZATION REPORT NUMBER

FZM-8407

9. SPONSORING/MONITORING AGENCY NAME(S) AND ADDRESS(ES)

Flight Dynamics Directorate
Wright Laboratory
Air Force Materiel Command
Wright-Patterson AFB OH 45433-7562
POC: William Gillard, WL/FIGC, 937-255-0412

10. SPONSORING/MONITORING AGENCY REPORT NUMBER

WL-TR-97-3059

11. SUPPLEMENTARY NOTES

12a. DISTRIBUTION AVAILABILITY STATEMENT

Distribution authorized to U.S. Government agencies and their contractors; Critical Technology; August 1997. Other requests for this document shall be referred to WL/FIGC, 2210 Eighth St., Suite 11, Wright-Patterson OH 45433-7521

12b. DISTRIBUTION CODE

13. ABSTRACT *(Maximum 200 words)*

This report describes the Phase II portion of a joint U.S. Air Force - U.S. Navy sponsored investigation of innovative aerodynamic control concepts for fighter aircraft without vertical tails. The Phase I work consisted of effector performance prediction, vehicle integration assessment, and transition studies for numerous control effector concepts. The Phase II effort is an extension of the Phase I work and consists mainly of three wind tunnel tests to acquire more information about the aerodynamic performance of all-moving wing tips (AMTs) and spoiler-slot-deflectors (SSDs). These tests clearly showed both the AMT and SSD can produce significant yaw control power and are strong control effector candidates for tailless fighters. Predicted vehicle dynamics from Phase I are compared with predictions developed utilizing the new aerodynamic data acquired in Phase II.

14. SUBJECT TERMS

Tailless Aircraft, Lateral-Directional Control Power, Flight Control Effectors, All Moving Wing Tips, Spoiler-Slot-Deflector, Effector Integration

15. NUMBER OF PAGES

413

16. PRICE CODE

17. SECURITY CLASSIFICATION OF REPORT	18. SECURITY CLASSIFICATION OF THIS PAGE	19. SECURITY CLASSIFICATION OF ABSTRACT	20. LIMITATION OF ABSTRACT
UNCLASSIFIED	UNCLASSIFIED	UNCLASSIFIED	

Standard Form 298 (Rev. 2-89) (EG)
Prescribed by ANSI Std. 239.18
Designed using Perform Pro, WHS/DIOR, Oct 94

Table of Contents

Table of Contents ____ *iii*

List of Figures ____ *v*

List of Tables ____ *x*

Nomenclature ____ *xi*

Foreword ____ *xv*

Summary ____ *xvi*

1 Introduction ____ *1-1*

1.1 Background ____ 1-2

1.2 Phase 2 Program Content ____ 1-5

2 Small-Scale ADF Wind-Tunnel Test Results and Analysis ____ *2-1*

2.1 Introduction and Background ____ 2-1

2.2 Facility Description and Test Conditions ____ 2-1

2.3 Description of Models ____ 2-1

2.4 Test Objectives ____ 2-5

2.5 Results and Analysis ____ 2-5

2.6 Conclusions and Recommendations ____ 2-11

3 Rotary Balance Testing and Analysis ____ *3-1*

3.1 Summary ____ 3-1

3.2 Introduction ____ 3-1

3.3 Test Facility ____ 3-2

3.4 Test Procedures ____ 3-2

3.5 Description of Models ____ 3-2

3.6 Test Conditions ____ 3-3

3.7 Data Presentation ____ 3-4

3.8 Discussion of ICE 201 Results ____ 3-4

3.9 Discussion of ICE 101 Results ____ 3-11

3.10 Predicted Spin Characteristics ____ 3-16

3.11 Concluding Remarks and Summary ____ 3-17

4 SARL Wind Tunnel Test ____ *4-1*

4.1 Summary ____ 4-1

4.2 Introduction ____ 4-1

Preceding Page Blank

4.3 Model Description 4-1
4.4 Facility Description 4-5
4.5 Test Conditions 4-5
4.6 Discussion of Results 4-7
4.7 Control Power Variations with Control Volume 4-11
4.8 Conclusions 4-11
5 Simulation Database *5-1*
6 Control Power Analysis *6-1*
6.1 Methodology 6-1
6.2 Land-Based: Configuration 101 Series 6-8
6.3 Carrier-Based: Configuration 201 Series 6-28
7 Conclusions *7-1*
7.1 All Moving Wing Tip 7-1
7.2 Spoiler-Slot-Deflector 7-1
7.3 Control Power Analysis 7-2
7.4 Recommendations 7-3
8 References *8-1*

List of Figures

Figure 1-1: Effect of Desire For High-AOA Agility and Low Observability On Technology Development Envelope 1-1
Figure 1-2: Land-Based Baseline Configuration (101-Series) 1-2
Figure 1-3: Carrier-Based Baseline Configuration (201-Series) 1-3
Figure 1-4: Phase 1 Control Concepts Selected For Further Investigation During Phase 2 1-3
Figure 1-5: Four Control Suites Studied During ICE Phase 2 1-4
Figure 1-6: Diagram Outlining Tasks Performed During Phase 2 of ICE Program 1-5
Figure 1-7: Configurations 101 (Left) and 201 (Right) in LMTAS 2'x3' ADF Wind Tunnel 1-6
Figure 1-8: ICE Rotary Balance Wind-Tunnel Models in LAMP Vertical Wind Tunnel 1-7
Figure 1-9: 1/18th-Scale High-Speed Wind-Tunnel Model in SARL Facility at WPAFB 1-7
Figure 2-1: LMTAS 2'X3' ADF Wind Tunnel 2-13
Figure 2-2: Wind-Tunnel Model of Land-Based Configuration 101 2-13
Figure 2-3: Configuration 101 Wind-Tunnel Model Parts 2-14
Figure 2-4: Wind-Tunnel Model Carrier-Based Configuration 201 2-15
Figure 2-5: Configuration 201 Wind-Tunnel Model Parts 2-16
Figure 2-6: IB Fwd SSD Deflected 60° 2-16
Figure 2-7: Configuration 201 Run Log 2-17
Figure 2-8: Configuration 101 Run Log 2-20
Figure 2-9: Configuration 101 Longitudinal Data 2-22
Figure 2-10: Configuration 101 Lateral-Directional Stability Characteristics 2-23
Figure 2-11: Small AMT Control Effectiveness on Configuration 101 2-24
Figure 2-12: Skewed AMT Control Effectiveness on Configuration 101 2-25
Figure 2-13: Large AMT Control Effectiveness on Configuration 101 2-26
Figure 2-14: AMT Control Effectiveness Variation with Geometry 2-27
Figure 2-15: Diagram of Side Force and Axial Force Generated By Skewed AMT Deflection 2-28
Figure 2-16: Axial Force and Side Force Increments due to AMT Deflection of 60° 2-29
Figure 2-17: Relationship Between AMT Yaw Control Power and Control Volume Ratio 2-30
Figure 2-18: Variation of Yaw Power Generated By Various AMTs With Deflection At AOA of 0° 2-30
Figure 2-19: Effect of AOA on Variation of Large AMT Yaw Power With Deflection Angle 2-31
Figure 2-20: Effect of Sidslip on AMT Yaw Power for Configuration 101 2-32
Figure 2-21: Alternate Large AMT Arrangements 2-33
Figure 2-22: Effect of Gurney Flap and Fillet on Large AMT for 30° Deflection 2-34
Figure 2-23: Effect of Gurney Flap and Fillet on Large AMT for 60° Deflection 2-35
Figure 2-24: LEF Interaction with Skewed AMT on Configuration 101 2-36
Figure 2-25: IB Aft SSD Control Effectiveness on Configuration 101 2-37
Figure 2-26: IB Fwd SSD Control Effectiveness on Configuration 101 2-38
Figure 2-27: OB Fwd SSD Control Effectiveness on Configuration 101 2-39
Figure 2-28: SSD Control Power Variation with Control Volume 2-40
Figure 2-29: Effect of Sideslip on SSD Control Power 2-41
Figure 2-30: Effect of Location on SSD Control Effectiveness 2-42
Figure 2-31: Comparison of OB Fwd Spoiler and SSD Control Effectiveness 2-43
Figure 2-32: Effect of Slot Geometry Variation on SSD Effectiveness 2-44
Figure 2-33: Effect of OB Fwd SSD Deflections on Control Power From -30° Elevon Deflection 2-45
Figure 2-34: Effect of OB Fwd SSD Deflections on Control Power From -10° Elevon Deflection 2-46
Figure 2-35: Effect of OB Fwd SSD Deflections on Control Power From 10° Elevon Deflection 2-47
Figure 2-36: Effect of OB Fwd SSD Deflections on Control Power From 30° Elevon Deflection 2-48
Figure 2-37: Effect of 60° OB Fwd Spoiler and SSD Deflections on Control Power From -30° Elevon Deflection 2-49
Figure 2-38: Effect of 60° OB Fwd Spoiler and SSD Deflections on Control Power From-10° Elevon Deflection 2-50
Figure 2-39: Effect of 60° OB Fwd Spoiler and SSD Deflections on Control Power From 10° Elevon Deflection 2-51
Figure 2-40: Effect of 60° OB Fwd Spoiler and SSD Deflections on Control Power From 30° Elevon Deflection 2-52
Figure 2-41: Effect of SSD Location on Control Power From -30° Elevon Deflection 2-53
Figure 2-42: Effect of SSD Location on Control Power From 30° Elevon Deflection 2-54
Figure 2-43: Effect of SSD Location on Control Power From 30° Pitch Flap Deflection 2-55
Figure 2-44: Longitudinal Characteristics of Configuration 201 2-56
Figure 2-45: Effect of Canard Deflection on Lateral-Directional Stability of Configuration 201 2-57
Figure 2-46: Small AMT Control Effectiveness on Configuration 201 2-58
Figure 2-47: Comparison of Small and Large AMT Control Effectiveness on Configuration 201 2-59
Figure 2-48: Effect of Skewed AMT on Configuration 201 2-60
Figure 2-49: AMT Control Power Comparison at Deflection of 60° on Configuration 201 2-61

Figure 2-50: Effects of Sideslip on Large AMT Control Power 2-62
Figure 2-51: Effect of Sideslip on Skewed AMT at High AOAs 2-63
Figure 2-52: Effect of Small AMT on Aileron Control Power 2-64
Figure 2-53: Effect of Skewed AMT on Aileron Control Power 2-65
Figure 2-54: Effect of Large AMT on Aileron Control Power 2-66
Figure 2-55: IB Aft SSD Control Power on Configuration 201 2-67
Figure 2-56: IB Fwd SSD Control Power on Configuration 201 2-68
Figure 2-57: OB Fwd SSD Control Power on Configuration 201 2-69
Figure 2-58: Effect of Location on SSD Control Power 2-70
Figure 2-59: Effect of Sideslip on IB Fwd SSD 2-71
Figure 2-60: Variation of Spoiler Control Power at IB Aft SSD Location With Deflection Angle 2-72
Figure 2-61: Effect of SSD Deflection Angle at IB Aft SSD Location on Pitching Moment 2-72
Figure 2-62: Configuration 201 Slot Blockage Configurations 2-73
Figure 2-63: Effect of Slot Blockage on SSD Control Power 2-74
Figure 2-64: Effect of Slot Blockage on SSD Axial Force 2-75
Figure 2-65: Effect of SSD Location on Aileron Control Interactions; Aileron = -30° 2-76
Figure 2-66: Effect of SSD Location on Aileron Control Interactions; Aileron = 30° 2-77
Figure 2-67: LEF Effects on SSD Control Power 2-78
Figure 2-68: Effect of Canard Deflections on SSD Control Effectiveness 2-79
Figure 2-69: Differential LEF Effectiveness on Configuration 201 2-80
Figure 2-70: Effect of Sideslip on DLEF Effectiveness; AOA = 20° 2-81
Figure 2-71: Effect of Sideslip on DLEF Effectiveness; AOA = 32.5° 2-82
Figure 2-72: AMT Effectiveness Efficiency 2-83
Figure 2-73: SSD Effectiveness Efficiency 2-83
Figure 13-1. Photograph of Rotary Balance Rig in the LAMP 10-ft Vertical Wind Tunnel. 3-46
Figure 3-2. Photograph of ICE 101 Model Installed on the Rotary Balance Rig. 3-47
Figure 3-3. Photograph of the ICE 201 Model Installed on the Rotary Balance Apparatus. 3-48
Figure 3-4. Three-view Drawing of the ICE 201 Configuration. 3-49
Figure 3-5. Three-view Drawing of the ICE 101 Configuration. 3-50
Figure 3-6. Photographs of Spoiler-slot-deflector (SSD) Deployed on ICE 101 Model. 3-51
Figure 3-7. Canard-on vs Canard-off Lift Coefficient for the ICE 201. 3-52
Figure 3-8. Effect of Sideslip on Static Pitching Moment for the ICE 201 (LEF=0). 3-54
Figure 3-9. Effect of Canard on Static Pitching Moment at β=0° for the ICE 201. 3-55
Figure 3-10. Effect of Rotation Rate and Sideslip on Pitching Moment for the ICE 201 (LEF=0). 3-56
Figure 3-11. Effects of Sideslip on Static Rolling Moment Characteristics of the ICE 201 (LEF=0). 3-59
Figure 3-12. Effect of Rotation Rate and Sideslip on Rolling Moment for the ICE 201 (LEF=0). 3-60
Figure 3-13. Effect of Sideslip on Static Yawing Moment Characteristics for the ICE 201 (LEF=0). 3-64
Figure 3-14. Effect of Rotation Rate and Sideslip on Yawing Moment for the ICE 201 (LEF=0). 3-65
Figure 3-15. Effect of Leading Edge Flap Deflection on Lift for the ICE 201 (β=0°). 3-68
Figure 3-16. Effect of Leading Edge Flap Deflection on Static Pitching Moment for the ICE 201 at Zero Sideslip. 3-69
Figure 3-17. Effect of Leading Edge Flap Deflection on Static Rolling Moment for the ICE 201. 3-70
Figure 3-18. Effect of Leading Edge Flap Deflection on Static Yawing Moment for the ICE 201. 3-71
Figure 3-19. Effect of Rotation Rate and LEF Deflection on Rolling Moment for the ICE 201 (β=0°). 3-72
Figure 3-20. Effect of Rotation Rate and LEF Deflection on Yawing Moment for the ICE 201 (β=0°). 3-75
Figure 3-21. Effect of Differential Leading Edge Flap Deflection on Rolling Moment for the ICE 201 (β=0°). 3-77
Figure 3-22. Effect of Differential Leading Edge Flaps on Side Force for the ICE 201 (β=0°). 3-78
Figure 3-23. Effect of Rotation Rate and Differential LEF on Rolling Moment for the ICE 201 (β=0°). 3-79
Figure 3-24. Effect of Rotation Rate and Differential LEF on Yawing Moment for the ICE 201 (β=0°). 3-81
Figure 3-25. Effect of Canard Deflection on Normal Force for the ICE 201 (LEF=30, β=0°). 3-83
Figure 3-26. Effect of Canard Deflection on Static Pitching Moment for the ICE 201 (LEF=30, β=0°). 3-84
Figure 3-27. ICE 201 Nose-Down Control Power (LEF=30, β=0°). 3-85
Figure 3-28. Effect of Canard Deflection on Static Rolling Moment at Zero Sideslip (LEF=30). 3-86
Figure 3-29. Effect of Canard Deflection on ICE 201 Static Lateral Stability (LEF=30, β=+10°). 3-87
Figure 3-30. Effect of LEF Deflection on Roll Increments due to dCanard=-60 (β=+10°). 3-88
Figure 3-31. Effect of Canard Deflection on ICE 201 Static Directional Stability (LEF=30, β=+10°). 3-89
Figure 3-32. Effect of LEF Deflection on Yaw Increments due to dCanard=-60 (β=+10°). 3-90
Figure 3-33. Effect of LEF and Canard Deflections on Rotational Pitching Moment for the ICE 201 (β=0°). 3-91
Figure 3-34. Effect of Canard Deflection on Roll Damping for the ICE 201 (β=0°). 3-93
Figure 3-35. Effect of LEF Deflection on Roll Damping due to dCanard=-60 for the ICE 201 (β=0°). 3-96

Figure 3-36. Effect of LEF Deflection on the Yaw Damping due to dCanard=-60 for the ICE 201 (β=0°). 3-99
Figure 3-37. Pitching Moment due to Left-Side Pitch Flap Deflection on the ICE 201 (LEF=30, β=0°). 3-101
Figure 3-38. Pitching Moment due to Left-Side Elevon Deflections on the ICE 201 (LEF=30, β=0°). 3-102
Figure 3-39. Effect of Left-Side Elevon Deflections on Rolling Moment for the ICE 201 (LEF=30, β=0°). 3-103
Figure 3-40. Yawing Moment due to Left-Side Elevon Deflection on the ICE 201 (LEF=30, β=0°). 3-104
Figure 3-41. Effect of Left-Side Aileron Deflection on Pitching Moment for the ICE 201 (LEF=30, β=0°). 3-105
Figure 3-42. Rolling Moment due to Left-Side Aileron Deflections on the ICE 201 (LEF=30, β=0°). 3-106
Figure 3-43. Yawing Moment due to Left-Side Aileron Deflections on the ICE 201 (LEF=30, β=0°). 3-107
Figure 3-44. Photograph of All Moving Wing Tip Deflected on the ICE 101 Model. 3-108
Figure 3-45. Axial Force due to AMT Deflections on the ICE 201 (LEF=30, β=0°). 3-109
Figure 3-46. Pitching Moment due to AMT Deflections on the ICE 201 (LEF=30, β=0°). 3-110
Figure 3-47. Effect of AMT Deflections on Control Power for the ICE 201 at Zero Sideslip (LEF=30). 3-111
Figure 3-48. Effect of AMT Deflections on Side Force for the ICE 201 (LEF=30, β=0°). 3-113
Figure 3-49. Influence of Sideslip Angle on AMT Control Effectiveness for the ICE 101 (LEF=30). 3-114
Figure 3-50. Effect of AMT Deflection on Rotational Rolling Moment for the ICE 201 (LEF=30, β=0°). 3-116
Figure 3-51. Effect of AMT Deflection on Rotational Yawing Moment for the ICE 201 (LEF=30, β=0°). 3-118
Figure 3-52. Effect of AMT/Aileron Interactions on Rolling Moment for the ICE 201 (LEF=30, β=0°). 3-120
Figure 3-53. Effect of Left-Hand Spoiler Deployment on Rolling Moment for the ICE 201 (LEF=30, β=0°). 3-121
Figure 3-54. Effect of Left-Hand Spoiler Deployment on Yawing Moment for the ICE 201 (LEF=30, β=0°). 3-122
Figure 3-55. Effect of Left-Hand Spoiler on Static Lateral Stability for the ICE 201 (LEF=30). 3-123
Figure 3-56. Effect of Left-Hand Spoiler Deployment on Directional Stability for the ICE 201 (LEF=30). 3-124
Figure 3-57. Effect of Rotation Rate and Left-Hand Spoiler on Rolling Moment for the ICE 201 (LEF=30, β=0°). 3-125
Figure 3-58. Effect of Rotation Rate and Left-Hand Spoiler on Yawing Moment for the ICE 201 (LEF=30). 3-127
Figure 3-59. Effect of Right-Hand SSD on Rolling Moment for the ICE 201 (LEF=30). 3-129
Figure 3-60. Effect of SSD on ICE 201 Lateral Stability (LEF=30, β=+10°). 3-130
Figure 3-61. Yawing Moment due to SSD Deployment on the ICE 201 at Zero Sideslip (LEF=30). 3-131
Figure 3-62. Effect of Left-Hand SSD on Directional Stability for the ICE 201 (LEF=30, β=+10°). 3-132
Figure 3-63. Effects of Spoiler or SSD on Rotational Rolling Moment for the ICE 201 (LEF=30, β=0°). 3-133
Figure 3-64. Effects of Spoiler or SSD on Rotational Rolling Moment for the ICE 201 (LEF=30, β=0°). 3-136
Figure 3-65. Effect of Canard/SSD Interactions on Rolling Moment for the ICE 201 (LEF=30, β=0°). 3-138
Figure 3-66. Effect of SSD/Elevon Interactions on Rolling Moment for the ICE 201 (LEF=30, β=0°). 3-139
Figure 3-67. Effect of SSD/Elevon Interactions on Pitching Moment for the ICE 201 (LEF=30, β=0°). 3-140
Figure 3-68. Effect of SSD/Elevon Interactions on Yawing Moment for the ICE 201 (LEF=30, β=0°). 3-141
Figure 3-69. Effect of SSD/Aileron Interactions on Rolling Moment for the ICE 201 (LEF=30, β=0°). 3-142
Figure 3-70. Lift Coefficient for the ICE 101 at Zero Sideslip (LEF=0). 3-143
Figure 3-71. Static Pitching Moment for the ICE 101 at Zero and Nonzero Sideslip Angles (LEF=0). 3-144
Figure 3-72. Effect of Rotation Rate and Sideslip Angle on Pitching Moment for the ICE 101 (LEF=0). 3-145
Figure 3-73. Effect of Sideslip Angle on the Static Rolling Moment Characteristics for the ICE 101 (LEF=0). 3-147
Figure 3-74. Effect of Rotation Rate and Sideslip Angle on the Rolling Moment for the ICE 101 (LEF=0). 3-148
Figure 3-75. Effect of Sideslip Angle on Static Yawing Moment Characteristics for the ICE 101 (LEF=0). 3-151
Figure 3-76. Effect of Rotation Rate and Sideslip Angle on Yawing Moment for the ICE 101 (LEF=0). 3-152
Figure 3-77. Effect of Leading Edge Flap Deflection on the Lift Coefficient for the ICE 101 (β=0°). 3-155
Figure 3-78. Effect of Leading Edge Flap Deflection on the Static Pitching Moment for the ICE 101 at β=0°. 3-156
Figure 3-79. Effect of Rotation Rate and LEF Deflection on the Yawing Moment for the ICE 101 (β=0°). 3-157
Figure 3-80. Effect of Differential LEF on Static Yawing Moment for the ICE 101 (β=0°). 3-159
Figure 3-81. Effect of Pitch Flap Deflections on Normal Force for the ICE 101 (LEF=30, β=0°). 3-160
Figure 3-82. Pitching Moment due to Right-Hand Pitch Flap Deflections on the ICE 101 (LEF=30, β=0°). 3-161
Figure 3-83. Pitching Moment due to Right-Hand Elevon Deflections on the ICE 101 (LEF=30, β=0°). 3-162
Figure 3-84. ICE 101 Maximum Nose Down Control Power for LEF=30. 3-163
Figure 3-85. Rolling Moment due to Right-Hand Elevon Deflections on the ICE 101 (LEF=30, β=0°). 3-164
Figure 3-86. Yawing Moment due to Right-Hand Elevon Deflections on the ICE 101 (LEF=30, β=0°). 3-165
Figure 3-87. Axial Force due to AMT Deflection on the ICE 101 (LEF=30, β=0°). 3-166
Figure 3-88. Side Force due to AMT Deflection on the ICE 101 (LEF=30, β=0°). 3-167
Figure 3-89. Effect of AMT Deflections on Yawing Moment for the ICE 101 (LEF=30, β=0°). 3-168
Figure 3-90. Effect of AMT Deflections on Rolling Moment for the ICE 101 (LEF=30, β=0°). 3-169
Figure 3-91. Effect of Sideslip on AMT Yaw Effectiveness for the ICE 101 (LEF=30, AMT=0/60). 3-170

Figure 3-92. Effect of Sideslip on AMT Roll Effectiveness for the ICE 101 (LEF=30, AMT=0/60). 3-171
Figure 3-93. Effect of AMT/LEF Interactions on Rolling Moment for the ICE 101 (β=0°). 3-172
Figure 3-94. Effect of AMT/LEF Interactions on Yawing Moment for the ICE 101 (β=0°). 3-173
Figure 3-95. Effect of Rotation Rate and AMT Deflections on Rolling Moment for the ICE 101 (LEF=30, β=0°). 3-174
Figure 3-96. Effect of Rotation Rate and AMT Deflections on Yawing Moment for the ICE 101 (LEF=30, β=0°). 3-177
Figure 3-97. Rolling Moment due to Left-Hand Spoiler Deployment on the ICE 101 (LEF=30, β=0°). 3-180
Figure 3-98. Yawing Moment due to Left-Hand Spoiler Deployment on the ICE 101 (LEF=30, β=0°). 3-181
Figure 3-99. Effect of Left-Hand Spoiler on Lateral Stability for the ICE 101 (LEF=30). 3-182
Figure 3-100. Effect of Left-Hand Spoiler on Directional Stability for the ICE 101 (LEF=30). 3-183
Figure 3-101. Effect of Rotation Rate and Left-Hand Spoiler on Rolling Moment for the ICE 101 (LEF=30, β=0°). 3-184
Figure 3-102. Pitching Moment due to Right-Hand SSD on the ICE 101 (LEF=30, β=0°). 3-186
Figure 3-103. Effect of Right-Hand SSD on Rolling Moment for the ICE 101 (LEF=30, β=0°). 3-188
Figure 3-104. Effect of Right-Hand SSD on Yawing Moment for the ICE 101 (LEF=30, β=0°). 3-189
Figure 3-105. Effect of Right-Hand SSD on Side Force for the ICE 101 (LEF=30, β=0°). 3-190
Figure 3-106. Effect of Rotation Rate and Right-Hand SSD on Rolling Moment for the ICE 101 (LEF=30, β=0°). 3-191
Figure 3-107. Effect of Rotation Rate and Right-Hand SSD on Yawing Moment for the ICE 101 (LEF=30, β=0°). 3-194
Figure 3-108. Effect of SSD/Elevon Interactions on Rolling Moment for the ICE 101 (LEF=30, β=0°). 3-197
Figure 3-109. Effect of SSD/Elevon Interactions on Pitching Moment for the ICE 101 (LEF=30, β=0°). 3-198
Figure 3-110. Effect of SSD/Elevon Interactions on Yawing Moment for the ICE 101 (LEF=30, β=0°). 3-199
Figure 4-1: 1/18th Scale LMTAS Tailless Fighter Wind Tunnel Model 4-12
Figure 4-2: Assembly Drawing of New Wing Constructed for ICE SARL Test 4-13
Figure 4-3: Various SSD Configurations Run During the SARL Test 4-14
Figure 4-4: AMT Geometry 4-14
Figure 4-5: Comparison of ADF, LAMP and High-Speed Wind Tunnel Model Controls Geometry 4-15
Figure 4-6: Longitudinal Data Tie-in with 1994 Test 4-16
Figure 4-7: Lateral-Directional Data Tie-in with 1994 Test 4-17
Figure 4-8: Longitudinal Data Tie-in Between New and Old Wings 4-18
Figure 4-9: Lateral-Directional Data Tie-in Between New and Old Wings 4-19
Figure 4-10: Pitching Moment Shift can be Explained by Presence of Actuator Fairings 4-20
Figure 4-11: Straight and Skewed AMT Control Effectiveness 4-21
Figure 4-12: Axial Force Changes with AMT Deflection 4-22
Figure 4-13: Deflected AMT Installed on the High Speed Model at SARL 4-23
Figure 4-14: Sideslip Effects on Straight AMT Control Power 4-24
Figure 4-15: Sideslip Effects on Skewed AMT Control Power 4-25
Figure 4-16: Skewed AMT Interaction with -30 deg Elevon 4-26
Figure 4-17: Skewed AMT Interaction with 30 deg Elevon 4-27
Figure 4-18: LEF Interaction with Skewed AMT = 30 deg 4-28
Figure 4-19: LEF Interaction with Skewed AMT = 60 deg 4-29
Figure 4-20: Outboard SSD Control Effectiveness 4-30
Figure 4-21: Summary of Sideslip Effects on Outboard SSD Control Power 4-31
Figure 4-22: Effect of Mach and Reynolds Number Variation on SSD Control Power 4-32
Figure 4-23: Outboard SSD Interaction with -30 deg Elevon 4-33
Figure 4-24: Outboard SSD Interaction with -10 deg Elevon 4-34
Figure 4-25: Outboard SSD Interaction with 10 deg Elevon 4-35
Figure 4-26: Outboard SSD Interaction with 30 deg Elevon 4-36
Figure 4-27: Outboard SSD Interaction with Pitch Flap Effectiveness 4-37
Figure 4-28: Effect of Venting the Spoiler and Deflector 4-38
Figure 4-29: Interaction of Vented SSD with -30 deg Elevon 4-39
Figure 4-30: Effect of Vented SSD with 30 deg Elevon 4-40
Figure 4-31: Effect of Slot Variations on SSD Control Power 4-41
Figure 4-32: Effect of SSD Variations on Elevon = -30 Interaction 4-42
Figure 4-33: Effect of SSD Variations on Elevon = 30 Interaction 4-43
Figure 4-34: Half-Sized SSD 4-44
Figure 4-35: Segmented SSD Control Effectiveness 4-45
Figure 4-36: IB Half SSD Interaction with -30 deg Elevon 4-46
Figure 4-37: IB Half SSD Interaction with -10 deg Elevon 4-47
Figure 4-38: IB Half SSD Interaction with 10 deg Elevon 4-48
Figure 4-39: IB Half SSD Interaction with 30 deg Elevon 4-49
Figure 4-40: Inboard SSD Control Effectiveness 4-50

Figure 4-41: Inboard SSD Interaction with -30 deg Elevon 4-51
Figure 4-42: Inboard SSD Interaction with 30 deg Elevon 4-52
Figure 4-43: Effect of SSD Location on -30 deg Elevon Interaction 4-53
Figure 4-44: Effect of Location on 30 deg Elevon Interaction 4-54
Figure 4-45: IB SSD Interactions with Pitch Flaps 4-55
Figure 4-46: AMT Roll Power Variation with Control Volume (AMT = 60 deg) 4-56
Figure 4-47: AMT Yaw Power Variation with Control Volume (AMT = 60 deg) 4-56
Figure 4-48: SSD Roll Power Variation with Control Volume (SSD = 60 deg) 4-57
Figure 4-49: SSD Yaw Power Variation with Control Volume (SSD = 60 deg) 4-57
Figure 6-1: Example of Control Power Envelope Computed By CPA 6-2
Figure 6-2: Example of Control Power Boundary Data Computed By CPA 6-3
Figure 6-3: Illustration of CPR Software Utilization 6-4
Figure 6-4: Longitudinal Axis Flight Control System Used In CPR 6-5
Figure 6-5 Lateral Axis Flight Control System Used In CPR 6-6
Figure 6-6 Directional Axis Flight Control System Used In CPR 6-6
Figure 6-7: Lateral-Directional Command Mixer Used In CPR 6-7
Figure 6-8: Comparison of SSD Effectiveness on Configuration 101-1 With Phase 1 Predictions 6-9
Figure 6-9: Comparison of AMT Effectiveness on Configuration 101-4 With Phase 1 Predictions 6-10
Figure 6-10: Configuration 101-1 Control Power Available at 300 KCAS/15K for Mil Power and Max A/B 6-13
Figure 6-11: Configuration 101-4 Control Power Available at 300 KCAS/15K for Mil Power and Max A/B 6-14
Figure 6-12: Configuration 101-1 Control Power Available at 108 KCAS/15K With Max A/B 6-15
Figure 6-13: Configuration 101-4 Control Power Available at 108 KCAS/15K With Max A/B 6-16
Figure 6-14: Configuration 101-1 Power Approach Control Power Available 6-17
Figure 6-15: Configuration 101-4 Power Approach Control Power Available 6-18
Figure 6-16: Maximum Coordinated Roll Power for Configurations 101-1 and 101-4 at 150 KCAS/15K 6-20
Figure 6-17: Configuration 101-1 High-AOA Lateral-Directional Departure Characteristics at 150 KCAS/15K 6-21
Figure 6-18: Configuration 101-4 High-AOA Lateral-Directional Departure Characteristics at 150 KCAS/15K 6-22
Figure 6-19: Time History of Configuration 101-1 Roll Performance at 194 KEAS/15K for Two Initial AOAs 6-23
Figure 6-20: Configuration 101 Time-To-Bank 90° at 194 KEAS/15K and FWV Roll Agility Metric 6-24
Figure 6-21: Comparison of Configuration 101-1 Lateral-Directional Flying Qualities With Phase 1 Results 6-26
Figure 6-22: Comparison of Configuration 101-4 Lateral-Directional Flying Qualities With Phase 1 Results 6-27
Figure 6-23: Comparison of Configuration 101 Roll Performance Predictions With Phase 1 Results 6-28
Figure 6-24: Comparison of SSD Effectiveness on Configuration 201-1 With Phase 1 Predictions 6-29
Figure 6-25: Comparison of AMT Effectiveness on Configuration 201-4 With Phase 1 Predictions 6-31
Figure 6-26: Configuration 201-1 Control Power Available at 300 KCAS/15K for Mil Power and Max A/B 6-33
Figure 6-27: Configuration 201-4 Control Power Available at 300 KCAS/15K for Mil Power and Max A/B 6-34
Figure 6-28: Configuration 201-1 Control Power Available at 108 KCAS/15K With Max A/B 6-35
Figure 6-29: Configuration 201-4 Control Power Available at 108 KCAS/15K With Max A/B 6-36
Figure 6-30: Maximum Coordinated Roll Power for Configurations 201-1 and 201-4 at 150 KCAS/15K 6-38
Figure 6-31: Configuration 201-1 High-AOA Lateral-Directional Departure Characteristics at 150 KCAS/15K 6-39
Figure 6-32: Configuration 201-4 High-AOA Lateral-Directional Departure Characteristics at 150 KCAS/15K 6-40
Figure 6-33: Comparison of Configurations 201-1 and 201-4 Roll Performance at 194 KCAS/15K 6-41
Figure 6-34: Configuration 201-Series Time-To-Bank 90° at 194 KEAS/15K and FWV Roll Agility Metric 6-41
Figure 6-35: Configuration 201 Power Approach Trim Conditions 6-45
Figure 6-36: Comparison of Configuration 201-1 PA Control Power Available With Phase 1 Results 6-46
Figure 6-37: Comparison of Configuration 201-1 Power Approach Roll Performance With Phase 1 Results 6-47
Figure 6-38: Comparison of Configuration 201-4 PA Control Power Available With Phase 1 Results 6-48
Figure 6-39: Comparison of Configuration 201-4 Power Approach Roll Performance With Phase 1 Results 6-49
Figure 6-40: Comparison of Configuration 201-1 Lateral-Directional Flying Qualities With Phase 1 Results 6-50
Figure 6-41: Comparison of Configuration 201-4 Lateral-Directional Flying Qualities With Phase 1 Results 6-51
Figure 6-42: Comparison of Configuration 201 Roll Performance Predictions With Phase 1 Results 6-52

List of Tables

Table 2-1: C-1.1-.55A Balance Data 2-2
Table 2-2: ICE Phase II ADF Test Conditions 2-2
Table 2-3: Control Surface Deflection Conventions 2-3
Table 2-4: Spoiler-Slot-Deflector Geometry Descriptions on Configuration 101 2-4
Table 2-5: All-Moving Tip Geometry Descriptions on Configuration 101 2-4
Table 2-6: All-Moving Tip Geometry Description on Configuration 201 2-5
Table 2-7: Spoiler-Slot-Deflector Geometry Description on Configuration 201 2-5
Table 3-1: Dimensional Characteristics of the Full-Scale ICE 201 3-19
Table 3-2: Dimensional Characteristics of the Full-Scale ICE 101 3-20
Table 3-3: Rotary Balance Run Schedule for the ICE 201 Configuration 3-21
Table 3-4: Rotary Balance Run Schedule for the ICE 101 Configuration 3-31
Table 3-5: Mass Properties Data for the ICE Configurations 3-41
Table 3-6: Predicted Spin Modes for the ICE 201 3-42
Table 3-7: Predicted Spin Modes for the ICE 101 3-44
Table 4-1: Description of Possible SSD Combinations on the ICE High-Speed Model 4-2
Table 4-2: All Moving Wing Tip Geometric Paramters 4-3
Table 4-3: SARL Test Model Reference Geometry 4-4
Table 4-4: High Speed Model Control Surface Deflection Convention 4-5
Table 4-5: 1996 ICE SARL Run Log 4-6
Table 5-1: Configuration 101-Series Simulation Database Description 5-3
Table 5-2: Configuration 201-Series Simulation Database Description 5-6
Table 6-1: Configuration 101-Series Roll Performance Summary 6-25
Table 6-2: Configuration 201-Series Up & Away Roll Performance Summary 6-42
Table 6-3: Effect of Power Setting on PA Roll Performance 6-44

Nomenclature

Symbol	*Definition*	*Units*
ADF	Aerodynamic Development Facility, Low-Speed Wind Tunnel at LMTAS	---
AMT	All Moving Wing Tip	---
AOA, α	Angle-of-Attack	deg
AOS, Beta, β	Angle-of-Sideslip	deg
$\dot{\beta}$	Sideslip Rate	deg/sec
b	Reference Span	ft
BAR	Bihrle Applied Research	---
$\bar{c}$, MAC	Mean Aerodynamic Chord	inches
C_A	Axial Force Coefficient	---
CAP	Longitudinal Control Anticipation Parameter	
C_D	Drag Coefficient	---
CFD	Computational Fluid Dynamics	---
CG	Center of Gravity	% MAC
C_l	Rolling Moment Coefficient	---
C_L	Lift Coefficient	---
C_{lr}	Rolling Moment due to Yaw Rate Stability Derivative	1/rad
$C'_{l_{max}}$	Maximum Coordinated Roll Control Power Coefficient	---
C_{l_β}	Lateral Stability Derivative Coefficient	---
C_m	Pitching Moment Coefficient	---
C_N	Normal Force Coefficient	---

Symbol	*Definition*	*Units*
C_n	Yawing Moment Coefficient	---
$C_{n\beta}$	Yawing Moment due to Sideslip	1/deg
C_{np}	Yawing Moment due to Roll Rate Stability Derivative	1/rad
$C_{n\beta_{DYN}}$ *Augmented*	Lateral-Directional Departure Parameter Augmented with Control Power	---
CPA	Control Power Available Software Tool	---
CPR	Control Power Required Software Tool	---
C_Y	Side Force Coefficient	---
δ	Control Surface Deflection	deg
DLEF	Differential Leading Edge Flap	---
ϕ	Bank Angle	deg
FCS	Flight Control System	---
FS	Fuselage Station	inches
FSLEMAC	Fuselage Station Location of the Leading Edge of the MAC	inches
FWV	Fixed Wing Vehicle	---
h	Altitude	ft
IB	Inboard	---
ICE	Innovative Control Effectors Program	---
IR&D	Independent Research & Development	---
I_{XX}	Roll Moment of Inertia	sl-ft^2
I_{XZ}	Cross Product of Inertia	sl-ft^2
I_{YY}	Pitch Moment of Inertia	sl-ft^2

Symbol	*Definition*	*Units*
I_{ZZ}	Yaw Moment of Inertia	sl-ft^2
KCAS	Knots Calibrated Airspeed	Knots
KEAS	Knots Equivalent Airspeed	Knots
KTAS	Knots True Airspeed	Knots
LAMP	Large Amplitude Multi-Purpose Vertical Wind Tunnel in Neuberg a.d. Donau, Germany	---
LaRC	NASA Langley Research Center, Hampton, VA	---
LED	Leading Edge Down	---
LEF	Leading Edge Flap	---
LMTAS	Lockheed Martin Tactical Aircraft Systems, Fort Worth, TX	---
LO	Low Observable	---
M	Mach Number	---
MATV	Multi Axis Thrust Vectoring	---
MRC	Moment Reference Center	%MAC
NAWCAD	Naval Air Warfare Center Aircraft Division, Patuxent River, MD	---
N_Z	Normal Acceleration at the CG	g's
OB	Outboard	---
p	Roll Rate	deg/sec
PA	Power Approach Flight Phase	---
PG1-PG6	Longitudinal FCS Gains	Various
PSTK	Pitch Stick Command	lbs
PTRIMC	Pitch Trim Command	deg
$\bar{q}$	Dynamic Pressure	lb/ft^2
$\dot{q}$	Pitch Acceleration	rad/sec^2

Symbol	*Definition*	*Units*
q	Pitch Rate	deg/sec
r	Yaw Rate	deg/sec
RAM	Roll Agility Metric	---
RCS	Radar Cross Section	---
RG1 - RG4	Lateral FCS Gains	Various
R_N	Reynolds Number	1/ft
RSTK	Roll Stick Command	lbs
RTRIMC	Roll Trim Command	deg
S	Reference Wing Area	ft^2
SARL	Subsonic Aerodynamic Research Laboratory, Subsonic Wind Tunnel at WPAFB, OH	---
SSD	Spoiler-Slot-Deflector	---
τ_r	Closed Loop Roll Mode Time Constant	sec
τ_a	Actuator Time Constant	sec
TED	Trailing Edge Down	---
TEU	Trailing Edge Up	---
UA	Up and Away Flight Phase	---
$\overline{V}$	Control Volume Ratio	---
V	Velocity	ft/sec
ω_{sp}	Closed Loop Short Period Frequency	rad/sec
$\Omega b/2V$	Non-dimensional Rotation Rate	---
WL	Wright Laboratory or Waterline Location	---
WOD	Wind Over Deck	Knots
WPAFB	Wright-Patterson Air Force Base, Ohio	---

Symbol	*Definition*	*Units*
X	Longitudinal Dimension	inches
2y/b	Span Station	---
Y	Lateral Dimension	inches
YG1 - YG6	Directional FCS Gains	Various
ζ_{sp}	Closed Loop Short Period Damping Ratio	---
Z	Vertical Dimension	inches

Subscripts

a	Aileron	---
AMT	All Moving Tip	---
c	Canard	---
D	Dive	---
e	Elevon	---
LEF	Leading Edge Flap	---
o	Initial Condition	---
pf	Pitch Flap	---
s	Stability Axis	---
sp	Spoiler	---
SSD	Spoiler-Slot-Deflector	---
wind	Wind Axis	---

Foreword

The Innovative Control Effectors (ICE) program was sponsored jointly by Wright Laboratory (WL/FIGC) at Wright-Patterson AFB, Ohio and the Naval Air Warfare Center Aircraft Division (NAWCAD) located in Warminster, Pennsylvania. The USAF program manager and technical monitor was Mr. Bill Gillard. The Navy program manager and technical monitor was Mr. Steve Hynes. The ICE program was a two-phase effort performed under USAF contract number F33615-94-C-3610 between September 1994 and July 1997. The current phase (Phase 2) began in March 1996. The prime contractor was Lockheed Martin Tactical Aircraft Systems (LMTAS) located in Fort Worth, Texas. Bihrle Applied Research (BAR) in Hampton, Virginia was subcontracted to perform the rotary balance testing and analysis. The LMTAS program manager was Mr. Ken Dorsett. Many people contributed their time and talents towards the completion of this effort. A few of the major contributors are listed below. This effort would not have been possible without their help.

- ADF wind tunnel models: the LMTAS engineering display model shop – Tom Blakeney, Doug Thompson, Phil Dougherty, and Don Downing.
- ADF and rotary balance wind-tunnel model drawings: Derek Bye.
- ADF test support: Rob Burchak, Eric Dean, Wink Baker, Bill Gillard (WL/FIGC), and Steve Hynes (NAWCAD).
- High-speed wind-tunnel model design and construction: Nelson Lehman, Fernando Meza, Don Morbitzer, Bob Solomon, and a host of talented model technicians.
- Rotary balance testing and analysis: Heather Houlden (BAR), Stefan Klock (BAR), and Bill Gillard (WL/FIGC).
- SARL test support: Wink Baker, Tom Tighe (WL/FIMO), Joe Martin (WL/FIMO), Bill Gillard (WL/FIGC), and the crew of the SARL wind tunnel.
- Stability and Control Analysis: Ken Dorsett and Scott Fears.

Summary

The Innovative Control Effectors (ICE) program was a two-phased effort that was jointly sponsored by the Air Force's Wright Laboratory (WL/FIGC) and the Naval Air Warfare Center Aircraft Division (NAWCAD). Technical work was performed by Lockheed Martin Tactical Aircraft Systems (LMTAS) in Fort Worth, Texas and Bihrle Applied Research (BAR) in Hampton, Virginia. The primary objectives of the ICE program were to identify and to quantify the stability and control, performance, and integration impacts of control concepts that would be useful on tailless or low-observable fighter aircraft which were also intended to be highly maneuverable. Two tailless fighter configurations were used as the focus of these studies: a land-based flying wing with a leading-edge sweep of 65° and a carrier-based concept with a canard-delta wing configuration. During Phase 1 of this research, numerous control concepts were evaluated on both types of aircraft, and this portion of the program is documented in WL-TR-96-3043. Based on these results, the all-moving wing tip (AMT) and spoiler-slot-deflector (SSD) concepts were identified for further study during Phase 2 because of their good aerodynamic effectiveness and less severe integration impacts.

One of the primary purposes of ICE Phase 2 was to expand the experimental database describing the capabilities of the AMT and the SSD. Three wind-tunnel tests were conducted: (1) a small-scale screening entry in the LMTAS 2'x3' Aerodynamic Development Facility (ADF); (2) a rotary balance test at the BAR 10' Large Amplitude Multi-Purpose (LAMP) vertical wind tunnel in Neuberg a.d. Donau, Germany; and (3) a low-speed test in the WL Subsonic Aerodynamic Research Laboratory (SARL) 7'x10' wind tunnel at Wright Patterson Air Force Base (WPAFB) in Dayton, Ohio. When considered together, the data from these tests covered an angle-of-attack (AOA) range of -3° to 90°, a sideslip (β) range of ±30°, and non-dimensional rotation rates ($\Omega b/2V$) between ±0.3. These tests investigated the effects of variations in control effector geometry (i.e., size, location, etc.) and the effects of sideslip and rotation rate on AMT and SSD control power. Additionally, aerodynamic interactions between either the AMTs or the SSDs and the other closely located control surfaces were obtained to improve the fidelity of the aerodynamic math model.

Three AMT variations were tested that included small and large unskewed tips with chordwise hingelines and a third skewed tip with a swept hinge line. On the skewed tip, the pivot trunion was swept aft such that the AMT-wing break was aligned with the opposite leading edge on the land-based configuration (25° hingeline sweep) or the opposite wing-fold line (10° hingeline sweep) on the carrier-based configuration. Skewing the pivot trunion aft improved AMT control effectiveness because favorable side forces were generated when the control surface was deflected trailing-edge down. These side forces acted aft of the aircraft center-of-gravity and thereby increased AMT yaw effectiveness by combining with the yawing-moment increments produced by the drag forces on the device. On the land-based configuration, the skewed AMT generated 25% to 30% more yawing moment per unit of control surface area than the unskewed AMT over a large AOA range, which meant that a smaller surface could be used to obtain the same level of control power. AMT deflection generated yaw control power throughout the AOA range that was tested, and favorable rolling- and pitching-moment increments were produced for most of these AOAs. AMT yaw effectiveness was not significantly affected by either sideslip or rotation rate, which is a highly desirable trait. AMT deflections provided sufficient control authority for spin recovery when deployed against the direction of rotation. Based on these results, the AMT was judged to be the best overall effector of all the concepts investigated during the ICE program for full-envelope operation of a highly maneuverable tailless fighter.

Variations in SSD location were tested, and the best place was determined to be as far outboard and as far forward of the hingeline of the trailing-edge control surfaces as possible. This location maximized the yaw control power produced by the SSDs and minimized the aerodynamic interaction between SSD deflection and the effectiveness of any trailing-edge control surfaces mounted downstream of the SSD. To further enhance SSD control effectiveness, the "slot" through the wing between the spoiler and the deflector should be as large as the control surfaces themselves. Models of internal wing structure were simulated in the slot, and they were found to have minimal effect on SSD effectiveness. SSD deflection produced higher yawing

moments at low AOAs than AMT deflection, but the AMTs were more effective at the higher AOAs. Similar to the AMTs, SSD effectiveness was relatively unaffected by sideslip or rotation rate, and SSD deflection provided sufficient control authority for spin recovery when deployed against the direction of rotation.

The second primary task performed during ICE Phase 2 was to conduct flying qualities analysis of both the land-based and carrier-based configurations when using either SSDs or AMTs as the primary yaw controller. To accomplish this objective, the new wind-tunnel data were used to construct updated simulation databases which were input into existing LMTAS simulation tools. When using aerodynamic control power alone, all the designs possessed sufficient control power for roll coordination and lateral-directional stability augmentation throughout the AOA range investigated with the exception of the land-based configuration that used SSDs for yaw control. This aircraft ran out of augmenting directional control power for AOAs above 30°. When using both aerodynamic control power and multi-axis thrust vectoring together, all the designs had substantially higher and essentially unlimited maneuvering potential. During Phase 1, the roll performance at various flight conditions was predicted using the aerodynamic data available at that time, and somewhat ambitious goals for maximum roll performance were established for these same flight conditions. Due primarily to better than predicted yaw- and roll-control effectiveness, each of the configurations met or exceeded the Phase 1 roll performance predictions, and the carrier-based designs achieved the Phase 1 goals. The land-based configurations achieved most of the roll performance goals but fell short of the 30 deg AOA roll performance goal. These results were attributed to the fact that the carrier-based control power required values were set by carrier suitability considerations (notably, power approach roll performance), whereas the land-based configurations control power sizing conditions were more balanced across the flight conditions that were investigated. The carrier-based configurations nearly achieved the Level 1 bank angle change requirement for power approach, but additional roll control power will be needed to meet this specification. All four configurations manifested values of the fixed wing vehicle (FWV) roll agility metric that were 30% to 40% larger than those for the highly agile F-16 MATV aircraft.

The following topics are recommended for future research efforts: (1) collection of transonic wind-tunnel data to validate the control effectiveness at the higher speeds, (2) evaluation of the hinge moments on the SSDs and AMTs to refine subsystem requirements by using either wind-tunnel data or computational methods, (3) determination of the aeroelastic effects on AMT and SSD control power by using computational structural modeling, and (4) RCS testing and analysis to evaluate the effects of actuation details on the aircraft's signature. These results are required to refine the structural, subsystem, signature, and flight control system (FCS) integration details needed to construct a flight vehicle. If performed, these follow-on studies could culminate in a flight demonstration of these effectors on a supersonic tailless aircraft. Several choices exist for performing this flight test. These options include building an unmanned flight demonstrator, modifying the NASA F-16XL (e.g., remove vertical tail, modify outboard aileron area, and formulate new FCS), or constructing new wings for either an F-16 or the F-16XL that incorporate SSDs and/or AMTs.

1 Introduction

To achieve increased survivability in the current and future air combat environments, most new aircraft designs incorporate some degree of low-observable (LO) technology. One of the primary ways to reduce the observability of an aircraft is to decrease its radar cross section (RCS). Low-radar-cross-section design practices manifest themselves in the form of external shaping, elimination of vertical control surfaces, and alignment of control surface edges with fixed airframe edges. The application of these LO technologies to high performance aircraft has added new constraints to the design process for this type of vehicle. As a result, aircraft designed for low RCS may require new control concepts to achieve the required maneuvering capability and tactical utility throughout the flight envelope while simultaneously satisfying the low-RCS shaping specifications.

Additionally, new benchmarks for fighter maneuverability have been demonstrated with the emergence of the YF-22, Su-27/Su-35 and the F-16 multi-axis thrust vectoring (MATV) aircraft. Piloted simulation studies have shown that the high angle-of-attack (AOA) or post-stall maneuvering capabilities of these aircraft can yield significant benefits during low-speed close-in air combat [Doane, 1990]. If this capability is to be included within a low-RCS design, trying to satisfy both the low-signature and the high agility requirements results in pushing the target design space further into the far corner of the technology envelope (Figure 1-1). In summary, the combination of signature-related geometry considerations and higher standards for maneuverability is driving the need for new and innovative control concepts for tactical aircraft.

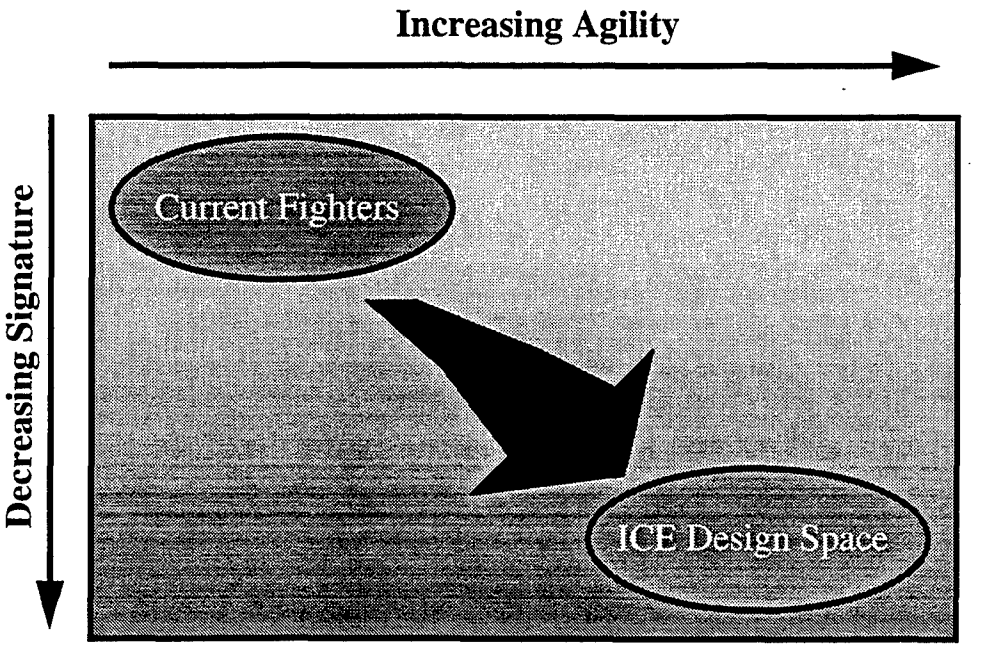

Figure 1-1: Effect of Desire For High-AOA Agility and Low Observability On Technology Development Envelope

In addition to aerodynamic design, these unique control concepts also offer challenges with respect to flight control system integration. Control suites for low-RCS aircraft often exhibit a high degree of coupling about all three axes (pitch, roll and yaw), and the individual control surfaces may interact aerodynamically to introduce complex nonlinearities into the problem of control allocation. It is also typical for tailless fighters to exhibit relaxed static stability in both the pitch and the yaw axes, which requires prioritization of

control power to the appropriate axes to retain control under conditions when surface rate or deflection limits may be reached. As a result, tailless fighters typically have more highly coupled, interactive control suites than their predecessors that require unique approaches to control power integration and allocation.

1.1 Background

The Innovative Control Effectors (ICE) program was conceived in 1993 to investigate the capabilities of new and original methods for stabilizing and/or controlling high performance fighters whose design has the potential for all-aspect reduced observability. The program was jointly sponsored by both the Air Force's Wright Laboratory (WL/FIGC) and the Naval Air Warfare Center (NAWC). The following tasks were previously accomplished during the 18-month Phase I segment of the ICE program: (1) selection of a baseline vehicle and the associated innovative control concept(s) to be evaluated, (2) investigation of the performance of each control effector concept, (3) assessment of the integration impacts of each concept, (4) development of a risk reduction plan for implementing the control concepts, and (5) documentation of the study.

1.1.1 Baseline Configurations

During Phase 1, two single-engine, multi-role fighter aircraft baselines were studied. Each vehicle incorporated internal or low-observable weapons carriage for reduced RCS. An all-wing tailless concept that employed a 65°-sweep delta wing was used for the USAF land-based configuration (Figure 1-2). To better provide for the low-speed control required during carrier landings, a canard-delta planform with a 42° leading-edge sweep angle was chosen for the Navy baseline (Figure 1-3).

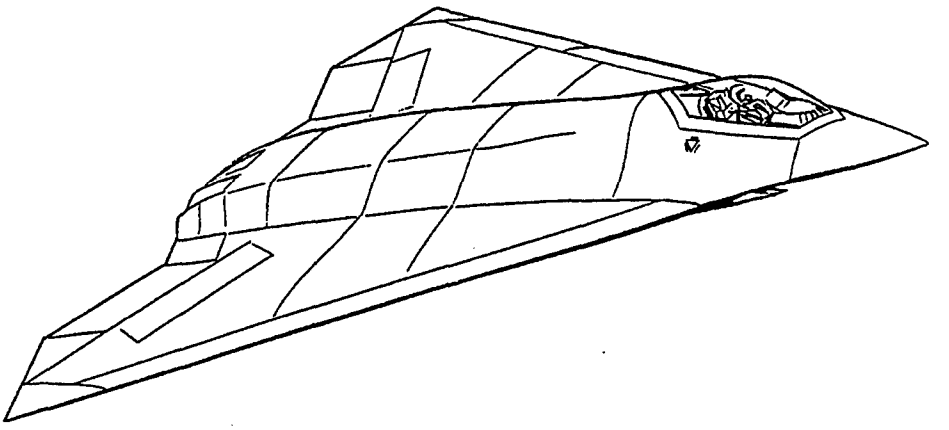

Figure 1-2: Land-Based Baseline Configuration (101-Series)

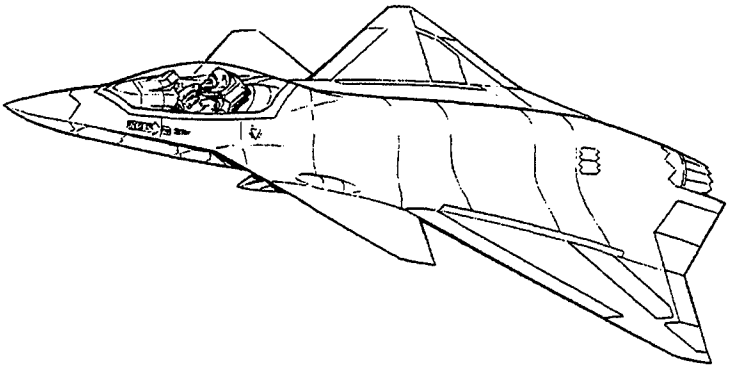

Figure 1-3: Carrier-Based Baseline Configuration (201-Series)

1.1.2 Previously Studied Control Suites

Six control suites, 3 each for the land-based and carrier-based airplanes, were studied in detail during Phase 1 of the ICE program. The lateral-directional control surfaces used within these suites consisted of various combinations of spoilers, spoiler slot deflectors, deployable rudders, symmetric and differential leading-edge flaps, and all-moving wing tips. Pitch control was provided by elevons and pitch flaps on all the designs, and each configuration had both pitch and yaw thrust vectoring. Based on a combination of their aerodynamic performance and integration impacts, the lateral-directional control concepts of all-moving wing tips (AMT), spoiler-slot-deflectors (SSD), and differential leading-edge flap deflections (DLEF) were identified during Phase 1 to yield the highest payoffs and therefore to be the most desirable for further investigation (Figure 1-4). These control concepts offered the best control effectiveness up to high AOAs and the lightest overall weight when integrated into a tailless vehicle [Dorsett & Mehl, 1996]. Both the SSDs and the AMTs produced some degree of control effectiveness throughout the AOA range investigated, but the effectiveness generated by DLEF was primarily confined to high AOAs. In addition, the F-22 is utilizing DLEF for high-AOA roll coordination, and data on DLEF effectiveness could therefore be obtained from this project. For these reasons, it was decided to focus on the AMT and SSD during Phase 2 of the ICE program. Figure 1-5 shows plan view sketches of the resulting control suites, and descriptions of each configuration are included below.

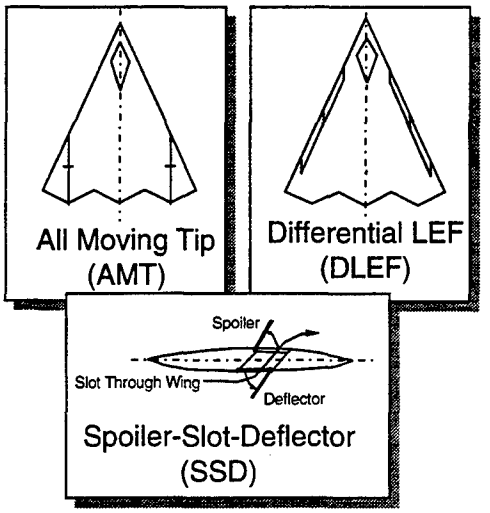

Figure 1-4: Phase 1 Control Concepts Selected For Further Investigation During Phase 2

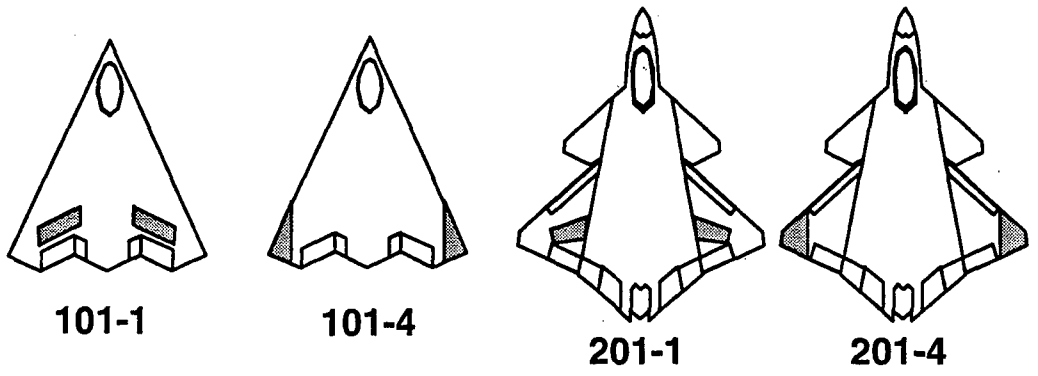

Figure 1-5: Four Control Suites Studied During ICE Phase 2

1.1.3 Land-Based Configurations: 101-1 and 101-4

The baseline configuration for both of the land-based designs studied during Phase 2 was the flying wing illustrated in Figure 1-2. Configuration 101-1 used SSDs for both roll and yaw control. SSD deployment generates yawing moments through differential drag. Due primarily to the spoiler component of the device, large rolling moments are also produced by SSD deflections. When implemented on an actual aircraft, the upper spoiler and lower surface deflector would be mechanically linked to provide aerodynamic balance and thereby reduce the hinge moments, and therefore a single actuator could most likely drive both surfaces. Configuration 101-4 used AMTs as its primary yaw control instead of SSDs. The AMT deploys trailing-edge down to generate yawing moments through differential drag at the wing tip. Both configurations incorporated elevons for pitch and roll control, pitch flaps for supplemental pitch control, and an MATV nozzle for additional low-speed pitch and yaw control.

1.1.4 Carrier-Based Configurations: 201-1 and 201-4

The baseline configuration for both of the carrier-based designs studied during Phase 2 was the canard-delta planform shown in Figure 1-3. Similar to the land-based designs, Configuration 201-1 employed SSDs as its primary yaw control device, and Configuration 201-4 used AMTs. Both configurations utilized canard and pitch flap deflections for pitch control, elevons and ailerons for roll and pitch, and an MATV nozzle for pitch and yaw. Symmetric leading-edge flap deflections (LEF) were scheduled to vary the wing camber with AOA and thereby provide increased lift and improved directional stability at the higher AOAs.

1.1.5 Phase 1 Recommendations

The following recommendations for follow-on work were formulated at the completion of the Phase 1 analysis.

- Conduct rotary balance wind-tunnel testing to determine the effects of steady rotation on the effectiveness of the control concepts. Evaluate the propensity for departures and spins and the control power available for departure and spin recovery.

- Determine the optimum SSD orientation and geometry that maximizes its lateral-directional control power while concurrently minimizing its impact on the effectiveness of the downstream trailing-edge control surfaces.

- Evaluate geometry and orientation changes that maximize the control effectiveness for the AMT.

- Evaluate the effects of sideslip on both the SSD and AMT control effectors.
- Determine the effects of blockage (e.g., internal structure) within the slot of the SSD on SSD performance.
- Acquire transonic wind tunnel data for both the AMT and SSD to validate the predictions made during Phase 1 of the ICE effort.

1.2 Phase 2 Program Content

Based on the recommendations from Phase 1, the following tasks were selected to comprise Phase 2 of the ICE program: 1) conduct additional wind-tunnel tests to increase the scope and the fidelity of the aerodynamic database, 2) construct new wind-tunnel models or modify existing models as needed, 3) analyze the wind-tunnel data to obtain updated assessments of the control concept effectiveness and to ascertain the validity of the Phase 1 predictions, 4) perform simulation analysis using LMTAS software tools to evaluate the flying qualities of the resulting configurations, and 5) document the results (Figure 1-6). An optional transonic wind-tunnel test was proposed, but this task was not completed due to funding limitations.

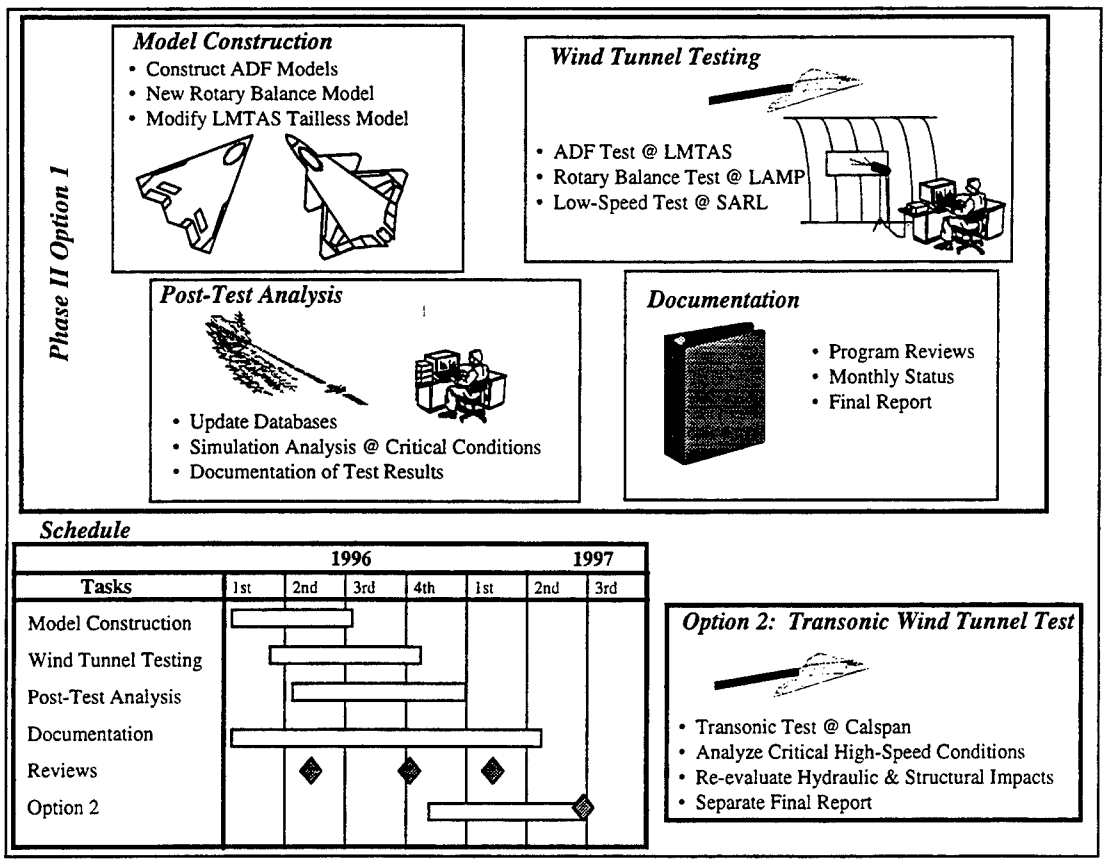

Figure 1-6: Diagram Outlining Tasks Performed During Phase 2 of ICE Program

This report is laid out in eight chapters. Chapters 2 through 4 cover the three wind tunnel tests conducted during Phase 2. Each of these three chapters was originally written as a stand-alone wind tunnel test report. As a result, all information regarding each test, including summary and introductory information as well as test conclusions are included.

1.2.1 ADF Wind-Tunnel Test

Three wind-tunnel tests were completed during ICE Phase 2. The first test was performed in the LMTAS Aerodynamic Development Facility (ADF), which has a 2'x3' test section. For this test, two 1/40th-scale models were constructed that represented the land-based (101) and carrier-based (201) configurations (Figure 1-7). The primary purpose of the test was to screen a range of SSD and AMT concepts at a low-cost facility to determine which concepts should be tested on larger scale models. A secondary goal was to enhance the aerodynamic database for Configuration 201 on which only limited testing was performed during Phase 1. Parametric studies in the arrangement of the various control effectors were performed to optimize the concepts. The variations in SSD design that were tested included spanwise location differences, chordwise position changes, and size modifications. The AMT configurations that were tested included two sizes that had the pivot trunion oriented normal to a buttline and a third skewed tip that had the pivot trunion swept aft. In addition, upwards and downwards Gurney flaps and a fillet were tested in conjunction with the larger, unskewed AMT in attempts to improve its roll-to-yaw characteristics. The following aerodynamic interactions between closely located control surfaces were also studied: SSD/aileron, SSD/canard, SSD/LEF, SSD/pitch flap, AMT/elevon, and AMT/LEF. Control effectiveness versus control volume relationships were also developed to aid in aerodynamic prediction and control surface sizing. A total of 135 hours of testing was performed. Six-component data was obtained over a range of AOA between 0° and 70° at sideslip angles between ±20°. This test is discussed in detail in Chapter 2.

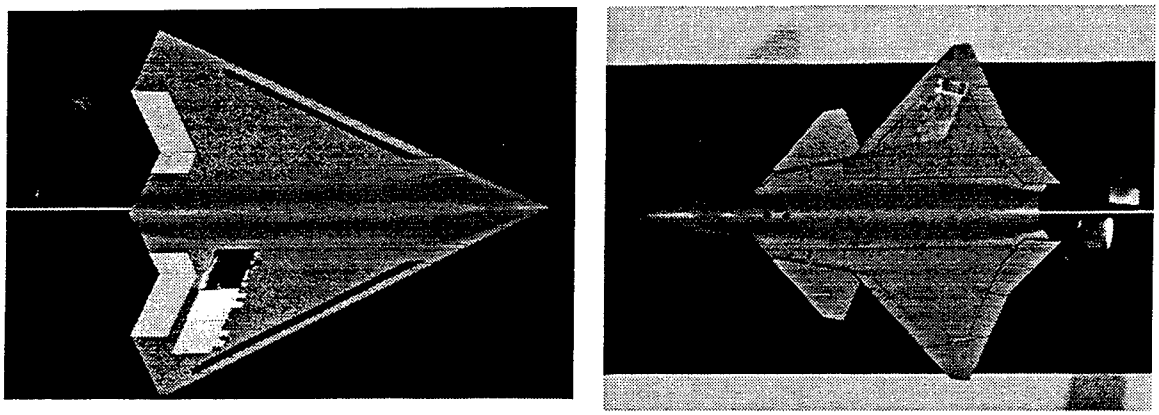

Figure 1-7: Configurations 101 (Left) and 201 (Right) in LMTAS 2'x3' ADF Wind Tunnel

1.2.2 Rotary Balance Test in LAMP Vertical Wind Tunnel

Two models that represented the land-based 101 series (1/13th-scale) and the carrier-based 201 series (1/13.5th-scale) aircraft were constructed by Birhle Applied Research (BAR) and tested in their Large Amplitude Multi-Purpose (LAMP) 10' vertical wind tunnel which is located in Neuberg a.d. Donau, Germany (Figure 1-8). These models each included SSDs at the outboard-forward location and skewed AMTs, which were both found during the ADF test to be the most favorable control effector arrangements. Both models also included a full complement of pitch and roll control surfaces: elevons, pitch flaps, canards, ailerons, leading-edge flaps, etc. The effects of large sideslip angles out to ±30° and steady wind-axis rotation rates with non-dimensional values between ±0.3 were tested over a wide range of AOA between 0° and 90°. Zero-control spin modes were identified for both configurations, and the appropriate recovery control settings were determined. A total of 220 hours of testing was completed. This test is documented in detail in Chapter 3.

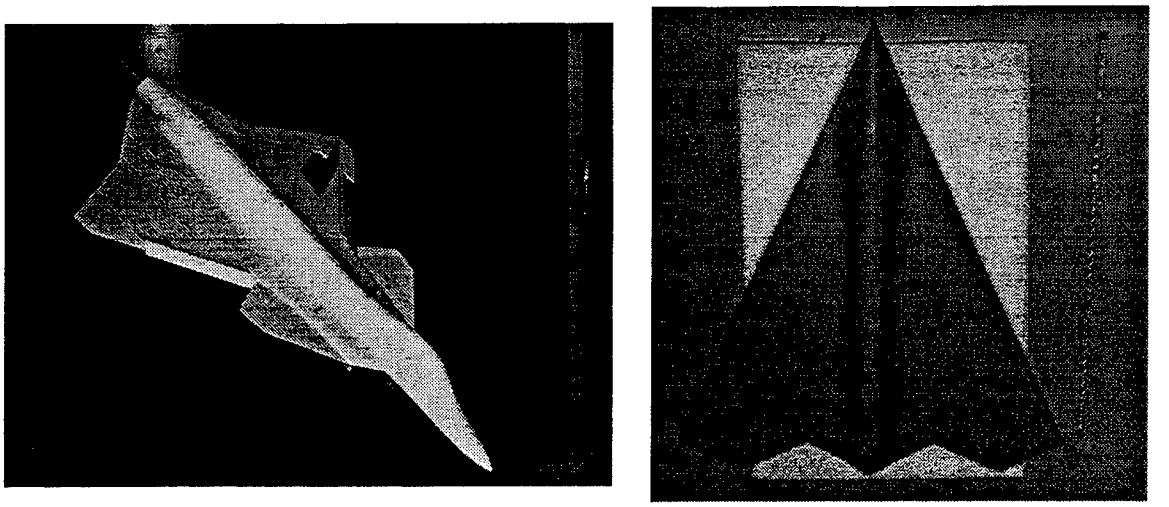

Figure 1-8: ICE Rotary Balance Wind-Tunnel Models in LAMP Vertical Wind Tunnel

1.2.3 SARL Low-Speed Wind-Tunnel Test

The final test conducted during ICE Phase 2 was performed in the Wright Laboratory Subsonic Aerodynamic Research Laboratory (SARL) 7'x10' wind tunnel at Wright-Patterson AFB, Ohio. The existing LMTAS 1/18th-scale high-speed tailless fighter research model was modified for this test by constructing a new left wing that incorporated the SSD and AMT control surfaces (Figure 1-9). This model was used to obtain higher fidelity data than the ADF results on the land-based configuration. No corresponding model was available for the carrier-based configuration, and sufficient funds were not obtainable for construction of a new high-speed model. As a result, no data was obtained during this test for the carrier-based series. Straight and skewed AMTs and both inboard and outboard SSDs were investigated. The effects of SSD size and slot geometry were also studied. Similar to the ADF test, interactions between either the AMTs or the SSDs and any other closely located control surfaces were quantified. A total of 77 hours of testing was completed. This test is described in more detail in Chapter 4.

Figure 1-9: 1/18th-Scale High-Speed Wind-Tunnel Model in SARL Facility at WPAFB

1.2.4 Simulation and Flying Qualities Analysis

The wind-tunnel data obtained during ICE Phase 2, together with previously existing ICE Phase 1 and LMTAS IR&D data, were compiled into two aerodynamic simulation databases that represented Configurations 101 and 201 (Chapter 5). These databases were used with LMTAS control power analysis tools to analyze the flight conditions that were identified during ICE Phase 1 to be critical for control

surface sizing. Analysis of control power envelopes, roll performance, lateral-directional stability augmentation, high-AOA capabilities, and comparisons with the original Phase 1 results can be found in Chapter 6.

2 Small-Scale ADF Wind-Tunnel Test Results and Analysis

2.1 Introduction and Background

As alluded to previously, the overall objective of the ICE program was to reduce the risk associated with integrating advanced control effectors into next generation fighter aircraft. Phase 1 of the program resulted in the selection of three concepts that were deemed worthy of further investigation: (1) the all-moving wing tip (AMT), (2) the spoiler-slot-deflector (SSD), and (3) differential leading-edge flap deflections (DLEF) [Dorsett & Mehl: 1996]. During Phase 1, both the AMT and SSD were demonstrated to be full envelope lateral-directional controls that exhibit good effectiveness and low hinge moments at high speeds. The AMT in particular performed well across the flight envelope and at high AOAs. DLEF was shown to have payoffs at approach conditions and at high AOA.

One of the primary objectives for Phase 2 of the ICE program was to increase the aerodynamic database for the three high payoff control concepts that were selected during Phase 1. This report describes the results and analyses from a two-segment wind-tunnel test in the LMTAS Aerodynamic Development Facility (ADF) in Fort Worth, Texas. These control concepts were tested on both the land-based and carrier-based configurations.

2.2 Facility Description and Test Conditions

The LMTAS ADF wind tunnel is an open circuit facility with a 2'x3' test section (Figure 2-1). It is primarily used to screen configuration concepts at the conceptual design level. Angle of attack (AOA) and sideslip are controlled using a sting motor drive system that can position the model anywhere between 0° and 90° AOA and ±20° of yaw angle. During this test, both yaw sweeps at fixed AOA and pitch sweeps at fixed yaw angle were conducted to acquire data throughout the AOA and sideslip range. The test section operates at a dynamic pressure of 18 psf, which corresponds to a Reynolds number of approximately 0.85 x 10^6 1/ft.

The balance used at ADF since early 1995 is the C-1.1-.55A. It has a 0.55-inch maximum diameter, pull-on tabs for the sting attachment, and a male taper with a pull-on screw for the model connection. It was originally manufactured and calibrated in San Diego, but it has been recalibrated for use at the ADF. Calibration ranges and balance capacities are listed in Table 2-1.

This test consisted of two entries. During the first entry (ADF 9604), the carrier-based configuration was tested, and the land-based configuration was tested during the second entry (ADF 9605). Table 2-2 describes the test conditions for each entry.

2.3 Description of Models

Two 1/40th-scale wind-tunnel models were constructed during Phase 2 for testing at the ADF. The models consisted of wooden fuselages with wings constructed of fiberglass cloth set in a urethane resin. Control surfaces were made from aluminum plate with balsa inserts that were shaped to form an aerodynamic surface. Table 2-3 lists the sign convention for each control surface deflection.

Table 2-1: C-1.1-.55A Balance Data

Load (lbs, in-lbs)	Normal Force	Axial Force	Pitching Moment	Rolling Moment	Yawing Moment	Side Force
Max Calibrated Load	35	7	56	10	12	6
Balance Capacity	110	24	100	15	30	25

Table 2-2: ICE Phase II ADF Test Conditions

Parameter	Value
Test Entry	ADF 9604
Date	3-April 1996 through 17-April 1996
Mach Number	0.1
AOA Schedules	A1: 0° to 32.5° by 2.5° A2: 15° to 45° by 2.5° A3: 0° to 40° by 2.5° A4: 45° to 70° by 5°
Sideslip Schedule	-20°, -15°, -10° to 10° by 2°, 15°, 20°
Reynolds Number	0.85 X 10^6 1/ft
Dynamic Pressure (psf)	18
Test Entry	ADF 9605
Date	18-April 1996 through 25-April 1996
Mach Number	0.1
AOA Schedules	A1: 0° to 32.5° by 2.5°
Sideslip Schedule	-20°, -15°, -10° to 10° by 2°, 15°, 20°
Reynolds Number	0.85 X 10^6 1/ft
Dynamic Pressure (psf)	18

Table 2-3: Control Surface Deflection Conventions

Control Surface	Deflection Range (deg)	Direction for Positive Deflection
Canard (201 only)	+10 to -60	TED
Trailing Edge Controls	-30 to +30	TED
Spoiler	0 to +60	TEU
Deflector	0 to +60	LED
All Moving Tips	-10 to +60	TED
Leading Edge Flaps	0 to +40 (101)	LED
	0 to +30 (201)	LED

Note: TED = Trailing Edge Down, TEU = Trailing Edge Up, and LED = Leading Edge Down

2.3.1 Land-Based Configuration (101)

The land-based configuration was a true flying wing that embodied a 65° leading-edge sweep with a serrated trailing edge. The control surfaces consisted of pitch flaps, elevons, leading-edge flaps (LEF), SSDs, and AMTs (Figure 2-2). Model reference geometry data are also shown in Figure 2-2. Inlets were not included on the model. Instead, aerodynamic fairings were molded into the model surface to represent the inlet face and thereby provide a smooth transition from the forebody to the bottom of the model.

Several variations in SSD and AMT geometry were modeled. The SSDs were located in the right wing of the model, and the AMTs were built into the left wing. Both wings contained the other pitch and roll control surfaces. A large cutout was made in the right wing to accommodate the following three possible SSD locations: (1) inboard aft (IB Aft), (2) inboard forward (IB Fwd), and (3) outboard aft (OB Aft). The right and left halves of the IB Aft SSD could also be tested separately. A set of five spoiler and deflector deflections were constructed to fit within the hole that was cut in the wing. Associated blocks molded from urethane were taped in place to fill the remaining void between the wing and the SSD control. Table 2-4 summarizes the SSD arrangements that were tested. The listed surface areas and locations are in model scale.

Three AMTs were tested that consisted of small and large unskewed AMTs and a third skewed AMT that had a swept hingeline. Table 2-5 summarizes the AMT configurations that were tested. The moment arm dimension was measured from the moment reference center (MRC) to the area centroid of the control surface. This dimension also accounts for any sweep associated with the surface (e.g., aft swept hingelines increase the effective arm with respect to the MRC).

Figure 2-3 shows the Configuration 101 model with its associated parts. The SSD is shown closed in the OB Fwd location. Silver tape covers the left portion of the slot cutout and holds the filler block in place. Each of the spoiler and deflector pieces are shown above the right wing. The left wing has the small AMT installed. The left wing of the model was modified each time an AMT change was made to incorporate the various AMT layouts.

Table 2-4: Spoiler-Slot-Deflector Geometry Descriptions on Configuration 101

Description	Model Part No	Area (in^2)	Arm (in)	Volume Ratio
IB Aft Location	SSD_1	1.80	3.27	0.0072
IB Fwd Location	SSD_2	1.80	3.18	0.0070
OB Fwd Location	SSD_3	1.80	4.50	0.0099
Aft IB Half SSD	$SSD_{1\,IB}$	0.90	2.75	0.0030
Aft OB Half SSD	$SSD_{1\,OB}$	0.90	3.80	0.0042

Table 2-5: All-Moving Tip Geometry Descriptions on Configuration 101

Description	Model Part No	Area (in^2)	Arm (in)	Volume Ratio
Small AMT	AMT_1	1.30	5.00	0.0079
Skewed AMT	AMT_2	1.79	6.24	0.0136
Large AMT	AMT_3	2.57	4.68	0.0147

2.3.2 Carrier-Based Configuration (201)

The carrier-based configuration was developed from a family of airplanes investigated during the initial Joint Strike Fighter efforts. Figure 2-4 illustrates the model and includes the model reference constants. The control surfaces consisted of pitch flaps, elevons, ailerons, canards, LEFs, AMTs, and SSDs. This model was originally constructed for ICE Phase I [Dorsett & Mehl: 1996] but modified for this test. Unlike the 101 model, the 201 model contained inlets, but the inlet air was ducted out the bottom of the model instead of flowing through the model to the nozzle exit area.

Figure 2-5 shows the 201 model and all of its associated parts. Similar to the Configuration 101 model, the SSDs were located on the right wing, and the AMTs were built into the left wing. Four separate wings were constructed to integrate the various AMT and SSD geometries that were tested. Tables 2-6 and 2-7 summarize these AMT and SSD arrangements. The right wing installed on the model in Figure 2-5 shows the SSD located at the IB Fwd location. The wing shown above and to the right of the model was used when testing the SSD in the aft location. Spoiler and deflector parts are shown above the model and between the two wings on the right. When viewed from top to bottom, the three wings located to the left of the model in Figure 2-5 incorporate the small, skewed, and large AMTs, respectively. Different LEF and aileron parts were constructed to integrate with each AMT configuration. Figure 2-6 shows a close-up of the IB Fwd SSD installation with both the spoiler and deflector surfaces deflected 60°.

Table 2-6: All-Moving Tip Geometry Description on Configuration 201

Description	Model Part No	Area (in^2)	Arm (in)	Volume Ratio
Small AMT	AMT_1	2.20	5.70	0.0152
Skewed AMT	AMT_2	2.32	6.20	0.0176
Large AMT	AMT_3	2.98	5.53	0.0200

Table 2-7: Spoiler-Slot-Deflector Geometry Description on Configuration 201

Description	Model Part No	Area (in^2)	Arm (in)	Volume Ratio
IB Aft Location	SSD_1	1.66	4.33	0.0088
IB Fwd Location	SSD_2	1.66	4.13	0.0084
OB Fwd Location	SSD_3	1.66	4.53	0.0092
Aft IB Half SSD	$SSD_{1\,IB}$	0.80	3.85	0.0038
Aft OB Half SSD	$SSD_{1\,OB}$	0.85	4.80	0.0050

2.4 Test Objectives

The primary objectives of the ADF testing conducted during ICE Phase 2 may be summarized as follows:

- Investigate effects of geometry variations in size, orientation, or location on both SSD and AMT effectiveness.
- Determine the aerodynamic potential of the skewed AMT.
- Develop an SSD geometry that minimizes the adverse aerodynamic impacts on the downstream trailing-edge control surfaces.
- Expand the aerodynamic database for the carrier-based configuration.

The run logs for both test entries are included in Figures 2-7 and 2-8. Because significantly less data were available on the carrier-based design, the bulk of this test focused on Configuration 201. Furthermore, the greater number of control surfaces (canard and aileron) on Configuration 201 resulted in it having a larger test matrix.

2.5 Results and Analysis

All data discussed in the following sections are referenced to the subject configuration's moment reference center (38% MAC for Configuration 101 and 20% MAC for Configuration 201). The body-axis coordinate system was used unless otherwise specified.

2.5.1 Land-Based Configuration (101)

The aerodynamic characteristics of Configuration 101 are summarized below.

Basic Aerodynamic Characteristics

Configuration 101 longitudinal data are shown in Figure 2-9. Tie-in data from a test at the Subsonic Aerodynamic Research Laboratory (SARL) wind tunnel at Wright-Patterson AFB, Ohio as well as previous ADF entries are also shown for comparison purposes in this figure. The discrepancies that occurred at high AOA were primarily due to wind tunnel blockage effects because this type of correction is not typically applied to ADF data. The ADF pitching moment data matched well at low AOA, but the unstable break at 15° AOA was not as severe as that shown in the other low-speed data. This result was thought to be attributed to the slightly different forebody geometry on the $1/40^{th}$-scale ADF model.

The basic lateral-directional stability characteristics are shown in Figure 2-10. The configuration was laterally stable between 0° and 26° AOA and was directionally unstable throughout the AOA range tested. Above 25° AOA, directional stability worsened considerably.

All-Moving Wing Tip

Control effectiveness results for the small, skewed, and large AMTs are shown in Figures 2-11, 2-12 and 2-13, respectively. Positive AMT deflections produced nearly constant body-axis yaw with increasing AOA up to the highest AOA tested. Roll power was adverse at low AOA, but it became favorable above 15° AOA. Positive AMT deflections created small nose-down or nose-up pitching moments depending on deflection and AOA. The yaw control effectiveness produced by the AMTs increased with increasing deflection for angles up to 60°, which was the highest deflection tested. Larger deflections were not pursued because previous testing had indicated that 60° is a reasonable maximum deflection limit for this type of control since larger deflections do not produce significant increases in control power [Dorsett, Mehl 1996].

Figure 2-14 shows the variation in control power with changes in AMT geometry for a 60° deflection. As expected, the large unskewed AMT provided the greatest lateral-directional control power. Interestingly, the skewed AMT produced considerably greater yaw control power than the small unskewed AMT for only a moderate increase in control surface area (1.8 in^2 vs. 1.3 in^2). This result was attributed to the effects of sweeping the pivot trunion on the side forces produced by AMT deflection (Figure 2-15). Figure 2-16 shows the incremental axial and side forces produced by each AMT geometry at 60° of deflection. As expected, axial force varied directly with control surface area. The small and large AMTs created small side-force components that aided the yawing couple, but the skewed AMT generated a significantly greater side-force component. As a result, these side-force yawing-moment increments combined with the axial-force yawing-moment contributions produced by the skewed AMT to yield a higher net moment.

Figure 2-17 shows the control power produced at an AOA of 0° versus the control volume ratio of the various control layouts on both Configurations 101 and 201. AMT yaw control power varied linearly with control volume ratio. It should be noted that the skewed AMT volume ratios were computed using the moment arm normal to the skewed hingeline. When computed in this manner, the skewed AMT control power data collapsed in line with the other AMT data.

Variation of AMT yaw control power with control deflection is shown in Figure 2-18 for 0° AOA. A yaw control deadband exists over the first 10° of control deflection for all three AMT configurations. Figure 2-19 shows data for the large AMT at several angles-of-attack. At 0° AOA, a deadband existed for AMT deflections below 10° on all three AMT geometries, but the data in Figure 2-19 indicated that the deadband was reduced with increasing AOA.

The effects of sideslip on a 60° AMT deflection are illustrated in Figure 2-20. Sideslip angles up to ±20° had little effect on AMT yaw power throughout the AOA range tested, which was a very beneficial result. Sideslip modified the roll characteristics of the AMT somewhat and generally reduced the amount of nose-up pitching moment compared to the 0° case. Leeward sideslip resulted in more nose-up pitching moment above 25° AOA.

Variations using the Large AMT

Three modifications to the large unskewed AMT were tested in attempts to increase its yaw power and to reduce the adverse rolling-moment increments that were produced at low AOA. Reduction of the adverse roll characteristics would simplify the control blending and allocation process. These modifications, shown in Figure 2-21, consisted of a fillet aft of the pivot trunion, a gurney flap deflected 90° TED, and a gurney flap deflected 90° TEU. These parts were constructed from brass shim stock and taped to the model during the test.

Figures 2-22 and 2-23 show the effects of the alternate large AMT configurations on control power at 30° and 60° of AMT deflection. The aft fillet reduced the amount of adverse roll from a 30° AMT deflection for AOAs below 10°. Unfortunately, it also reduced the yaw power of the AMT at all AOAs. The TED gurney flap increased yaw power and low AOA adverse roll at this deflection. The TEU gurney flap decreased yaw power and adverse roll at low AOA, but yaw control was unchanged above 10° AOA. For the 60° deflection (Figure 2-23), minimal changes in control characteristics were seen except for an increase in yaw power due to TED gurney flap deflections and an increase in adverse roll with the aft fillet. Consequently, none of these modifications was entirely successful. The aft fillet reduced the roll/yaw ratio of the AMT from 2:1 to approximately 1:1 at low AOA for the 30° deflection, but unfortunately this beneficial result came at the expense of reduced yaw control power. For the 60° AMT deflection, the aft fillet increased the unfavorable roll/yaw ratio. Additional work with these concepts may yield more favorable results.

Interaction with LEF

Figure 2-24 shows the aerodynamic interaction between the skewed AMT and the LEF. The LEF increases the AMT yaw power slightly in the 10° to 25° AOA range, but the effects of deflecting the LEF on AMT effectiveness are generally small.

Spoiler-Slot-Deflector

Figures 2-25 through 2-27 show SSD effectiveness curves for the IB aft, IB fwd, and OB fwd locations. The 60° deflection generated large values of yaw power at low to moderate AOAs, but this yaw power generally decreased with increasing AOA. The 15° and 30° deflections lost yaw effectiveness above 20° to 25° AOA. Roll effectiveness was maintained and actually increased through 32.5° AOA. All three locations generated considerable nose-up pitching moments at maximum deflection.

Figure 2-28 shows SSD yaw control effectiveness versus control volume ratio for both Configurations 101 and 201. SSD yaw effectiveness followed a predictable trend with increasing control volume ratio.

The effect of sideslip on SSD control power is shown in Figure 2-29 for several AOAs. Yaw power was relatively unaffected by sideslip angles up to ±20°, but roll power varied more significantly with sideslip changes.

Effect of Location

Figure 2-30 shows the effect of location on the SSD control power produced by 60° deflections. The OB fwd location generated the greatest yaw power at low AOA due to its increased moment arm with respect to

the MRC. Above 20° AOA, all three locations generate the same amount of yaw power. The two IB locations generated less roll effectiveness than the OB location at low AOA but produced greater roll power at high AOA. This was a result of flow separation on the OB portion of the wing at higher AOA. Large nose-up pitching moments were generated by all three concepts with the IB locations generating larger pitching-moment increments for AOAs between 10° and 20°.

The OB fwd SSD control effectiveness is compared with the OB fwd spoiler in Figure 2-31. The SSD created considerably greater lateral-directional control power at any given deflection. For example, a 15° SSD deflection generated as much lateral-directional control power as a 30° spoiler deflection. The 60° SSD generated over 2.5 times the yaw power of the 60° spoiler by itself. However, the 15° and 30° SSD deflections resulted in a yaw power reversal above 20° AOA, whereas the spoiler did not. The pitching-moment increments generated by the spoiler were not nearly as significant as those produced by the SSD.

Effect of Slot Blockage

Figure 2-32 shows the effect of closing the slot between the upper and lower wing surface for a 60° SSD deflection. Yaw control power with the slot closed was less than that for the slot-open case for AOA<12°, but high-AOA yaw power was improved by closing the slot. Roll control power was significantly reduced with the slot closed, especially at low AOAs. Closing the slot reduced the nose-up pitching-moment increments that were produced at low AOAs. But for AOA'a above 10°, nose-up pitch was the same whether the slot was open or closed.

Effect of SSD and Spoiler Deflection on Effectiveness of Trailing-Edge Controls

Figures 2-33 through 2-36 respectively illustrate the effects of OB fwd SSD deflections on right-side elevon deflections of -30°, -10°, 10°, and 30°. Maximum SSD deflections destroyed elevon pitch- and roll-control effectiveness at low to moderate AOAs.

Figures 2-37 through 2-40 compare the effects of 60° OB fwd spoiler and SSD deflections on the effectiveness of the right elevon. The spoiler and the SSD had similar effects on TEU elevon roll power, but the SSD clearly reduced the elevon TEU (nose-up) pitch effectiveness more than did the spoiler alone. The SSD also affected TED elevon deflections more severely than did the spoiler alone. These results showed that the deflector portion of the SSD had a stronger influence on the downstream elevon that did the spoiler component of the SSD.

Figures 2-41 and 2-42 respectively show the effects of SSD location on the effectiveness of elevon deflections of -30° and 30°. Deflections of the SSDs at both of the IB locations resulted in elevon control reversals at low AOAs. The OB fwd SSD location also reduced elevon effectiveness, but it did not create the control reversal. As a result, the OB fwd location enabled the elevons to produce greater nose-down control power at high AOAs.

The effects of SSD location on the effectiveness of a 30° pitch flap (right side only) deflection is shown in Figure 2-43. Deflection of the SSD at the two IB locations adversely impacted nose-down pitch flap performance, and the OB fwd SSD location actually improved pitch flap nose-down control power at all AOAs. More research is required to better understand why this benefit occurs only for the OB fwd SSD.

2.5.2 Carrier-Based Configuration (201)

The aerodynamic characteristics of Configuration 201 are summarized below.

Basic Aerodynamic Characteristics

Figure 2-44 shows longitudinal tie-in data with an earlier ADF entry of Configuration 201. The canard-off normal force data compared very closely, whereas the current test data indicated a more nose-down trend at moderate AOAs. The current canard-on data were compared with a LEF=25° run from the previous test, which caused the differences in the high-AOA normal-force coefficients. In general, the new data showed the airplane to be slightly more stable than the old data. The older entry utilized a different balance than the current test, which perhaps resulted in some of the differences.

Figure 2-45 shows the effects of canard deflection on lateral-directional stability for the LEF=0° case. Depending on canard deflection, the configuration was laterally stable for AOAs up to 20° to 25°, and the degree of lateral instability in the stall region was also a function of canard setting. The configuration was directionally unstable at all AOAs. The degree of instability was insensitive to canard deflection for AOAs below 15°, but canard deflection affected directional stability at the higher AOAs.

All-Moving Wing Tip

The control effectiveness produced by deflections of the small AMT is shown in Figure 2-46. This control had very similar characteristics on Configuration 201 as it did on Configuration 101. TED deflections resulted in good yaw control power values for AOAs up to 32.5°. Roll power was adverse at low AOAs, but it became favorable at higher AOAs. The effect of size on AMT control power is shown in Figure 2-47. AMT size primarily affected yaw power at 30° and 60° deflections. Substantial effects on roll power were observed at low AOA. The AOA=0° results shown in this figure were used to construct the effectiveness versus control volume trends that were previously shown in Figure 2-17. Finally, Figure 2-48 illustrates the effect of sweeping the AMT trunion aft slightly. As discussed previously, the skewed AMT hingeline was made to line up with the wing fold line on the opposite side of the airplane for RCS reduction purposes, resulting in a 10° skew angle. The skewed AMT provided greater yaw control power than the small AMT at a 60° deflection. The surface area of the skewed AMT was 2.32 in^2 compared to 2.20 in^2 for the small AMT. A control power comparison for all three AMT geometries at 60° deflection is provided in Figure 2-49.

Effect of Sideslip on AMT Control Power

The effects of sideslip on the lateral-directional control power produced by deflections of the large AMT are shown in Figure 2-50. Sideslip primarily affected the roll power produced by the AMT, and yaw power was relatively unaffected. Figure 2-51 shows the effects of sideslip on the skewed AMT control power at high AOA. Yaw power generally increased with increasing windward sideslip and decreased with leeward sideslip.

Aerodynamic Interaction Between AMT and Aileron

Figures 2-52 through 2-54 show the impacts of small, skewed, and large AMT deflections on aileron control power. Keeping in mind that the AMT may be used for roll coordination, the deflections shown represent cases where the ailerons are deflected for roll, and the AMTs are deflected to coordinate the roll (i.e., opposite the aileron deflection). In general, TED tip deflections reduced the pitch and roll power generated by the aileron, and TEU tip deflections created only small differences in the aileron control power. The skewed and large AMT had smaller impacts on aileron control power than the small AMT did.

Spoiler-Slot-Deflector

Control power data for SSD deflections at the IB aft, IB fwd and OB fwd SSD locations are respectively shown in Figures 2-55 through 2-57. At the OB fwd location, SSD deflection generated greater yaw control power for AOAs up to 20° than when positioned at the other two locations. Similar to Configuration 101,

SSD deflection at this location also generated less roll power at high AOAs than it did at the other locations. The smallest nose-up pitching moments were generated when the SSD was located at the IB fwd position. Figure 2-58 summarizes the effects of location on SSD control power.

The effects of sideslip on SSD control power are shown in Figure 2-59. Yaw power was relatively unaffected by sideslip. Decreased roll power occurred for windward sideslip angles at low AOAs. For AOAs above 20°, roll power increased with windward sideslip.

Spoiler control power at an AOA of 0° versus deflector angle for the IB aft SSD location is shown in Figure 2-60. Peak roll power occurred when the spoiler and deflector angles were equal. At both the 30° and 60° deflections, opening the deflector in a 1:1 relationship with the spoiler approximately doubled the roll power generated by the spoiler alone. For a 15° spoiler alone deflection, no roll power was generated because the surface was immersed in the boundary layer flow. When both the spoiler and the deflector were opened 15°, more roll power was generated than for the 30° spoiler-only deflection. Yaw power increased with increasing deflector angle for any given spoiler deflection. At a 1:1 spoiler-deflector deflection combination, the SSD generated as much as 250% of the spoiler-alone yaw power.

The effects on pitching moment at an AOA of 0° of various spoiler-deflector combinations at the IB aft position are shown in Figure 2-61. A small nose-down pitching moment was generated when the spoiler was opened, but it was relatively insensitive to deflection. Opening the deflector at any given spoiler deflection generated a nose-up pitching moment trend. The 60° spoiler-deflector combination resulted in a significant nose-up pitching moment.

Effect of Slot Blockage

The effects of blocking the slot between the upper and lower wing surfaces were investigated by placing tape over various portions of the slot in a similar fashion as to what was done on Configuration 101. It was recognized that there were probably Reynolds number effects on the slot. These configurations were tested to get an idea of the trends that might be expected with varying slot geometry. Figure 2-62 illustrates the three blocked-slot configurations that were tested. Each slot geometry was tested with 60° spoiler and deflector combinations at the IB aft SSD location.

The effects of the various blocked-slot configurations on SDD effectiveness are shown in Figure 2-63. The greatest yaw control power was generated by the no-blockage SSD configuration at low AOAs, and the fully blocked configuration generated the greatest yaw power at high AOAs. The two partially blocked configurations generated more high-AOA yaw power than the no blockage, or baseline, configuration but less than the fully blocked slot. The fully-blocked slot on Configuration 101 showed similar trends. The baseline configuration possessed the greatest roll control power at all AOAs, and the least roll effectiveness occurred when the slot was fully blocked. The pitching-moment characteristics were also sensitive to slot configuration with the 50%-aft-blockage concept being less nose-up than the others in the moderate AOA range. Further analysis of these control increments showed substantial increases in the axial force increments at high AOA as the slot was blocked off, resulting in improved high AOA yaw control effectiveness. This trend makes sense, as a completely open slot would allow airflow straight through the slot at high AOA with little separation due to the deflector; whereas a closed slot would allow the deflector to trap a large separation bubble, resulting in increased drag and yawing moment (Figure 2-64).

Aerodynamic Interaction Between SSD and Aileron

The effects of SSD location on SSD/aileron interaction are respectively shown in Figures 2-64 and 2-65 for -30° and 30° aileron deflections. The data represent SSD and aileron deflections on the right wing. For both aileron deflections, all three SSD locations resulted in similar detrimental effects on aileron control power. However, the OB fwd SSD location does not degrade aileron control power as much as the other two locations. A similar result was observed on Configuration 101.

Effect of LEF and Canard Deflection on SSD Effectiveness

The LEF/SSD and the canard/SSD interactions are respectively shown in Figures 2-66 and 2-67. The IB aft SSD location was used for these comparisons. LEF deflections improved SSD yaw power at high AOAs, presumably due to delayed flow separation over the wing. LEF deflections had a nonlinear effect on SSD roll power in the same AOA region. Like any other airfoils, the canards generated strong tip vortices and downwash which acted on the wings. Therefore, changing canard deflections was expected to have significant effects on SSD control power. Lateral-directional control power was generally increased for TEU canard settings up to -10°. The -30° canard deflection resulted in increased yaw power over the baseline setting at high AOA, but roll power reversed sign above an AOA of 30°. Large negative canard deflections would typically be used for trim at the higher AOAs. For this reason, the increased SSD yaw power that occurred for these canard settings was considered favorable.

Differential LEF

The control effectiveness of differential LEF (DLEF) deflections is shown in Figure 2-68. The data show that this device became effective in yaw for AOAs above 10°. The accompanying rolling-moment increments were adverse for AOAs up to 20° beyond which they became favorable. The control effectiveness produced by DLEF was not increased for deflections above 20°.

The effects of sideslip on DLEF control power are respectively shown in Figures 2-69 and 2-70 for AOAs of 20° and 32.5°. At an AOA of 20°, yaw power was relatively unaffected by sideslip, and roll power became more adverse with windward sideslip. At an AOA of 32.5°, yaw power was degraded for sideslips between 2° and 8°, and roll power was nonlinear with sideslip angle.

2.6 Conclusions and Recommendations

A low-speed wind-tunnel test was performed in the LMTAS ADF facility on two 1/40th-scale models of the land-based and carrier-based ICE configurations. The capabilites of various innovative control concepts were evaluated. These concepts consisted of all-moving wing tips (AMT), spoiler-slot-deflectors (SSD), and differential leading-edge flap deflections (DLEF). The effects of size, geometry variation, control interactions, and sideslip on the effectiveness of each control surface were determined.

Summary of AMT Control Characteristics

- The AMT provided large body-axis yaw control power over a wide AOA range on both the land-based and carrier-based configurations.

- TED deflections created adverse roll at low AOAs that became favorable at the higher AOAs.

- A nonlinear deadband in the AMTs control effectiveness existed for small AMT deflections at an AOA of 0°, but the degree of deadband decreased with increasing AOA.

- The skewed AMT generated larger yaw control power than the unskewed AMTs because it produced axial forces as well as favorable side forces that both contributed to the yawing moments generated by the device. The degree of beneficial side force generated by the tip was proportional to the magnitude of trunion sweepback . Even small sweep angles noticeably improved AMT control power.

- AMT yaw control effectiveness was found to be scalable with control volume ratio when the sweep of the pivot trunion was accounted for. This result indicated that this scaling relationship could be used to estimate the effectiveness of the AMT on other configurations.

- AMT yaw control power was relatively unaffected by sideslip angles as large as ±20°, but the roll characteristics were more significantly affected by sideslip.

- Three alternative AMT arrangements were tested in attempts to reduce the adverse roll that occurred on the flying wing configuration at low AOAs. A fixed fillet that covered the portion of the tip aft of the pivot trunion decreased the low-AOA roll/yaw ratio from 2:1 to 1:1 for an AMT deflection of 30°. This effect was nonlinear with deflection and reduced AMT yaw power at moderate deflections. Lateral-directional control power at maximum deflection was unaffected by the fillet.

- TED AMT deflections generally degraded the effectiveness of the adjacent ailerons. The degree of interaction was strongly affected by AMT geometry.

Summary of SSD Control Characteristics

- The SSD provided larger lateral-directional control moments than those produced by conventional spoilers alone. Roll power was approximately doubled and yaw power increased by as much as 250% when a slot-deflector was added to the conventional spoiler arrangement.

- Maximum SSD deflections resulted in useable lateral-directional control power for AOAs up to 32.5°. Yaw power decreased with increasing AOA, but roll power remained relatively constant.

- SSD yaw power was relatively unaffected by sideslip, whereas the corresponding roll power was more extensively affected by sideslip.

- Spoiler/deflector deflection ratios of 1:1 maximized the roll power produced by the control. For any given spoiler deflection, increasing the corresponding deflector deflection up to the 1:1 value increased the yaw power that was produced.

- Large nose-up pitching moments were created by maximum SSD deflections. This result indicated that the other controls will be required to generate significant pitch control power to trim the vehicle when the SSD is deflected.

- The OB fwd SSD location created more yaw control power at low to moderate AOAs than did the IB locations due to an increased moment arm about the yaw axis.

- SSD deflections adversely affected the control power produced by the downstream trailing-edge surfaces. The lower surface deflector had a larger adverse effect than did the upper surface spoiler on elevon and aileron control power. Modifications to this surface may be able to reduce this adverse interaction.

- When located at the OB fwd position, SSD deflections did not affect the control power produced by the trailing-edge controls as severely as when it was located at either of the IB positions. In fact, the nose-down effectiveness of the pitch flaps was actually improved by a 60° SSD deflection at the OB fwd position, but the SSD deflections at the IB locations degraded pitch flap control power.

- LEF deflections in front of the SSD resulted in favorable aerodynamic interactions at high AOAs. Canard deflections significantly affected SSD control power. Canard settings that were consistent with high-AOA flight generally improved SSD yaw power at these AOAs.

- Similar to the AMTs, SSD lateral-directional control power scaled with control volume ratio, and this method can be used to estimate the effectiveness of SSDs on other configurations.

Differential LEF Control Characteristics

- Differential LEF created appreciable lateral-directional control moments on both configurations for AOAs above about 10° to 15°.
- DLEF control power was nonlinear with deflection angle.
- DLEF yaw control power was insensitive to sideslip, but roll power was affected by sideslip.

Recommendations

Based on the results of this test, it is recommended that future ICE wind-tunnel tests more closely investigate the skewed AMT and the OB forward SSD concepts. Research on the SSD should include efforts to reduce the adverse interaction with the downstream trailing-edge controls. A vent in the lower-surface deflector is recommended as a possible way to reduce these unfavorable interactions.

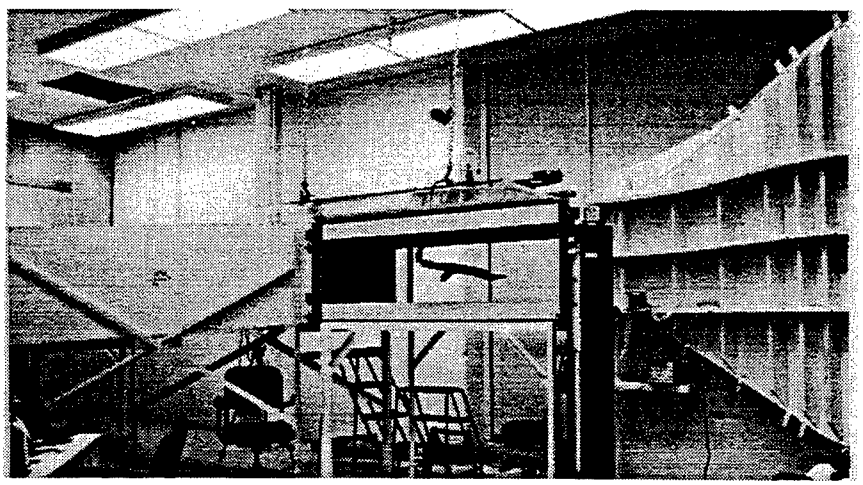

Figure 2-1: LMTAS 2'X3' ADF Wind Tunnel

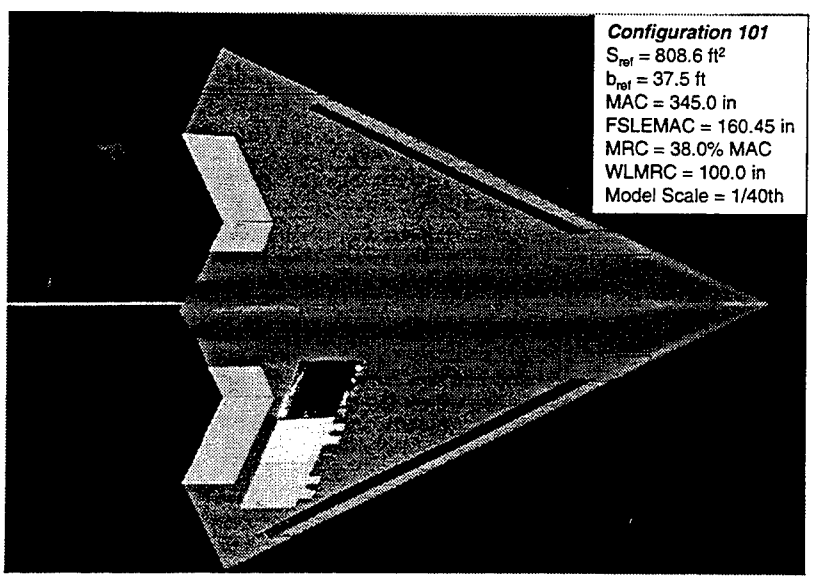

Figure 2-2: Wind-Tunnel Model of Land-Based Configuration 101

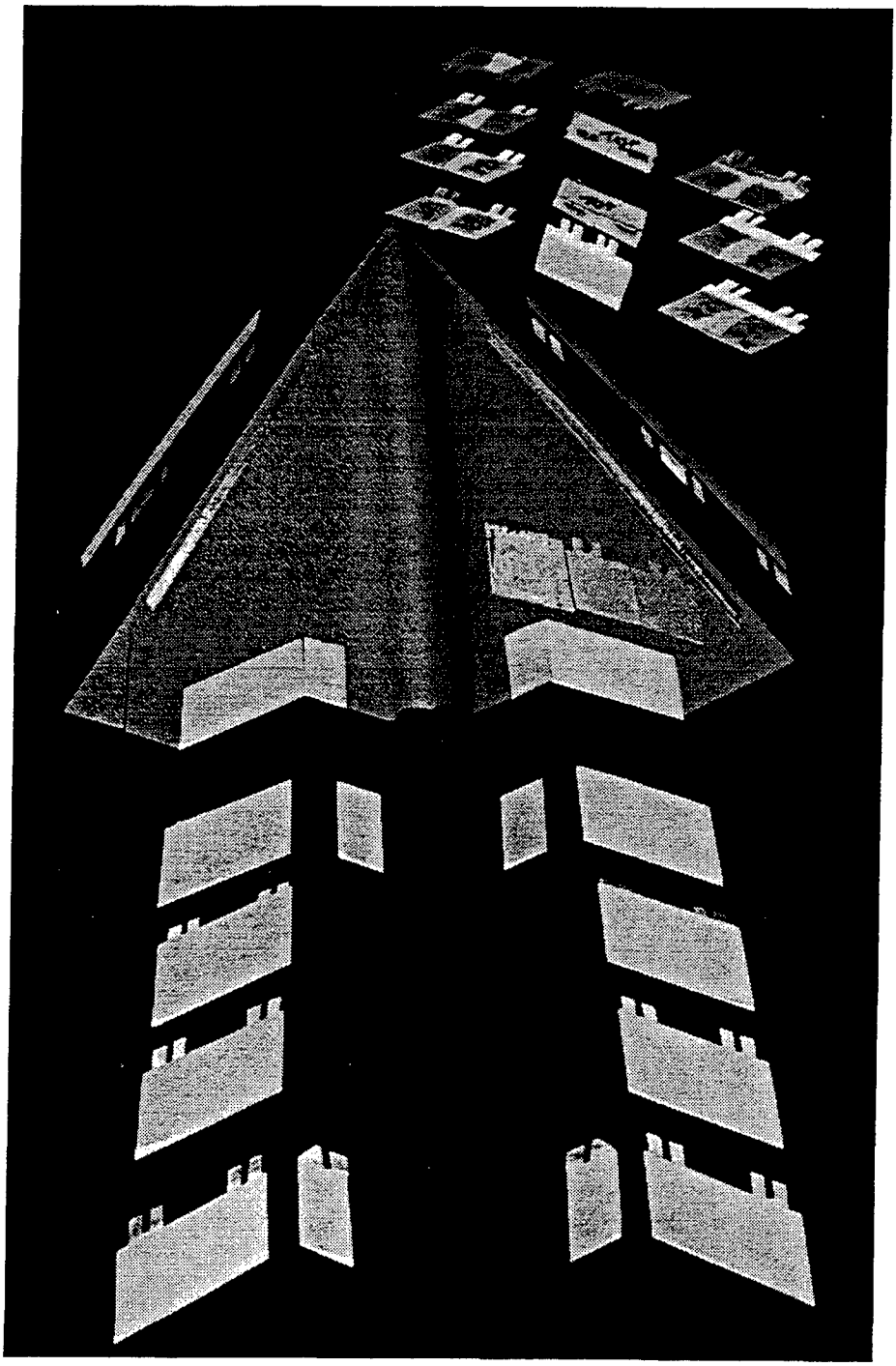

Figure 2-3: Configuration 101 Wind-Tunnel Model Parts

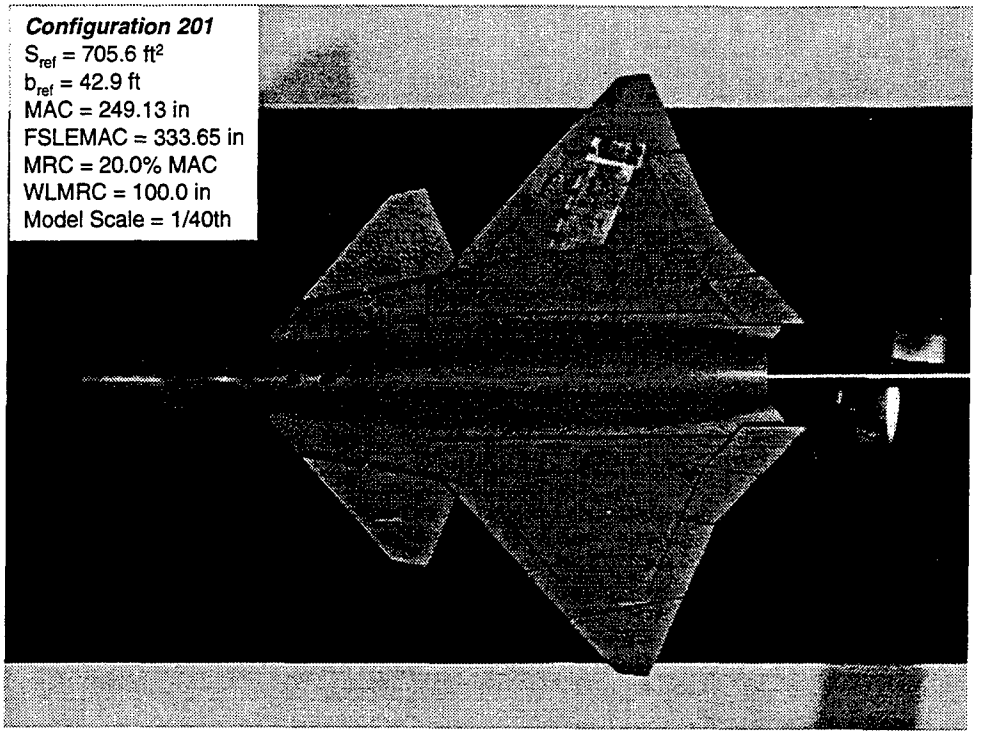

Figure 2-4: Wind-Tunnel Model Carrier-Based Configuration 201

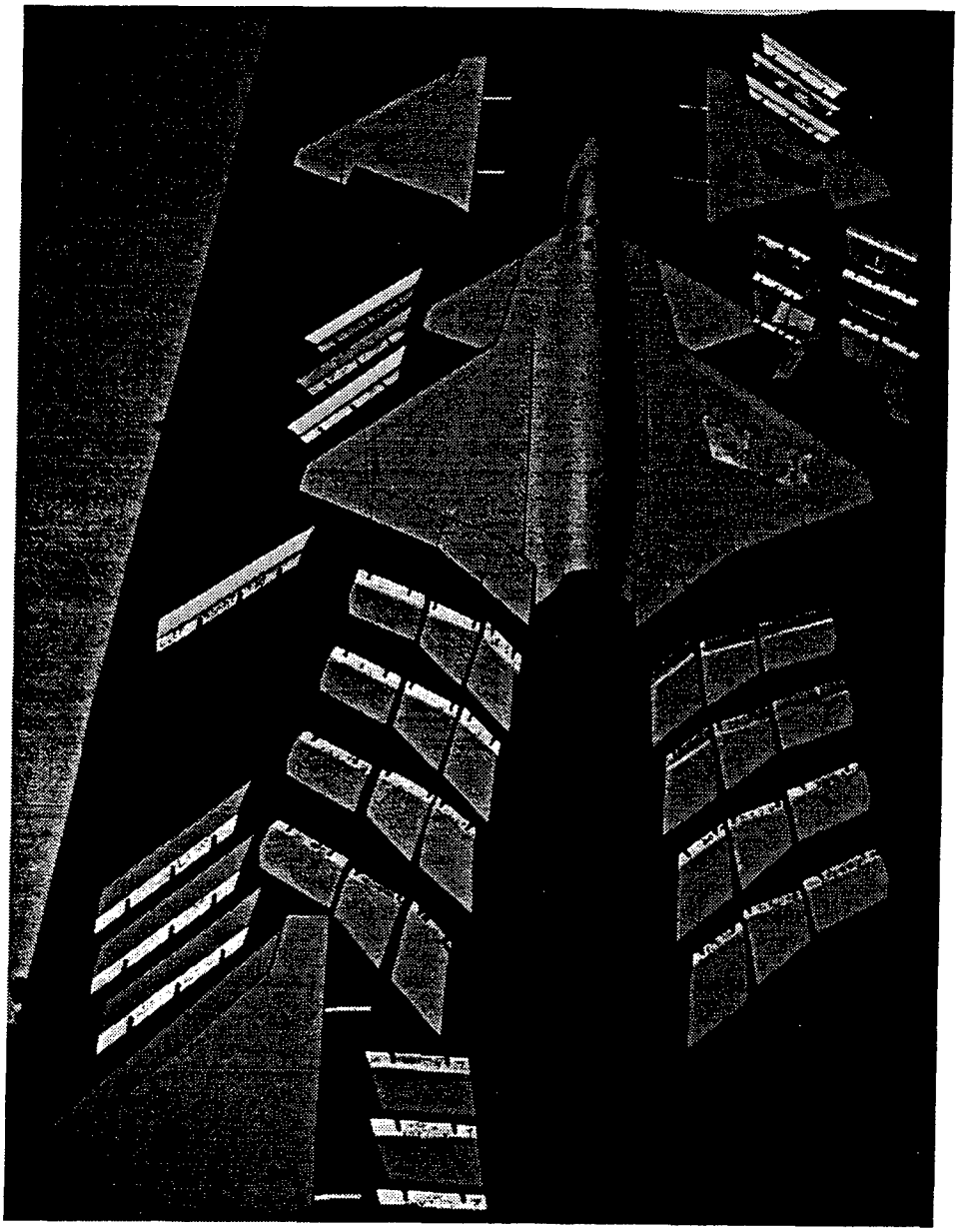

Figure 2-5: Configuration 201 Wind-Tunnel Model Parts

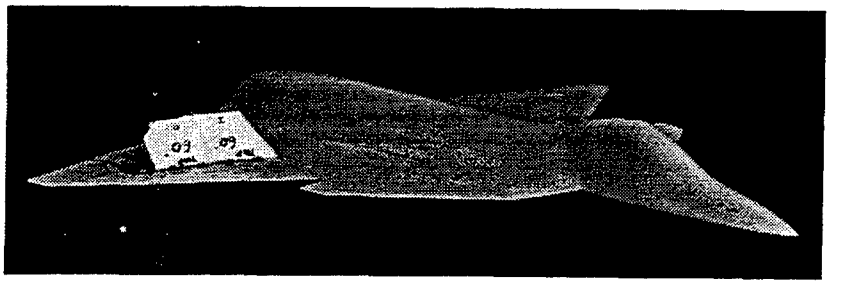

Figure 2-6: IB Fwd SSD Deflected 60°

ICE Phase II ADF Run Plan

Configuration 201-Series

	Full Scale		1/40th Scale	
Ref. Area	705.6	ft^2	63.5	in^2
Ref. Span	42.9	ft	12.9	in
MAC	249.13	in	6.23	in
FSLEMAC	333.65	in	8.34	in
FSMRC (20%)	383.48	in	9.59	in
WLMRC	100	in	2.5	in
FS Nose Tip	12	in	0.3	in

	Pitch Flaps		Elevons		Ailerons		Canard		LEF		Spoiler		Deflector		AMT		AOA=var; AOS=							AOS=var; AOA=								
Configuration	L	R	L	R	L	R	L	R	L	R	L	R	L	R	L	R	-20	-10	-5	0	5	10	20	0	10	20	22.5	25	27.5	30	32.5
Basic 201 (Can Off)	0	0	0	0	0	0	Off	Off	0	0	0	0	0	0	0	0	10	11	12	9	13	14	15	16	17	18	19	20	21	22	23
Basic 201							0	0												364											
Repeats																				28											
																				85											
																				103					104						
																				132											
																		148		147		149									
																		151		150		152									
																				174											
																				219											
																				381											
Wing 2																		221		220		222									
Wing 3																		295		294		296									
Wing 4																		336		335		337									
Basic 201 w/ A2																		393		392		394				395		396	397	398	399
Canard Series																	25	26	27	24	29	30	31	32	33	34	35	36	37	38	39
							15	15										44		43		45									
							10	10										47		46		48									
							-10	-10										50		49		51									
							-20	-20										53		52		54									
							-30	-30										56		55		57									
							-40	-40										404		403		405									
							-60	-60										419		418		420									
Pitch Flap Series		-30					0	0												365											
		-10																		366											
		10																		367											
		30																		368											
Elevon Series	0	0	0	-30																369											
				30																370											
				-10																371											
				10																372											
Aileron Series				0	-30	0														382											
(Small Aileron)					30															383											
					-10															384											
					10															385											
Aileron Series				0	0	-30														373											
(Baseline Aileron)						30														374											
						-10														376											
						10														375											

A1 (Model Inverted) AOA=0 - 32.5 by 2.5 deg

A2 (15 deg Sector) AOA=15 - 45 by 2.5 deg

A3 (Wings Vertical) AOA=0 - 40 by 2.5 deg; 45 - 70 by 5 deg

AOS Schedule AOS= -20, -15, -10 - 10 by 2.0 deg, 15, 20

ICE Phase II ADF Run Plan

	Pitch Flaps		Elevons		Ailerons		Canard		LEF		Spoiler		Deflector		AMT		AOA=var; AOS=							AOS=var; AOA=							
Configuration	L	R	L	R	L	R	L	R	L	R	L	R	L	R	L	R	-20	-10	-5	0	5	10	20	0	10	20	22.5	25	27.5	30	32.5
SSD1	0	0	0	0	0	0	0	0	0	0	0	60	0	0	0	0				156											
IB Aft Location														15						191											
														30						192											
														60						157				158	159	160	161	162	163	164	165
												30								195											
														30						166											
														15						196											
														0						167											
												15								168											
														15						169											
														30						193											
														60						194											
SSD1/Aileron						-30						60								189					190							
						-10														188											
						10														187											
						30														185					186							
												30		30						175											
						10														176											
						-10														177											
						-30														178											
												15		15						170											
						-10														171											
						10														172											
						30														173											
Spoiler 1/Aileron												60		0						183					184							
						10														182											
						-10														181											
						-30														179					180							
SSD1/LEF						0			10	10				60				198		197		199										
									30	30								201		200		202										
SSD1/Canard							10	10	0	0								204		203		205										
							-10	-10												206											
							-30	-30										208		207		209										
Tape Over 100% Slot							0	0												210											
Tape over Fwd 50%																				212											
Tape over Aft 50%																				211											
IB SSD 1												IB 60		IB 60				214		213		215										
OB SSD 1												OB60		OB60				217		216		218										

Figure 2-7: Configuration 201 Run Log

ICE Phase II ADF Run Plan

Configuration	Pitch Flaps L	Pitch Flaps R	Elevons L	Elevons R	Ailerons L	Ailerons R	Canard L	Canard R	LEF L	LEF R	Spoiler L	Spoiler R	Deflector L	Deflector R	AMT L	AMT R	AOA=var; AOS= -20	-10	-5	0	5	10	20	AOS=var; AOA= 0	10	20	22.5	25	27.5	30	32.5
SSD2/Aileron	0	0	0	0	0	0	0	0	0	0	0	60	0	0	0	0				263											
with Wing 2														60						279				280	281	282	283	284	285	286	287
												30		30						262											
														0						261											
												15								260											
														15						259											
SSD2/Aileron						-30						60		60						270					271						
						30														268					269						
Spoiler 2/Aileron														0						266					267						
						-30														264					265						
SSD 2/LEF						0			10	10								289		288		290									
									30	30								292		291		293									
SSD 2/Canard							10	10	0	0								273		272		274									
							-10	-10												275											
							-30	-30										277		276		278									

Configuration	Pitch Flaps L	Pitch Flaps R	Elevons L	Elevons R	Ailerons L	Ailerons R	Canard L	Canard R	LEF L	LEF R	Spoiler L	Spoiler R	Deflector L	Deflector R	AMT L	AMT R	AOA=var; AOS= -20	-10	-5	0	5	10	20	AOS=var; AOA= 0	10	20	22.5	25	27.5	30	32.5
SSD3	0	0	0	0	0	0	0	0	0	0	0	60	0	0	0	0				244											
OB Fwd Location														60						227				228	229	230	231	232	233	234	235
												30		30						226											
														0						225											
												15								224											
														15						223											
SSD3/Aileron						-30						60		60						236					237						
						30														238					239						
Spoiler 3/Aileron														0						240					241						
						-30														242					243						
SSD 3/LEF						0			10	10								246		245		247									
									30	30								249		248		250									
SSD 3/Canard							10	10	0	0								252		251		253									
							-10	-10												254											
							-30	-30										256		255		257									

ICE Phase II ADF Run Plan

Configuration	Pitch Flaps L	Pitch Flaps R	Elevons L	Elevons R	Ailerons L	Ailerons R	Canard L	Canard R	LEF L	LEF R	Spoiler L	Spoiler R	Deflector L	Deflector R	AMT L	AMT R	AOA=var; AOS= -20	-10	-5	0	5	10	20	AOS=var; AOA= 0	10	20	22.5	25	27.5	30	32.5
Small AMT (AMT1)	0	0	0	0	0	0	0	0	0	0	0	0	0	0	30	0				390											
															60					391											
AMT 1/Aileron					-30															76											
(Baseline Aileron)					-10															77											
					10															78											
					30															79											
															30					135											
					10															136											
					-10															137											
					-30															138											
															10					139											
					-10															140											
					10															141											
					30															142											
															-10					143											
					10															144											
					-10															145											
					-30															146											
Skewed AMT					0										30					377											
(No 2)															60					380											
AMT 2/Aileron					-30															358											
(Baseline Aileron)					-10															357											
					10															356											
					30															355											
															30					354											
					10															353											
					-10															352											
					-30															351											
															10					346											
					-10															345											
					10															344											
					30															343											
															-10					342											
					10															341											
					-10															340											
					-30															339											

Figure 2-7: Configuration 201 Run Log (Continued)

ICE Phase II ADF Run Plan

Configuration	Pitch Flaps L	Pitch Flaps R	Elevons L	Elevons R	Ailerons L	Ailerons R	Canard L	Canard R	LEF L	LEF R	Spoiler L	Spoiler R	Deflector L	Deflector R	AMT L	AMT R	AOA=var; AOS= -20	-10	-5	0	5	10	20	AOS=var; AOA= 0	10	20	22.5	25	27.5	30	32.5
Large AMT	0	0	0	0	0	0	0	0	0	0	0	0	0	0	30	0				386											
(No 3)															60					387											
AMT3/Aileron					-30															325											
(Small Aileron)					-10															324											
					10															323											
					30															322											
															30					313											
					10															312											
					-10															311											
					-30															310											
															10					305											
					-10															304											
					10															303											
					30															302											
															-10					301											
					10															300											
					-10															299											
					-30															298											
DLEF Series					0					10					0					97					98	99					153
										20										94					95	96					154
										30										91					92	93					155
DLEF/Canard							10	10										112		111		113									
										20								109		108		110									
										10								106		105		107									
							-20	-20										121		120		122									
										20								118		117		119									
										30								115		114		116									
							-30	-30										130		129		131									
										20								127		126		128									
										10								124		123		125									
							-40	-40										416		415		417									
										20								413		412		414									
										30								410		409		411									
							-60	-60		30								428		427		429									
										20								425		424		426									
										10								422		421		423									

ICE Phase II ADF Run Plan

Configuration	Pitch Flaps L	Pitch Flaps R	Elevons L	Elevons R	Ailerons L	Ailerons R	Canard L	Canard R	LEF L	LEF R	Spoiler L	Spoiler R	Deflector L	Deflector R	AMT L	AMT R	AOA=var; AOS= -20	-10	-5	0	5	10	20	AOS=var; AOA= 0	10	20	22.5	25	27.5	30	32.5
Sym LEF/Canard	0	0	0	0	0	0	10	10	10	10	0	0	0	0	0	0		68		67		69									
							-10	-10										71		70		72									
							-20	-20										65		64		66									
							-30	-30	30	30								434		433		435									
							-40	-40										407		406		408									
							-60	-60										431		430		432									
							-10	-10	20	20								74		73		75									
							-20	-20										62		61		63									
							-30	-30										59		58		60									
Skewed AMT/LEF							0	0	30	0					30					378											
Interaction															60					379											
Small AMT(1)									0									81		80		82			83					84	
															30			87		86		88									
															10					89											
															-10					90											
Large AMT(3)																				297											
															10					306											
															30			308		307		309									
															60			308		317		319			320					321	
Skewed AMT(2)																		360		359		361			362					363	
															30			349		348		350									
															10					347											
															-10					338											
															60		437	438		436		439	440		441		442			443	
Tape Over Inlet Exhaust															0					326					327					328	
							Off	Off												329					330					331	

Figure 2-7: Configuration 201 Run Log (Concluded)

| ICE Phase II ADF Run Plan | | |

ICE Phase II ADF Run Plan
Configuration 101-Series

	Pitch Flaps		Elevons		LEF		Spoiler		Deflector		AMT		AOA=var; AOS=							AOS=var; AOA=								Schedule
Configuration	L	R	L	R	L	R	L	R	L	R	L	R	-20	-10	-5	0	5	10	20	0	15	20	22.5	25	27.5	30	32.5	
SSD3				0				60		0						27												A1
OB Fwd Location										60						40				41	42	43	44	45	46	47	48	
								30		30						39/49												
										0						28												
								15								29												
										15						30/58												
SSD 3/Elevon				-30				60		60						60					61							
				-10												62												
				10												63												
				30												64					65							
								30		30						35/50												
				10												36/51												
				-10												37/52												
				-30												38/53												
								15		15						31/54												
				-10												32/55												
				10												33/56												
				30												34/57												
Spoiler 3/Elevon								60		0						21					22							
				10												23												
				-10												24												
				-30												25					26							
SSD3/Pitch Flap		30		0						60						66												

Note: Runs 30 - 39 were inadvertently run with Fwd Spoilers and Aft Deflectors. Configurations were re-run using correct spoiler/deflector geometry (runs 49 - 58).

ICE Phase II ADF Run Plan
Configuration 101-Series

	Pitch Flaps		Elevons		LEF		Spoiler		Deflector		AMT		AOA=var; AOS=							AOS=var; AOA=								Schedule
Configuration	L	R	L	R	L	R	L	R	L	R	L	R	-20	-10	-5	0	5	10	20	0	15	20	22.5	25	27.5	30	32.5	
Small AMT (No 1)	0	0	0	0	0	0	0	0	0	0	-10	0				132												A1
											10					133												
											30		135	136		134		137	138									
											40					139												
											60		141	142		140		143	144									
Skewed AMT (No 2)											-10					190												
											10					191												
											30		193	194		192		195	196									
											40					208												
											60		204	205		203		206	207									
Large AMT (No 3)											-10					168												
											10					169												
											30		171	172		170		173	174									
											40					175												
											60		177	178		176		179	180									
Skewed AMT/LEF					40									201		200		202										
											30			198		197		199										
LEF											0			210		209		211										
Large AMT + Fillet					0						30					182												
											60					181												
Large AMT +																184												
Gurney Flap TEU 90											30					183												
Large AMT +																186												
Gurney Flap TED 90											60					185												

Figure 2-8: Configuration 101 Run Log (Concluded)

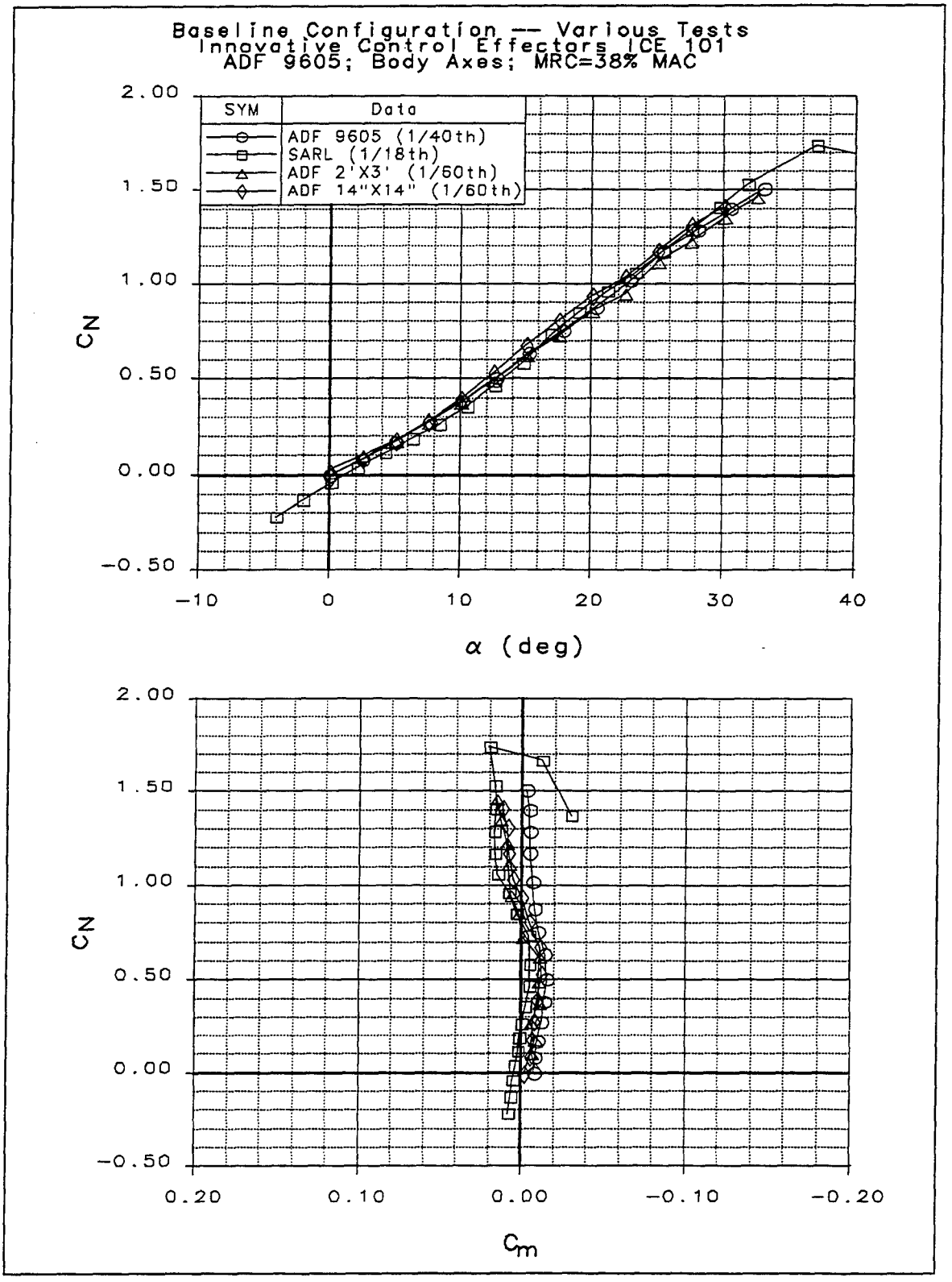

Figure 2-9: Configuration 101 Longitudinal Data

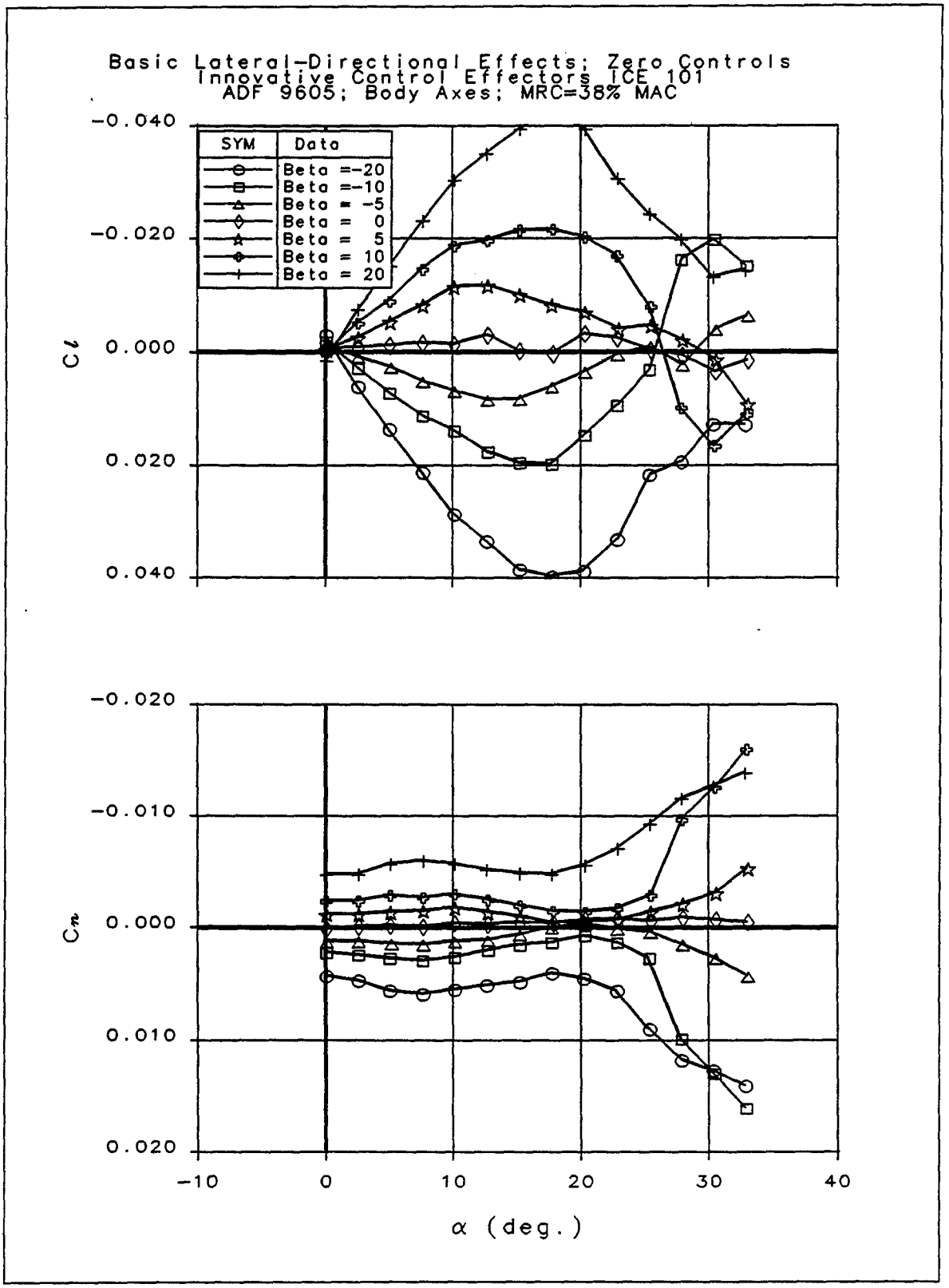

Figure 2-10: Configuration 101 Lateral-Directional Stability Characteristics

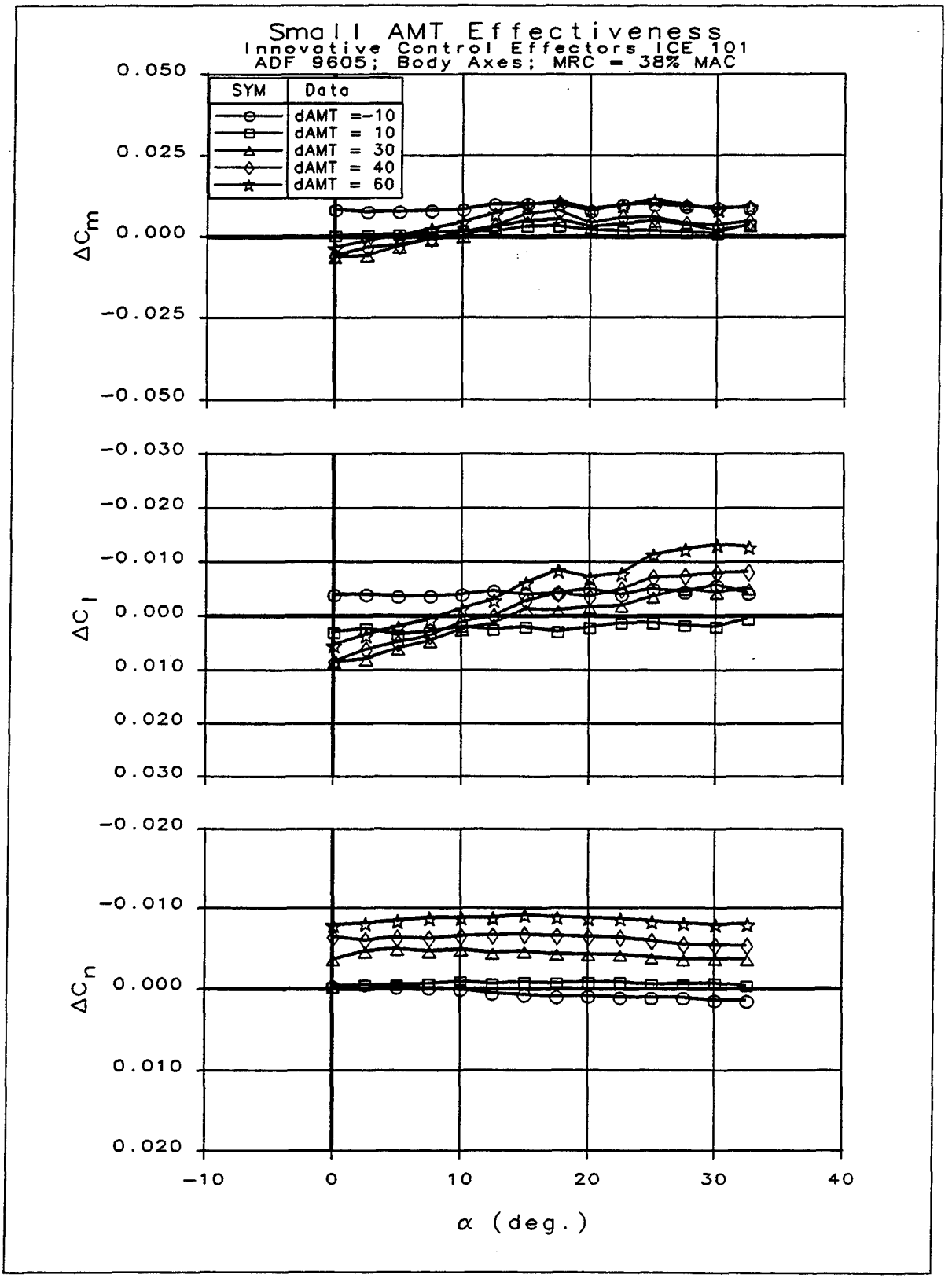

Figure 2-11: Small AMT Control Effectiveness on Configuration 101

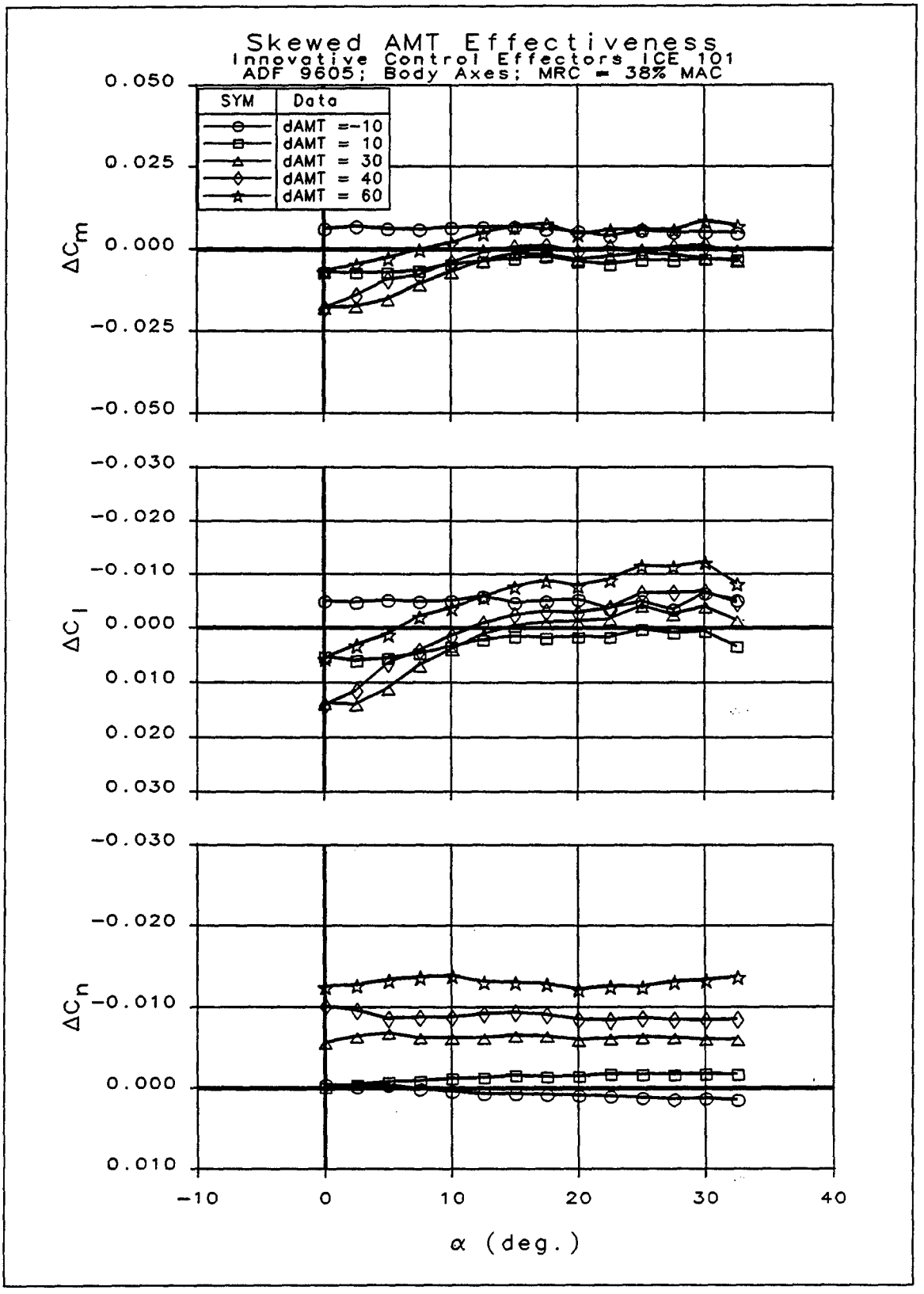

Figure 2-12: Skewed AMT Control Effectiveness on Configuration 101

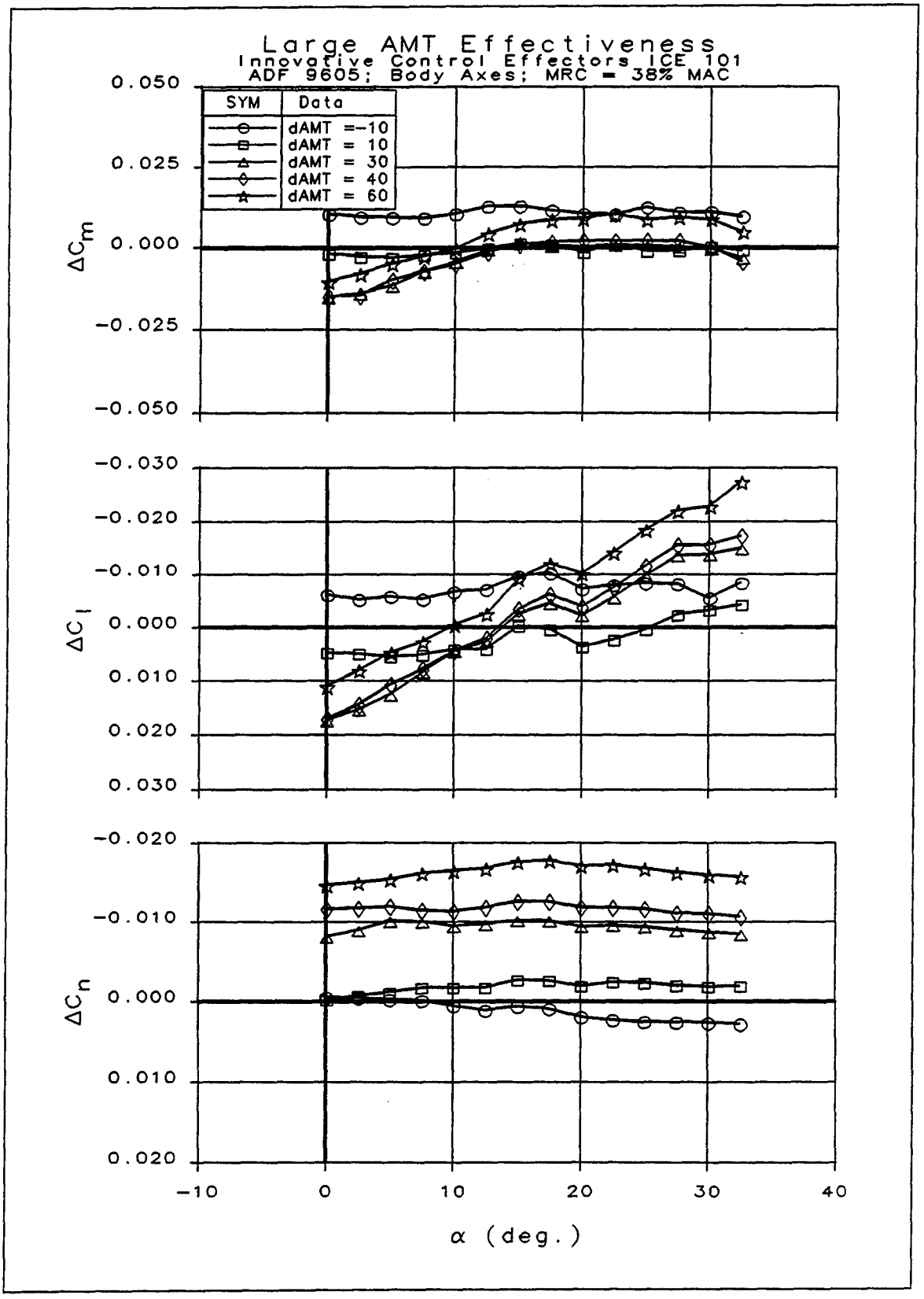

Figure 2-13: Large AMT Control Effectiveness on Configuration 101

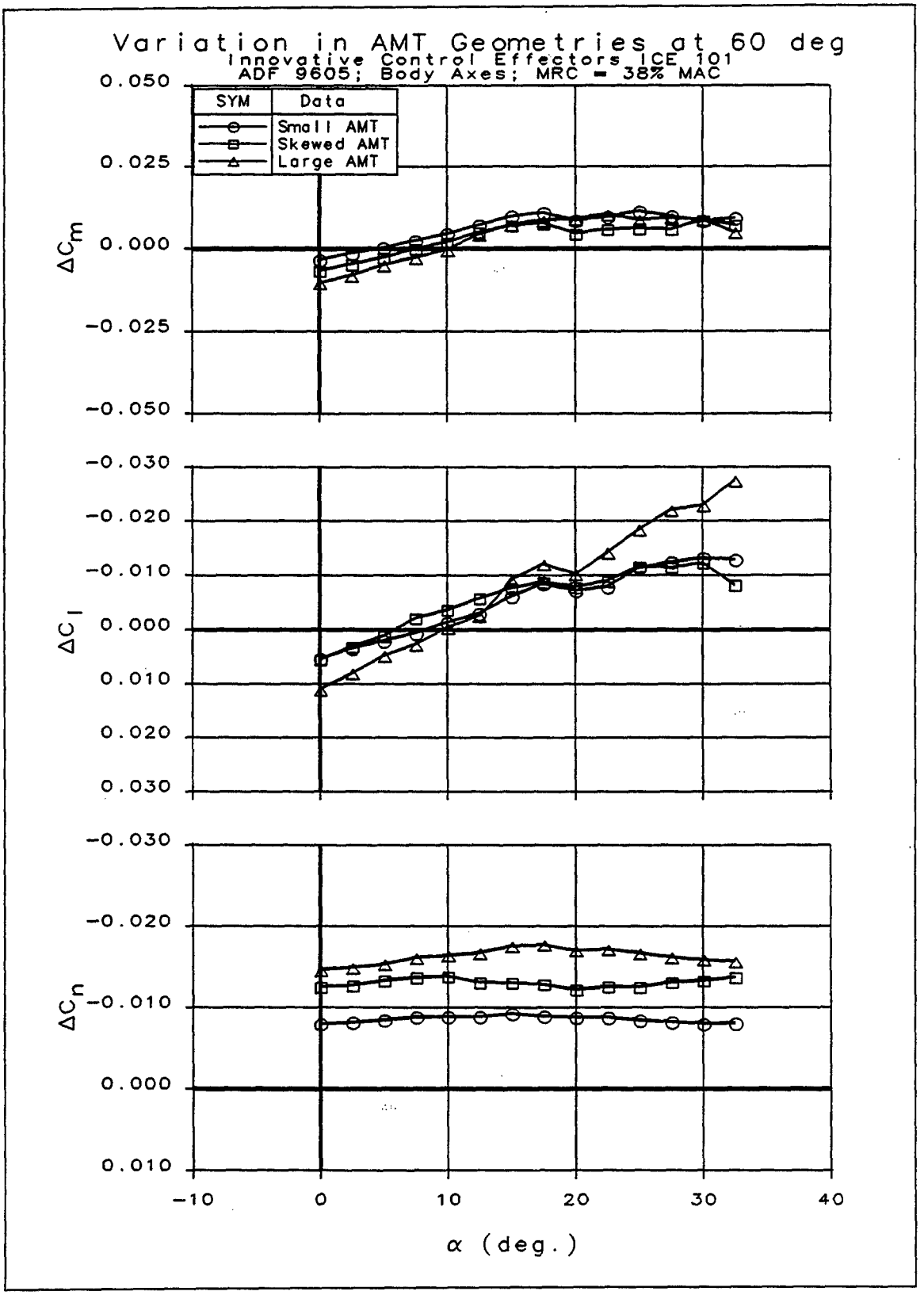

Figure 2-14: AMT Control Effectiveness Variation with Geometry

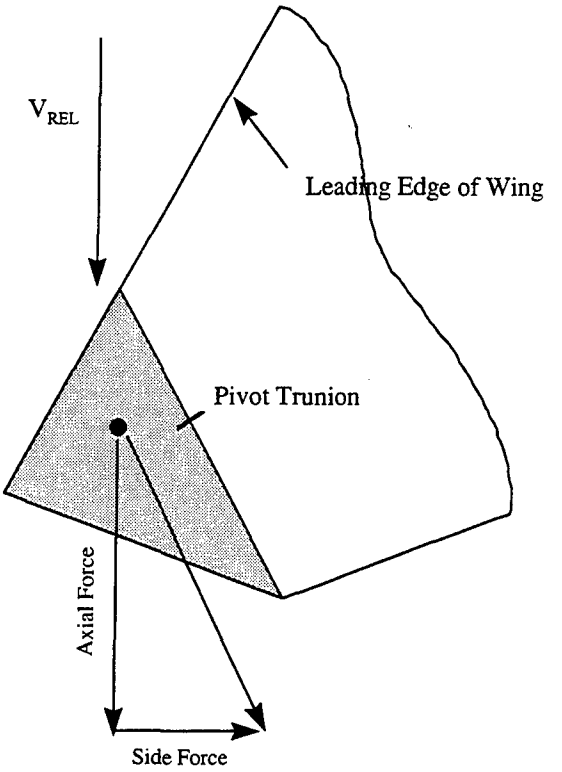

Figure 2-15: Diagram of Side Force and Axial Force Generated By Skewed AMT Deflection

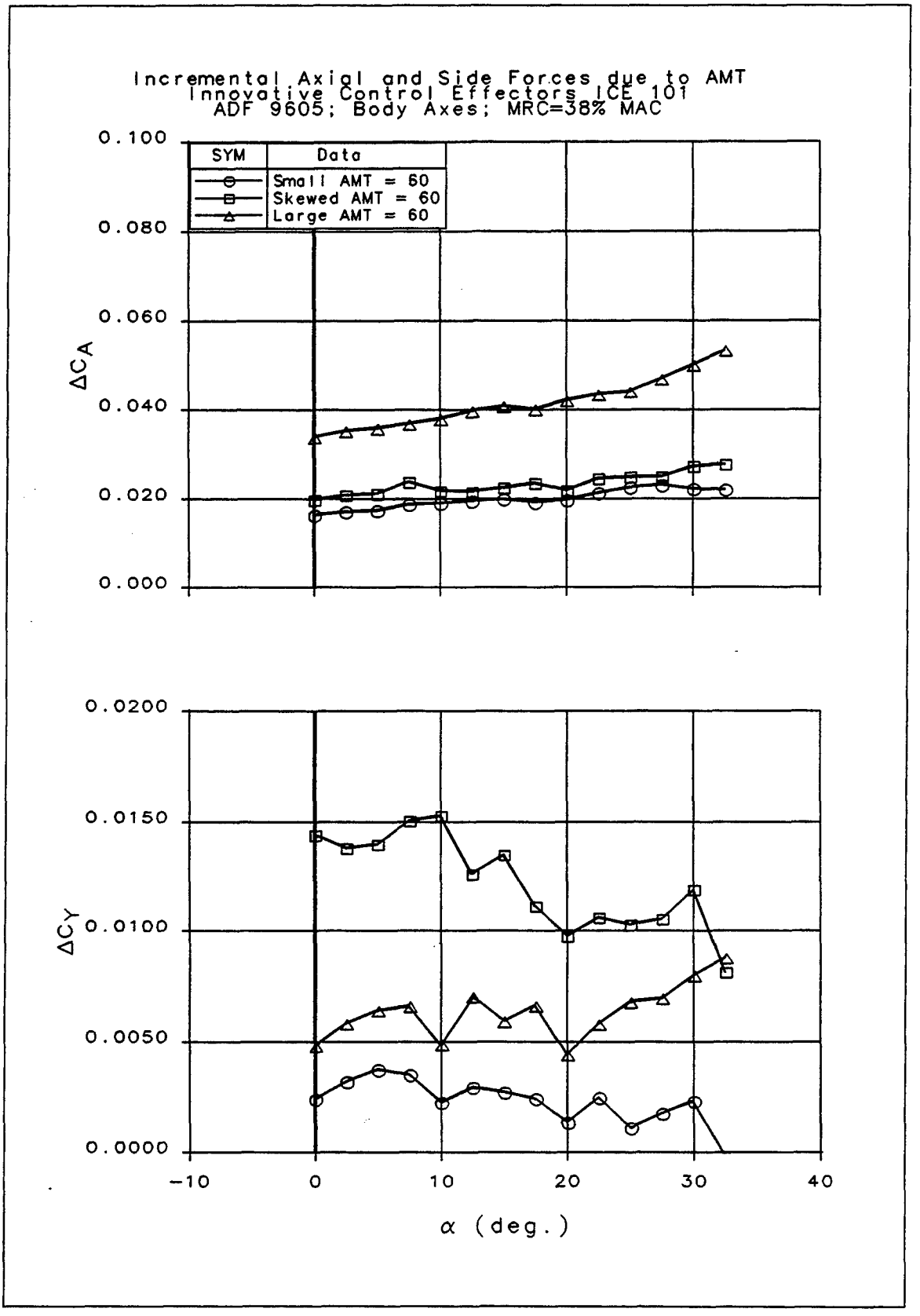

Figure 2-16: Axial Force and Side Force Increments due to AMT Deflection of 60°

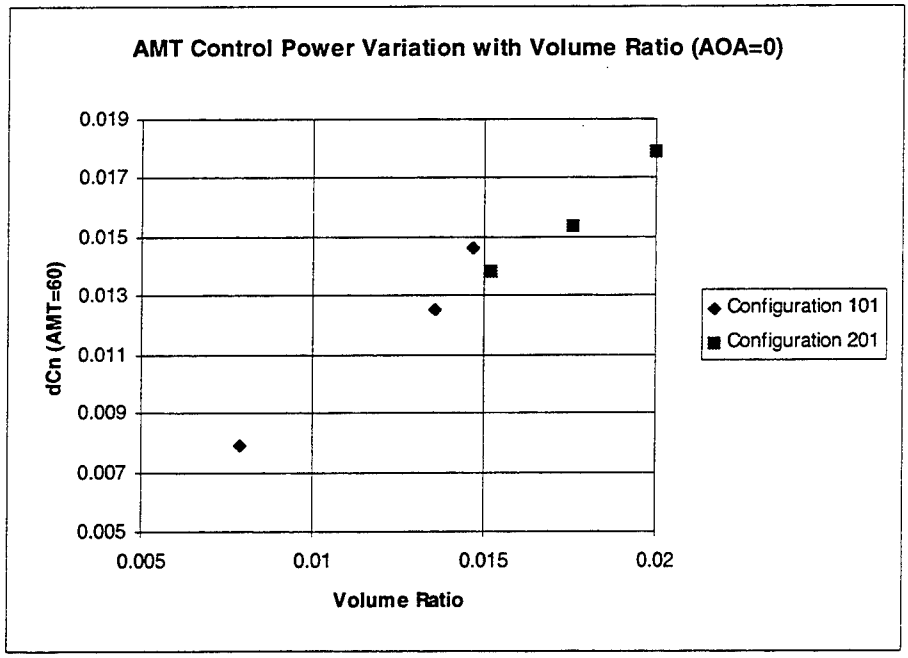

Figure 2-17: Relationship Between AMT Yaw Control Power and Control Volume Ratio

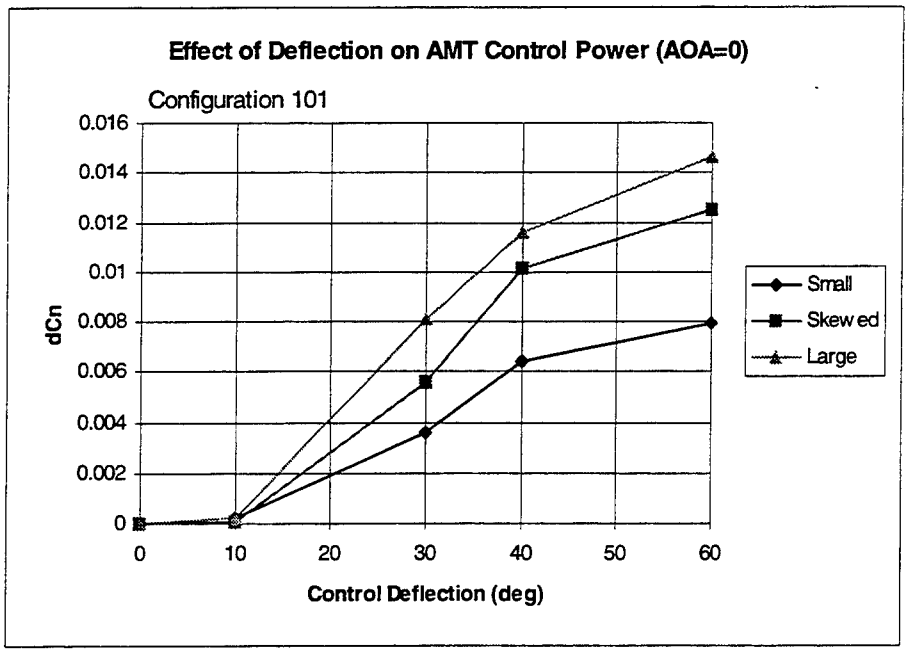

Figure 2-18: Variation of Yaw Power Generated By Various AMTs With Deflection At AOA of 0°

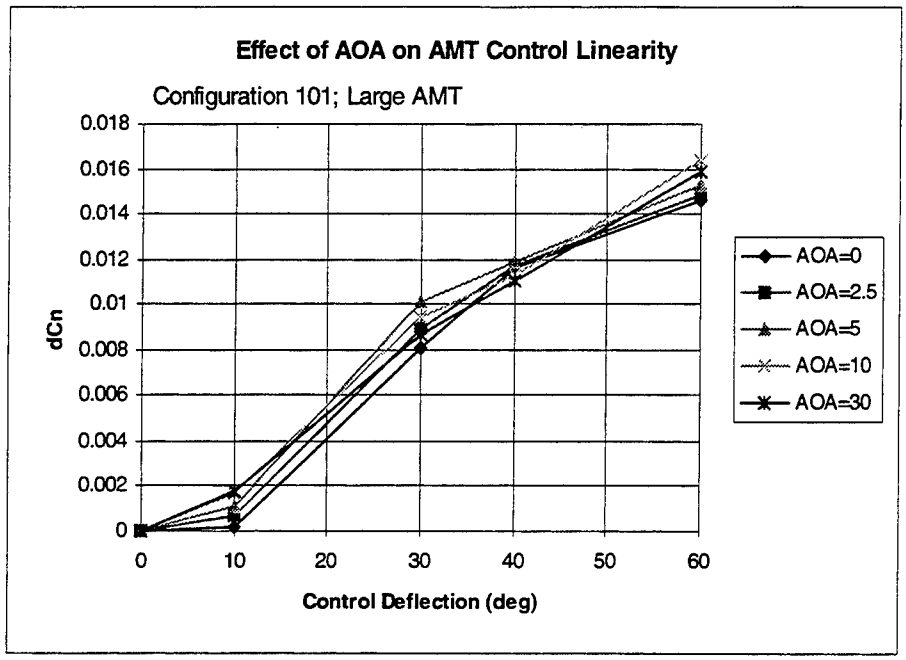

Figure 2-19: Effect of AOA on Variation of Large AMT Yaw Power With Deflection Angle

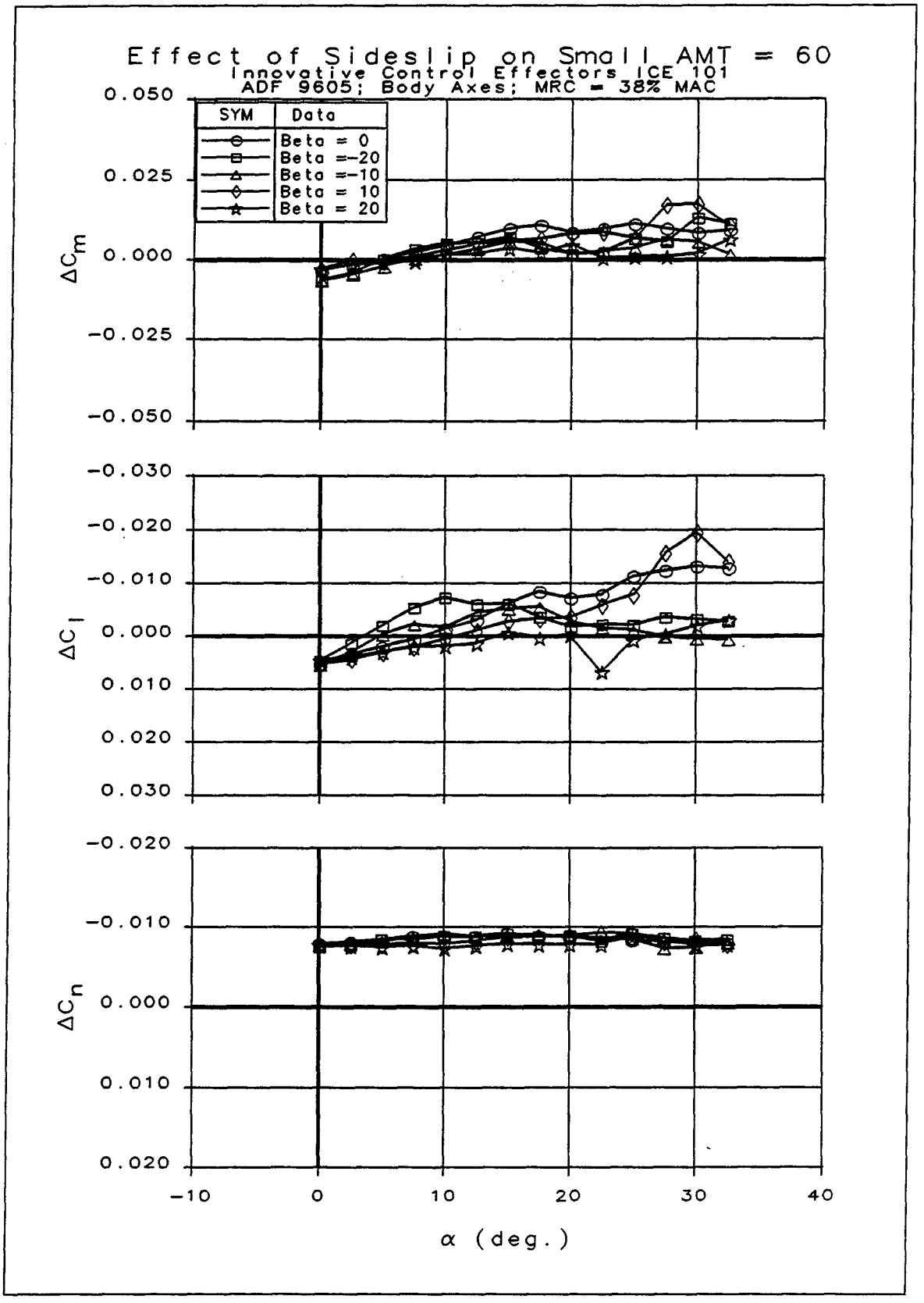

Figure 2-20: Effect of Sidslip on AMT Yaw Power for Configuration 101

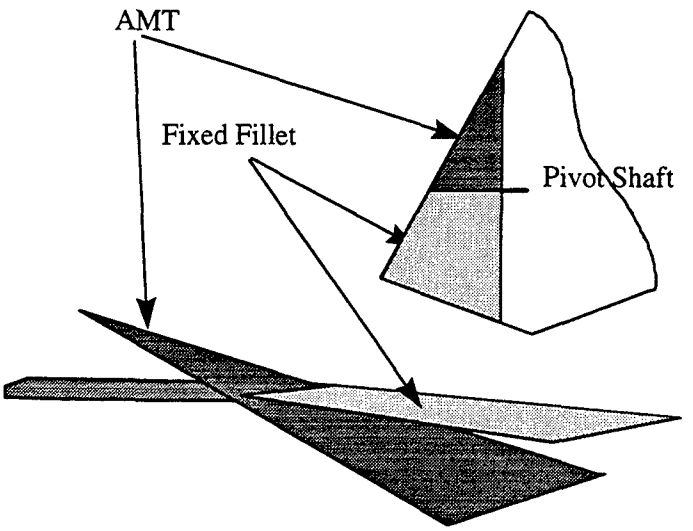

AMT with Aft Fillet

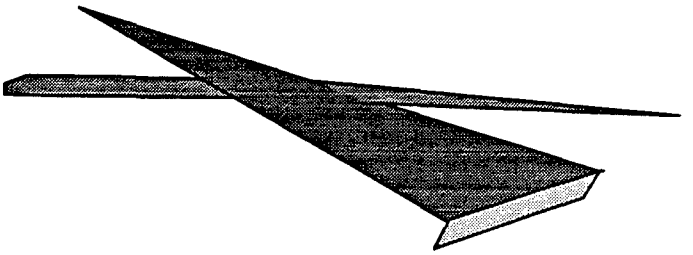

AMT with Gurney Flap Deflected 90 deg TED

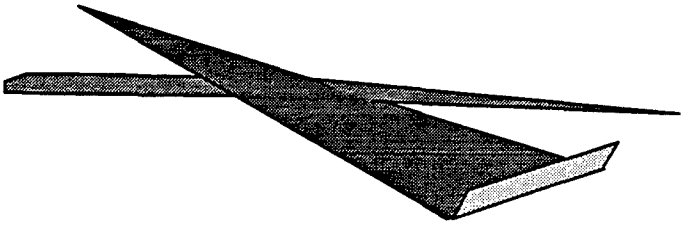

AMT with Gurney Flap Deflected 90 deg TEU

Figure 2-21: Alternate Large AMT Arrangements

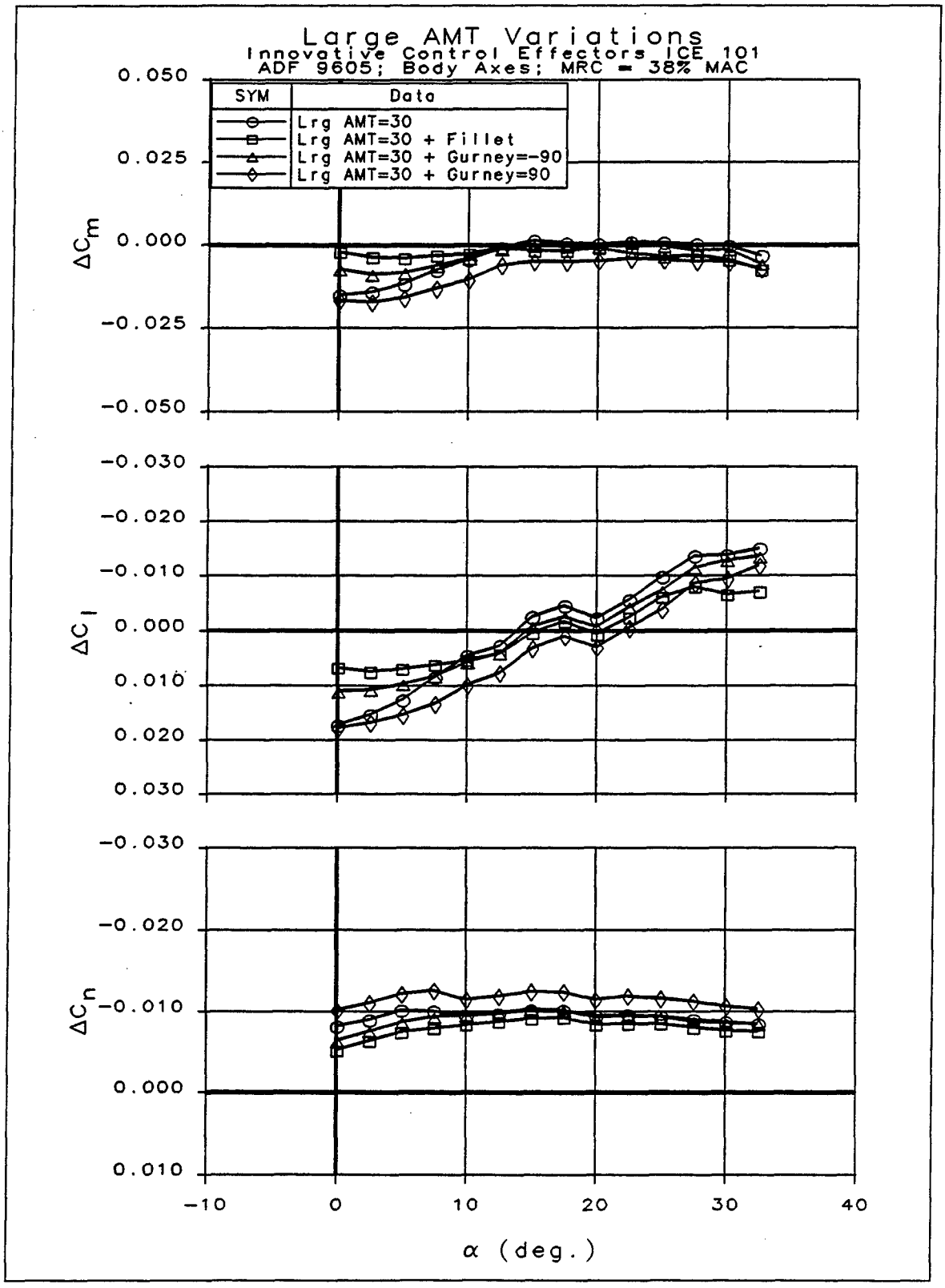

Figure 2-22: Effect of Gurney Flap and Fillet on Large AMT for 30° Deflection

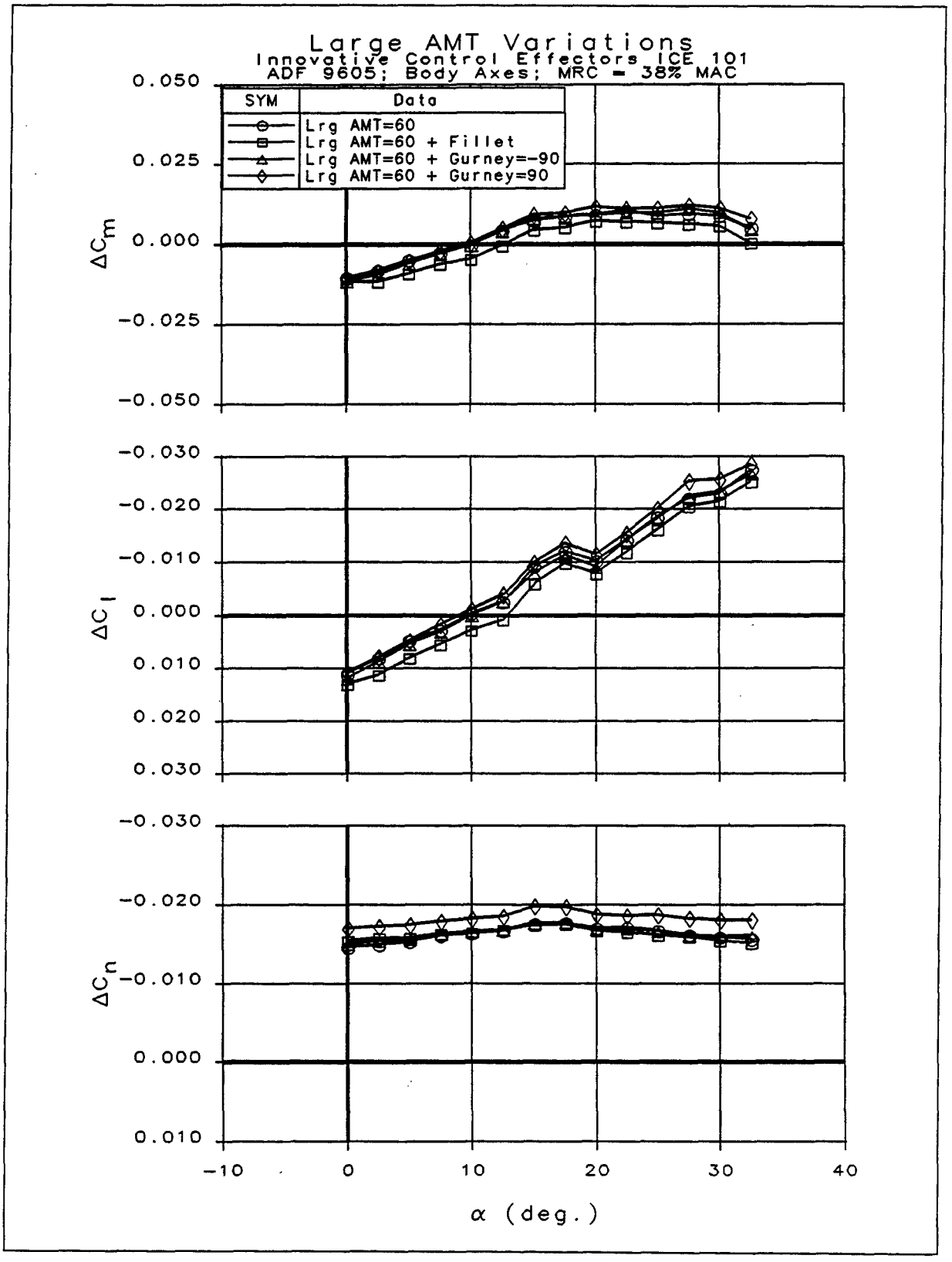

Figure 2-23: Effect of Gurney Flap and Fillet on Large AMT for 60° Deflection

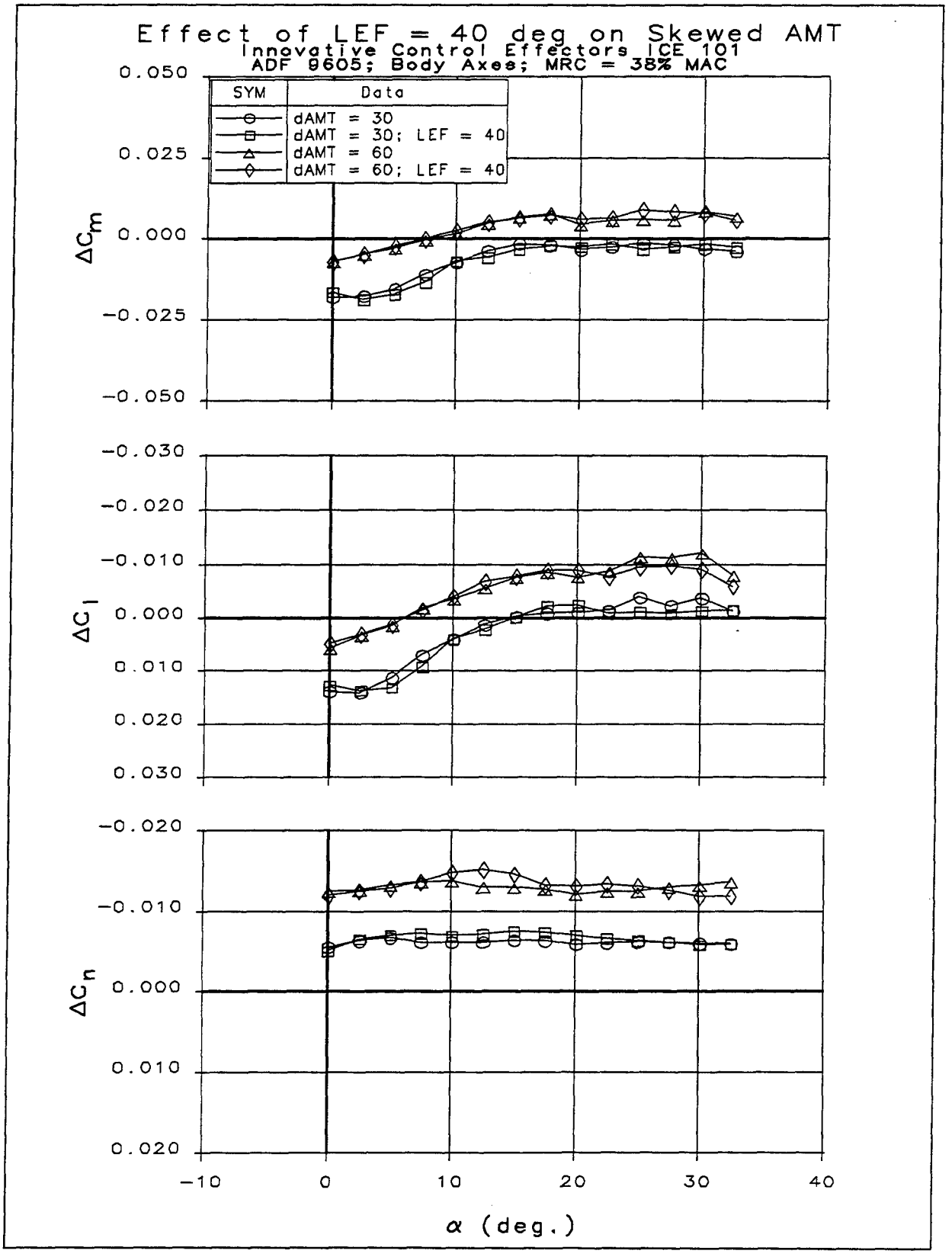

Figure 2-24: LEF Interaction with Skewed AMT on Configuration 101

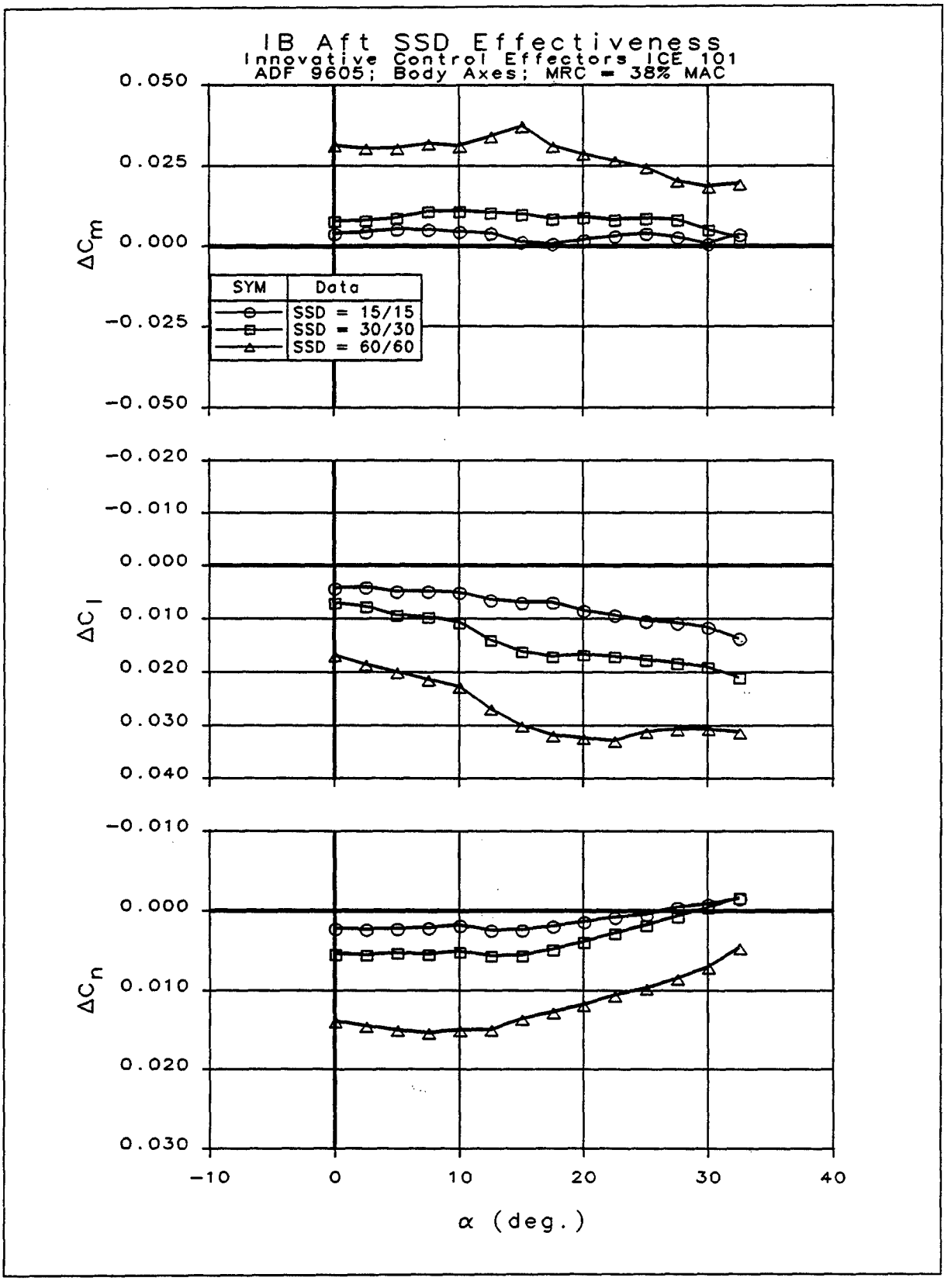

Figure 2-25: IB Aft SSD Control Effectiveness on Configuration 101

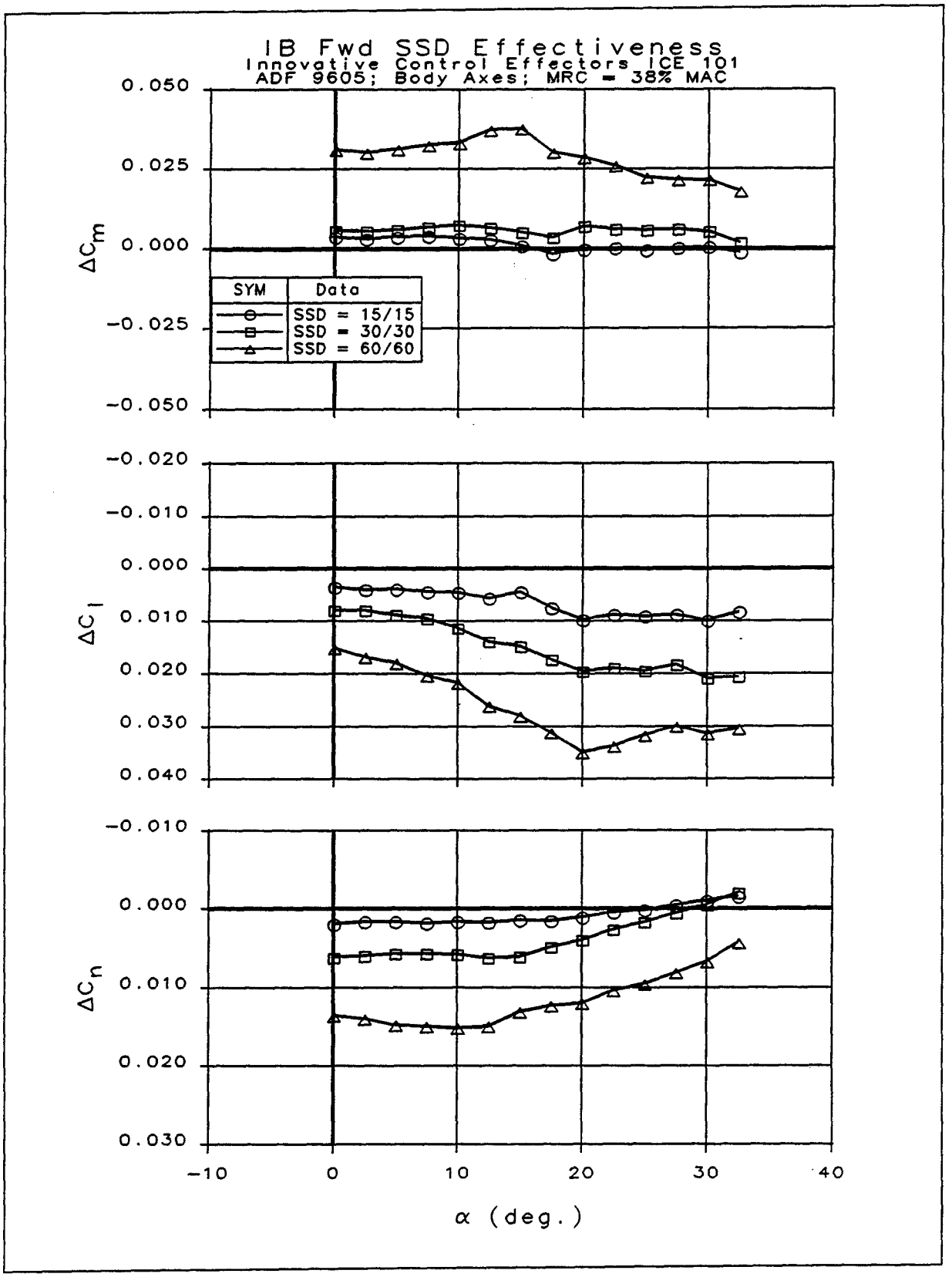

Figure 2-26: IB Fwd SSD Control Effectiveness on Configuration 101

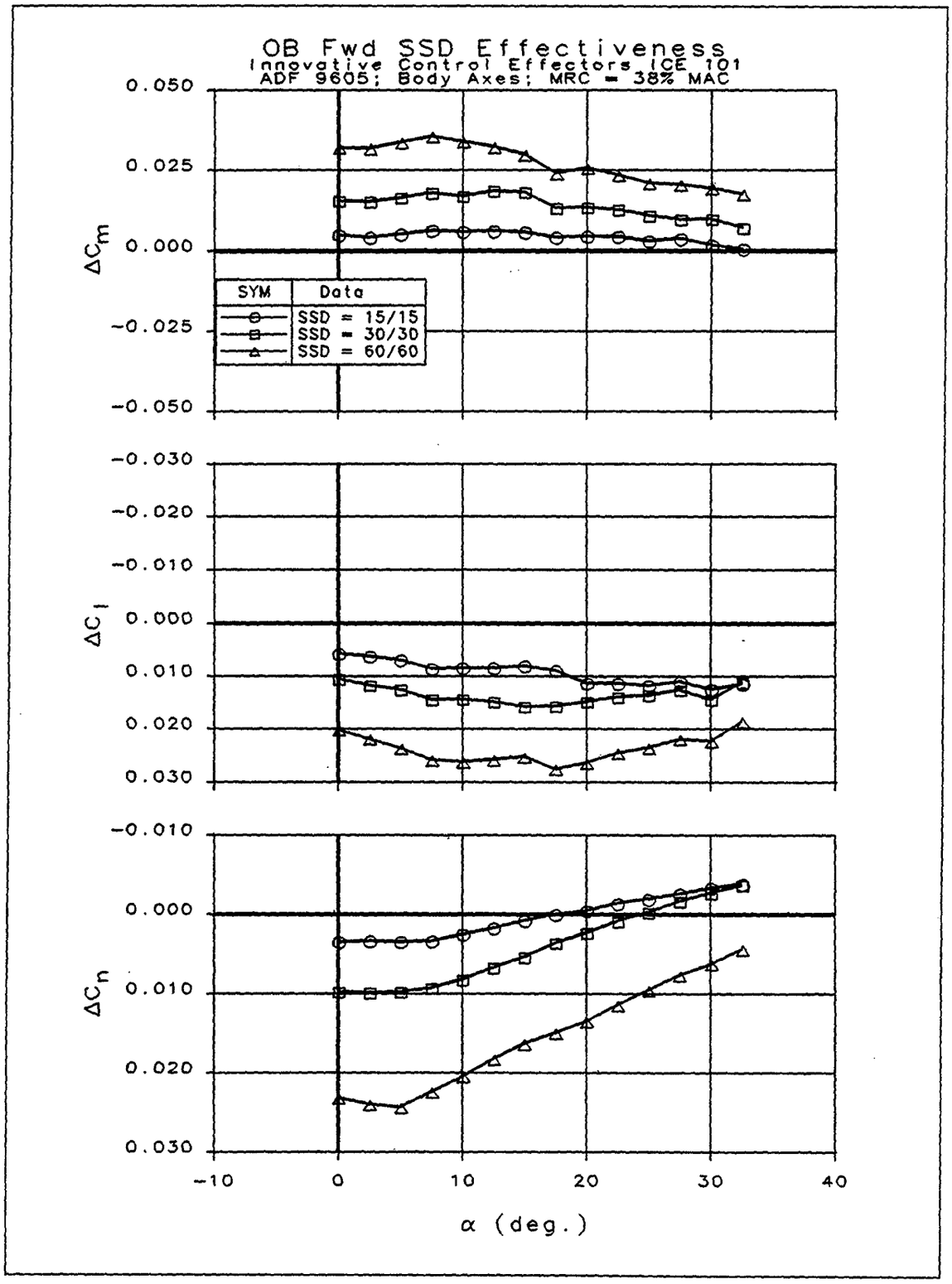

Figure 2-27: OB Fwd SSD Control Effectiveness on Configuration 101

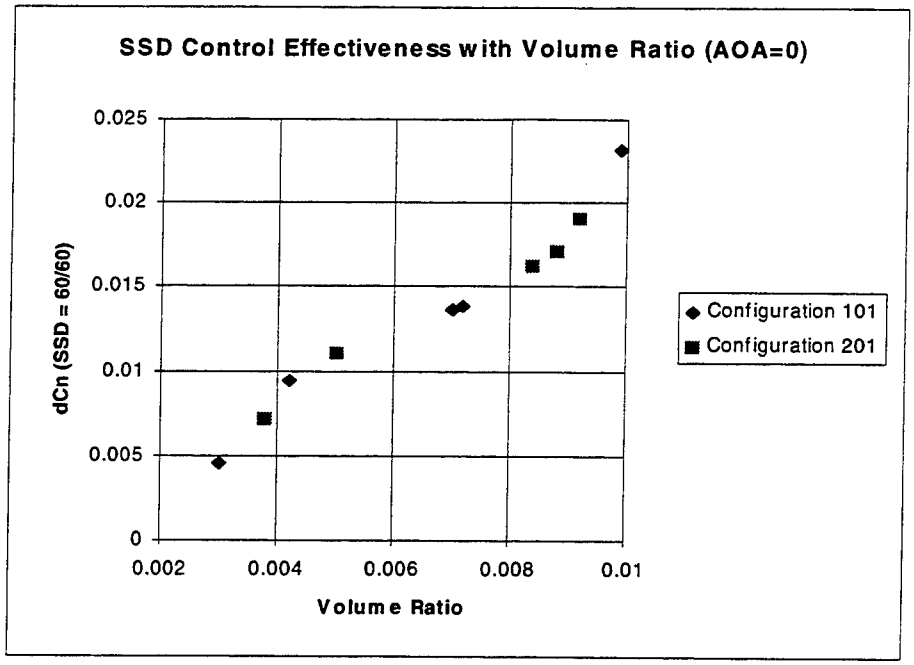

Figure 2-28: SSD Control Power Variation with Control Volume

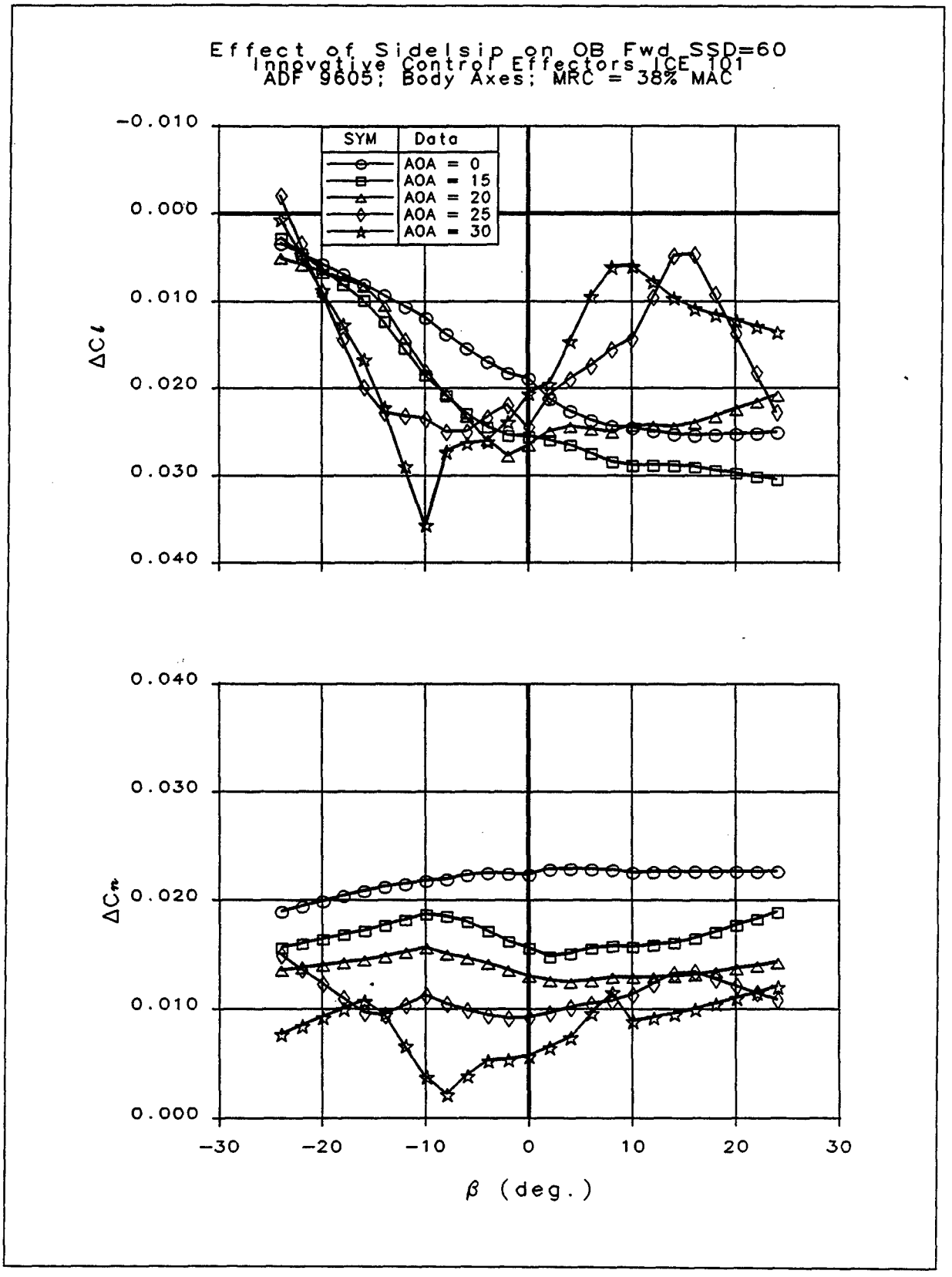

Figure 2-29: Effect of Sideslip on SSD Control Power

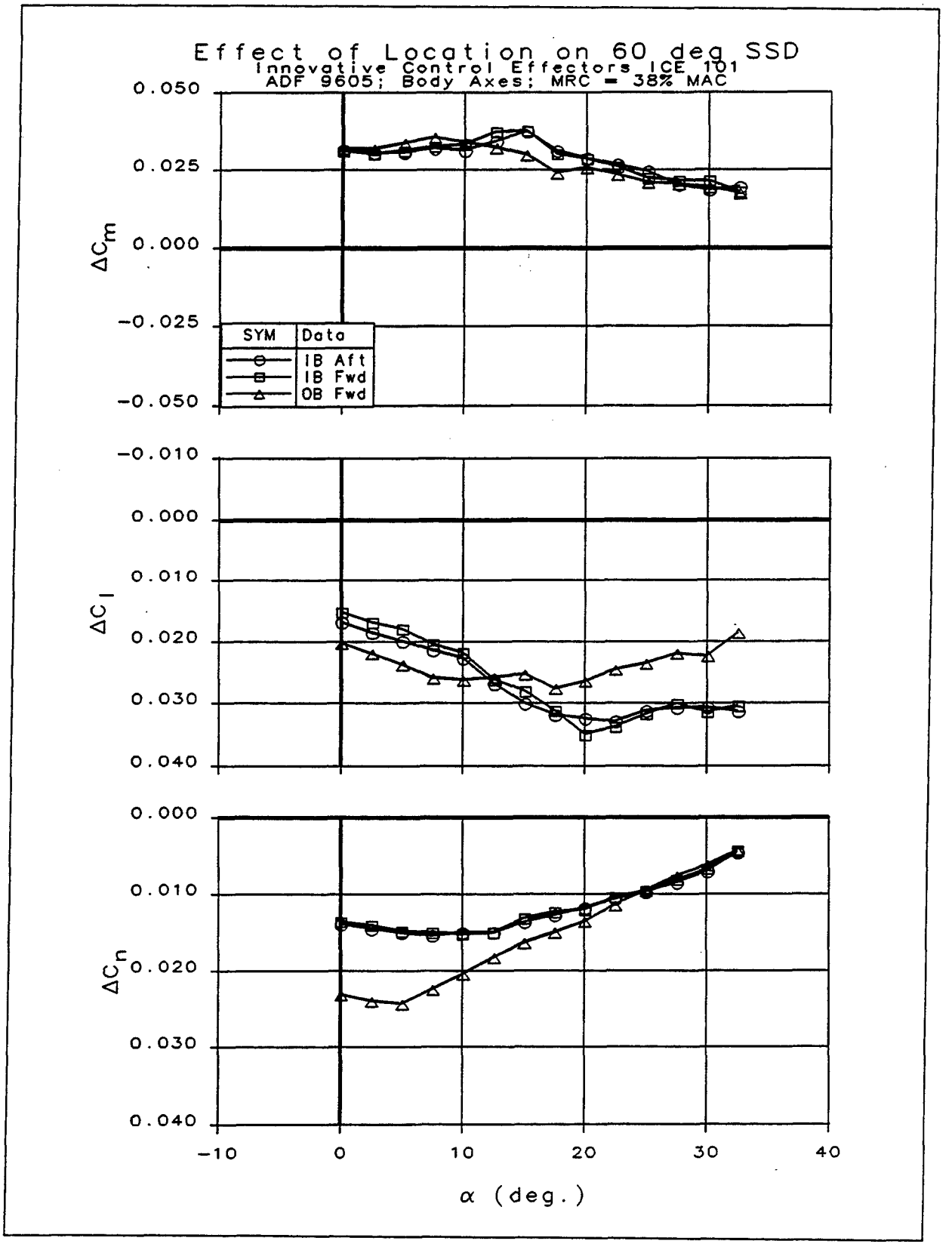

Figure 2-30: Effect of Location on SSD Control Effectiveness

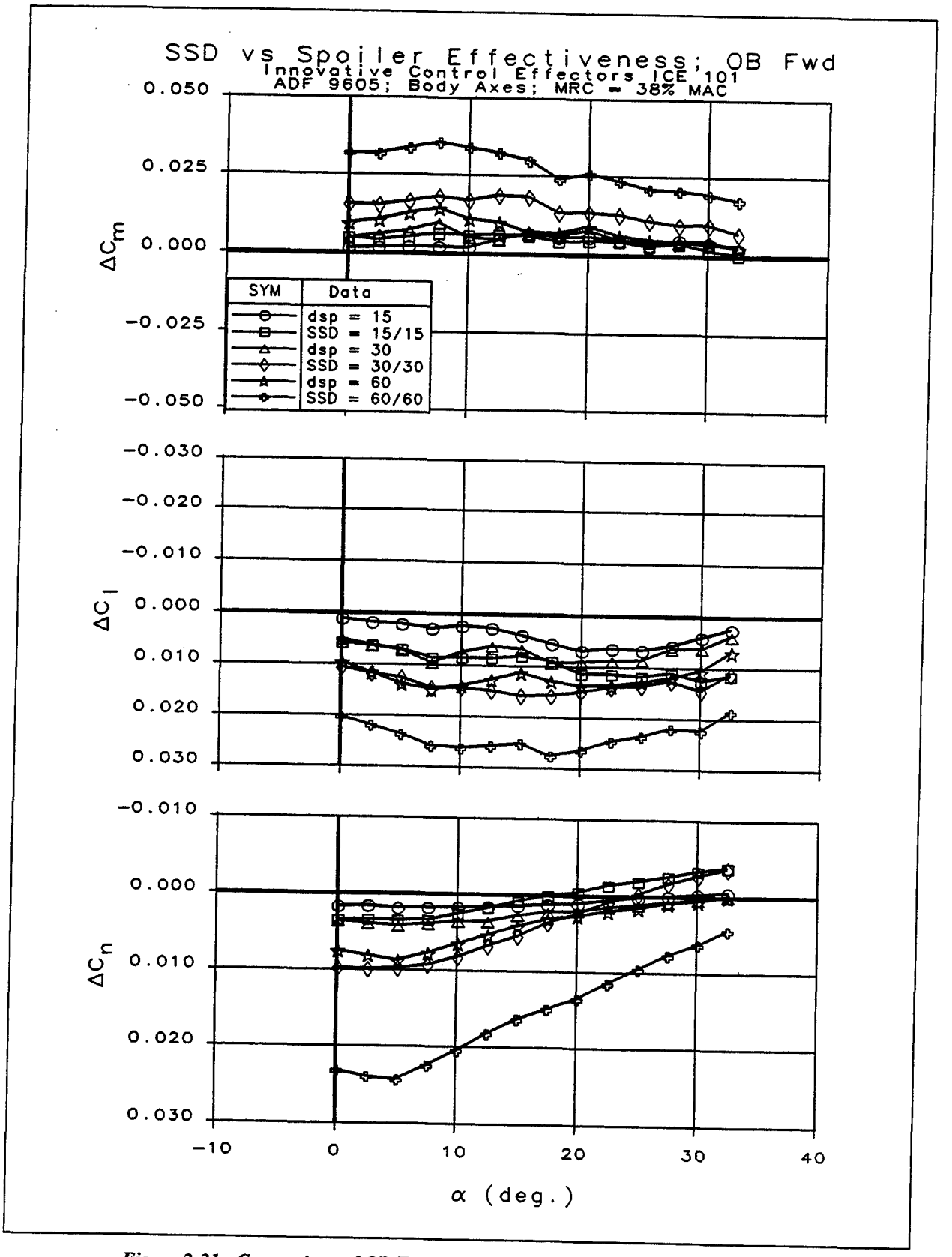

Figure 2-31: Comparison of OB Fwd Spoiler and SSD Control Effectiveness

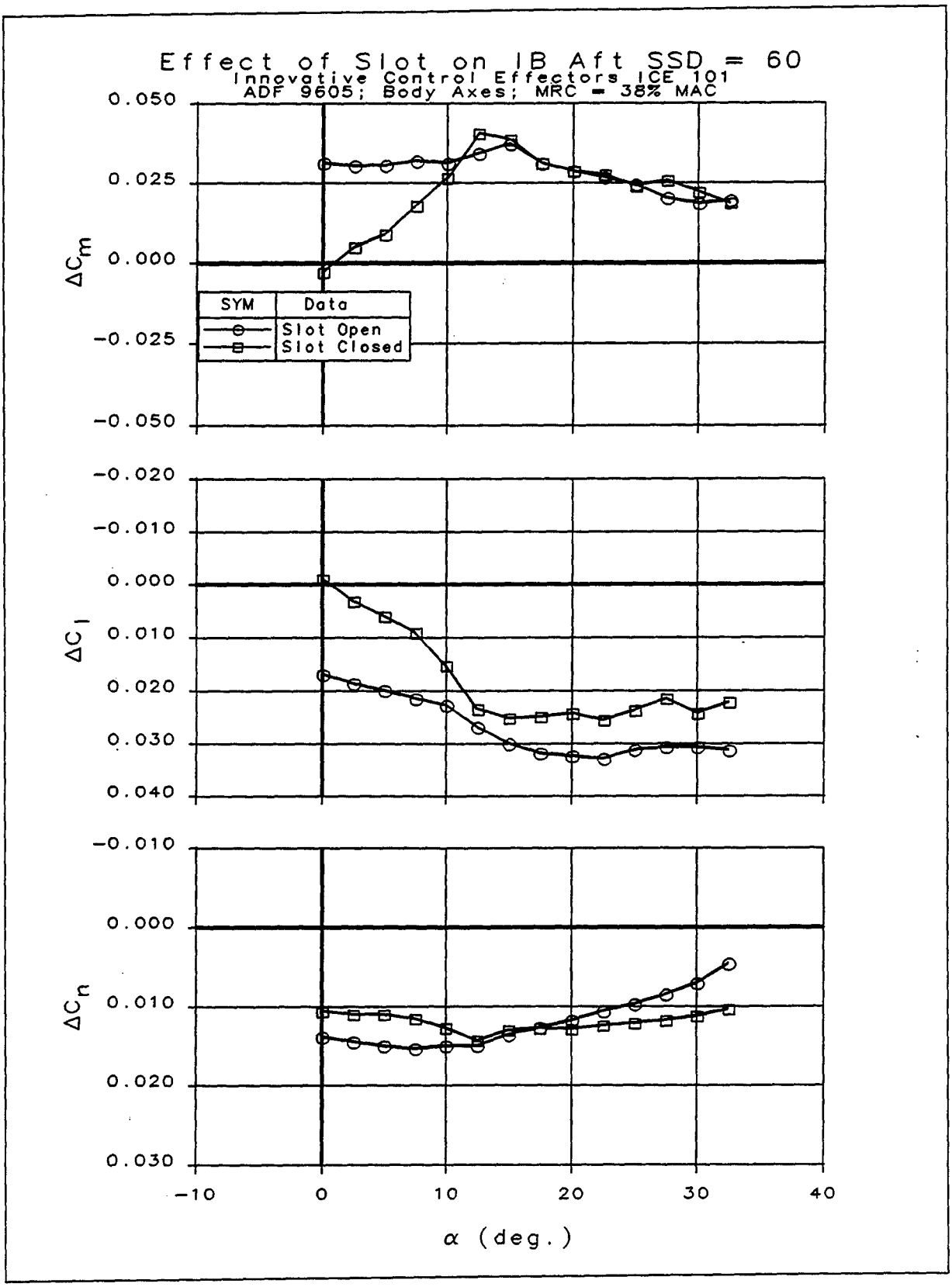

Figure 2-32: Effect of Slot Geometry Variation on SSD Effectiveness

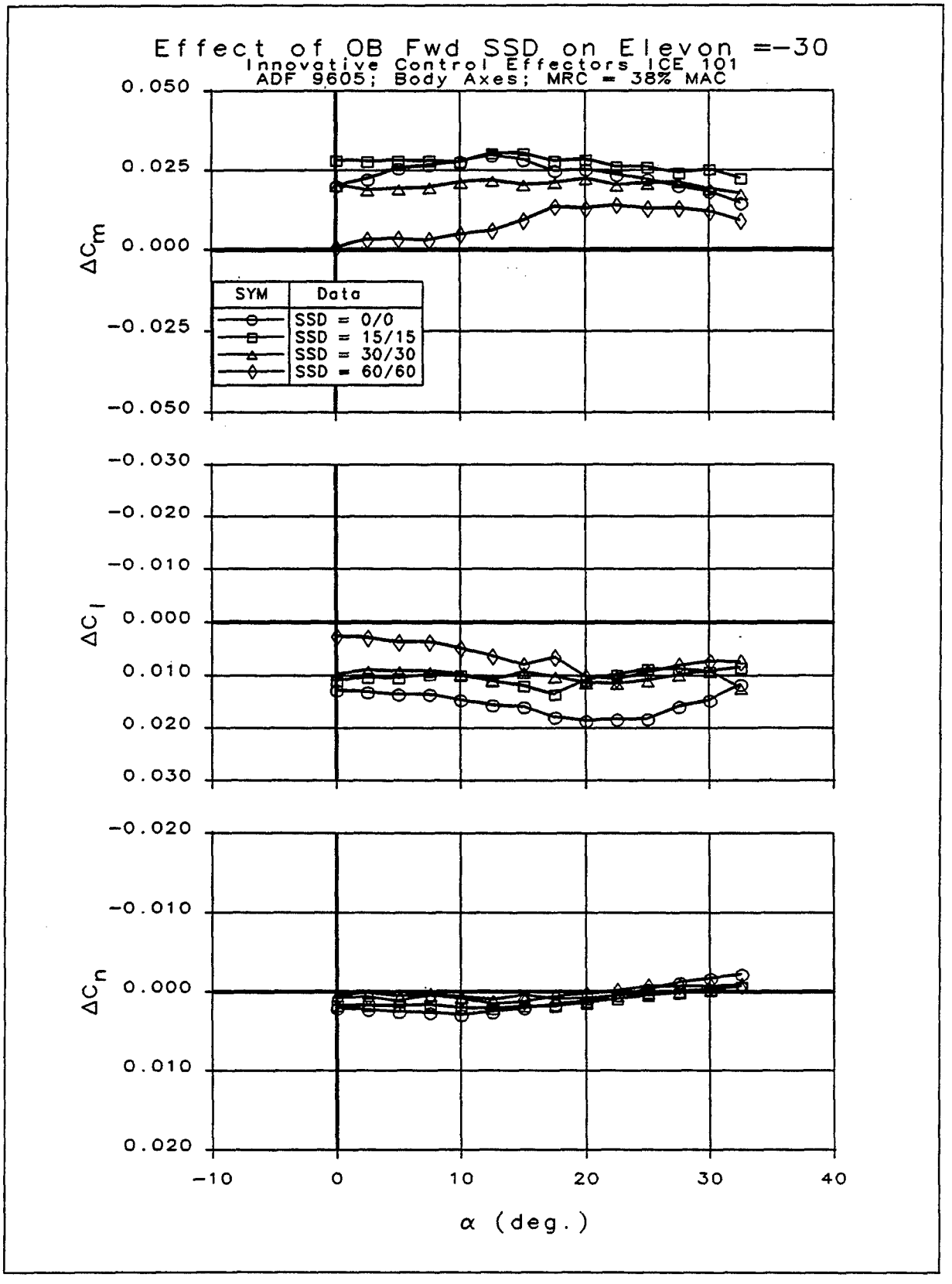

Figure 2-33: Effect of OB Fwd SSD Deflections on Control Power From -30° Elevon Deflection

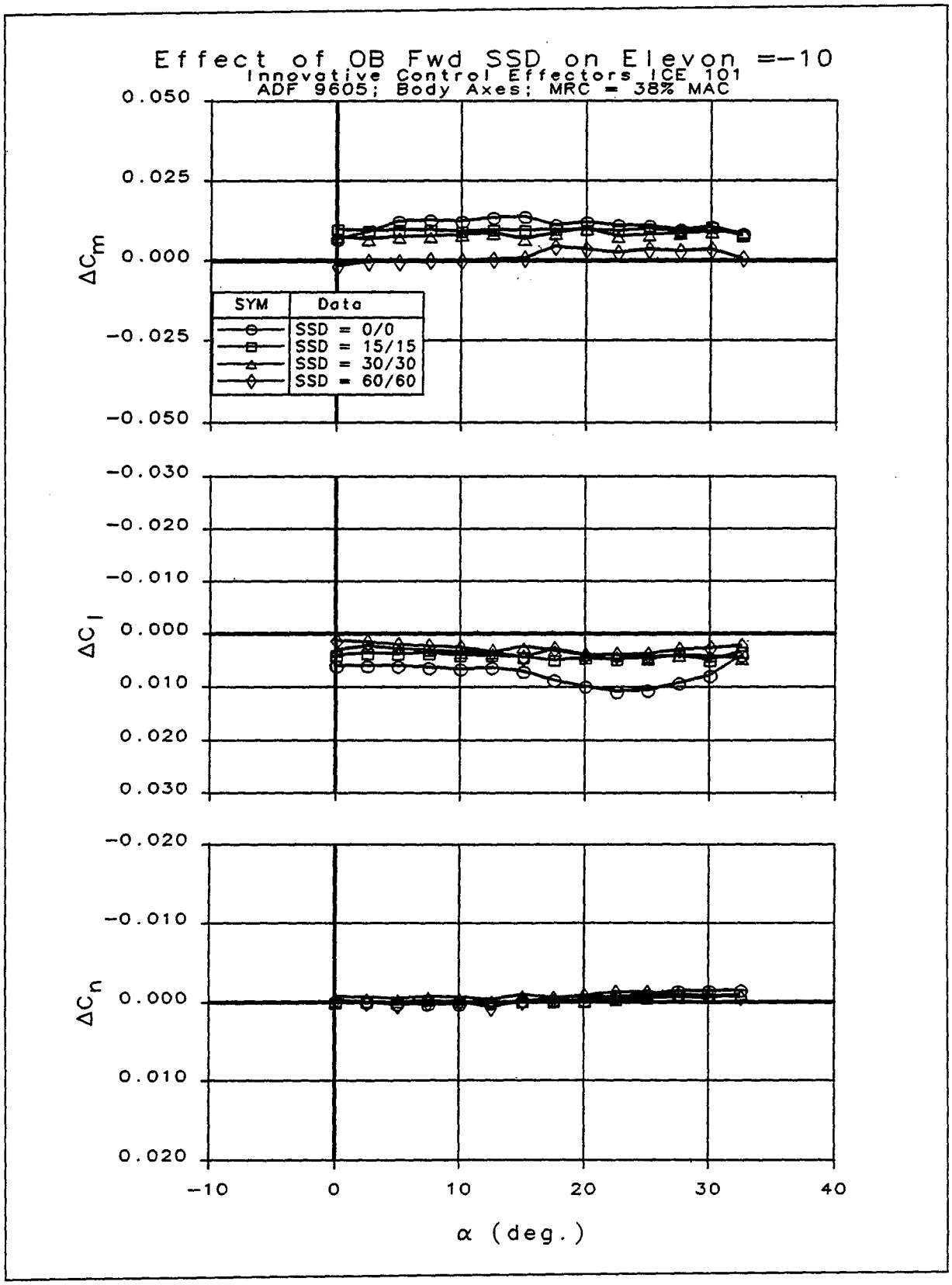

Figure 2-34: Effect of OB Fwd SSD Deflections on Control Power From -10° Elevon Deflection

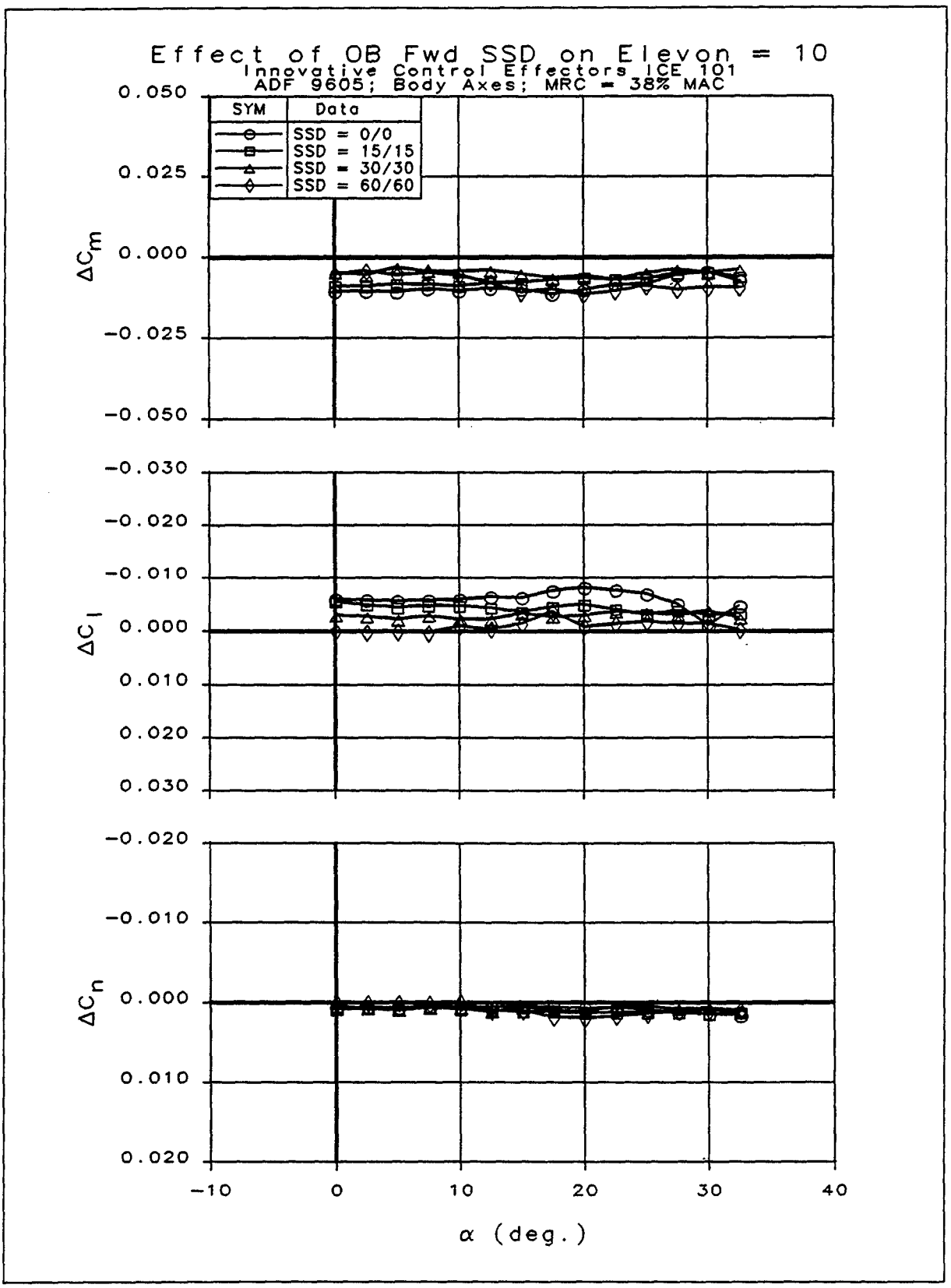

Figure 2-35: Effect of OB Fwd SSD Deflections on Control Power From 10° Elevon Deflection

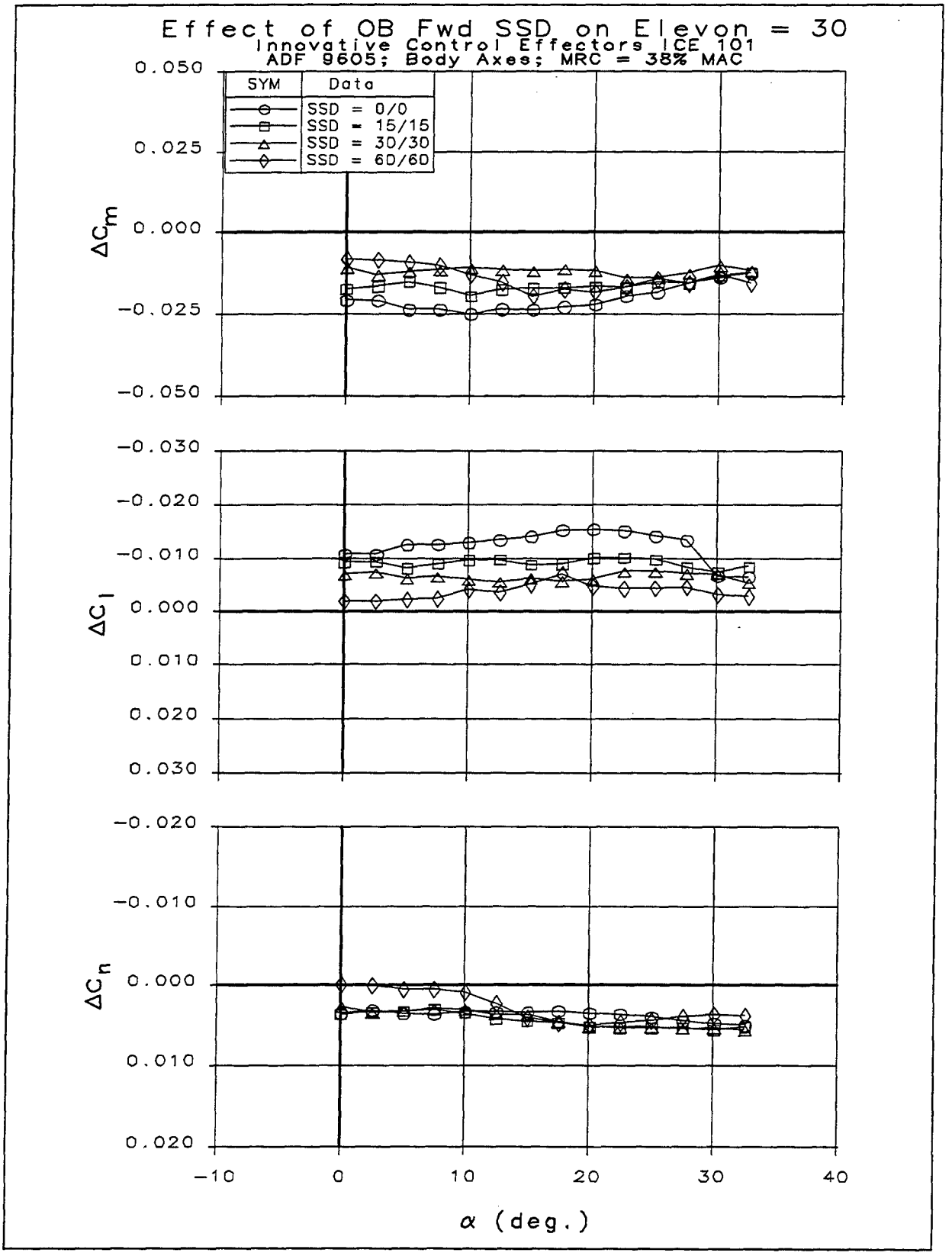

Figure 2-36: Effect of OB Fwd SSD Deflections on Control Power From 30° Elevon Deflection

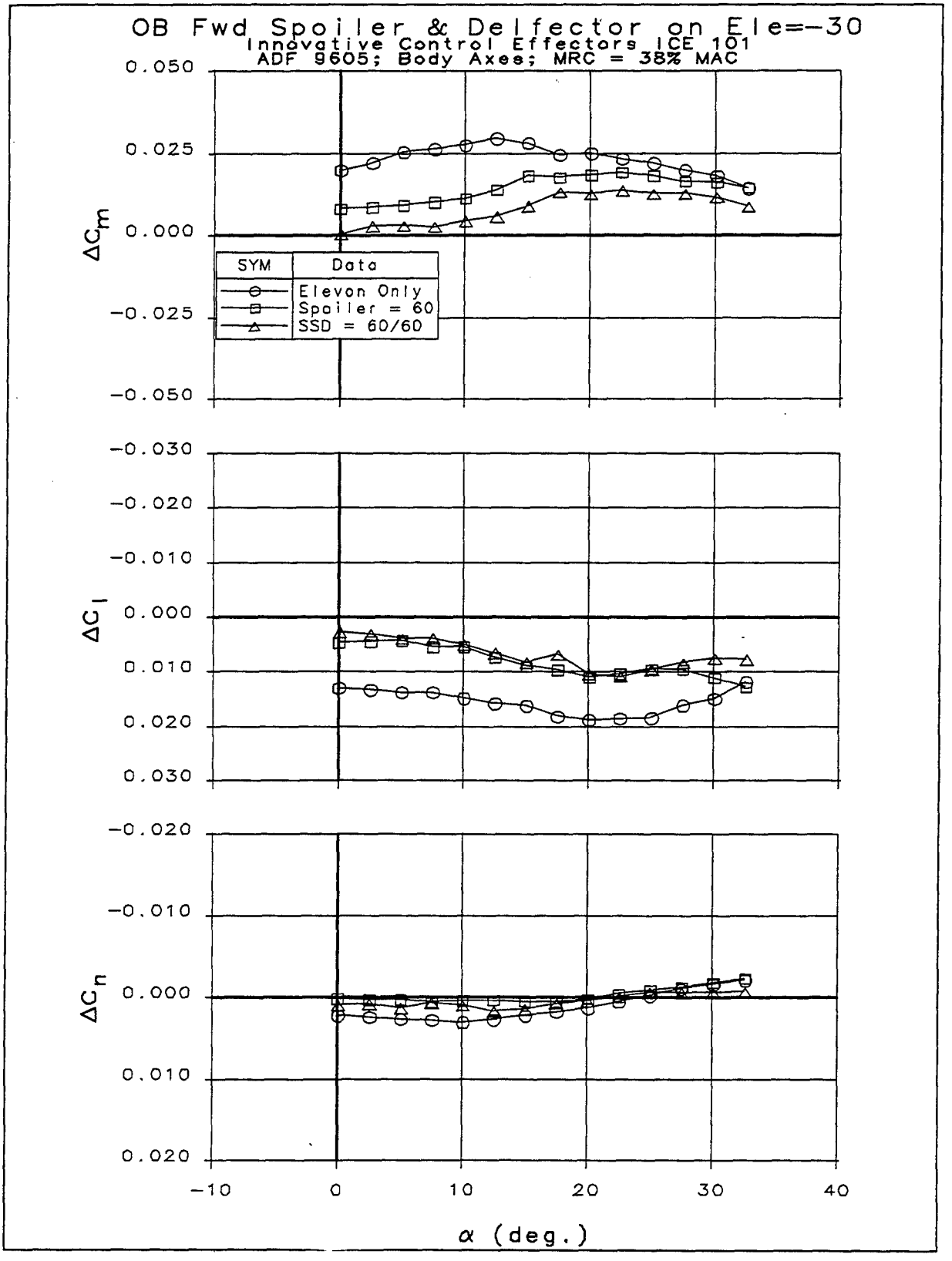

Figure 2-37: Effect of 60° OB Fwd Spoiler and SSD Deflections on Control Power From -30° Elevon Deflection

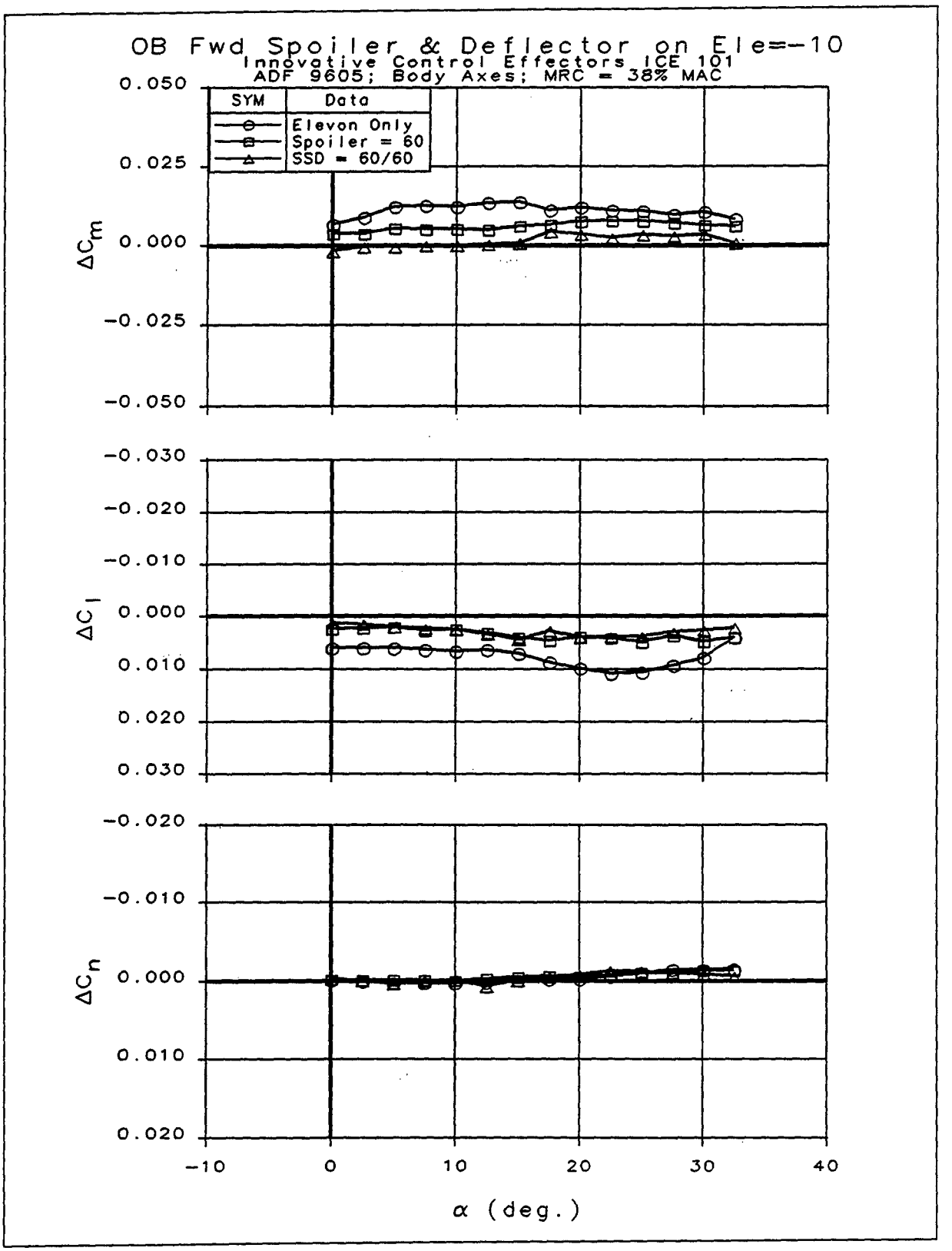

Figure 2-38: Effect of 60° OB Fwd Spoiler and SSD Deflections on Control Power From-10° Elevon Deflection

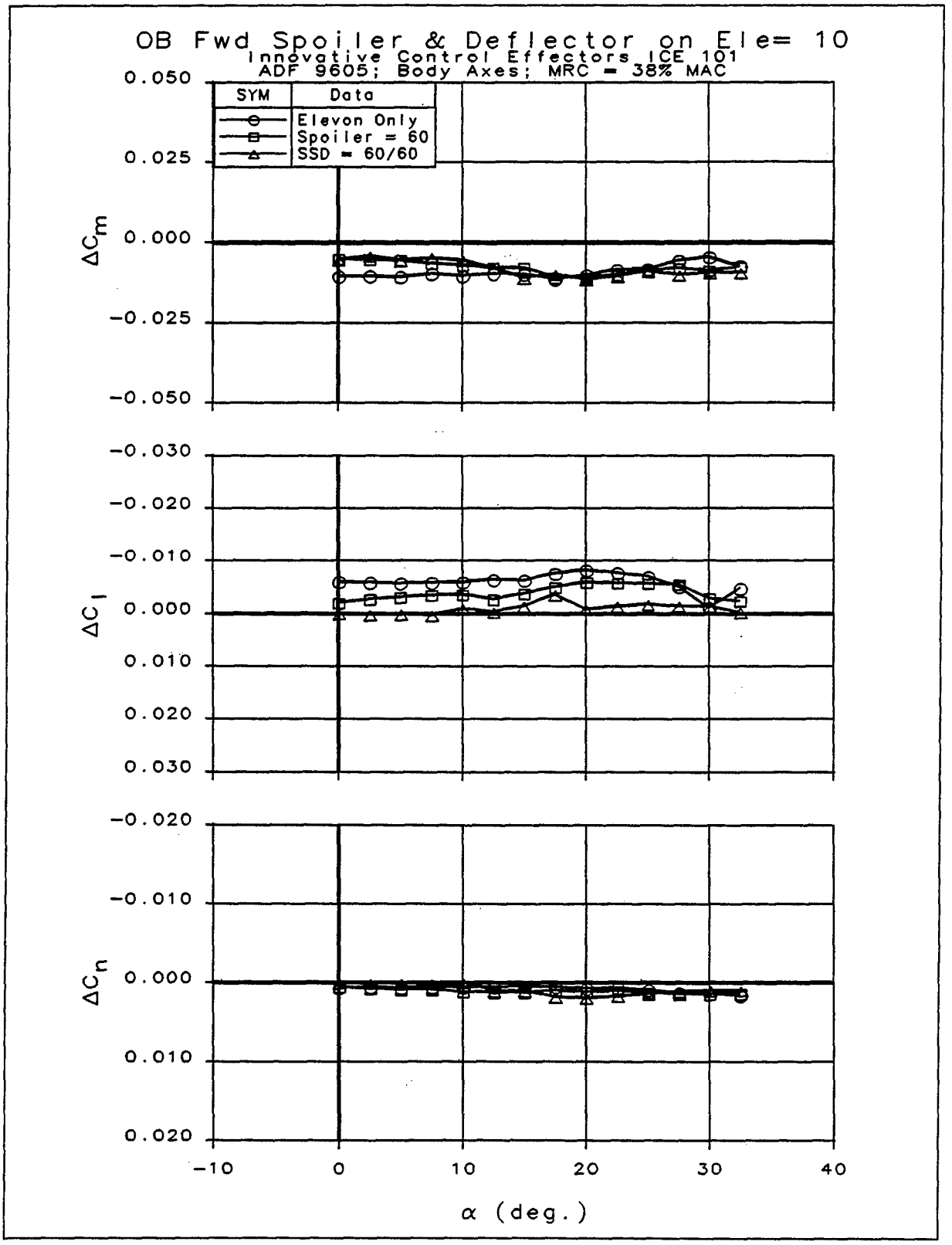

Figure 2-39: Effect of 60° OB Fwd Spoiler and SSD Deflections on Control Power From 10° Elevon Deflection

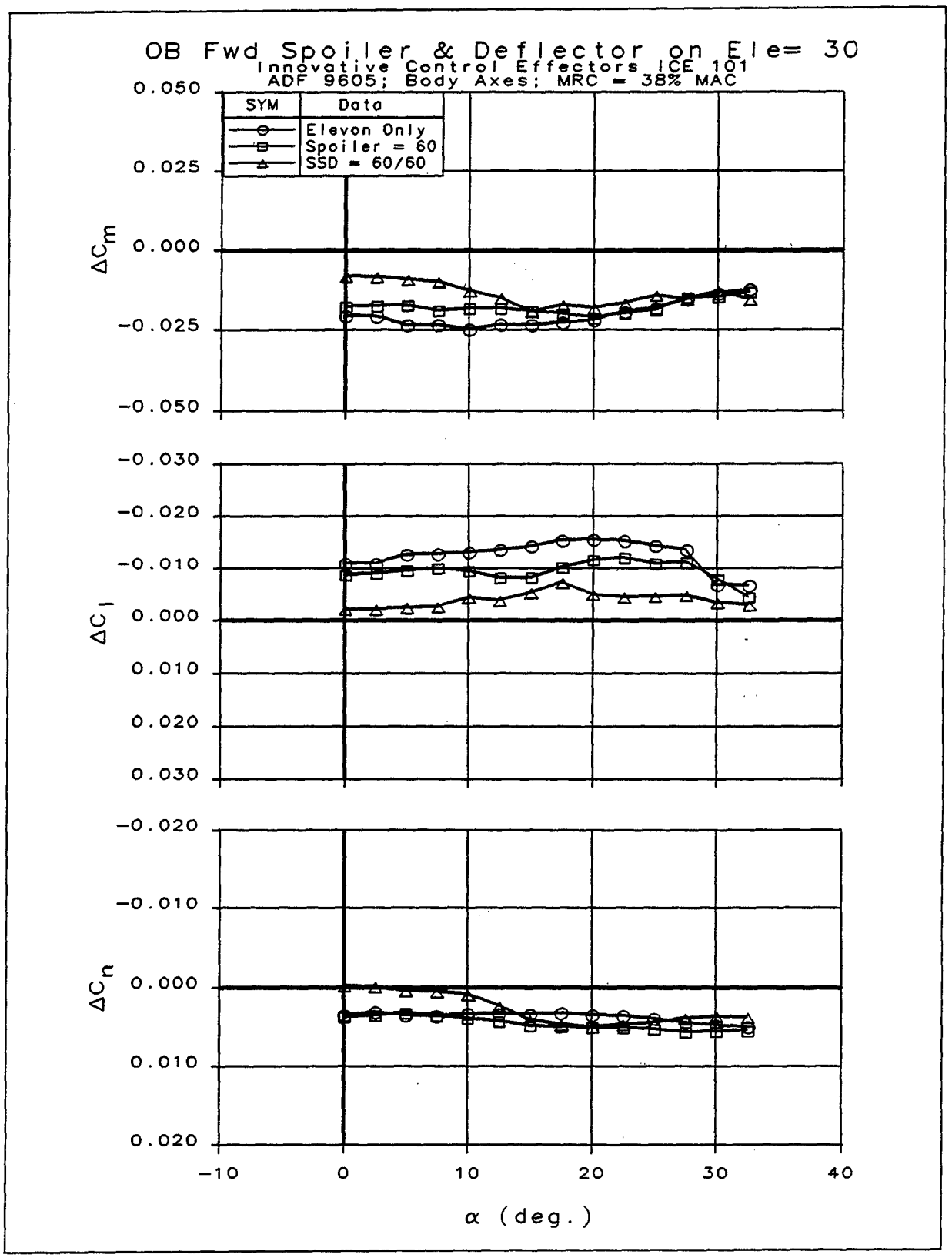

Figure 2-40: Effect of 60° OB Fwd Spoiler and SSD Deflections on Control Power From 30° Elevon Deflection

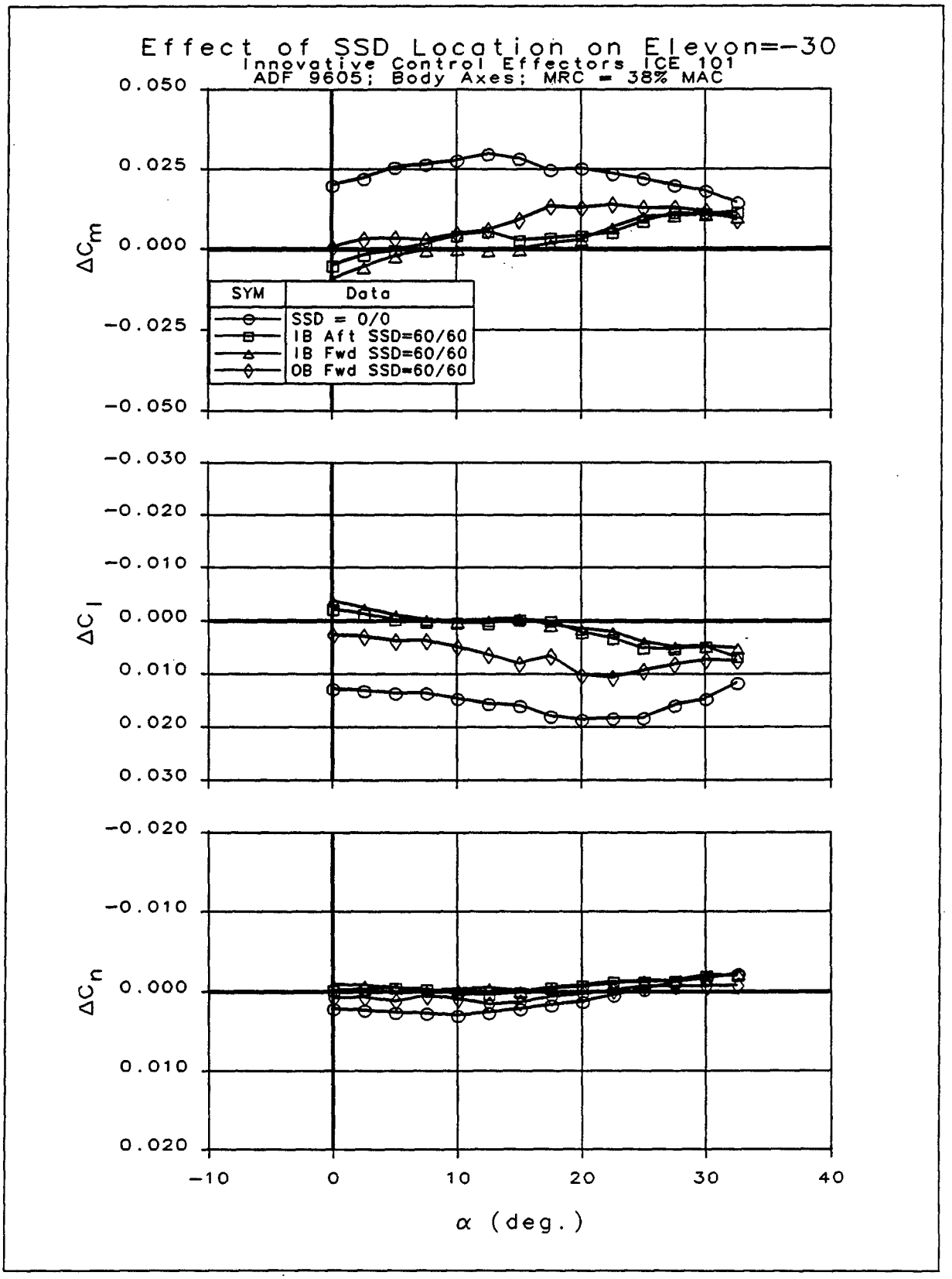

Figure 2-41: Effect of SSD Location on Control Power From -30° Elevon Deflection

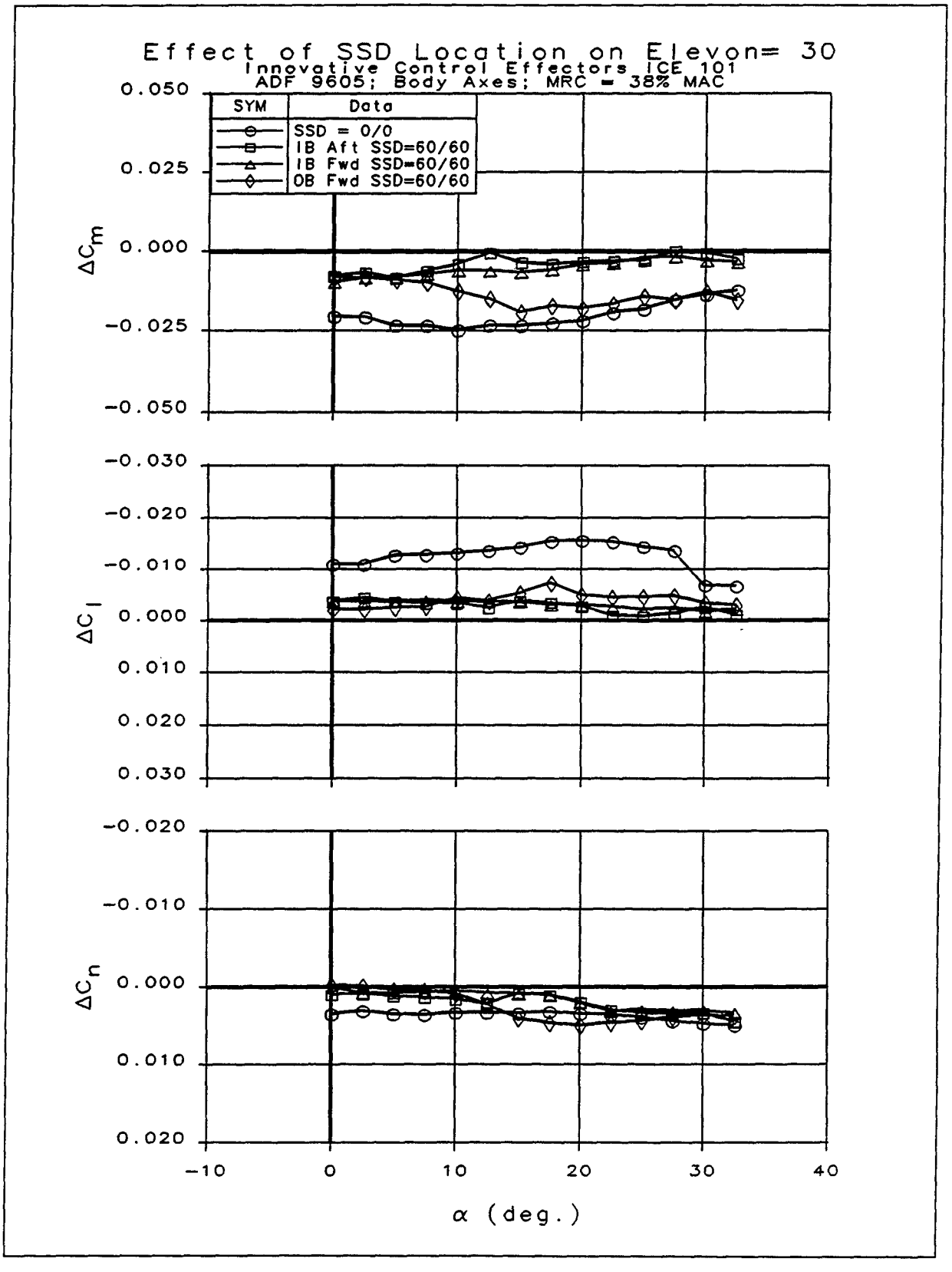

Figure 2-42: Effect of SSD Location on Control Power From 30° Elevon Deflection

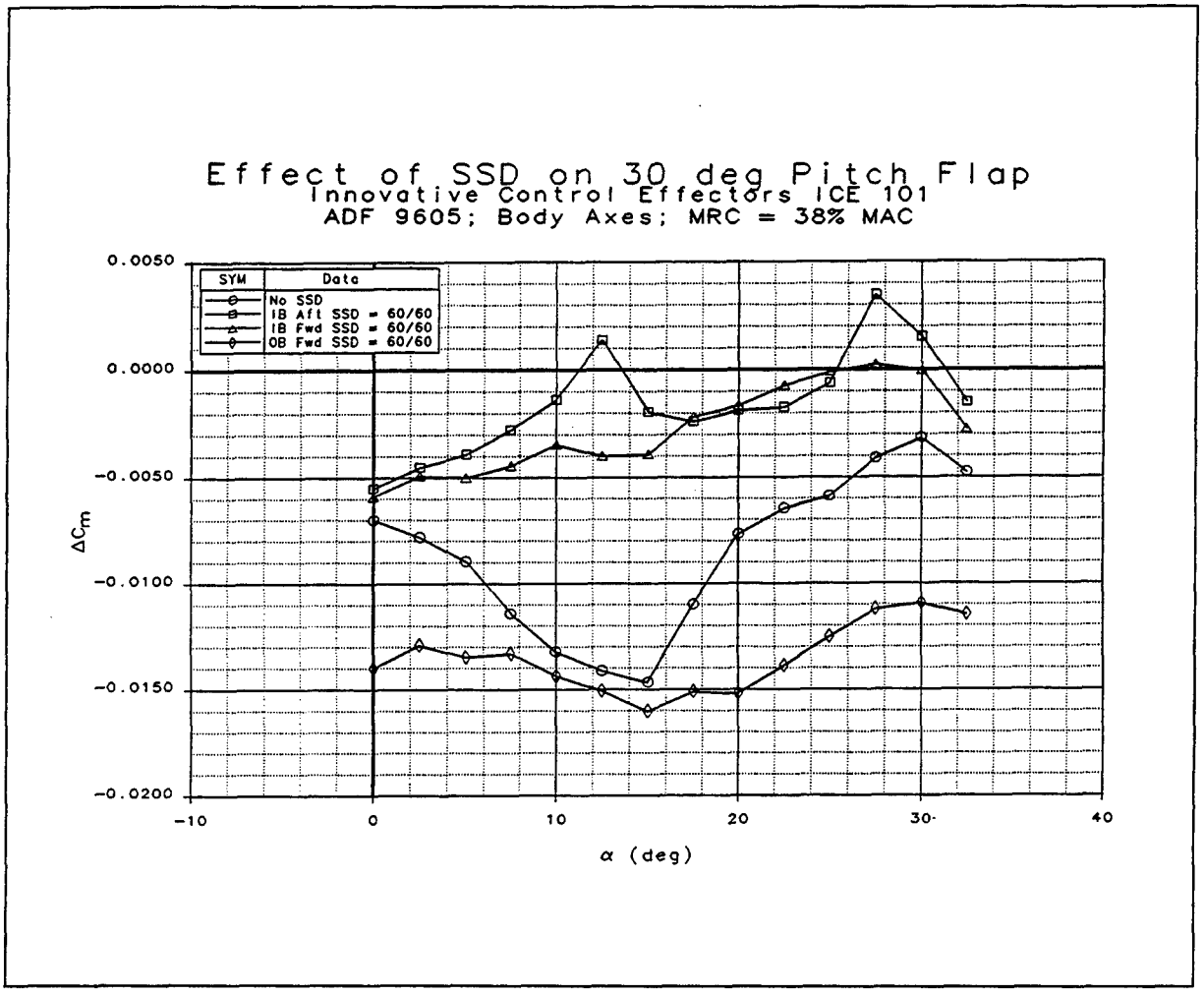

Figure 2-43: Effect of SSD Location on Control Power From 30° Pitch Flap Deflection

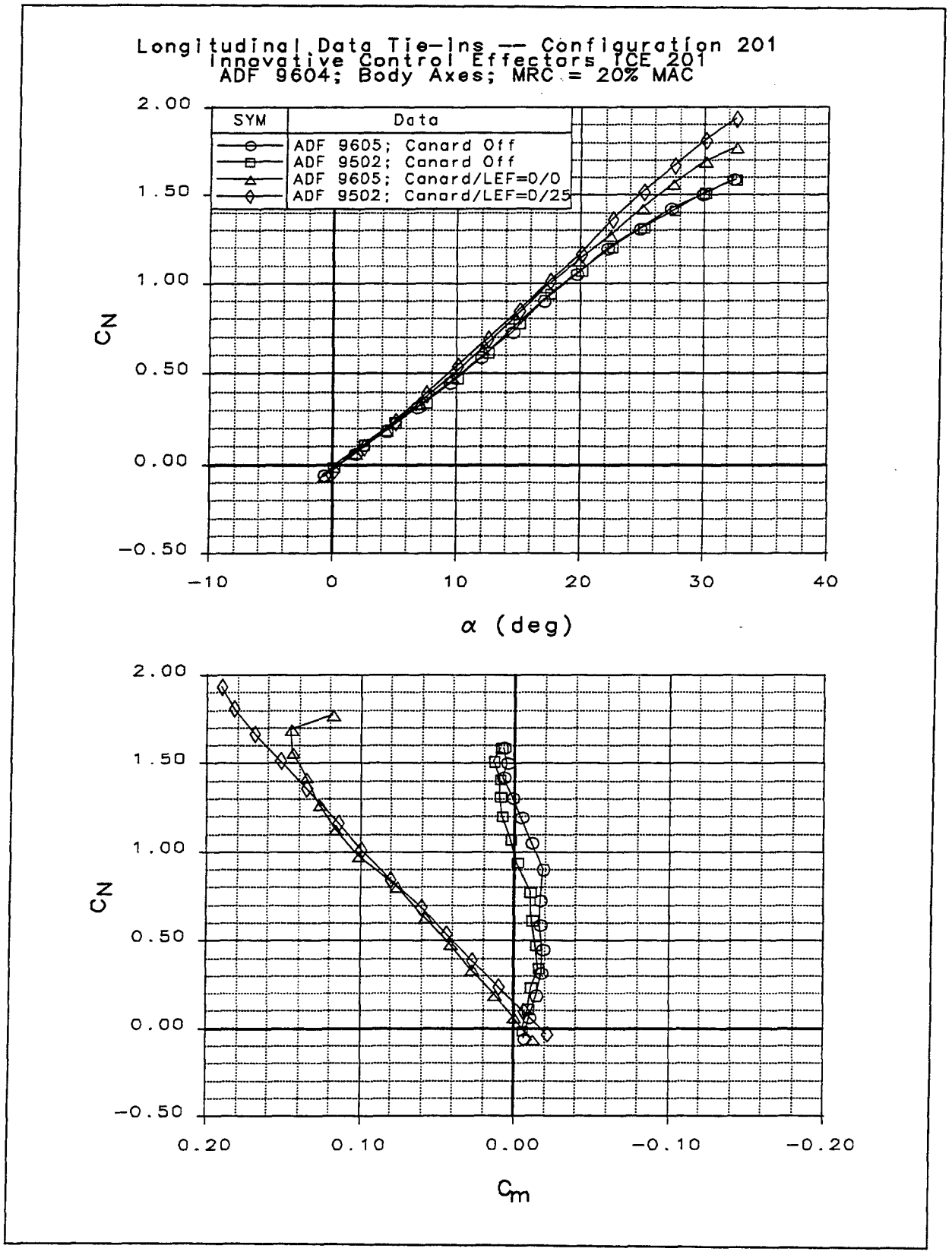

Figure 2-44: Longitudinal Characteristics of Configuration 201

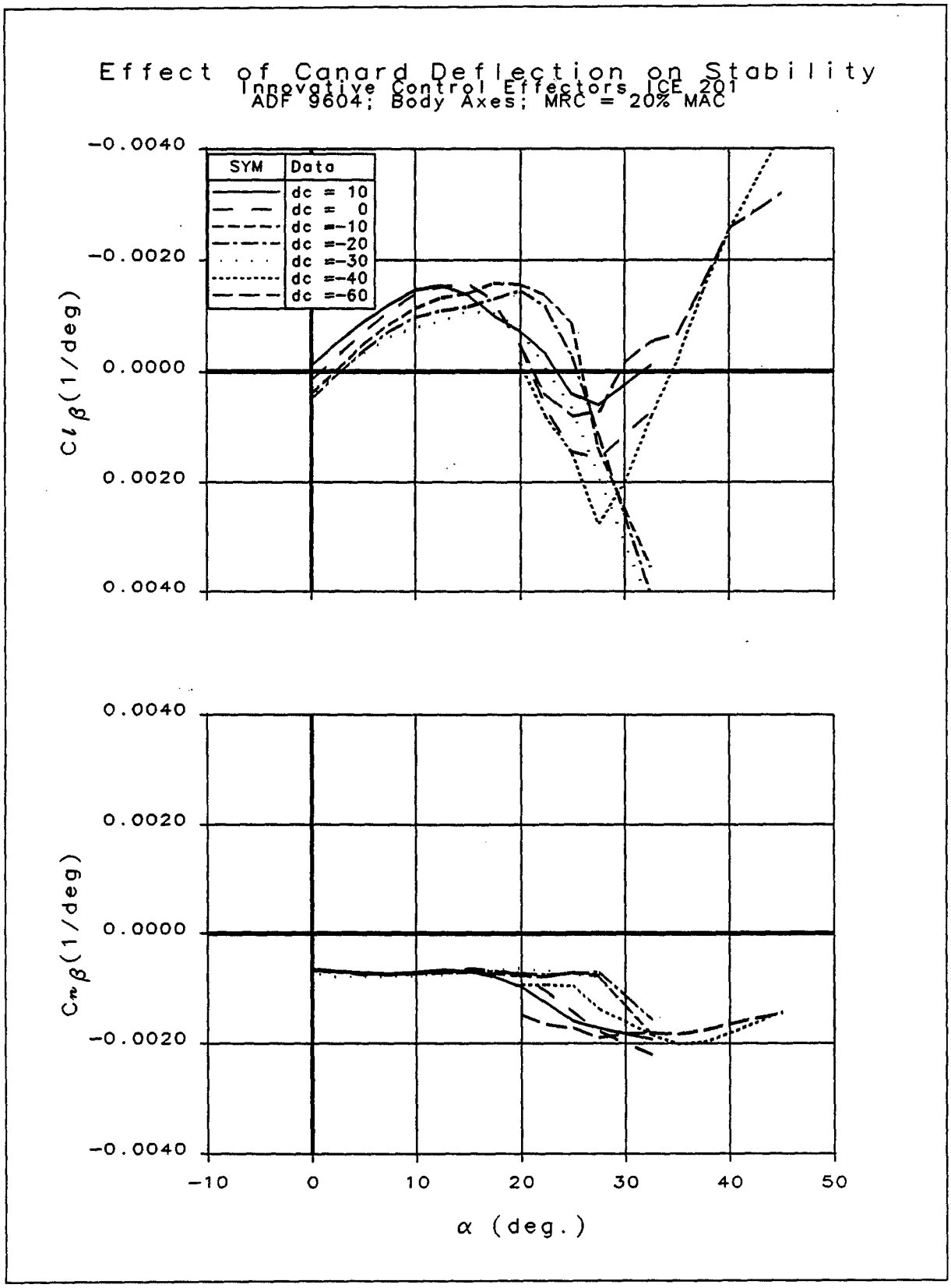

Figure 2-45: Effect of Canard Deflection on Lateral-Directional Stability of Configuration 201

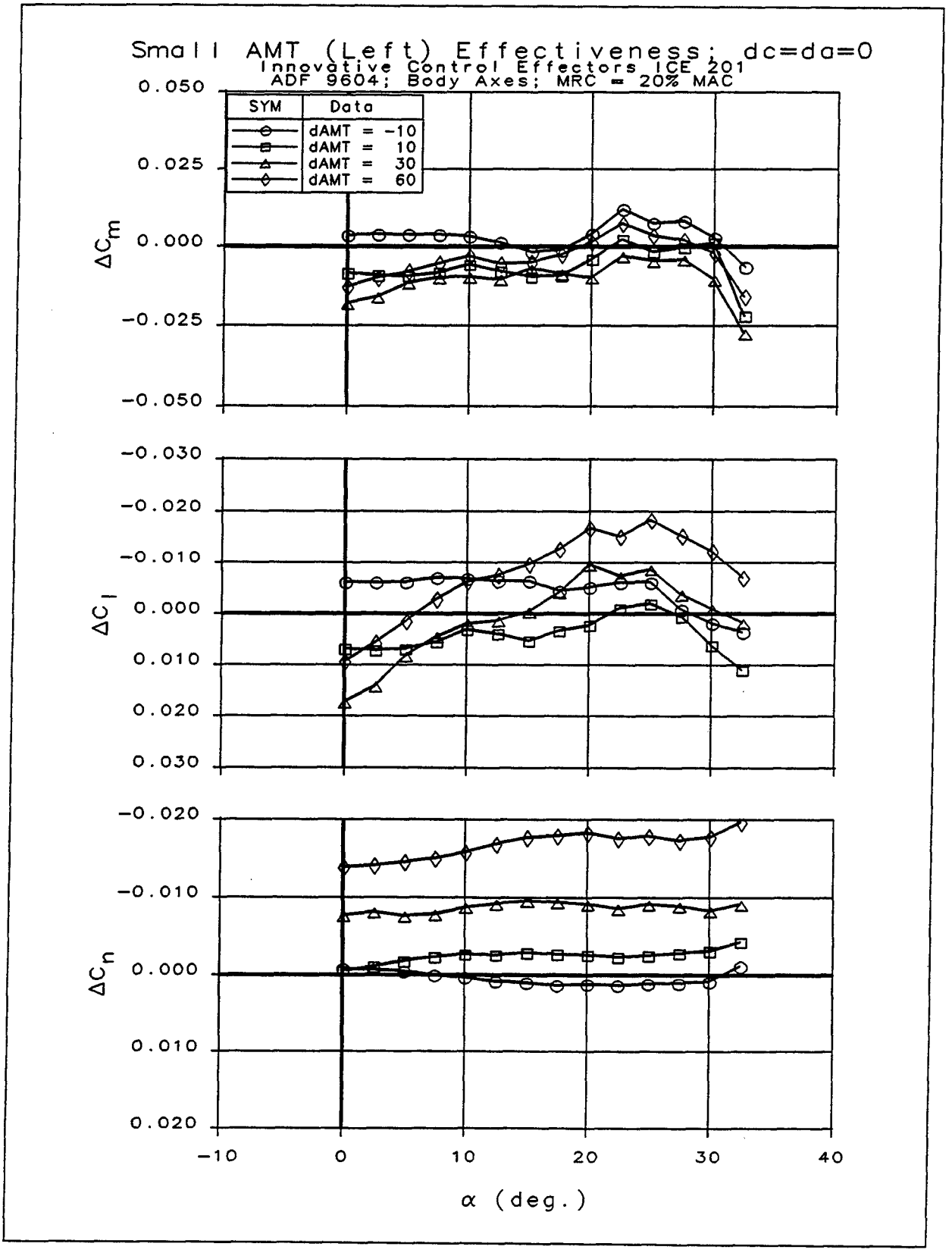

Figure 2-46: Small AMT Control Effectiveness on Configuration 201

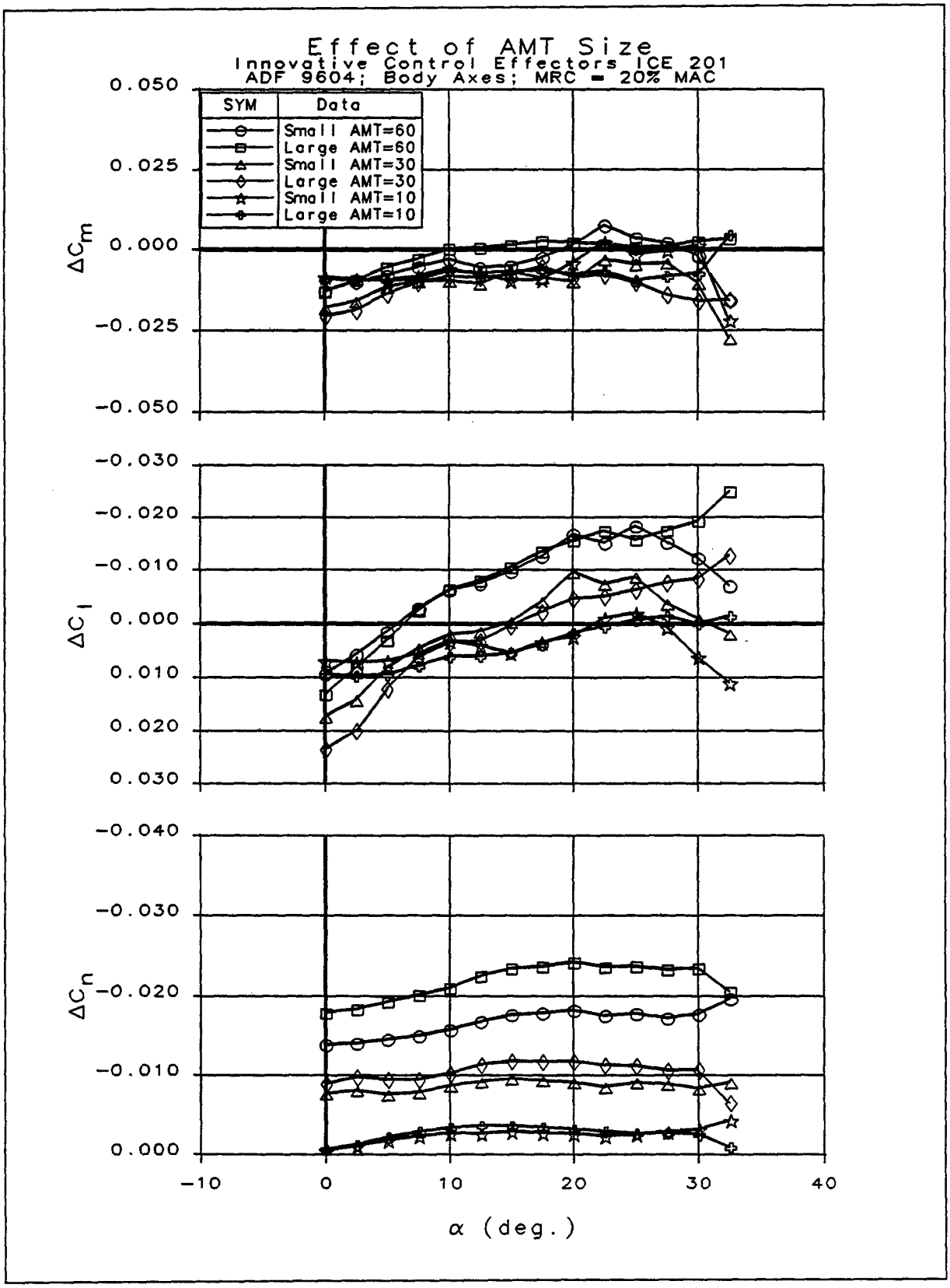

Figure 2-47: Comparison of Small and Large AMT Control Effectiveness on Configuration 201

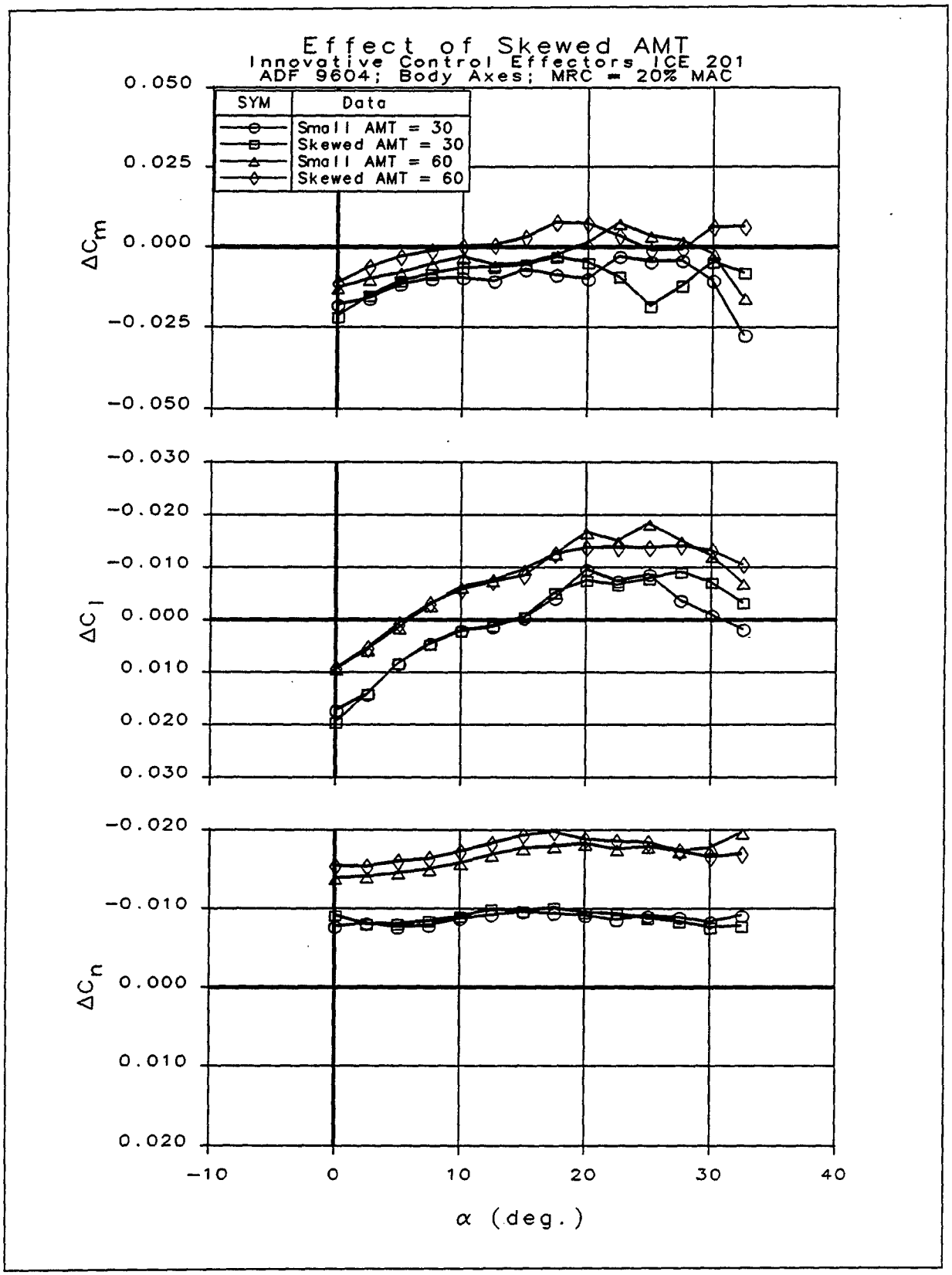

Figure 2-48: Effect of Skewed AMT on Configuration 201

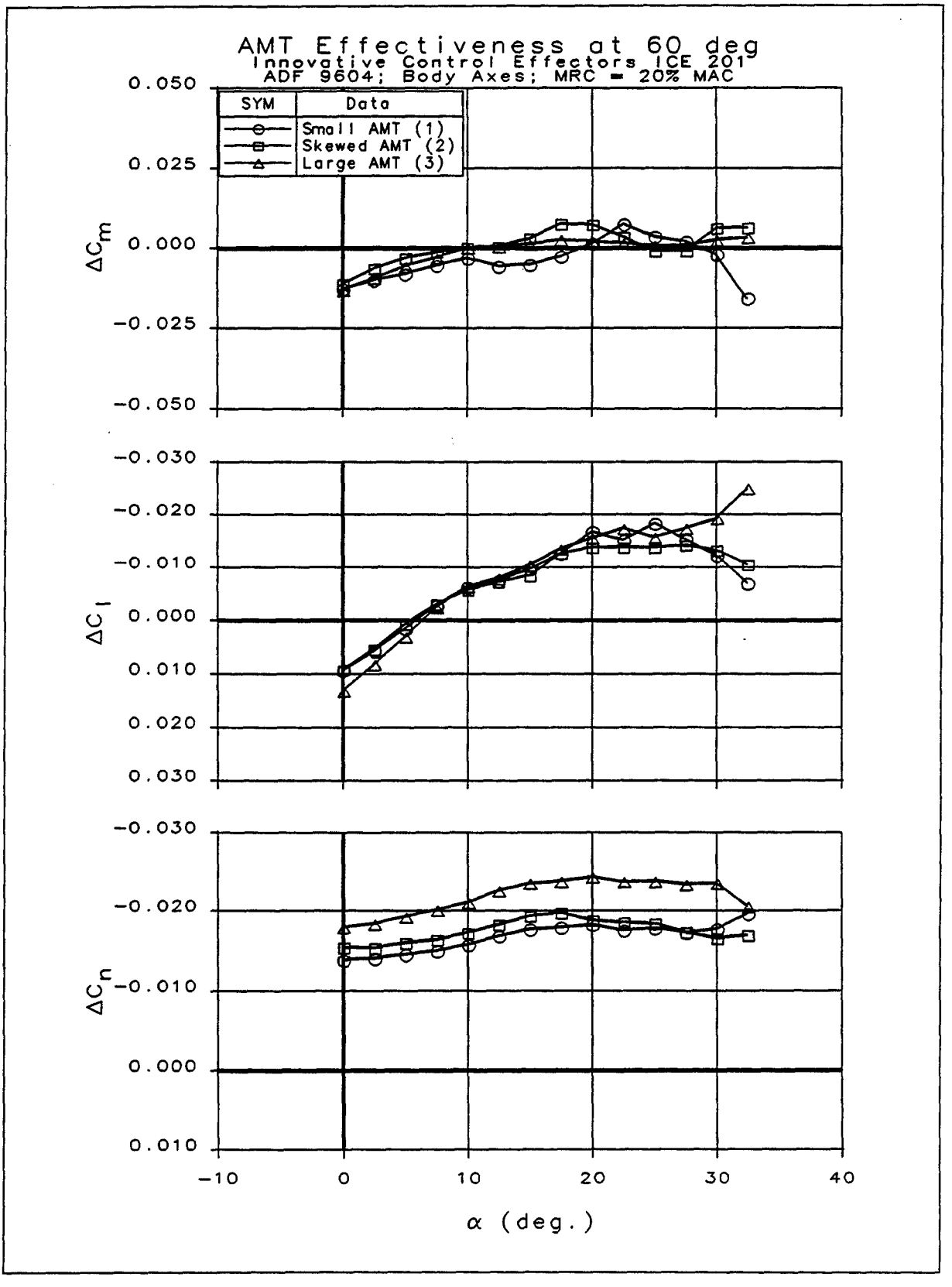

Figure 2-49: AMT Control Power Comparison at Deflection of 60° on Configuration 201

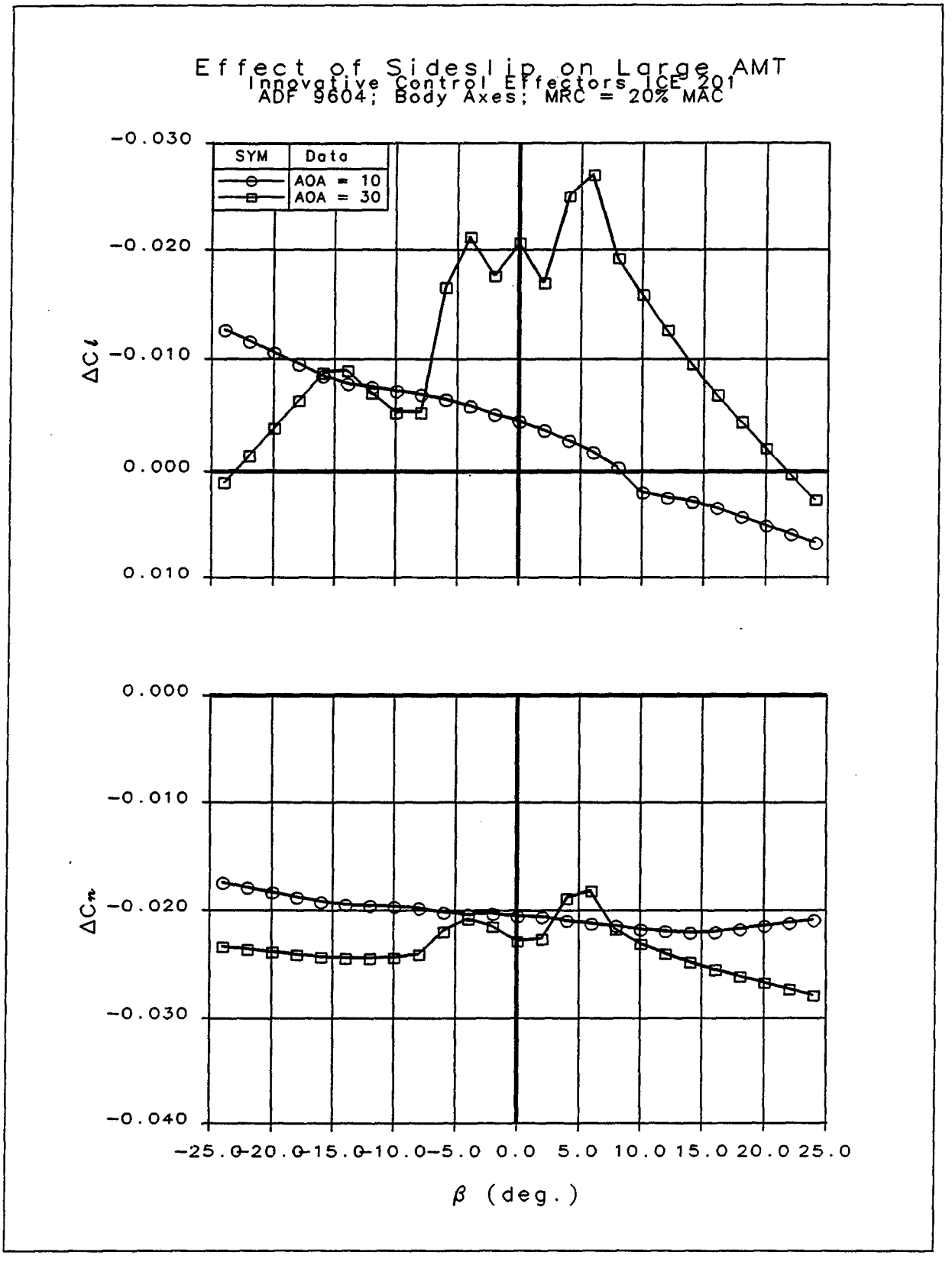

Figure 2-50: Effects of Sideslip on Large AMT Control Power

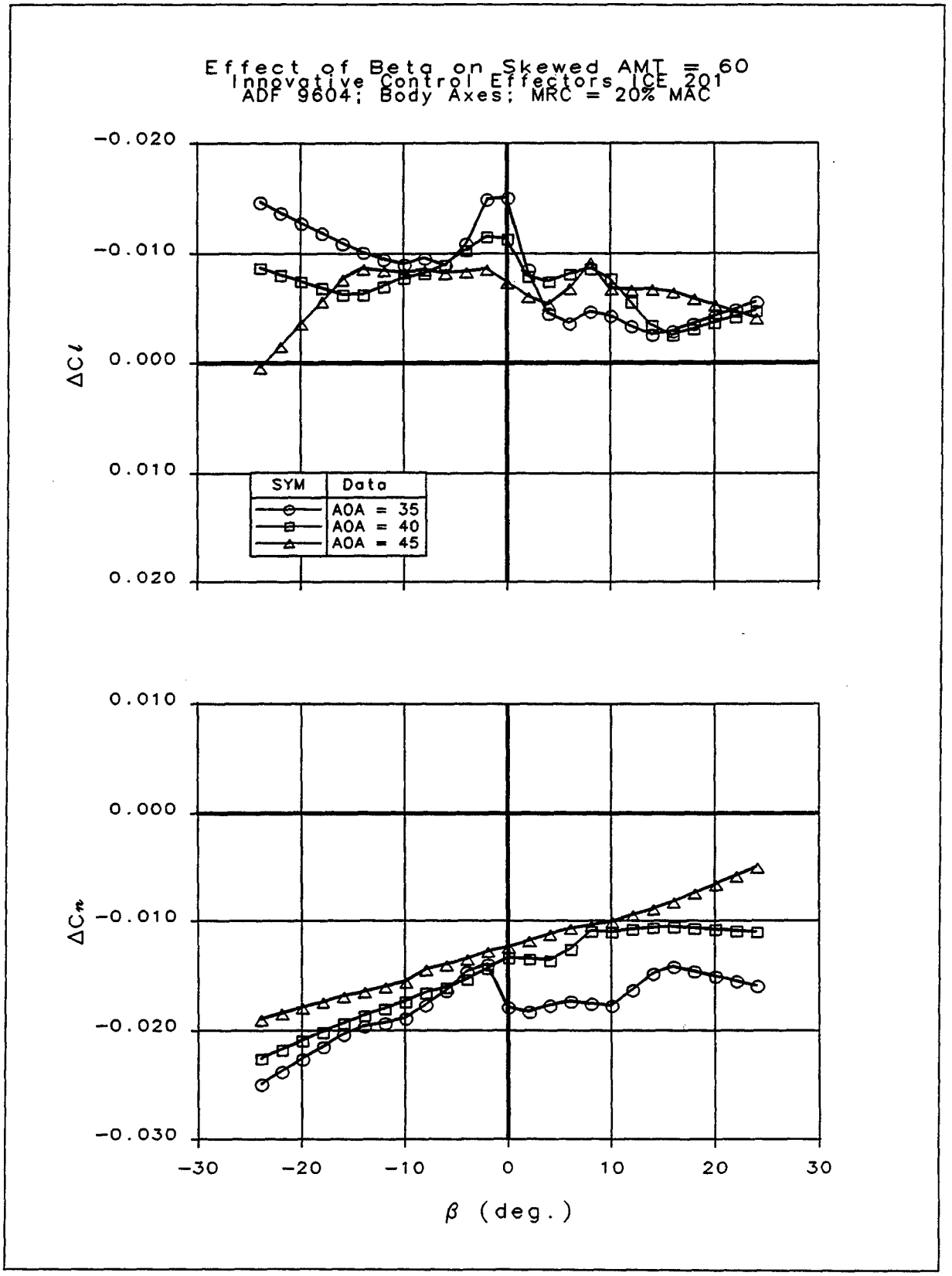

Figure 2-51: Effect of Sideslip on Skewed AMT at High AOAs

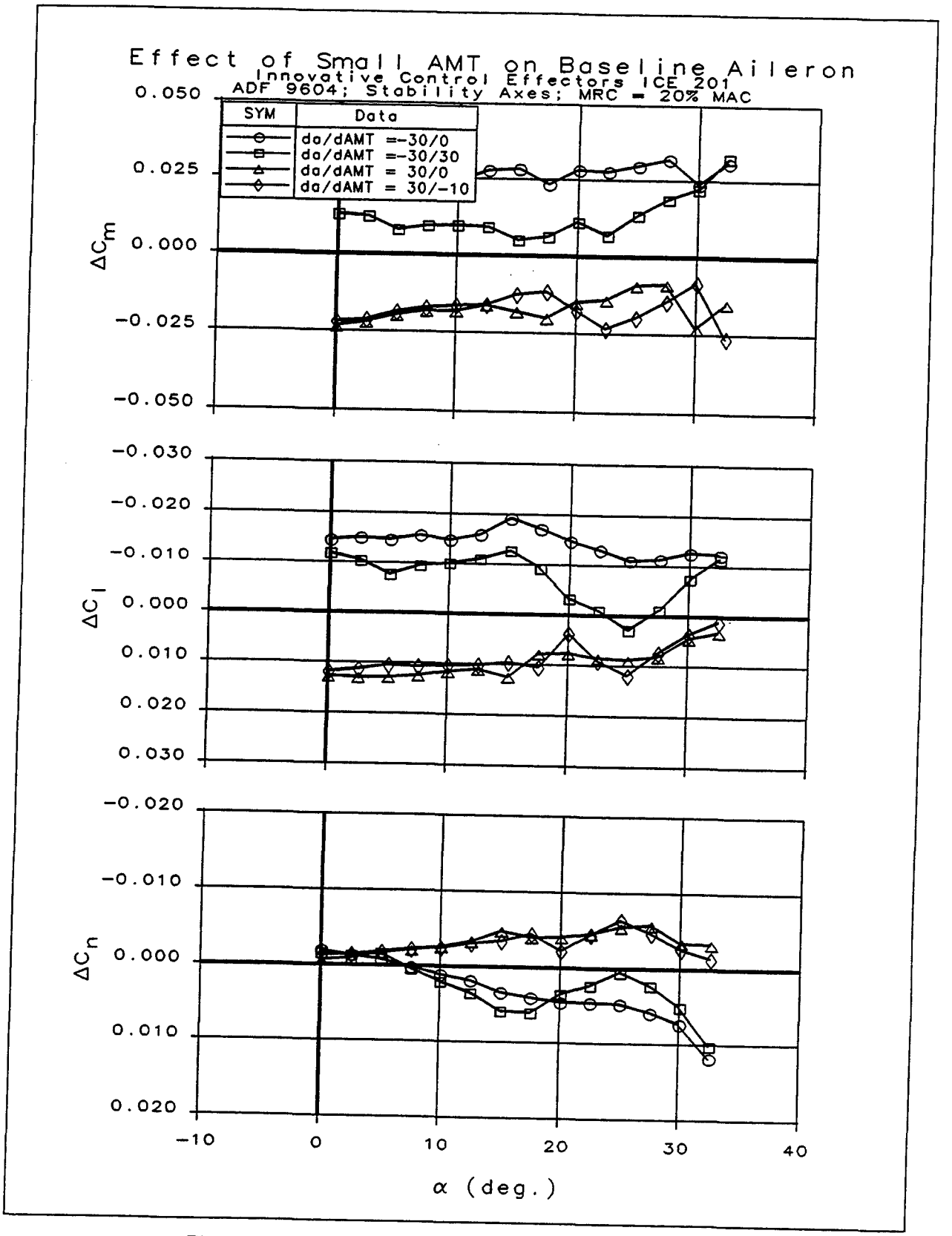

Figure 2-52: Effect of Small AMT on Aileron Control Power

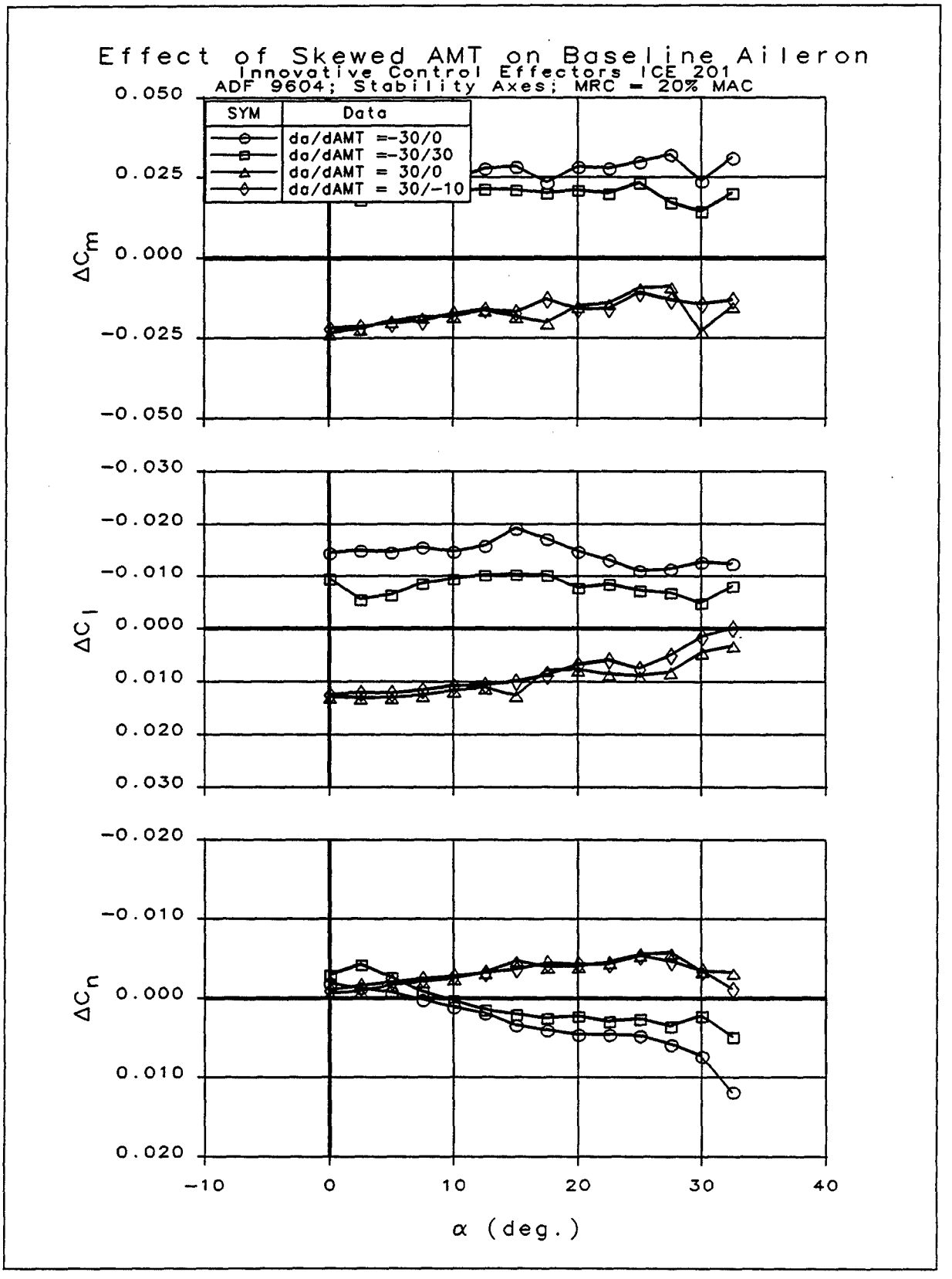

Figure 2-53: Effect of Skewed AMT on Aileron Control Power

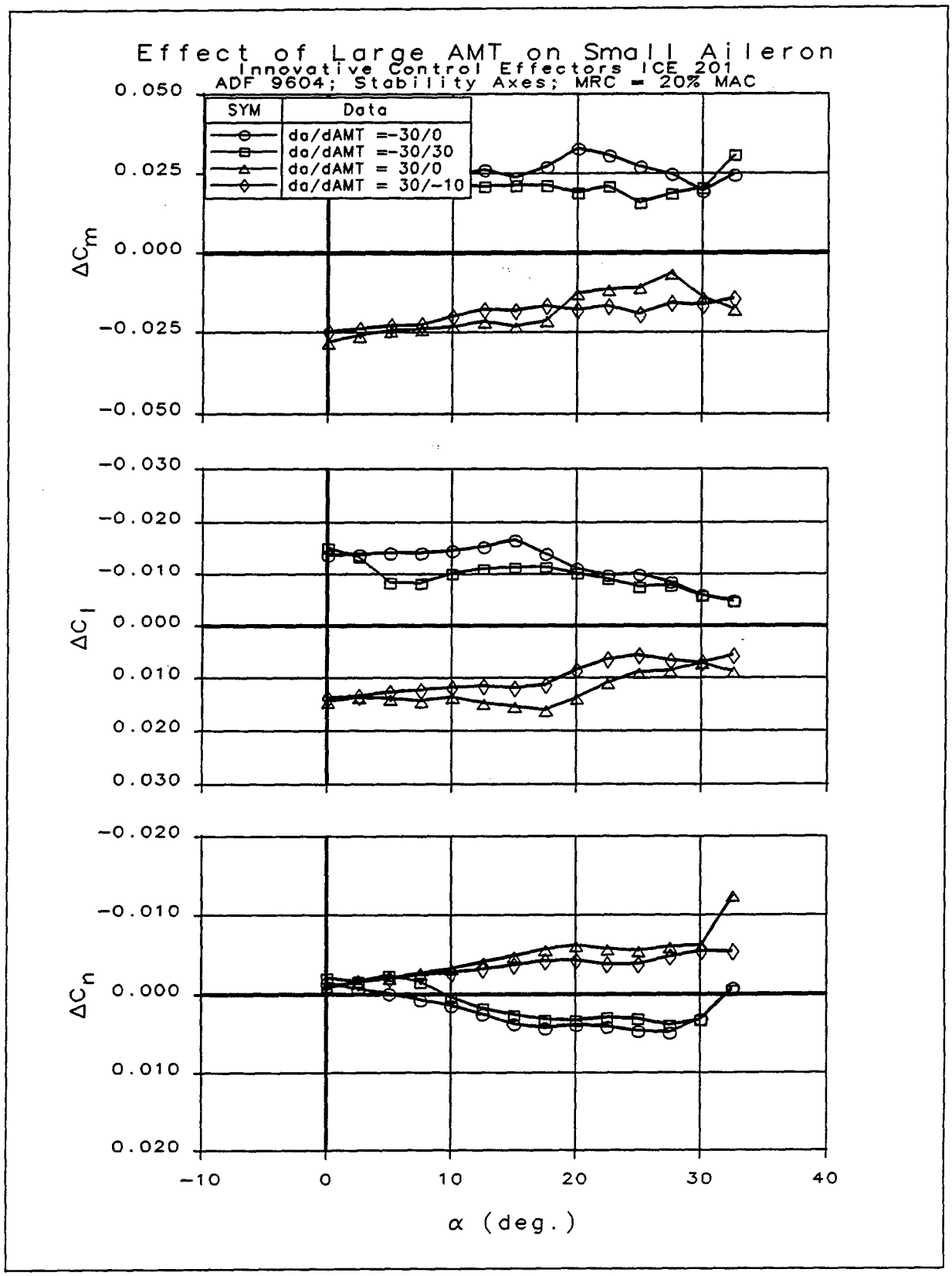

Figure 2-54: Effect of Large AMT on Aileron Control Power

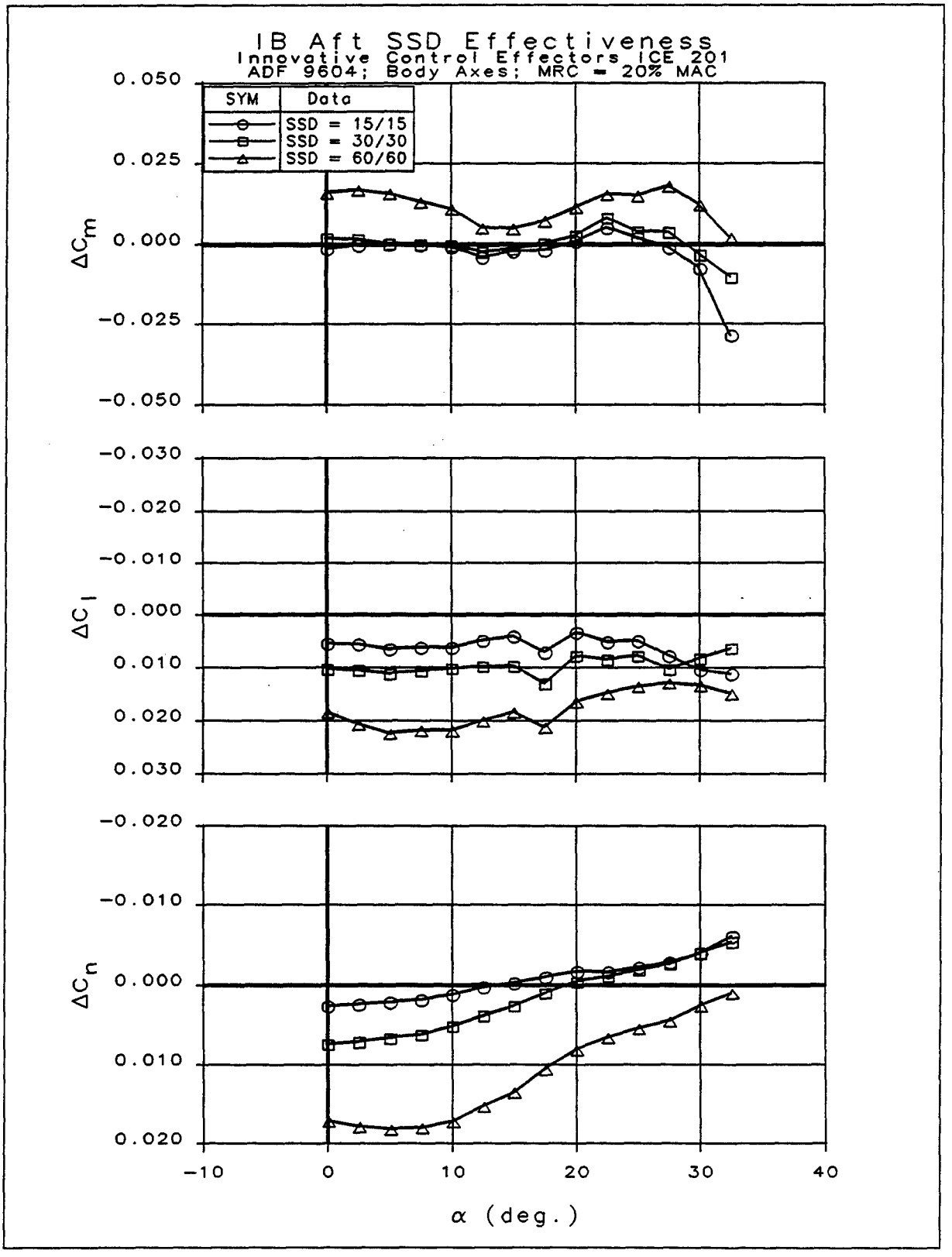

Figure 2-55: IB Aft SSD Control Power on Configuration 201

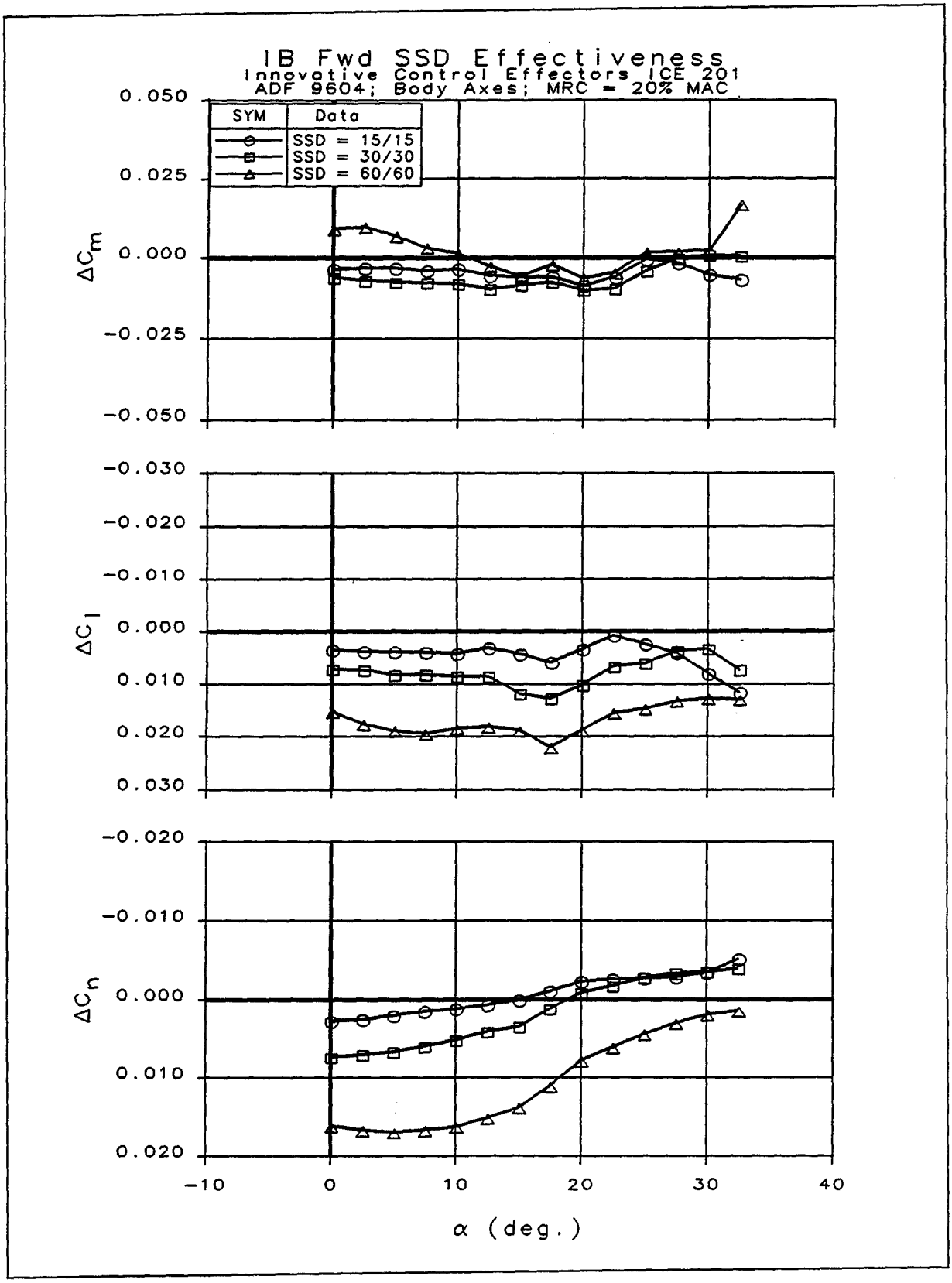

Figure 2-56: IB Fwd SSD Control Power on Configuration 201

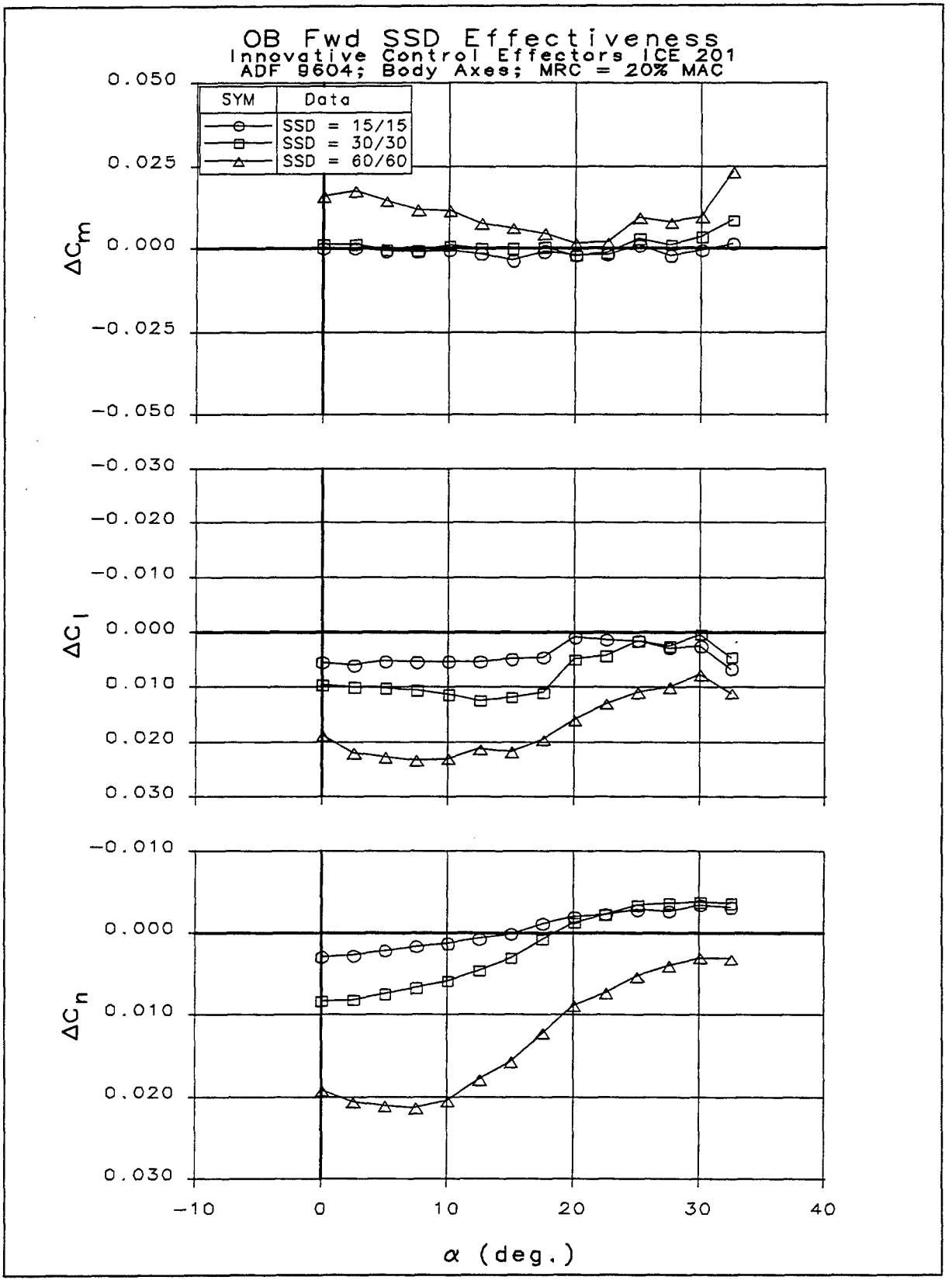

Figure 2-57: OB Fwd SSD Control Power on Configuration 201

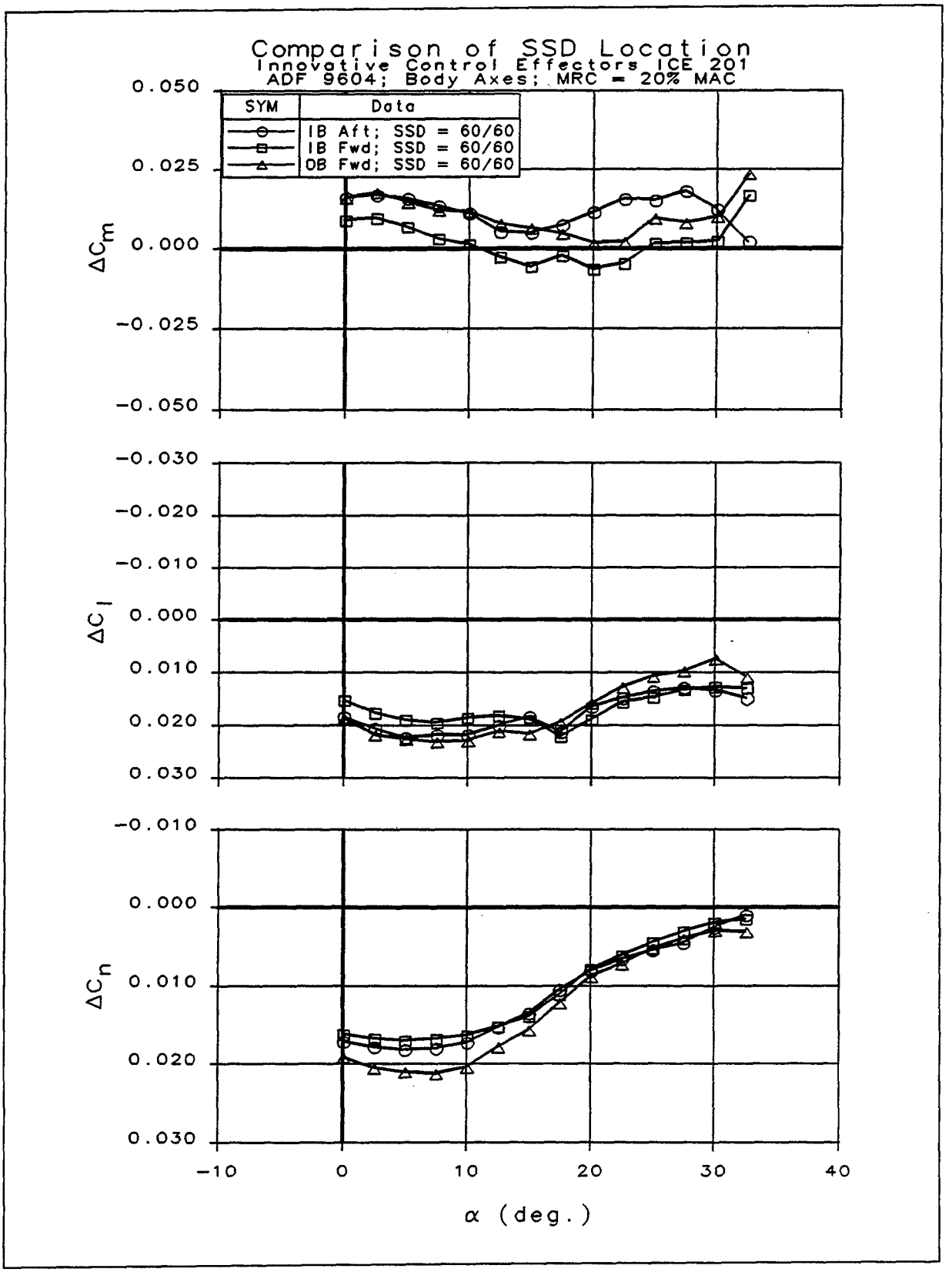

Figure 2-58: Effect of Location on SSD Control Power

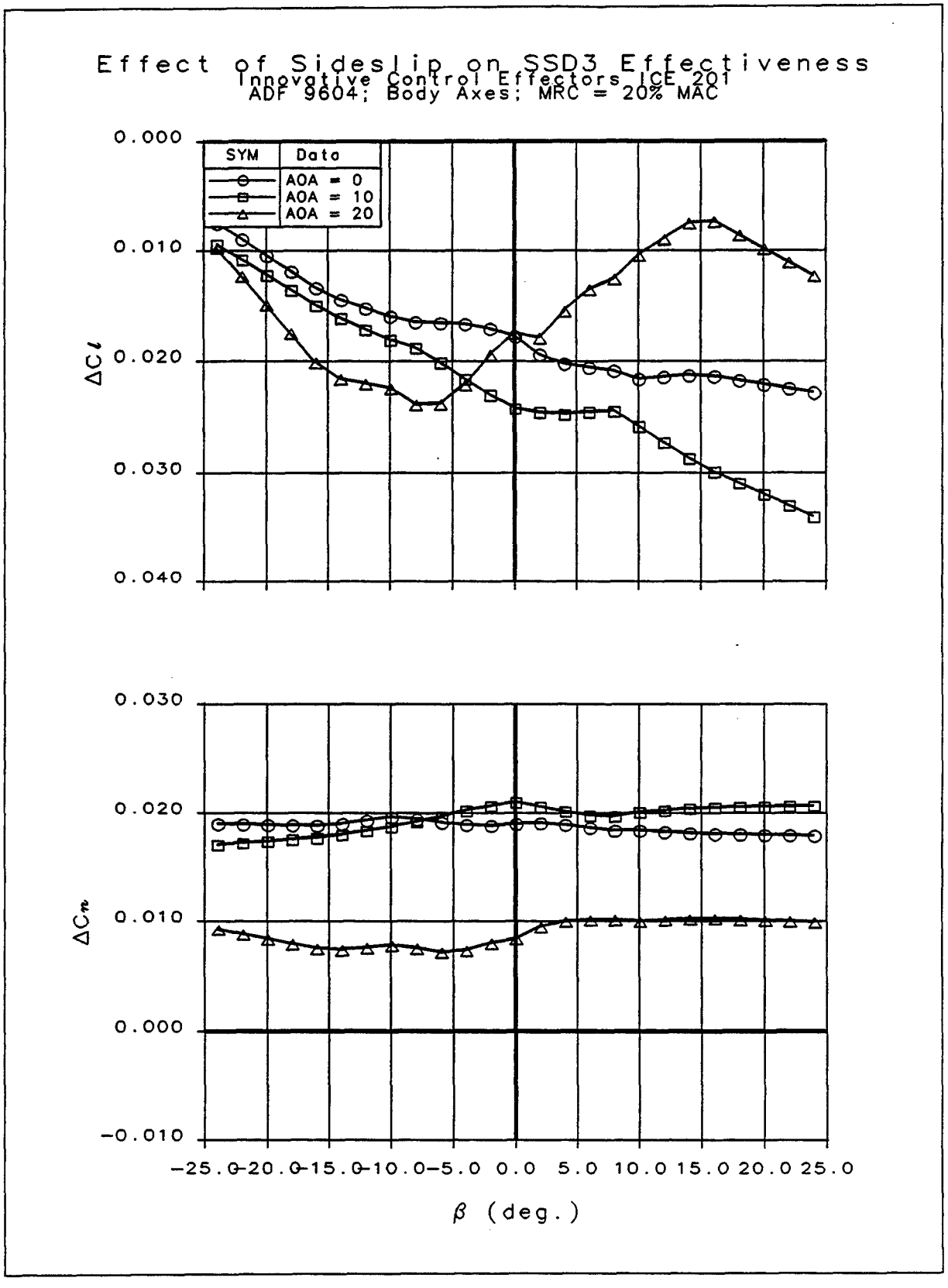

Figure 2-59: Effect of Sideslip on IB Fwd SSD

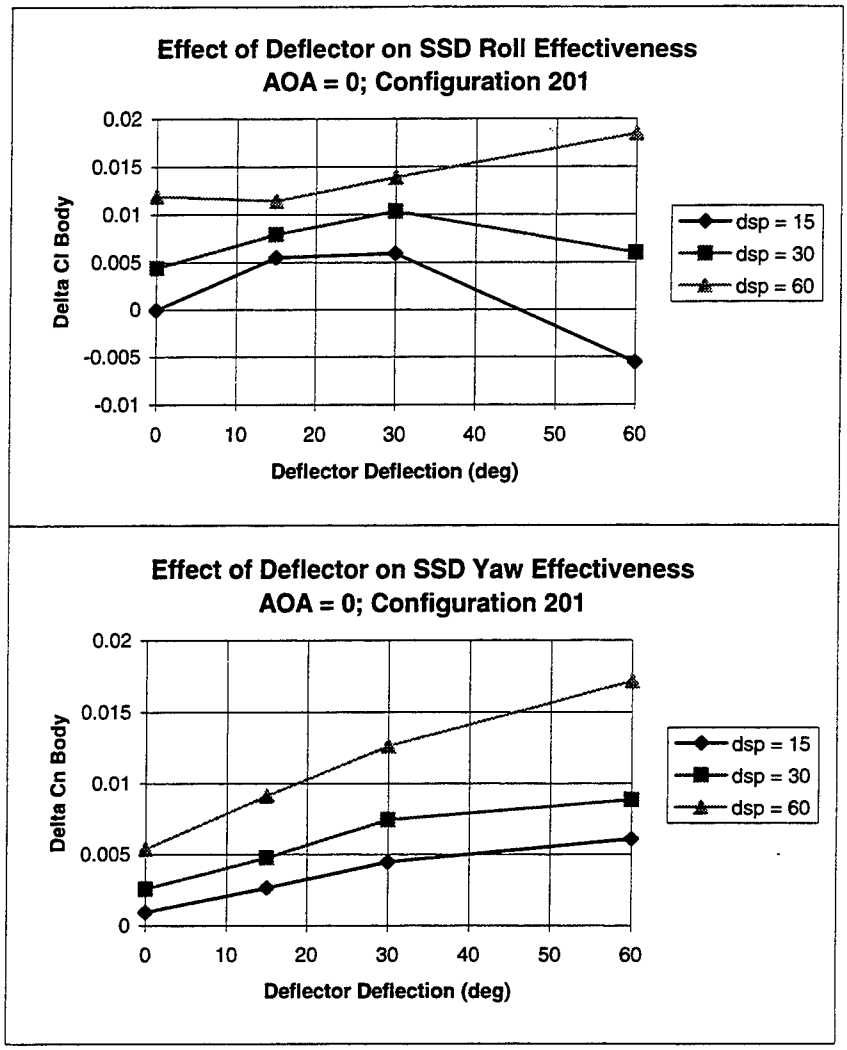

Figure 2-60: Variation of Spoiler Control Power at IB Aft SSD Location With Deflection Angle

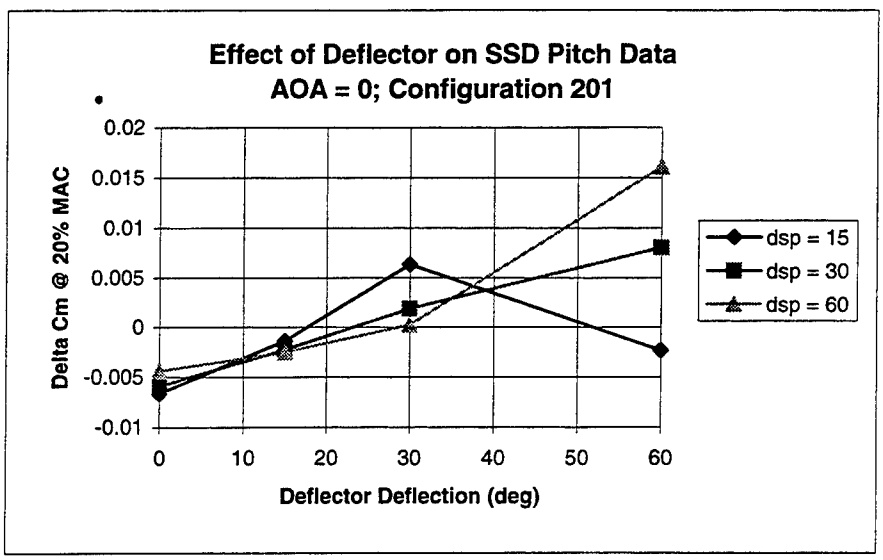

Figure 2-61: Effect of SSD Deflection Angle at IB Aft SSD Location on Pitching Moment

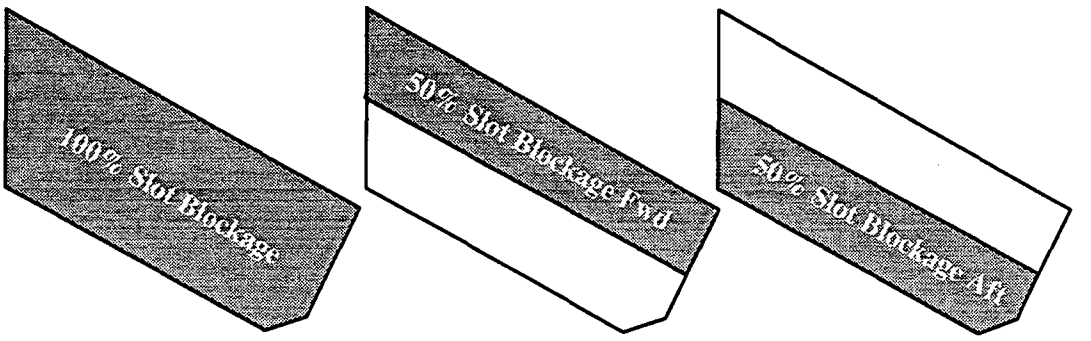

Figure 2-62: Configuration 201 Slot Blockage Configurations

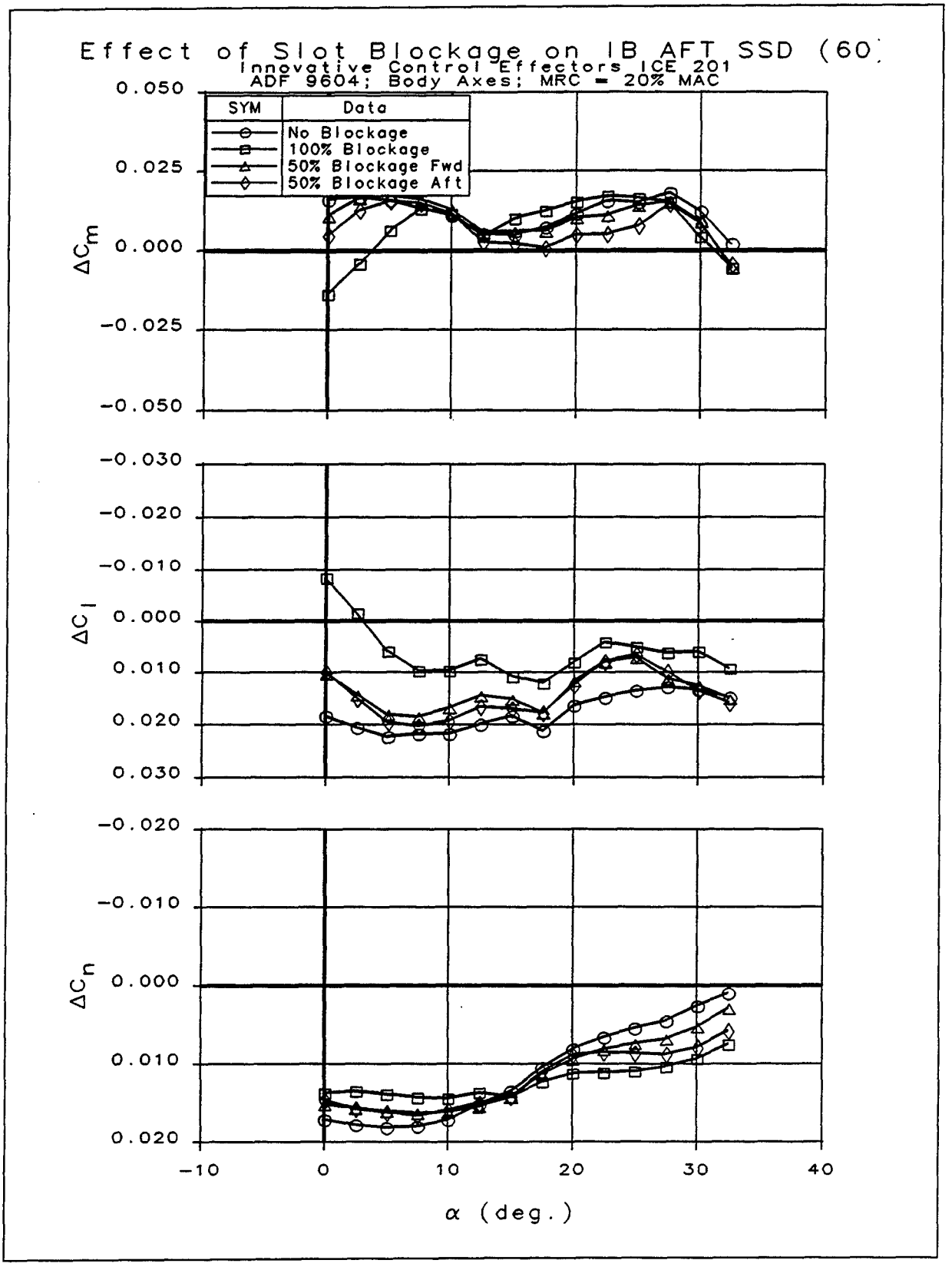

Figure 2-63: Effect of Slot Blockage on SSD Control Power

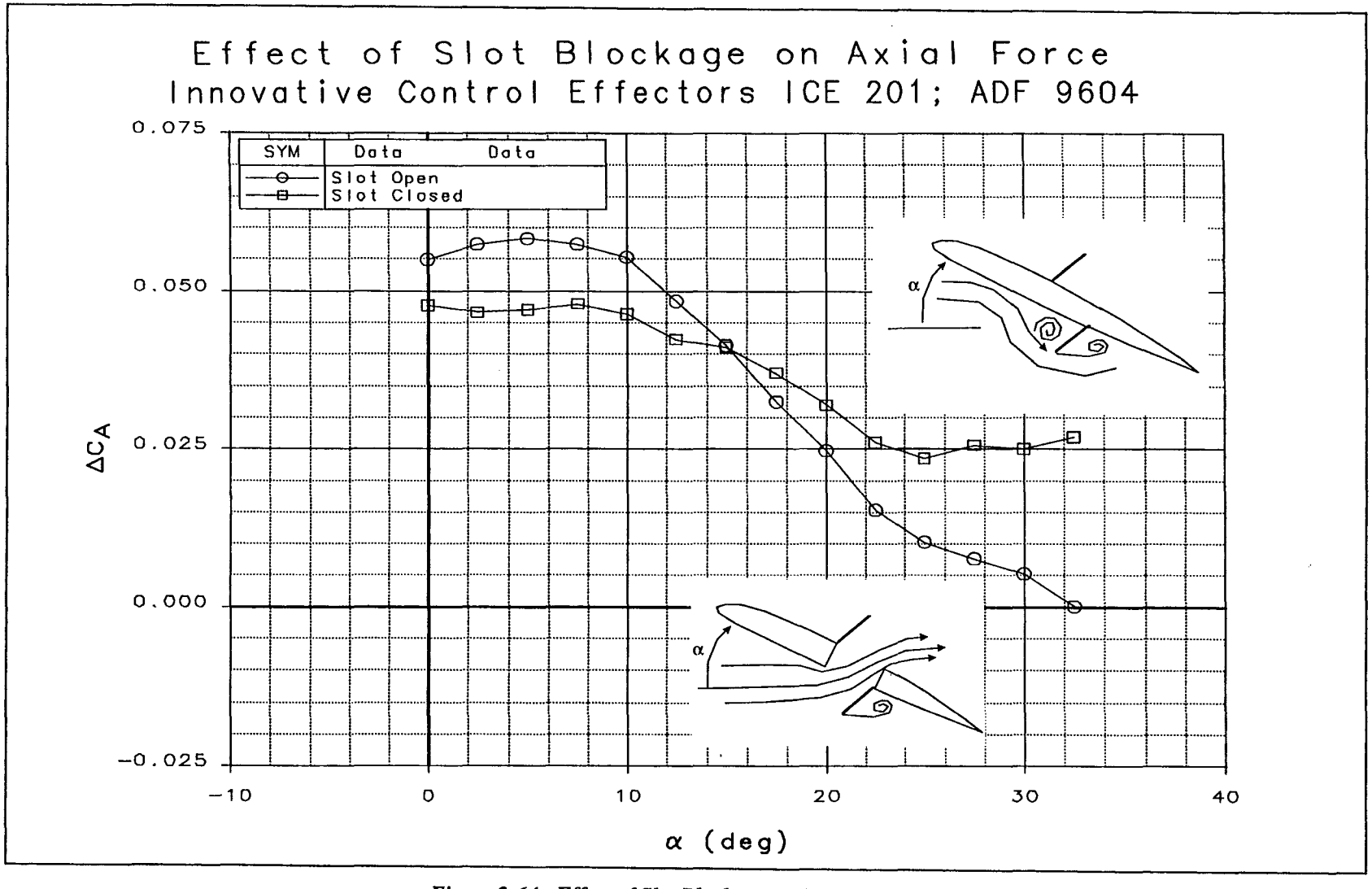

Figure 2-64: Effect of Slot Blockage on SSD Axial Force

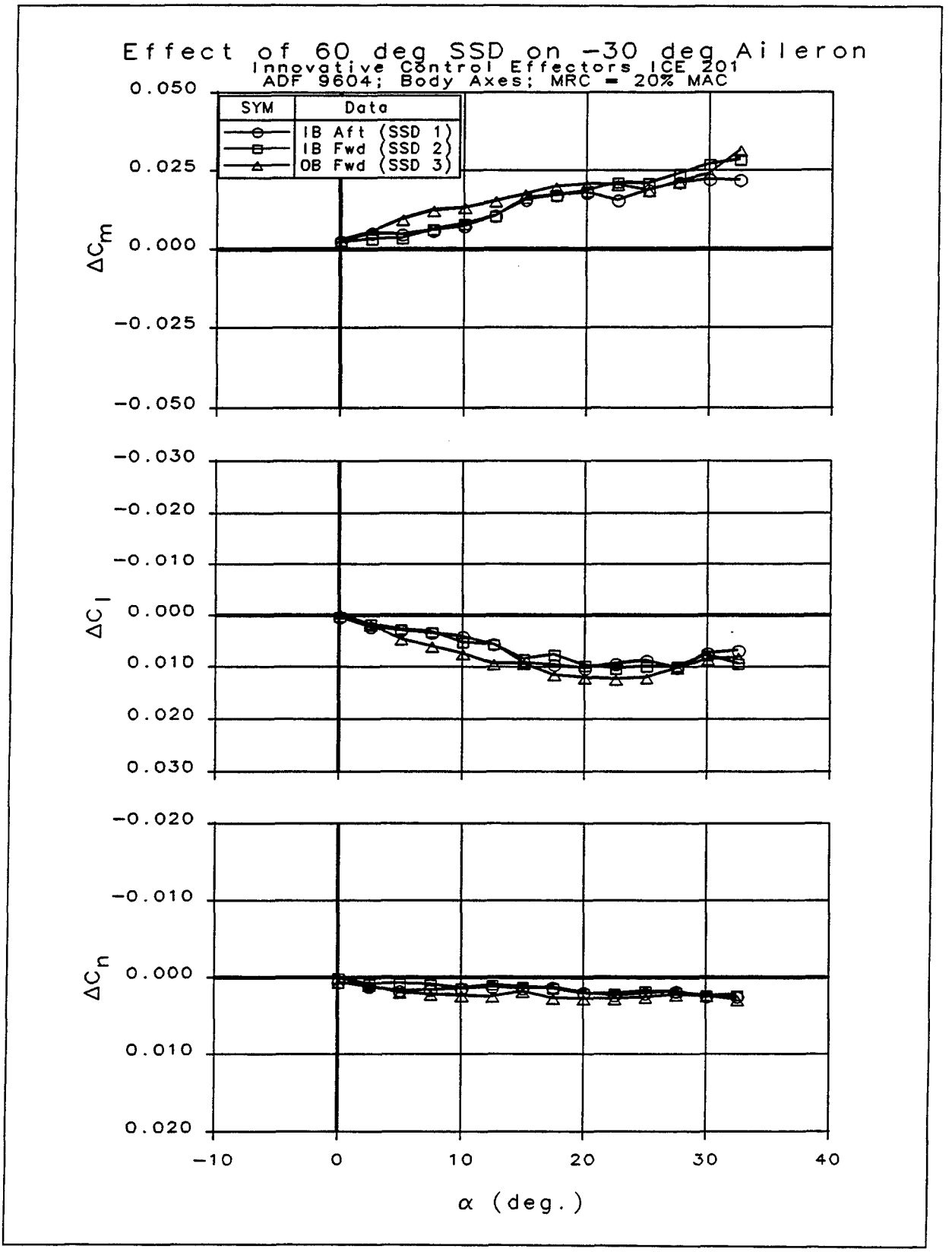

Figure 2-65: Effect of SSD Location on Aileron Control Interactions; Aileron = -30°

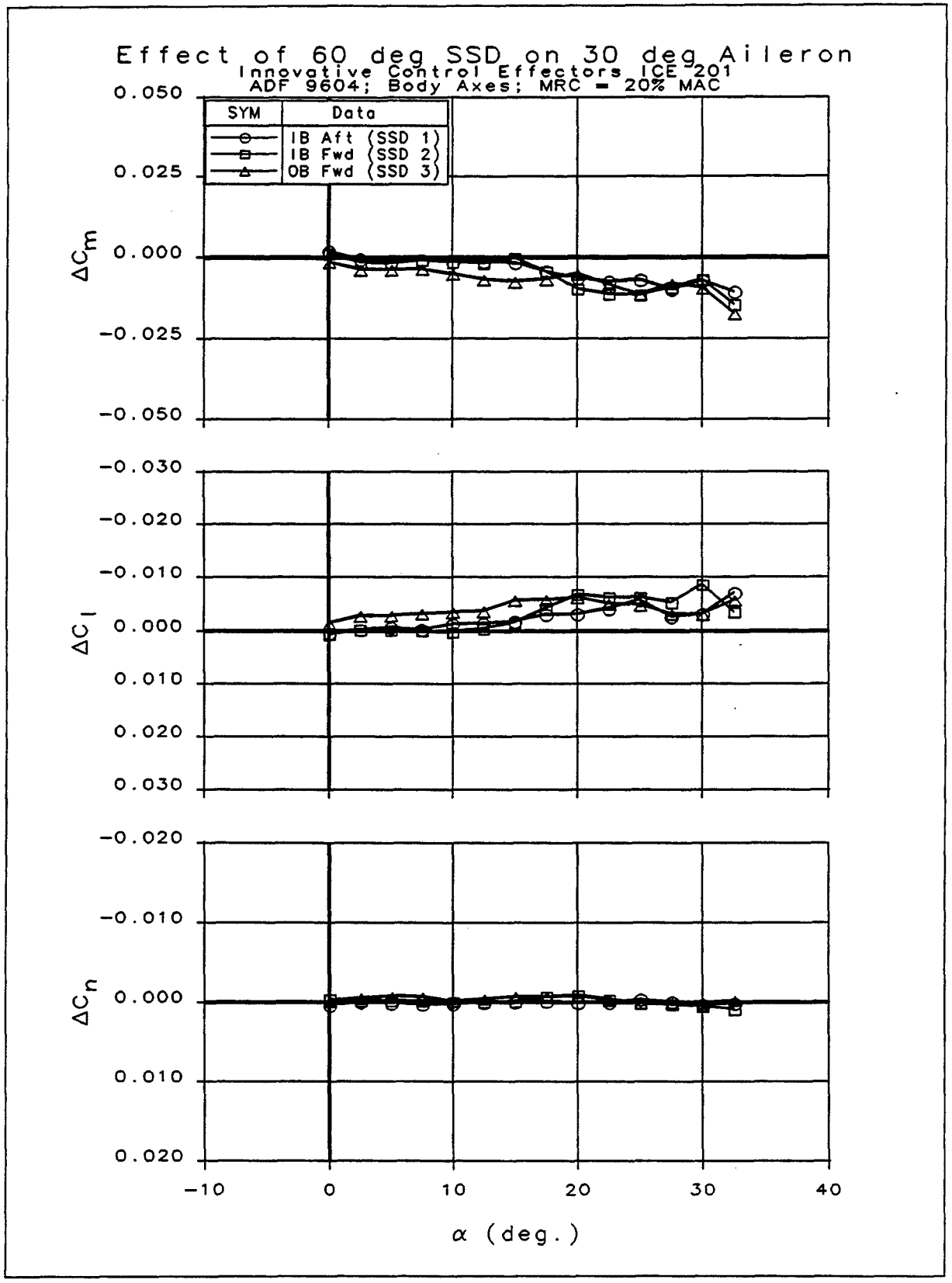

Figure 2-66: Effect of SSD Location on Aileron Control Interactions; Aileron = 30°

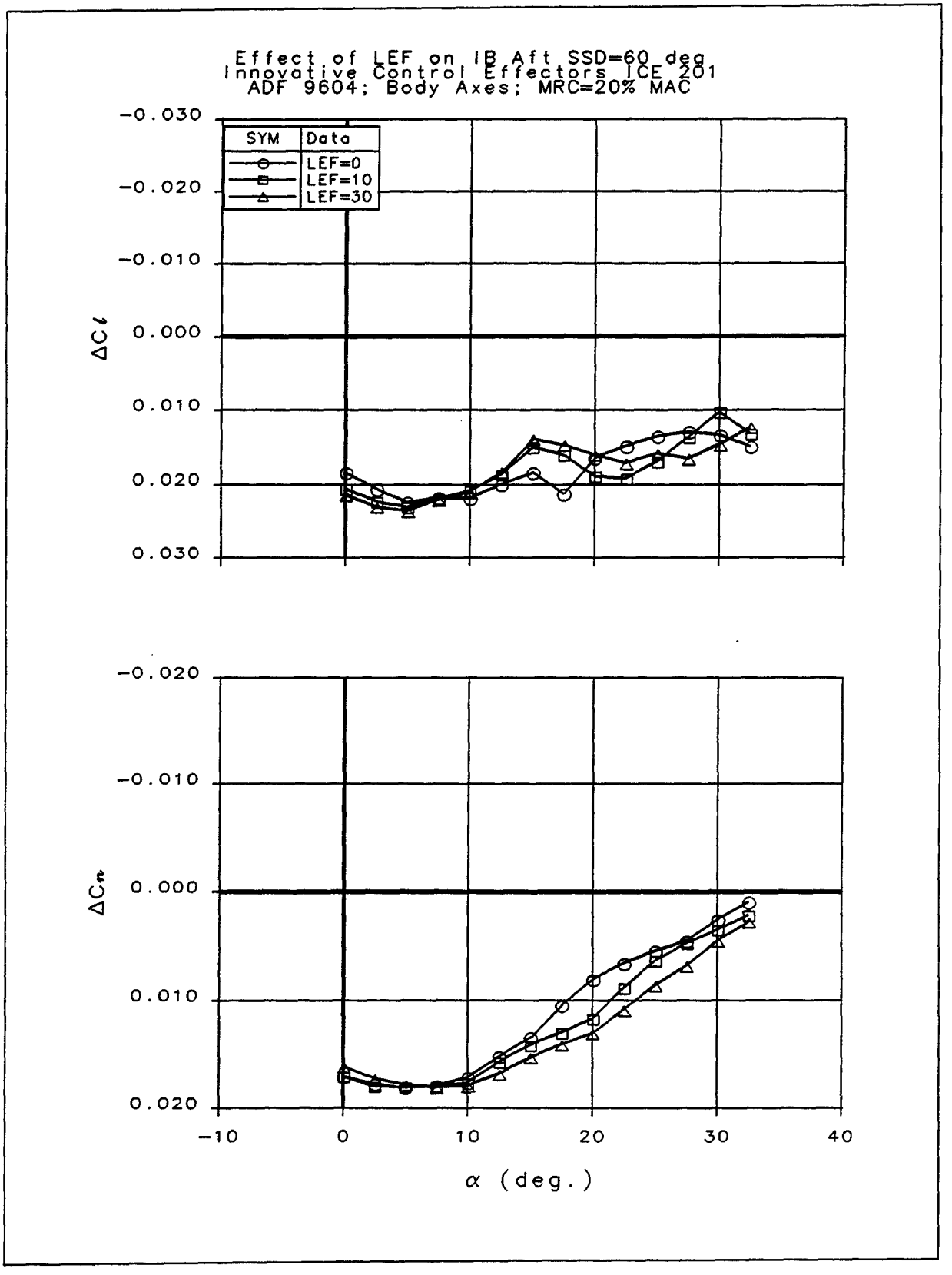

Figure 2-67: LEF Effects on SSD Control Power

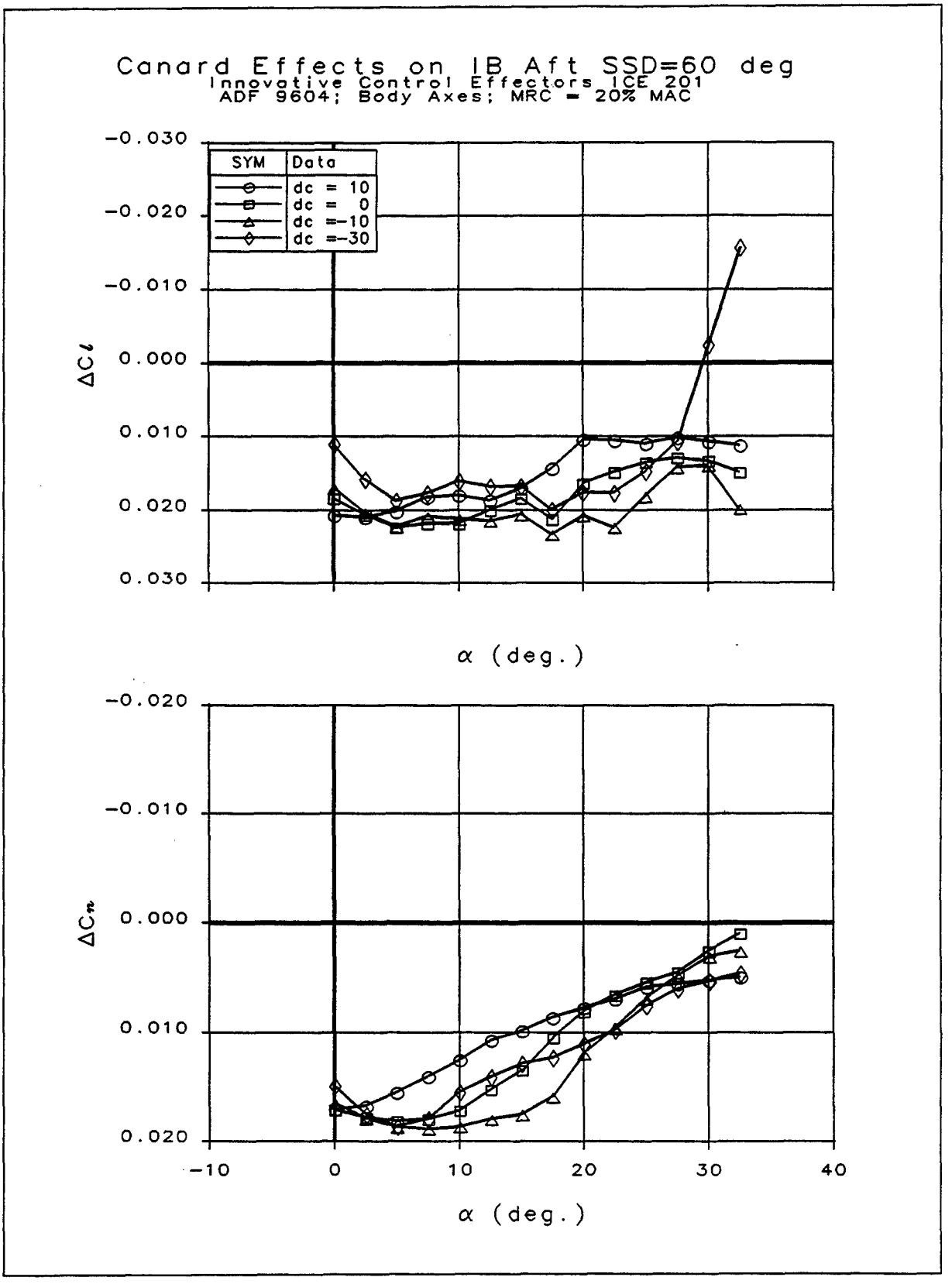

Figure 2-68: Effect of Canard Deflections on SSD Control Effectiveness

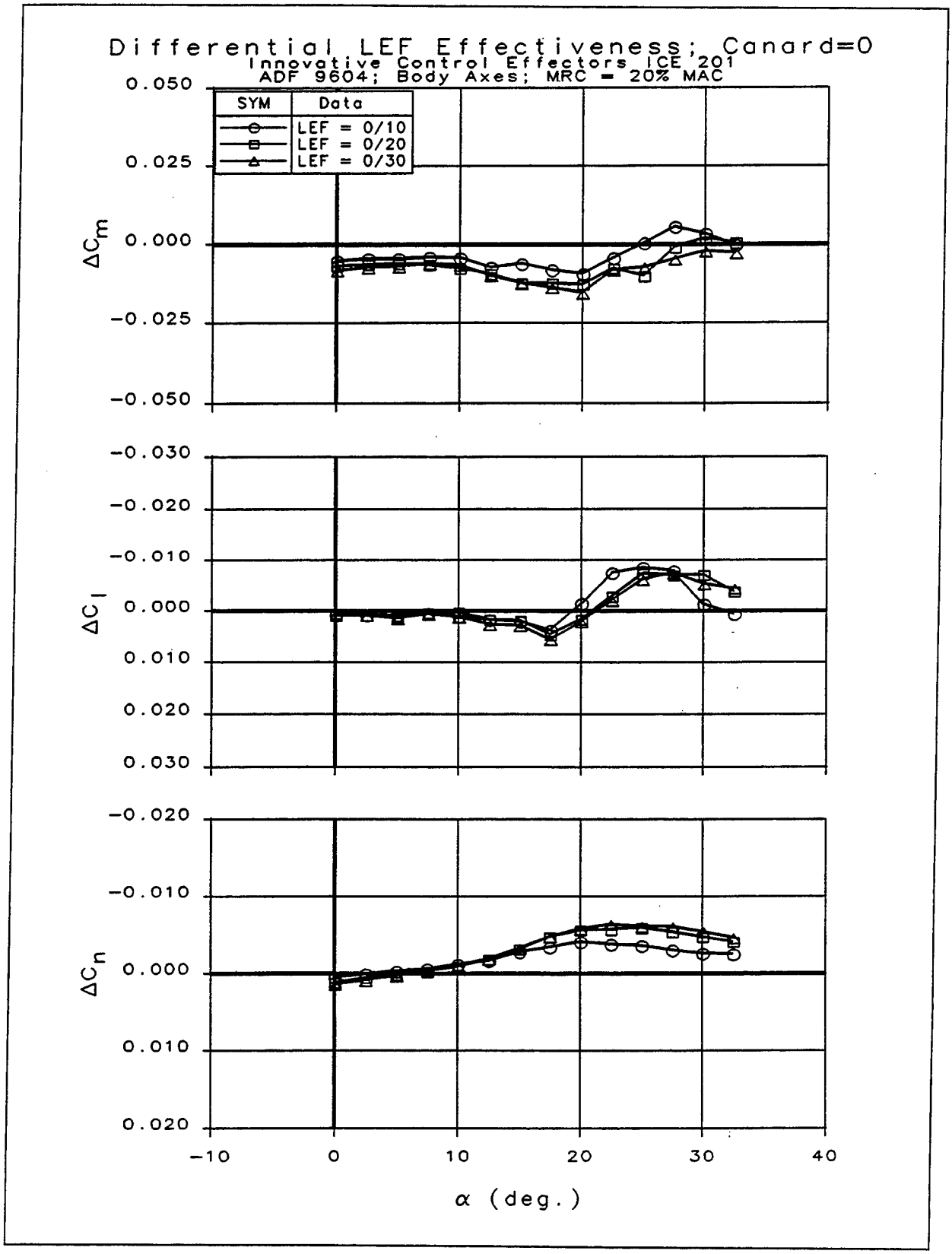

Figure 2-69: Differential LEF Effectiveness on Configuration 201

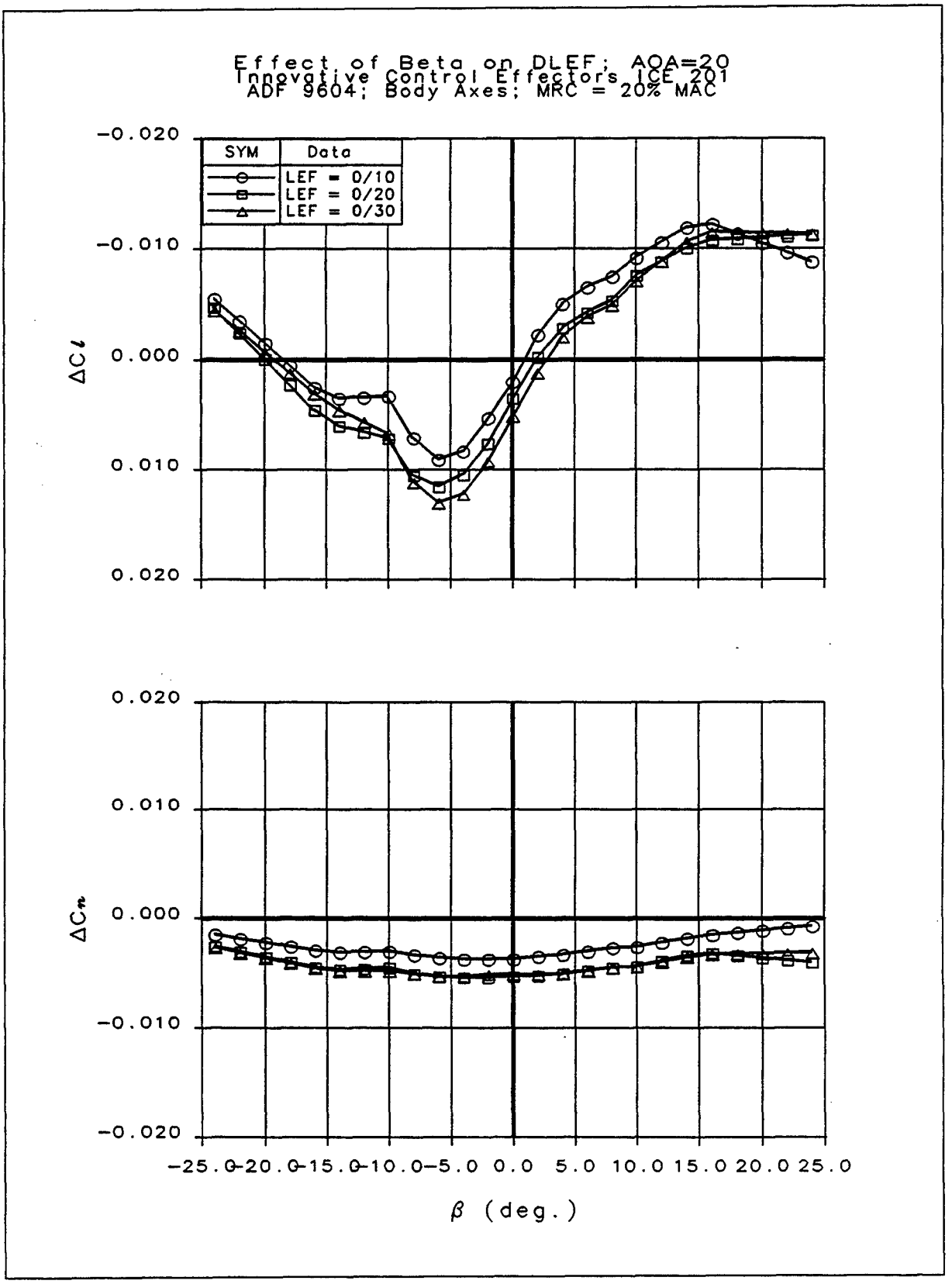

Figure 2-70: Effect of Sideslip on DLEF Effectiveness; AOA = 20°

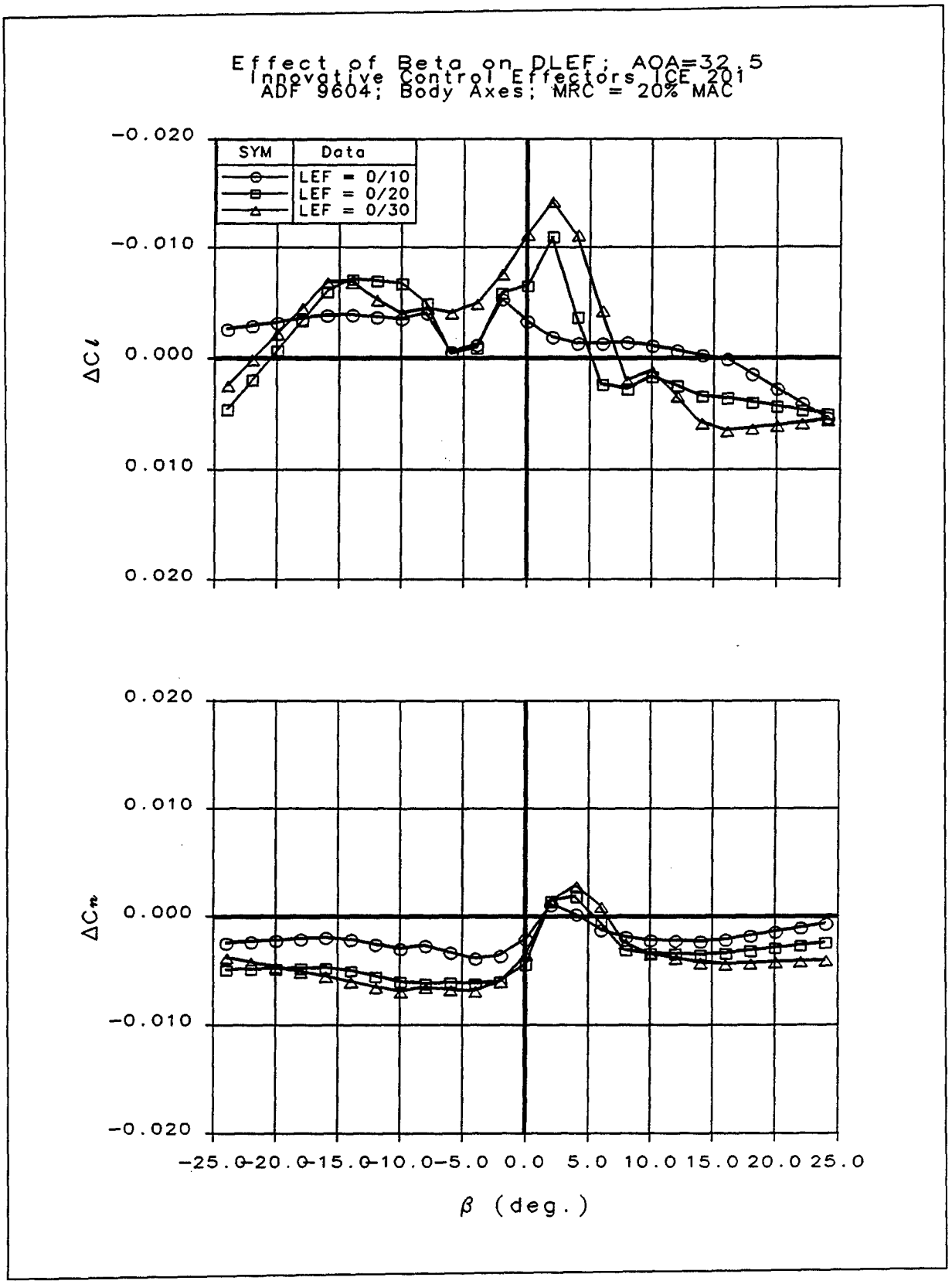

Figure 2-71: Effect of Sideslip on DLEF Effectiveness; AOA = 32.5°

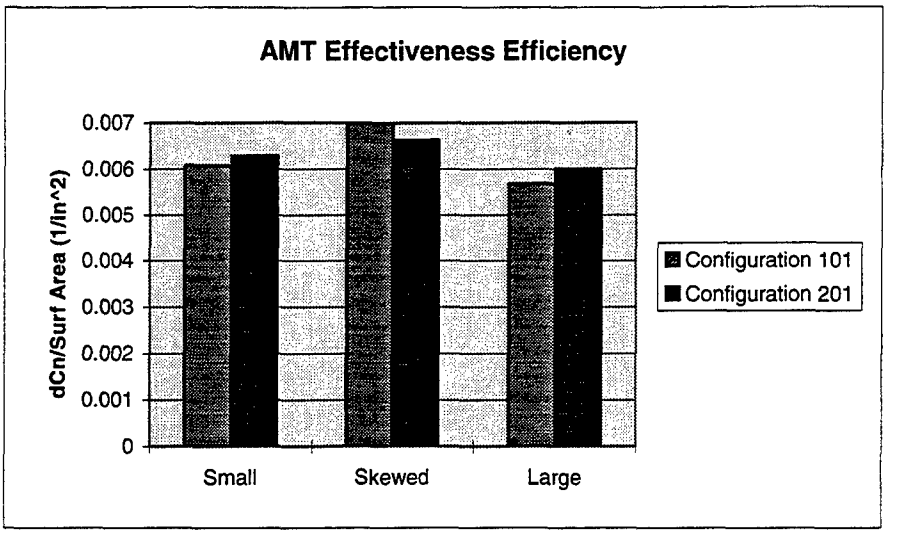

Figure 2-72: AMT Effectiveness Efficiency

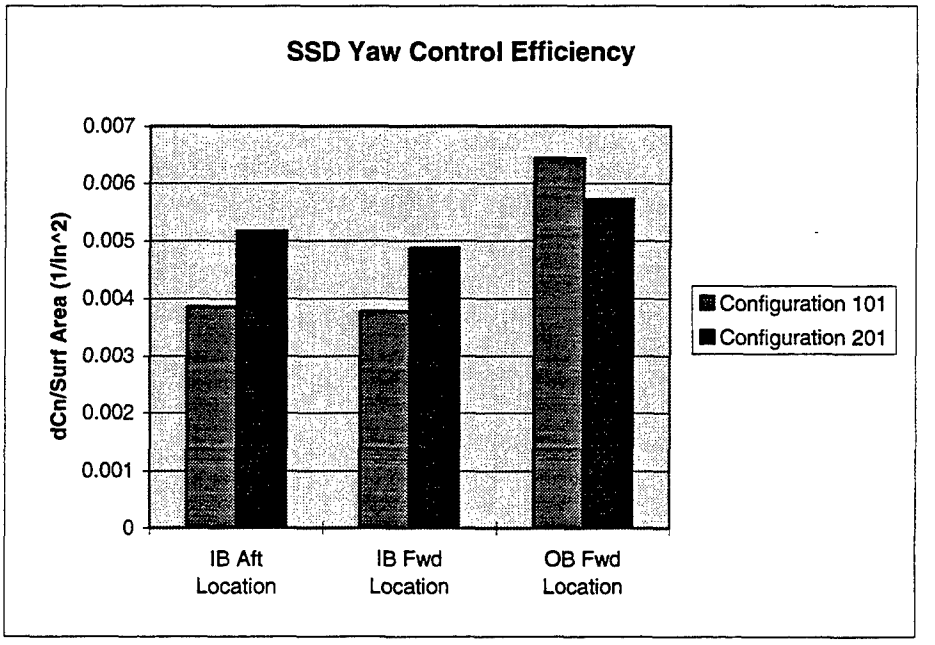

Figure 2-73: SSD Effectiveness Efficiency

3 Rotary Balance Testing and Analysis

3.1 Summary

Rotary balance wind tunnel tests were conducted on scale models of two tailless fighter configurations in order to determine the effects of rotation on various control effectors. These tests were conducted for Lockheed Martin Tactical Aircraft Systems under Phase II of the Innovative Control Effectors program that is sponsored by the U.S. Air Force and Navy. The two configurations tested were a land-based flying wing concept (ICE 101) and a carrier-based canard delta concept (ICE 201). The aerodynamic characterisitics of each model were obtained at rotational and static flow conditions at the Bihrle Applied Research Large Amplitude Multiple Purpose (LAMP) Corporate Research Facility in Neuberg a.d. Donau, Germany. The rotation characteristics of each basic ICE model were established from 0° to 90° angle of attack and for sideslip angles between -30° and +30°. The static and rotational control effectivness of the various control effectors were investigated during this test.

The basic ICE 201 model with neutral controls is damped in roll for angles of attack below maximum lift, and becomes propelling briefly in the stall region. Propelling rolling moments are also exhibited between 75° and 90° angle of attack. The basic model is neutrally damped in yaw for angles of attack below maximum lift. Yaw damping is exhibited for all other angles of attack. The all moving wing tip has little effect on the rotational characteristics. However, the spoiler-slot-deflector improves roll damping in the stall region. The baseline configuration exhibits static directional instability for all angles of attack and sideslip. A roll-stability reversal occurs in the maximum lift region for sideslip angles less than 20°. Lateral stability is observed at all other angles of attack and sideslip.

As part of the analysis, steady-state spin modes were calculated for the 201 configuration using the rotational data. A high angle of attack pitch trim condition is predicted for the 201 with neutral control deflections. Various pro-spin control deflections result in moderate spins predicted to occur around 70°-75° angle of attack.

The basic ICE 101 model with neutral controls is well damped in roll for angles of attack below 25°. Above 70° angle of attack the model becomes propelling in roll. The configuration is neutrally damped in yaw below 30° angle of attack. Yaw damping is observed at all other angles of attack. Large unstable static yawing moments develop between 20° and 50° angle of attack for sideslip angles less than 30°. Deflecting the all moving tip trailing edge down reduces roll damping below 50° angle of attack and increases yaw damping for angles of attack above 45°. The spoiler-slot-deflector results in improved yaw damping on the 101 configuration. Lateral stability is observed for all angles of attack except in the immediate post-stall region, where a roll-stability reversal occurs for sideslip angles less than 10°.

Steady-state spin modes were calculated for the ICE 101 configuration as well. Two equilibrium conditions are predicted for the basic configuration with neutral controls. A fast spin is predicted at $\alpha = 76°$, and a slower mode is predicted at $\alpha = 50°$ (5.7 sec/turn). Pro-spin elevons, in combination with the spoiler-slot-deflector deployed against the direction of the spin results in no predicted spin mode. Finally, 60° AMT deflections deployed against the direction of the spin were sufficient for spin recovery.

3.2 Introduction

Extensive rotary balance wind tunnel tests were conducted on scale models of the two ICE concepts at the Bihrle Applied Research LAMP 10-ft vertical wind tunnel. A 1/13-scale model of the land-based flying wing (designated ICE 101) and a 1/13.5-scale model of the carrier-based canard-delta (designated ICE 201) configuration were constructed for the ICE program.

These tests covered an angle of attack range from 0° to 90° and a sideslip range of ±30° for clockwise and counter-clockwise rotation rates up to 0.3 Ωb/2V. The effects of rotation on the basic model were determined. The rotational characteristics of the following four control concepts were evaluated: the all moving wing tip (AMT), the spoiler-slot-deflector (SSD), differential leading edge flaps, and upper surface spoiler. The effectiveness of the AMT and SSD as spin recovery controls were also investigated.

This report documents the ICE rotary balance test program and presents an analysis of the results. As part of the analysis, steady-state spin modes were calculated using the rotary balance data, and are presented in this report in the form of a table.

3.3 Test Facility

The ICE rotary balance test program was conducted during the month of August 1996 in the Bihrle Applied Research LAMP vertical wind tunnel located in Neuberg a.d. Donau, Germany. A photograph of the ICE 101 model mounted on the rotary balance rig in the LAMP wind tunnel is shown in Figure 3-1. Photographs of each model mounted on the aft sting are shown in Figures 3-2 and 3-3.

A double C-sector sting support system is capable of continuous angle of attack sweeps from -4° to +90° for sideslip angles out to ±30°. The angle of attack sector has sting attachment points at each end to allow for either top or aft-sting mounting. A full angle of attack range of ±180° is possible with these sting mounts.

A six-component strain gauge balance, affixed to the end of the sting and mounted inside the model, is used to measure the forces and moments acting about the body axis of the model. A control panel located outside of the tunnel test section is used to activate motors on the rig, which position the model to the desired attitude. Electrical currents from the balance and to the motors on the rig are conducted through the slip rings.

The system is capable of rotating up to 150 rpm in either the clockwise or counter-clockwise direction. A range of Ωb/2V values can be attained by adjusting the rotational speed of the rig and/or the tunnel flow velocity. Static aerodynamic forces and moments are measured when Ωb/2V=0.

The data acquisition, reduction, and presentation system is composed of a NEFF System 470 16-channel scanner/voltmeter, a personal computer, and printer. This equipment permits data to be viewed via on-line digital print-outs and/or graphical plots.

3.4 Test Procedures

A rotary balance rig measures the forces and moments acting on a model subjected to rotational flow conditions. Historical background for this test technique is presented by Bihrle, 1981. Rotary aerodynamic data are obtained in two steps. First, the inertial forces and moments (tares) acting on the model at different attitudes and rotation rates must be determined. Ideally these inertial terms would be measured by rotating the model in a vacuum. As a practical approach, the model is enclosed in a sealed spherical structure that rotates with the model, but without touching it. In this manner, the surrounding air moves with the model, thus eliminating any aerodynamic forces and moments that may be generated if the model were rotated in open air. As the rig is rotated at the desired attitude and rate, the inertial forces and moments generated by the model are measured and stored on magnetic disc for later use. Before the air-on test begins, the spherical enclosure is removed, and force and moment data are measured with the wind tunnel in operation. The tares that were recorded earlier are then subtracted from these data, leaving only the aerodynamic forces and moments which are then converted into coefficient form.

3.5 Description of Models

The models were constructed of fiberglass, balsa, and plywood, with carbon fiber added for additional stiffness. A 1/13-scale model of the land-based flying wing concept (ICE 101) and a 1/13.5-scale model of the carrier-based canard-delta concept (ICE 201) were built for the rotary balance test program.

A three-view drawing of the 201 configuration is shown in Figure 3-4, and the dimensional characteristics of the model are given in Table 3-1. The 201 model was constructed with removable canards for component tests. The control surfaces could be set to any deflection within the following limits:

Wing LE Flaps	0°, +30° TED
Pitch Flap	-30° TEU, +30° TED
Elevons	-30° TEU, +30° TED
Ailerons	-30° TEU, +30° TED
All Moving Tip	-10° TEU, +60° TED
Upper Spoiler	0° or 60°
Spoiler-slot-deflector	0° or 60°

A three-view drawing of the 101 configuration is shown in Figure 3-5, and the dimensional characteristics of the model are presented in Table 3-2. The control surfaces could be set to any deflection within the following limits:

Wing LE Flaps	0°, +30° TED
Pitch Flap	-30° TEU, +30° TED
Elevons	-30° TEU, +30° TED
All Moving Tip	-10° TEU, +60° TED
Upper Spoiler	0° or 60°
Spoiler-slot-deflector	0° or 60°

Note that only one SSD and one upper spoiler position were tested for each model. As a result, both the 101 and 201 configurations were built with spoiler-slot-deflectors that only deployed to one setting of 60°. Figure 3-6 shows the SSD deployed on the right wing of the flying wing configuration.

3.6 Test Conditions

The rotary balance tests were conducted in the LAMP 10-ft vertical tunnel at a dynamic pressure of 1.5 lb/ft^2 or freestream velocity of 36 ft/sec, which corresponds to a Reynolds number of approximately 229,000 per foot. The 101 model was tested with the spin axis located at the model c.g. location of 0.38 $\bar{c}$, but slightly below the waterline of the c.g. such that the balance moment center was located at FS 291.94, WL 95.06 (full-scale). The vertical offset was accounted for when the overall forces and moments were computed. Therefore, all ICE 101 data presented in this report are referenced to FS 291.94, WL 100.0 (0.38 $\bar{c}$).

The spin axis of the 201 was intended to be at the model c.g. location of 0.20 $\bar{c}$. However, due to a discrepancy over the fuselage station of the nose tip the balance moment center was placed 28.4 inches aft of the nose tip at FS 395.4,

WL 100 (full-scale). This corresponds to 0.248 $\bar{c}$. Note that all ICE 201 moment data presented in this report were transferred to 0.20 $\bar{c}$.

All configurations were tested through an angle of attack range of 0° to 90° and sideslip angles of up to ±30°. Table 3-3 lists all of the 201 configurations tested, and Table 3-4 lists the 101 configurations tested. Unless otherwise noted in the tables, data were obtained from 0° to 90° in 5° increments and Ωb/2V values of 0.0 (static value), 0.05, 0.1, 0.2, and 0.3 in both the clockwise (pilot's right) and counter-clockwise directions.

3.7 Data Presentation

Selected comparison plots are included herein to support the analysis. All data are presented in body axes unless otherwise noted. Rotary balance data are presented by plotting the aerodynamic coefficients versus the non-dimensional rotation rate, Ωb/2V. The rotary plots are divided into four quadrants by the coordinate axes. Static data points occur on the ordinate axis (Ωb/2V=0). All points to the right of the this axis (positive Ωb/2V) represent data measured during rotation to the pilot's right. Conversely, all data to the left of the ordinate axis represent data points obtained while rotating to the pilot's left. To an outside observer looking down, this means the airplane will rotate clockwise when it is upright and counter-clockwise when inverted.

Rotary balance data indicate the behavior of the airplane due to rotation and thus, the potential for departing from controlled flight and entering a spin. Rotational aerodynamics are also experienced during coordinated roll maneuvers. For clockwise rotation on an upright airplane, positive rolling or yawing moments increase the rotation rate and are therefore defined as propelling moments. Conversely, a negative rolling or yawing moment with clockwise rotation is described as a damping moment, because the moment will tend to resist the rotation. The opposite is true for counter-clockwise rotation, where negative rolling and yawing moments are propelling and positive moments are damping. Therefore, a negative slope of roll or yaw versus rotation indicates the moments are damped. Conversely, a positive slope indicates propelling moments.

3.8 Discussion of ICE 201 Results

Rotary balance tests were conducted on the ICE 201 carrier-based canard-delta configuration from 0° to 90° angle of attack and out to ±30° angle of sideslip. The baseline 201 configuration was tested first and the influence of the various control effectors was then investigated both statically and at rotation.

The benefits of canard-wing configurations are widely known and documented [Behrbohm: 1965; Stoll & Koenig: 1983; Das & Longo: 1995]. Downwash from the canard induces a non-uniform distribution of local angle of attack at the front and inner portion of the wing that is beneath the canard vortex wake. The effective incidence on this section of the wing is reduced, which suppresses flow separation and delays the formation of the wing leading edge vortex. The slower build-up of the leading edge vortex along the part of the wing under the canard wake results in a wing vortex that is weaker when it encounters an adverse pressure gradient near the wing trailing edge. As a result, wing leading edge vortex separation is delayed to higher angles of attack [Hummel & Oelker: 1994; Hoeijmakers: 1990]

3.8.1 Baseline Static and Rotary Characteristics

The baseline 201 configuration, as referred to in this report, has neutral control deflections, including both the leading edge flaps and canard. This section of the report presents the static and rotational characteristics of the baseline model. The rotational effects of the all moving wing tip (AMT), differential leading edge flap, spoiler, spoiler-slot-deflector (SSD), and canard were all evaluated in this test series.

Longitudinal

Maximum lift is attained by α=25°, as illustrated in Figure 3-7. Note that both the canard-on and canard-off configurations produce nearly the same amount of lift at low to moderate angles of attack; this effect has been observed in other tests [Stoll: 1983; Das: 1995]. As discussed previously, the wing of a canard-wing configuration works at a lower effective angle of attack than a wing alone configuration and thus produces less lift. However, the additional lift from the canard compensates for the loss of lift at the wing [Hummel: 1994]. As a result, both the canard-on and canard-off configurations generate nearly the same amount of lift, as shown in Figure 3-7. The lift curve slope is the same below α=5° for both the canard-on and canard-off configurations, beyond which the lift curve slope becomes slightly steeper for the canard-on configuration.

The static pitching moment data is presented in Figure 3-8. At zero sideslip the 201 is increasingly nose-up from 0° to 20° angle of attack. At α=20°, a slope reversal occurs and the airplane becomes less nose-up with angle of attack. At α=30°, the pitch curve levels off somewhat, exhibiting a slightly positive slope up through α=45°. Above α=45°, the 201 model gradually becomes less nose up with angle of attack until it breaks nose down at about α=66°. The pitching moments are increasingly nose down as the angle of attack continues to increase through 90°.

At nonzero sideslip angles, the 201 is less nose up between 35° and 65° angle of attack as shown in Figure 3-8. This nose down increment increases as sideslip angle increases. In the 45° to 65° angle of attack region, the slope of the pitching moment curve becomes more linear with increasing sideslip angle. The pitching moment curve is nearly linear for all angles of attack above 25° when β=30°.

Tests conducted with the canards removed revealed that at very low angles of attack the pitching moment is neutral on the wing-alone configuration, as shown in Figure 3-9. Removing the canards resulted in less nose up pitching moments throughout the entire angle of attack range. Note also that the change in pitching moment slope near the region of maximum lift is less extreme when the canards are removed. Correspondingly, the post-stall decrease in the lift coefficient is less severe for the canard-off configuration (see Figure 3-7).

The effects of rotation rate on pitching moment are presented in Figure 3-10. At zero sideslip and low angles of attack, pitching moment is fairly constant with rotation. At higher angles of attack the 201 becomes slightly less nose up with rotation. The effects of sideslip on the rotational pitch characteristics are typical of those observed on other fighter configurations [Kay & Ralston: 1995; Dickes: 1991]. A nose down increment is produced when the signs of sideslip and rotation rate are both the same. Conversely, a nose-up increment results when the signs of sideslip and rotation rate are opposite one another.

Lateral

The 201 exhibits very small levels of lateral instability below α=5°, as shown in Figure 3-11. However, stable rolling moments are observed between 5° and 20° angle of attack. At sideslip angles of 10°, a roll-stability reversal occurs between 18° and 32° angle of attack. The occurrence of a roll-stability reversal has been observed in previous experiments on delta wing configurations [Johnson, Grafton & Yip: 1980]. One explanation for the occurrence of a reversal in roll-stability on a canard-delta configuration is that at sideslip the canard tip vortex reinforces the wing leading edge vortex on the leeward side, but not on the windward side. This causes the windward leading edge vortex to burst first, decreasing the lift on the windward wing [Stoll: 1983]. The roll-stability degradation occurs for sideslip angles out to 20°, although at β=20° the rolling moments do not become unstable. At larger sideslip angles no roll reversal is evident. Above α=30° the stability levels increase slightly up to 90°α for all sideslip angles tested.

The 201 configuration is well damped in roll for angles of attack below maximum lift as shown in Figure 3-12. At 25° and 30° α, the 201 model exhibits neutral to slightly propelling roll characteristics that are typical of military configurations in the stall region. From 35° to 70° angle of attack the model once again exhibits roll damping, with

reduced levels of damping occurring for increasing angles of attack. At α=75°, the model transitions from damped to propelling rolling moments that persist on up to 90° angle of attack.

Directional

The effect of sideslip on the static yawing moment is presented in Figure 3-13. The model exhibits unstable yawing moments for all angles of attack and sideslip. At β=10°, the magnitude of the yawing moments increase between 15° and 30° angle of attack. Generally constant yawing moments are produced for angles of attack above 30°. The effect of increasing sideslip angle is fairly linear at low angles of attack, but above α=15° larger sideslip angles have less effect on the magnitude of the yawing moments produced. Also note the small static asymmetry that occurs at zero sideslip between 40° and 60° angle of attack.

The rotational yawing moment characteristics are presented in Figure 3-14. The model is neutrally damped (constant with rotation) in yaw below 20° angle of attack. At α=20° the model is very lightly damped in yaw. The model then becomes increasingly damped as the angle of attack increases, and the model remains well damped up through 90°.

3.8.2 Control Effectiveness

The effectiveness of the various 201 control effectors are discussed in this section. The following were investigated for their control effectiveness: symmetric and differential leading edge flaps, symmetric canard deflection, pitch flaps, elevons, ailerons, all moving wing tip (AMT), spoilers, and spoiler-slot deflectors (SSD). The effect of the AMT or SSD on the effectiveness of various control surfaces is also discussed here. The control effectiveness was investigated using left-side deflections for each control surface. Unless otherwise specified, the leading edge flaps were deflected thirty degrees for all control power runs.

Leading Edge Flaps

Symmetric Leading Edge Flaps

Static

The effects of leading edge flap deflection on lift are presented in Figure 3-15 for flap angles of zero and thirty degrees. As expected, maximum lift is increased by deflecting the leading edge flaps. However, the angle of attack of maximum lift did not change. Also, the post-stall reduction in lift is less severe with the leading edge flaps deflected thirty degrees.

Deflecting the leading edge flaps only affects pitching moment in the region of maximum lift, as shown in Figure 3-16. The model is more nose up in this region (between 20° and 35°) when the flaps are deflected thirty degrees. Leading edge flap deflection has virtually no effect on the pitching moment at nonzero sideslip angles.

The effect of leading edge flap deflection on the static lateral stability characteristics is presented in Figure 3-17. Deflecting the leading edge flaps reduces the angle of attack range of the roll reversal that occurs at low sideslip angles, by delaying the onset of the reversal. With the leading edge flaps deflected and β=10°, the roll-stability reversal onset is delayed from α=18° to about α=22°. In general, the level of roll instability is reduced when the leading edge flaps are deflected.

The effect of the leading edge flaps on the static yawing moment characteristics are shown in Figure 3-18. Yaw is only slightly influenced by deflecting the leading edge flaps. At nonzero sideslip angles, deflecting the leading edge flaps has a slightly more destabilizing influence on yaw.

Rotational

Figure 3-19 illustrates the effect of leading edge flap deflection on the rotational rolling moment characteristics. Deflecting the leading edge flaps significantly increases the roll damping just below the angle of maximum lift (α=20°). Beyond the maximum lift region, the model is more propelling in roll and remains propelling out to higher angles of attack when the leading edge flaps are deflected. This effect is typical of airplanes with leading edge devices, and has been observed in other rotary balance tests [Dickes: 1991; Houlden: 1995]. Above α=55°, the leading edge flaps have no significant effect on roll damping.

Deflecting the leading edge flaps reduces the yaw damping at certain angles of attack, as illustrated in Figure 3-20. Below the angle of maximum lift, the leading edge flaps have no effect on the rotational yaw characteristics. At α=25° the yaw damping is significantly reduced when the leading edge flaps are deflected. For angles of attack above α=25°, deflecting the leading edge flaps generally reduces yaw damping. Note that as the angle of attack approaches 90°, the effect of leading edge flap deflection on yaw damping decreases.

Differential Leading Edge Flaps

The effect of differential leading edge flap deflection on static rolling moment is shown in Figure 3-21 for LEF=30°/0° (left/right). The differential flaps produce rolling moments just above α=15° and remain effective up through α=55°. At α=30° the roll produced by differential flaps is adverse. This may be the result of a sudden decrease in side force at α=30°, shown in Figure 3-22.

The effect of differential leading edge flaps on the rotational roll characteristics is presented in Figure 3-23. Note that during rotation, the flap angle of the leeward wing has no effect on the roll damping. When rotating to the left (negative $\Omega b/2V$), where the windward wing has zero flap deflection, the roll damping matches the roll damping of the symmetric zero flap configuration. Similarly, for positive $\Omega b/2V$ the windward wing has a thirty degree flap deflection, and the rolling moments match those obtained with a symmetric flap deflection of thirty degrees. Differential leading flap deflections have no effect on the rotational yaw characteristics, as illustrated in Figure 3-24.

Canard Effectiveness

Only symmetric canard deflections were investigated during this test program. Canard deflections of +10° (TED), -20, -40, and -60° were tested with the leading edge flaps deflected thirty degrees. Canard deflections of -60° were also tested with zero leading edge flaps.

Static

The effect of canard deflection on normal force is presented in Figure 3-25. Maximum normal force is achieved with a canard deflection of -20° (trailing edge up). Larger TEU canard deflections actually reduce normal force slightly.

The effects of canard deflection on the static longitudinal characteristics are presented in Figure 3-26. Trailing edge up canard deflections are effective in generating nose down pitching moments up to 80° angle of attack. For nose-down canard deflections (trailing edge up), the pitch control effectiveness is linear between 10° and 25° angle of attack. Nose-down control power below 10° angle of attack is reduced for larger canard deflections of -40° and -60°. At low angles of attack, deflecting the canard -40° generates the maximum nose down pitching moment. Above α=25°, canard deflections of -60° are most effective in generating nose down pitching moments. Nose-up canard (TED) is only effective up to 20° angle of attack. Beyond 20° α, nose-down pitch increments are produced with TED canard. Deflecting the canard 60° TEU and all trailing edge controls 30° TED gives the maximum nose down pitching moment, as shown in Figure 3-27.

The effect of canard deflection on the static zero sideslip rolling moment is shown in Figure 3-28. Deflecting the canards results in a roll offset in the stall region (25°-40°α). Trailing edge down canard produces positive rolling moments between 30° and 45° angle of attack. Negative rolling moment offsets are the result when the canard is deflected trailing edge up. The effects due to canard deflection at sideslip are presented in Figure 3-29. Positive (TED) canard deflection has no effect on the lateral stability characteristics except to slightly reduce the magnitude of the roll-stability reversal. Negative (TEU) canard deflections have a slightly destabilizing influence on the basic configuration at low to moderate angles of attack. The angle of attack range of the roll-stability reversal is also reduced by deflecting the canard. Beyond α=35°, deflecting the canard has no effect on the static lateral characteristics of the 201. Additionally, deflecting the leading edge flaps in the presence of the canard has little influence on the lateral characteristics, except to reduce the level of instability observed in the stall region, as shown in the incremental plot of Figure 3-30.

The effects of canard deflection on the static directional characteristics are shown in Figure 3-31. TED canard has virtually no effect on the directional characteristics, while TEU canard deflections have a slightly destabilizing effect at angles of attack between about 30° and 65°. At high angles of attack, leading edge flap deflections influence the directional characteristics due to the canard as shown in Figure 3-32. The destabilizing influence of the canard is aggravated if the leading edge flaps are set to zero.

Rotational

The effects of rotation rate and canard deflection on pitching moment are presented in Figure 3-33. Trailing edge down canards have no effect on the rotational pitching moment at any angle of attack. Trailing edge up canard deflections have no effect on the rotational pitch characteristics below α=25°. However, TEU canard tends to "flatten" out the rotational pitch curve for angles above the angle of maximum lift, as illustrated in Figure 3-33. Figure 3-33 also shows that leading edge flap deflection has little effect on the rotational pitch characteristics with the canard deflected.

The effects of canard deflection on the rotational roll characteristics are presented in Figure 3-34. Below α=20° the rolling moments are slightly less damped with trailing edge up canard deflections. At 20° and 25° α, roll damping is increased due to TEU canard. No other effects due to TEU canard deflections are observed until α=40°, where the roll damping increases slightly. As the angle of attack continues to increase, only at higher rotation rates is a slight improvement in roll damping observed. Trailing edge down canard deflections have much less influence on the rotational roll characteristics. The primary effect due to TED canard is to reduce roll damping at α=20° (just below the angle of maximum lift). In the immediate post-stall region, deflecting the canard TED significantly improves the propelling characteristics exhibited by the baseline configuration.

Leading edge flap deflection also influences the roll damping due to canard deflections, as shown in Figure 3-35. Deflecting the canard TEU without deflecting the leading edge flaps has a detrimental effect on the rotational roll characteristics from 20° to 25°. From α=20° to 25°, higher levels of roll damping are observed when the leading edge flaps are deflected thirty degrees. From 30° to 35° angle of attack, deflecting the leading edge flaps results in slightly more propelling rolling moments with TEU deflected canard. While these effects are similar to the leading edge flap effect observed with zero canard deflection, these data do reflect some interactive effects between the leading edge flaps and canard.

Figure 3-36 shows the effect of rotation and canard deflection on yawing moment. Deflecting the canard TEU generates slightly propelling yawing moments at angles of attack below 10°. Yaw damping is increased for all other angles of attack. The effects of TED canard on rotational yaw characteristics are negligible. Note that leading edge flap deflection has little influence on the yaw damping due to canard deflection.

Pitch Flap Effectiveness

The control effectiveness of the pitch flaps (inboard trailing edge flaps) is presented in Figure 3-37. The pitch flaps provide good nose-up control power throughout the entire angle of attack range. Nose-down pitch flap (trailing edge down) is effective up to about 60° angle of attack. Note that at most angles of attack, the magnitude of the pitch increment due to nose-down pitch flaps is slightly less than that due to nose-up deflections.

Elevon Effectiveness

The elevon (middle trailing edge flap) control effectiveness is shown in Figures 3-38 through 3-40. Figure 3-38 shows the elevon effectiveness in pitch. Nose up elevon (TEU) is effective up to 90°. Nose-down (TED) elevon is effective only up to about 50° angle of attack. The roll control power due to elevon deflection is presented in Figure 3-39. A corresponding loss of roll effectiveness due to trailing edge down elevon occurs at about α=45°, as shown in Figure 3-39. The elevons exhibit good roll effectiveness below 30° angle of attack. Elevon deflection has little effect on the yaw characteristics, as illustrated in Figure 3-40.

Aileron Effectiveness

Aileron control effectiveness is presented in Figures 3-41 through 3-43. As with the other trailing edge controls, TED aileron exhibits nose-down effectiveness up to about 50° angle of attack (Figure 3-41). Figure 3-42 shows that the ailerons are very effective in roll below about 30° angle of attack, with the roll effectiveness becoming reduced at higher angles of attack. Small levels of adverse yaw are generated by trailing edge down aileron deflections, as shown in Figure 3-43. Trailing edge up aileron deflection does not appear to produce any accompanying yawing moment.

Effectiveness of the All Moving Wing Tip

The all moving wing tip (AMT) is employed primarily as a yaw control device. An all moving wing tip produces axial force to generate a yawing moment. This all moving tip design is unique in that it has an aft-swept hingeline that also generates a substantial side force that contributes to the yaw control power. The skewed hingeline of the all moving wing tip is pictured in Figure 3-44. The AMT control effectiveness for left-side deflections is presented in Figures 3-45 through 3-49.

Static

Figure 3-45 presents the axial force produced when the AMT is deflected. The AMT does not have any effect on pitching moment when deflected TED, as shown in Figure 3-46. However, TEU deflections did produce very small nose up moments at low to moderate angles of attack.

The AMT exhibits yaw effectiveness above 25° angle of attack when deflected trailing edge up, as shown in Figure 3-47a. Positive yaw is produced with left-hand TEU deflections. The AMT exhibits good yaw control power for all angles of attack with TED deflections. The yaw effectiveness appears to be linear with TED deflection angle up to α=60°. Above 60° angle of attack, the yaw control power is generally not influenced by the AMT deflection angle. Note the yaw reversal that occurs near stall at α=30° with trailing edge down AMT. This corresponds to a spike in side force at the same angle of attack, as shown in Figure 3-48. Figure 3-48 indicates that although side force increases at this angle, the center of pressure has moved forward, resulting in a positive yaw increment.

The influence of sideslip angle on the yaw effectiveness of the AMT is presented in Figure 3-49a for a trailing edge down deflection of 60° on the left wing. Negative yaw increments are produced for all sideslip angles. Above α=40°, the yaw effectiveness is significantly reduced when the leeward AMT is deflected (left-hand AMT, positive β).

Figure 3-47b shows that while trailing edge up AMT deflections are very effective in roll below 35° angle of attack, the effectiveness is quite non-linear. The AMT loses effectiveness entirely at about 60°. The rolling moments produced with left-hand TED AMT deflections are adverse below 10° angle of attack. Above 10°α, favorable roll increments are produced with either TEU or TED deflections. The AMT remains effective in roll up through 90° when deflected TED. The control power appears to be linear with deflection angle. Trailing edge up deflected AMT exhibits good roll control effectiveness for angles of attack below 20°.

Figure 3-49b illustrates the effect of sideslip angle on AMT roll control power. Adverse roll is produced for angles of attack below 10° and for both positive and negative sideslip angles. Favorable roll is exhibited with the leeward AMT (positive β for left-hand AMT) for all angles of attack above 10°. Deflecting the windward AMT (negative β) eliminates the non-linear roll characteristics observed on the baseline configuration by producing constant rolling moments up through α=20°. Also note that the level of instability is reduced in the region where the roll-stability reversal occurs.

Rotational

Deflecting the AMT trailing edge up has no effect on the rotational roll characteristics, as illustrated in Figure 3-50. Trailing edge down deflections reduce roll damping slightly for angles of attack below 25°. For α=25°-30°, trailing edge down AMT improves the propelling characteristics slightly at higher rotation rates. For angles of attack above 30°, TED deflections have no significant effect on the rotational rolling moment characteristics.

TEU deflections have no effect on the yawing moment due to rotation, as shown in Figure 3-51. Deflecting the AMT trailing edge down slightly reduces the yaw damping at angles of attack below 35°. Otherwise, deflecting the AMT primarily results in a static shift of the rotational characteristics.

AMT/Aileron Interactions

The aileron roll effectiveness is reduced when in the presence of an AMT deflection, as shown in Figure 3-52. Note that aileron roll power is most seriously affected at angles of attack below 35°.

Spoiler Effectiveness

Static

The spoiler effectiveness is shown in Figures 3-53 through 3-56 for left-side upper surface spoiler deployment. The spoiler exhibits good roll control power up to 30° angle of attack, as shown in Figure 3-53. Figure 3-54 shows that favorable yaw is generated for angles of attack up to 25°. Above α=25°, no yawing moment is produced by the spoiler.

The effects of sideslip angle on spoiler deflection are primarily limited to angles of attack below about 30°. Figure 3-55 shows that left-side spoiler deflections produce negative roll increments at low angles of attack for all sideslip angles tested. Deploying the leeward spoiler (left spoiler in positive sideslip) results in roll effectiveness similar to that seen at zero sideslip. When the spoiler is deployed on the windward wing (negative β in this case) greater roll power is exhibited up through α=20°. However, the control effectiveness reverses at α=25°, with positive roll increments produced with a windward spoiler deployment. This characteristic is reversed for the spoiler effectiveness in yaw, as shown in Figure 3-56. The windward spoiler exhibits yaw effectiveness similar to that seen at zero sideslip with negative yaw produced by left-side spoiler deployment. Meanwhile the leeward spoiler is effective up through 90° with a reversal in effectiveness occurring at α=30°. Note that greater yaw control power at low angles of attack is achieved with the windward spoiler.

Rotational

The effects of spoiler deployment on the rotational roll characteristics are limited to certain angles of attack and rotation rates, as shown in Figure 3-57. At α=25°, the spoiler significantly increases the roll damping. Beyond 25°α, roll damping is affected only when the spoiler is deployed on the advancing wing (positive $\Omega b/2V$ for left-side spoiler). Figure 3-57 also shows that from 30° to 45° α, the roll damping is improved for positive rotation rates.

Similar effects, although to a lesser degree, are noted in the rotational yaw characteristics. Figure 3-58 shows that the model is slightly more damped in yaw at positive rotation rates for angles of attack below 30°. The spoiler has no effect on the rotational yaw characteristics at higher angles of attack.

Effectiveness of the Spoiler-Slot-Deflector

A photograph of the spoiler-slot-deflector (SSD) deployed on the ICE 101 configuration is shown in Figure 3-6. The shape of the SSD is the same on both ICE models.

Static

The roll effectiveness of the SSD is shown in Figure 3-59 for a left-side deployment of the control. Note that the SSD generates almost twice as much roll power as the spoiler. The SSD is also effective out to higher angles of attack than the spoiler. The SSD exhibits roll effectiveness up to α=40°, while the spoiler is effective in roll up to 30° angle of attack. The effects of sideslip on the SSD roll control power are similar to those observed with the spoiler, as shown in Figure 3-60.

In Figure 3-61 the influence of the SSD on the static yawing moment is compared with the effects due to the spoiler. The SSD exhibits significantly more favorable yaw control power and remains effective up to much higher angles of attack (α=60°) than the spoiler. Above 60° α, however, a control reversal occurs such that positive yaw (nose-right) is produced with a left-side SSD deployment. Figure 3-62 shows that the SSD yaw effectiveness is influenced by nonzero sideslip angles in a similar fashion as the upper surface spoiler.

Rotational

The effect of rotation rate and SSD deployment on rolling moment is presented in Figure 3-63. The SSD improves roll damping from 25° to 35° angle of attack. Figure 3-63 shows that roll damping due to the SSD is greater than the roll damping due to the spoiler. Above 35°α roll damping is increased only when the spoiler/SSD wing is advancing (positive $\Omega b/2V$ in this case). Note that the SSD has a greater overall effect on the rotational roll characteristics than the spoiler alone. Although, as the angle of attack approaches 90°, neither the spoiler nor the SSD significantly influence roll damping. The effect of the SSD on the rotational yaw characteristics is illustrated in Figure 3-64. Yaw damping is slightly increased for angles of attack below 30°, and no effects are noted at any higher angles of attack.

SSD/Canard Interactions

Deflecting the canard TEU slightly reduces the roll effectiveness of the SSD at low angles of attack, as shown in Figure 3-65. Between 20° and 45° angle of attack, however, greater roll power is exhibited by the SSD/canard configuration than by the SSD alone configuration.

SSD/Elevon Interactions

Figure 3-66 shows the effect of the SSD on elevon roll effectiveness. Elevon roll power is slightly reduced by the SSD. Note that the SSD has more effect on TED elevon deflections. The elevon effectiveness in pitch or yaw is not affected by the SSD, as shown in Figures 3-67 and 3-68.

SSD/Aileron Interactions

The effect of the SSD on aileron roll effectiveness is presented in Figure 3-69. Figure 3-69 shows that the SSD has a significant impact on the aileron control power. The SSD completely neutralizes TED aileron roll effectiveness. In addition, the roll power due to TEU aileron is sharply reduced at angles of attack below 20°.

3.9 Discussion of ICE 101 Results

Rotary balance tests were conducted on the ICE 101 land-based delta wing configuration from 0° to 90° angle of attack and sideslip angles of 0°, ±10°, ±20, and ±30°. The baseline 101 configuration was tested first, then the influence of the various control effectors was investigated both statically and at rotation. The interaction between certain control surfaces was also investigated. The rotational effects of the all moving wing tip (AMT), differential leading edge flap, spoiler, and spoiler-slot-deflector were all evaluated in this test program.

3.9.1 Baseline Static and Rotary Characteristics

The baseline configuration for the 101, as referred to in this report, has neutral control surface deflections, including zero leading edge flaps. This section of the report presents the baseline static and rotational characteristics.

Longitudinal

Maximum lift is attained on the baseline configuration at 25° angle of attack, as shown in Figure 3-70. The static pitching moment characteristics are presented in Figure 3-71. The model exhibits neutral pitch stability between 0° and 10°α at zero sideslip. At α=10° a nose-up break occurs, with an unstable slope continuing up to 25° angle of attack. A slope reversal occurs at α=25° and the model becomes less nose-up as the angle of attack increases to 35°, where the model first exhibits nose-down pitching moments. The model once again becomes neutral in pitch from 35° to 45° angle of attack. A nose-down break in the pitch curve occurs at α=45°, and increasingly nose-down moments develop as the angle of attack increases to 90°.

The effects of sideslip on static pitching moment can also be seen in Figure 3-71. As the angle of sideslip increases, the model becomes more nose-down between 25° and 45° angle of attack. No other significant effects of sideslip are noted.

At zero sideslip, pitching moments are generally constant with rotation. Although the model does become slightly more nose-down at high rotation rates for angles of attack above 50° (Figure 3-72). Figure 3-72 also shows the effects of sideslip on the rotational pitch characteristics of the basic airplane. The sideslip effects are similar to those of the 201 configuration. When the signs of sideslip and rotation rate are the same, nose-down moments are produced, and when the signs are opposite, nose-up increments are the result.

Lateral

The 101 model exhibits high levels of lateral stability at all sideslip angles for low angles of attack, as shown in Figure 3-73. Similar to the 201 configuration, a roll-stability reversal occurs between 15° and 35° α for sideslip angles of 10°. As discussed in section 8.1, it is not uncommon for a roll reversal to occur on delta wing

configurations at sideslip conditions. Above 35° α, stable rolling moments that increase slightly with angle of attack occur for all sideslip angles tested.

The rotational roll characteristics of the ICE 101 baseline configuration are shown in Figure 3-74. The model is well damped in roll below 25° angle of attack. From α=25° to 65°, slightly lower levels of roll damping are observed. The model is neutrally damped at α=70° and then becomes propelling on up through 90° angle of attack.

Directional

The static directional characteristics are presented in Figure 3-75 for sideslip angles up to 30°. Fairly constant levels of directional instability are observed from 0° to 20° and 50° to 90° angles of attack. Large levels of unstable yawing moments develop between 20° and 50° angle of attack that are independent of sideslip angle. Note that for sideslip angles of 30° the yawing moments are fairly constant for all angles of attack.

The effects of rotation on the yaw characteristics of the baseline configuration are shown in Figure 3-76 for both zero and nonzero sideslip angles. The model is neutrally damped (constant with rotation) for angles of attack below 30° and well damped from 30° to 45°. As in the static case, considerable non-linear effects are observed in this angle of attack range while rotating at sideslip angles. Above 45° α, progressively lower levels of yaw damping are observed.

3.9.2 Control Effectiveness

The effectiveness of control effectors on the ICE 101 configuration are discussed in this section. The following were investigated for their control effectiveness: symmetric and differential leading edge flaps, pitch flaps, elevons, all moving wing tip (AMT), spoilers and spoiler-slot deflectors (SSD). The effect of various control surfaces on AMT and SSD control power is also discussed in this section as well. The effectiveness of trailing edge controls, the AMT, and SSD was investigated using right-side deflections unless stated otherwise. Additionally, the leading edge flaps were deflected thirty degrees for all control deflections unless otherwise specified.

Leading Edge Flaps

Symmetric Flap Deflection

The ICE 101 model was tested with both leading edge flaps deflected thirty degrees. The effect of leading edge flap deflection on lift coefficient is presented in Figure 3-77. Leading edge flaps extend the angle of maximum lift to 30°. Deflecting the leading edge flaps produces pitching moments that are slightly less nose-up for angles of attack between 10° and 25°, as shown in Figure 3-78. The model is slightly more nose-up in the region of maximum lift with the leading edge flaps deflected thirty degrees. The leading edge flaps do not influence the static lateral-directional characteristics significantly.

Rotational effects due to leading edge flap deflection are much less significant on the flying wing than on the canard-delta configuration. Deflecting the leading edge flaps has no effect on roll damping for the 101 configuration. However, Figure 3-79 shows that yaw damping is increased slightly at low angles of attack by deflecting the leading edge flaps.

Differential Flap Deflection

Differential leading edge flaps have very little influence on the static or rotational characteristics of the delta wing model. Figure 3-80 shows that only a small positive yaw increment is produced by differentially deflecting the flaps (LEF=30/0).

Pitch Flap Effectiveness

Figures 3-81 and 3-82 show the pitch flap effectiveness for deflections of +30° and -30°. The normal force increment produced by TED pitch flap is smaller than that produced by TEU pitch flap, as illustrated in 3-81. Figure 3-82 shows that nose-up (TEU) pitch flap is effective up to 45° angle of attack. TED deflections are effective only to α=30°.

Elevon Effectiveness

The elevon effectiveness is presented in Figures 3-83 through 3-86 for elevon deflections of +30° and -30°. Elevon pitch control power is shown in Figure 3-83. The elevon exhibits good nose-up pitch authority throughout the entire angle of attack range. Nose-down elevon remains effective up to 45° angle of attack.

Maximum nose down control power is shown in Figure 3-84. All trailing edge control surfaces (elevons and pitch flaps) are set to +30°. Deflecting all trailing edge surfaces results in nose down pitching moment for all angles of attack below 30°. The pitching moment is neutral at α=30° with maximum nose-down deflections. Maximum nose-down control power begins to diminish at α=45° and loses its effectiveness entirely by about α=65°.

The elevon exhibits good roll control power at low angles of attack, as shown in Figure 3-85. Roll effectiveness begins to decrease for angles of attack above 20°. Trailing edge up elevon is effective in roll for all angles of attack, while TED roll control power is exhibited up to about 60° angle of attack. Figure 3-86 shows that small positive (nose-right) yaw increments are produced with either TEU or TED elevon deflections on the right-hand wing.

Effectiveness of the All Moving Wing Tip

The all moving wing tip (AMT) was described in section 3.8.2. The AMT control effectiveness for right-hand AMT deflections are presented in Figures 3-87 through 3-92.

Static

As discussed earlier in this report, the purpose of the skewed hinge line AMT is to generate both axial and side forces to produce yaw control power. Figure 3-87 shows the axial force produced by deflecting the AMT. Figure 3-88 shows that deflecting the right-hand AMT trailing edge down produces negative side force increments. Since the AMT is aft of the c.g., negative side force due to the AMT generates positive yawing moment that is shown in Figure 3-89. Trailing edge down AMT deflections exhibit good yaw effectiveness for all angles of attack. The rolling moments due to TED deflections are adverse at low angles of attack, becoming favorable above 10° α, as illustrated in Figure 3-90. Trailing edge up deflections exhibit very good roll control power up to high angles of attack. The yaw associated with trailing edge up AMT deflections is favorable at low angles of attack and becomes adverse at the higher angles. Above α=10°, positive roll is produced by any right-side AMT deflection.

The influence of sideslip angle on AMT effectiveness in yaw is presented in Figure 3-91 for a right-hand deflection of 60°. The AMT generates slightly more yaw control power when deflected on the windward wing (positive β for right-hand AMT). Figure 3-91 shows that the AMT remains effective in yaw through α=90° for both positive and negative sideslip angles. The effects of sideslip angle on AMT roll control power for the ICE 101 are similar to those observed on the ICE 201 configuration, as illustrated in Figure 3-92. Deflecting the windward AMT (positive β, right-hand AMT) results in constant rolling moments that are adverse up through α=20°. Note that the leeward AMT (negative β) is effective in roll only up to about α=30°, while the windward AMT is effective for all angles of attack.

The effect of leading edge flap deflection on AMT effectiveness is presented in Figures 3-93 and 3-94. Figure 3-93 shows that the AMT exhibits slightly more roll control effectiveness when the leading edge flap deflection is zero. However, the AMT is more effective in yaw with the leading edge flaps deflected thirty degrees, as illustrated in Figure 3-94.

Rotational

The effects of rotation rate and AMT deflection on the 101 configuration are presented in Figures 3-95 and 3-96. The rotational roll characteristics due to the AMT are presented in Figure 3-95 for right-side deflections of -10° and +60°. Roll damping at low angles of attack is reduced slightly by positive deflections, but no other significant effects are observed above 15° angle of attack. The TEU deflection has no effect on the rotational roll characteristics.

Figure 3-96 shows that TED deflections slightly improve yaw damping for angles of attack above 45°. TEU deflections have no significant effects on the rotational yaw characteristics.

Spoiler Effectiveness

Static

The upper spoiler configurations were tested with the left-hand spoiler deflected. The roll control power due to deployment of the left-hand spoiler is shown in Figure 3-97. The spoiler is effective in roll up to α=30°. The associated yawing moment is favorable, as shown in Figure 3-98. The influence of sideslip angle on the roll control power of the spoiler, shown in Figure 3-99, is similar to that seen in the ICE 201, where the greatest effect is due to the windward spoiler (negative β for left-hand spoiler). Deploying the spoiler on the leeward wing has little effect on the rolling moment characteristics at sideslip.

Figure 3-100 shows the effect of sideslip on the spoiler yaw effectiveness. At low angles of attack the spoiler produces negative yaw increments for both zero and nonzero sideslip angles. beyond stall, the yaw effectiveness reverses, where positive yaw increments are produced due to left-side spoiler deployment at both positive and negative sideslip angles.

Rotational

The effects of the left-hand spoiler on the rotational roll characteristics are presented in Figure 3-101. Figure 3-101 shows that the spoiler has no effect on roll damping when the left wing is retreating (negative $\Omega b/2V$). However, roll damping is significantly increased at α=25°-30° and positive rotation rates, due to the spoiler effects on the advancing wing. There are no significant effects on yaw damping due to the spoiler being deployed.

Effectiveness of the Spoiler-Slot-Deflector

Figure 3-5 shows a photograph of the ICE 101 model with the spoiler-slot-deflector deployed on the right-hand wing.

Static

The effect of the SSD on static pitching moment is presented in Figure 3-102. The SSD produces more nose-up pitching moments throughout most of the angle of attack range.

The SSD exhibits very good roll effectiveness up to 30° angle of attack, as shown in Figure 3-103. The roll power decreases slightly above 30°, but the SSD remains effective up to 70° angle of attack. Figure 3-103 also shows that the SSD generates more roll power than the spoiler and remains effective in roll out to higher angles of attack than the spoiler.

The SSD is very effective in generating yaw, as shown in Figure 3-104. Significant favorable yawing moments are produced by the SSD at low angles of attack. Yaw control power decreases slightly with angle of attack up to α=55°, where the resulting yawing moment is zero. Above 55° a control reversal occurs that is sustained up to 90° angle of attack. Note a sudden decrease in yawing moment that occurs at α=30°. This corresponds to a sudden increase in negative side force, as shown in Figure 3-105. Figure 3-105 also illustrates the change in sign of side force that occurs at high angles of attack that correlates with the SSD yaw control reversal.

Rotational

The effect of rotation rate and spoiler or SSD deployment on rolling moment is shown in Figure 3-106. Roll damping is increased slightly for α=20° to 35° due to the SSD. Note that a greater increase in roll damping is observed when the SSD is on the advancing wing (negative $\Omega b/2V$ in this case). However, the SSD has no substantial effect on the rotational roll characteristics for angles of attack above 35°. The SSD has a more significant impact on the yaw damping characteristics, as shown in Figure 3-107. Slightly higher levels of yaw damping are exhibited due to the SSD for angles of attack below 20°. At 20° and 25° α, the baseline configuration is slightly propelling in yaw, but deploying the SSD results in damped yawing moments. From α=30° on up to 90° the SSD improves yaw damping.

SSD/Elevon Interactions

The elevon effectiveness is significantly reduced by the SSD, as shown in Figures 3-108 through 3-110. Figure 3-108 shows that the elevon roll control power is sharply degraded when in the presence of the SSD. The elevon pitch control power is also reduced by the interaction of the SSD, as shown in Figure 3-109. The yaw effectiveness due to TEU elevon is almost completely eliminated by the SSD for all angles of attack, as shown in Figure 3-110. Below α=55°, TED elevon yaw control power is also seriously degraded by the SSD. However, TED elevon is not influenced by the SSD and remains effective in yaw for angles of attack above 55°.

3.10 Predicted Spin Characteristics

Rotary balance data can be used to predict the aircraft's steady-state spin modes at any specified altitude for a given set of weight and inertial conditions. An outline of the method and historical background are presented by Bihrle, 1983. For steady spins to occur, the aerodynamic pitching, rolling, and yawing moments must simultaneously balance their respective inertial moments. Since an upright rotating airplane always produces a positive inertial pitching moment, negative aerodynamic pitching moments must exist to produce the balance and hence, permit a spin. A propelling aerodynamic moment must exist in order to maintain the aircraft's rotation, with body axis rolling moment being the primary driving moment at low angles of attack and body axis yawing moment becoming the dominant factor as angle of attack increases to the flat spin attitude.

Experience has shown that the full-scale airplane will either have a steady spin as predicted, or it will have an oscillatory spin mode whose average values of angle of attack and turn rate will equal the predicted steady values. Also, in some extreme cases, the oscillatory motions will be so severe that the airplane will not stabilize in the spin. All spin modes presented in this report are calculated for an altitude of 25,000 feet. The full-scale weights and inertias used to compute the spin modes are listed in Table 3-5.

3.10.1 ICE 201

The predicted steady-state spin modes for the ICE 201 canard-delta configuration with various controls deflected are presented in Table 3-6. Spin modes were computed for two sets of inertial configurations, but the inertial properties had no effect on most of the spin predictions. Due to its rotationally damped characteristics, the predicted spin behavior of the 201 configuration are relatively mild. For the basic airplane with neutral controls and either zero or thirty degree leading edge flap deflections, only a high angle of attack pitch trim condition is predicted.

Effect of Controls

When the canard is deflected -60°, another pitch trim condition develops at about 25° angle of attack. Pro-spin (to the right) trailing edge controls, combined with TEU canard, produces a moderate spin to the left at about 76° angle of attack.

With maximum nose down controls, the high angle of attack pitch trim occurs at lower angles of attack, as should be expected.

Deflecting the left-hand all moving tip TED produces an equilibrium near α=70° that is a result of the nose-left yawing moment generated by the AMT. When the canard is deflected TEU in conjunction with the AMT, an equilibrium occurs at α=63°.

Spin modes were also calculated for full TEU canard with left-hand SSD deployed. This configuration was the only one affected by the inertial properties. A pitch trim near 60° angle of attack is predicted for both inertial configurations. Also, a moderate spin (4.6 sec/turn) at α=70° is predicted for the 10K BB inertial configuration that is not predicted for the 5K BB configuration.

3.10.2 ICE 101

The predicted steady-state spin modes for the ICE 101 flying wing configuration with various controls deflected are presented in Table 3-7. A fast spin (2.8 sec/turn) at α=76° is predicted for the basic 101 with neutral controls and zero leading edge flaps. This spin condition is very sensitive to any static asymmetry in yaw, and may not occur if the static yawing moment at this angle is zero. A high angle of attack pitch trim condition also exists near α=50°. Deflecting the leading edge flaps modifies the flat spin mode by reducing its angle of attack and turn rate to α=72° and 3.4 sec/turn. Differential leading edge flaps have no effect on the pitch trim condition but does weaken the flat, fast spin mode so that it occurs at a lower angle of attack and has a slower turn rate (α=67°, 3.8 sec/turn).

Effect of Controls

Maximum nose down control deflection (full TED elevons and pitch flaps) results in a moderate spin mode at α=54° and 4.6 sec/turn. Additionally, a pitch trim condition occurs near α=25°, the region where the static pitching moment becomes zero with nose down controls.

Spin predictions showed that the all moving wing tip (AMT) can be successfully employed as an anti-spin device. Deflecting the right-hand AMT trailing edge down eliminates the baseline high angle of attack spin mode. However, when the same control is examined for a right spin condition (a pro-spin control), a moderate spin of 4.3 sec/turn is predicted at α=63°. Applying pro-spin elevons with the AMT results in a very fast, flat spin (α=88.6°, 1 sec/turn) in the pro-spin direction.

Deploying the right-hand SSD is ineffective in recovering from the baseline flat spin mode to the left at α=76°. Due to the yaw reversal that occurs with this SSD configuration, the model develops a flatter and much faster (α=85°, 1.6 sec/turn) spin mode. Figure 3-110 showed that anti-spin elevons (deflected for left roll in a left spin) generate enough adverse yaw at high angles of attack to neutralize the yaw reversal due to the SSD alone. Consequently, spin recovery can be accomplished in spite of the pro-spin qualities of the SSD as long as anti-spin elevons are applied as well. Therefore, anti-spin SSD (left-hand SSD for spin to pilot's left) combined with anti-spin elevons would be even more effective in spin recovery.

3.11 Concluding Remarks and Summary

An analysis of the ICE 201 rotary balance data has led to the following observations:

- Maximum lift is attained at α=25°. The basic, neutral control configuration is nose-up in pitch through α=66°. Stable rolling moments occur for all sideslip angles throughout most of the angle of attack range. However, the configuration exhibits a roll-stability reversal in the region of maximum lift for sideslip angles of 20° and below. The neutral control configuration is directionally unstable for all angles of attack and sideslip.

- The model with neutral controls is damped in roll below α=20°, and then becomes propelling in the stall region. Beyond stall, the model becomes damped once again, and then at high angles of attack transitions to propelling rolling moments that persist on up to 90°. The model is neutrally damped in yaw for angles of attack below maximum lift. Yaw is damped for all other angles of attack.

- The canard exhibits very good pitch control power. Nose-down (TEU) deflections are effective up to very high angles of attack. TEU canard increases the roll damping over much of the angle of attack range.

- Pitch flaps provide good pitch control power up to high angles of attack. Nose up deflections (TEU) are effective to higher angles of attack than nose-down pitch flap deflections. Elevons are effective in pitch and roll up to about 30° angle of attack. Good aileron roll effectiveness is exhibited for almost all angles of attack. Low levels of adverse yaw are observed with TED aileron deflections.

- The all moving wing tip (AMT) is very effective in yaw because of its skewed hinge line that produces both axial and side force. The all moving tip also exhibits roll control power for all angles of attack. Adverse roll is generated by TED deflections for angles of attack below about 10°. The rotational characteristics are not significantly influenced by deflecting the AMT. Aileron roll power is reduced when in the presence of an all moving tip deflection.

- Both the upper surface spoiler and the spoiler-slot-deflector (SSD) exhibit good roll control power. The corresponding yawing moments are favorable. The SSD control power is greater than the control power due to the spoiler. Roll damping is improved in the stall region when either the SSD or spoiler is deployed. Aileron roll power is reduced when deflected in the presence of the SSD.

- A high angle of attack pitch trim is predicted on the basic model with neutral control deflections. Nose down longitudinal controls result in a pitch trim condition at lower angles of attack. Pro-spin controls result in a slow spin mode around 70°-75° angle of attack.

An analysis of the ICE 101 rotary balance data has led to the following observations:

- Maximum lift is attained at α=25° with neutral control deflections. The basic neutral control configuration exhibits neutral pitch stability up to 10° angle of attack and then breaks nose up. The model breaks nose down at

about α=45°. High levels of lateral stability are observed for all angles of attack and sideslip except for a roll-stability reversal that occurs in the region of maximum lift for sideslip angles of ±20° and less. The baseline configuration is directionally unstable for all angles of attack and sideslip, with high levels of instability that develop between 20° and 50° angle of attack.

- The neutral control configuration is well damped in roll for angles of attack below maximum lift. Lower levels of roll damping occur for angles of attack between 25° and 65°, and propelling rolling moments are observed above 65°. Neutral yaw damping occurs up through stall, and damped yawing moments are observed for all other angles of attack.

- Nose down pitch flaps are effective up to about 30° angle of attack, and nose up pitch flaps are effective up to about 65°. Elevons are effective in pitch, roll, and yaw. Trailing edge up elevon deflections exhibit both roll and pitch effectiveness throughout the entire angle of attack range.

- The all moving wing tip (AMT) exhibits good yaw control effectiveness for all angles of attack. The associated rolling moments are adverse for angles of attack below about 10°, but are favorable for all higher angles of attack. Trailing edge down AMT deflections reduce roll damping slightly below 50° angle of attack and increase the yaw damping slightly for angles of attack above 45°.

- Good roll and yaw control effectiveness are observed when the spoiler or the spoiler-slot-deflector (SSD) is deployed. Higher levels of roll and yaw are produced with the SSD than with the spoiler. A yaw control reversal occurs at high angles of attack with the SSD deployed. The SSD increases yaw damping for all angles of attack. Elevon effectiveness is sharply reduced when deflected TEU in the presence of the SSD.

- A high angle of attack, fast spin (α=76°, 2.8sec/turn) is predicted for the ICE 101 with neutral control deflections. This spin condition is due to the very low level of yaw damping at this angle of attack, combined with a small static shift in the yawing moment. A slower mode (5.7 sec/turn) is also predicted at α=50°. Deflecting the leading edge flaps results in slower turn rates.

- The AMT alone appears sufficient for recovering from the neutral control flat spin mode. Pro-spin AMT results in a moderate spin at α=63° and 4.3 sec/turn. An extremely flat, fast spin is predicted with the AMT deflected in combination with pro-spin elevons.

- Deploying the SSD on the windward wing during a left spin condition results in a flatter, faster spin (α=85°, 1.6 sec/turn) due to the SSD yaw control reversal observed at high angles of attack. Applying pro-spin elevons with the SSD results in no predicted spin.

Table 3-1. - Dimensional Characteristics of the Full-Scale ICE 201

Model Scale	1/13
Overall Length, in	517.49
FS Nose Tip, in	0.0
Reference Area, ft^2	808.6
Reference Span, ft	37.5
Mean Aerodynamic Chord, in	345.0
Aspect Ratio	1.74
FS LEMAC, in	160.84
LE Sweep, deg	65
TE Chevron Sweep, deg	25
Elevon Area (each side), ft^2	22.77
Pitch Flap Area (each side), ft^2	7.77
All Moving Tip Area (each side), ft^2	19.89

Table 3-2. - Dimensional Characteristics of the Full-Scale ICE 101

Model Scale	1/13.5
FS Nose Tip, in	12.0
Wing:	
Reference Area, ft^2	705.6
Reference Span, ft	42.9
Mean Aerodynamic Chord, in	249.13
FS LEMAC, in	333.65
LE Sweep, deg	42
IB Wing TE Sweep, deg	-42
OB Wing TE Sweep, deg	-24
LEF Area, ft^2	17.69
Control Surfaces:	
Canard Area, ft^2	43.92
Pitch Flap Area (each side), ft^2	15.48
Elevon Area (each side), ft^2	13.43
Aileron Area (each side), ft^2	14.48
All Moving Tip Area (each side), ft^2	19.89

Table 3-3. - Rotary Balance Run Schedule for the ICE 201 Configuration

Configuration Name	AOA	Beta	Canard	LEF	Elevon	dAil.	Pitch Flap	AMT	SSD	Filename	Notes
				(L/R)	(L/R)	(L/R)	(L/R)	(L/R)	(L/R)		
ICE201 Canard Off	0-90,Δ5	0	-	0/0	0/0	0/0	0/0	0/0	0/0	IC2A0	Canard OFF
Baseline Runs											
ICE201W0	0-90,Δ5	0	0	0/0	0/0	0/0	0/0	0/0	0/0	IC2A	w+b+canard
ICE201W0p+10	"	+10	0	0/0	0/0	0/0	0/0	0/0	0/0	IC2B	
ICE201W0p-10	"	-10	0	0/0	0/0	0/0	0/0	0/0	0/0	IC2C	
ICE201W0p+20	"	+20	0	0/0	0/0	0/0	0/0	0/0	0/0	IC2F	
SICE201W0p-20	"	-20	0	0/0	0/0	0/0	0/0	0/0	0/0	SIC2G	**STATIC**
SICE201W0p+30	"	+30	0	0/0	0/0	0/0	0/0	0/0	0/0	SIC2H	**STATIC**
SICE201W0p-30	"	-30	0	0/0	0/0	0/0	0/0	0/0	0/0	SIC2J	**STATIC**
Canard Effectiveness											
ICE201W1 dc=10	0-90,Δ5	0	TED 10	30/30	0/0	0/0	0/0	0/0	0/0	IC2AC1	
SICE201W1 dc=10p+10	"	+10	TED 10	30/30	0/0	0/0	0/0	0/0	0/0	SIC2BC1	**STATIC**
SICE201W1 dc=-20	"	0	TEU 20	30/30	0/0	0/0	0/0	0/0	0/0	SIC2AC2	**STATIC**
SICE201W1 dc=-20p+10	"	+10	TEU 20	30/30	0/0	0/0	0/0	0/0	0/0	SIC2BC2	**STATIC**
SICE201W1 dc=-40	"	0	TEU 40	30/30	0/0	0/0	0/0	0/0	0/0	SIC2AC3	**STATIC**
SICE201W1 dc=-40p+10	"	+10	TEU 40	30/30	0/0	0/0	0/0	0/0	0/0	SIC2BC3	**STATIC**
ICE201W1 dc=-60	"	0	TEU 60	30/30	0/0	0/0	0/0	0/0	0/0	IC2AC4	
ICE201W1 dc=-60p+10	"	+10	TEU 60	30/30	0/0	0/0	0/0	0/0	0/0	IC2BC4	
ICE201W0 dc=-60	"	0	TEU 60	0/0	0/0	0/0	0/0	0/0	0/0	IC2ACF	
ICE201W0 dc=-60p+10	"	+10	TEU 60	0/0	0/0	0/0	0/0	0/0	0/0	IC2BCF	
LEF Effectiveness											
ICE201W1	0-90,Δ5	0	0	30/30	0/0	0/0	0/0	0/0	0/0	IC2AF1	
ICE201W1p+10	"	+10	0	30/30	0/0	0/0	0/0	0/0	0/0	IC2BF1	
ICE201W2	"	0	0	30/0	0/0	0/0	0/0	0/0	0/0	IC2AF2	
SICE201W2p+10	"	+10	0	30/0	0/0	0/0	0/0	0/0	0/0	SIC2BF2	**STATIC**
SICE201W2p-10	"	-10	0	30/0	0/0	0/0	0/0	0/0	0/0	SIC2CF2	**STATIC**

All TED deflections are **positive.** Configuration abbreviations: **W0**:≡lef=0/0, **W1**:≡ lef=30/30, **W2**:≡ lef=30/0

β: A=0, B=+10, C=-10, F=+20, G=-20, H=+30, J=-30 **Ωb/2V Schedule: 0.0, .05, .1, .2, .3**

Table 3-3 Continued

Configuration Name	AOA	Beta	Canard	LEF	Elevon	dAil.	Pitch Flap	AMT	SSD	Filename	Notes
				(L/R)	(L/R)	(L/R)	(L/R)	(L/R)			
Elevon Effectiveness											
SICE201W1 de=-30/0	0-90,Δ5	0	0	30/30	-30/0	0/0	0/0	0/0	0/0	SIC2AE1	**STATIC**
SICE201W1 de=-30/0 p+10	"	+10	0	30/30	-30/0	0/0	0/0	0/0	0/0	SIC2BE1	**STATIC**
SICE201W1 de=-30/0 p-10	"	-10	0	30/30	-30/0	0/0	0/0	0/0	0/0	SIC2CE1	**STATIC**
SICE201W1 de=+30/0	"	0	0	30/30	30/0	0/0	0/0	0/0	0/0	SIC2AE2	**STATIC**
SICE201W1 de=+30/0 p+10	"	+10	0	30/30	30/0	0/0	0/0	0/0	0/0	SIC2BE2	**STATIC**
SICE201W1 de=+30/0 p-10	"	-10	0	30/30	30/0	0/0	0/0	0/0	0/0	SIC2CE2	**STATIC**
Aileron Effectiveness											
SICE201W1 da=-30/0	0-90,Δ5	0	0	30/30	0/0	-30/0	0/0	0/0	0/0	SIC2AL1	**STATIC**
SICE201W1 da=-30/0 p+10	"	+10	0	30/30	0/0	-30/0	0/0	0/0	0/0	SIC2BL1	**STATIC**
SICE201W1 da=-30/0 p-10	"	-10	0	30/30	0/0	-30/0	0/0	0/0	0/0	SIC2CL1	**STATIC**
SICE201W1 da=+30/0	"	0	0	30/30	0/0	30/0	0/0	0/0	0/0	SIC2AL2	**STATIC**
SICE201W1 da=+30/0 p+10	"	+10	0	30/30	0/0	30/0	0/0	0/0	0/0	SIC2BL2	**STATIC**
SICE201W1 da=+30/0 p-10		-10	0	30/30	0/0	30/0	0/0	0/0	0/0	SIC2CL2	**STATIC**
Pitch Flap Effectiveness											
SICE201W1 PF=-30/0	0-90,Δ5	0	0	30/30	0/0	0/0	-30/0	0/0	0/0	SIC2AP1	**STATIC**
SICE201W1 PF=+30/0	"	0	0	30/30	0/0	0/0	+30/0	0/0	0/0	SIC2AP2	**STATIC**
AMT Effectiveness											
ICE201W1 AMT=-10/0	0-90,Δ5	0	0	30/30	0/0	0/0	0/0	TEU 10/0	0/0	IC2AT1	
SICE201W1 AMT=-10/0 p+10	"	+10	0	30/30	0/0	0/0	0/0	TEU 10/0	0/0	SIC2BT1	**STATIC**
SICE201W1 AMT=-10/0p-10	"	-10	0	30/30	0/0	0/0	0/0	TEU 10/0	0/0	SIC2CT1	**STATIC**
SICE201W1 AMT=+30/0	"	0	0	30/30	0/0	0/0	0/0	TED30/0	0/0	SIC2AT2	**STATIC**
SICE201W1 AMT=+30/0 p+10	"	+10	0	30/30	0/0	0/0	0/0	TED30/0	0/0	SIC2BT2	**STATIC**

All TED deflections are **positive.** Configuration abbreviations: **W0**:≡lef=0/0, **W1**:≡ lef=30/30, **W2**:≡ lef=30/0

β: A=0, B=+10, C=-10, F=+20, G=-20, H=+30, J=-30

Ωb/2V Schedule: 0.0, .05, .1, .2, .3

Table 3-3. - Continued

Configuration Name	AOA	Beta	Canard	LEF	Elevon	dAIL	Pitch Flap	AMT	SSD	Filename	Notes
				(L/R)	(L/R)	(L/R)	(L/R)	(L/R)			
AMT Effectiveness											
SICE201W1AMT=+30/0p-10	"	-10	0	30/30	0/0	0/0	0/0	TED30/0	0/0	SIC2CT2	**STATIC**
SICE201W1 AMT=+30/0 p+10	"	+10	0	30/30	0/0	0/0	0/0	TED30/0	0/0	SIC2BT2	**STATIC**
SICE201W1AMT=+30/0p-10	"	-10	0	30/30	0/0	0/0	0/0	TED30/0	0/0	SIC2CT2	**STATIC**
SICE201W1 AMT=+40/0	"	0	0	30/30	0/0	0/0	0/0	TED40/0	0/0	SIC2AT3	**STATIC**
SICE201W1 AMT=+40/0 p+10	"	+10	0	30/30	0/0	0/0	0/0	TED40/0	0/0	SIC2BT3	**STATIC**
SICE201W1 AMT=+40/0 p-10	"	-10	0	30/30	0/0	0/0	0/0	TED40/0	0/0	SIC2CT3	**STATIC**
ICE201W1 AMT=60/0	0-90,Δ5	0	0	30/30	0/0	0/0	0/0	TED60/0	0/0	IC2AT4	
SICE201W1 AMT=60/0 p+10	"	+10	0	30/30	0/0	0/0	0/0	TED60/0	0/0	SIC2BT4	**STATIC**
SICE201W1 AMT=60/0 p+20	"	+20	0	30/30	0/0	0/0	0/0	TED60/0	0/0	SIC2FT4	**STATIC**
SICE201W1 AMT=60/0 p+30	"	+30	0	30/30	0/0	0/0	0/0	TED60/0	0/0	SIC2HT4	**STATIC**
SICE201W1 AMT=60/0 p-10	"	-10	0	30/30	0/0	0/0	0/0	TED60/0	0/0	SIC2CT4	**STATIC**
SICE201W1 AMT=60/0 p-20	"	-20	0	30/30	0/0	0/0	0/0	TED60/0	0/0	SIC2GT4	**STATIC**
SICE201W1 AMT=60/0 p-30	"	-30	0	30/30	0/0	0/0	0/0	TED60/0	0/0	SIC2JT4	**STATIC**
SSD Effectiveness											
ICE201W1 SSD=U60-L0/0-0	0-90,Δ5	0	0	30/30	0/0	0/0	0/0	0/0	LH SPLR	IC2AS1	
SICE201W1 SSD=U60-L0/0-0 p+10	"	+10	0	30/30	0/0	0/0	0/0	0/0	LH SPLR	SIC2BS1	**STATIC**
SICE201W1 SSD=U60-L0/0-0 p-10	"	-10	0	30/30	0/0	0/0	0/0	0/0	LH SPLR	SIC2CS1	**STATIC**
ICE201W1SSD=U60-L60/0-0	"	0	0	30/30	0/0	0/0	0/0	0/0	LH SSD	IC2AS2	
SICE201W1 SSD=U60-L60/0-0 p+10	"	+10	0	30/30	0/0	0/0	0/0	0/0	LH SSD	SIC2BS2	**STATIC**
SICE201W1 SSD=U60-L60/0-0 p+20	"	+20	0	30/30	0/0	0/0	0/0	0/0	LH SSD	SIC2FS2	**STATIC**
SICE201W1 SSD=U60-L60/0-0 p+30	"	+30	0	30/30	0/0	0/0	0/0	0/0	LH SSD	SIC2HS2	**STATIC**

All TED deflections are **positive.** Configuration abbreviations: **W0**:≡lef=0/0, **W1**:≡ lef=30/30, **W2**:≡ lef=30/0

β: A=0, B=+10, C=-10, F=+20, G=-20, H=+30, J=-30

Ωb/2V Schedule: 0.0, .05, .1, .2, .3

Table 3-3. - Continued

Configuration Name	AOA	Beta	Canard	LEF	Elevon	dAil.	Pitch Flap	AMT	SSD	Filename	Notes
				(L/R)	(L/R)	(L/R)	(L/R)	(L/R)			
SICE201W1 SSD=U60-L60/0-0p-10	0-90,Δ5	-10	0	30/30	0/0	0/0	0/0	0/0	LH SSD	SIC2CS2	STATIC
SICE201W1 SSD=U60-L60/0-0 p-20	"	-20	0	30/30	0/0	0/0	0/0	0/0	LH SSD	SIC2GS2	STATIC
SICE201W1 SSD=U60-L60/0-0 p-30	"	-30	0	30/30	0/0	0/0	0/0	0/0	LH SSD	SIC2JS2	STATIC
SSD/Aileron Interactions											
SICE201W1 da=-30/0 SSD=U60-L60/0-0	0-90,Δ5	0	0	30/30	0/0	-30/0	0/0	0/0	LH SSD	SIC2ASL1	STATIC
SICE201W1 da=+30/0 SSD=U60-L60/0-0	"	0	0	30/30	0/0	30/0	0/0	0/0	LH SSD	SIC2ASL2	STATIC
SSD/Elevon Interactions											
SICE201W1 de=-30/0 SSD=U60-L60/0-0	0-90,Δ5	0	0	30/30	-30/0	0/0	0/0	0/0	LH SSD	SIC2ASE1	STATIC
SICE201W1 de=+30/0 SSD=U60-L60/0-0	"	0	0	30/30	30/0	0/0	0/0	0/0	LH SSD	SIC2ASE2	STATIC
Canard/SSD Interactions											
SICE201W1 dc=-60 SSD=U60-L60/0-0	0-90,Δ5	0	TEU 60	30/30	0/0	0/0	0/0	0/0	LH SSD	SIC2ASC1	STATIC
SICE201W1 dc=-60 SSD=U60-L60/0-0	"	0	TEU 60	30/30	0/0	0/0	0/0	0/0	LH SPLR	SIC2ASC2	STATIC
Canard/AMT Interactions											
SICE201W1 dc=-60 AMT=40/0	0-90,Δ5	0	TEU 60	30/30	0/0	0/0	0/0	TED40/0	0/0	SIC2ATC1	STATIC
AMT/Aileron Interactions											
SICE201W1 da=-30/0 AMT=40/0	0-90,Δ5	0	0	30/30	0/0	-30/0	0/0	TED40/0	0/0	SIC2ATL1	STATIC
SICE201W1 da=30/0 AMT=40/0	"	0	0	30/30	0/0	+30/0	0/0	TED40/0	0/0	SIC2ATL2	STATIC

All TED deflections are **positive.** Configuration abbreviations: **W0**:≡lef=0/0, **W1**:≡ lef=30/30, **W2**:≡ lef=30/0

β: A=0, B=+10, C=-10, F=+20, G=-20, H=+30, J=-30

Ωb/2V Schedule: 0.0, .05, .1, .2, .3

Table 3-3. - Concluded

Configuration Name	AOA	Beta	Canard	LEF	Elevon	dAil.	Pitch Flap	AMT	SSD	Filename	Notes
				(L/R)	(L/R)	(L/R)	(L/R)	(L/R)			
SSD/Pitch Flap Interactions											
SICE201W1 pf=-30/0 SSD=U60-L60/0-0	0-90,Δ5	0	0/0	30/30	0/0	0/0	-30/0	0/0	LH SSD	SIC2APS1	**STATIC**
SICE201W1 pf=30/0 SSD=U60-L60/0-0	"	0	0/0	30/30	0/0	0/0	+30/0	0/0	LH SSD	SIC2APS2	**STATIC**
ICE201W1 dc=-60 de=30/30 da=30/30 pf=30/30	0-90,Δ5	0	TEU 60	30/30	30/30	30/30	30/30	0/0	0/0	IC2A5	(max nose down)
ICE201W1 dc=-60 de=30/30 da=30/30 pf=30/30p+10	"	+10	TEU 60	30/30	30/30	30/30	30/30	0/0	0/0	IC2B5	
SICE201W1 dc=-60 de=30/30 da=30/30 pf=30/30p+20	"	+20	TEU 60	30/30	30/30	30/30	30/30	0/0	0/0	SIC2F5	**STATIC**
SICE201 W1 dc=-80 de=30/30 da=30/30 pf=30/30	"	0	TEU 80	30/30	30/30	30/30	30/30	0/0	0/0	SIC2A6	**STATIC**
SICE201 W1 p+20	"	+20	0/0	30/30	0/0	0/0	0/0	0/0	0/0	SIC2FF1	**STATIC**
SICE201 W1 p+30	"	+30	0/0	30/30	0/0	0/0	0/0	0/0	0/0	SIC2HF1	**STATIC**
ICE201 W1 AMT=60/0 p+10 ROT	"	+10	0/0	30/30	0/0	0/0	0/0	60/0	0/0	IC2BT4	
ICE201 W1 AMT=60/0 p-10 ROT	"	-10	0/0	30/30	0/0	0/0	0/0	60/0	0/0	IC2CT4	
ICE201 W1 dc=-60 AMT=60/0	40-90,Δ5	0	TEU 60	30/30	0/0	0/0	0/0	60/0	0/0	IC2A20	
ICE201 W1 dc=-60 AMT=60/0p+10	"	+10	TEU 60	30/30	0/0	0/0	0/0	60/0	0/0	IC2B20	
ICE201 W1 dc=-60 AMT=60/0p+10	"	-10	TEU 60	30/30	0/0	0/0	0/0	60/0	0/0	IC2C20	
ICE201W1 dc=-60 de=30/-30 da=30/-30 pf=30/-30	"	0	TEU 60	30/30	30/-30	30/-30	30/-30	0/0	0/0	IC2A21	
" "p+10	"	+10	TEU 60	30/30	30/-30	30/-30	30/-30	0/0	0/0	IC2B21	
" "p-10	"	-10	TEU 60	30/30	30/-30	30/-30	30/-30	0/0	0/0	IC2C21	
ICE201W1 dc=-60SSD=U60-L60/0-0	"	0	TEU 60	30/30	0/0	0/0	0/0	0/0	LH SSD	IC2A22	
ICE201W1 dc=-60SSD=U60-L60/0-0 p+10	"	+10	TEU 60	30/30	0/0	0/0	0/0	0/0	LH SSD	IC2B22	
ICE201W1 dc=-60 SSD=U60-L60/0-0 p-10	"	-10	TEU 60	30/30	0/0	0/0	0/0	0/0	LH SSD	IC2C22	

All TED deflections are **positive.** Configuration abbreviations: **W0**:≡lef=0/0, **W1**:≡ lef=30/30, **W2**:≡ lef=30/0

β: A=0, B=+10, C=-10, F=+20, G=-20, H=+30, J=-30 **Ωb/2V Schedule: 0.0, .05, .1, .2, .3**

Table 3-4. - Rotary Balance Run Schedule for the ICE 101 Configuration

Configuration Name	AOA	Beta	LEF	Elevon	Pitch Flap	AMT	SSD	COND.	Filename	Notes
				(L/R)	(L/R)	(L/R)		Stat/Rot		
ICE101W0	0-90,Δ5	0	0/0	0/0	0/0	0/0	0/0	ROT	IC1A	Baseline
ICE101W0 p+10	"	+10	0/0	0/0	0/0	0/0	0/0	ROT	IC1B	
ICE101W0 p-10	"	-10	0/0	0/0	0/0	0/0	0/0	ROT	IC1C	
ICE101W0 p+20	"	+20	0/0	0/0	0/0	0/0	0/0	ROT	IC1F	
SICE101W0 p-20	"	-20	0/0	0/0	0/0	0/0	0/0	STATIC	SIC1G	
SICE101W0 p+30	"	+30	0/0	0/0	0/0	0/0	0/0	STATIC	SIC1H	
SICE101W0 p-30	"	-30	0/0	0/0	0/0	0/0	0/0	STATIC	SIC1J	
LEF Effectiveness										
ICE101W2	0-90,Δ5	0	30/0	0/0	0/0	0/0	0/0	ROT	IC1AF2	Differential LEF
ICE101W2 p+10	"	+10	30/0	0/0	0/0	0/0	0/0	ROT	IC1BF2	
ICE101W2 p-10	"	-10	30/0	0/0	0/0	0/0	0/0	ROT	IC1CF2	
ICE101W1	"	0	30/30	0/0	0/0	0/0	0/0	ROT	IC1AF1	Symmetric LEF
ICE101W1 p+10	"	+10	30/30	0/0	0/0	0/0	0/0	ROT	IC1BF1	
Elevon Effectiveness										
SICE101W1 de=0/-30	0-90,Δ5	0	30/30	0/-30	0/0	0/0	0/0	STATIC	SIC1AE1	
SICE101W1 de=0/+30	"	0	30/30	0/+30	0/0	0/0	0/0	STATIC	SIC1AE2	
Pitch Flap Effectiveness										
SICE101W1 pf=0/-30	0-90,Δ5	0	30/30	0/0	0/-30	0/0	0/0	STATIC	SIC1AP1	
SICE101W1 pf=0/+30	"	0	30/30	0/0	0/+30	0/0	0/0	STATIC	SIC1AP2	
AMT Effectiveness										
ICE101W1 AMT=0/-10	0-90,Δ5	0	30/30	0/0	0/0	0/TEU 10	0/0	ROT	IC1AT1	
SICE101W1 AMT=0/-10 p+10	"	+10	30/30	0/0	0/0	0/TEU 10	0/0	STATIC	SIC1BT1	
SICE101W1 AMT=0/-10 p-10	"	-10	30/30	0/0	0/0	0/TEU 10	0/0	STATIC	SIC1CT1	

All TED deflections are **positive.** Configuration abbreviations: **W0**:≡lef=0/0, **W1**:≡ lef=30/30, **W2**:≡ lef=30/0

β: A=0, B=+10, C=-10, F=+20, G=-20, H=+30, J=-30

Ωb/2V Schedule: 0.0, .05, .1, .2, .3

Table 3-4. - Continued

Configuration Name	AOA	Beta	LEF	Elevon	Pitch Flap	AMT	SSD	COND.	Filename	Notes
				(L/R)	(L/R)	(L/R)		Stat /Rot		
AMT Effectiveness										
SICE101W1 AMT=0/30	0-90,Δ5	0	30/30	0/0	0/0	0/TED 30	0/0	STAT	SIC1AT2	
SICE101W1 AMT=0/30 p+10	"	+10	30/30	0/0	0/0	0/TED 30	0/0	STAT	SIC1BT2	
SICE101W1 AMT=0/30 p-10	"	-10	30/30	0/0	0/0	0/TED 30	0/0	STAT	SIC1CT2	
SICE101W1 AMT=0/40	"	0	30/30	0/0	0/0	0/TED 40	0/0	STAT	SIC1AT3	
SICE101W1 AMT=0/40 p+10	"	+10	30/30	0/0	0/0	0/TED 40	0/0	STAT	SIC1BT3	
SICE101W1 AMT=0/40 p+10	"	-10	30/30	0/0	0/0	0/TED 40	0/0	STAT	SIC1CT3	
ICE101W1 AMT=0/60	"	0	30/30	0/0	0/0	0/TED 60	0/0	ROT	IC1AT4	
ICE101W1 AMT=0/60p+10	"	+10	30/30	0/0	0/0	0/TED 60	0/0	ROT	IC1BT4	
ICE101W1 AMT=0/60p-10	"	-10	30/30	0/0	0/0	0/TED 60	0/0	ROT	IC1CT4	
SICE101W1 AMT=0/60p+20	"	+20	30/30	0/0	0/0	0/TED 60	0/0	STAT	SIC1FT4	
SICE101W1 AMT=0/60p-20	"	-20	30/30	0/0	0/0	0/TED 60	0/0	STAT	SIC1GT4	
SICE101W1 AMT=0/60p+30	"	+30	30/30	0/0	0/0	0/TED 60	0/0	STAT	SIC1HT4	
SICE101W1 AMT=0/60p-30	"	-30	30/30	0/0	0/0	0/TED 60	0/0	STAT	SIC1JT4	
SSD Effectiveness										
ICE101W1 SSD=U60-L0/0-0	0-90,Δ5	0	30/30	0/0	0/0	0/0	LH SPLR	ROT	IC1AS1	
SICE101W1 SSD=U60-L0/0-0 p+10	"	+10	30/30	0/0	0/0	0/0	LH SPLR	STAT	SIC1BS1	
SICE101W1SSD=U60-L0/0-0 p-10	"	-10	30/30	0/0	0/0	0/0	LH SPLR	STAT	SIC1CS1	
ICE101W1 SSD=0-0/U60-L60	"	0	30/30	0/0	0/0	0/0	RH SSD	ROT	IC1AS2	
ICE101W1 SSD=0-0/U60-L60 p+10	"	+10	30/30	0/0	0/0	0/0	RH SSD	ROT	IC1BS2	
ICE101W1 SSD=0-0/U60-L60 p-10	"	-10	30/30	0/0	0/0	0/0	RH SSD	ROT	IC1CS2	
SICE101W1 SSD=0-0/U60-L60 p+20	"	+20	30/30	0/0	0/0	0/0	RH SSD	STAT	SIC1FS2	

All TED deflections are **positive.** Configuration abbreviations: **W0**:≡lef=0/0, **W1**:≡ lef=30/30, **W2**:≡ lef=30/0

β: A=0, B=+10, C=-10, F=+20, G=-20, H=+30, J=-30

Ωb/2V Schedule: 0.0, .05, .1, .2, .3

Table 3-4. - Continued

Configuration Name	AOA	Beta	LEF	Elevon	Pitch Flap	AMT	SSD	COND.	Filename	Notes
				(L/R)	(L/R)	(L/R)		Stat /Rot		
SSD Effectiveness										
SICE101W1 SSD=0-0/U60-L60 p-20	0-90,Δ5	-20	30/30	0/0	0/0	0/0	RH SSD	STAT	SIC1GS2	
SICE101W1 SSD=0-0/U60-L60 p+30	"	+30	30/30	0/0	0/0	0/0	RH SSD	STAT	SIC1HS2	
SICE101W1 SSD=0-0/U60-L60 p-30	"	-30	30/30	0/0	0/0	0/0	RH SSD	STAT	SIC1JS2	
SSD/Elevon Interactions										
SICE101W1 de=0/-30 SSD=0-0/U6-L60	0-90,Δ5	0	30/30	0/-30	0/0	0/0	RH SSD	STAT	SIC1ASE1	
SICE101W1 de=0/+30 SSD=0-0/U6-L60	"	0	30/30	0/+30	0/0	0/0	RH SSD	STAT	SIC1ASE2	
SSD/Pitch Flap Interactions										
SICE101W1 pf=0/-30 SSD=0-0/U60-L60	0-90,Δ5	0	30/30	0/0	0/-30	0/0	RH SSD	STAT	SIC1ASP1	
SICE101W1 pf=0/+30 SSD=0-0/U60-L60	"	0	30/30	0/0	0/+30	0/0	RH SSD	STAT	SIC1ASP2	
ICE101W1 de=30/30 pf=30/30	"	0	30/30	30/30	30/30	0/0	0/0	R	IC1A5	**Max nose down**
ICE101W1 de=30/30 pf=30/30 p+10	"	+10	30/30	30/30	30/30	0/0	0/0	R	IC1B5	
SICE101W1 de=30/30 pf=30/30 p+20	"	+20	30/30	30/30	30/30	0/0	0/0	S	SIC1F5	
SICE101 W1 de=30/30 pf=30/30 p+30	"	+30	30/30	30/30	30/30	0/0	0/0	S	SIC1H5	

All TED deflections are **positive.** Configuration abbreviations: **W0**:≡lef=0/0, **W1**:≡ lef=30/30, **W2**:≡ lef=30/0

β: A=0, B=+10, C=-10, F=+20, G=-20, H=+30, J=-30

Ωb/2V Schedule: 0.0, .05, .1, .2, .3

Table 3-4. - Continued

Configuration Name	AOA	Beta	LEF	Elevon	Pitch Flap	AMT	SSD	COND.	Filename	Notes
				(L/R)	(L/R)	(L/R)		Stat /Rot		
SICE101 W1 p+20	0-90,Δ5	+20	30/30	0/0	0/0	0/0	0/0	STAT	SIC1FF1	
SICE101 W1 p+30	"	+30	30/30	0/0	0/0	0/0	0/0	STAT	SIC1HF1	
SICE101 W0 de=30/30 pf=30/30	"	0	0/0	30/30	30/30	0/0	0/0	STAT	SIC1A6	max n.d w/ lef=0
SICE101 W0 de=30/30 pf=30/30p+10	"	+10	0/0	30/30	30/30	0/0	0/0	STAT	SIC1B6	
SICE101 W0 de=30/30 pf=30/30p-10	"	-10	0/0	30/30	30/30	0/0	0/0	STAT	SIC1C6	
Pitch flap/Elevon Interac.										
SICE101 W1 de=0/30 pf=0/30	"	0	30/30	0/30	0/30	0/0	0/0	STAT	SIC1APE2	
SICE101 W1 de=0/-30 pf=0/30p+10	"	0	30/30	0/-30	0/30	0/0	0/0	STAT	SIC1APE1	
AMT/Elevon Interactions										
SICE101 W1 de=0/-30 AMT=0/60	"	0	30/30	0/-30	0/0	0/TED 60	0/0	STAT	SIC1ATE1	
SICE101 W1 de=0/+30 AMT=0/60	"	0	30/30	0/+30	0/0	0/TED 60	0/0	STAT	SIC1ATE2	
AMT/Lef Interactions										
SICE101 W0 AMT=0/60	"	0	0/0	0/0	0/0	0/TED 60	0/0	STAT	SIC1ATF1	
SICE101 W0 AMT=0/30	"	0	0/0	0/0	0/0	0/TED 30	0/0	STAT	SIC1ATF2	
SICE101 W0 AMT=0/-10	"	0	0/0	0/0	0/0	0/TEU 10	0/0	STAT	SIC1ATF3	

All TED deflections are **positive.** Configuration abbreviations: **W0**:≡lef=0/0, **W1**:≡ lef=30/30, **W2**:≡ lef=30/0

β: A=0, B=+10, C=-10, F=+20, G=-20, H=+30, J=-30

Ωb/2V Schedule: 0.0, .05, .1, .2, .3

Table 3-4. - Concluded

Configuration Name	AOA	Beta	LEF	Elevon	Pitch Flap	AMT	SSD	COND.	Filename	Notes
				(L/R)	(L/R)	(L/R)		Stat /Rot		
ICE101 W0 AMT=0/60	40-90,Δ5	0	0/0	0/0	0/0	0/TED60	0/0	ROT	IC1A20	
ICE101 W0 AMT=0/60 p+10	40-90,Δ5	+10	0/0	0/0	0/0	0/TED60	0/0	ROT	IC1B20	
ICE101 W1 AMT=0/60 de=-30/+30	40-90,Δ5	0	30/30	-30/30	0/0	0/TED60	0/0	ROT	IC1A21	
ICE101W1 AMT=0/60 de=-30/+30p+10	40-90,Δ5	0	30/30	-30/30	0/0	0/TED60	0/0	ROT	IC1B21	
ICE101 W0 SSD=0-0/U60-L60	40-90,Δ5	0	0/0	0/0	0/0	0/0	RH SSD	ROT	IC1A30	
ICE101W0 SSD=0-0/U60-L60 p+10	40-90,Δ5	+10	0/0	0/0	0/0	0/0	RH SSD	ROT	IC1B30	
ICE101W0 SSD=0-0/U60-L60 de=-30/30	40-90,Δ5	0	0/0	-30/+30	0/0	0/0	RH SSD	ROT	IC1A31	
ICE101W0 SSD=0-0/U60-L60 de=-30/30 p+10	40-90,Δ5	+10	0/0	-30/+30	0/0	0/0	RH SSD	ROT	IC1B31	

All TED deflections are **positive.** Configuration abbreviations: **W0**:≡lef=0/0, **W1**:≡ lef=30/30, **W2**:≡ lef=30/0

β: A=0, B=+10, C=-10, F=+20, G=-20, H=+30, J=-30

Ωb/2V Schedule: 0.0, .05, .1, .2, .3

Table 3-5. - Mass Properties Data for the ICE Configurations

Configuration	Weight (lbs)	CG (% MAC)	I_{XX}	I_{YY}	I_{ZZ}
ICE 101					
101-TV	32750	38.84	35479	78451	110627
ICE 201-TV					
5K BB	34247	20.0	37925	77685	117935
10K BB	39347	20.0	43446	88994	135103

Table 3-6. - Predicted Spin Modes for the ICE 201

CONFIGURATION	LEFT SPIN					RIGHT SPIN				
	α (deg)	β (deg)	Spin Radius (ft)	Turn Rate (sec/turn)	V_D (ft/sec)	α (deg)	β (deg)	Spin Radius (ft)	Turn Rate (sec/turn)	V_D (ft/sec)
201-TV 5K BB										
LEF=0						pitch trim near α=66°				
LEF=30	pitch trim near α=65°					pitch trim near α=74°				
LEF=30, dCanard=-60	pitch trim near α=25°					pitch trim near α=25°				
						pitch trim near α=61°				
LEF=30, Max nose down controls	pitch trim region α=25°-40°									
	pitch trim near α=55°									
LEF=30, AMT=60/0	pitch trim α=71°					NO SPIN				
LEF=30, dCanard=-60, AMT=60/0	pitch trim α=63°					NO SPIN				
LEF=30, dCanard=-60, dE=dA=pf=30/-30	76.3	5.1	4.5	4.0	250	NO SPIN				
LEF=30, dCanard=-60, Left-Hand SSD	pitch trim near α=60°					NO SPIN				
201-TV 10K BB										
LEF=0						pitch trim near α=65°				
LEF=30						pitch trim near α=65°				
LEF=30, dCanard=-60	pitch trim near α=25°					pitch trim near α=25°				
						pitch trim near α=61°				
LEF=30, Max nose down controls	pitch trim region α=25°-40°									
	pitch trim near α=55°									
LEF=30, AMT=60/0	72	-1.9	8.0	5.7	261	NO SPIN				
LEF=30, dCanard=-60, AMT=60/0	pitch trim α=64°					NO SPIN				
LEF=30, dCanard=-60, dE=dA=pf=30/-30	76.8	4.8	4.1	4.0	267	NO SPIN				
LEF=30, dCanard=-60, LH SSD	pitch trim near α=60°					70.4	-3.4	8.0	4.6	274

Table 3-7. - Predicted Spin Modes for the ICE 101

CONFIGURATION	LEFT SPIN					RIGHT SPIN				
	α (deg)	β (deg)	Spin Radius (ft)	Turn Rate (sec/turn)	V_D (ft/sec)	α (deg)	β (deg)	Spin Radius (ft)	Turn Rate (sec/turn)	V_D (ft/sec)
LEF=0	pitch trim α=50°									
	76.2	0.7	1.9	2.8	260					
LEF=30/0	pitch trim α=50°									
	67.3	3.0	5.4	3.8	269					
LEF=30	pitch trim α=50°									
	72.3	1.7	3.5	3.4	261					
LEF=30, AMT=0/60	pitch trim near α=50°					pitch trim near α=50°				
						63.1	1.7	7.5	4.3	280
LEF=30, Right-hand SSD	85	0.2	0.1	1.6	247	pitch trim near α=50°				
LEF=30, dE=30, pf=30	pitch trim region α=20°-40°					pitch trim region α=20°-25°				
	pitch trim near α=53°									
LEF=0, AMT=0/60	NO SPIN					pitch trim region α=50°-60°				
LEF=30, AMT=0/60, dE=-30/+30	NO SPIN					pitch trim near α=50°				
						88.6	1.0	0	0.8	213
LEF=0, Right-hand SSD	83	0.2	0.4	1.9	254	pitch trim near α=50°				
LEF=0, Right-hand SSD, de=-30/+30	NO SPIN					63	-1.2	7.9	4.6	287

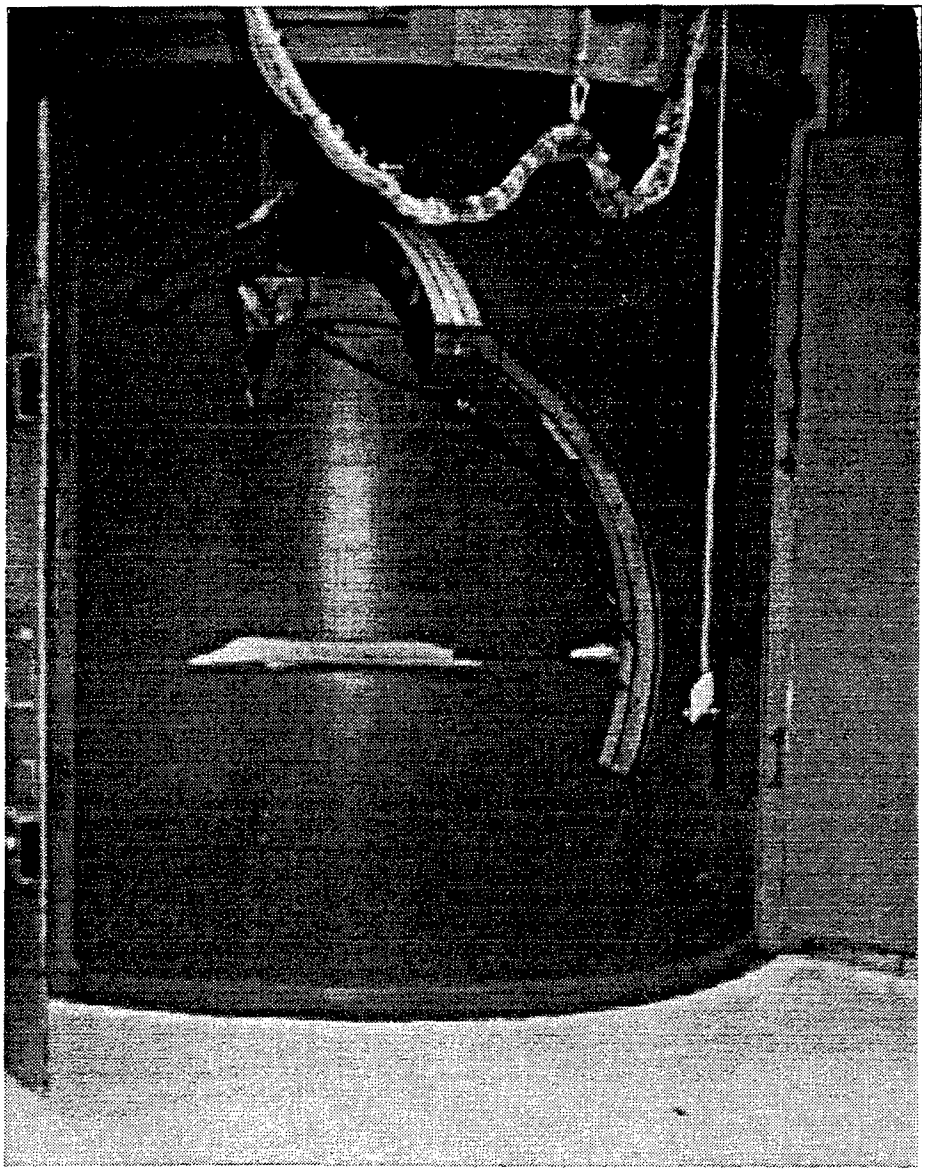

Figure 3-1. Photograph of Rotary Balance Rig in the LAMP 10-ft Vertical Wind Tunnel.

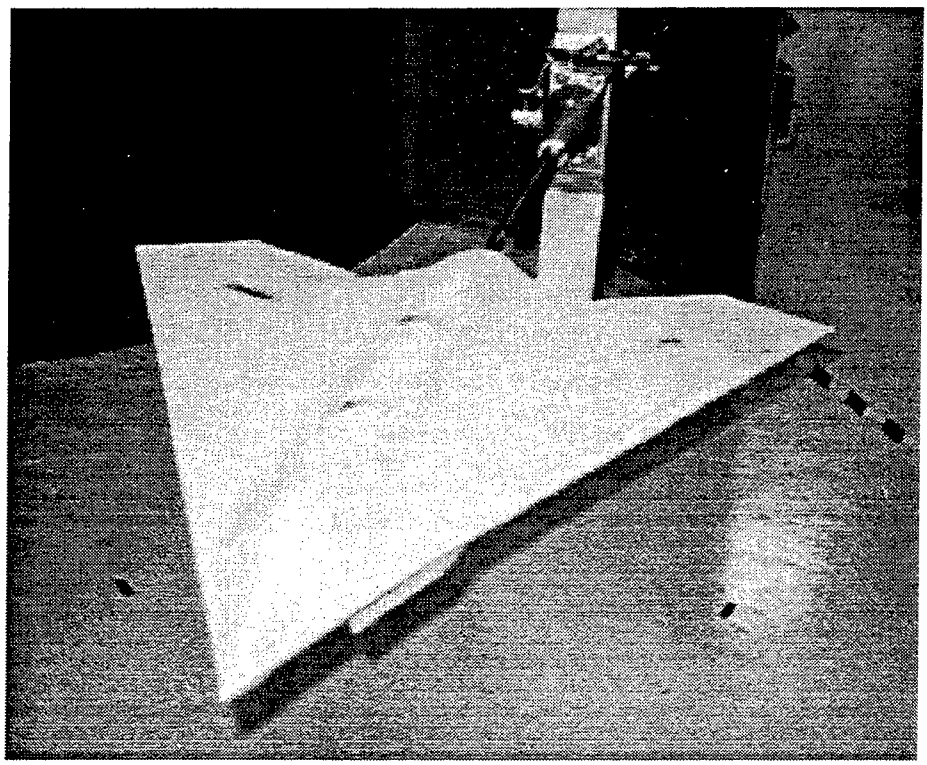

Figure 3-2. Photograph of ICE 101 Model Installed on the Rotary Balance Rig.

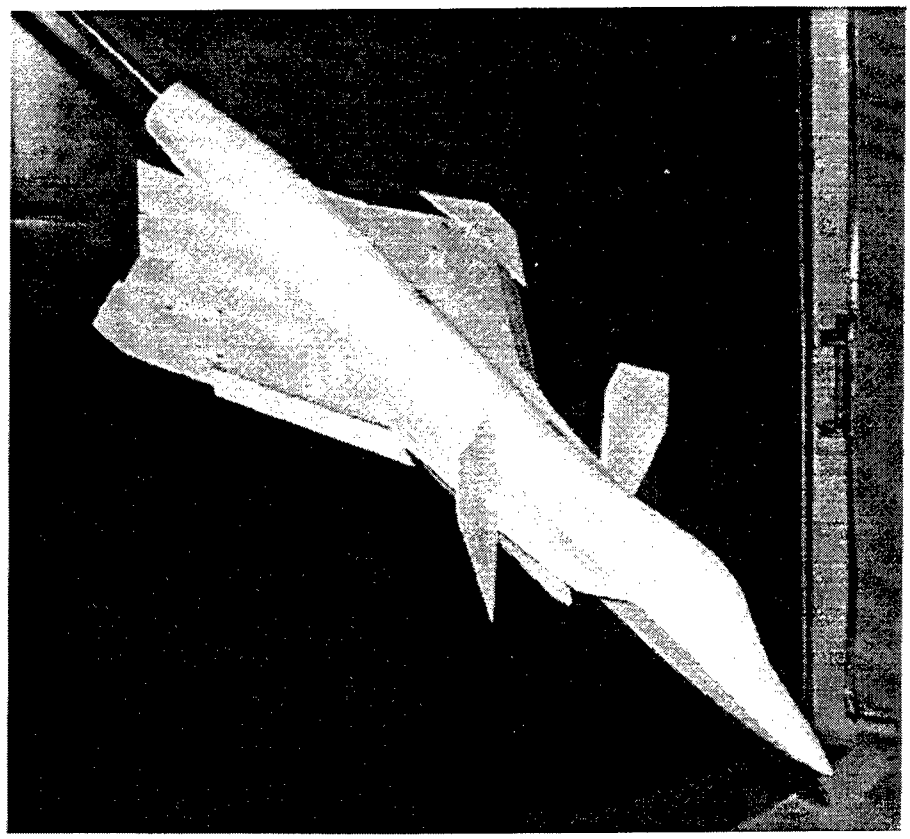

Figure 3-3. Photograph of the ICE 201 Model Installed on the Rotary Balance Apparatus.

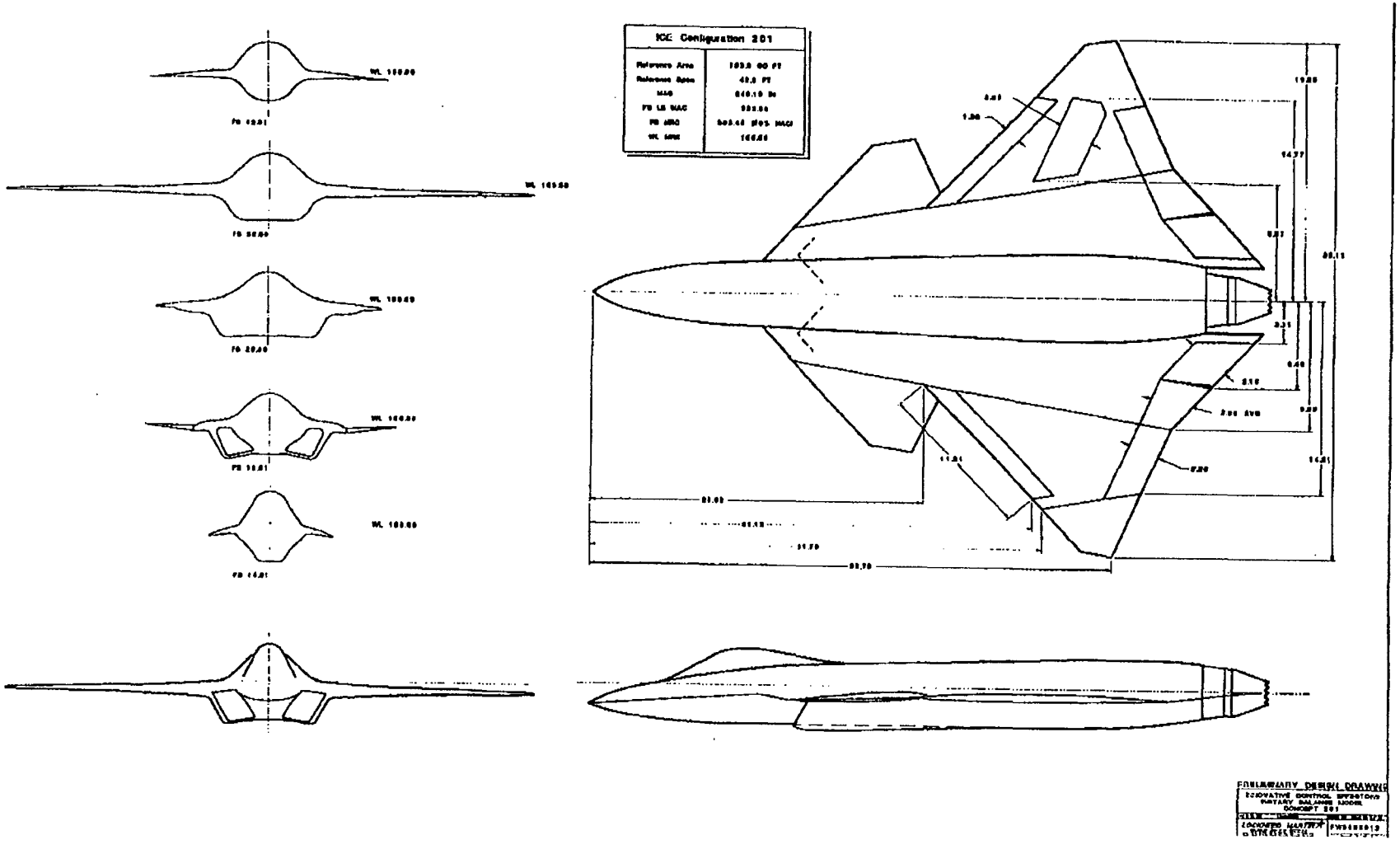

Figure 3-4. Three-view Drawing of the ICE 201 Configuration.

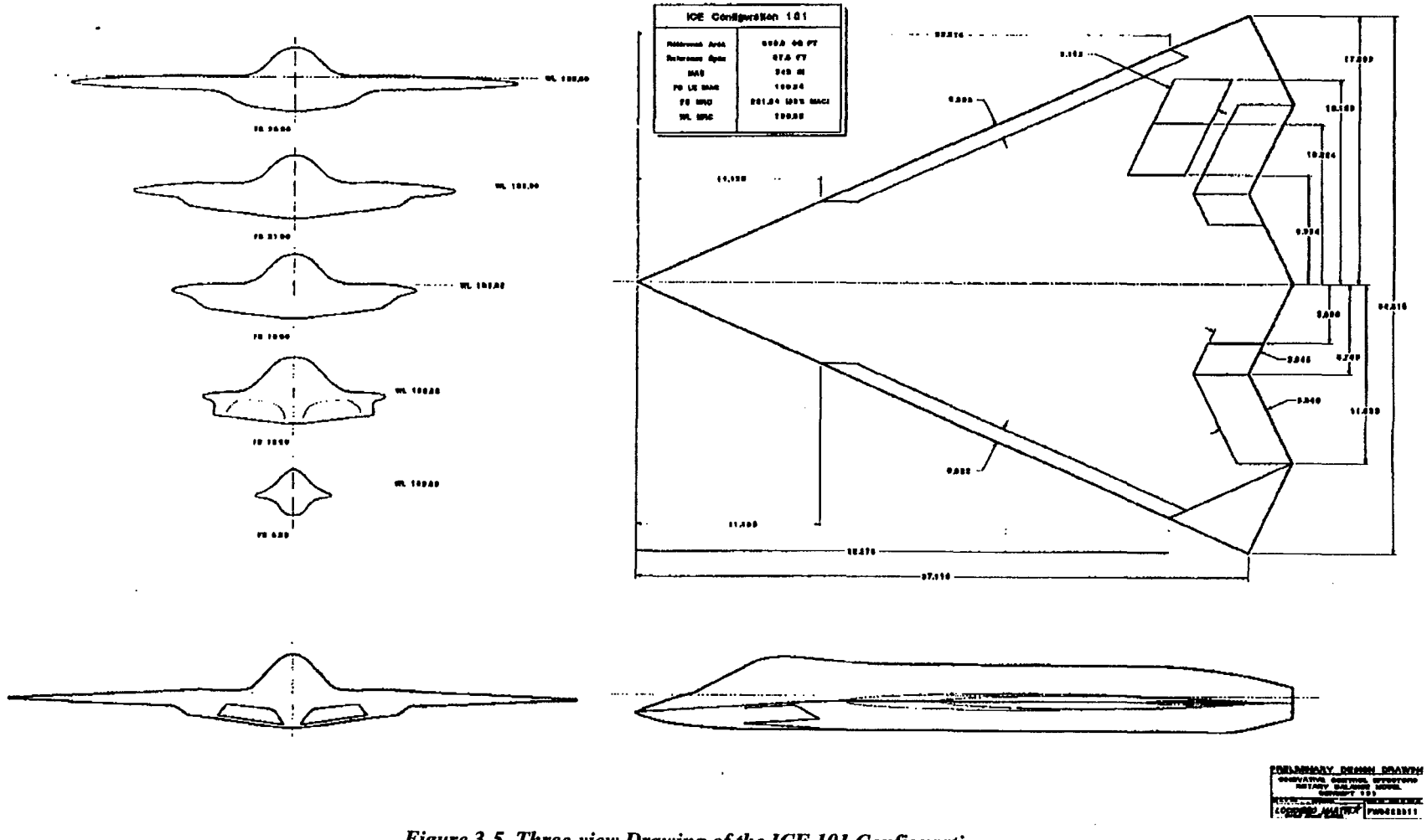

Figure 3-5. Three-view Drawing of the ICE 101 Configuration.

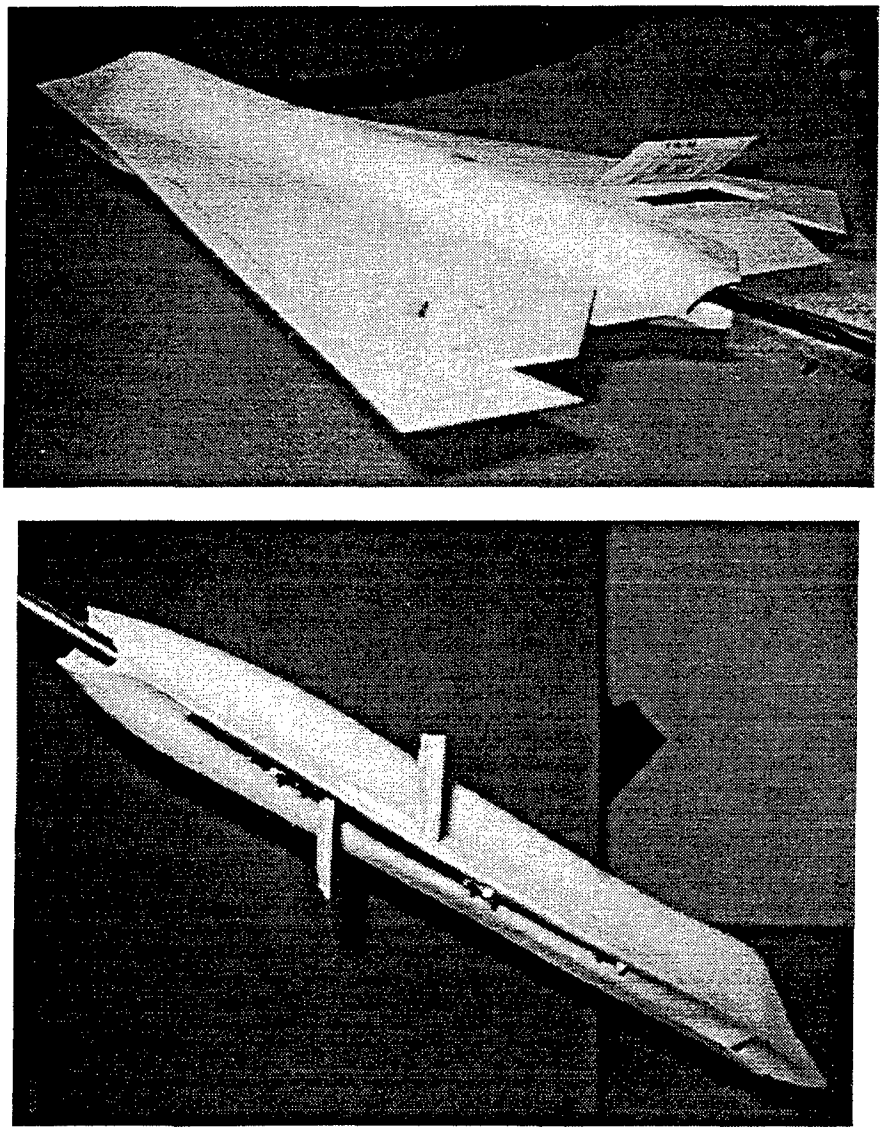

Figure 3-6. Photographs of Spoiler-slot-deflector (SSD) Deployed on ICE 101 Model.

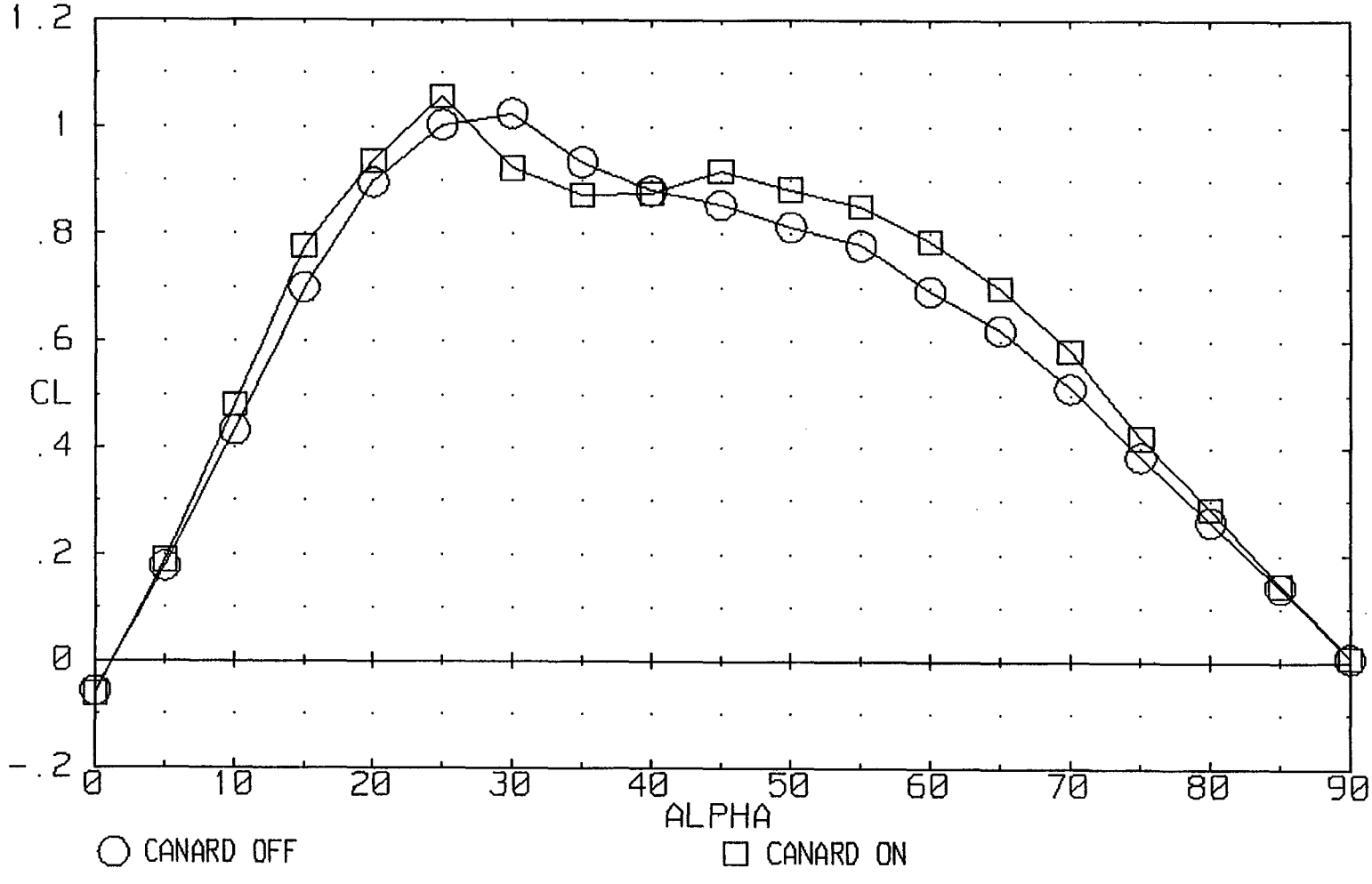

Figure 3-7. Canard-on vs Canard-off Lift Coefficient for the ICE 201.

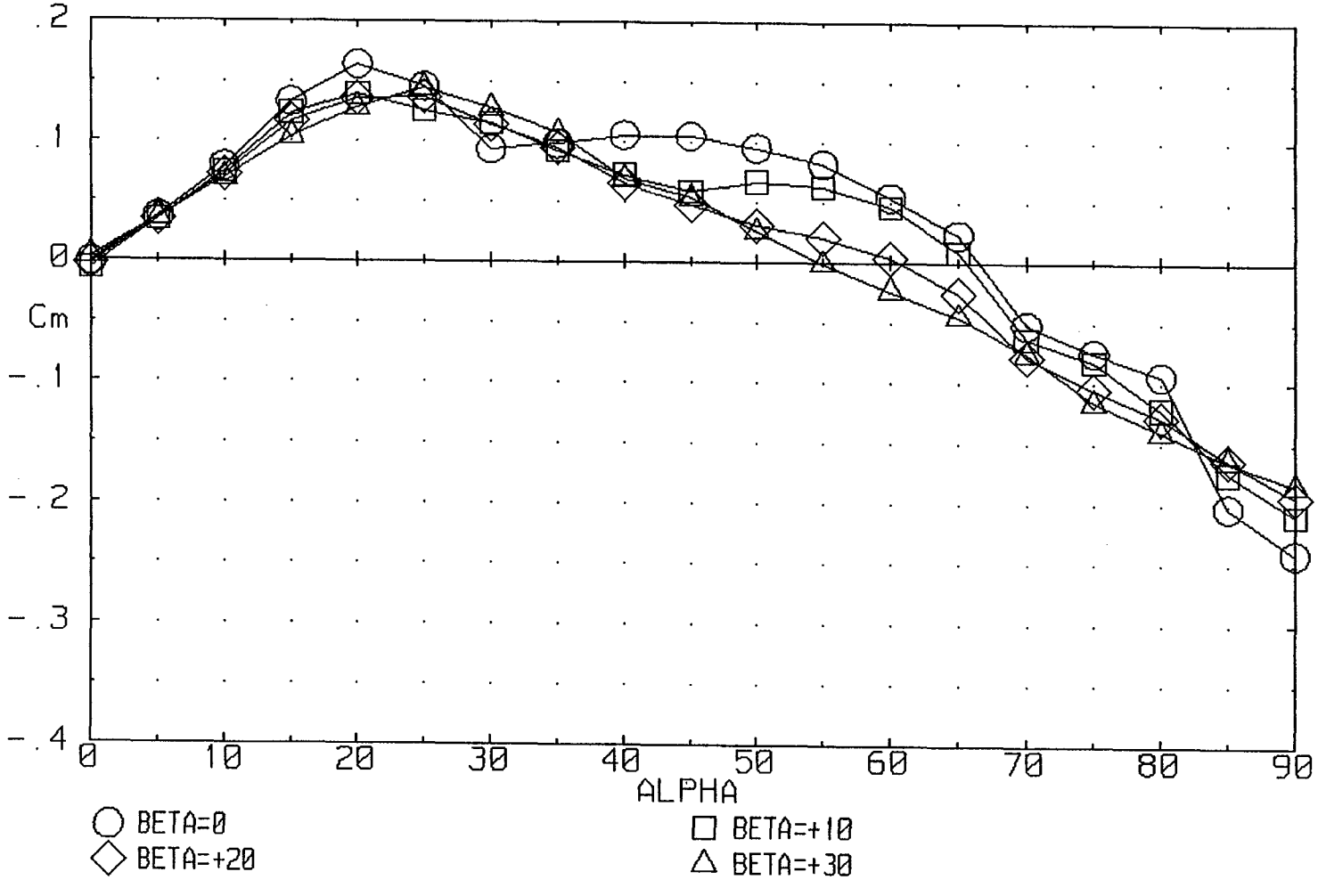

Figure 3-8. Effect of Sideslip on Static Pitching Moment for the ICE 201 (LEF=0).

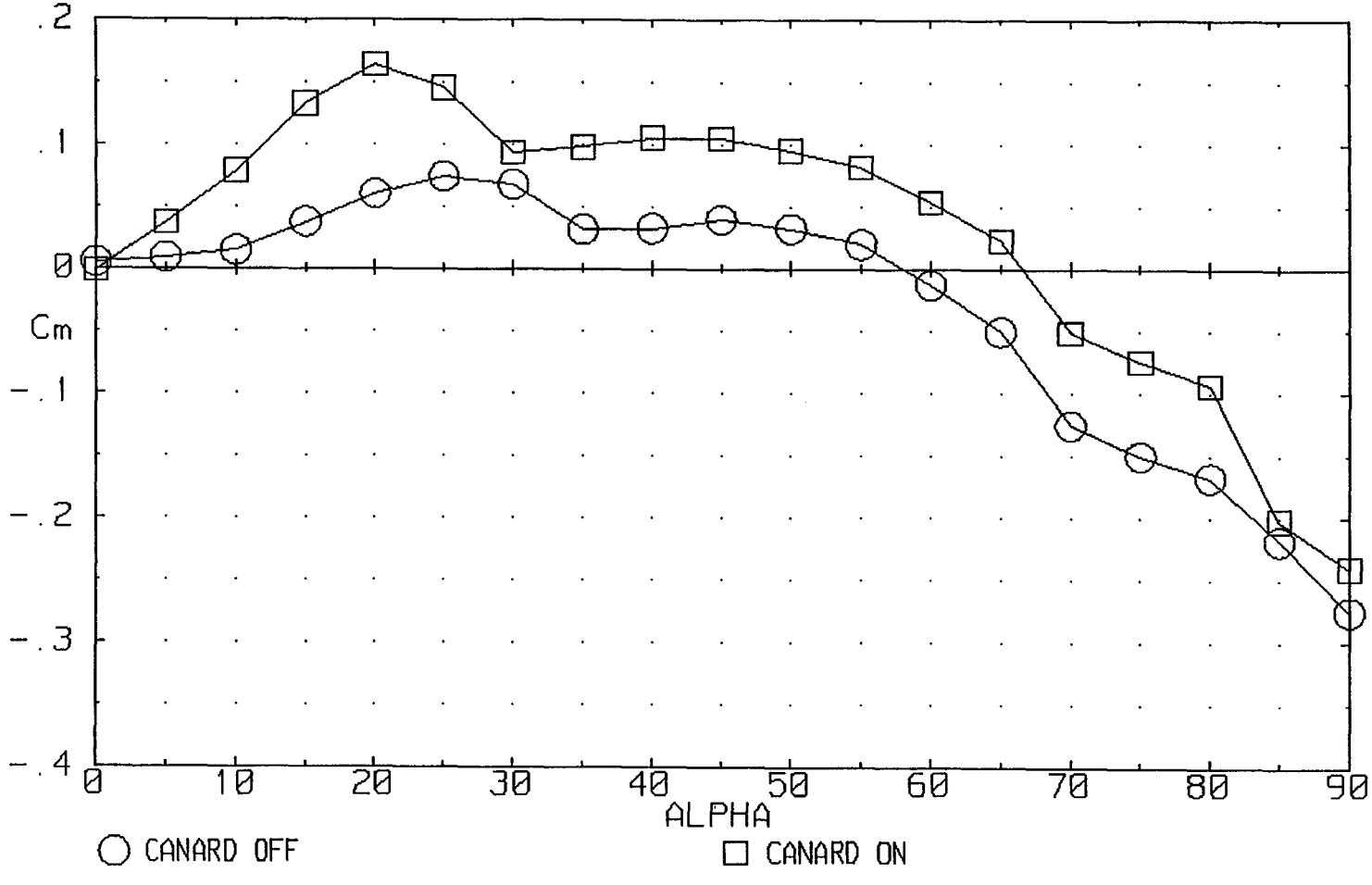

Figure 3-9. Effect of Canard on Static Pitching Moment at β=0° for the ICE 201.

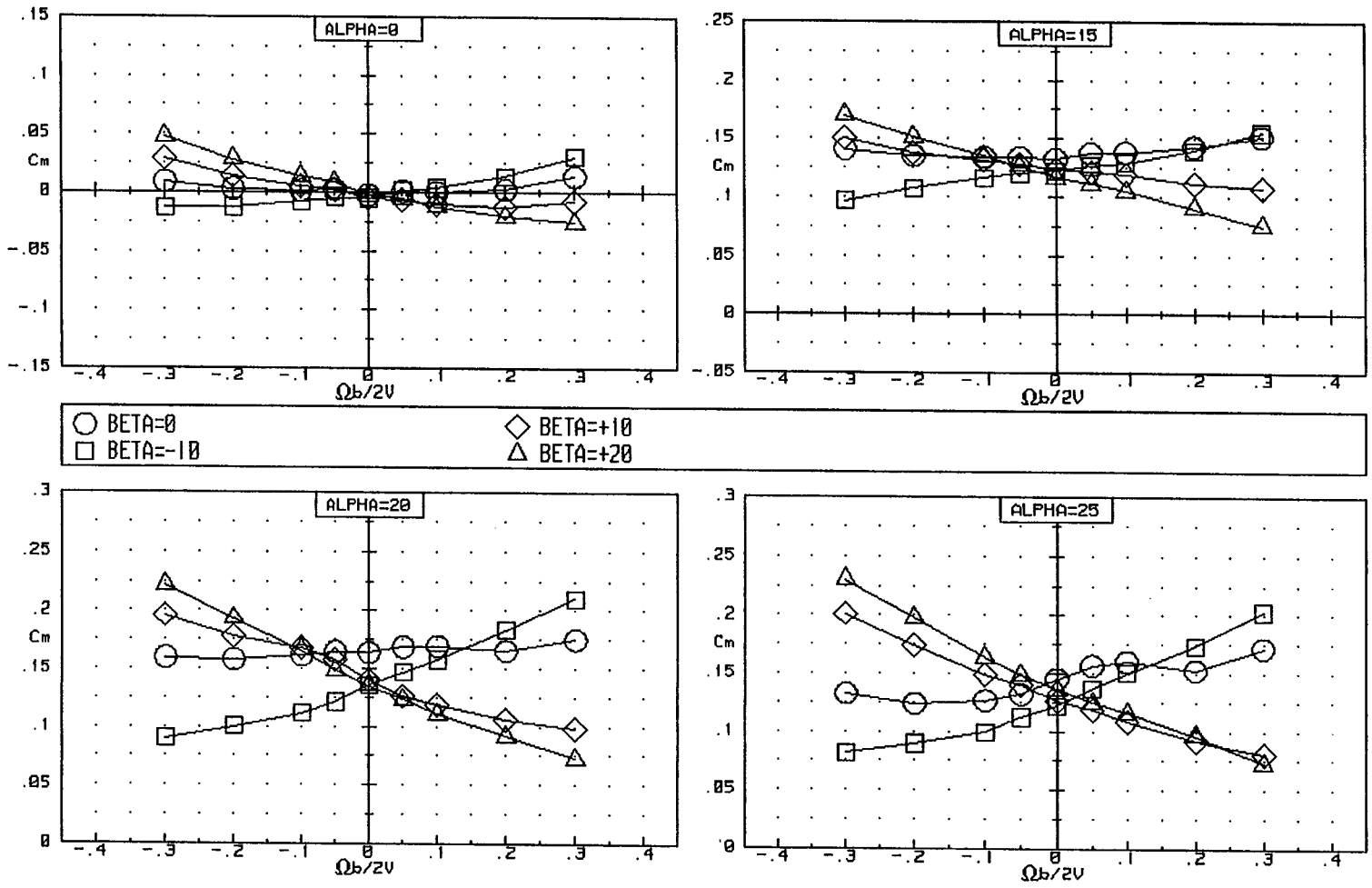

Figure 3-10. Effect of Rotation Rate and Sideslip on Pitching Moment for the ICE 201 (LEF=0).

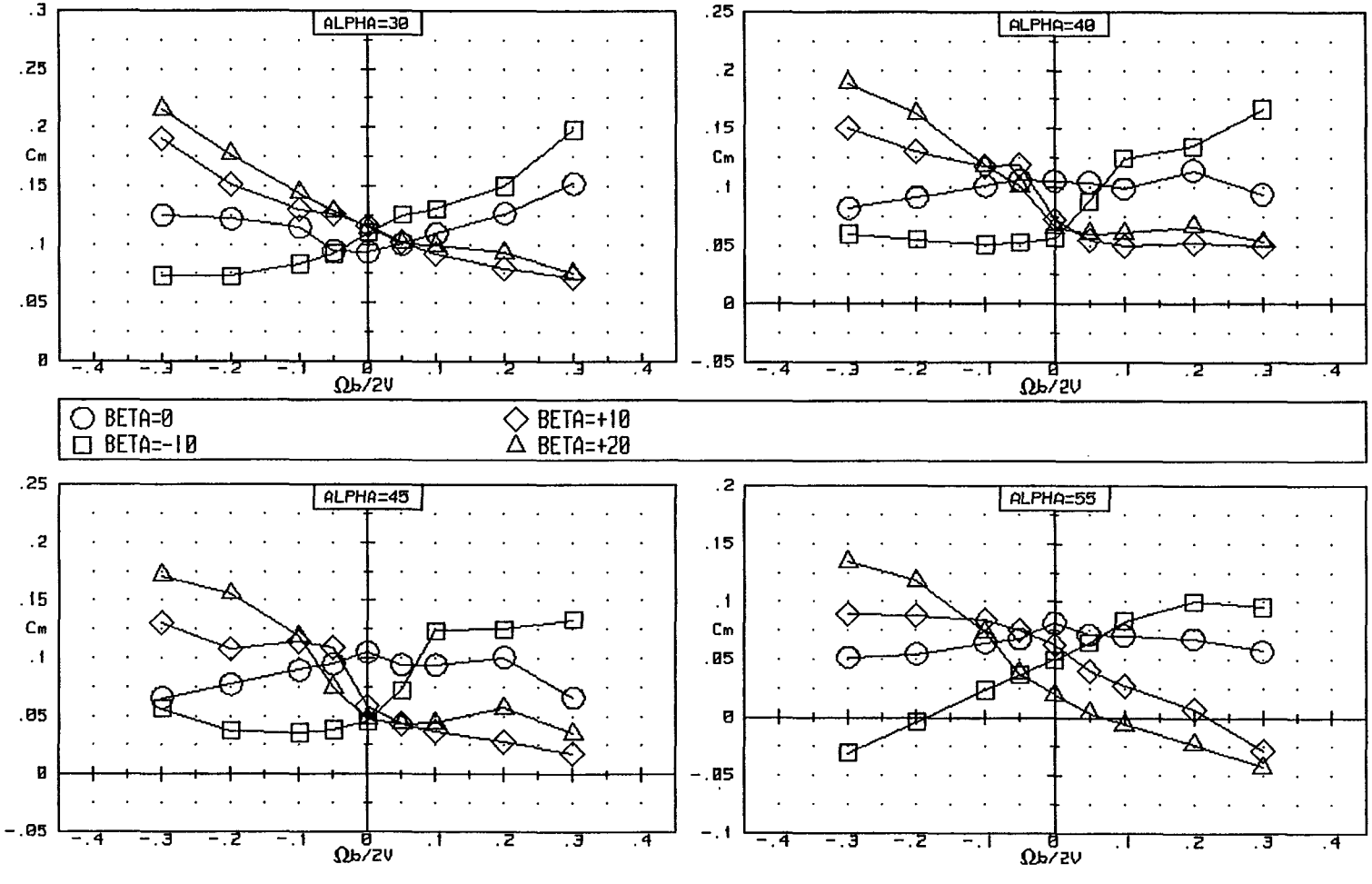

Figure 3-10. Continued.

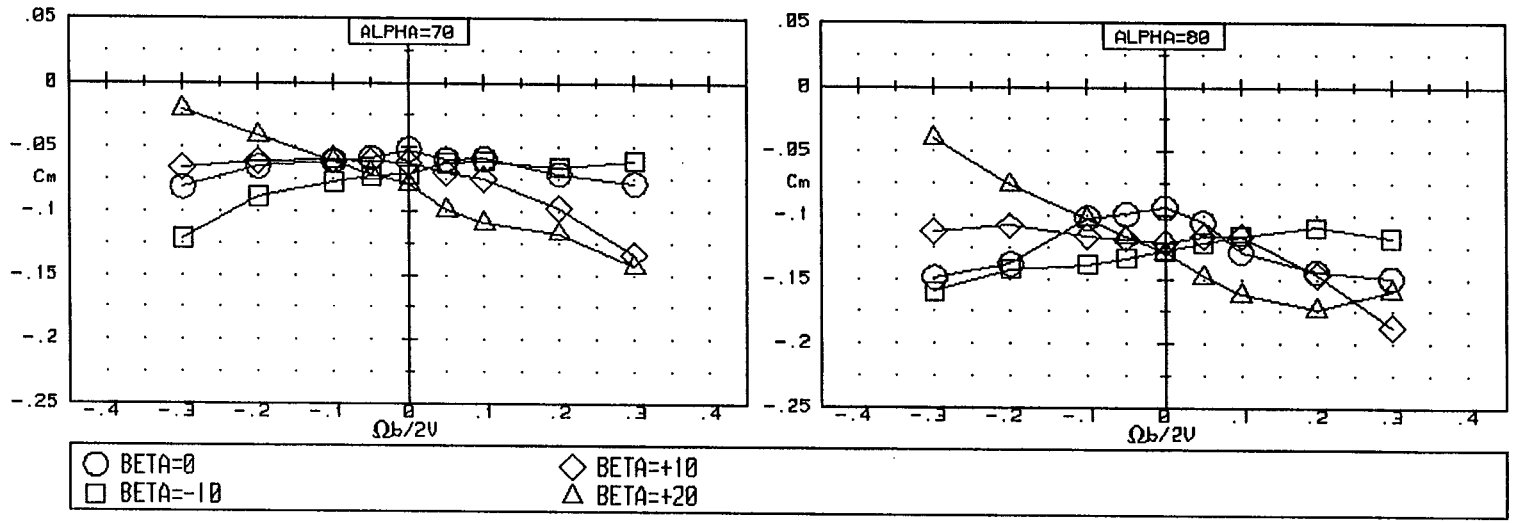

Figure 3-10. Concluded.

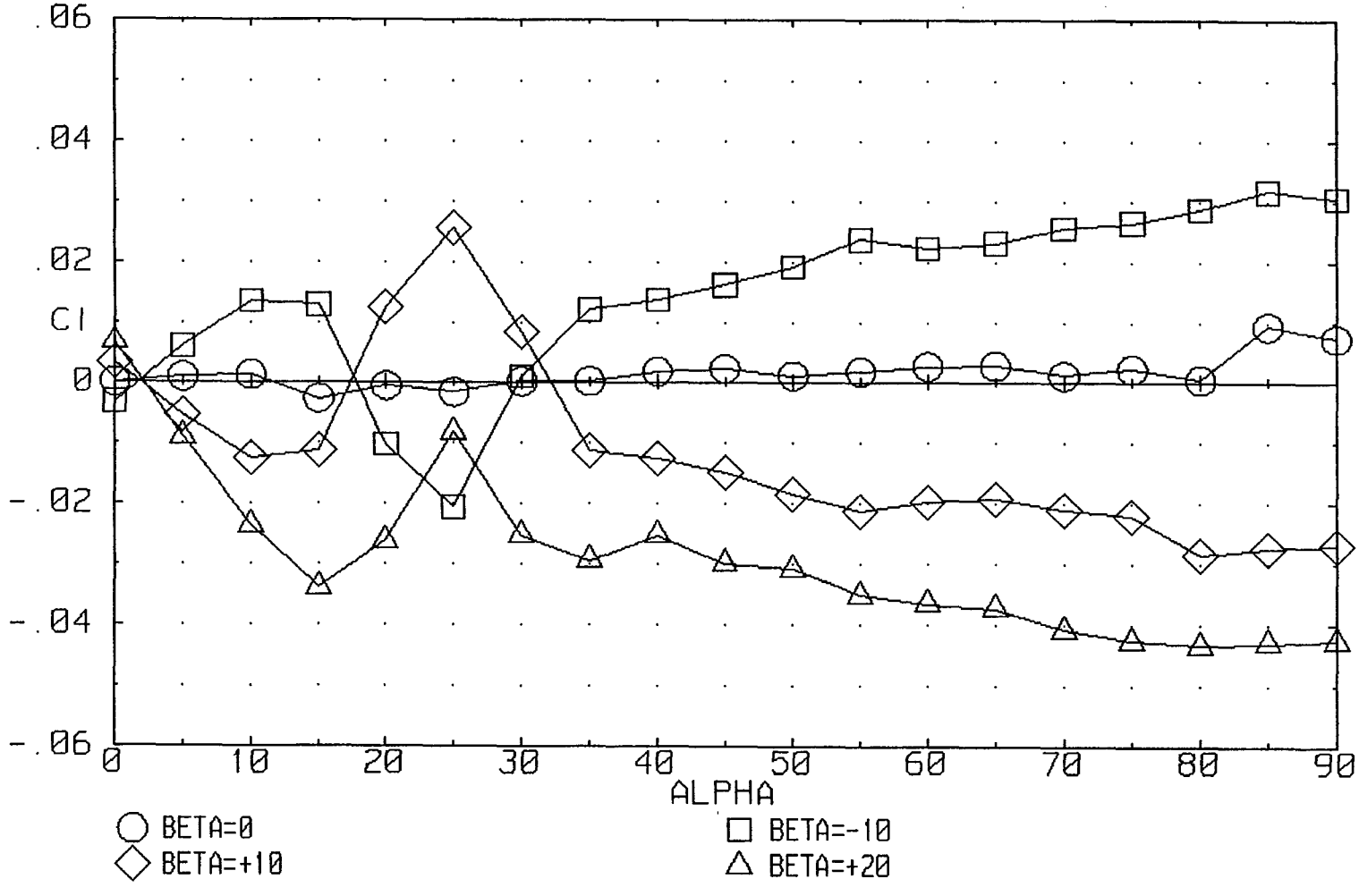

Figure 3-11. Effects of Sideslip on Static Rolling Moment Characteristics of the ICE 201 (LEF=0).

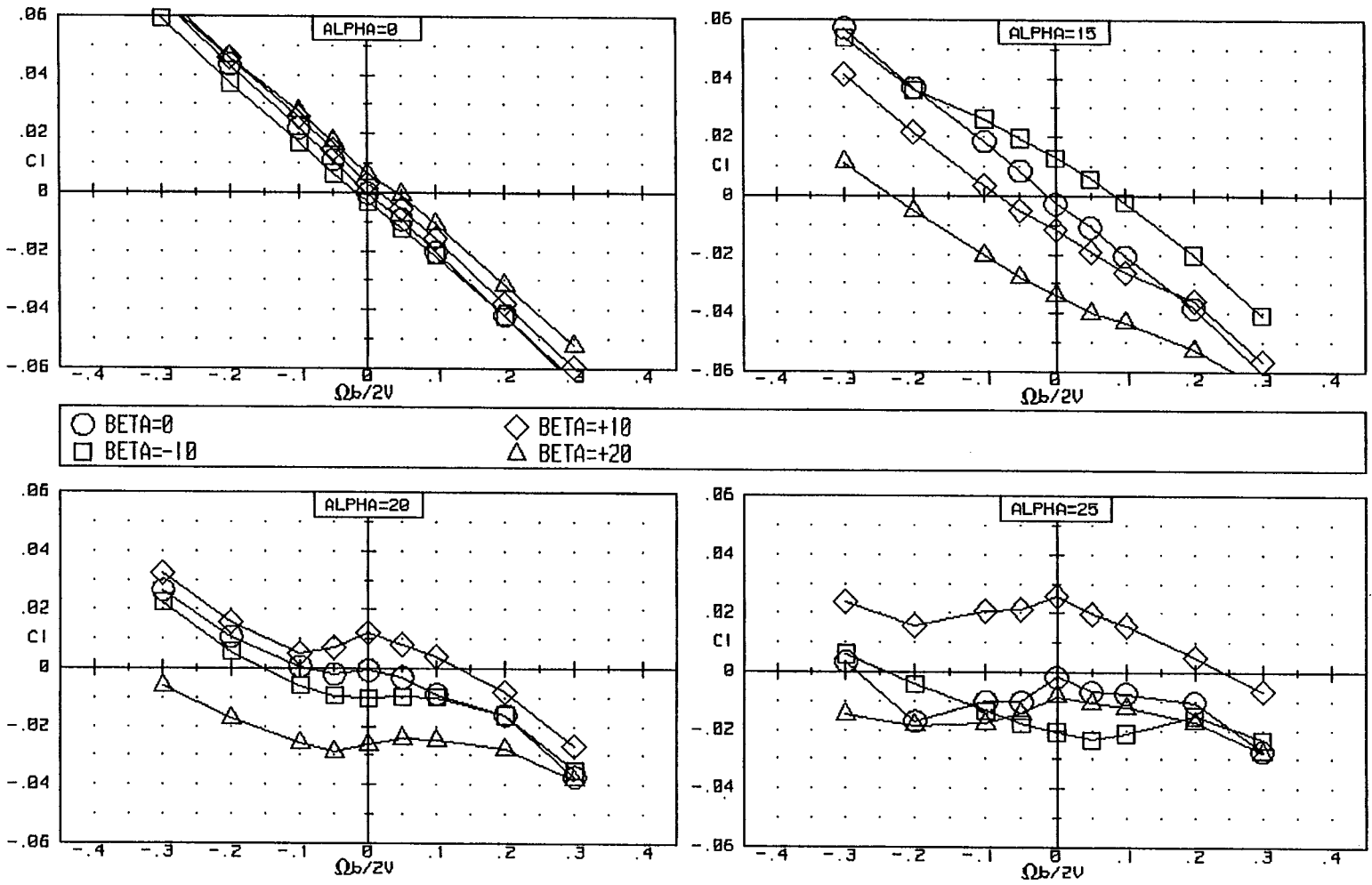

Figure 3-12. Effect of Rotation Rate and Sideslip on Rolling Moment for the ICE 201 (LEF=0).

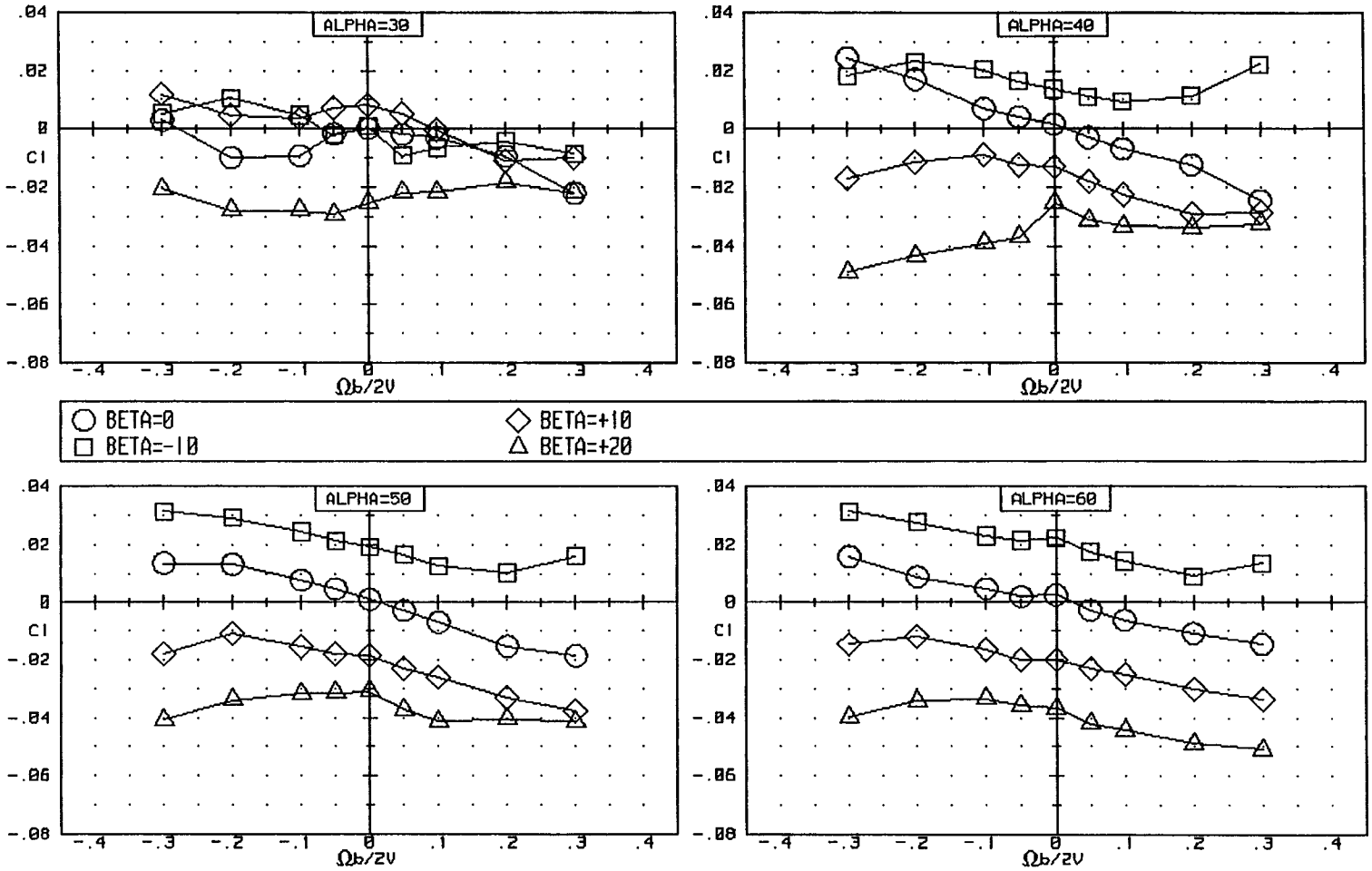

Figure 3-12. Continued.

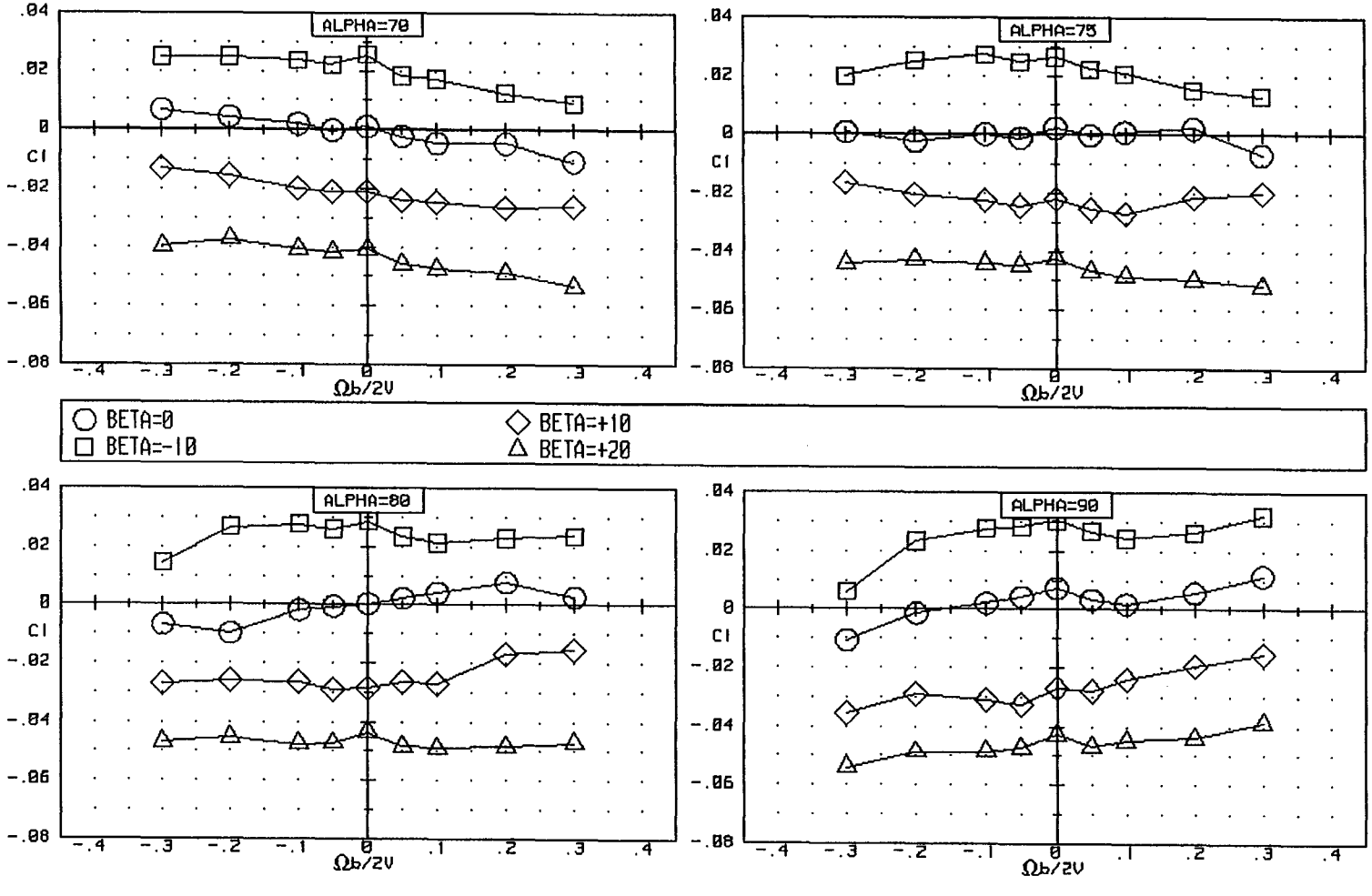

Figure 3-12. Concluded.

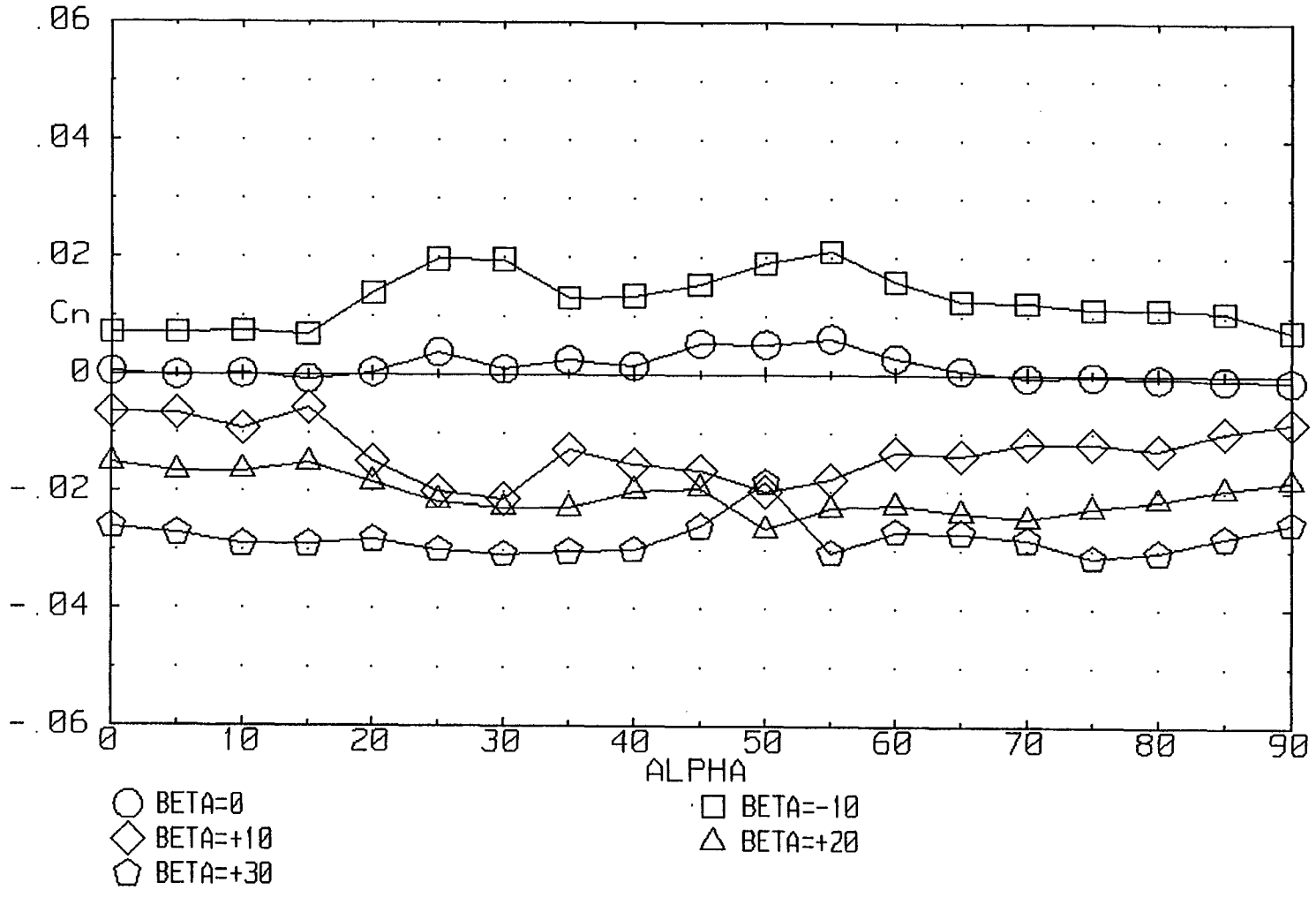

Figure 3-13. Effect of Sideslip on Static Yawing Moment Characteristics for the ICE 201 (LEF=0).

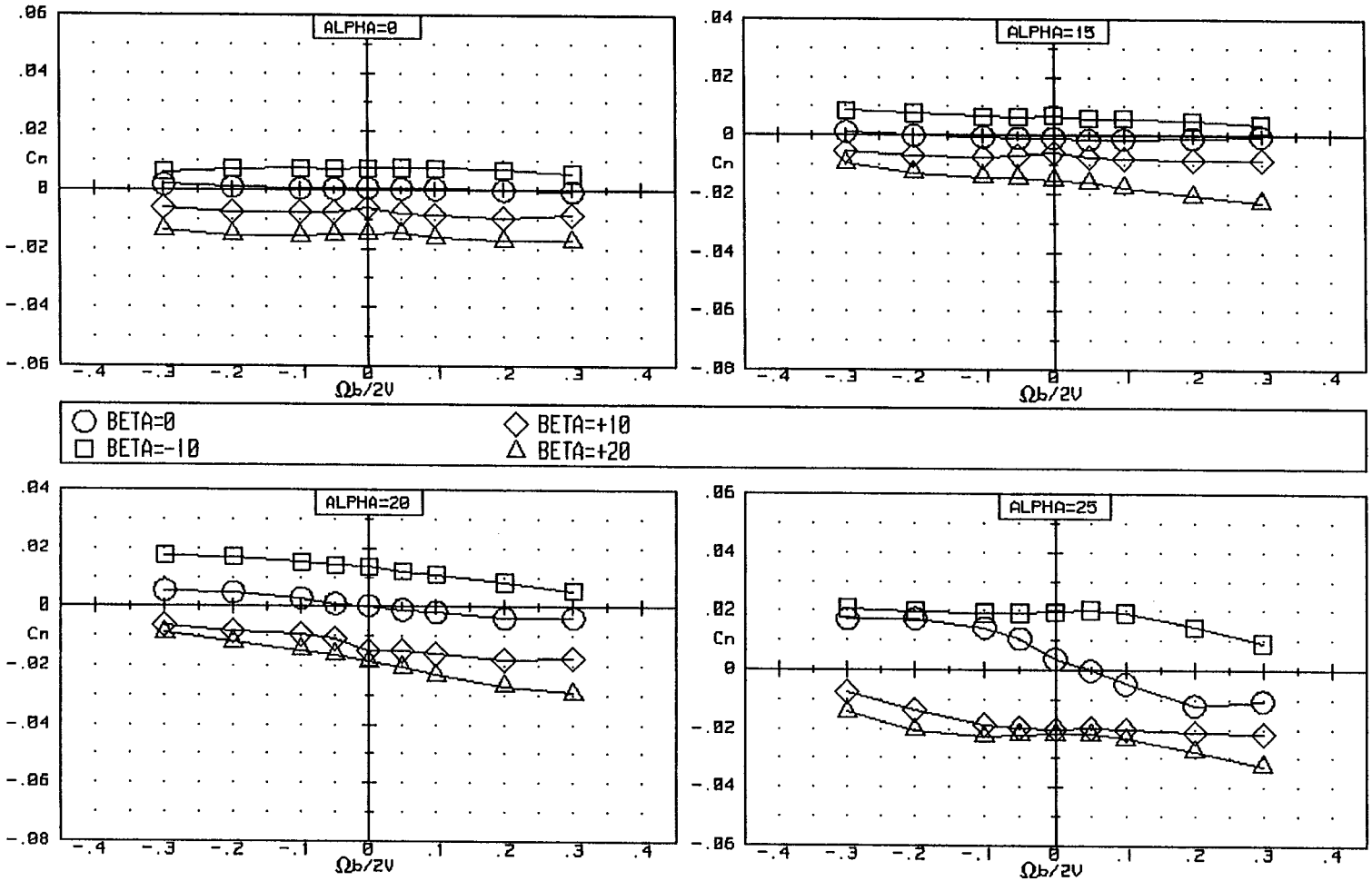

Figure 3-14. Effect of Rotation Rate and Sideslip on Yawing Moment for the ICE 201 (LEF=0).

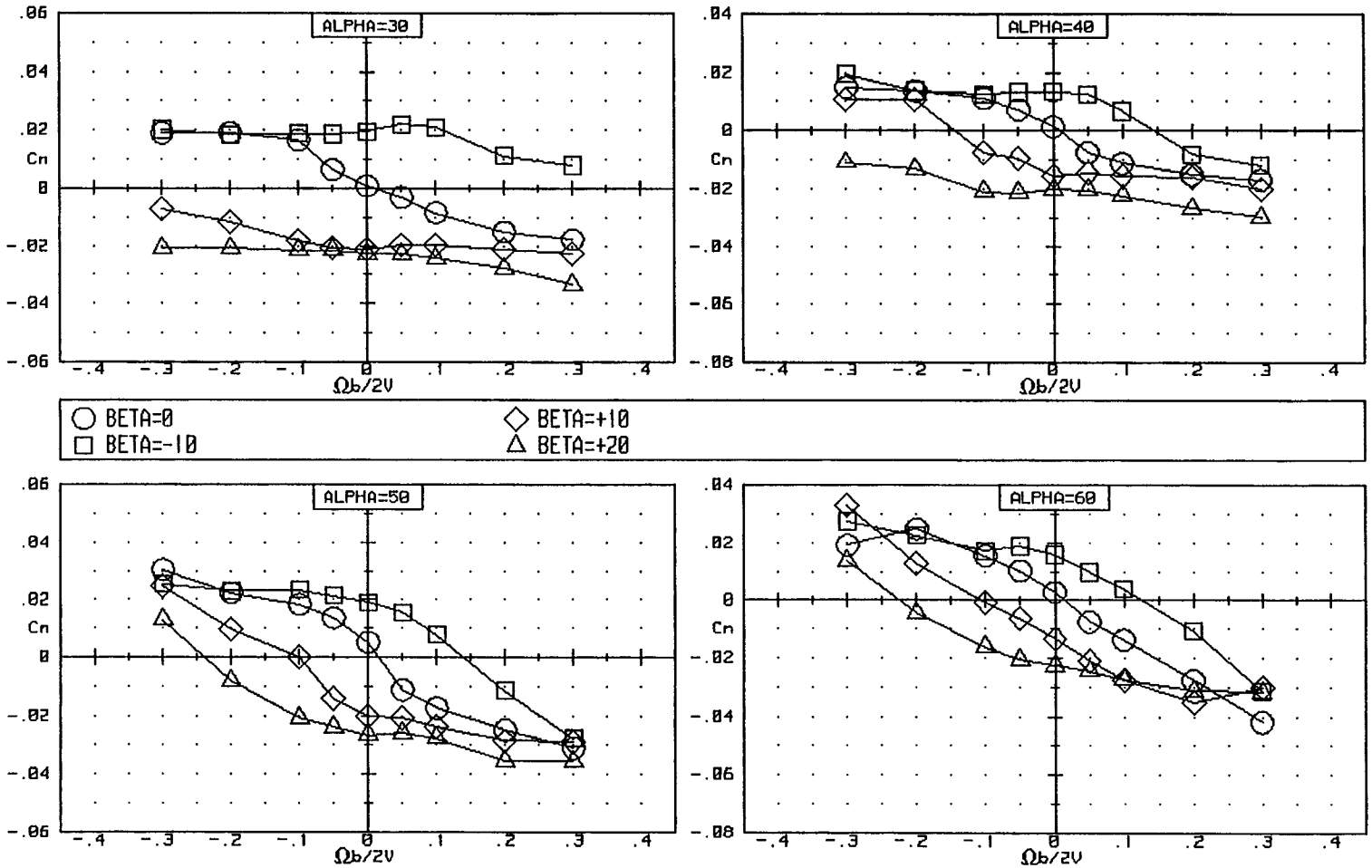

Figure 3-14. Continued.

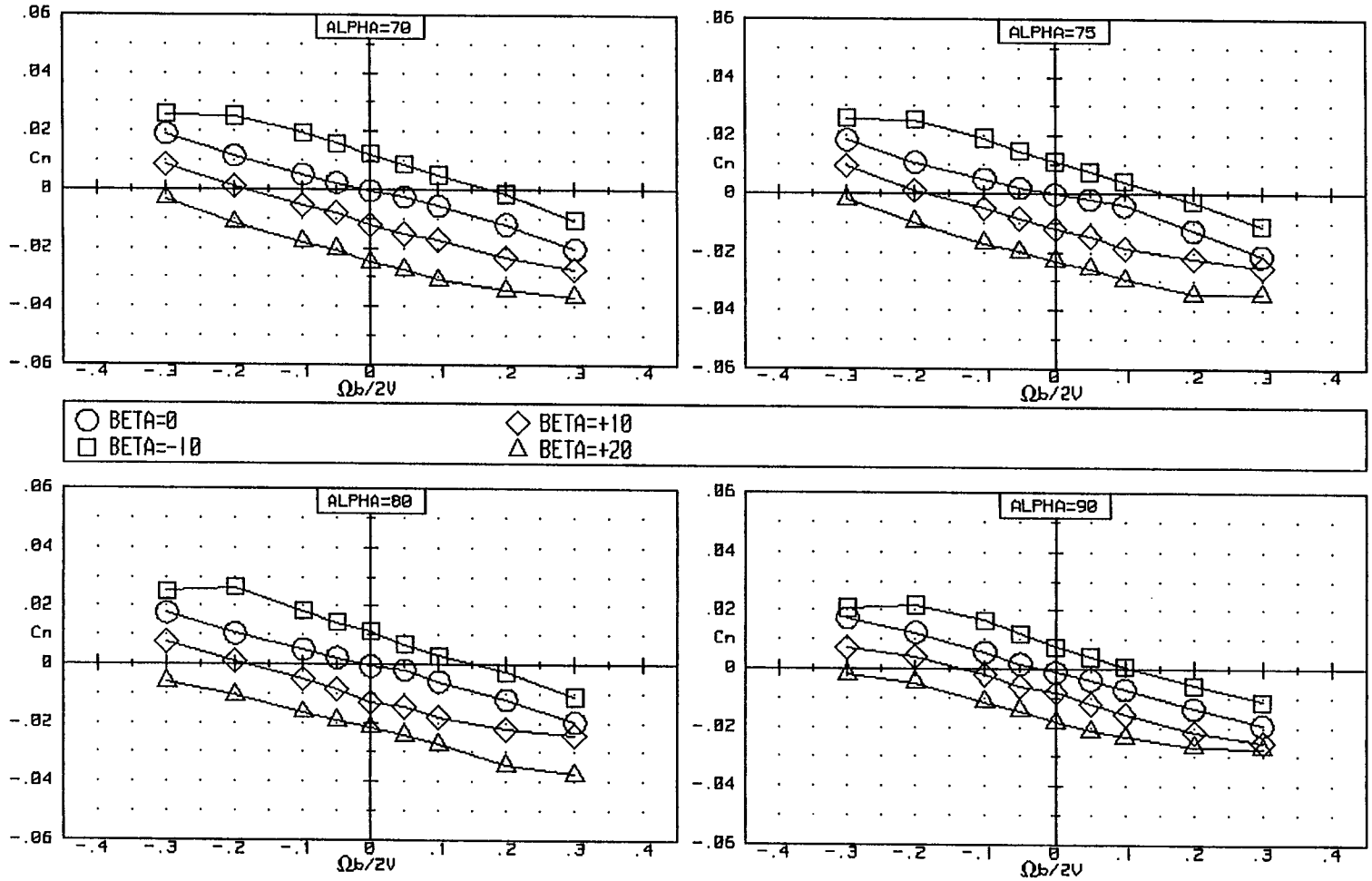

Figure 3-14. Concluded.

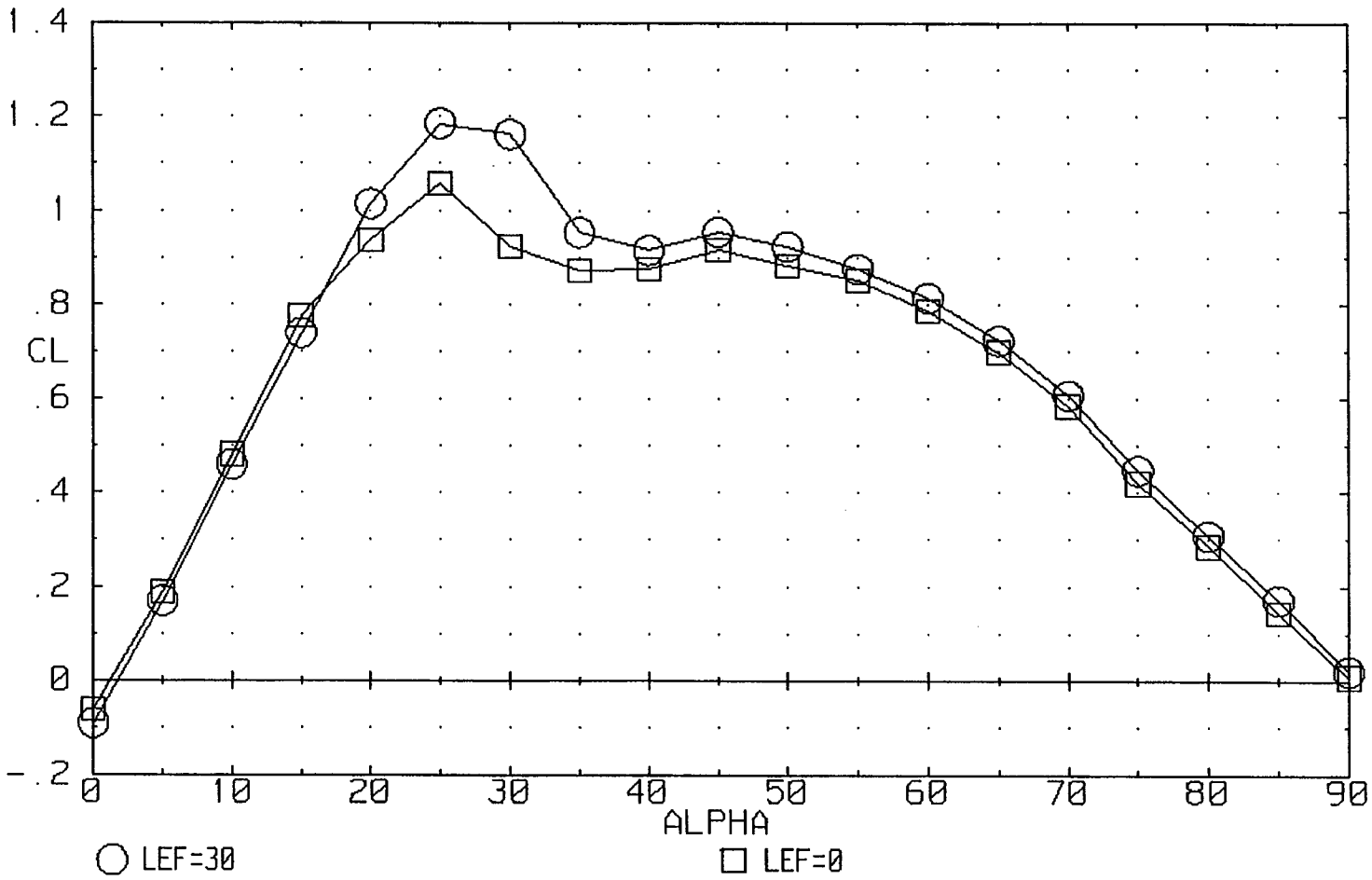

Figure 3-15. Effect of Leading Edge Flap Deflection on Lift for the ICE 201 (β=0°).

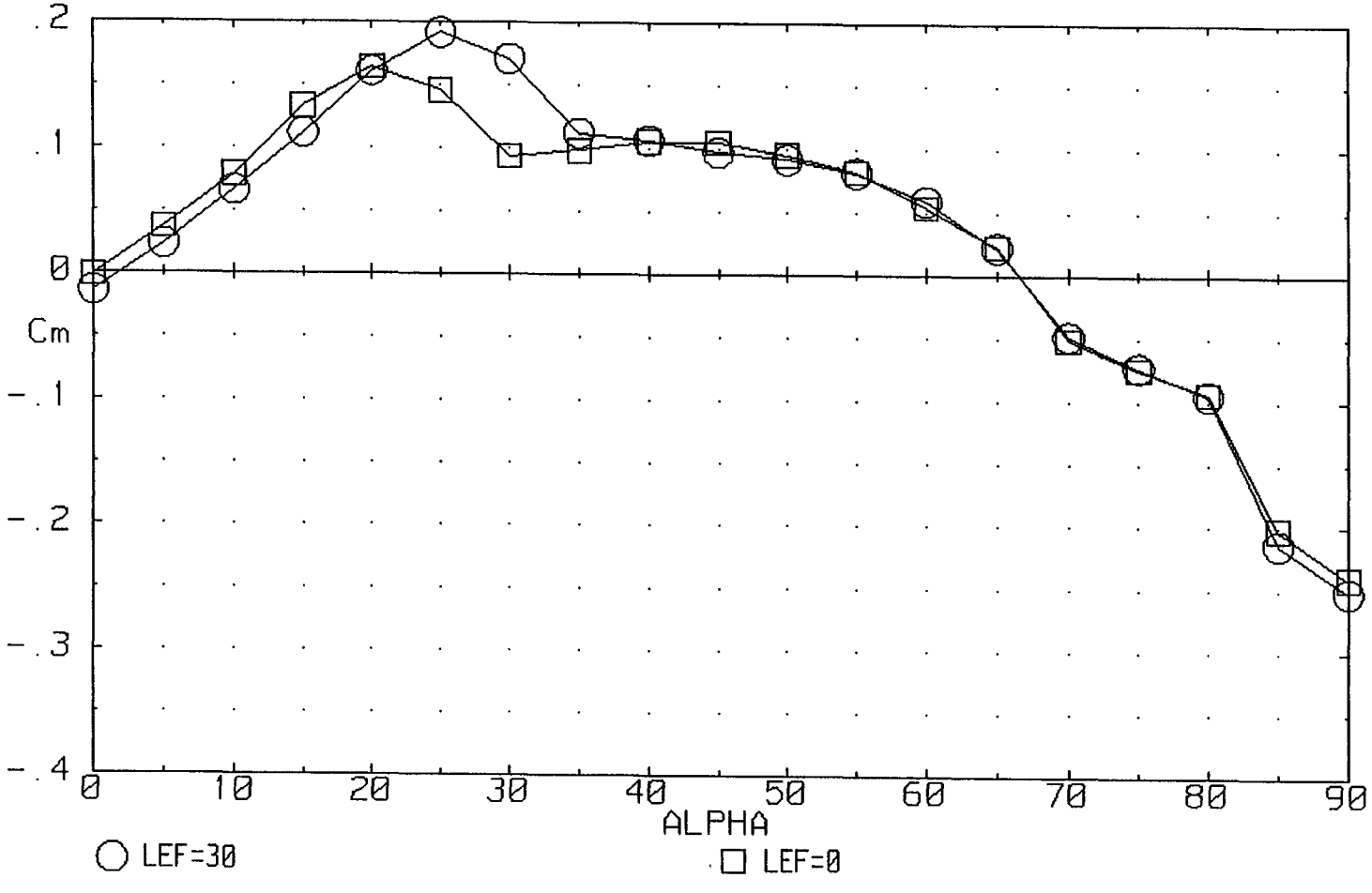

Figure 3-16. Effect of Leading Edge Flap Deflection on Static Pitching Moment for the ICE 201 at Zero Sideslip.

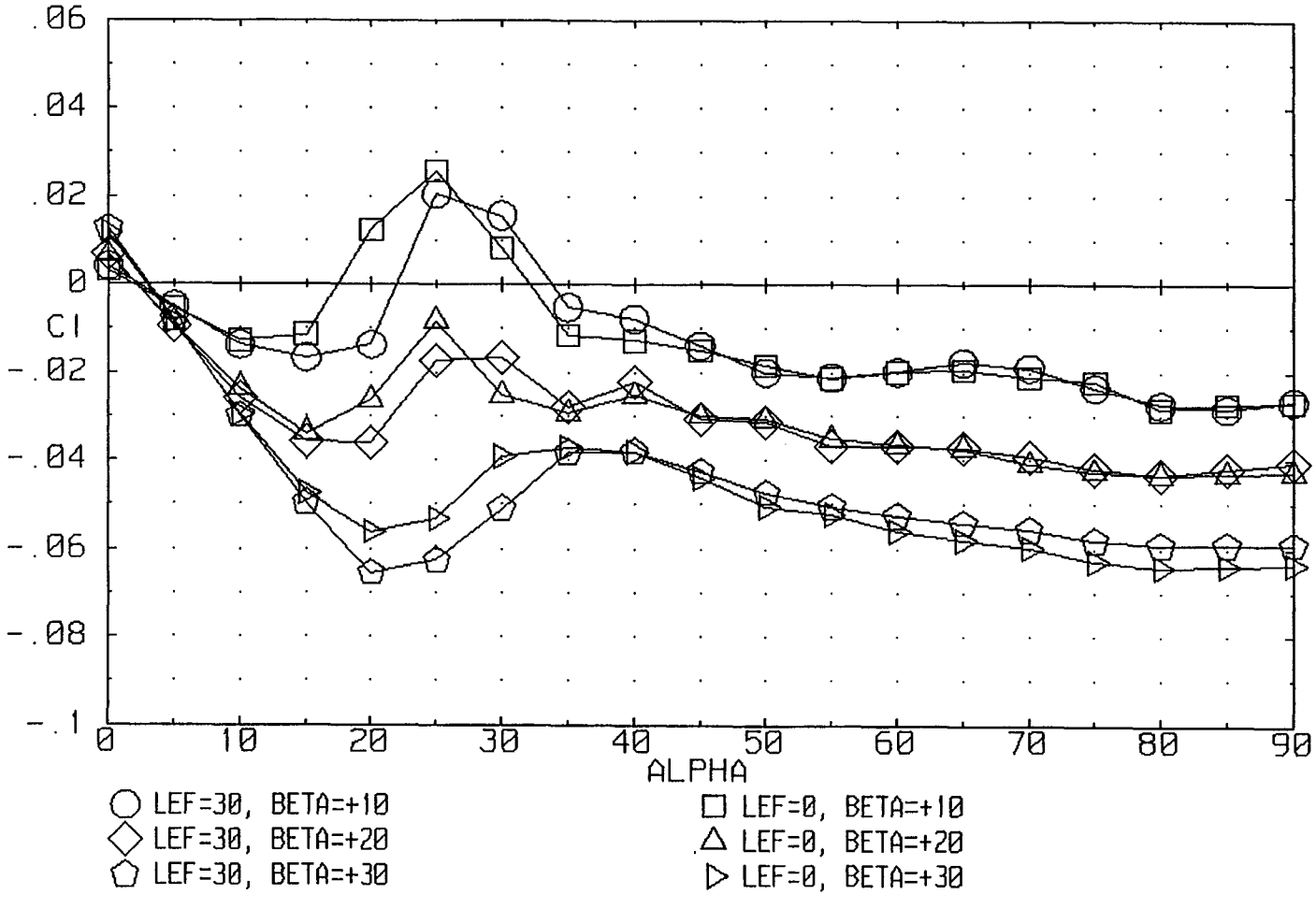

Figure 3-17. Effect of Leading Edge Flap Deflection on Static Rolling Moment for the ICE 201.

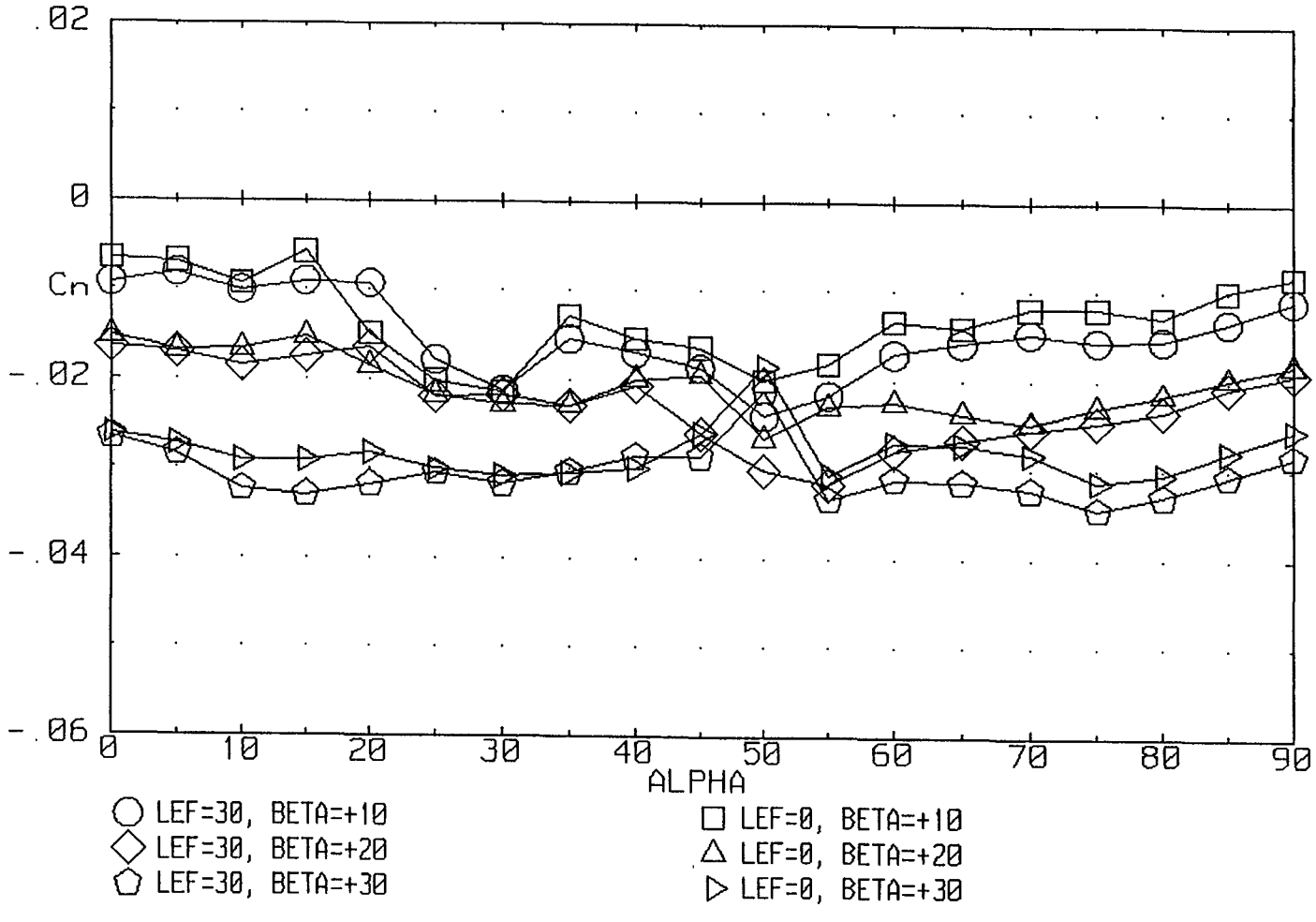

Figure 3-18. Effect of Leading Edge Flap Deflection on Static Yawing Moment for the ICE 201.

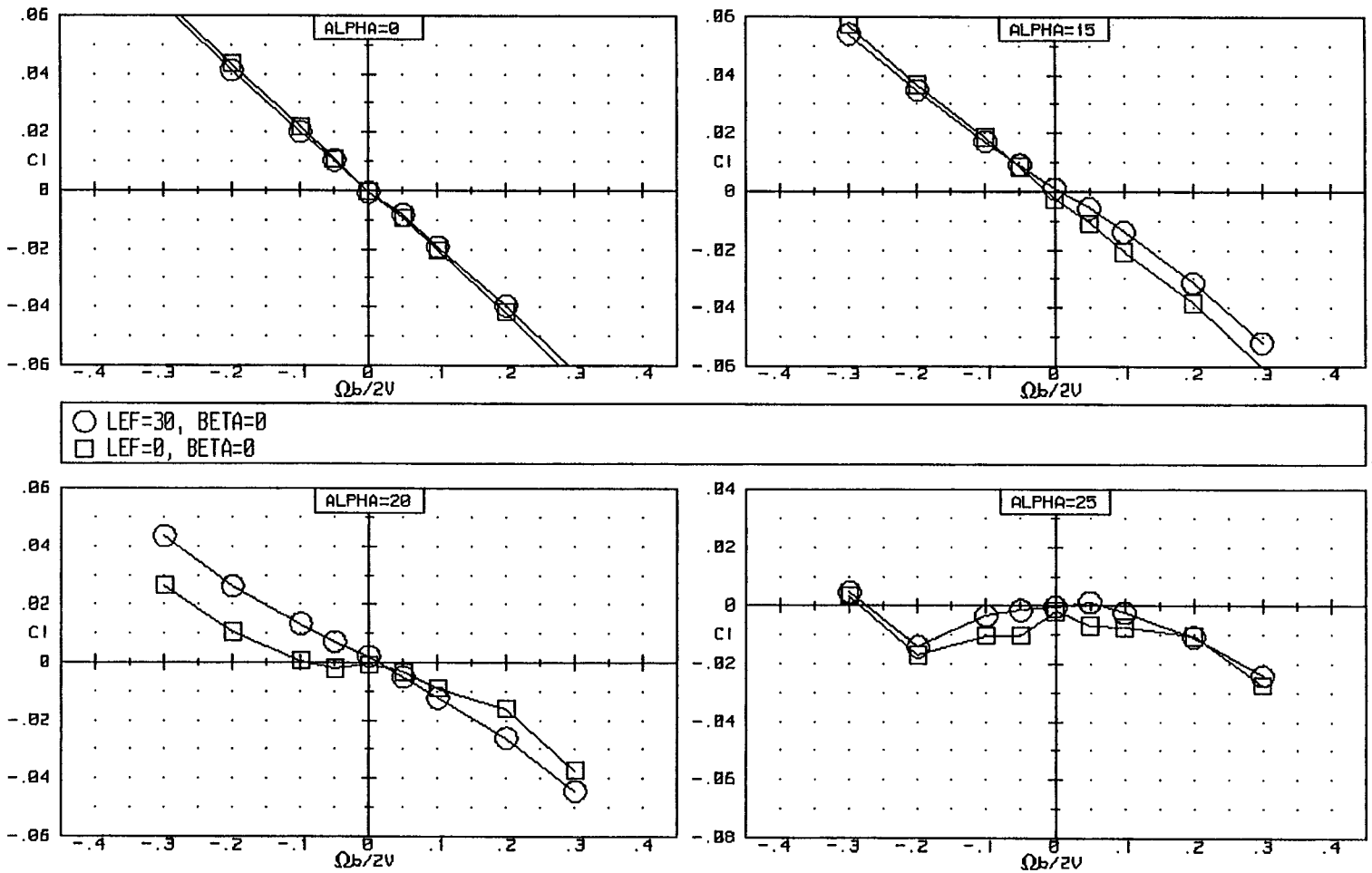

Figure 3-19. Effect of Rotation Rate and LEF Deflection on Rolling Moment for the ICE 201 (β=0°).

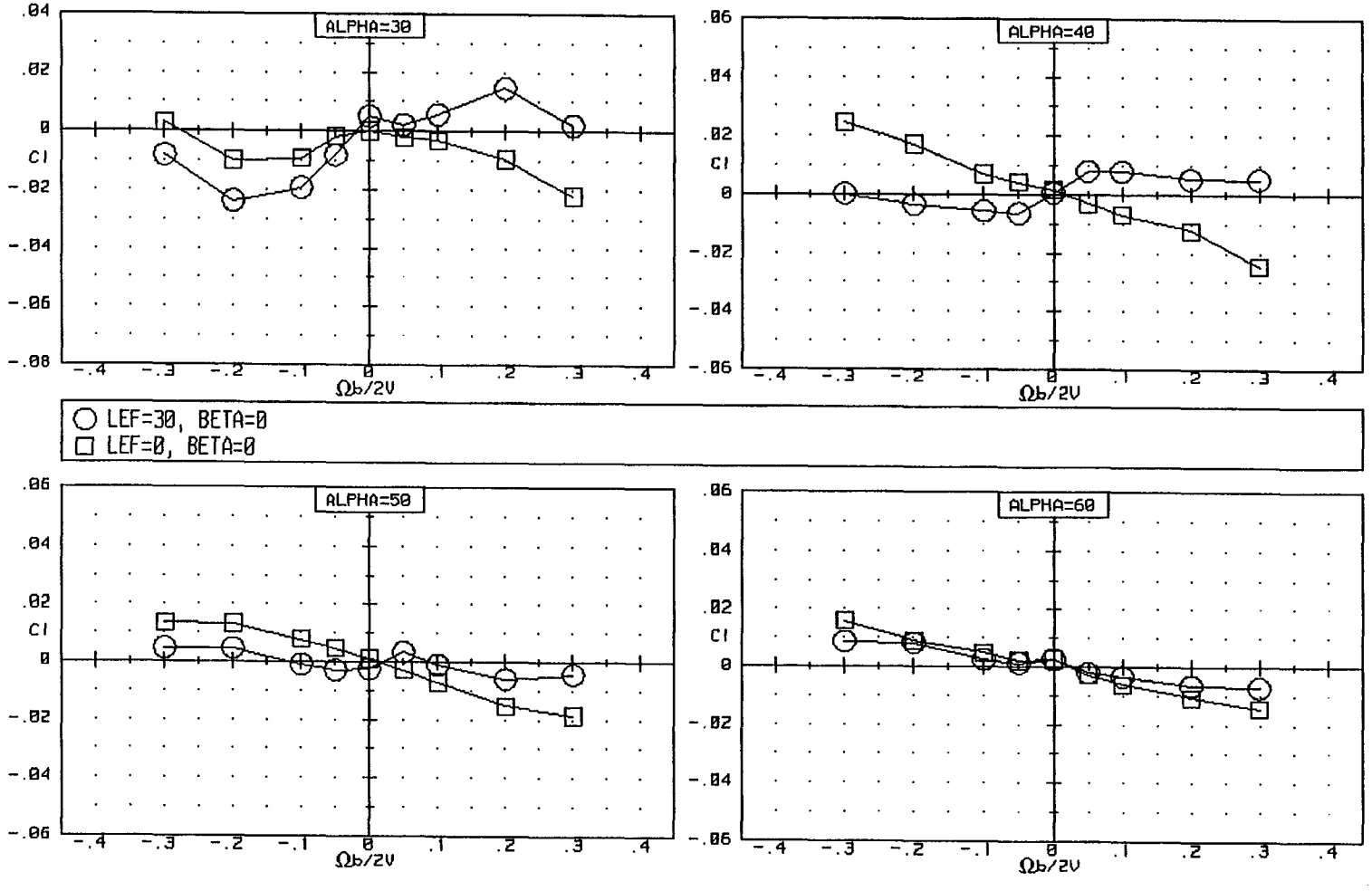

Figure 3-19. Continued.

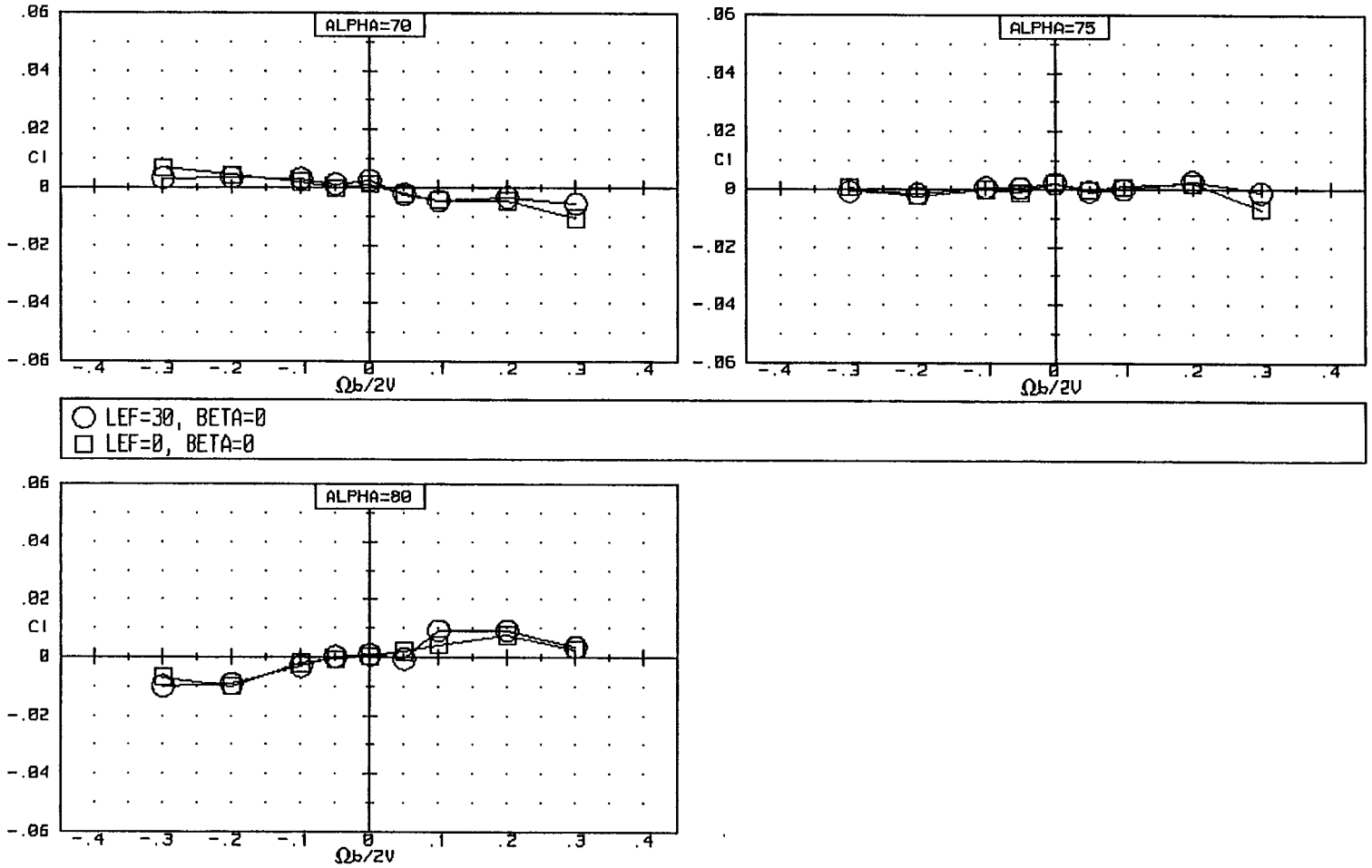

Figure 3-19. Concluded.

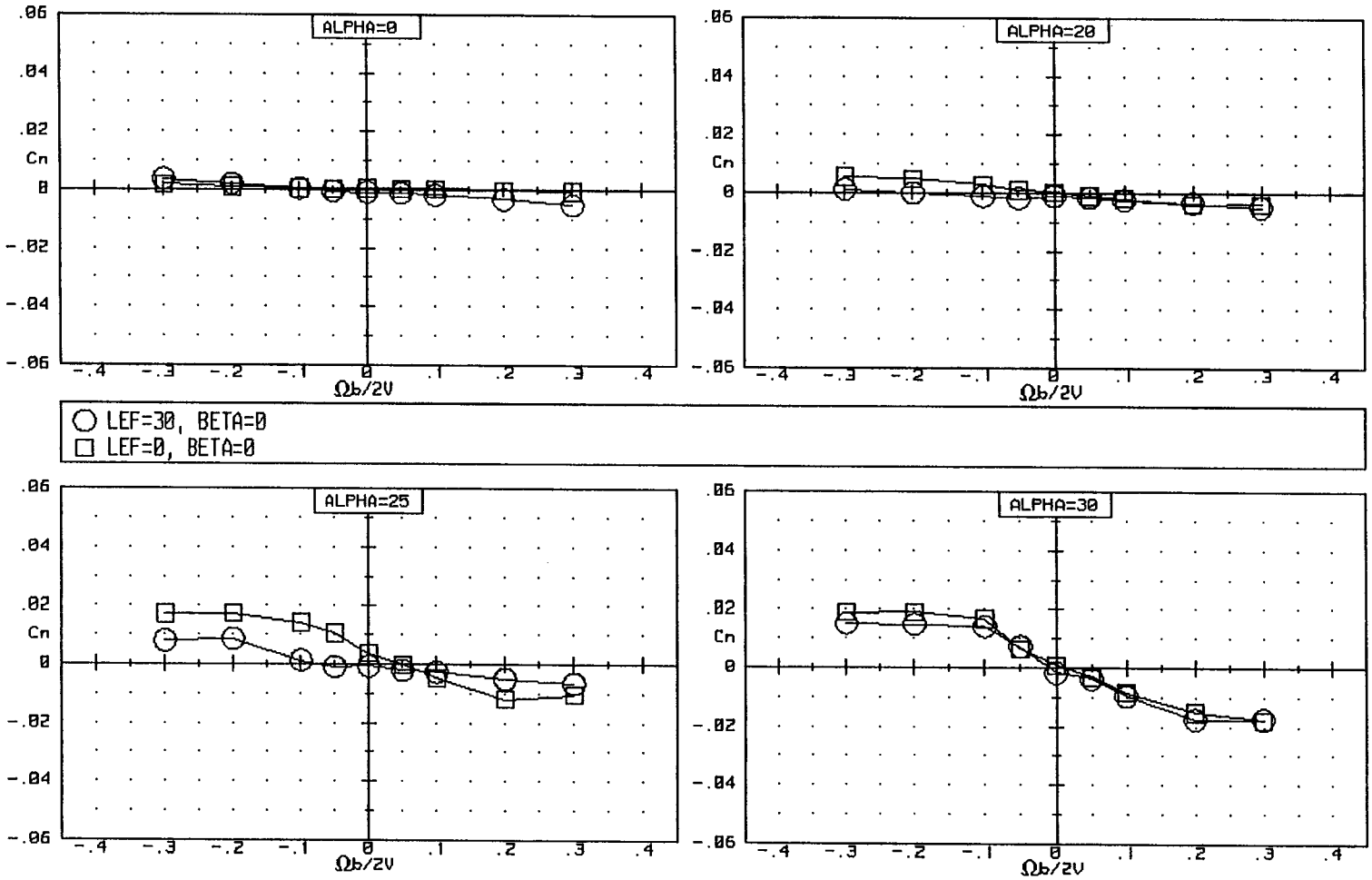

Figure 3-20. Effect of Rotation Rate and LEF Deflection on Yawing Moment for the ICE 201 (β=0°).

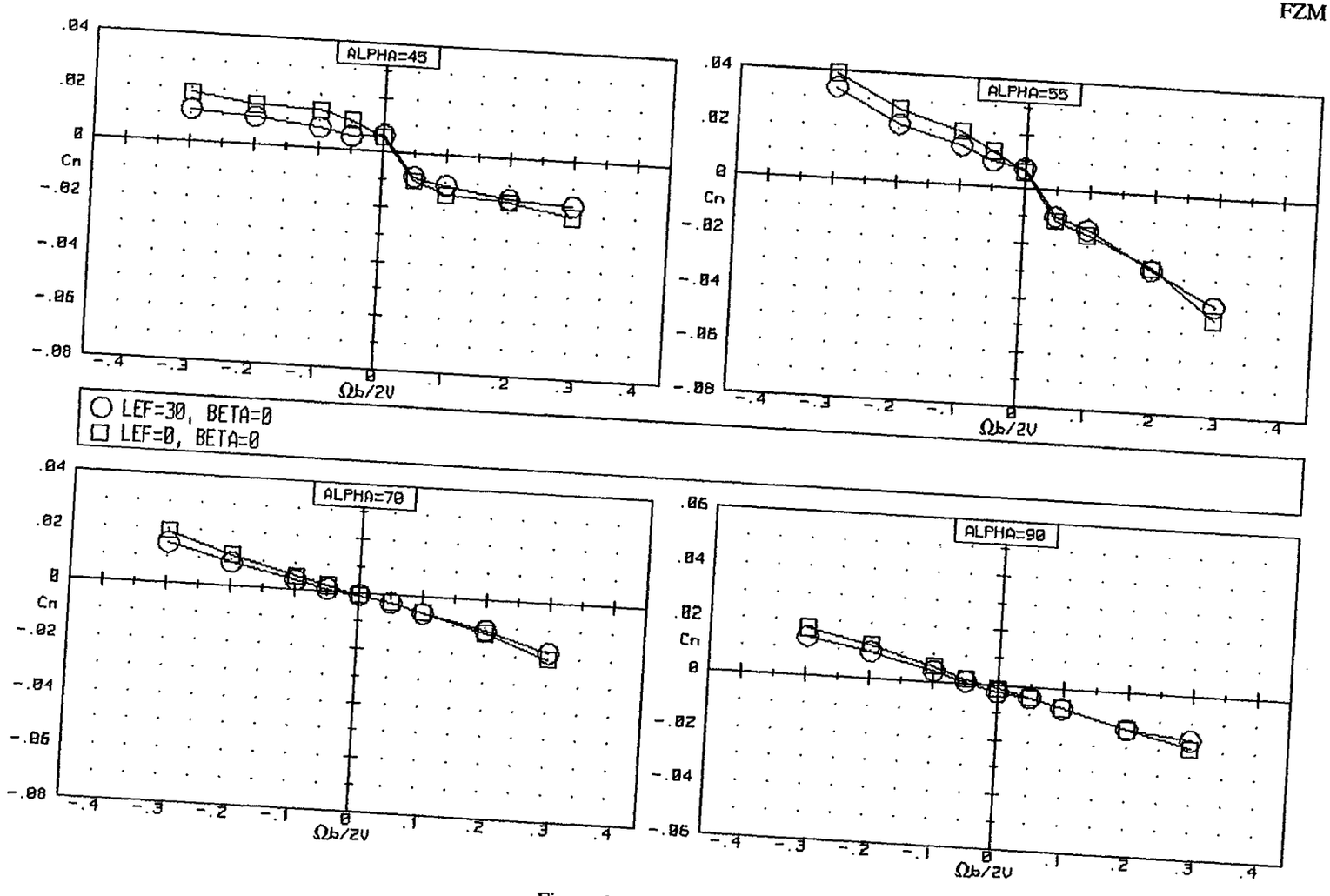

Figure 3-20. Concluded.

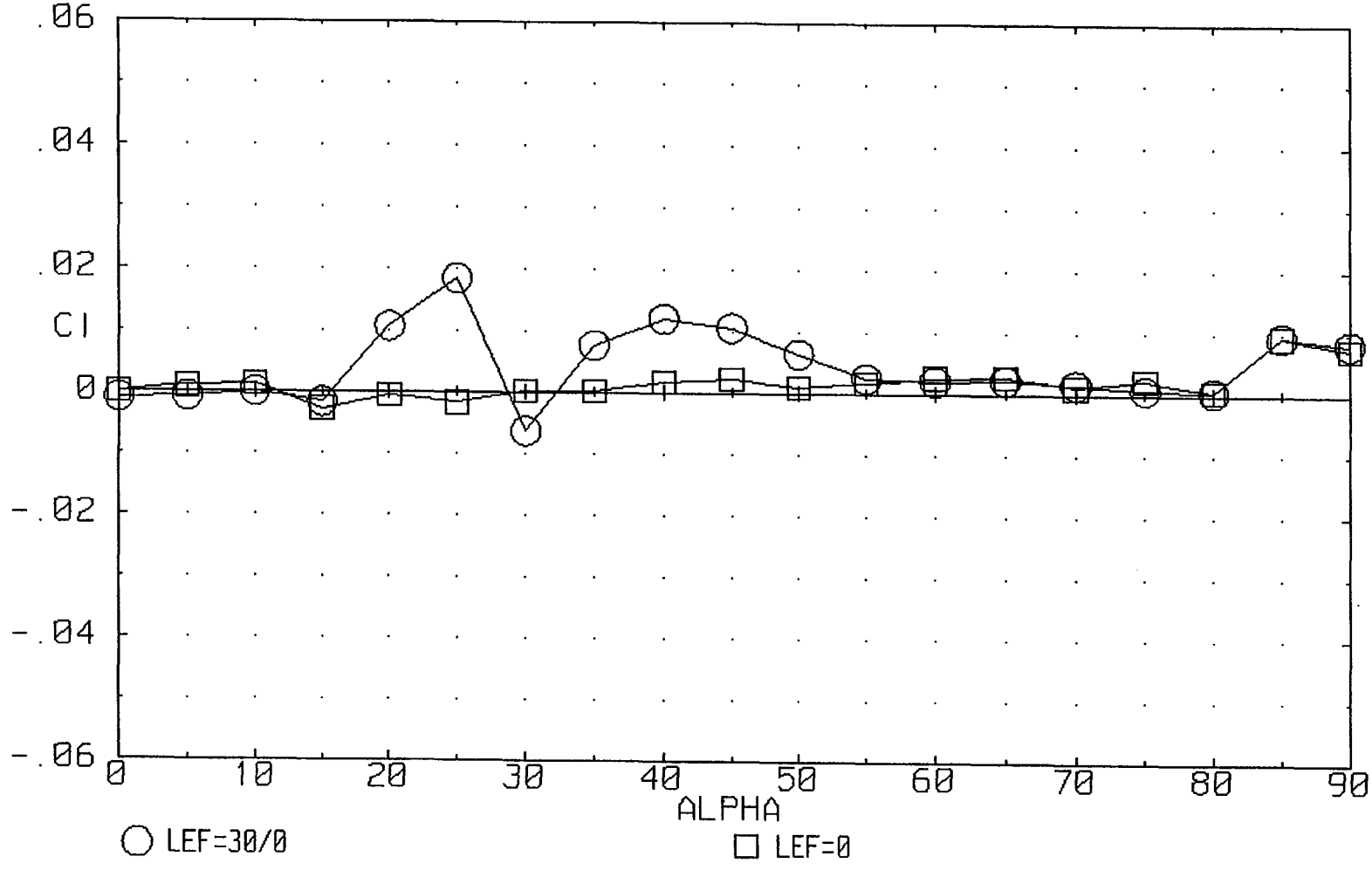

Figure 3-21. Effect of Differential Leading Edge Flap Deflection on Rolling Moment for the ICE 201 (β=0°).

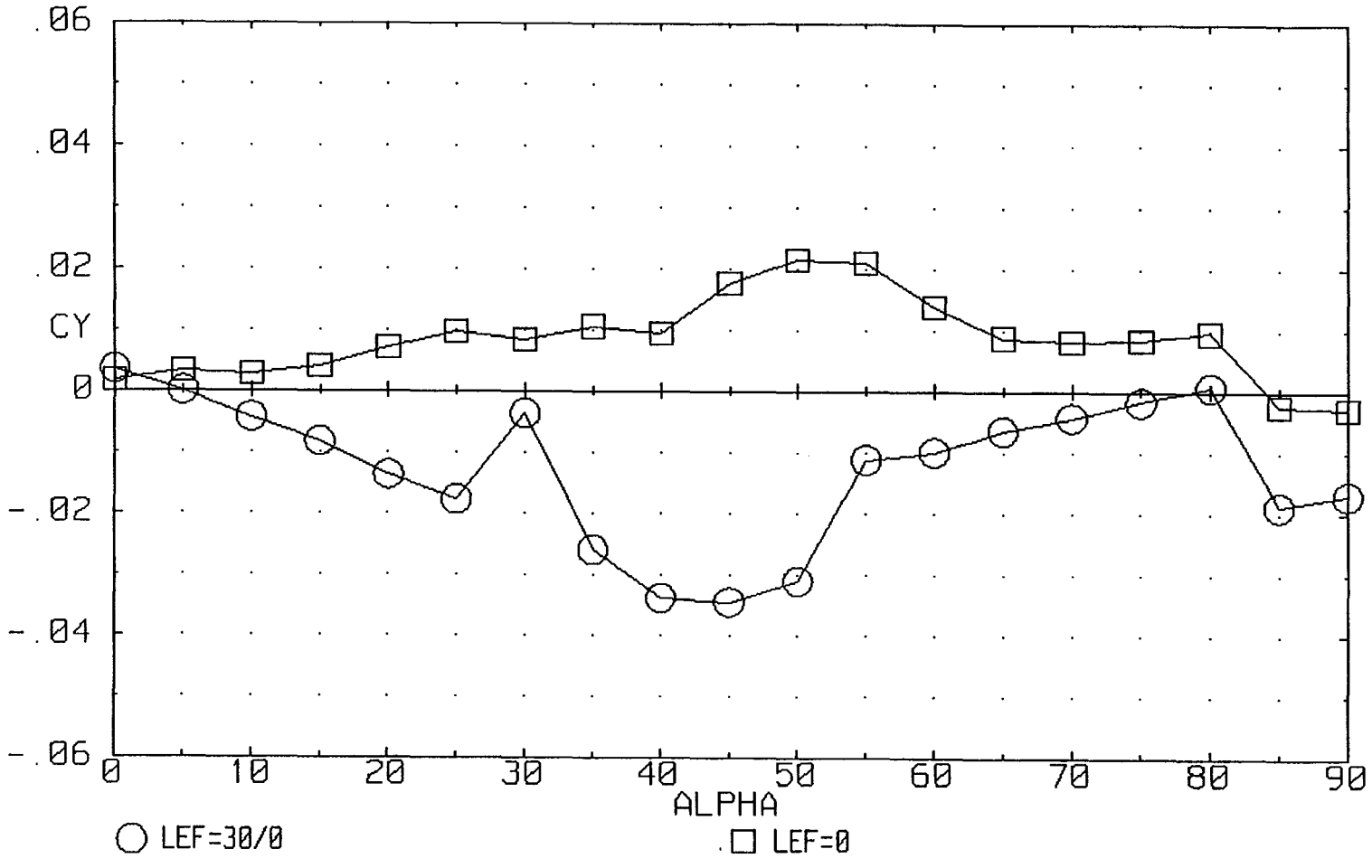

Figure 3-22. Effect of Differential Leading Edge Flaps on Side Force for the ICE 201 (β=0°).

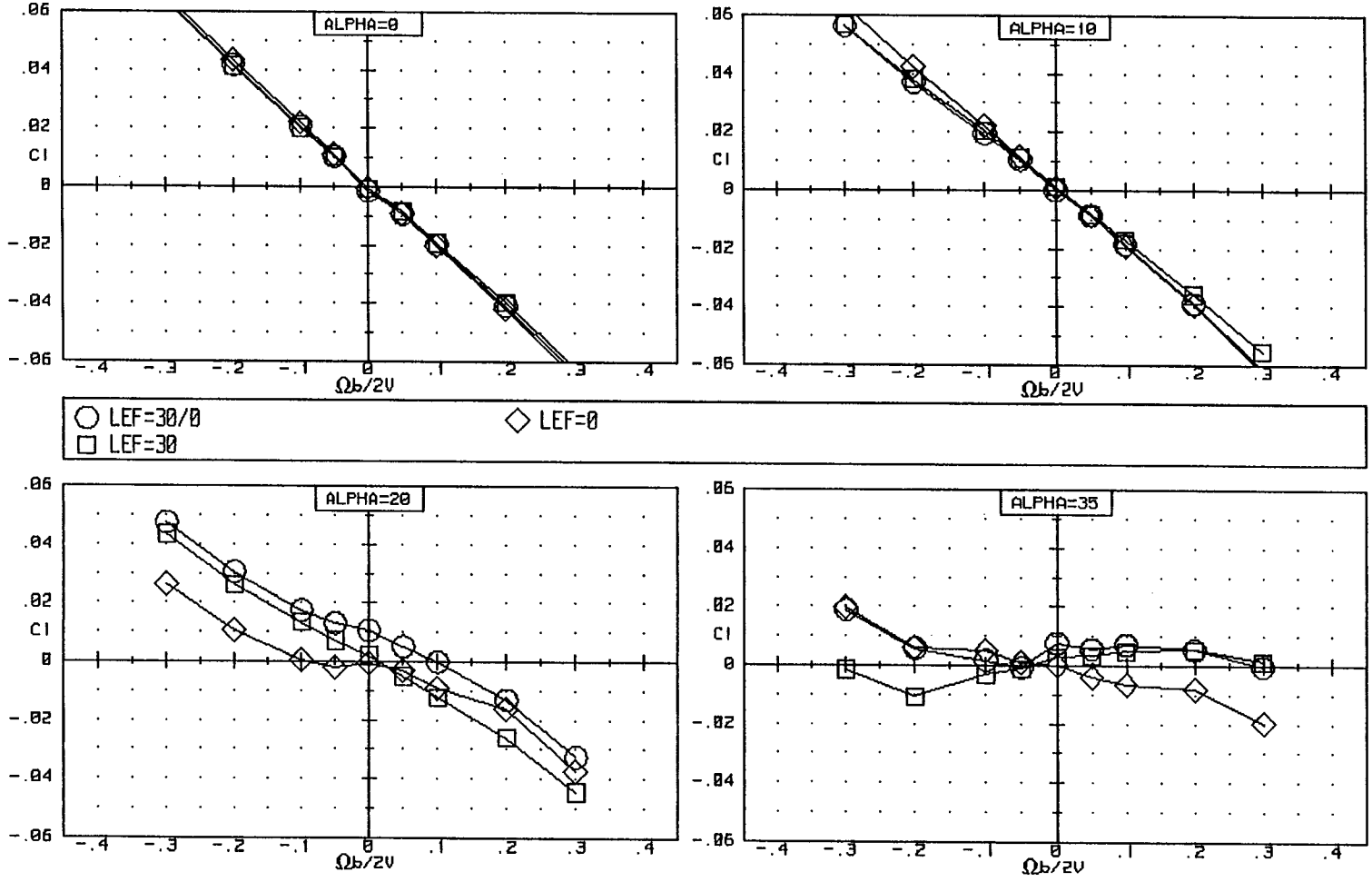

Figure 3-23. Effect of Rotation Rate and Differential LEF on Rolling Moment for the ICE 201 (β=0 °).

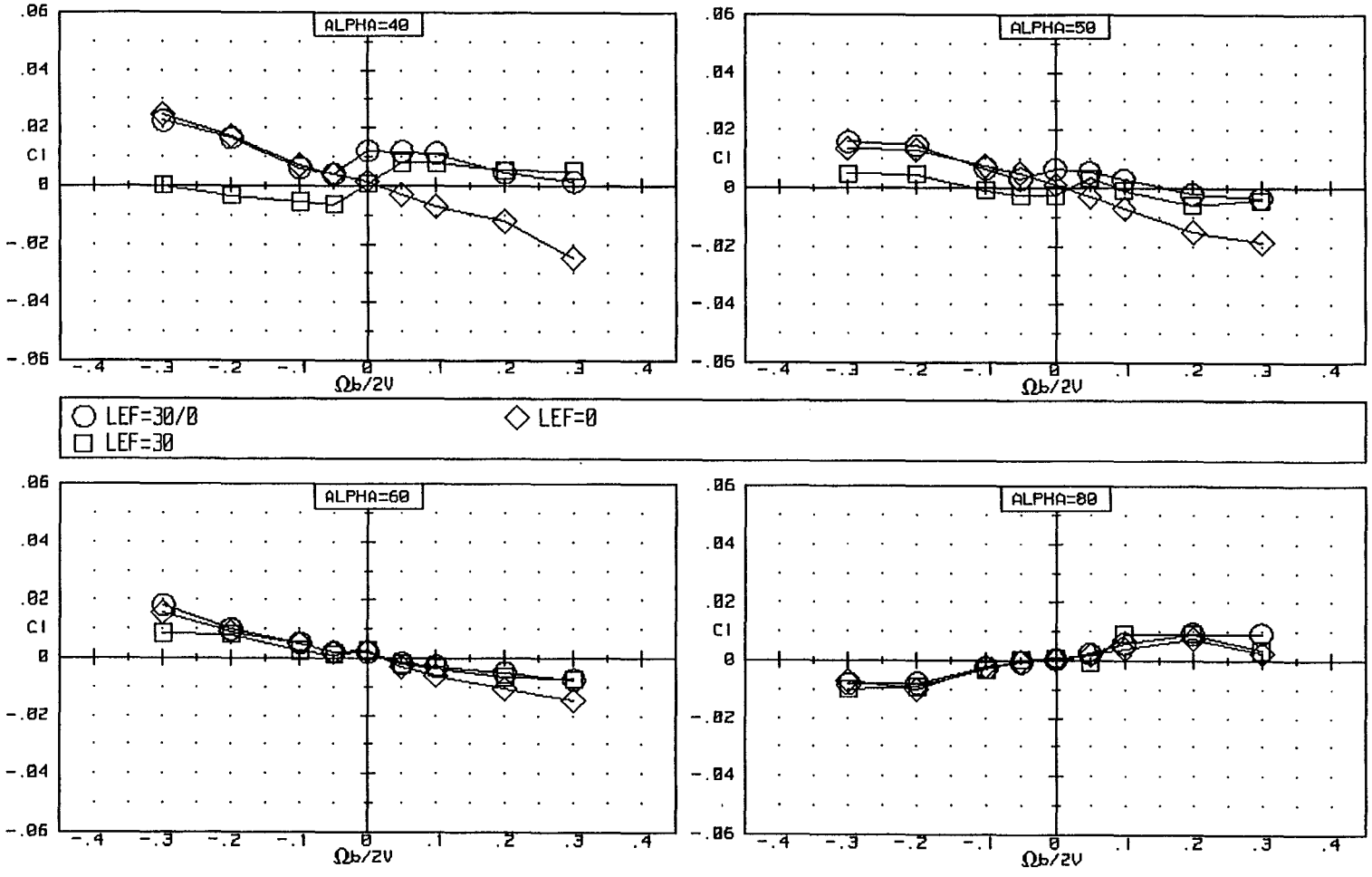

Figure 3-23. Concluded.

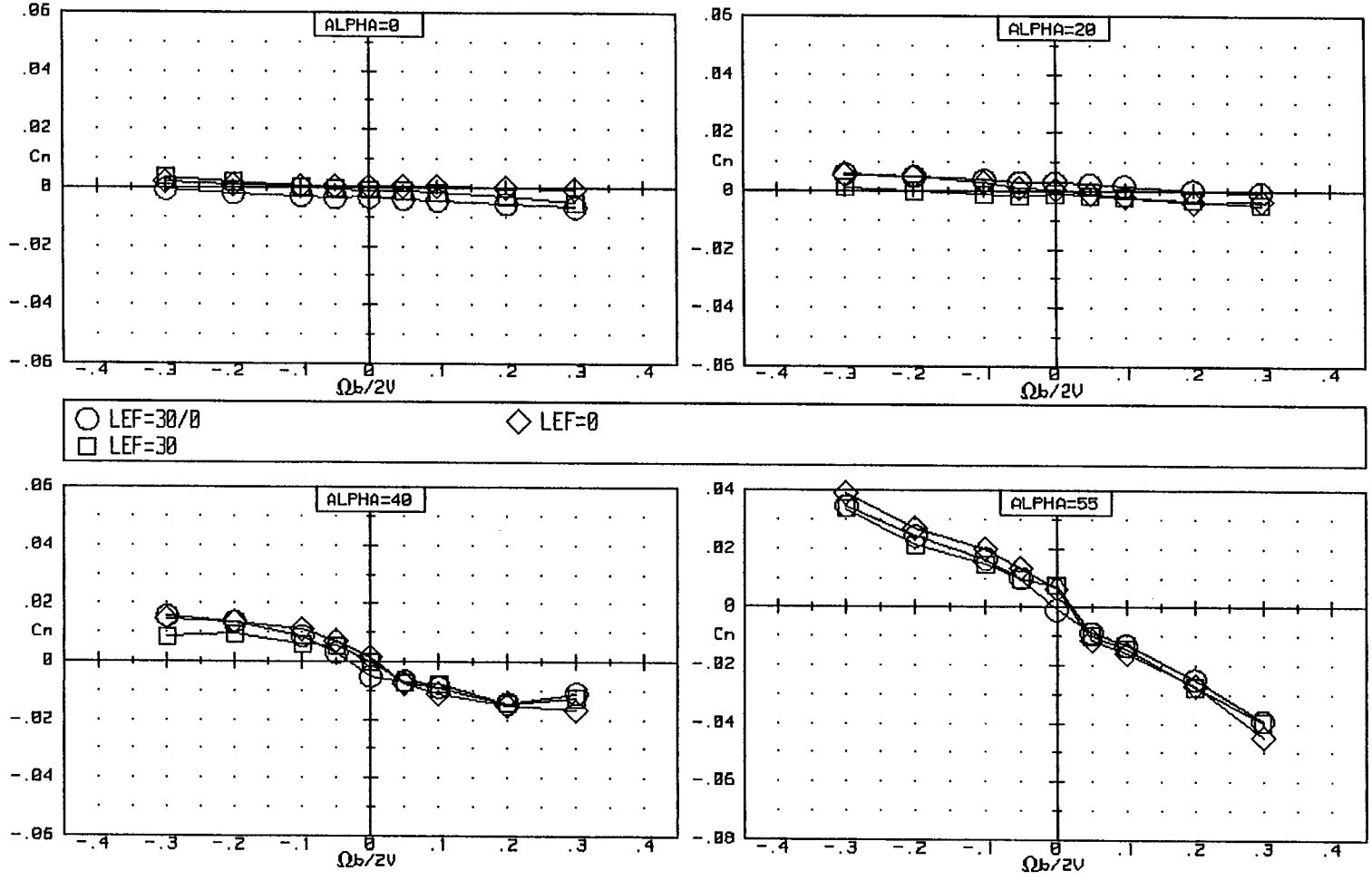

Figure 3-24. Effect of Rotation Rate and Differential LEF on Yawing Moment for the ICE 201 (β=0°).

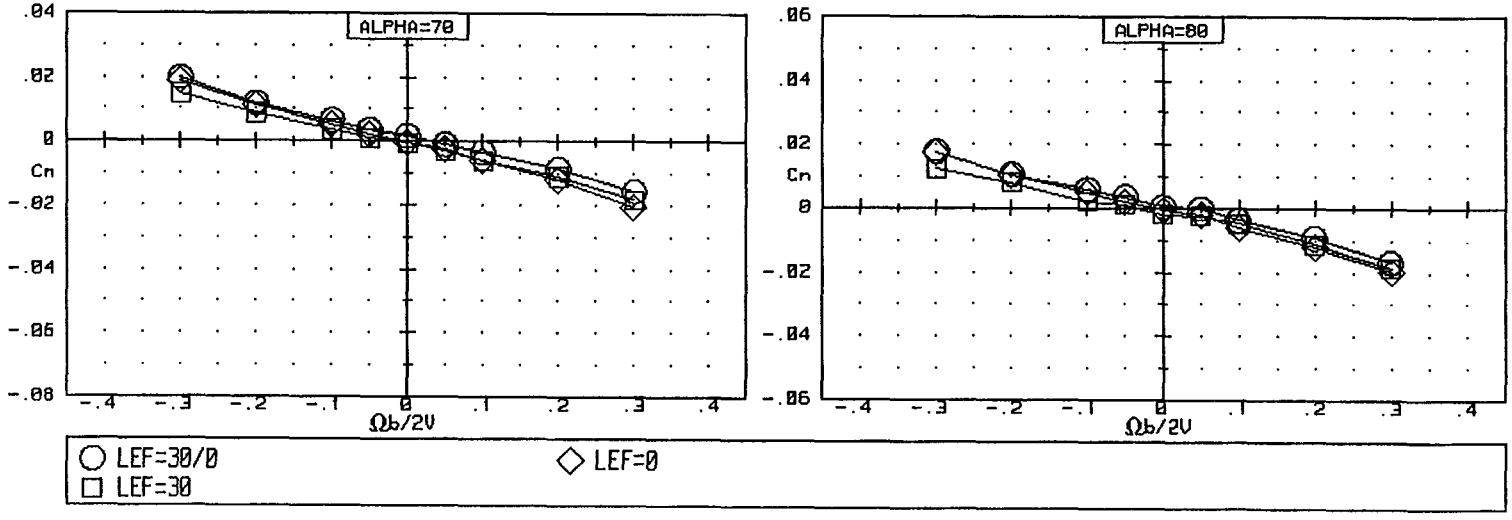

Figure 3-24. Concluded.

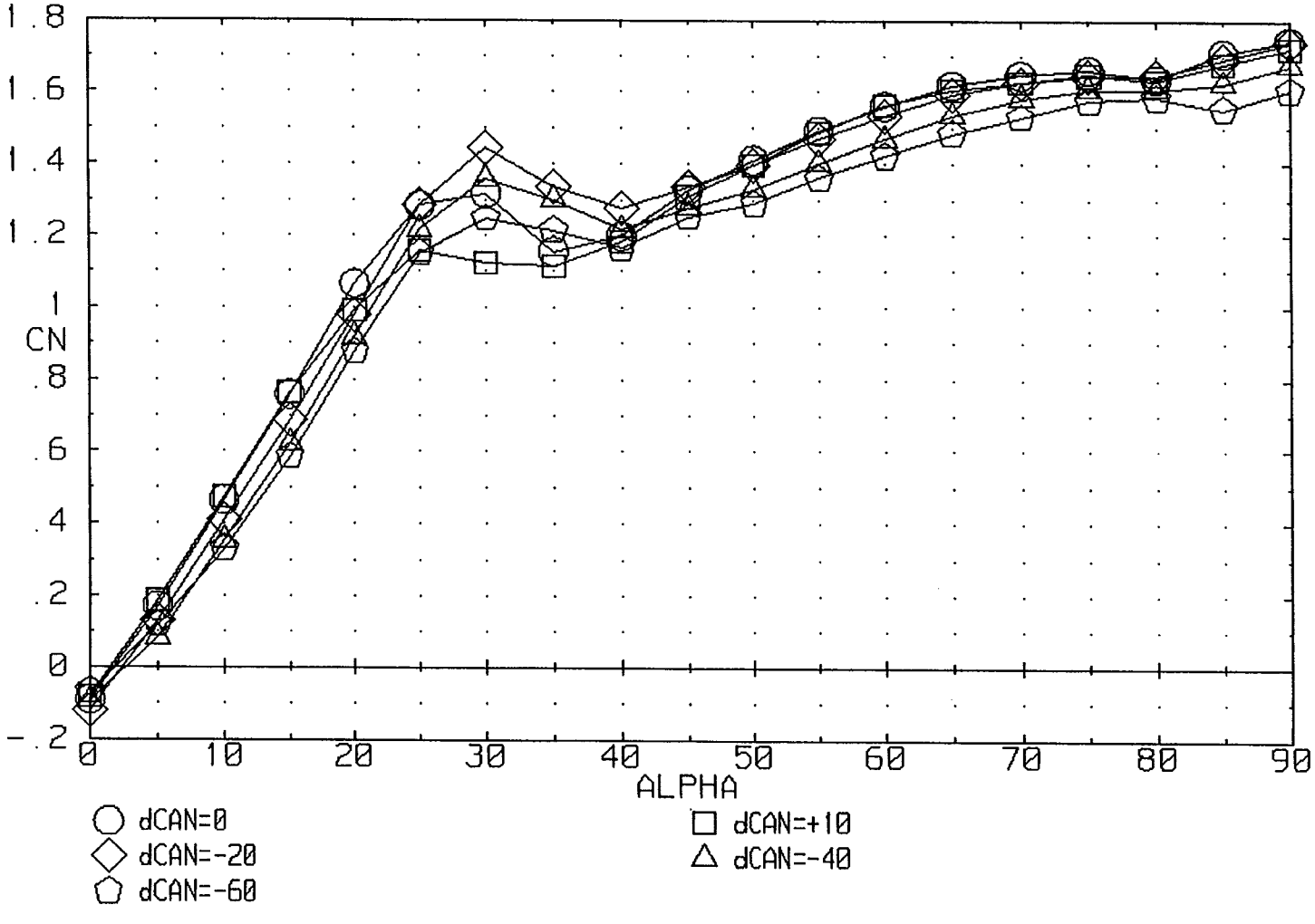

Figure 3-25. Effect of Canard Deflection on Normal Force for the ICE 201 (LEF=30, β=0°).

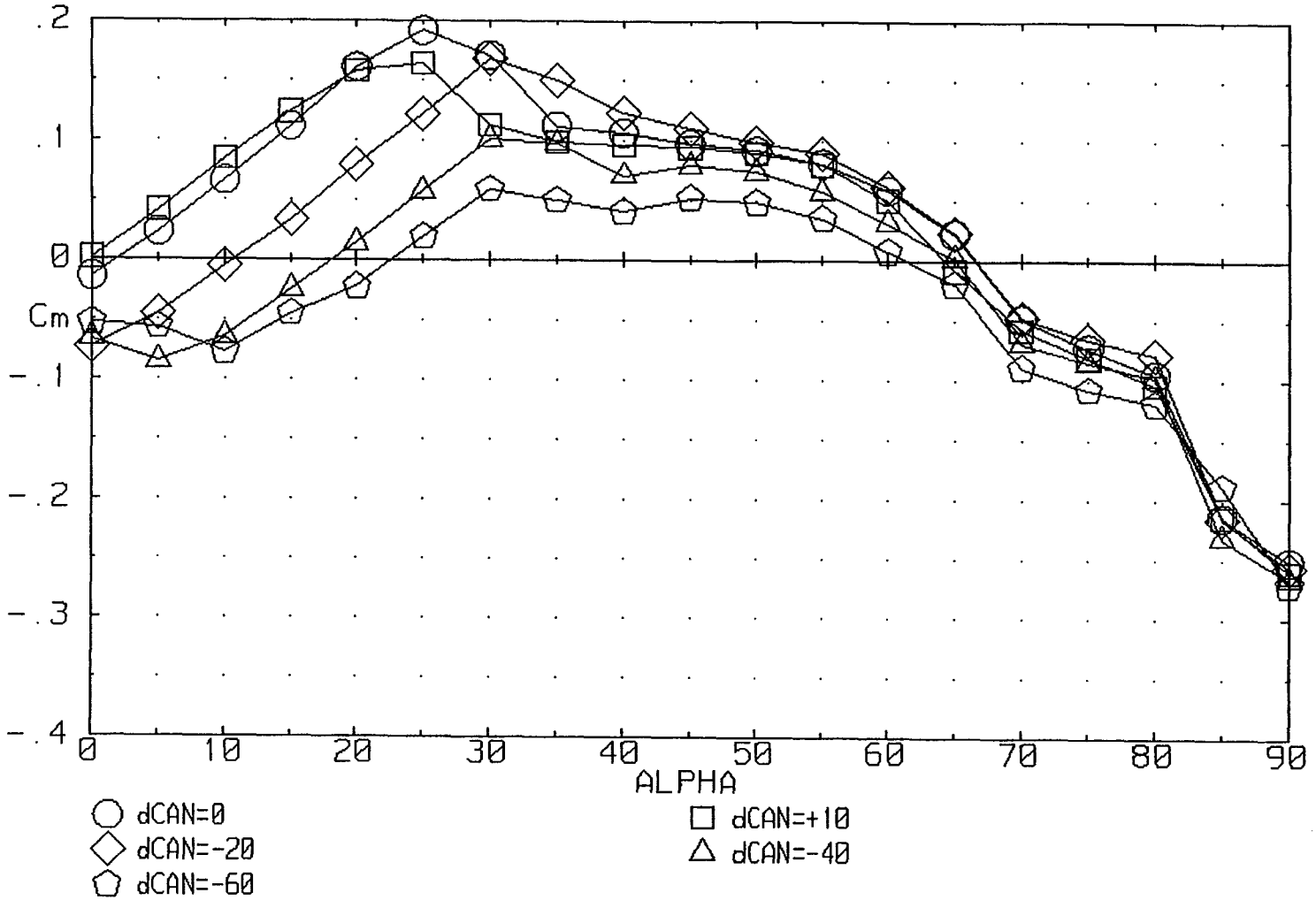

Figure 3-26. Effect of Canard Deflection on Static Pitching Moment for the ICE 201 (LEF=30, β=0°).

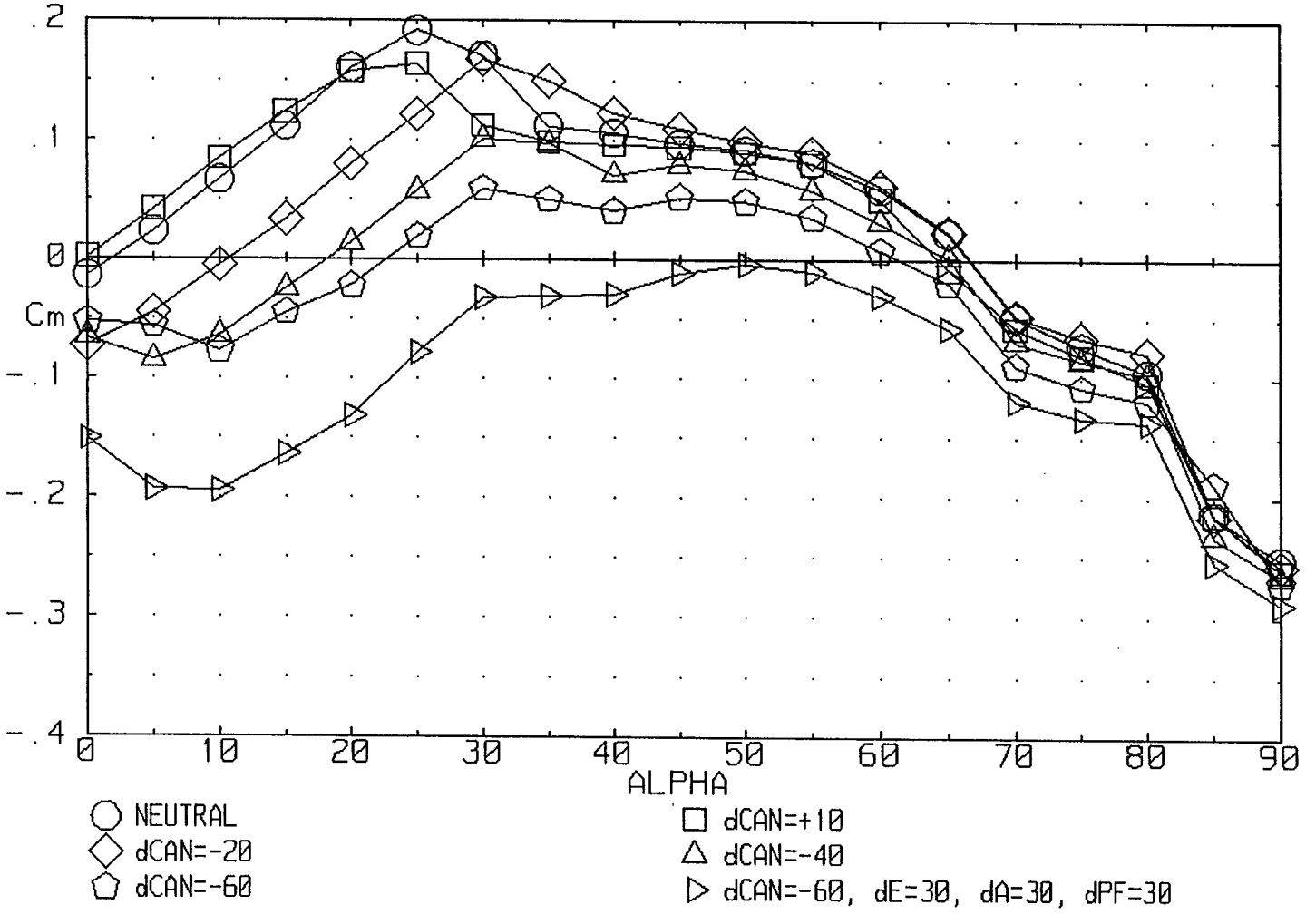

Figure 3-27. ICE 201 Nose-Down Control Power (LEF=30, β=0°).

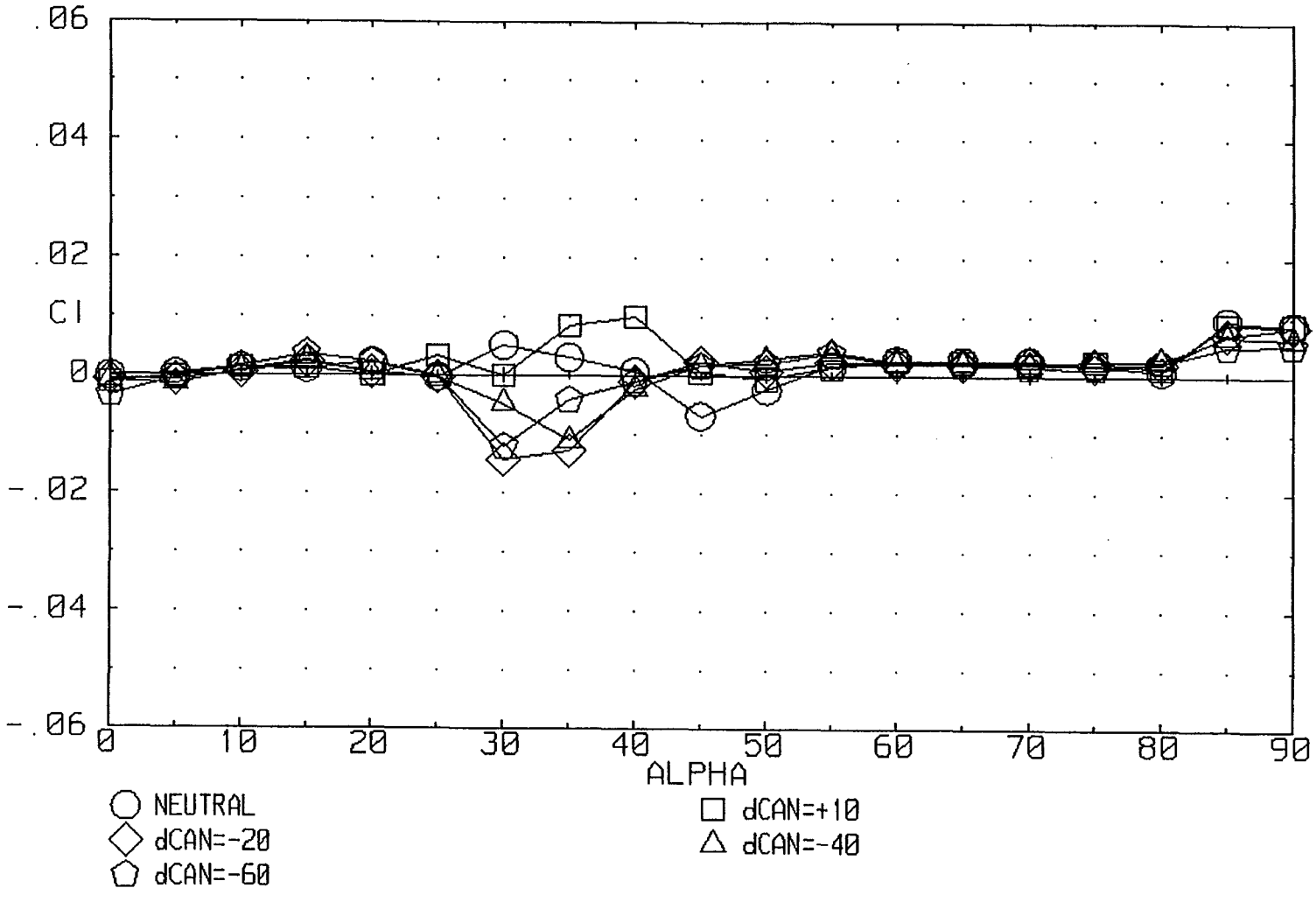

Figure 3-28. Effect of Canard Deflection on Static Rolling Moment at Zero Sideslip (LEF=30).

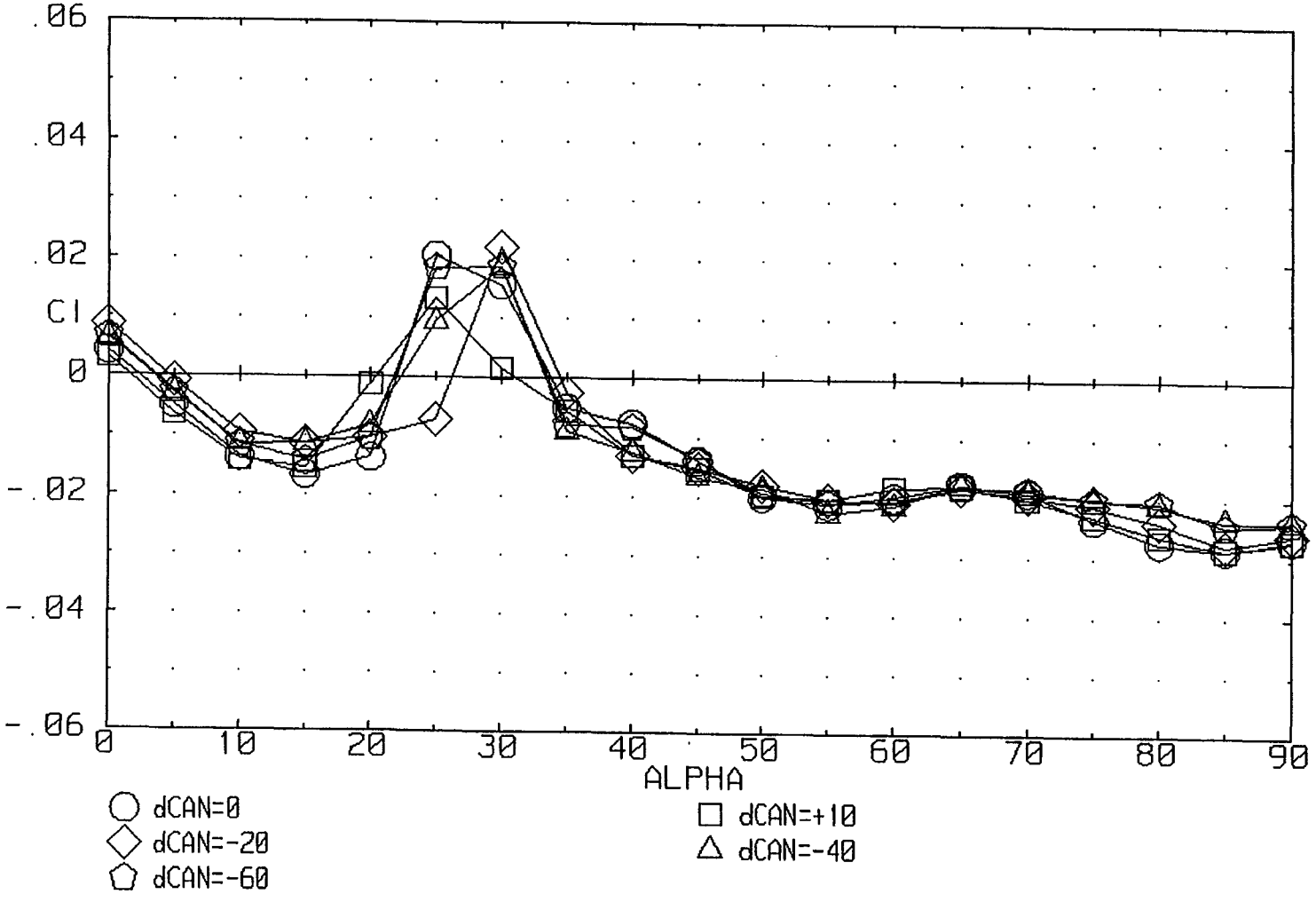

Figure 3-29. Effect of Canard Deflection on ICE 201 Static Lateral Stability (LEF=30, β=+10°).

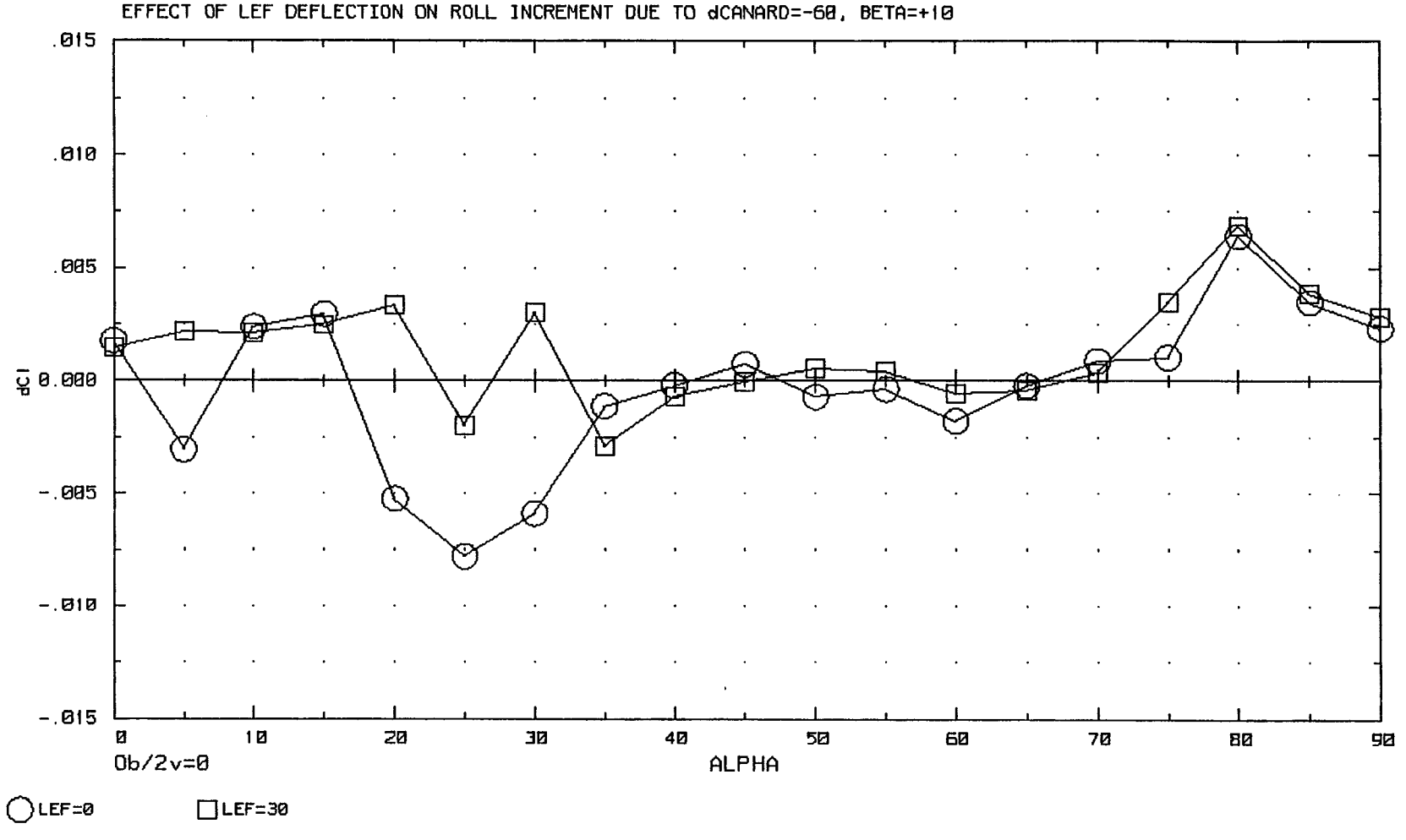

Figure 3-30. Effect of LEF Deflection on Roll Increments due to dCanard=-60 (β=+10 °).

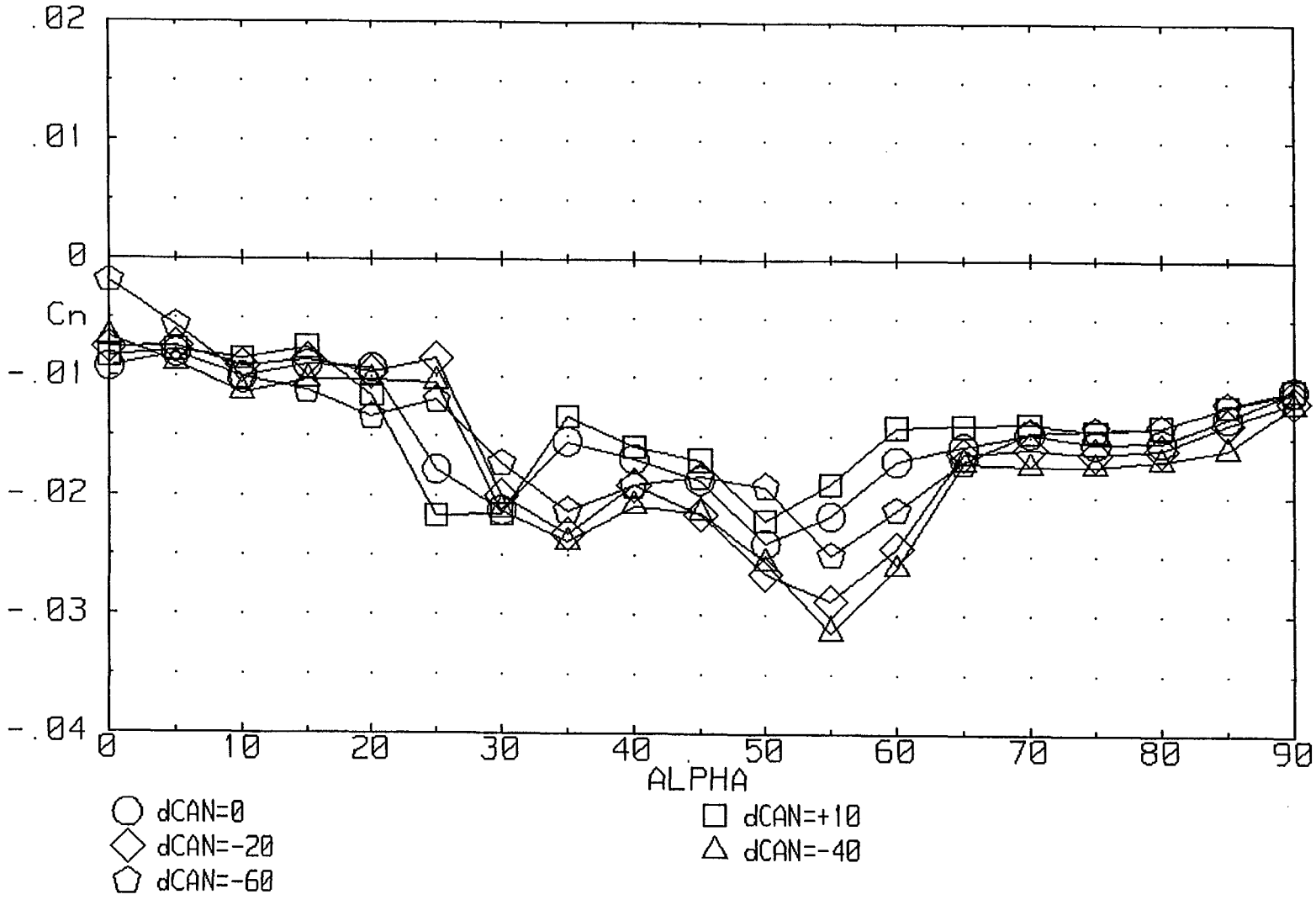

Figure 3-31. Effect of Canard Deflection on ICE 201 Static Directional Stability (LEF=30, β=+10°).

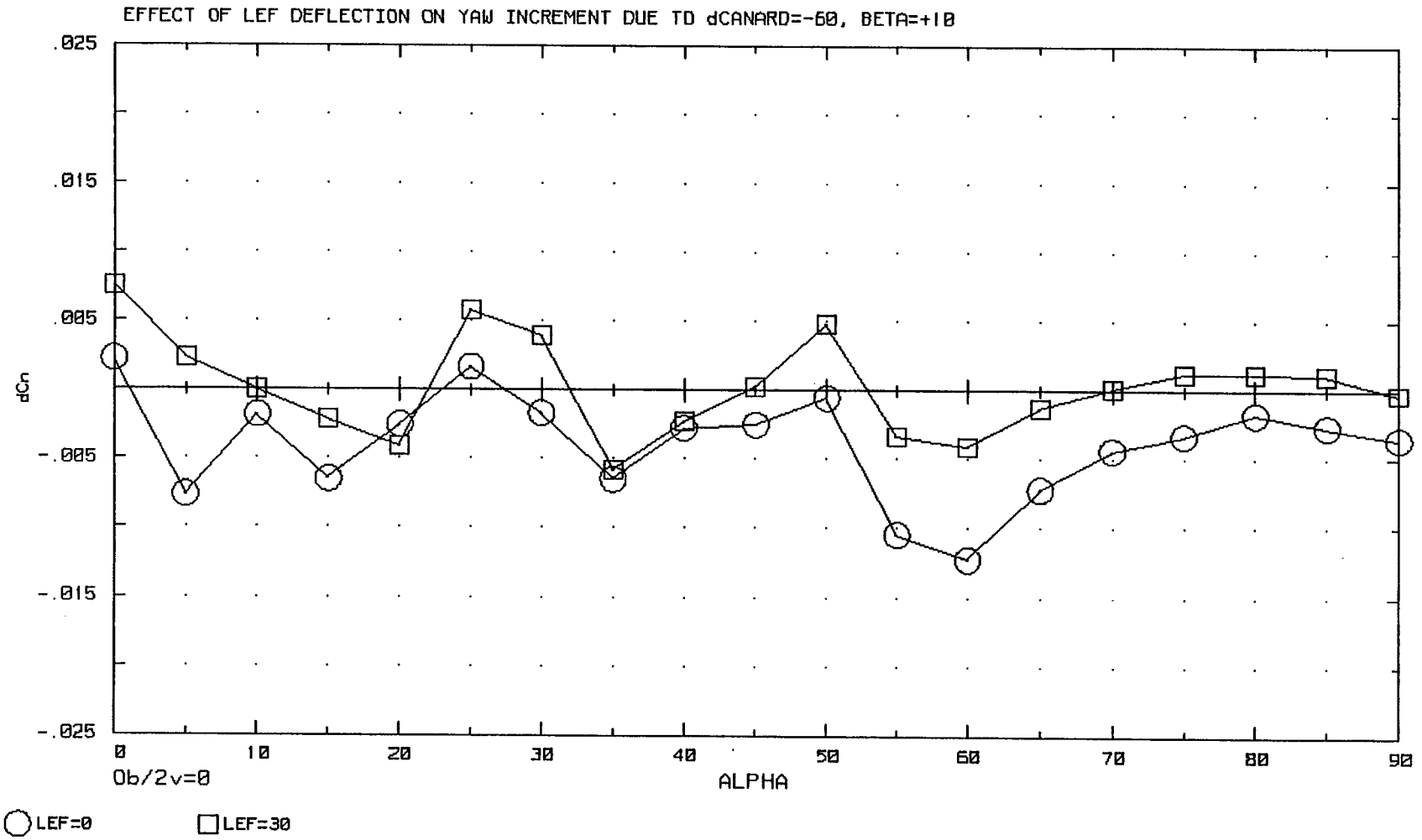

Figure 3-32. Effect of LEF Deflection on Yaw Increments due to dCanard=-60 (β=+10°).

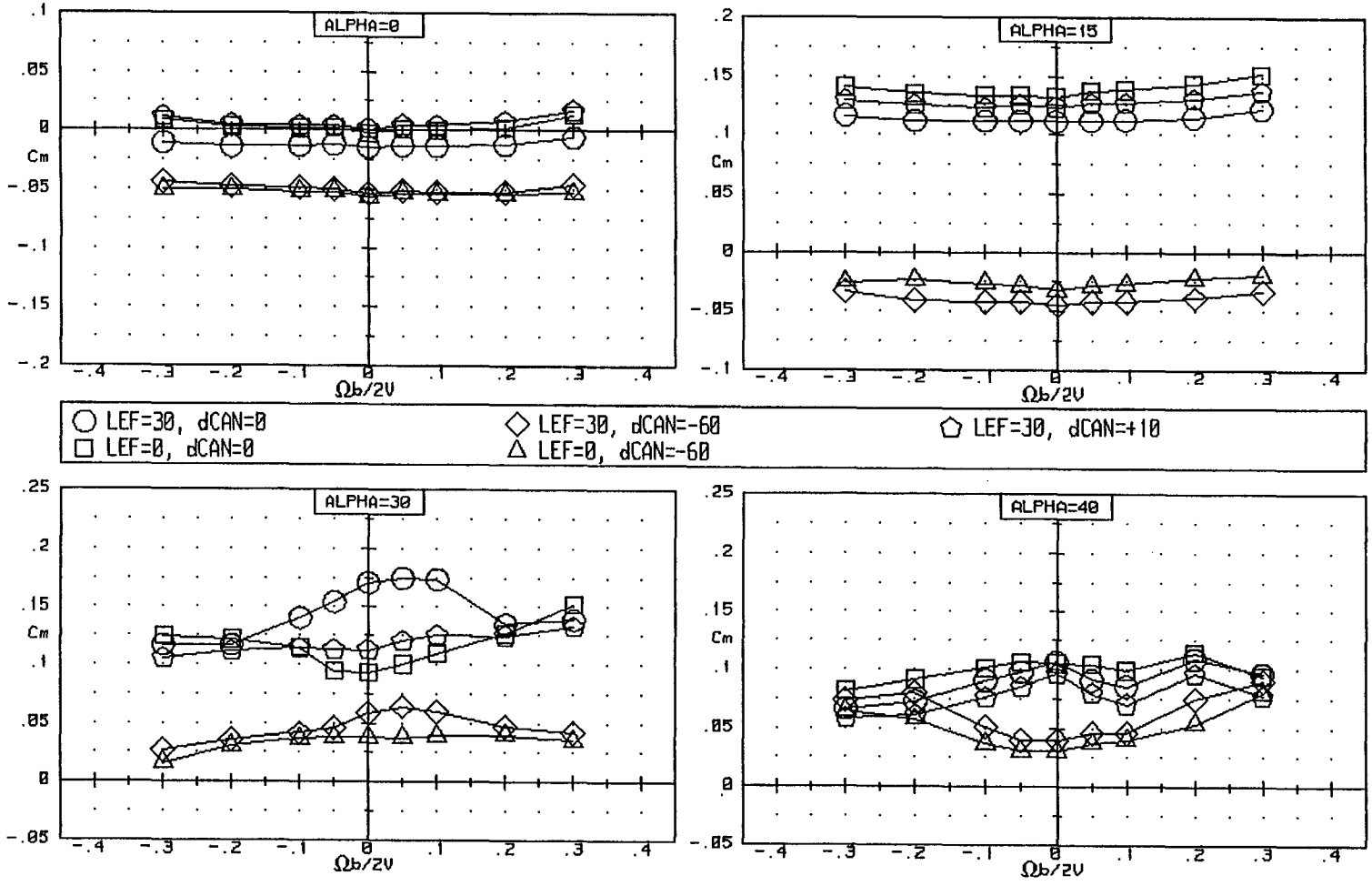

Figure 3-33. Effect of LEF and Canard Deflections on Rotational Pitching Moment for the ICE 201 (β=0°).

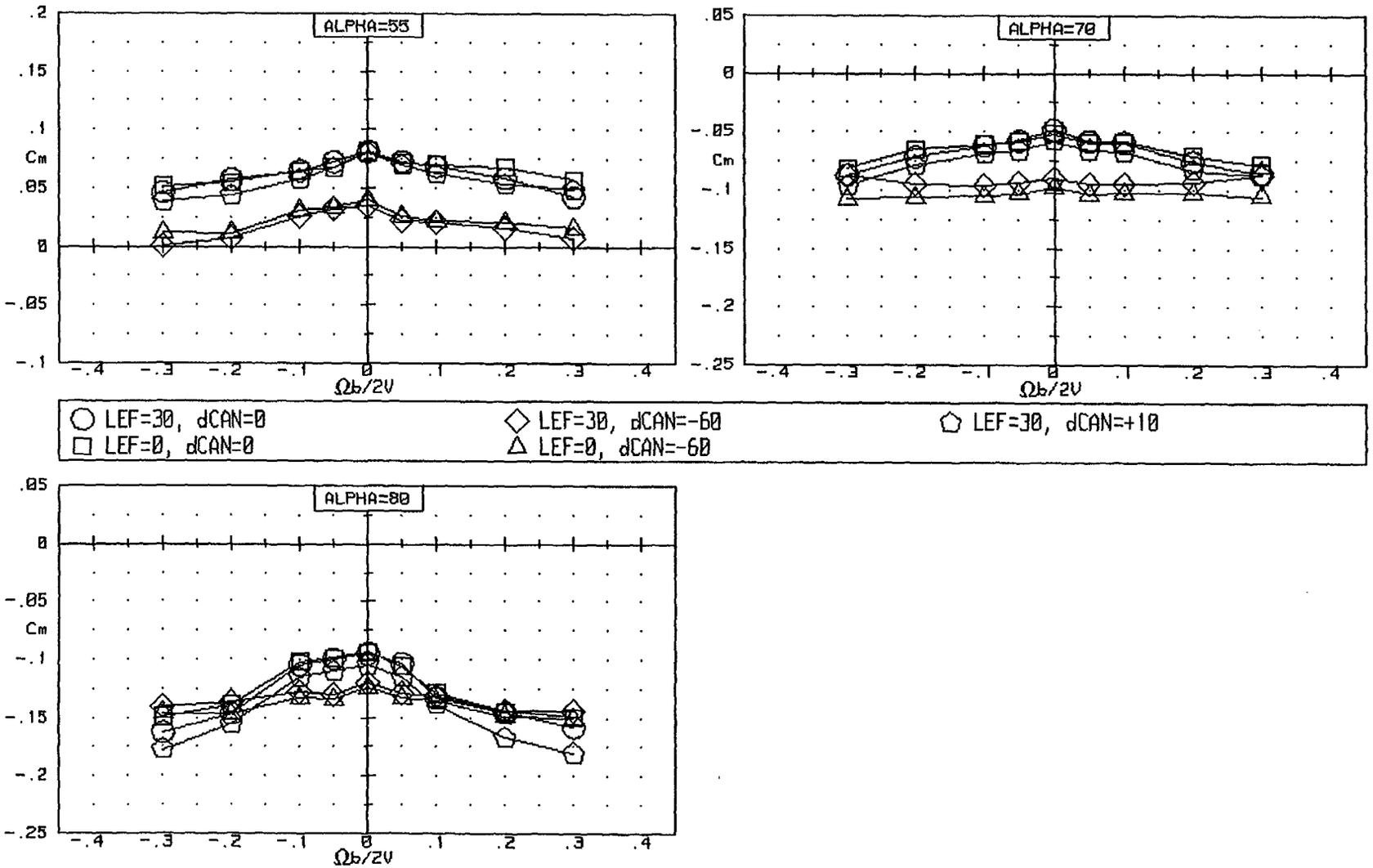

Figure 3-33 Concluded.

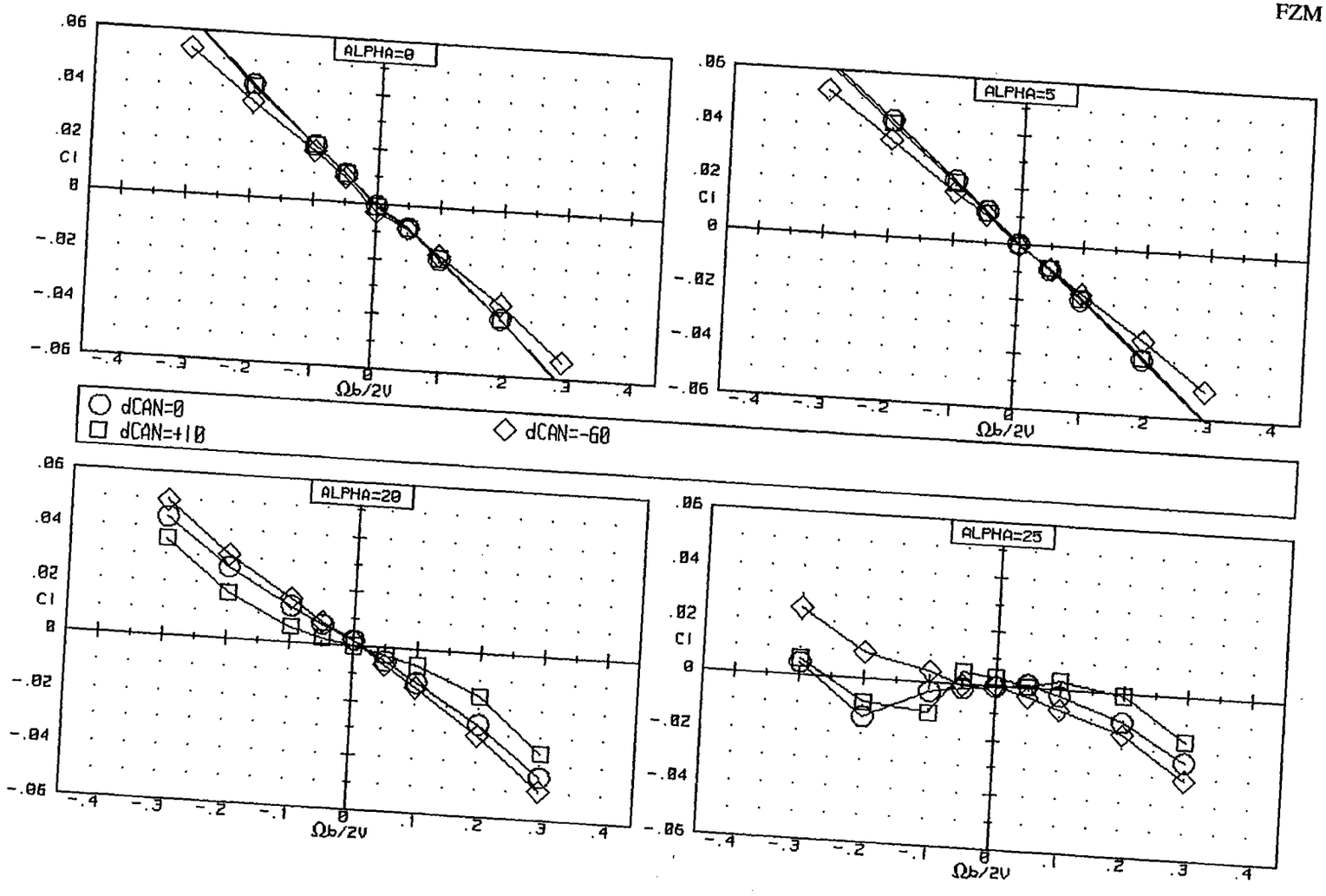

Figure 3-34. Effect of Canard Deflection on Roll Damping for the ICE 201 (β=0°).

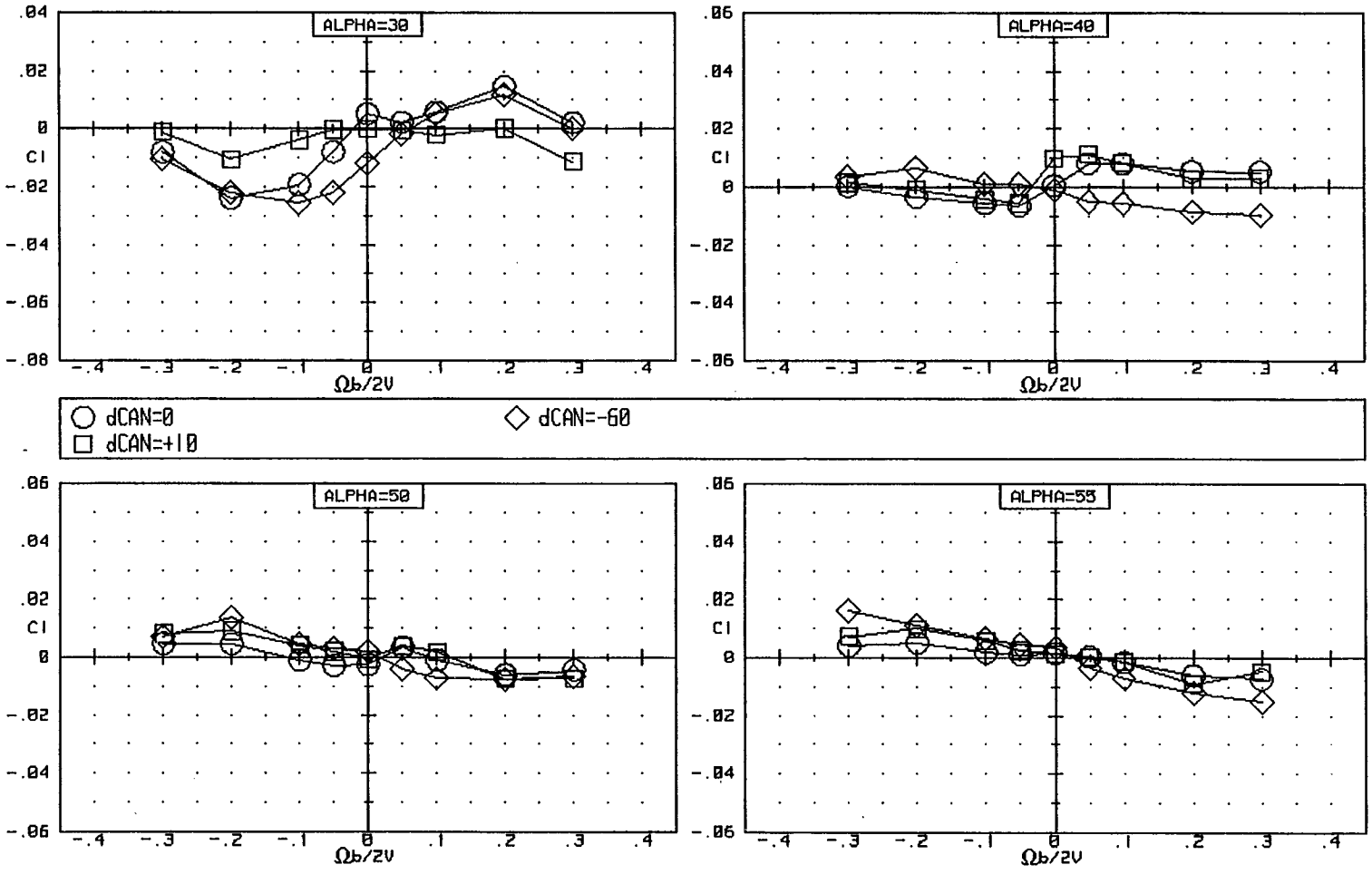

Figure 3-34 Continued.

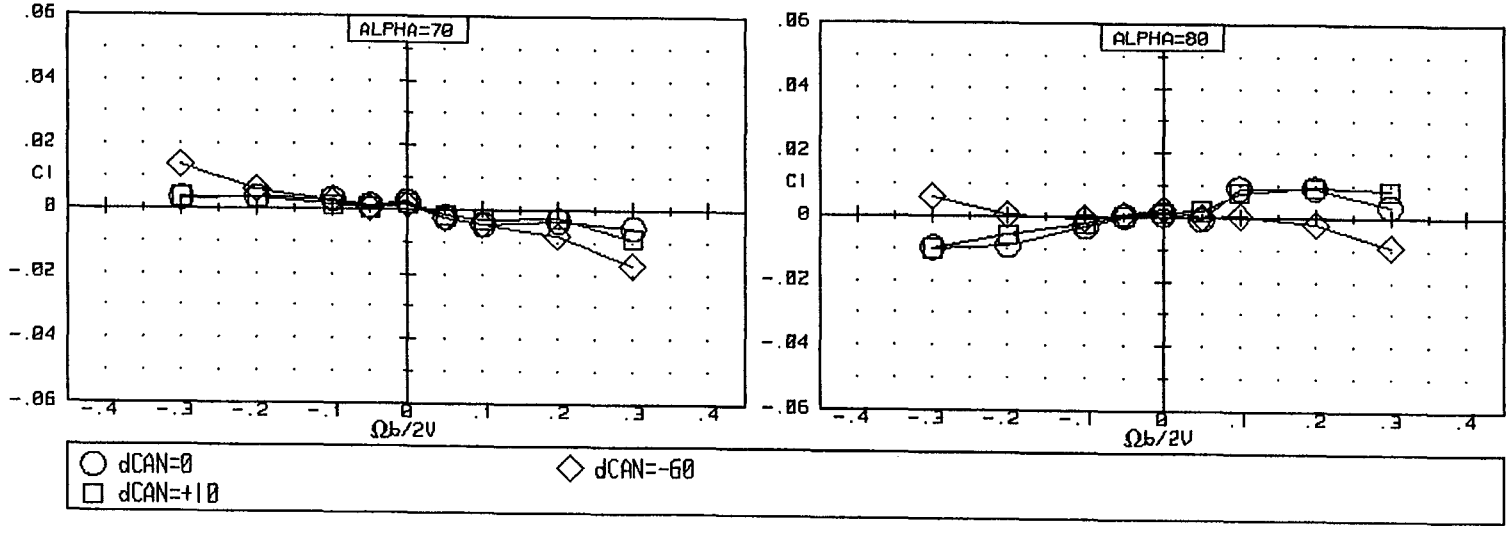

Figure 3-34 Concluded.

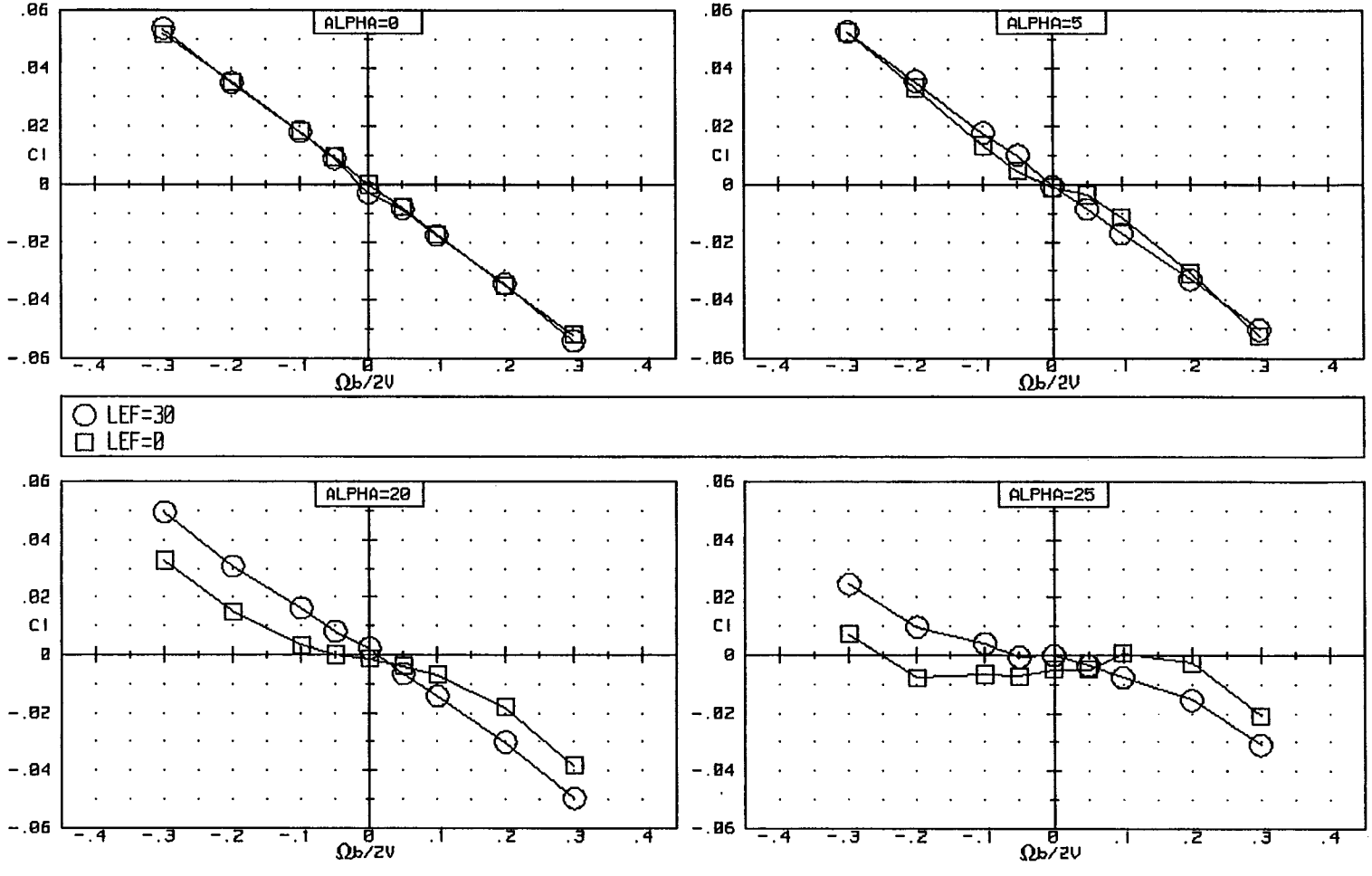

Figure 3-35. Effect of LEF Deflection on Roll Damping due to dCanard=-60 for the ICE 201 (β=0 °).

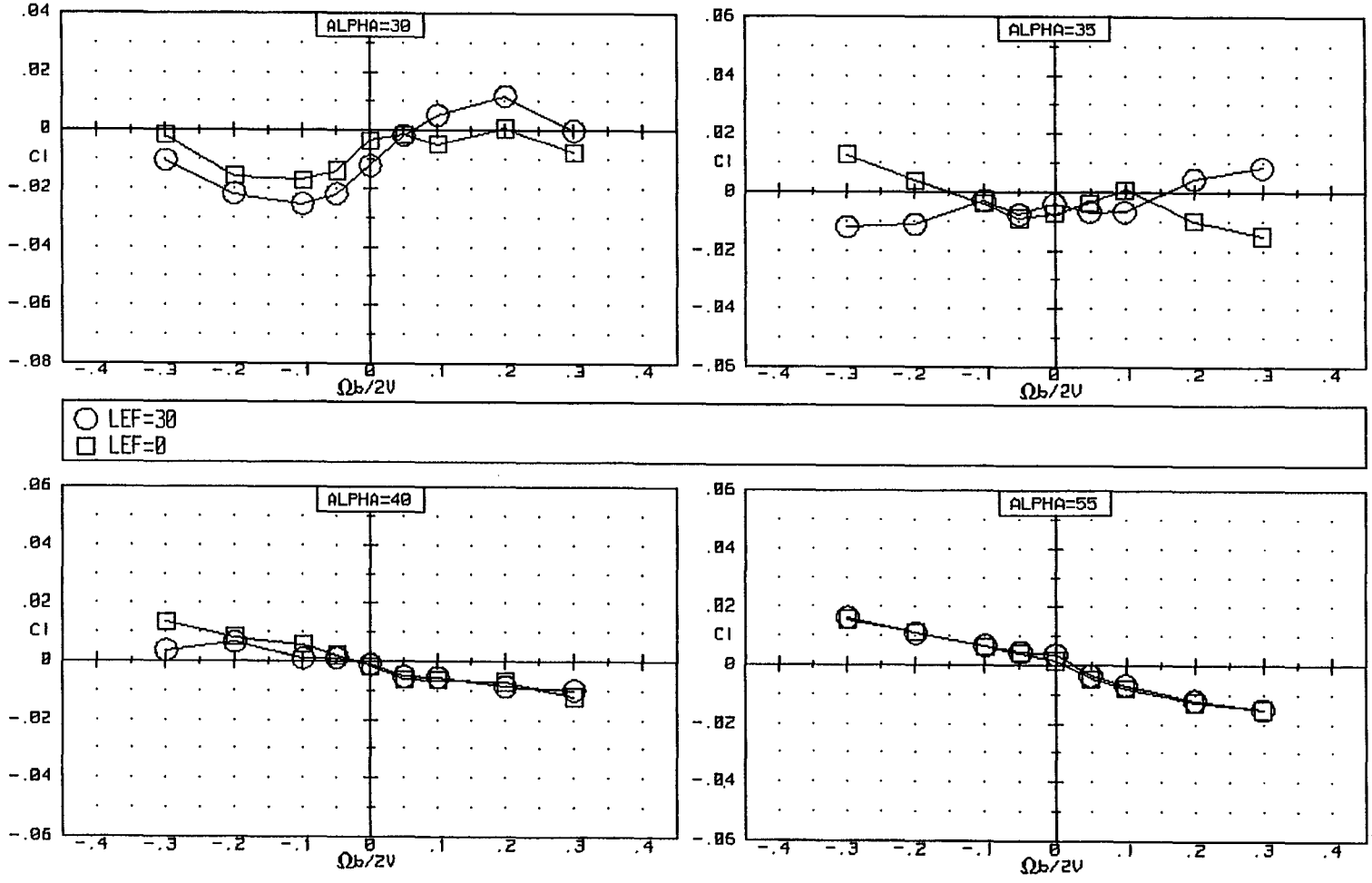

Figure 3-35 Continued.

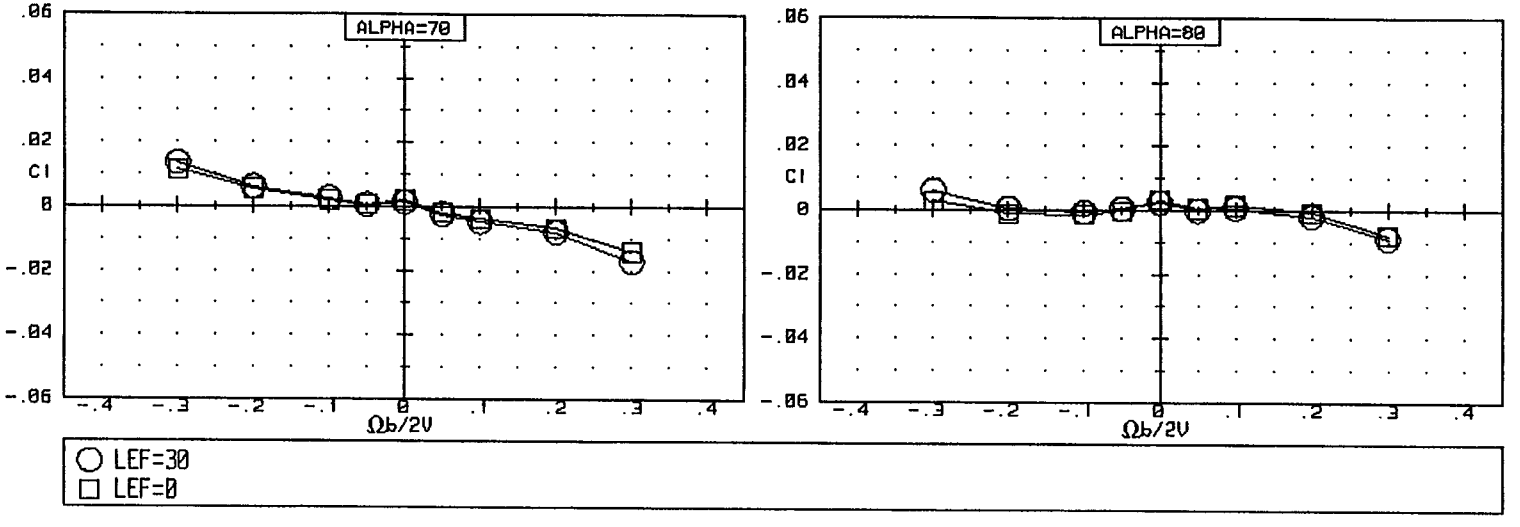

Figure 3-35 Concluded.

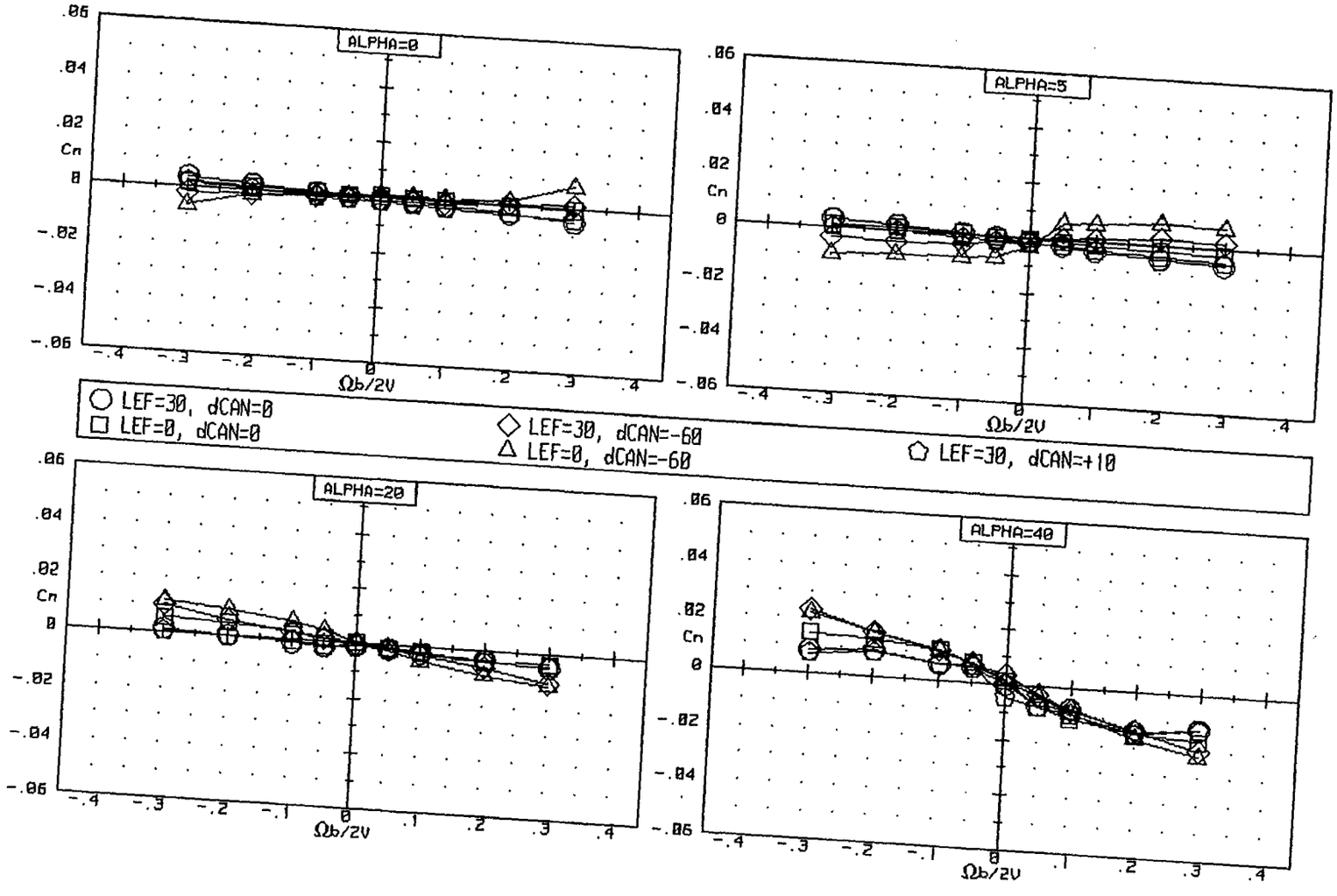

Figure 3-36. Effect of LEF Deflection on the Yaw Damping due to dCanard=-60 for the ICE 201 (β=0 °).

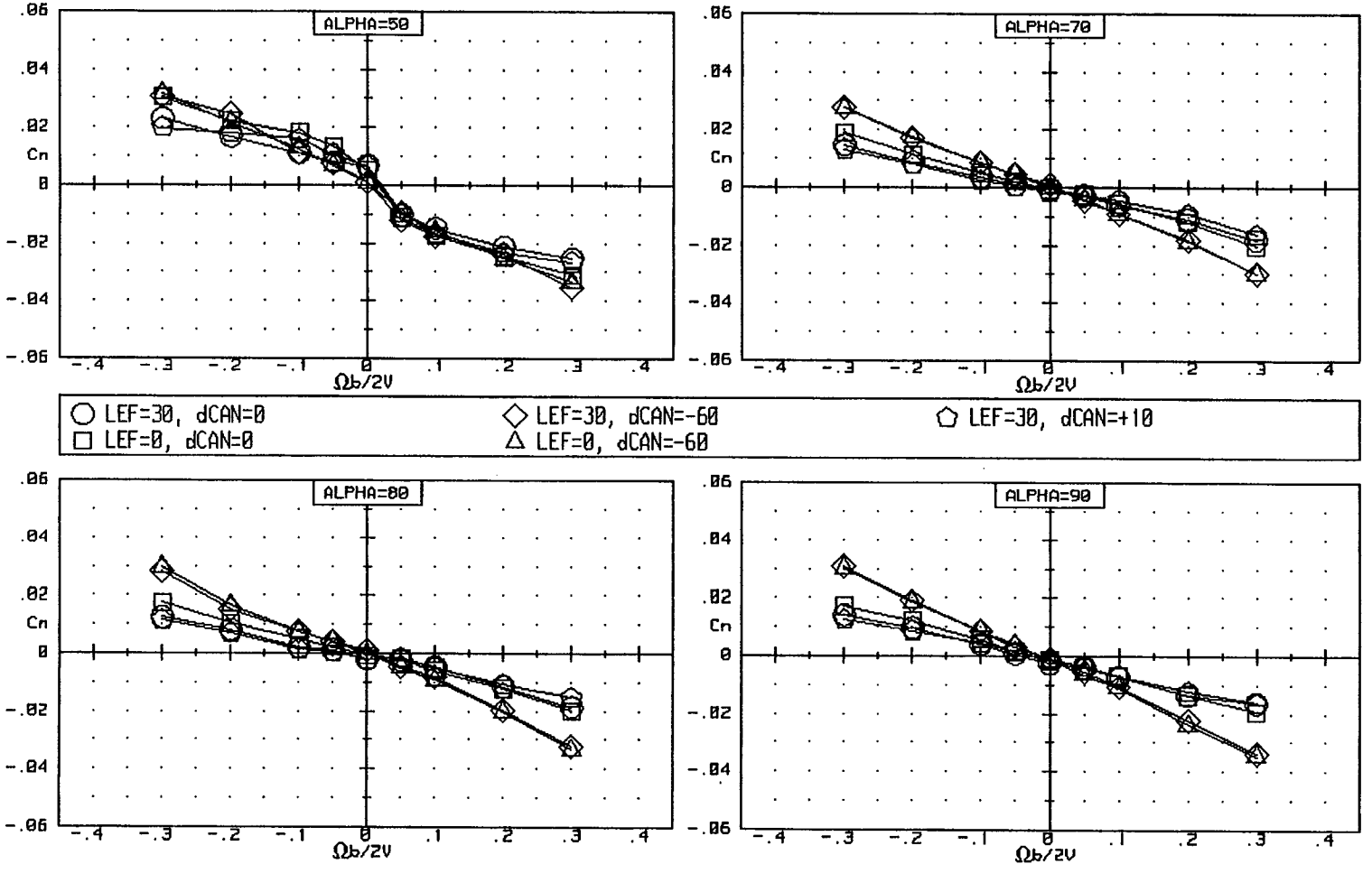

Figure 3-36 Concluded.

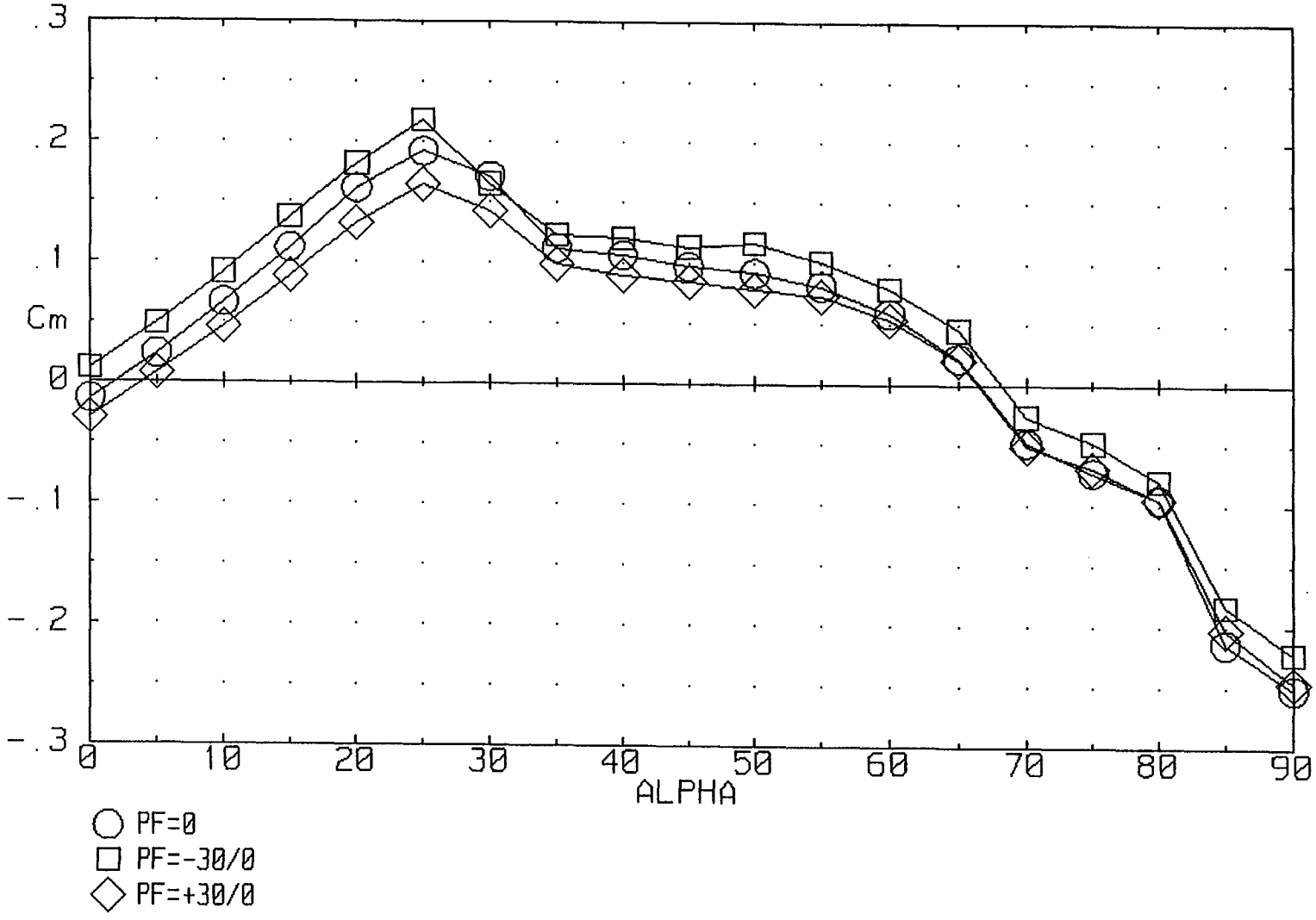

Figure 3-37. Pitching Moment due to Left-Side Pitch Flap Deflection on the ICE 201 (LEF=30, β=0°).

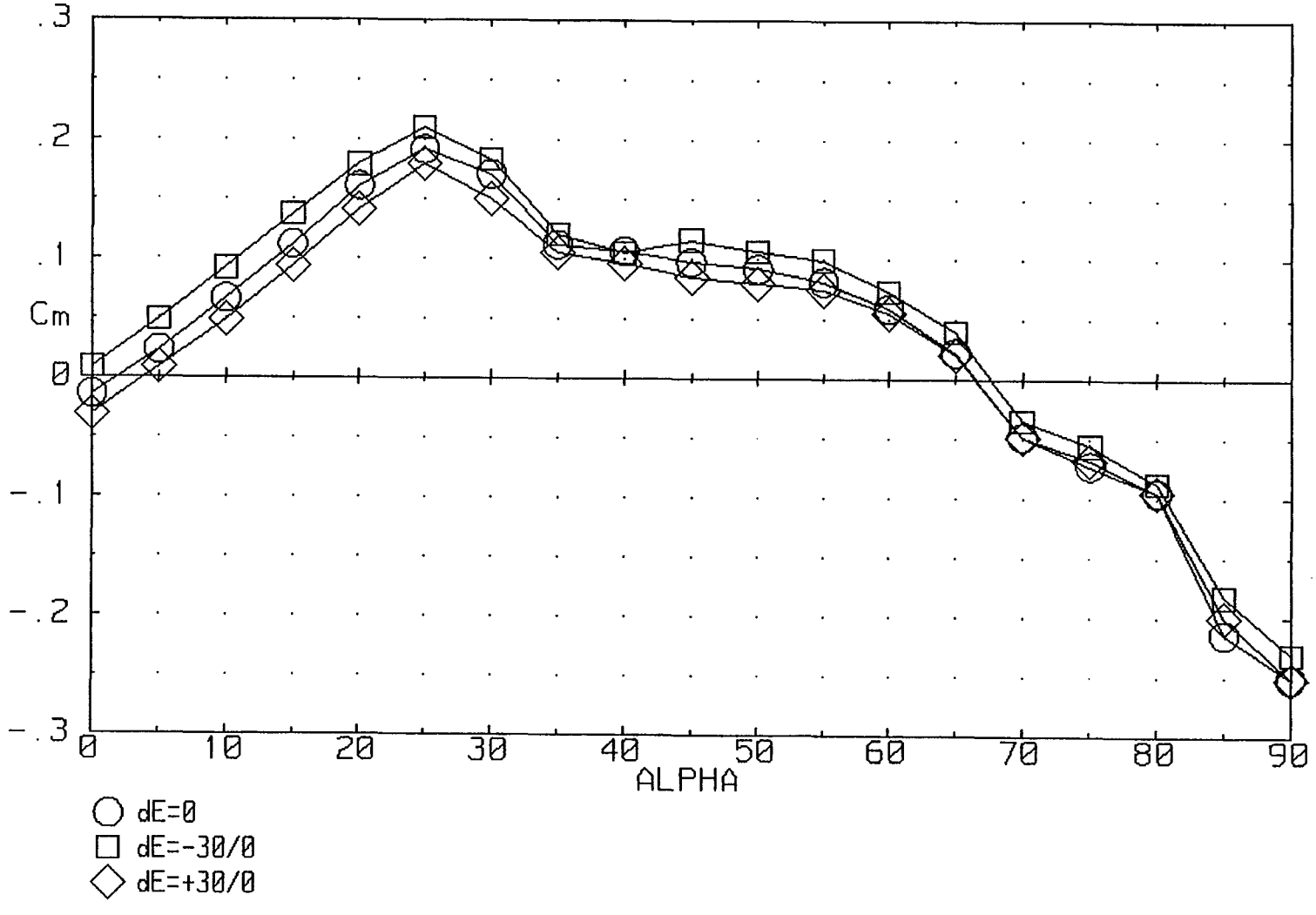

Figure 3-38. Pitching Moment due to Left-Side Elevon Deflections on the ICE 201 (LEF=30, β=0°).

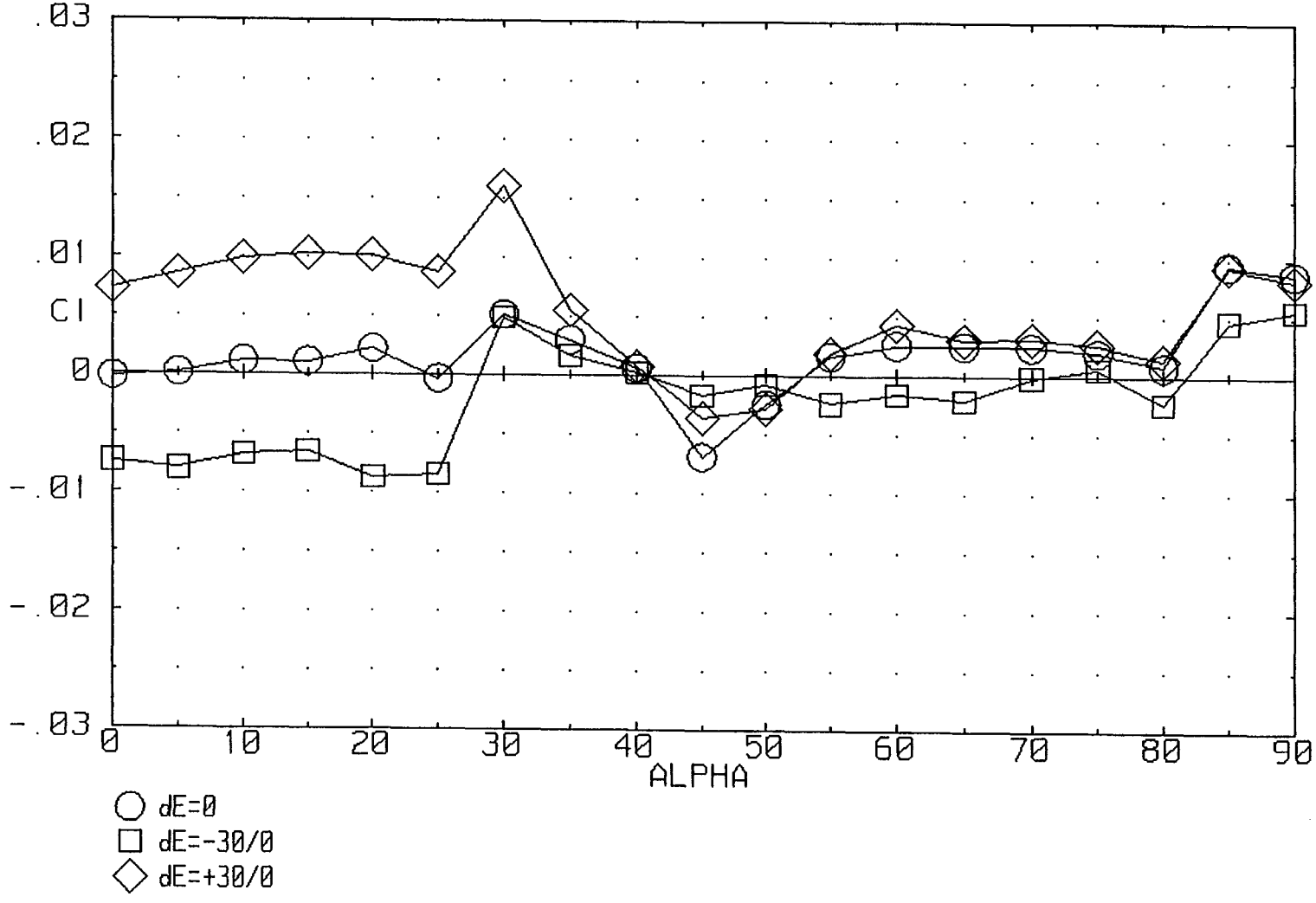

Figure 3-39. Effect of Left-Side Elevon Deflections on Rolling Moment for the ICE 201 (LEF=30, β=0°).

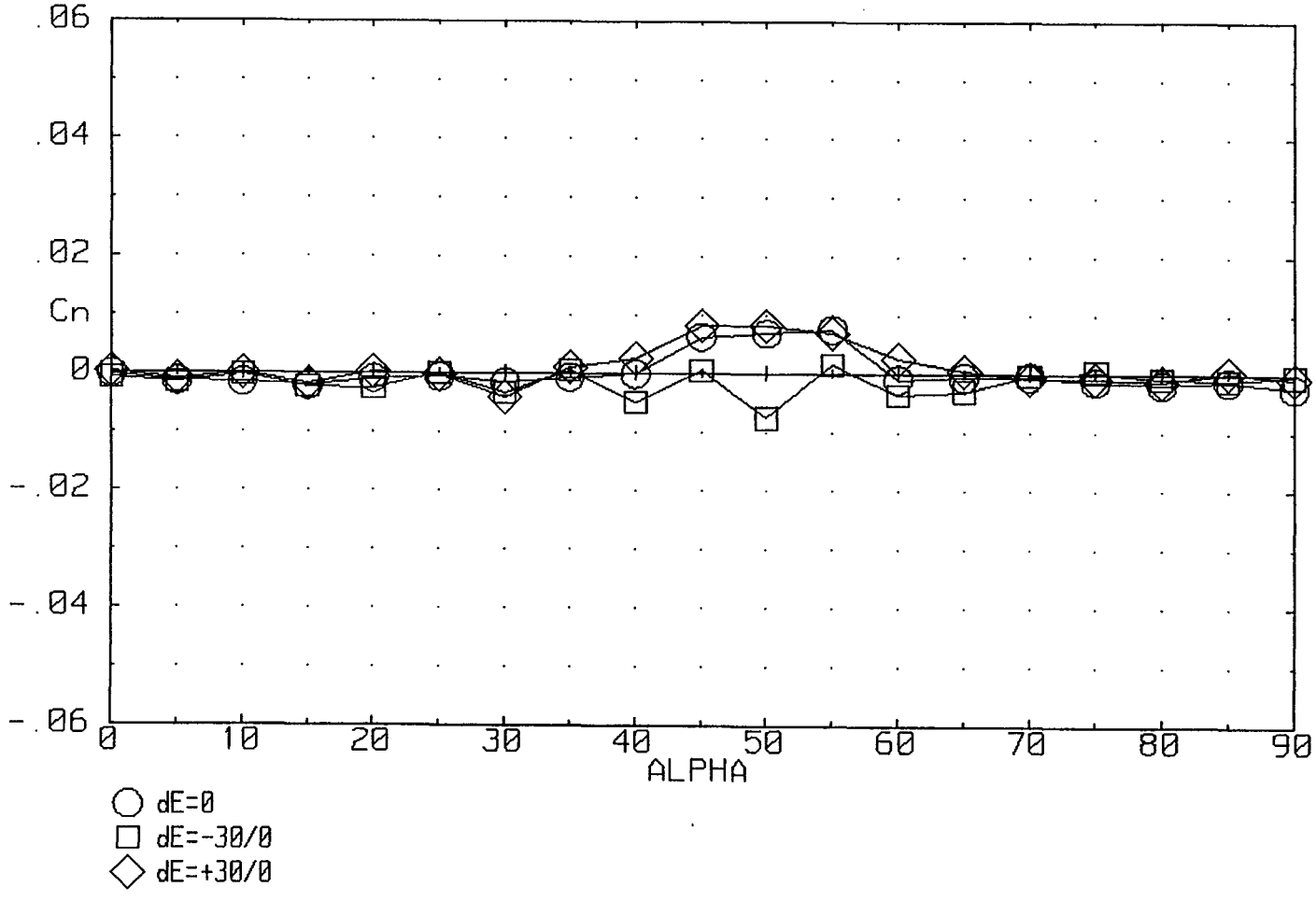

Figure 3-40. Yawing Moment due to Left-Side Elevon Deflection on the ICE 201 (LEF=30, β=0°).

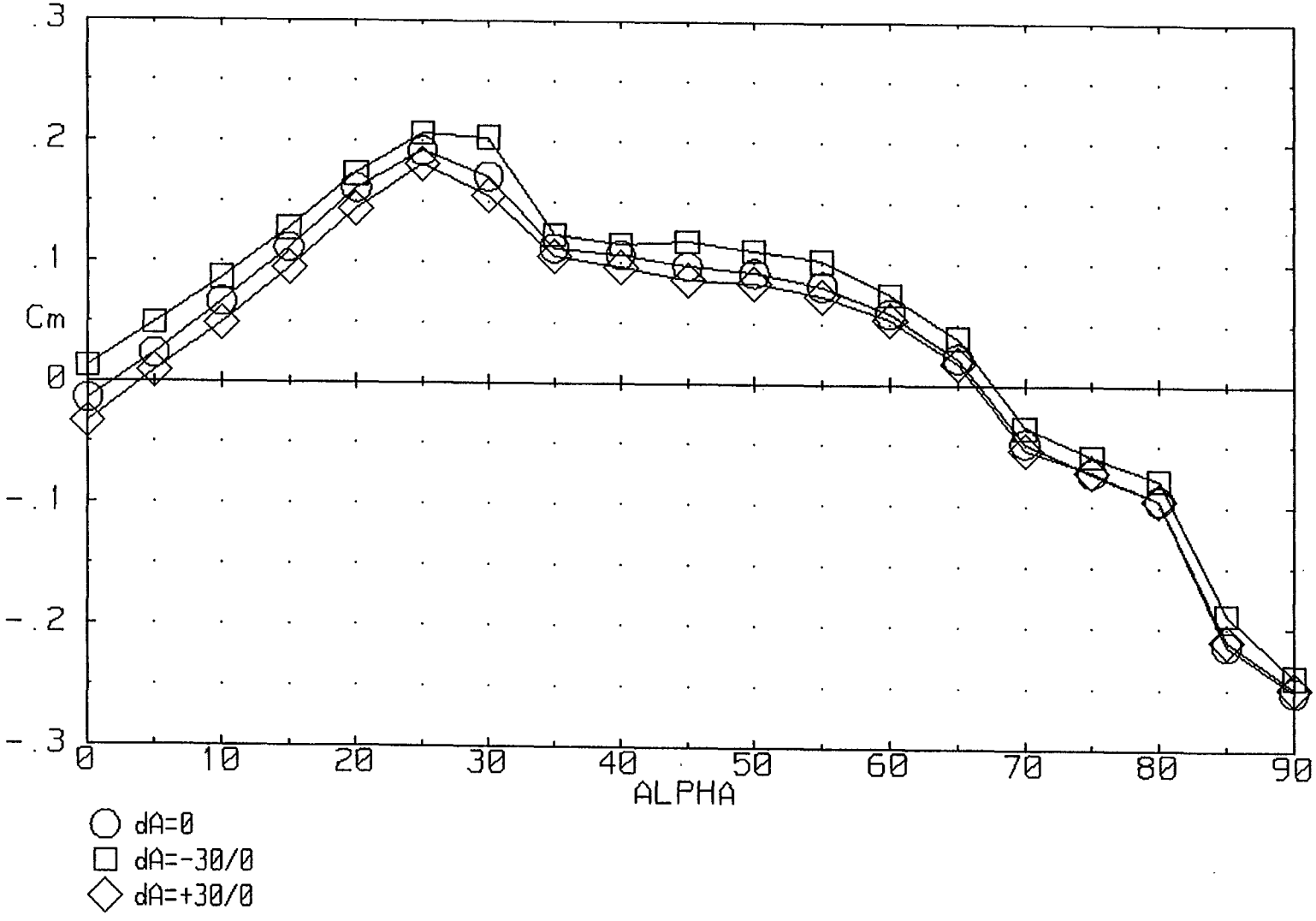

Figure 3-41. Effect of Left-Side Aileron Deflection on Pitching Moment for the ICE 201 (LEF=30, β=0°).

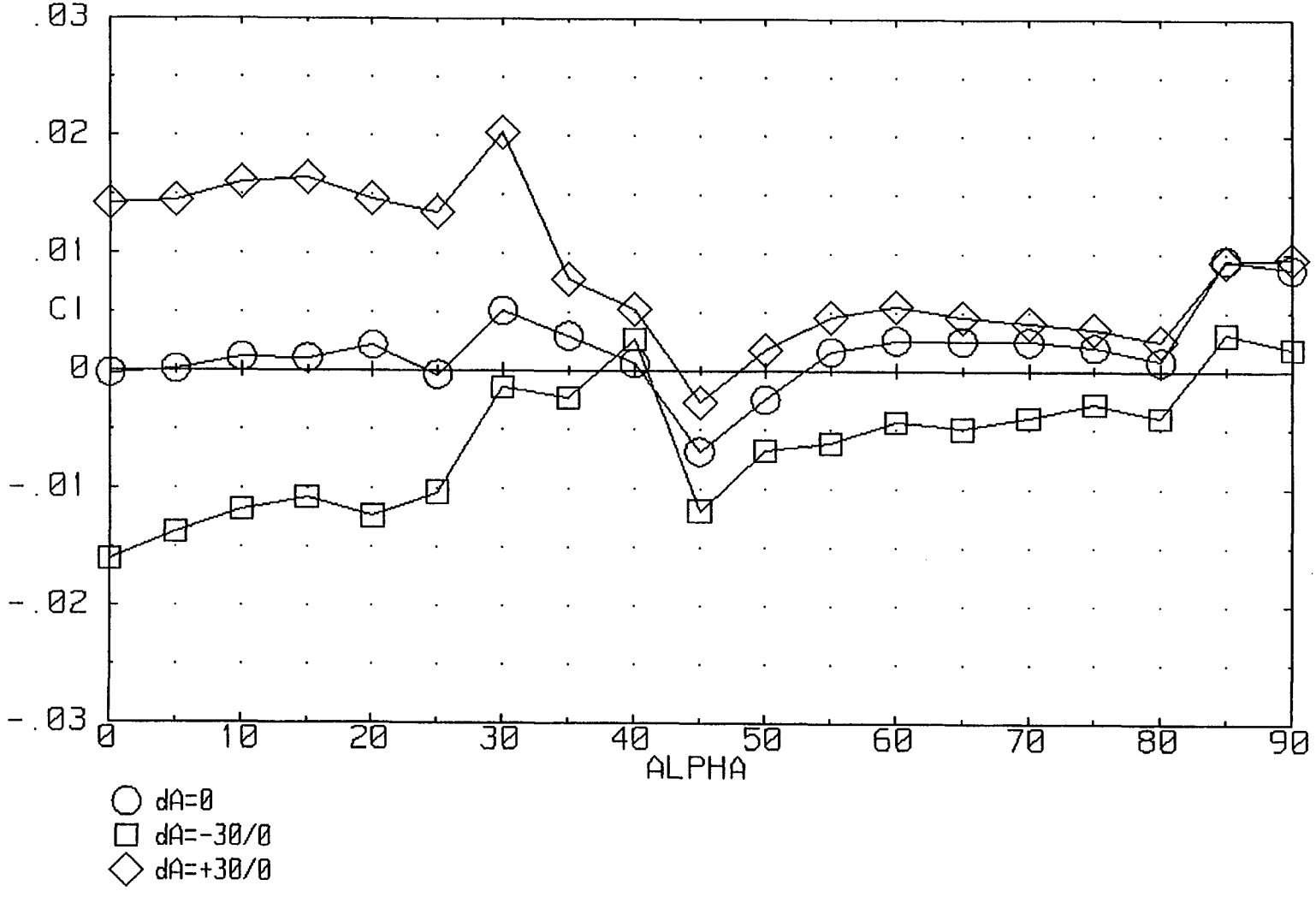

Figure 3-42. Rolling Moment due to Left-Side Aileron Deflections on the ICE 201 (LEF=30, β=0°).

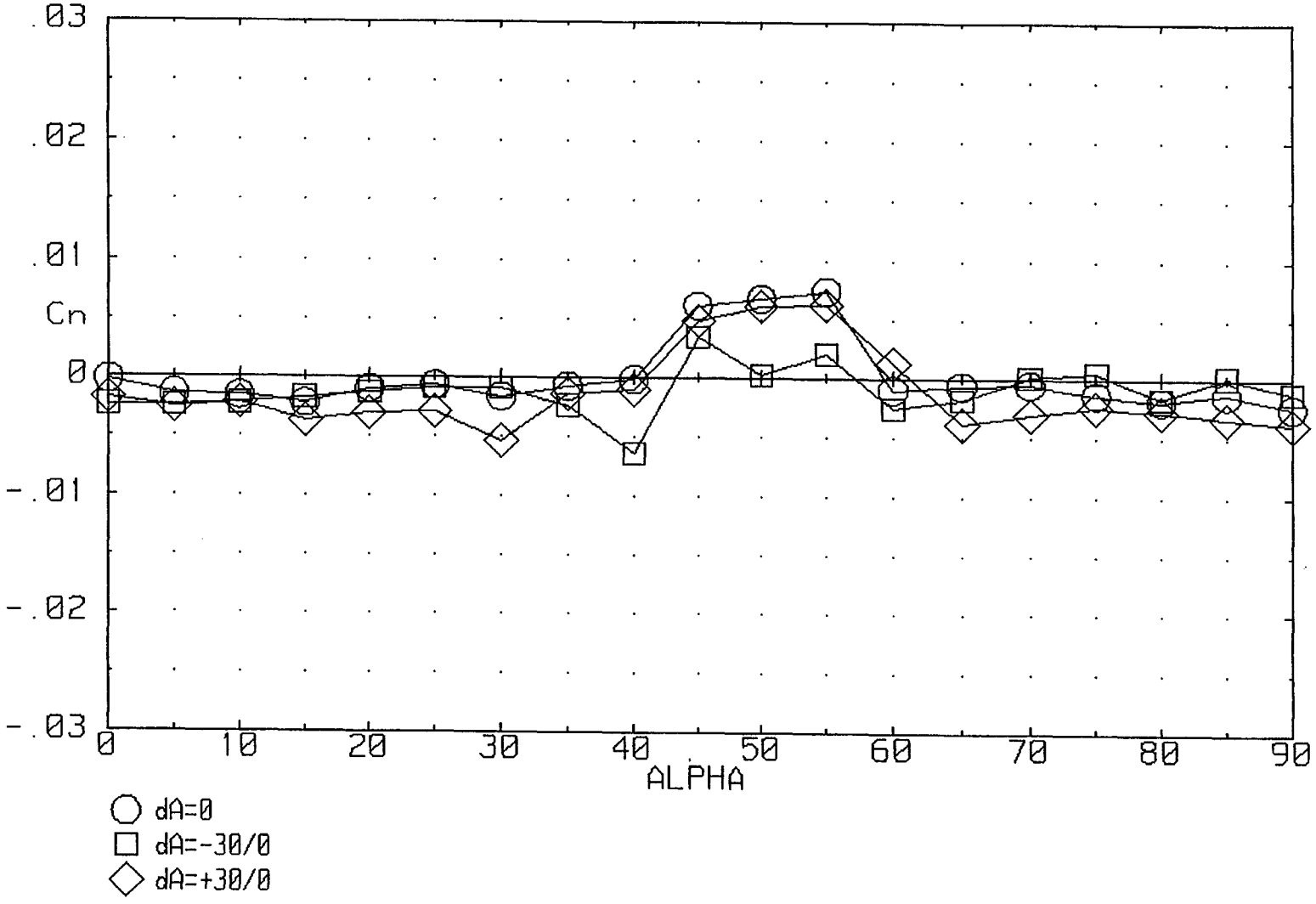

Figure 3-43. Yawing Moment due to Left-Side Aileron Deflections on the ICE 201 (LEF=30, β=0°).

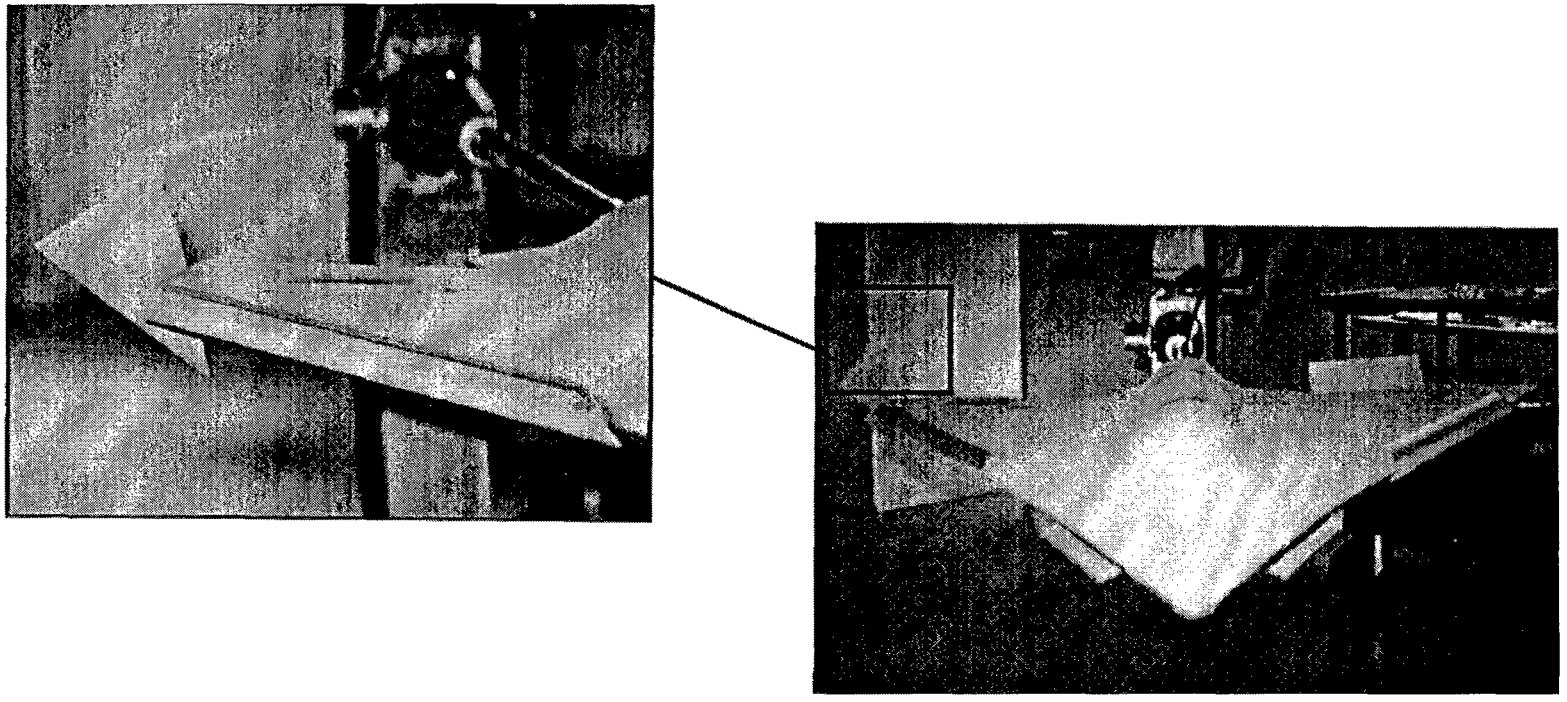

Figure 3-44. Photograph of All Moving Wing Tip Deflected on the ICE 101 Model.

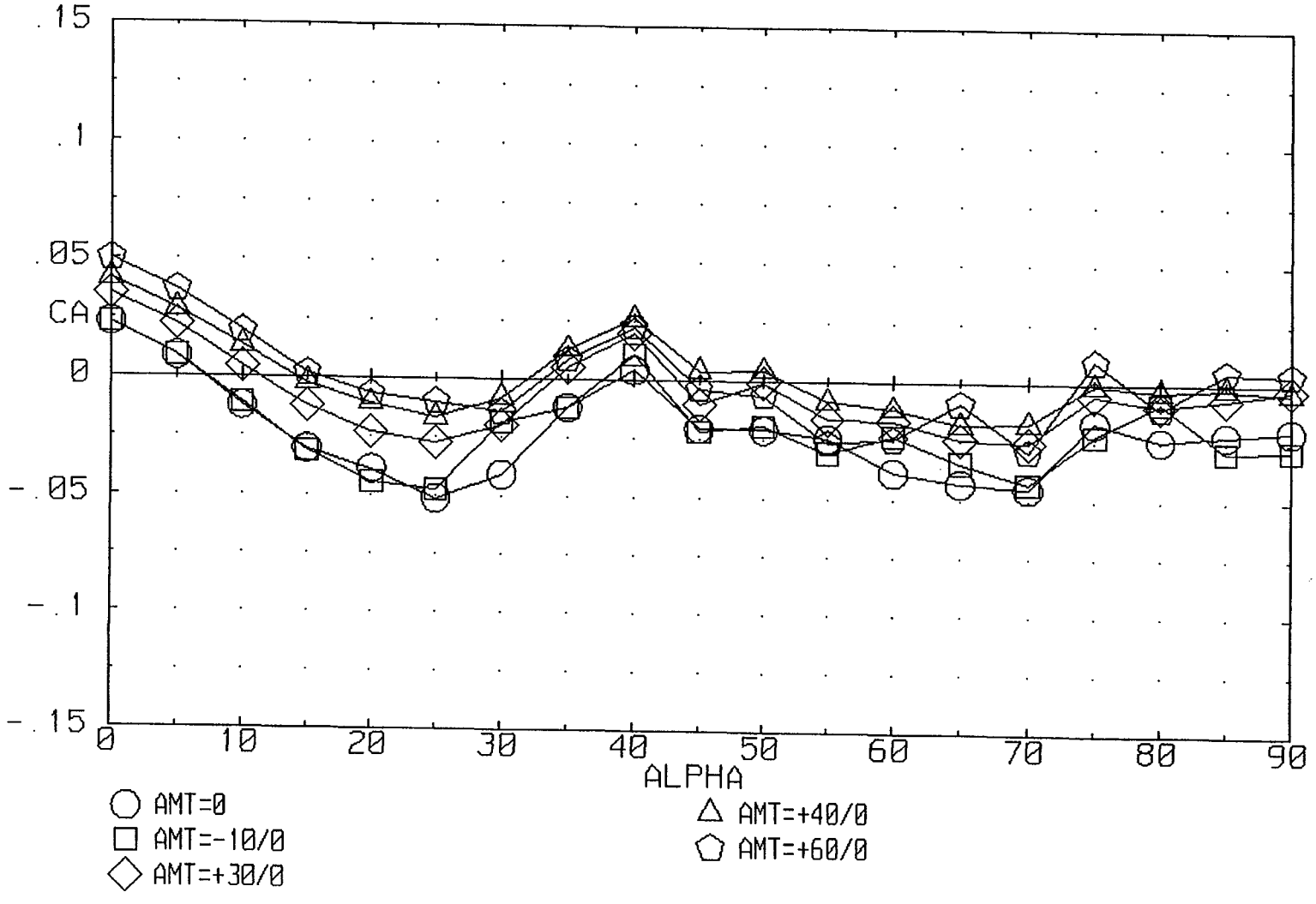

Figure 3-45. Axial Force due to AMT Deflections on the ICE 201 (LEF=30, β=0°).

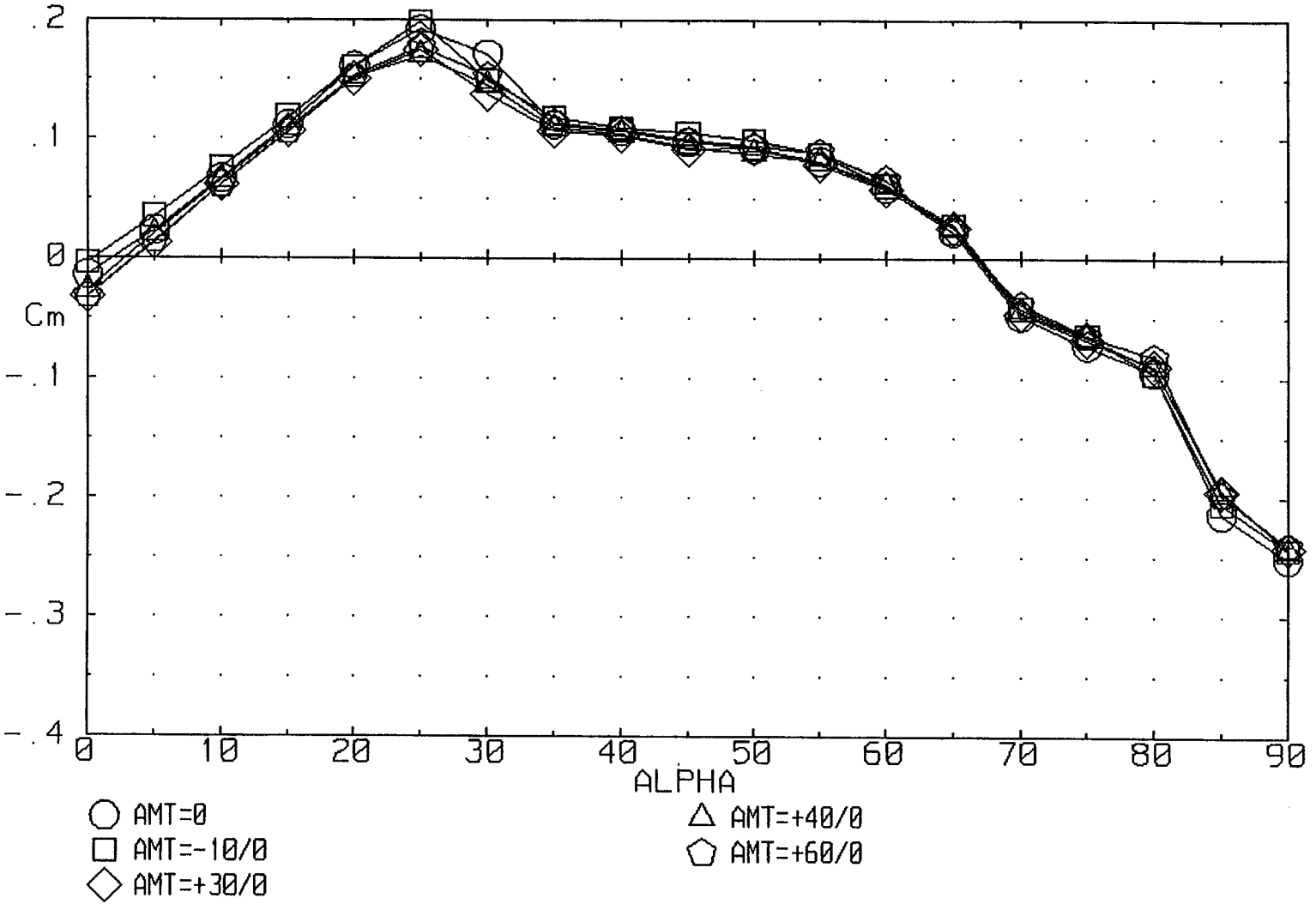

Figure 3-46. Pitching Moment due to AMT Deflections on the ICE 201 (LEF=30, β=0°).

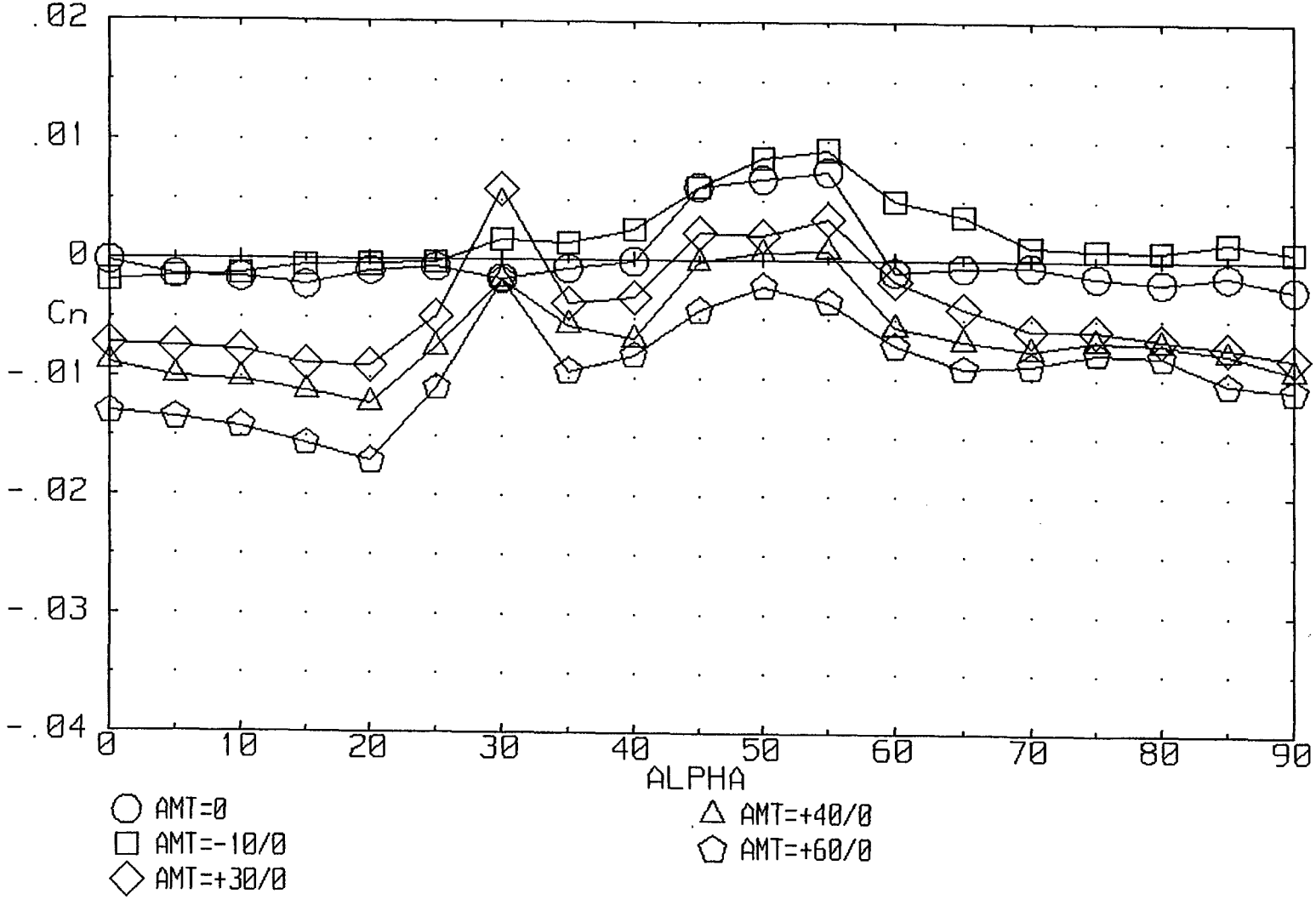

a) Yawing Moment

Figure 3-47. Effect of AMT Deflections on Control Power for the ICE 201 at Zero Sideslip (LEF=30).

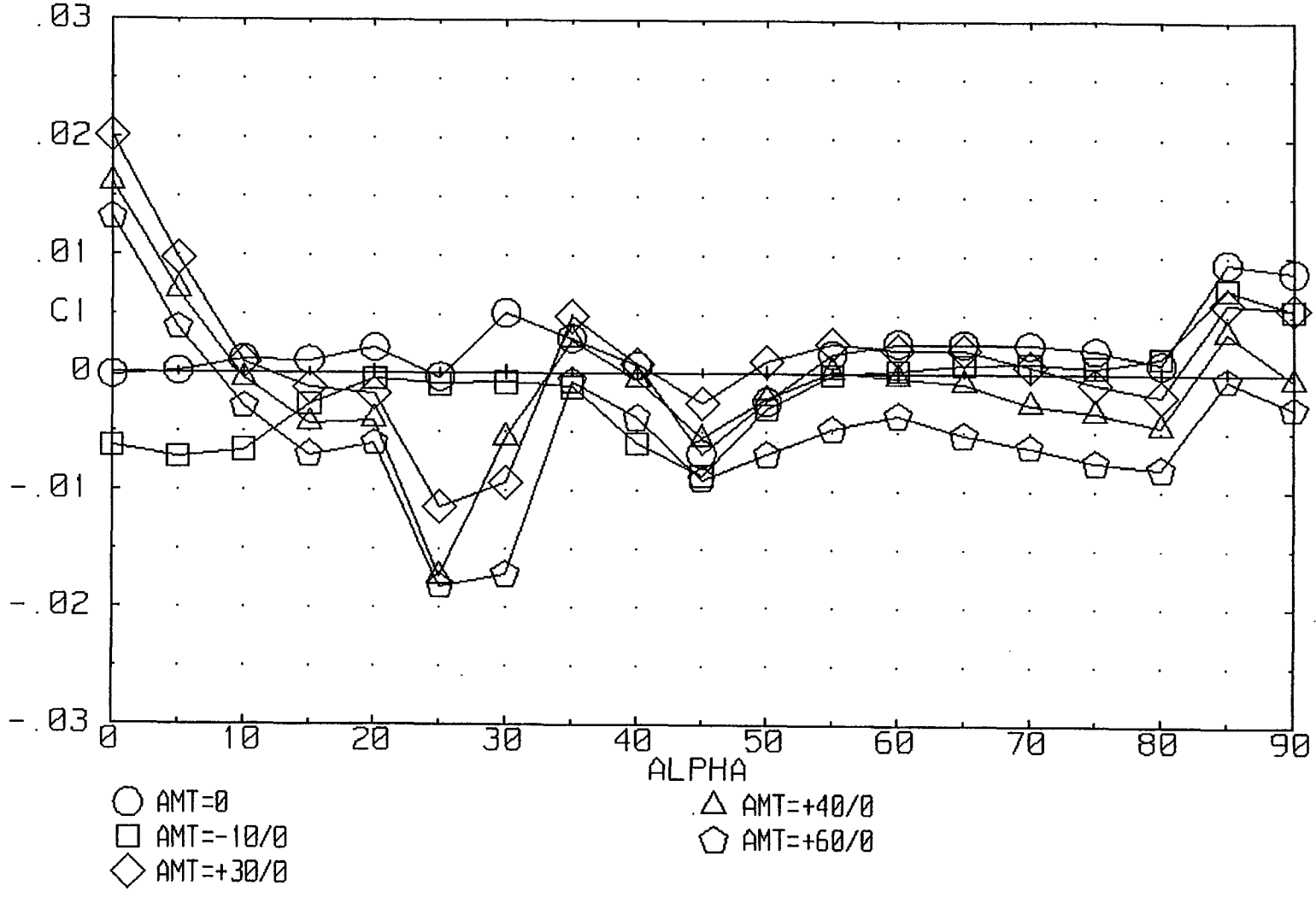

b) Rolling Moment

Figure 3-47 Concluded.

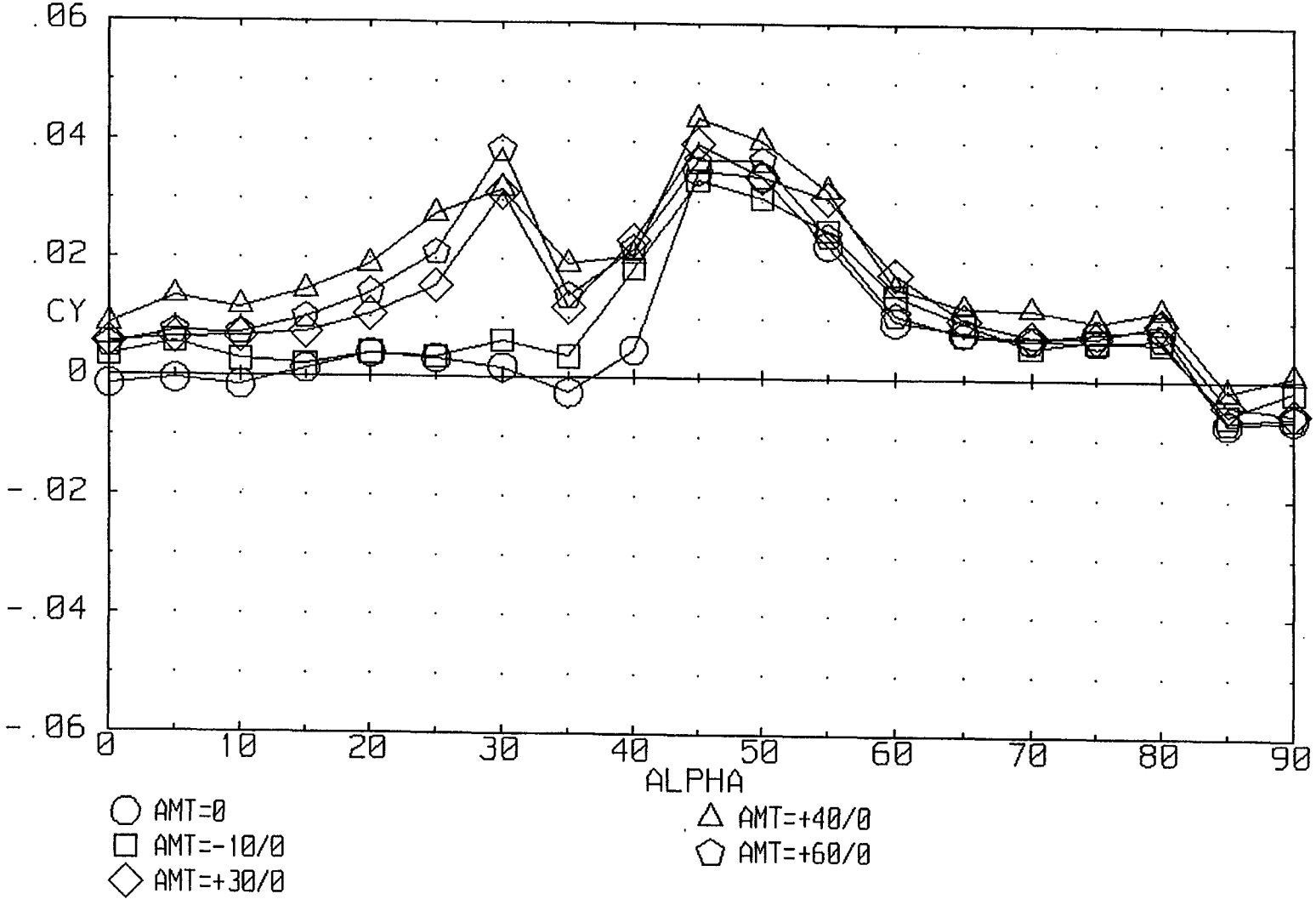

Figure 3-48. Effect of AMT Deflections on Side Force for the ICE 201 (LEF=30, β=0°).

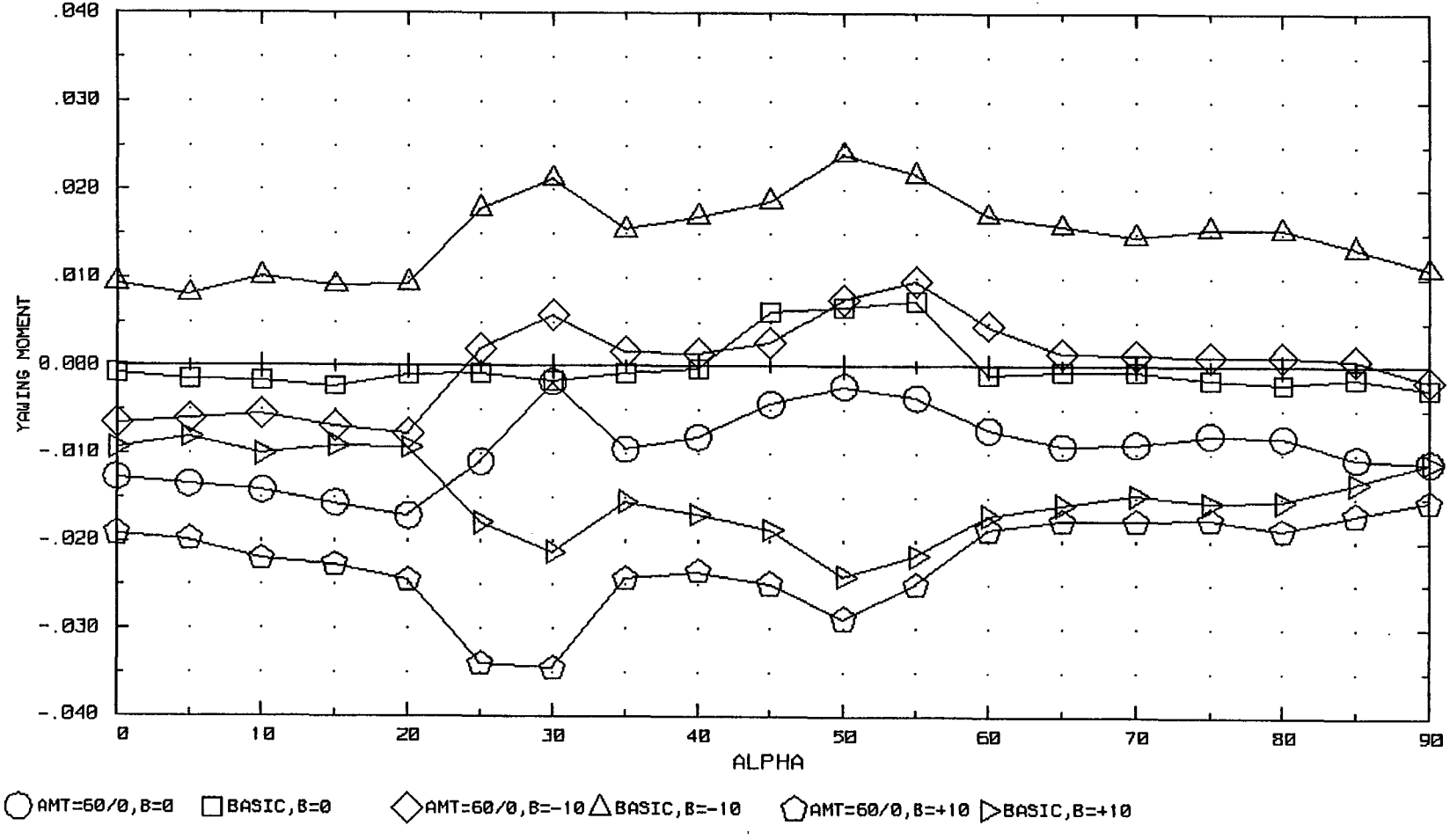

a) Yawing Moment

Figure 3-49. Influence of Sideslip Angle on AMT Control Effectiveness for the ICE 101 (LEF=30).

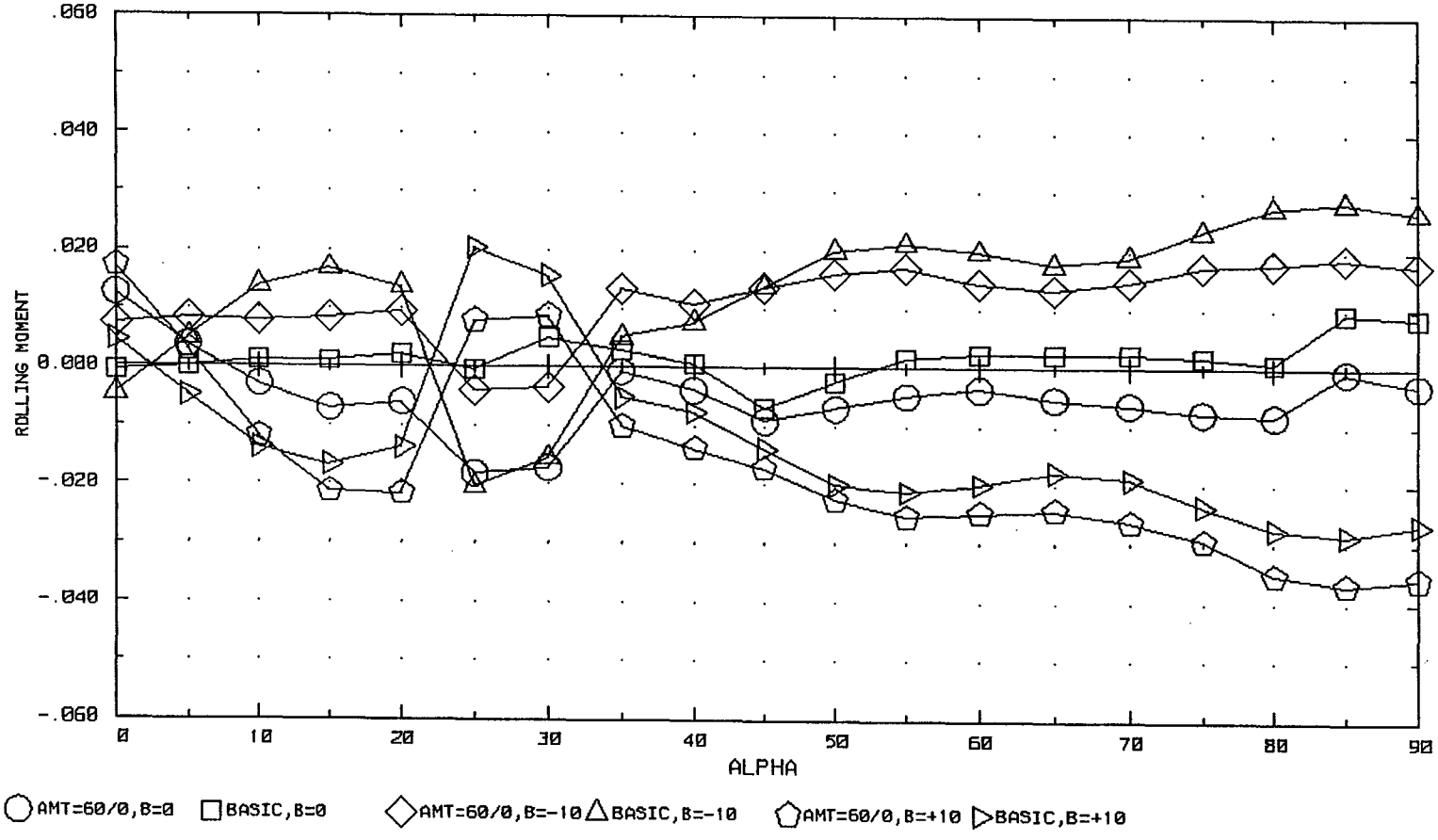

b) Rolling Moment

Figure 3-49 Concluded.

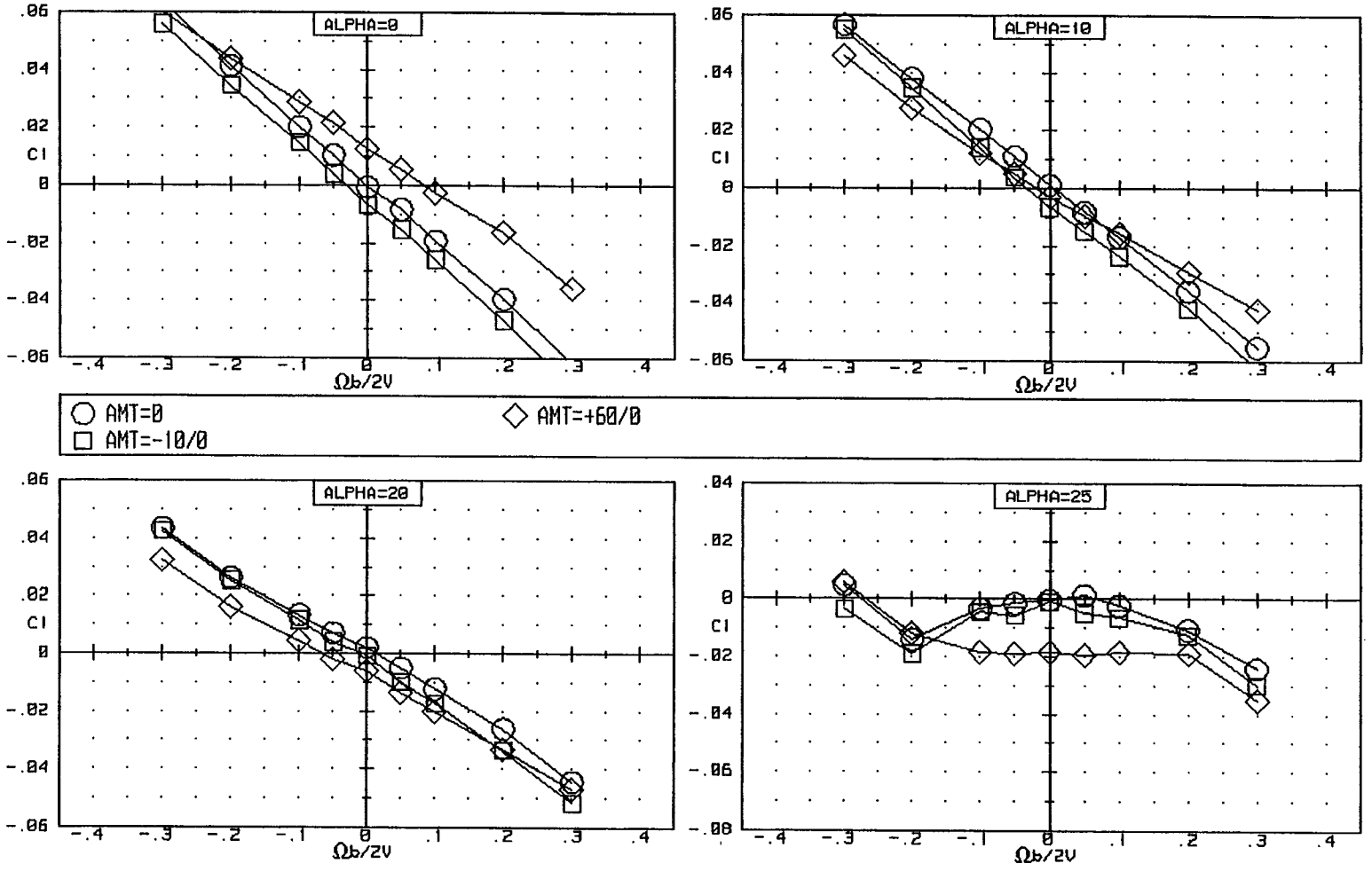

Figure 3-50. Effect of AMT Deflection on Rotational Rolling Moment for the ICE 201 (LEF=30, β=0°).

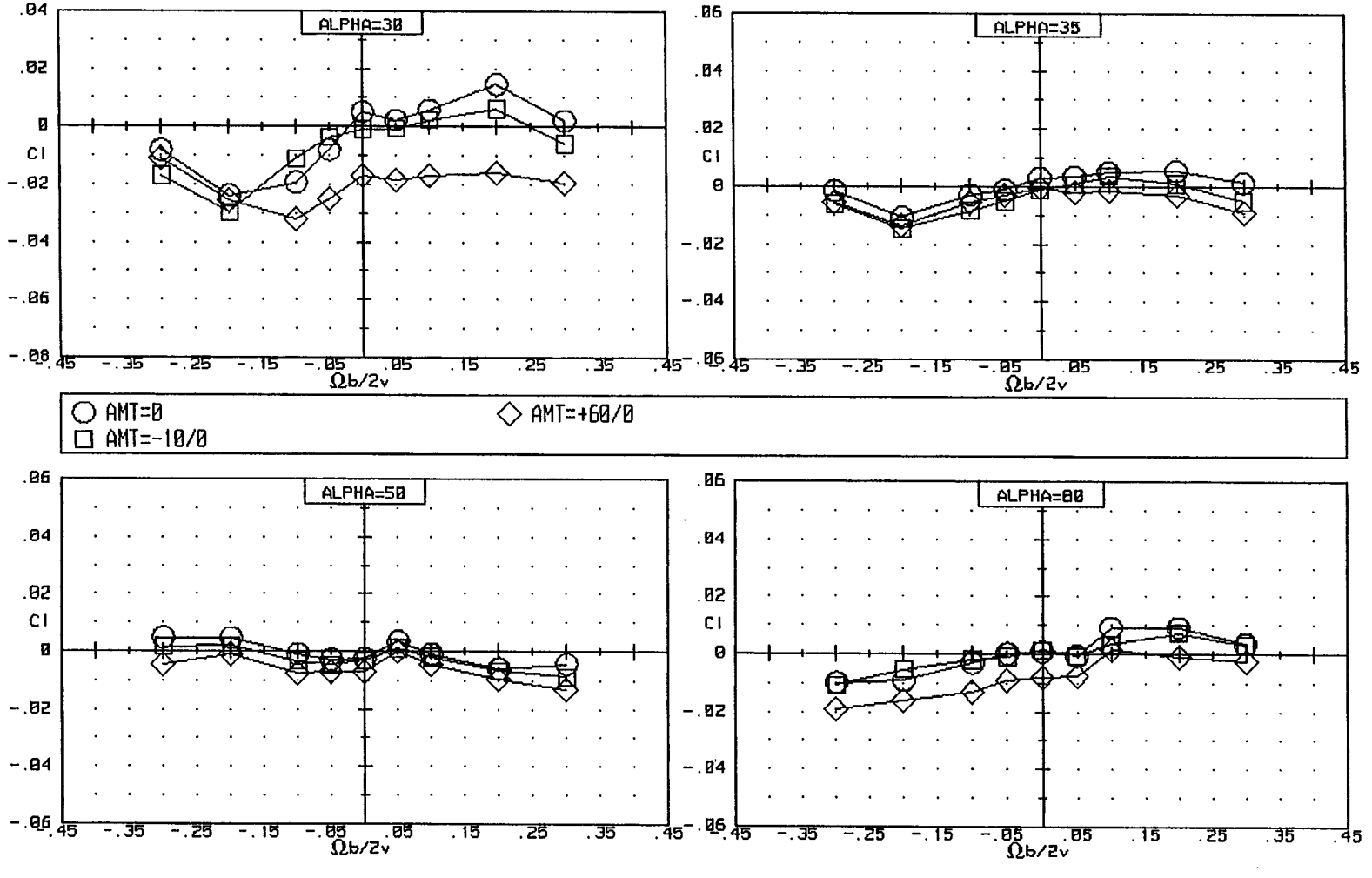

Figure 3-50 Concluded.

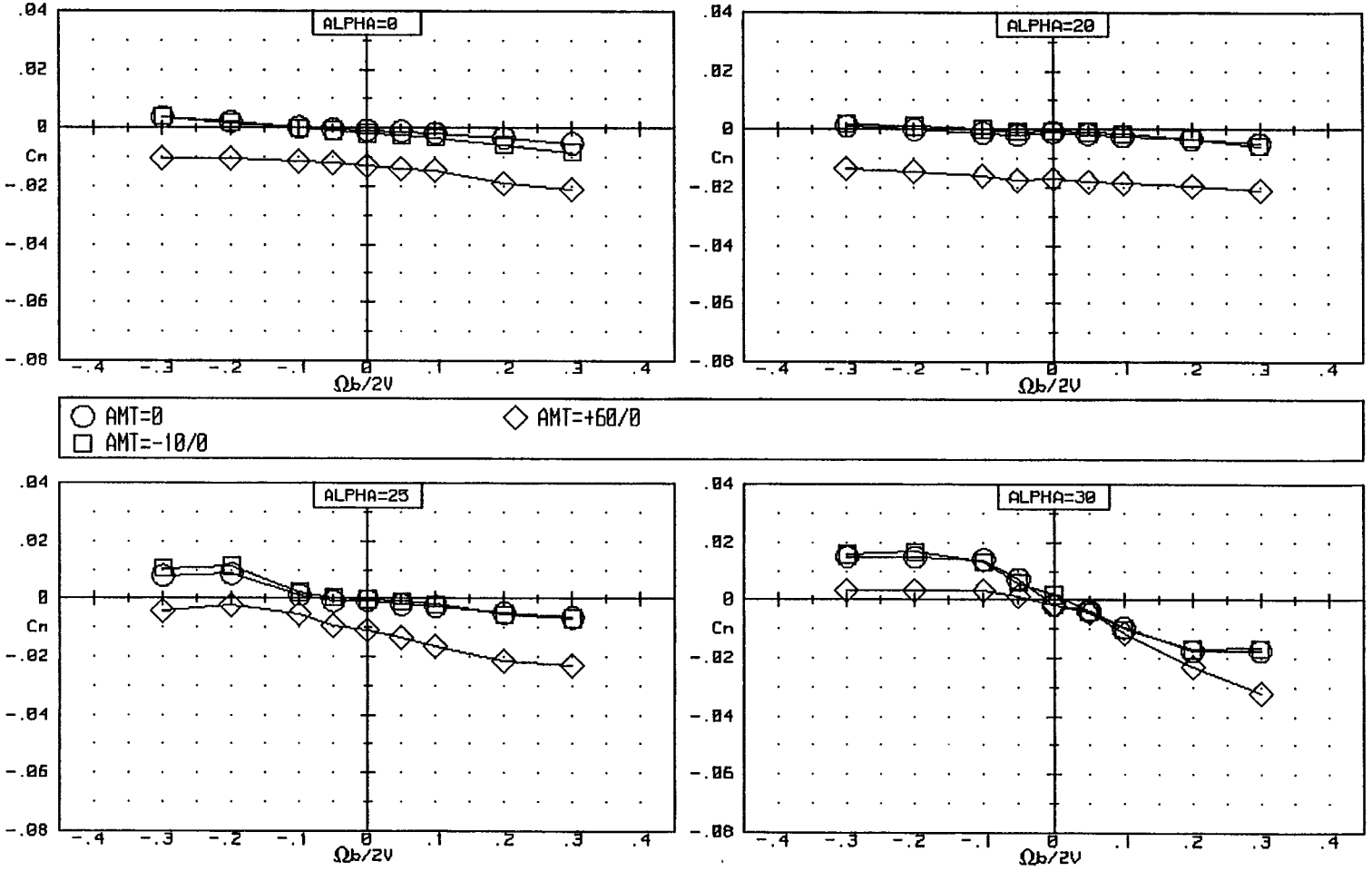

Figure 3-51. Effect of AMT Deflection on Rotational Yawing Moment for the ICE 201 (LEF=30, β=0°).

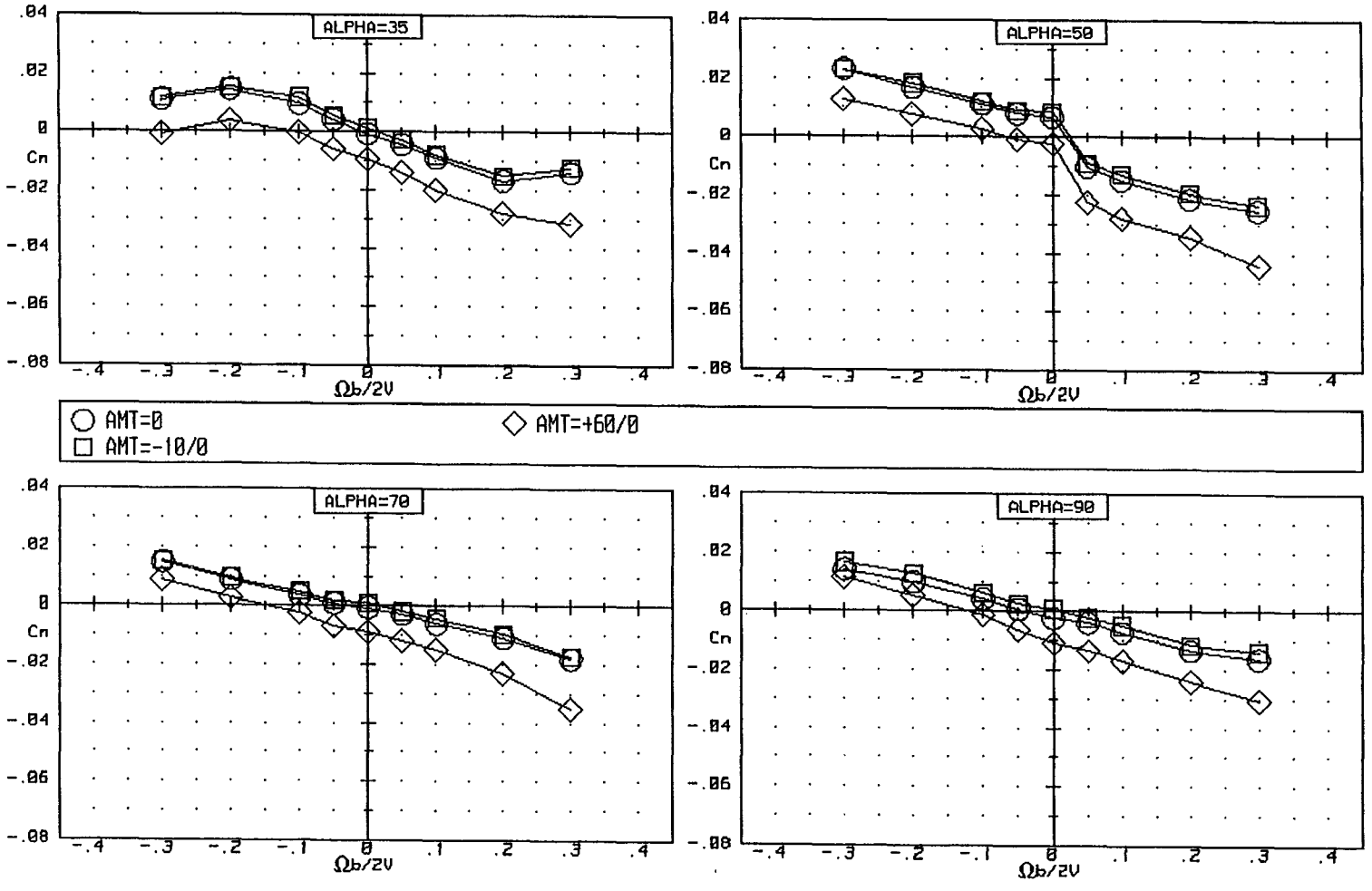

Figure 3-51 Concluded.

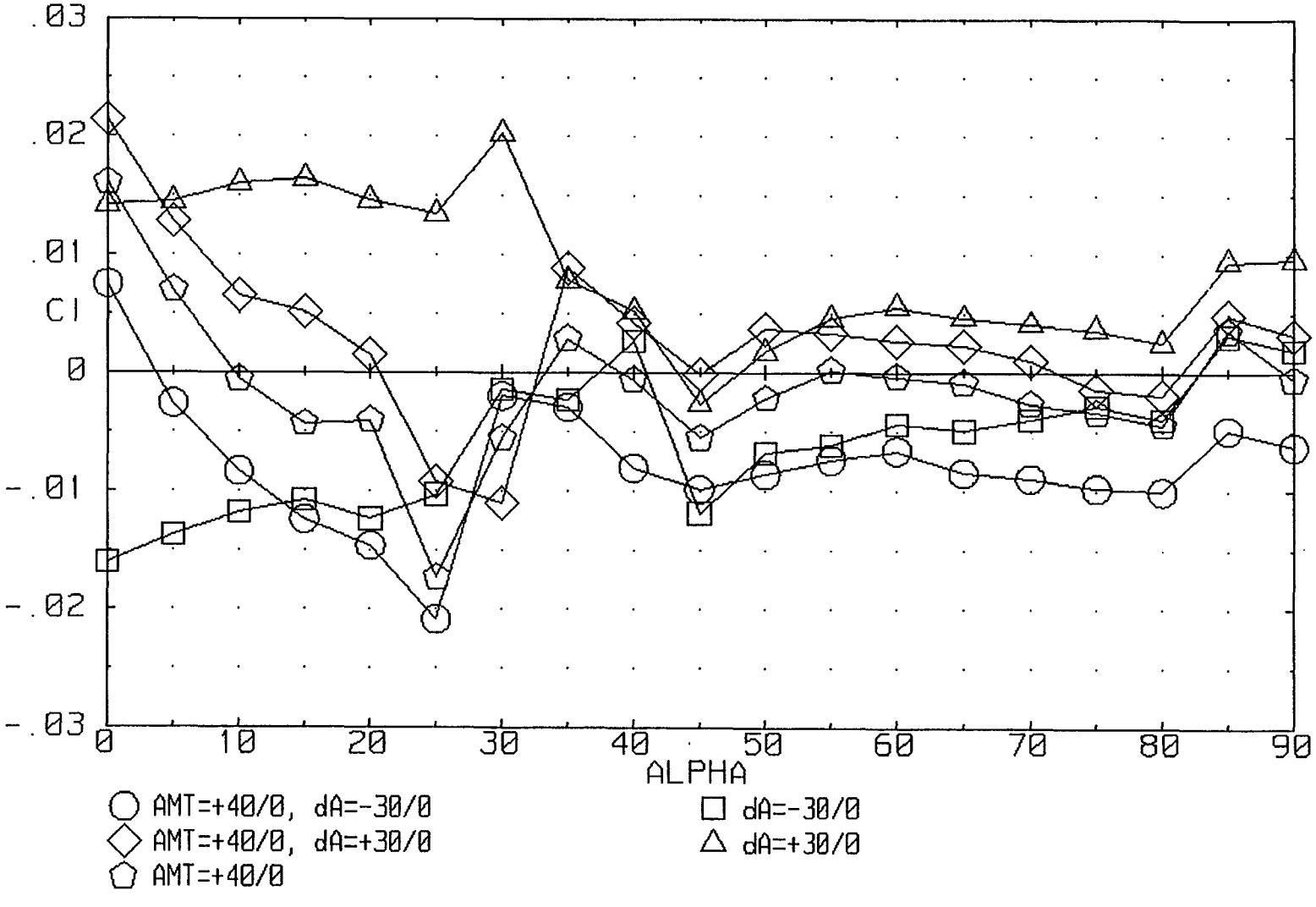

Figure 3-52. Effect of AMT/Aileron Interactions on Rolling Moment for the ICE 201 (LEF=30, β=0°).

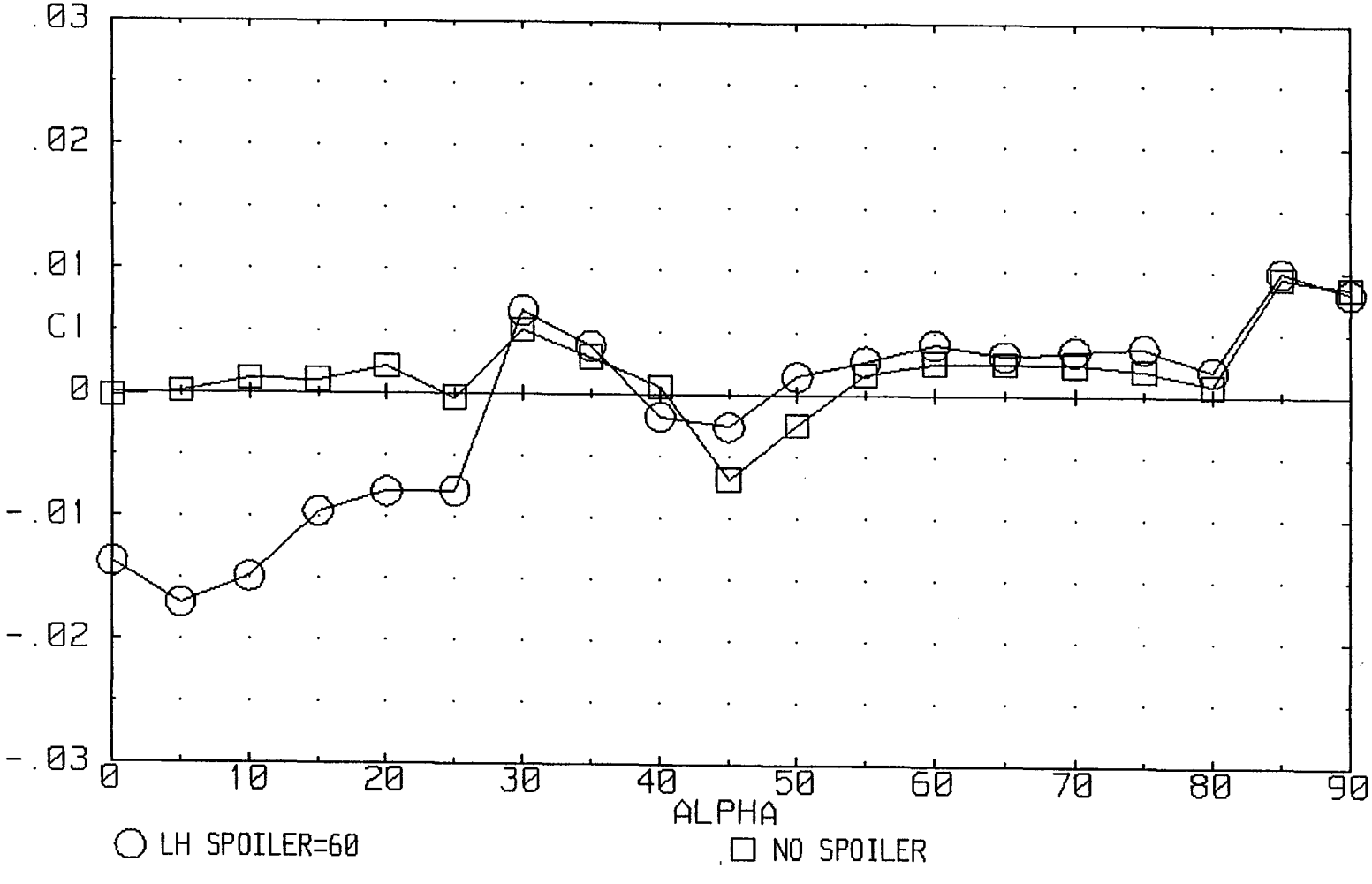

Figure 3-53. Effect of Left-Hand Spoiler Deployment on Rolling Moment for the ICE 201 (LEF=30, β=0°).

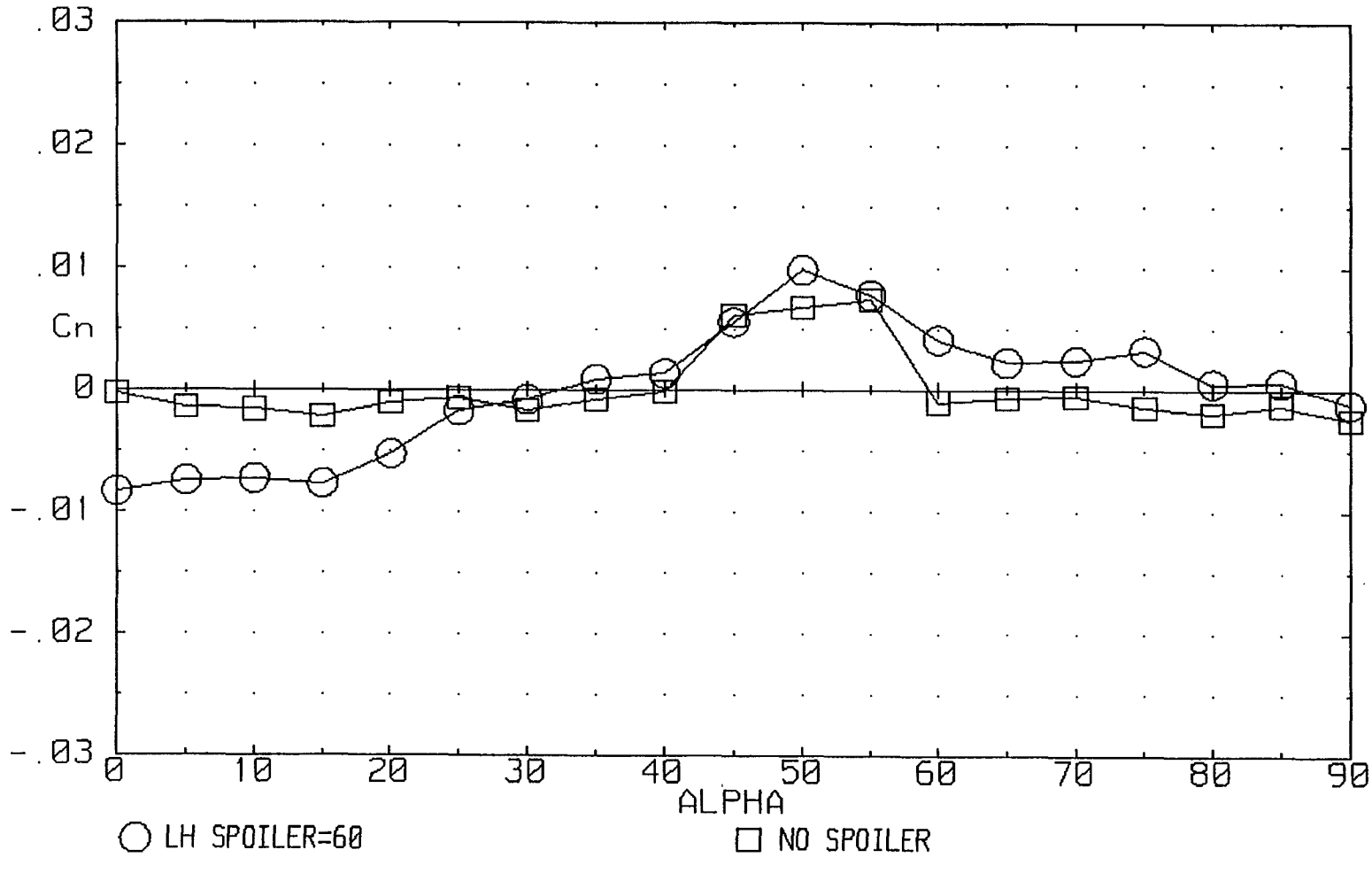

Figure 3-54. Effect of Left-Hand Spoiler Deployment on Yawing Moment for the ICE 201 (LEF=30, β=0°).

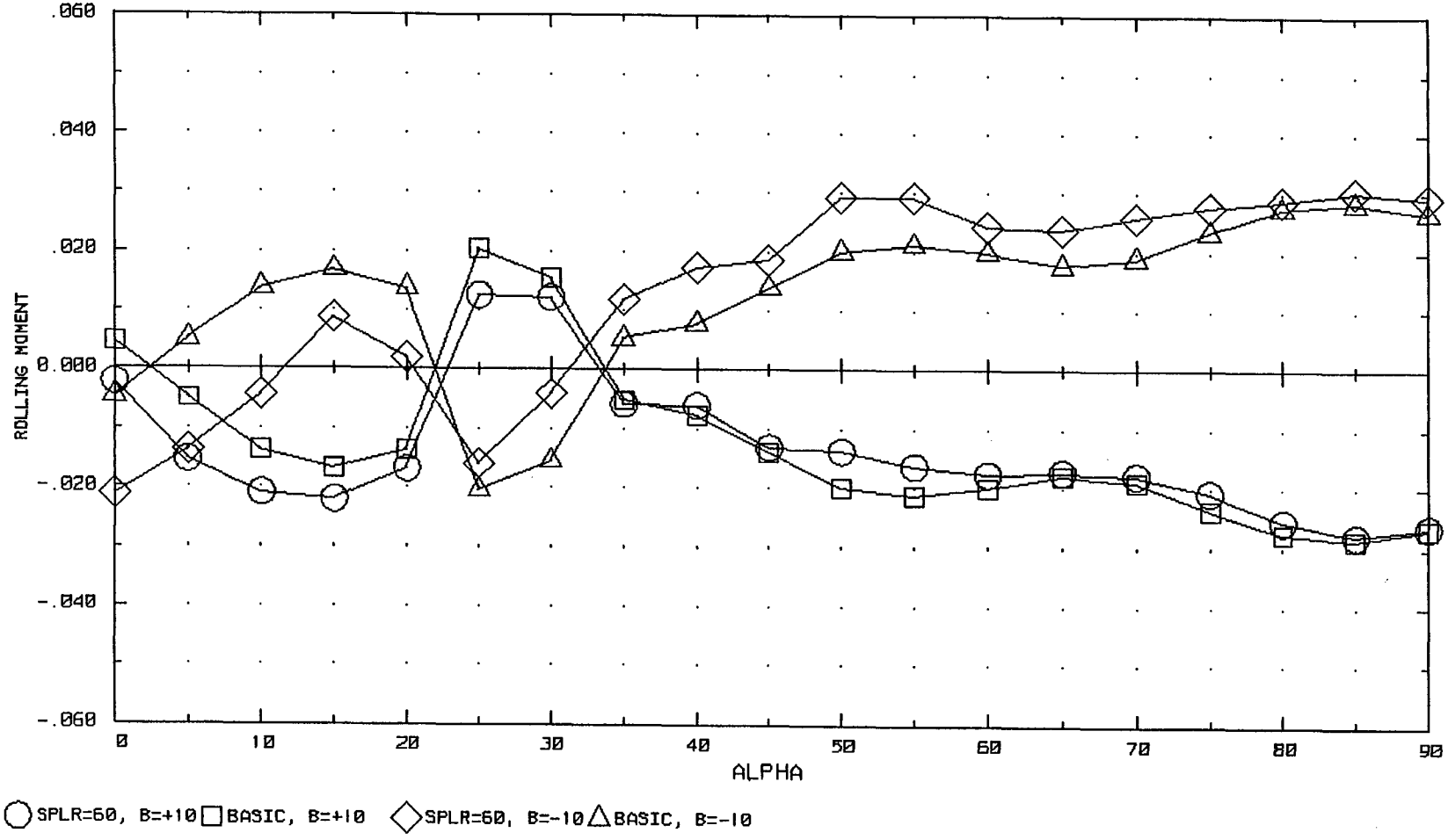

Figure 3-55. Effect of Left-Hand Spoiler on Static Lateral Stability for the ICE 201 (LEF=30).

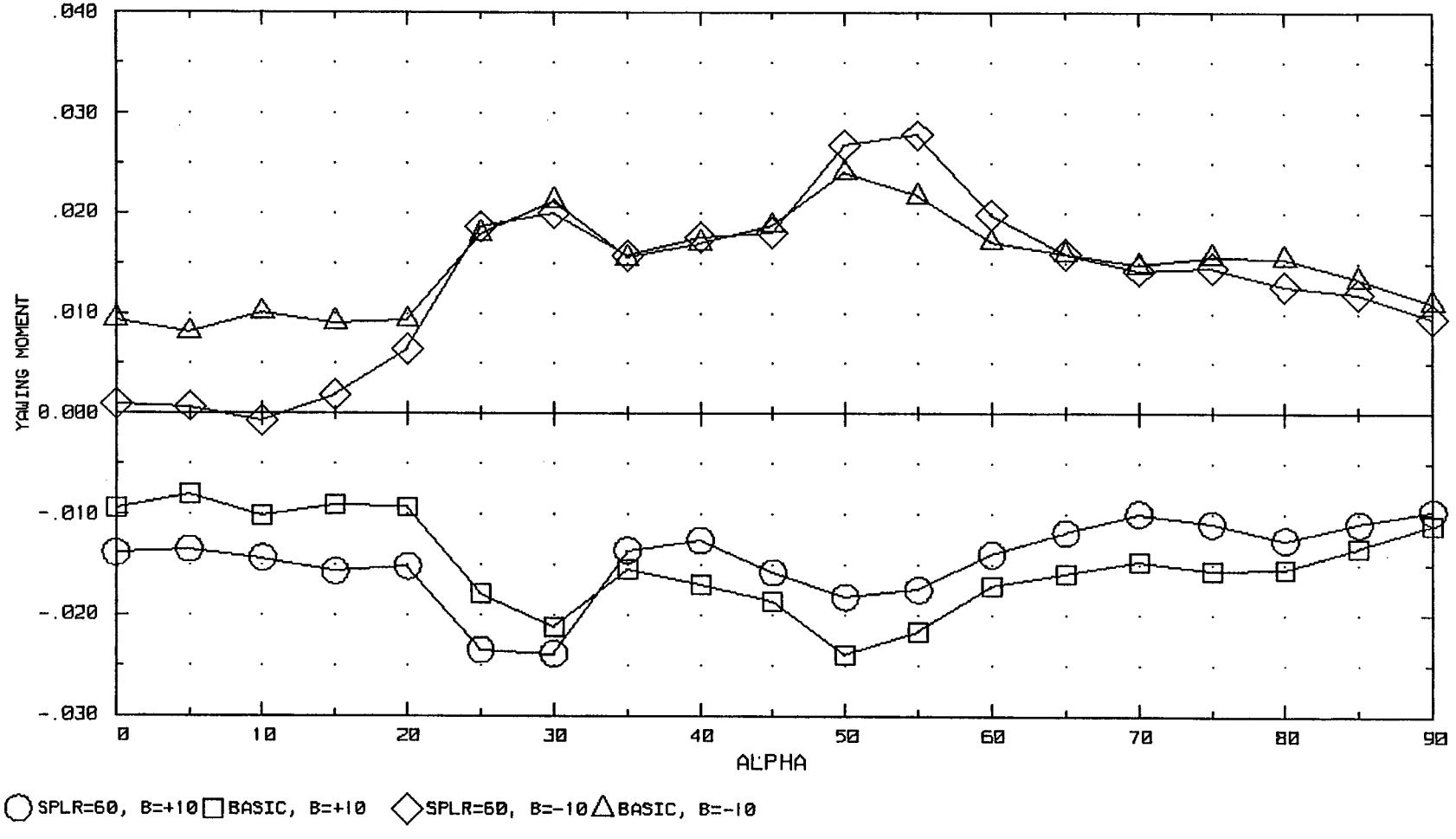

Figure 3-56. Effect of Left-Hand Spoiler Deployment on Directional Stability for the ICE 201 (LEF=30).

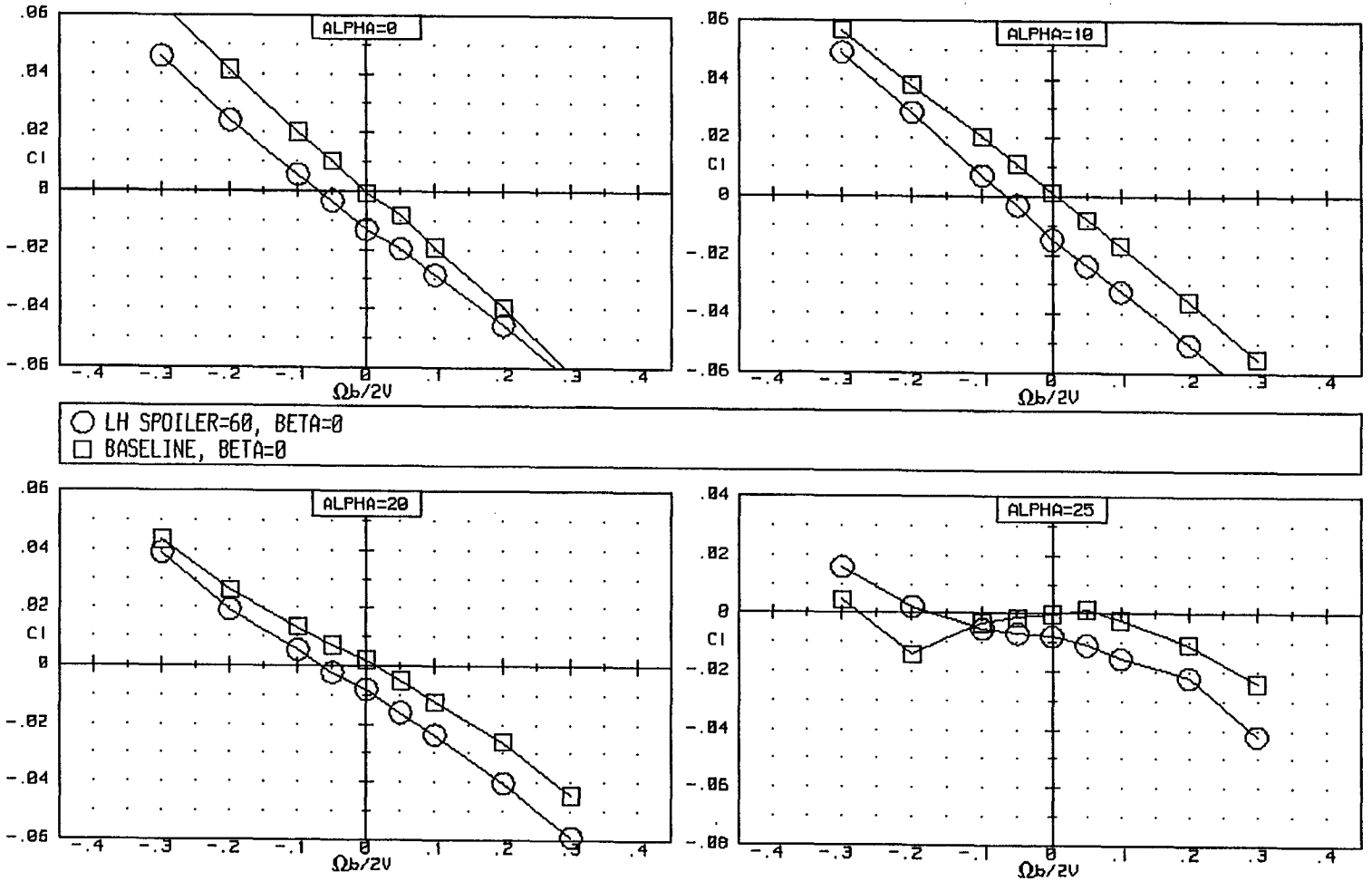

Figure 3-57. Effect of Rotation Rate and Left-Hand Spoiler on Rolling Moment for the ICE 201 (LEF=30, β=0°).

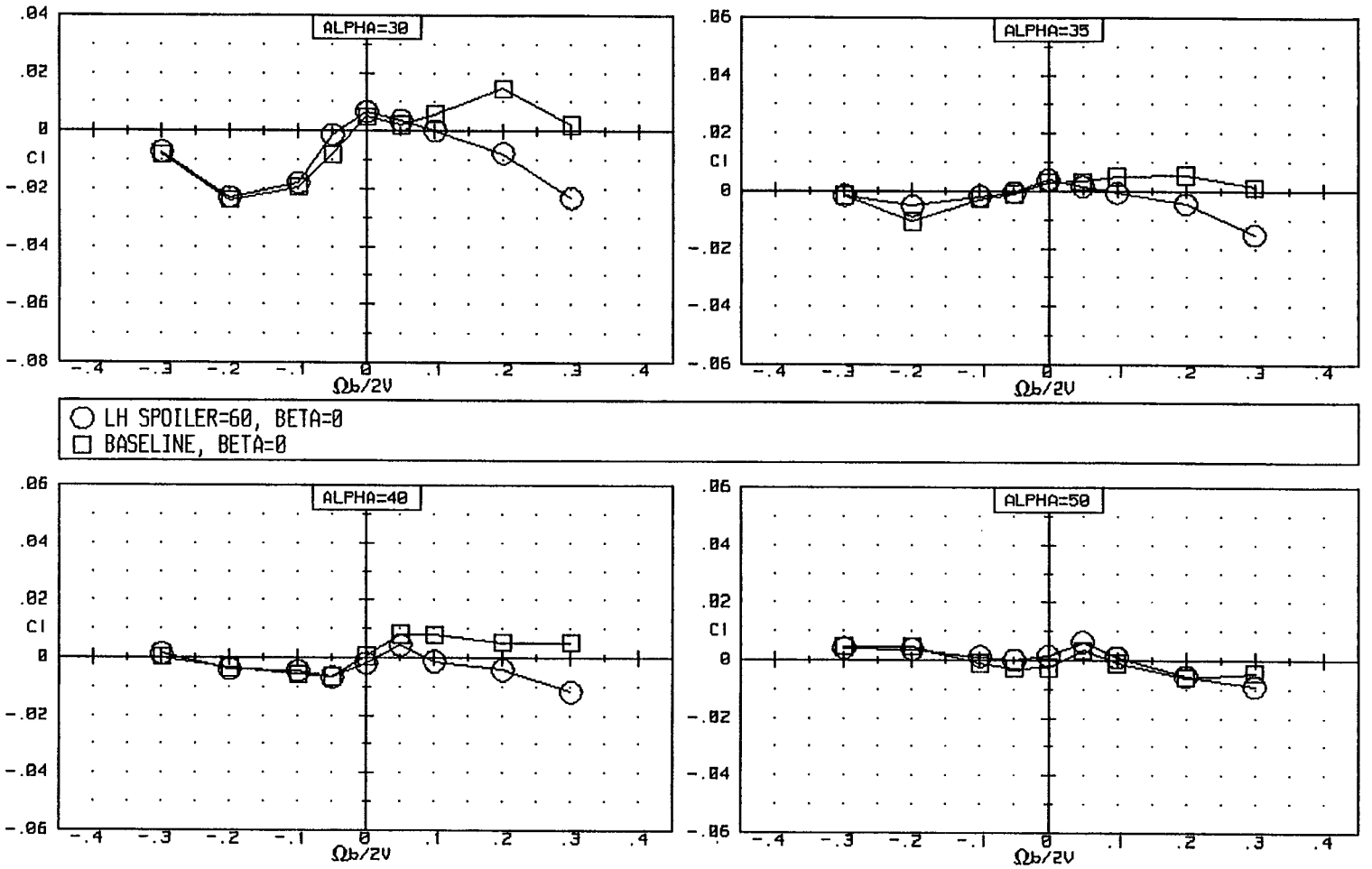

Figure 3-57. Concluded.

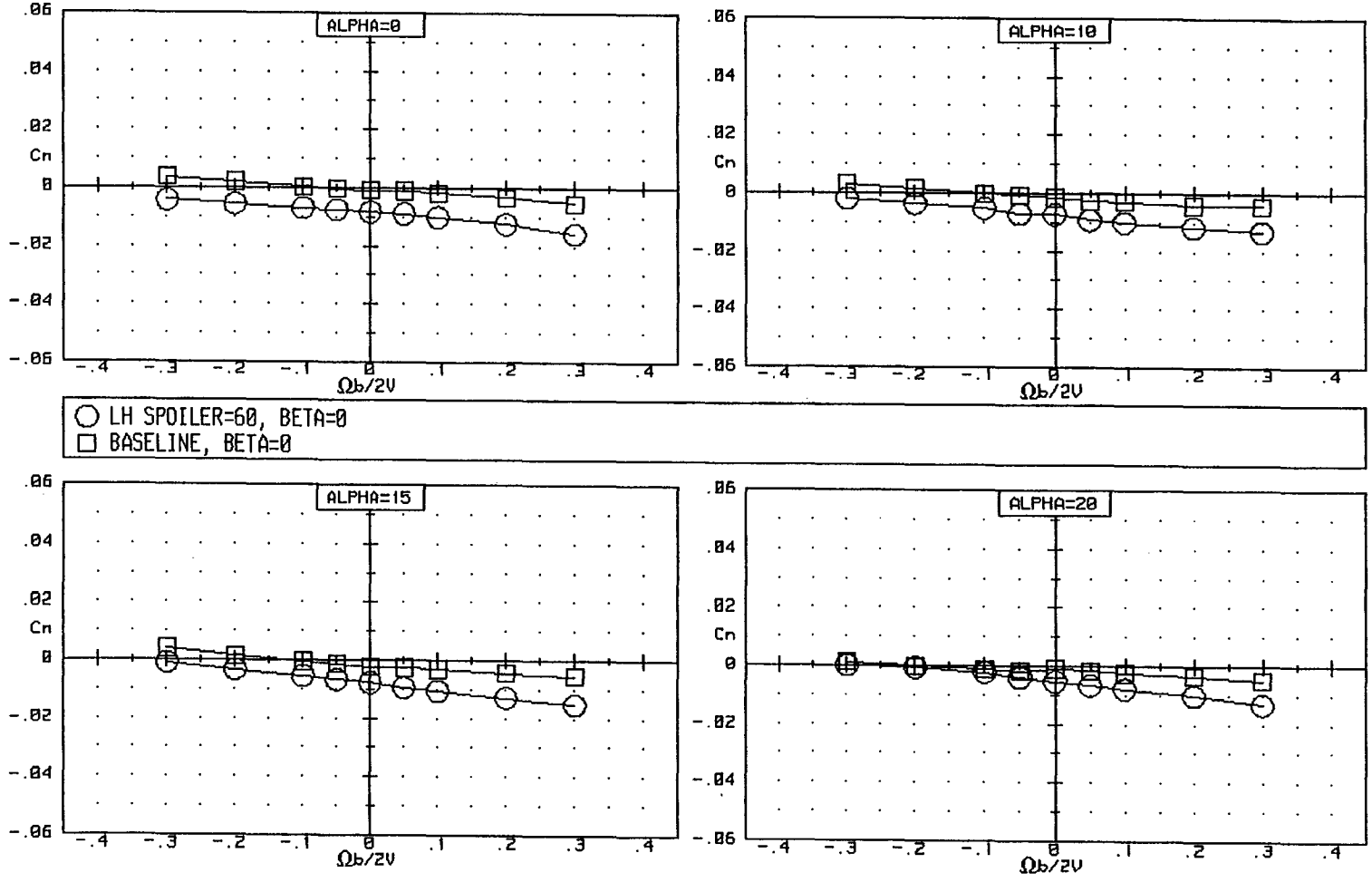

Figure 3-58. Effect of Rotation Rate and Left-Hand Spoiler on Yawing Moment for the ICE 201 (LEF=30).

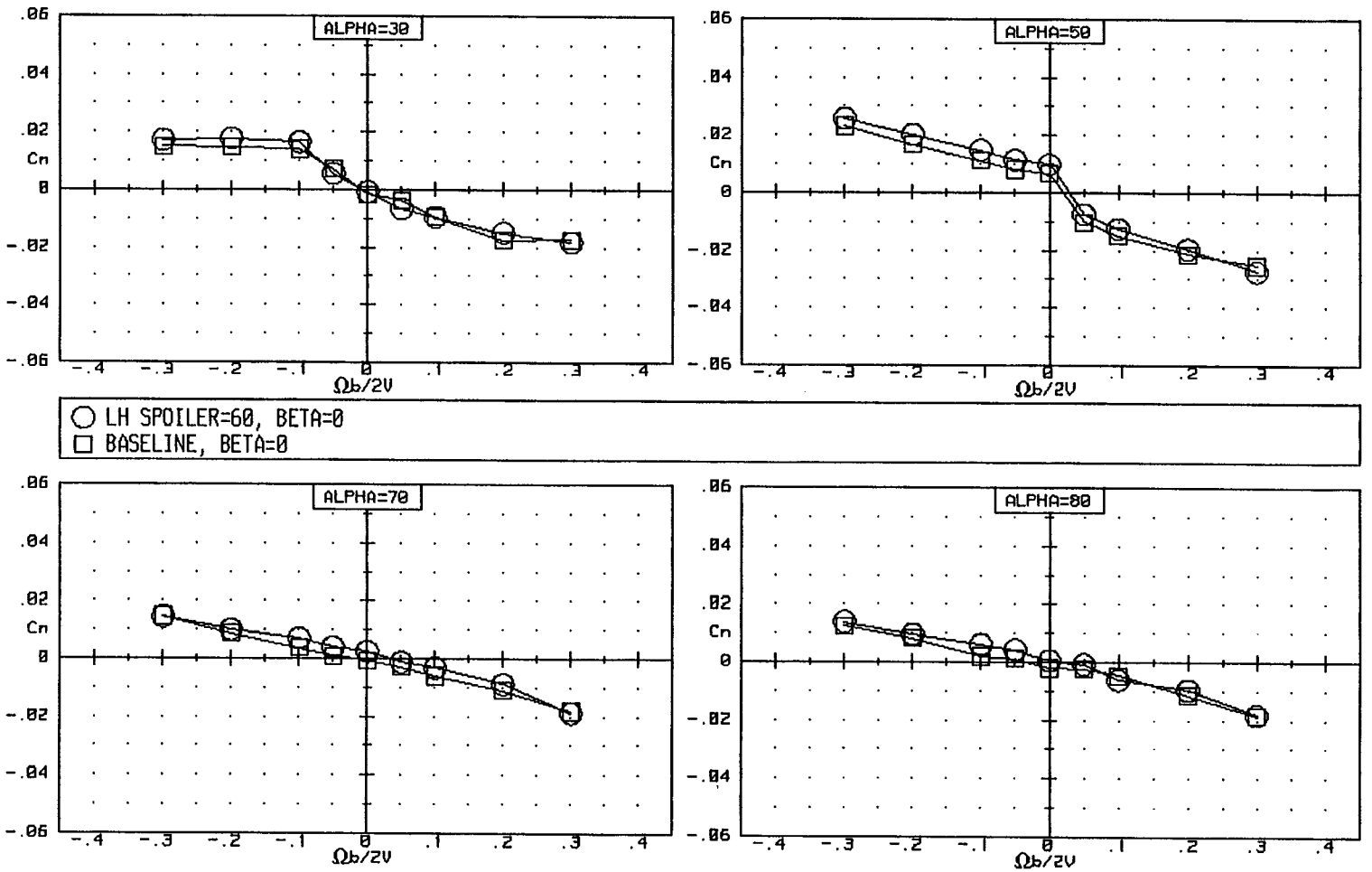

Figure 3-58. Concluded.

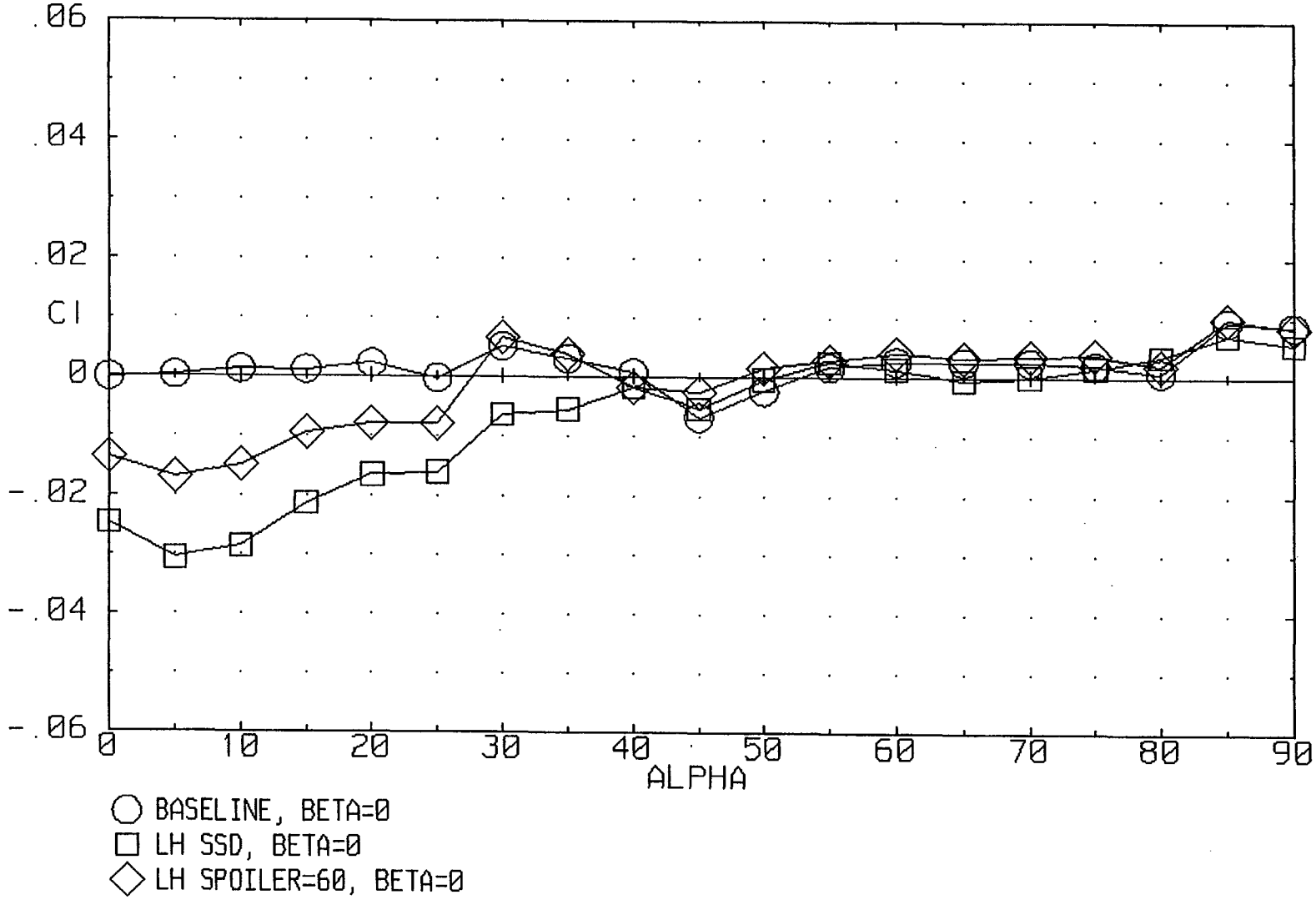

Figure 3-59. Effect of Right-Hand SSD on Rolling Moment for the ICE 201 (LEF=30).

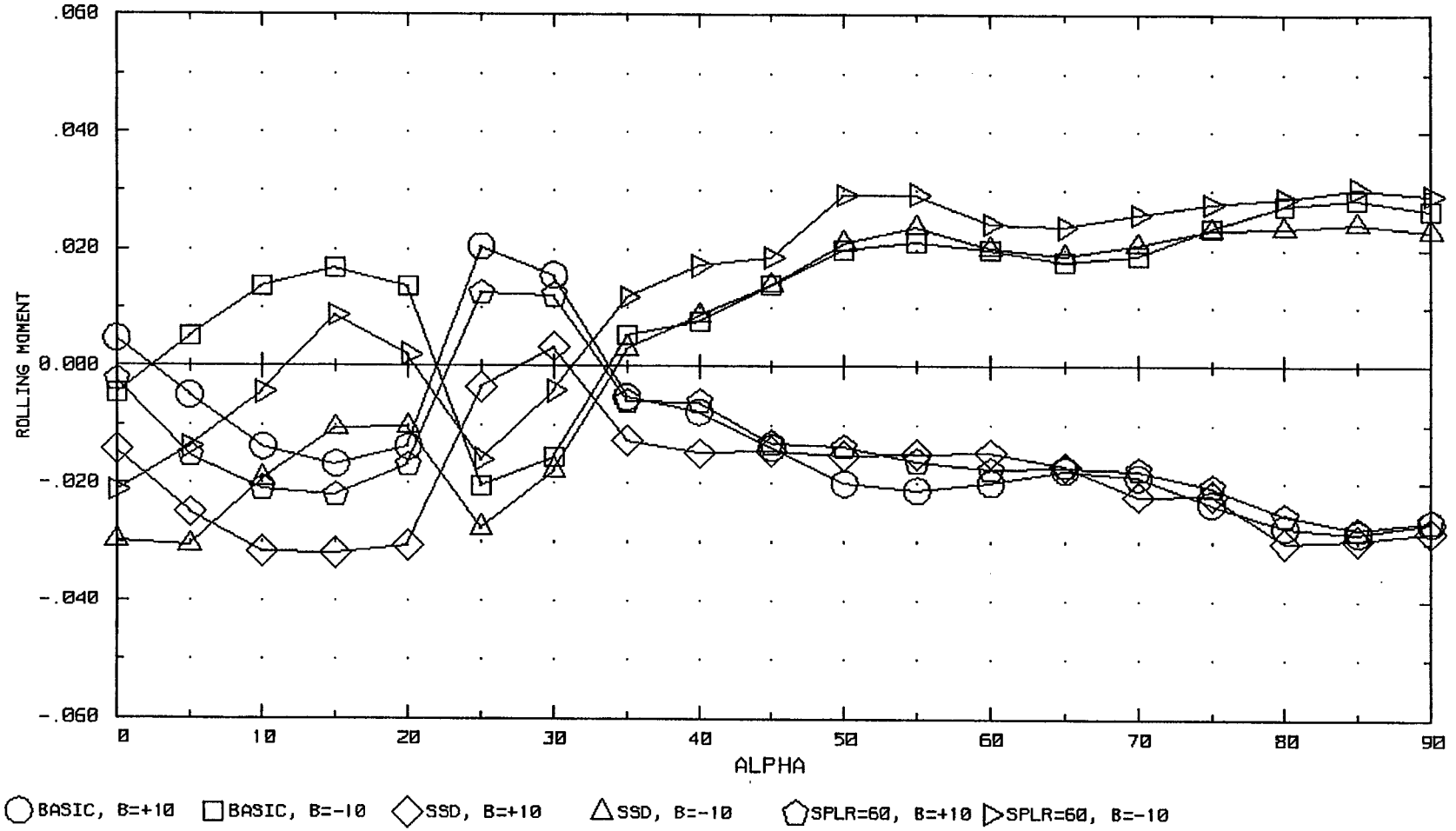

Figure 3-60. Effect of SSD on ICE 201 Lateral Stability (LEF=30, β=+10°).

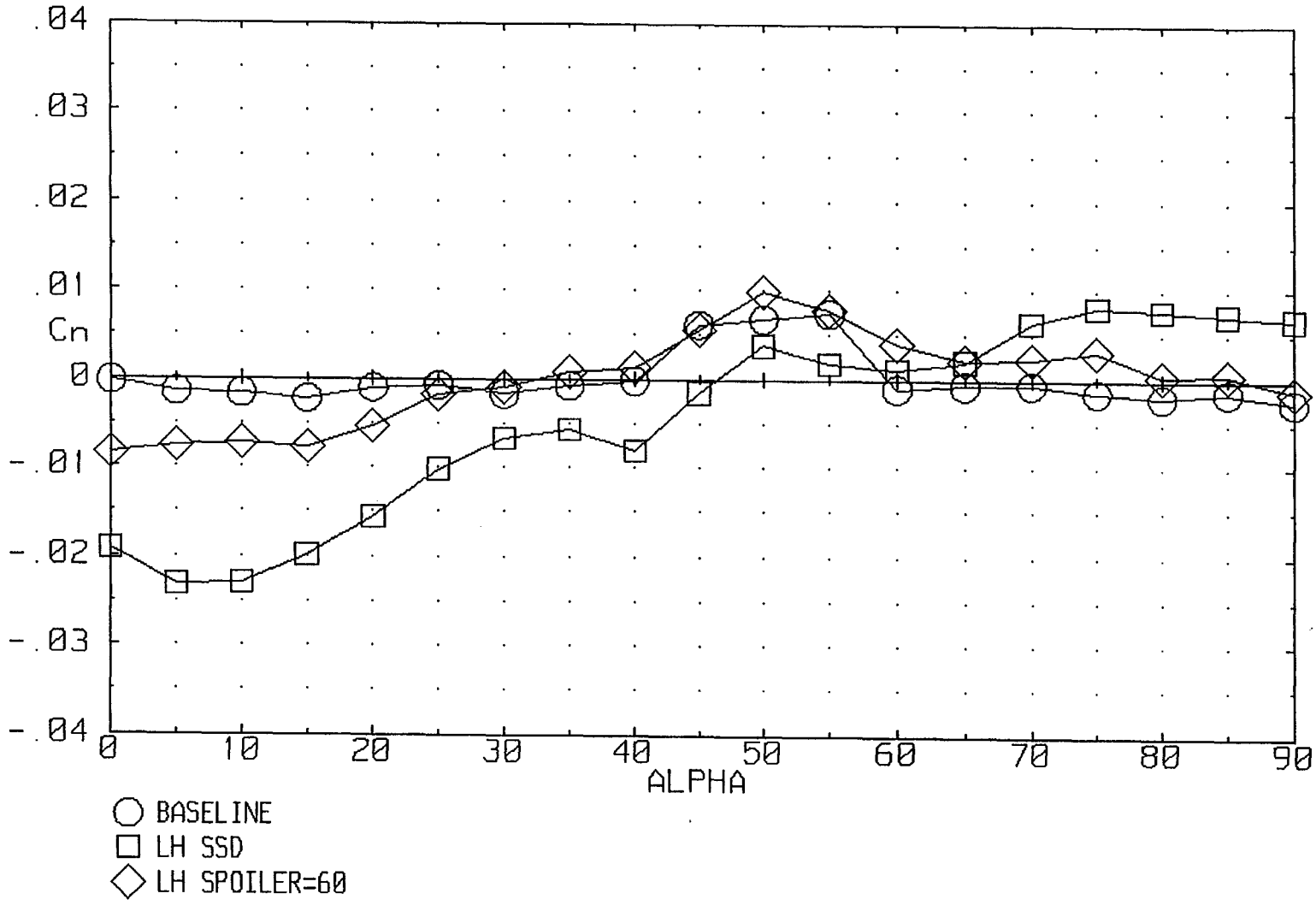

Figure 3-61. Yawing Moment due to SSD Deployment on the ICE 201 at Zero Sideslip (LEF=30).

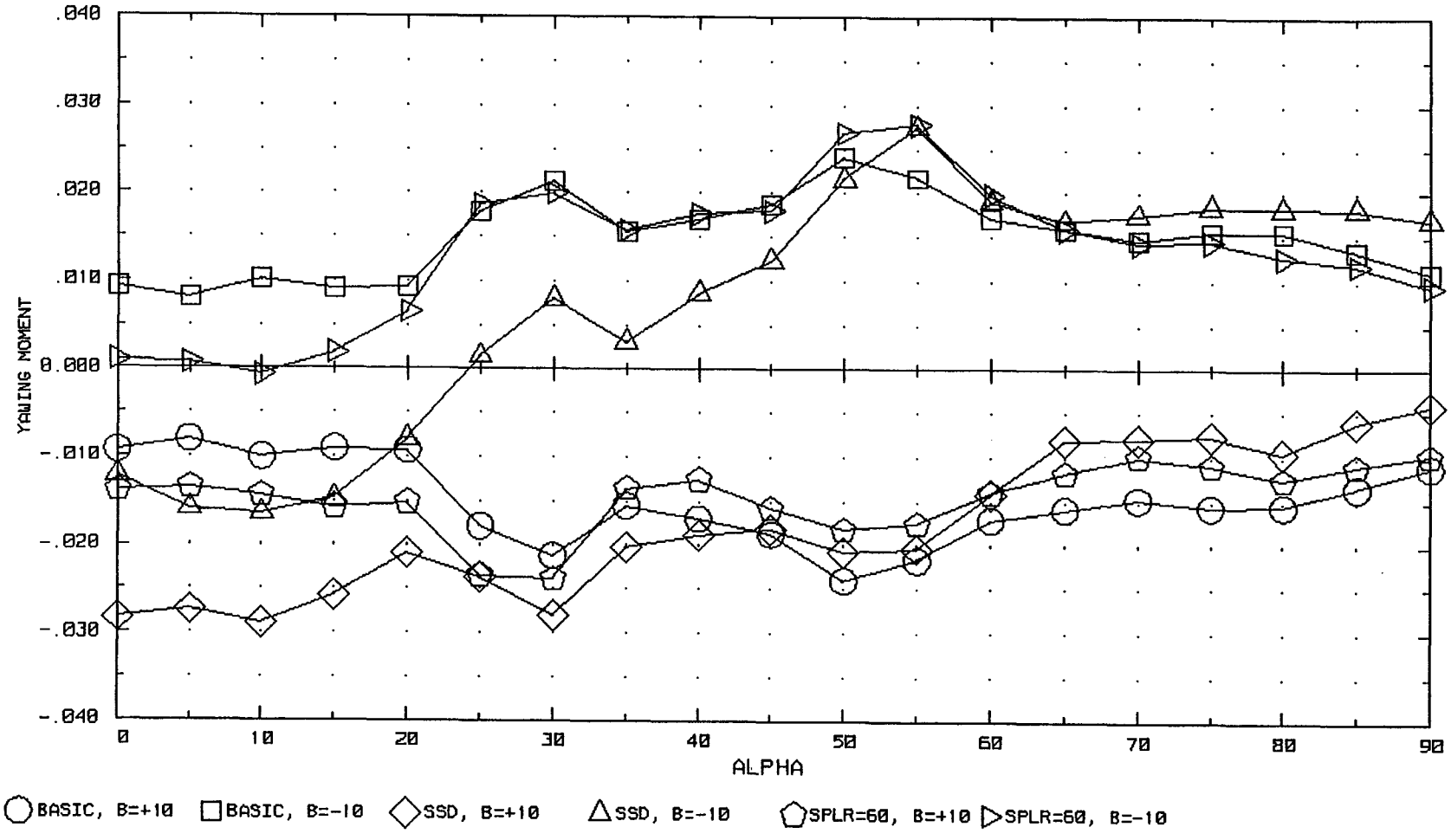

Figure 3-62. Effect of Left-Hand SSD on Directional Stability for the ICE 201 (LEF=30, β=+10°).

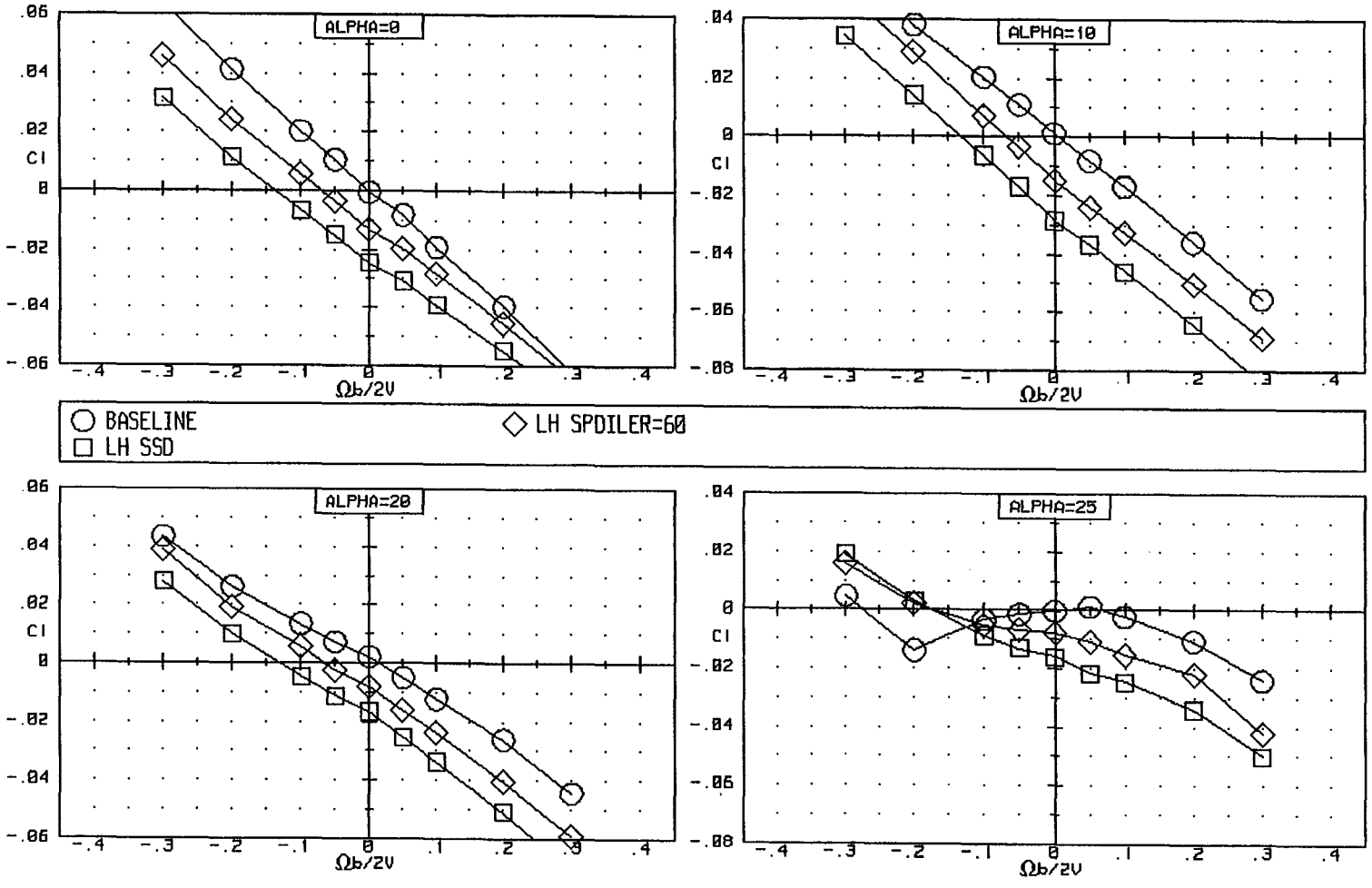

Figure 3-63. Effects of Spoiler or SSD on Rotational Rolling Moment for the ICE 201 (LEF=30, β=0°).

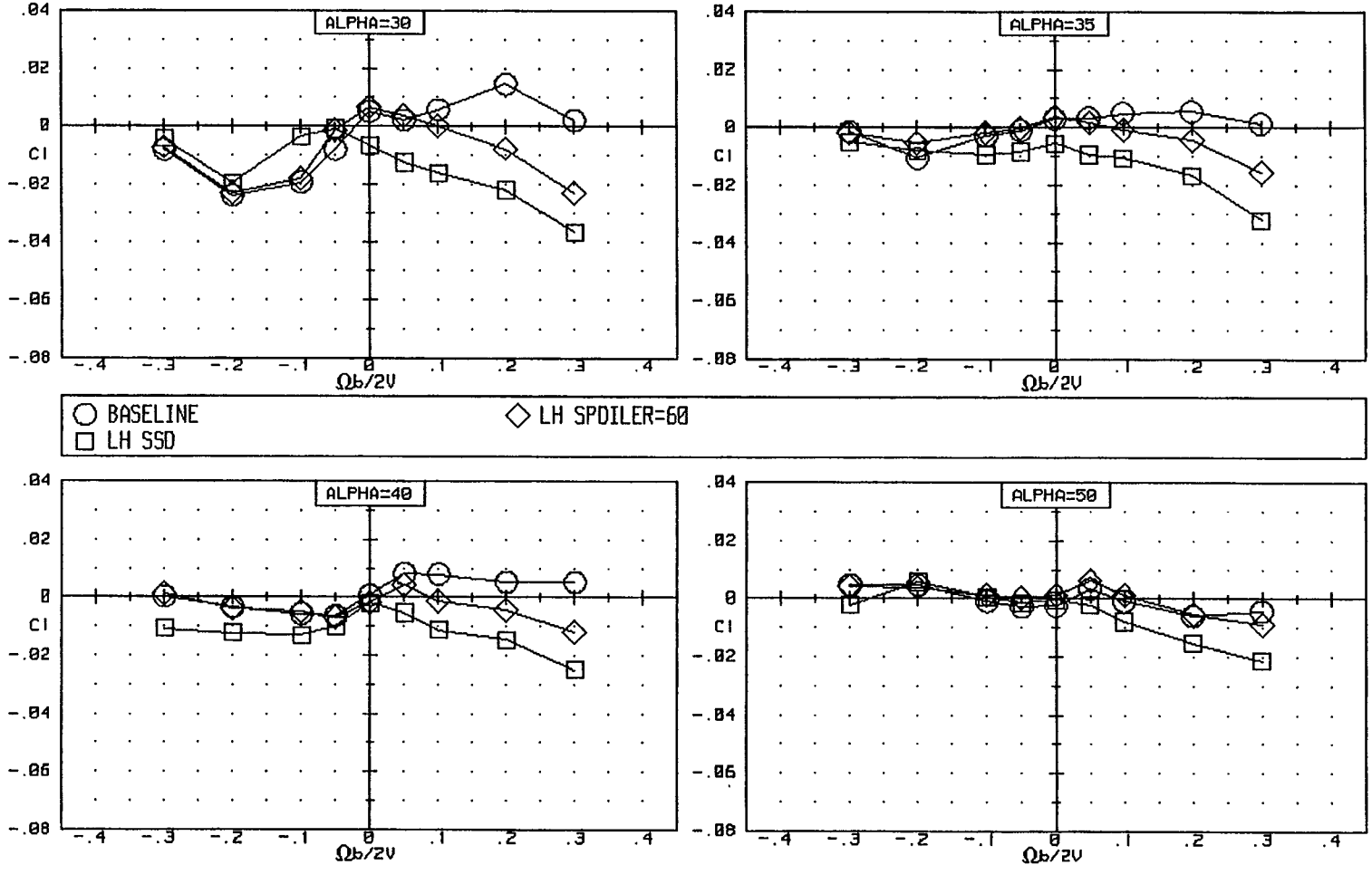

Figure 3-63. Continued.

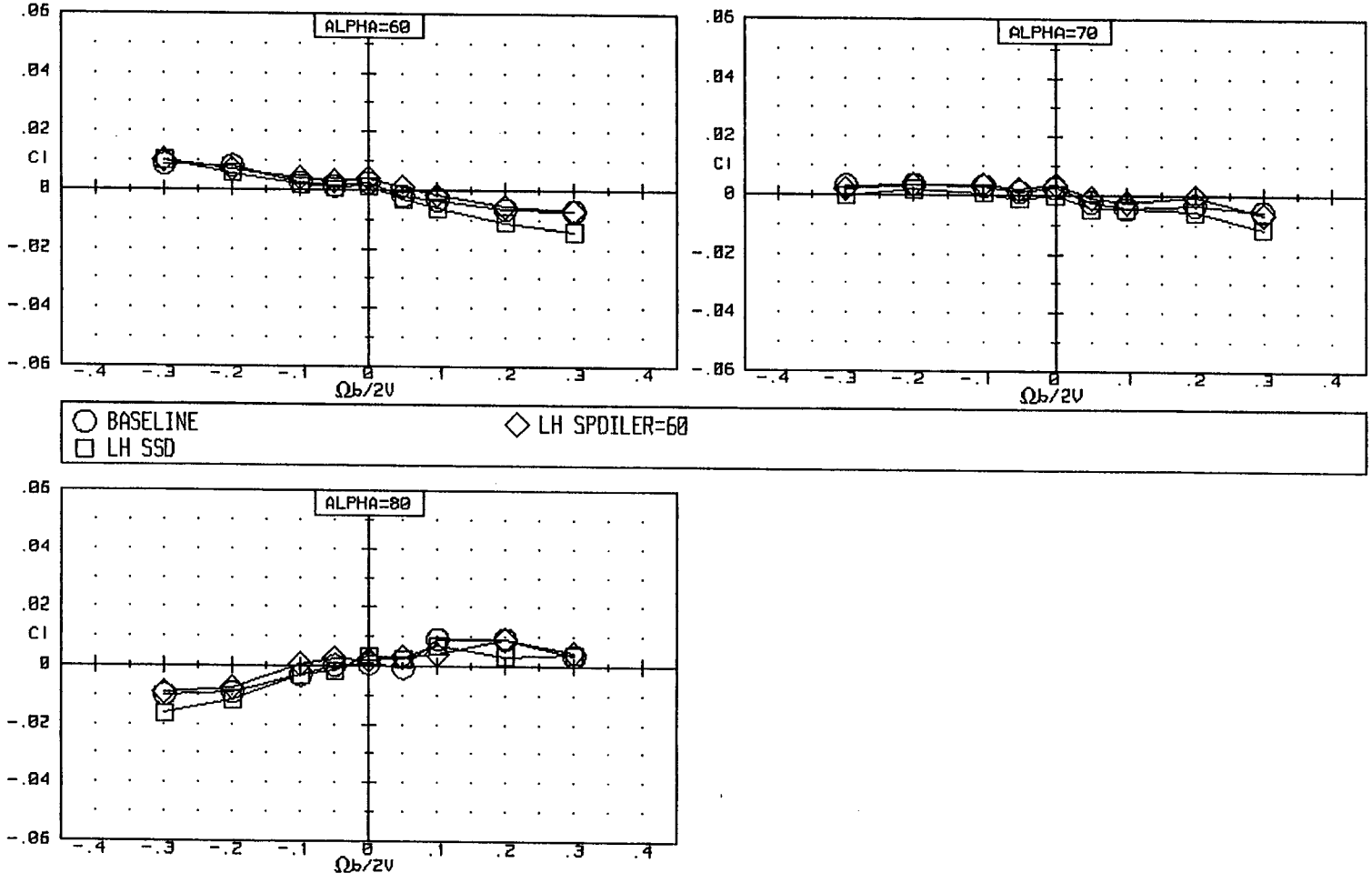

Figure 3-63. Concluded.

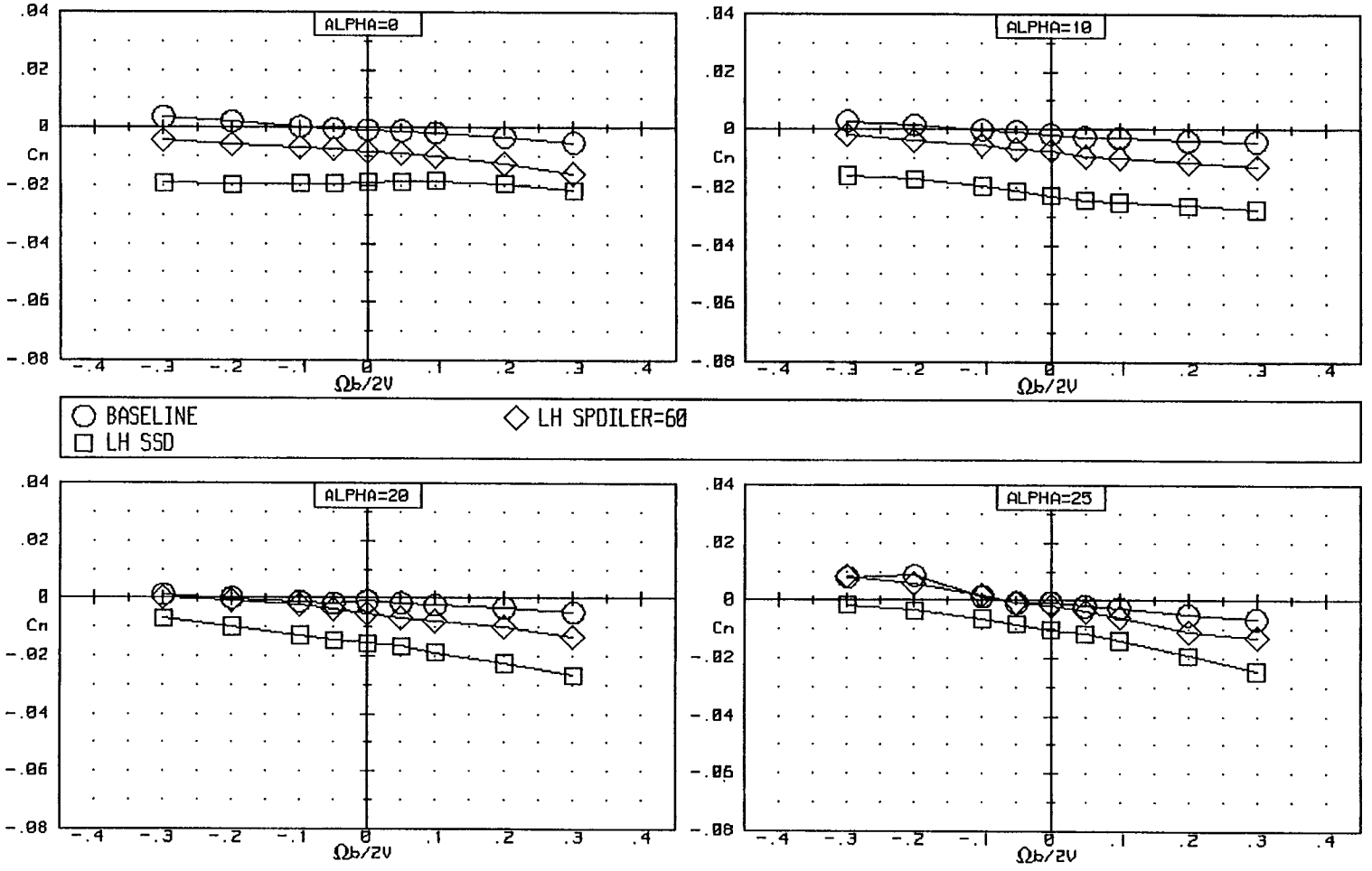

Figure 3-64. Effects of Spoiler or SSD on Rotational Rolling Moment for the ICE 201 (LEF=30, β=0°).

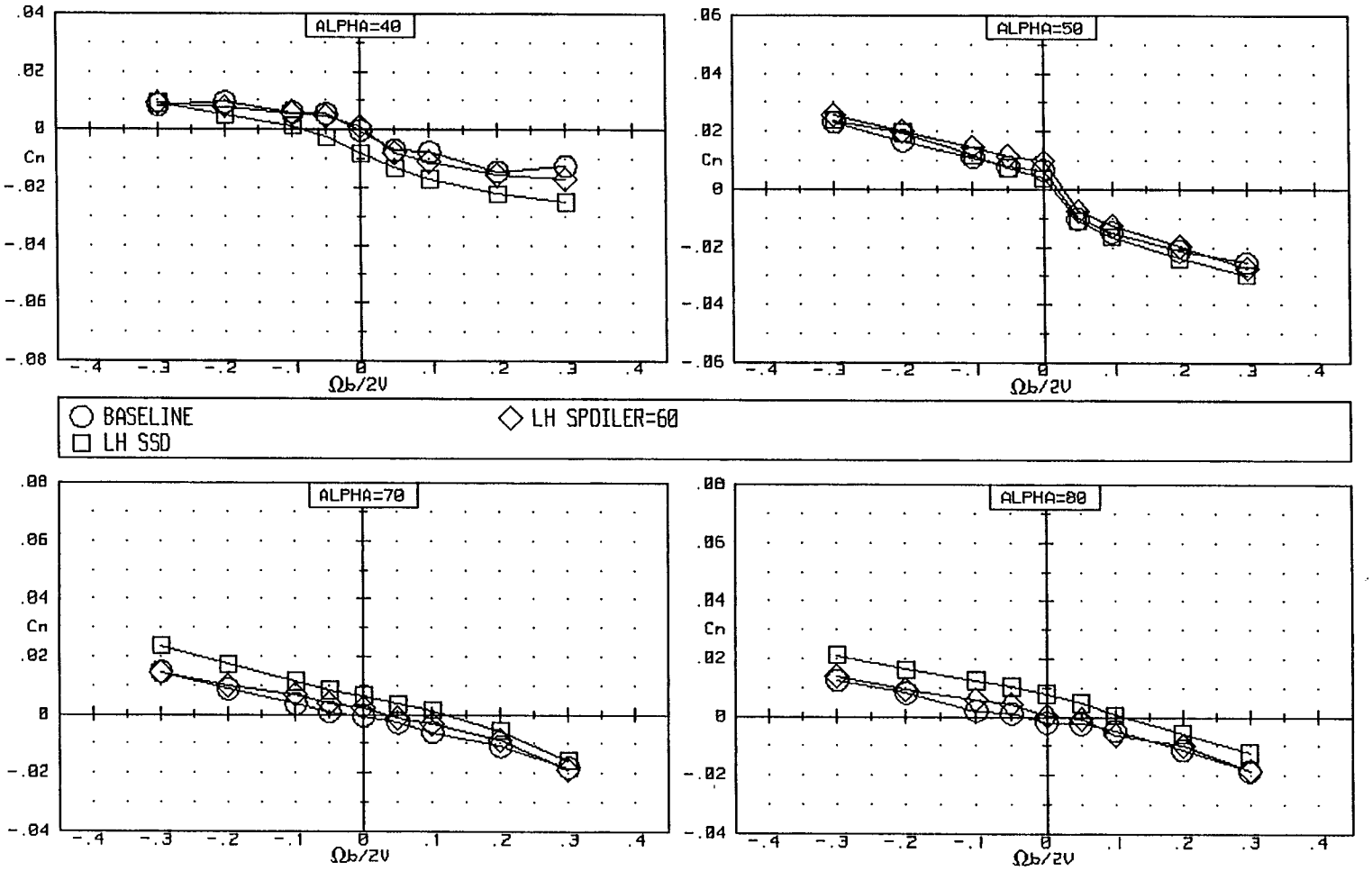

Figure 3-64. Concluded.

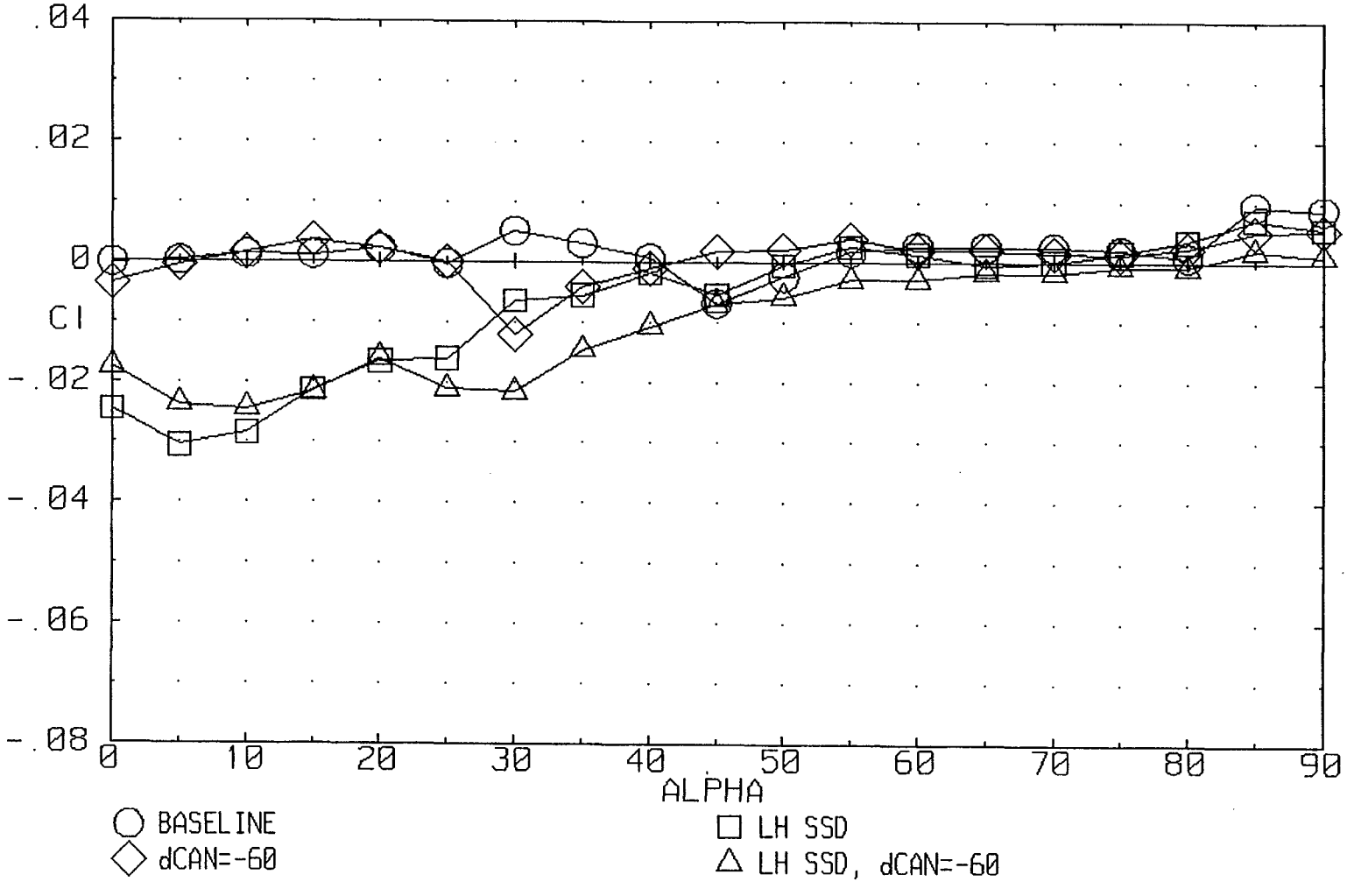

Figure 3-65. Effect of Canard/SSD Interactions on Rolling Moment for the ICE 201 (LEF=30, β=0°).

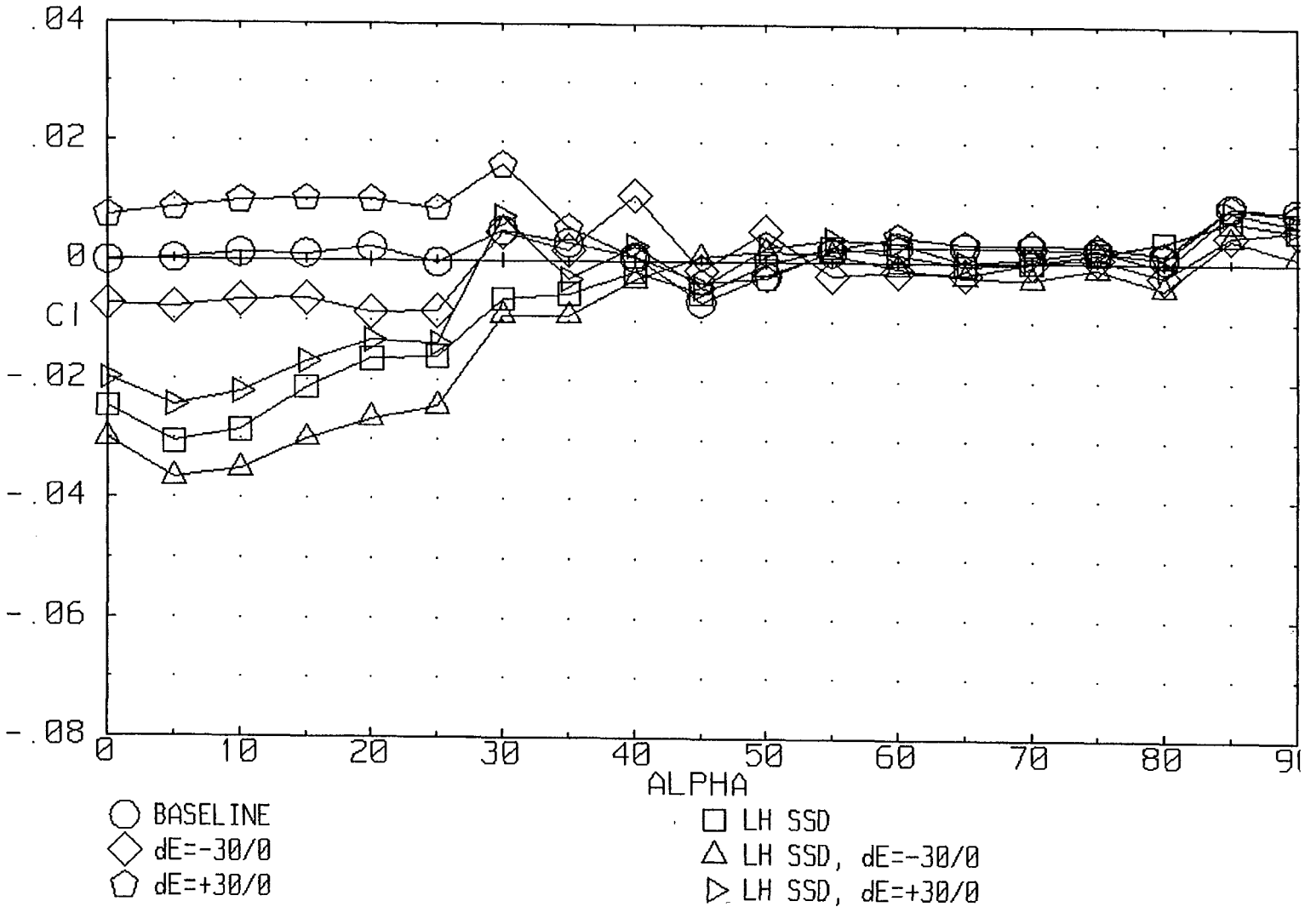

Figure 3-66. Effect of SSD/Elevon Interactions on Rolling Moment for the ICE 201 (LEF=30, β=0°).

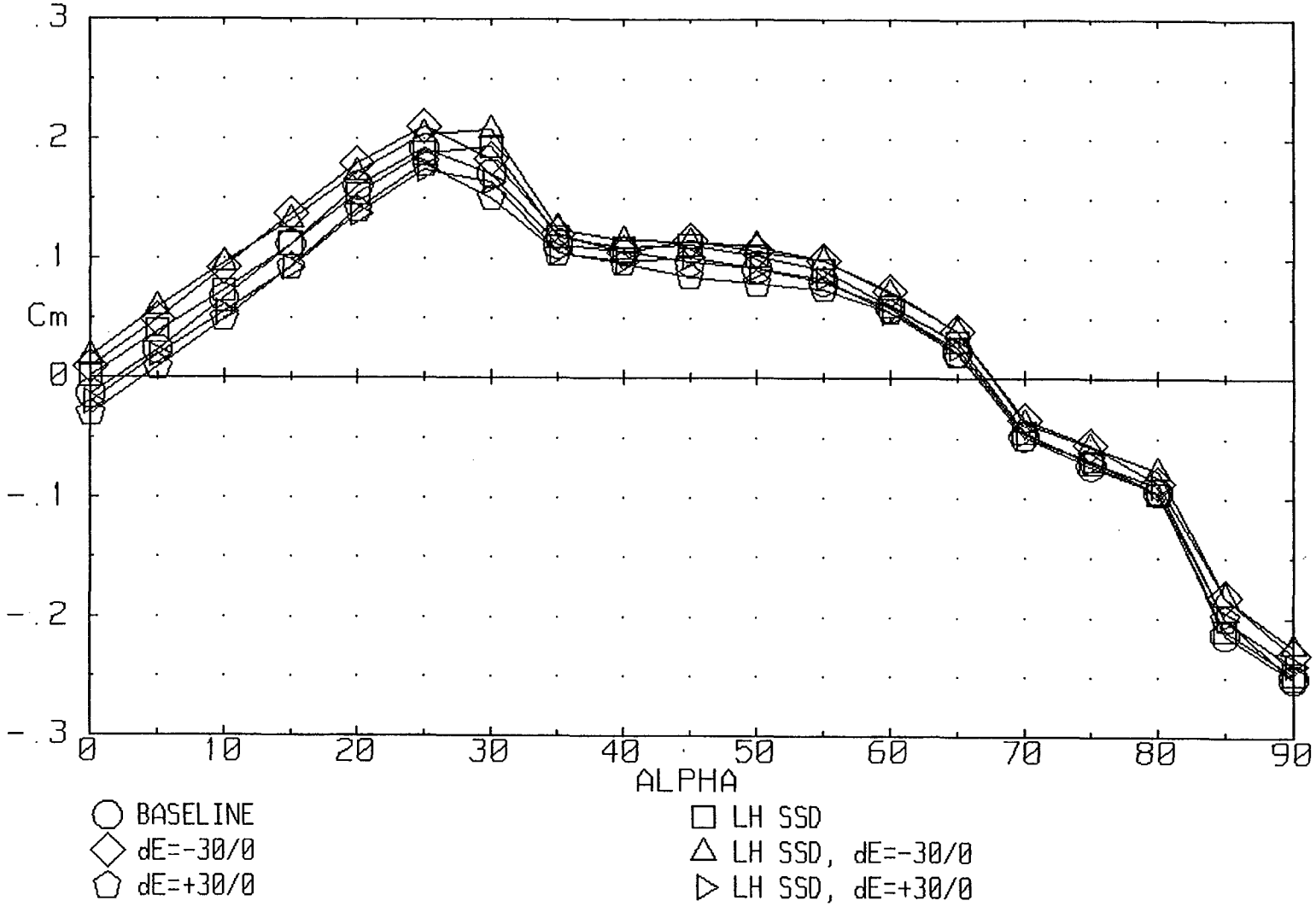

Figure 3-67. Effect of SSD/Elevon Interactions on Pitching Moment for the ICE 201 (LEF=30, β=0°).

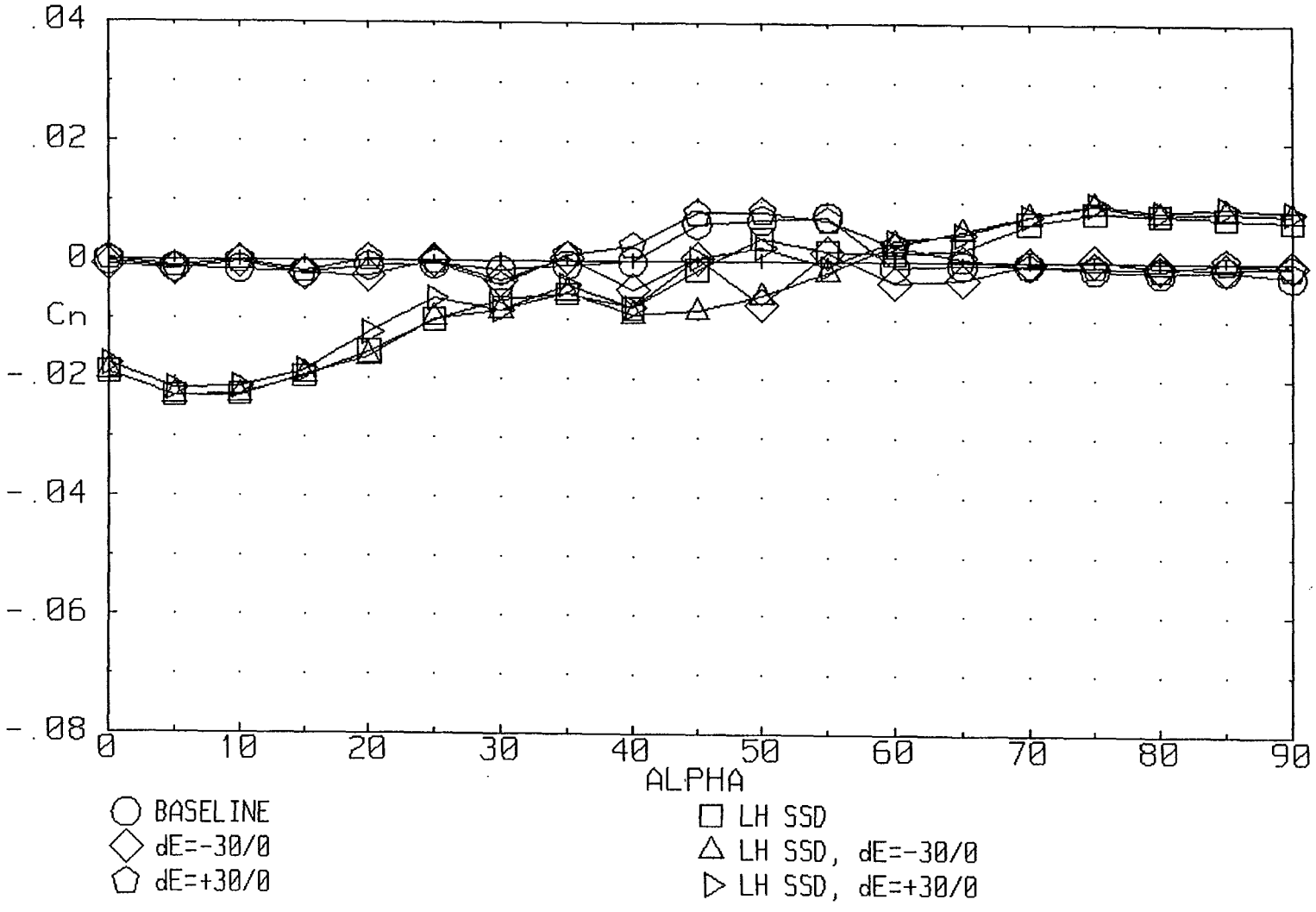

Figure 3-68. Effect of SSD/Elevon Interactions on Yawing Moment for the ICE 201 (LEF=30, β=0°).

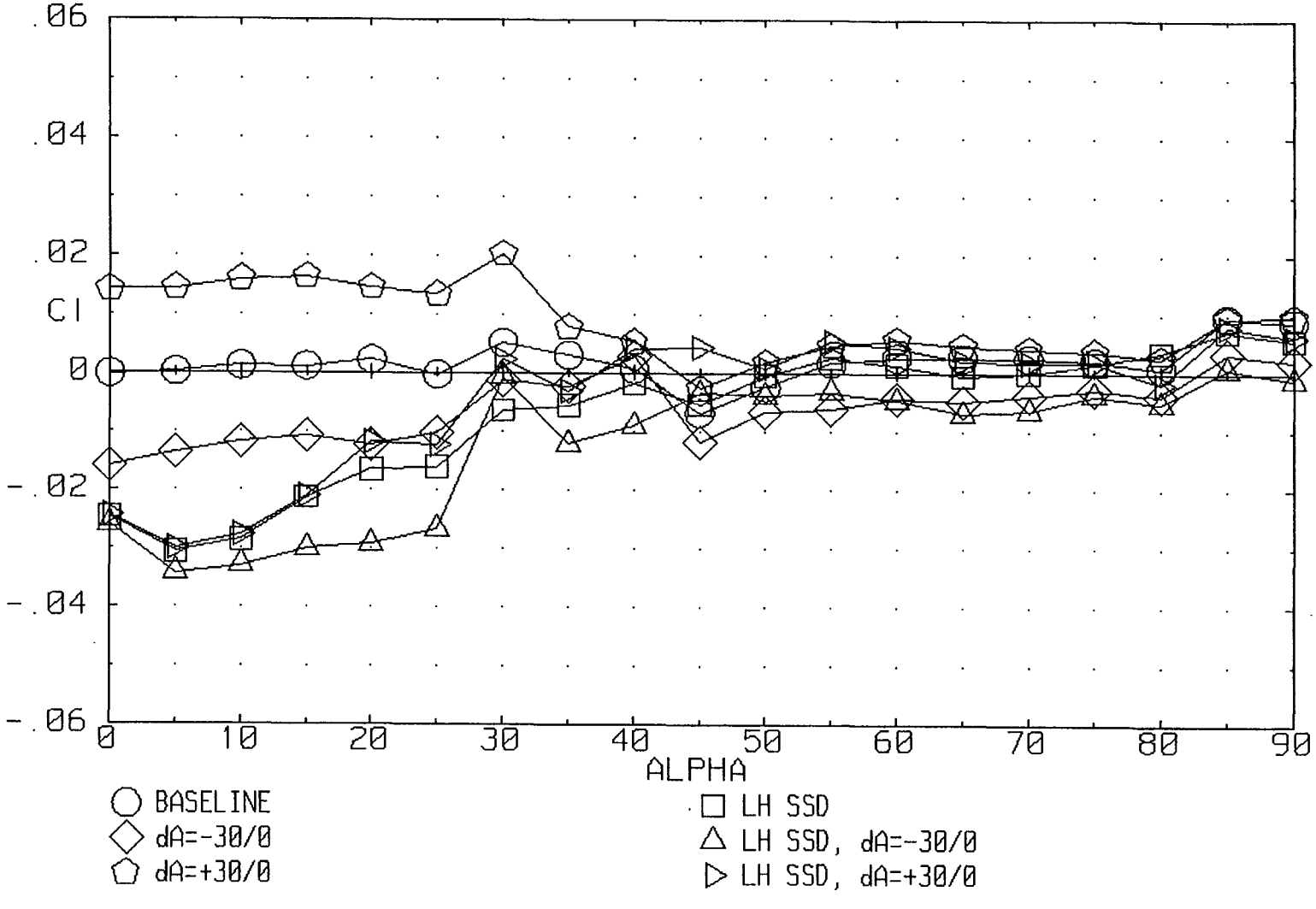

Figure 3-69. Effect of SSD/Aileron Interactions on Rolling Moment for the ICE 201 (LEF=30, β=0°).

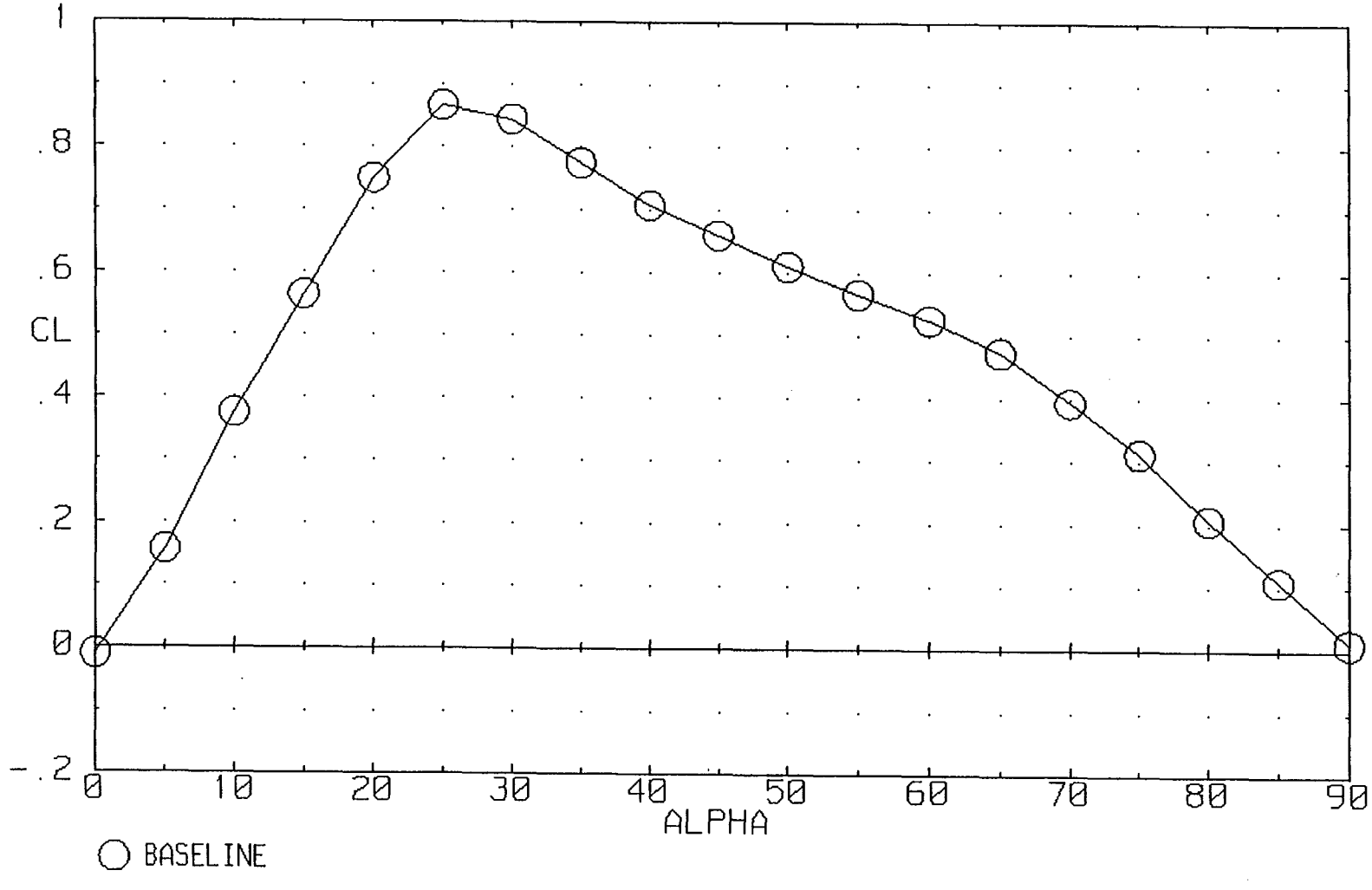

Figure 3-70. Lift Coefficient for the ICE 101 at Zero Sideslip (LEF=0).

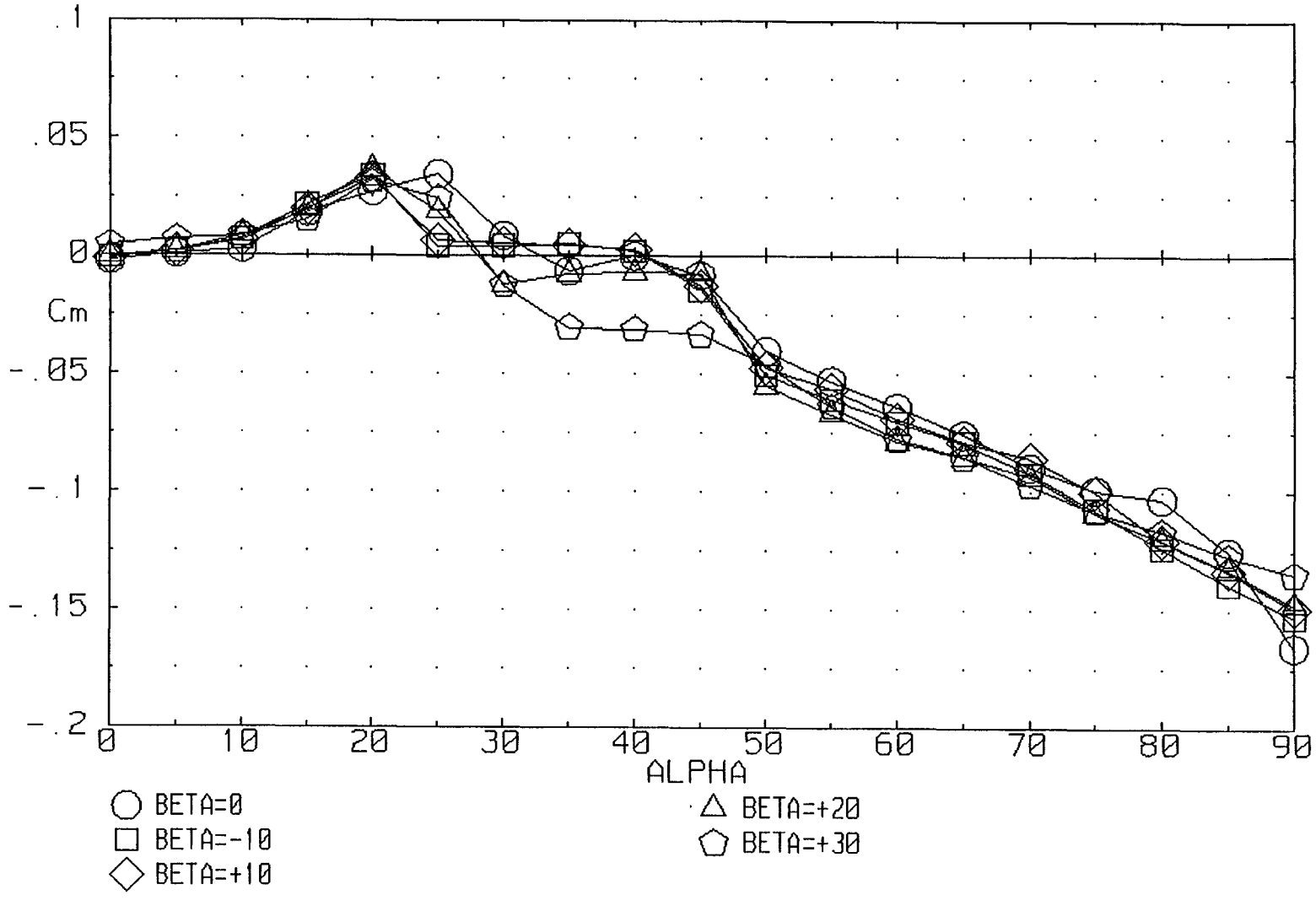

Figure 3-71. Static Pitching Moment for the ICE 101 at Zero and Nonzero Sideslip Angles (LEF=0).

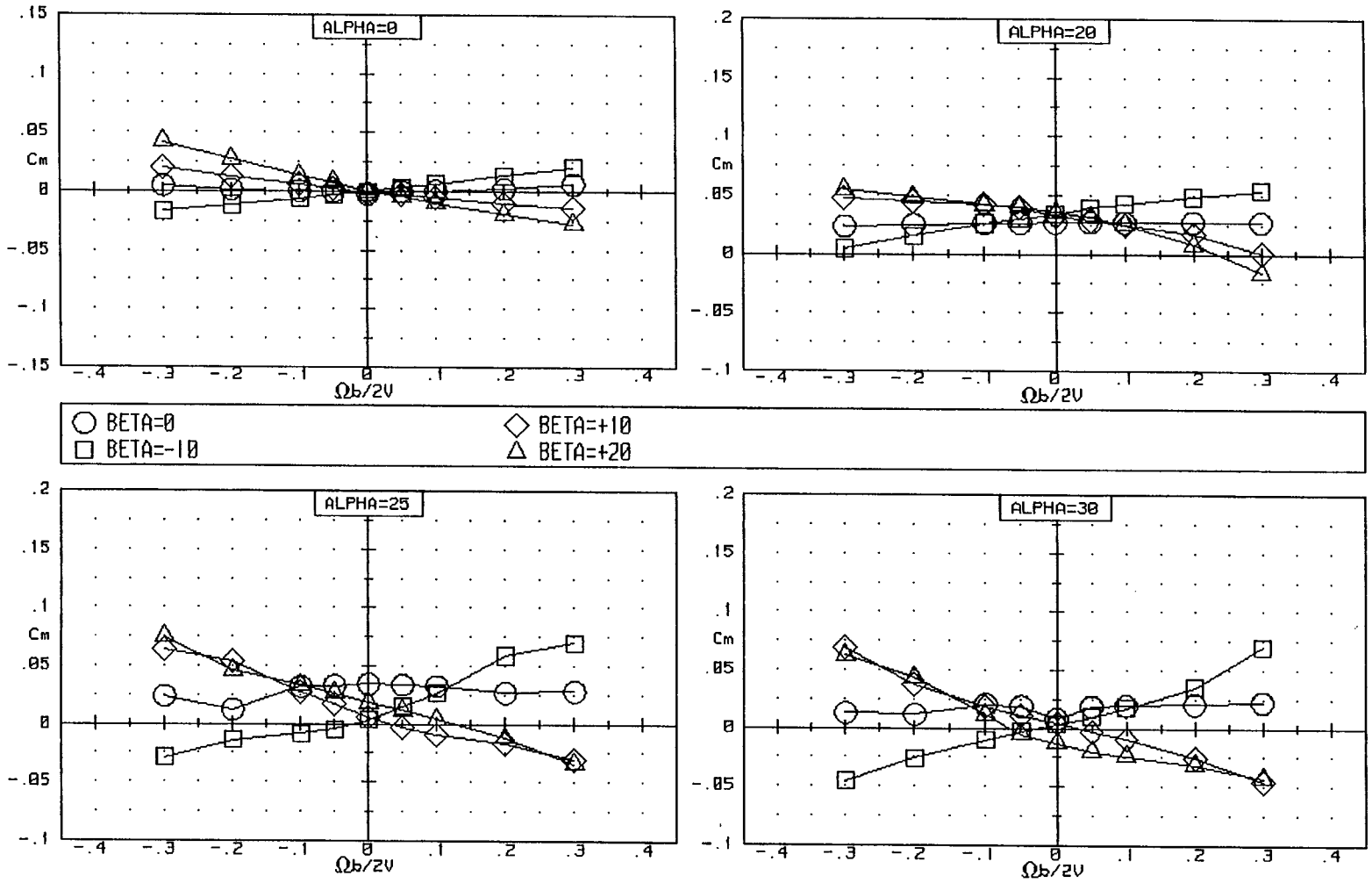

Figure 3-72. Effect of Rotation Rate and Sideslip Angle on Pitching Moment for the ICE 101 (LEF=0).

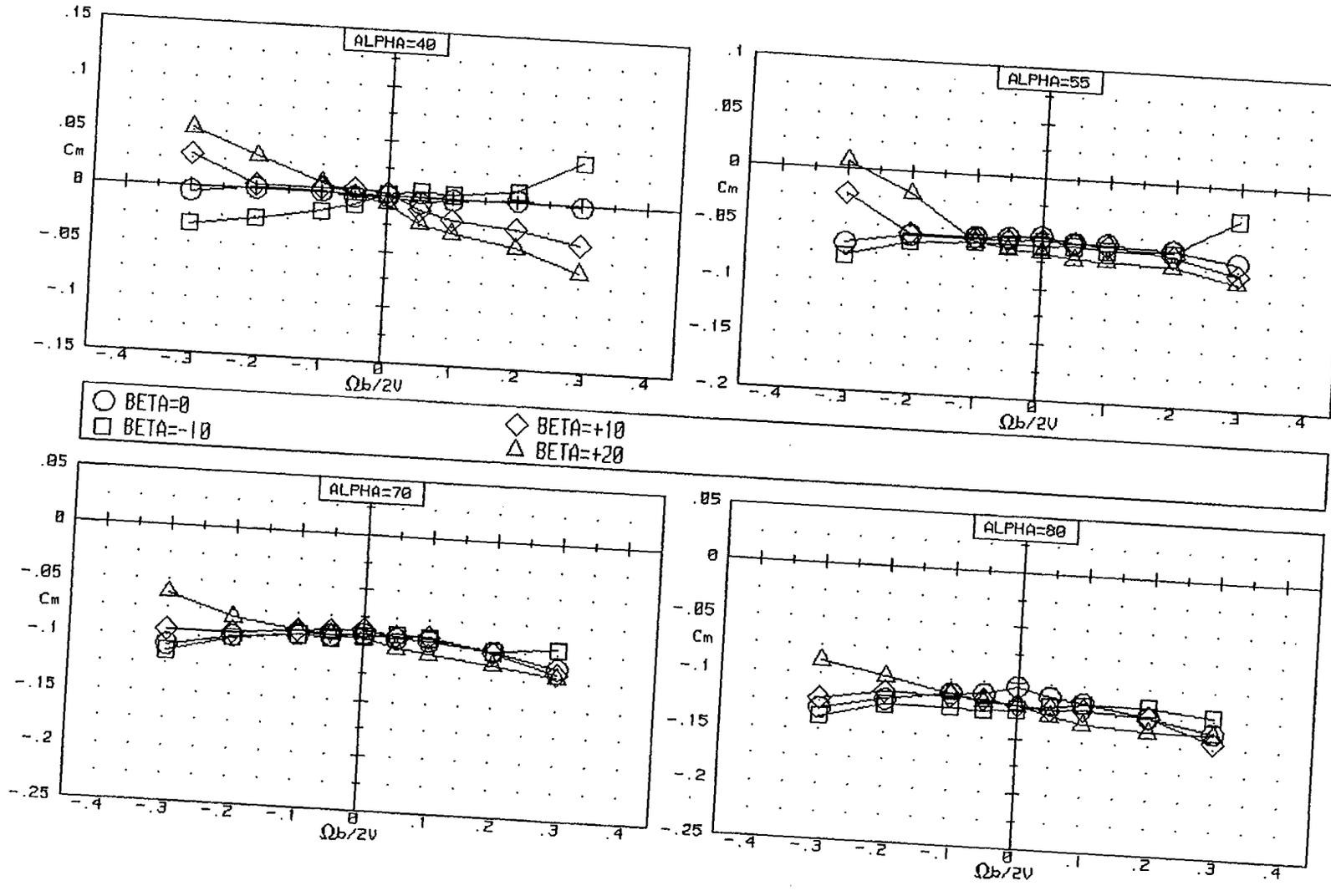

Figure 3-72. Concluded.

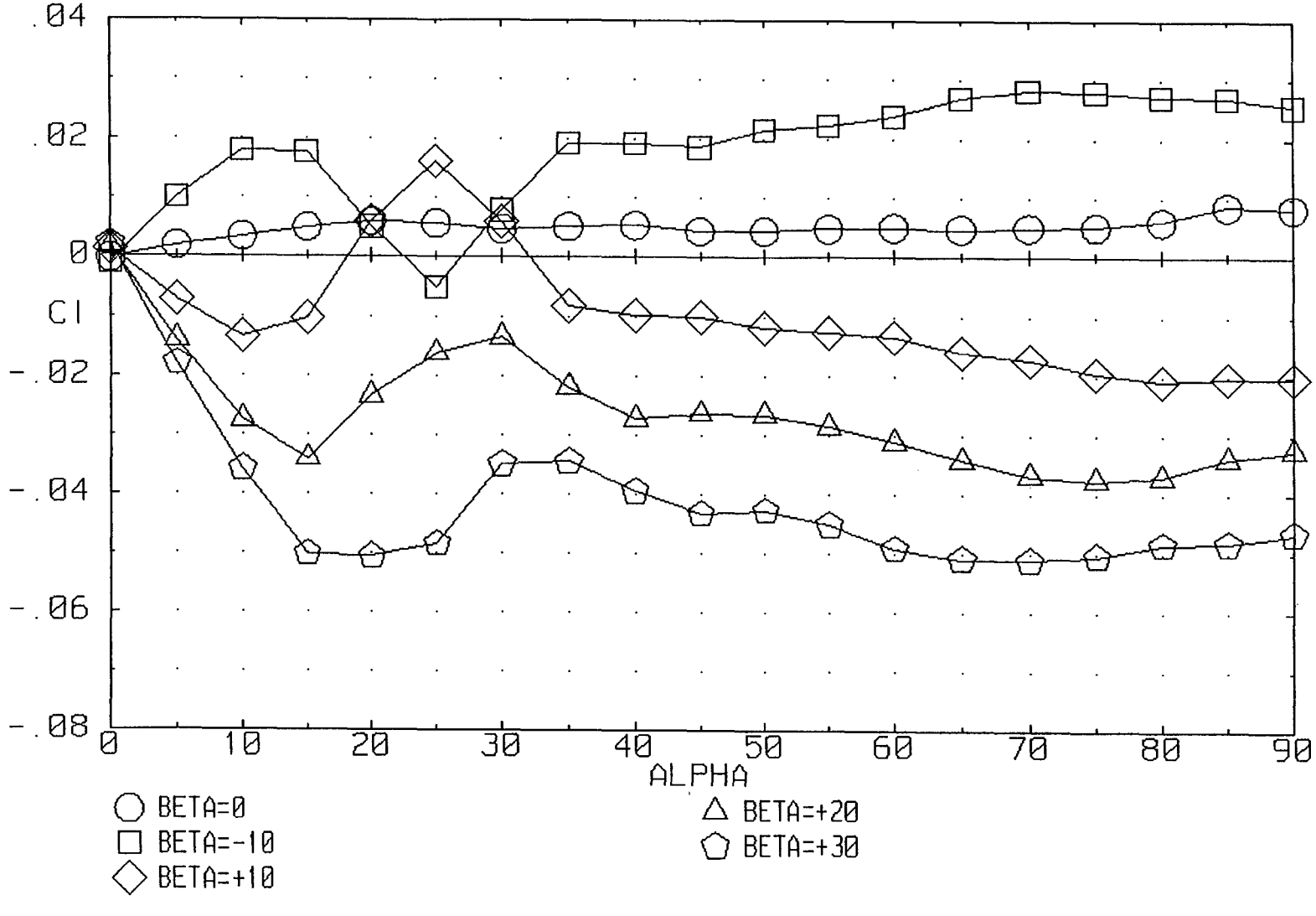

Figure 3-73. Effect of Sideslip Angle on the Static Rolling Moment Characteristics for the ICE 101 (LEF=0).

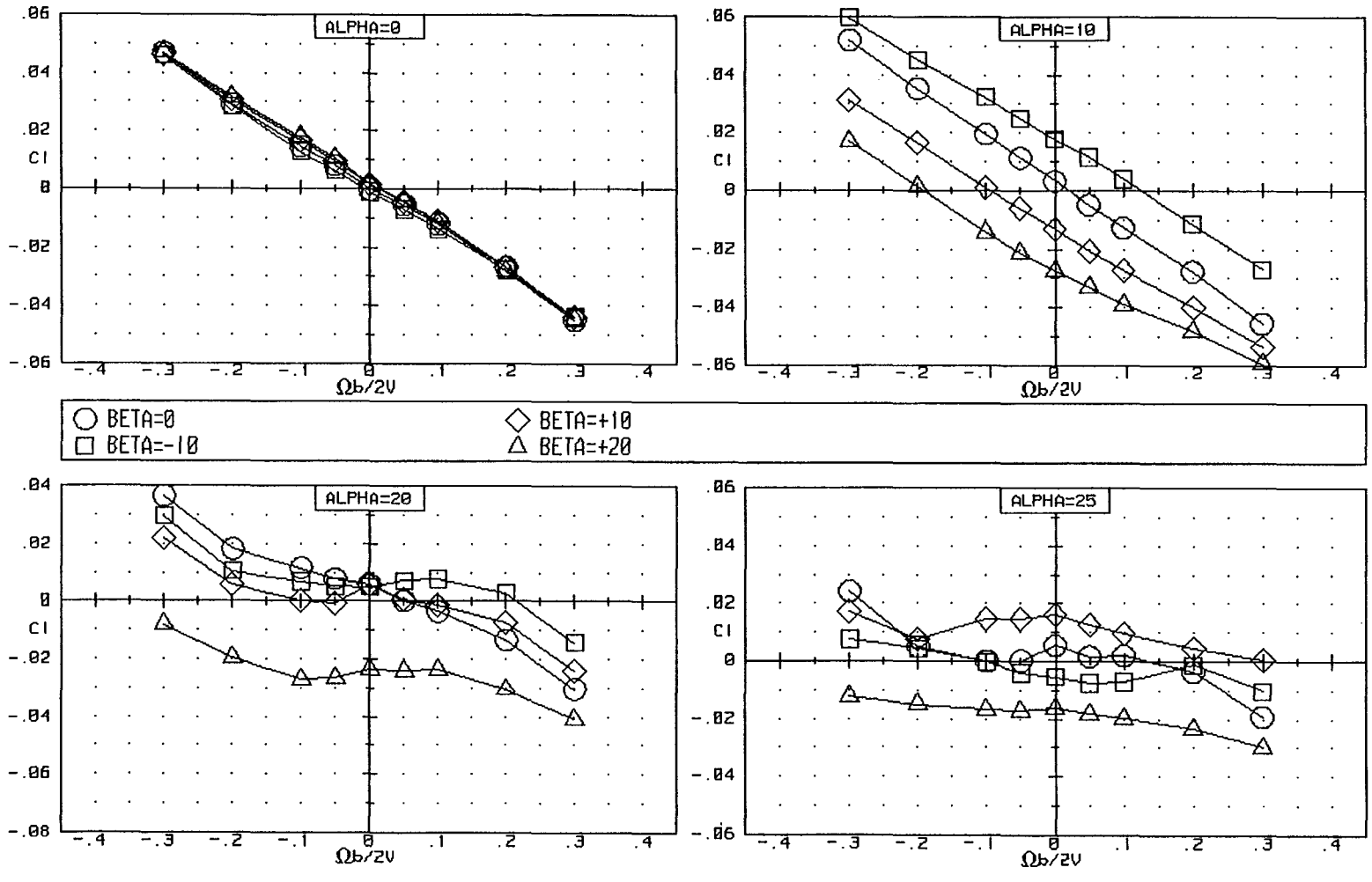

Figure 3-74. Effect of Rotation Rate and Sideslip Angle on the Rolling Moment for the ICE 101 (LEF=0).

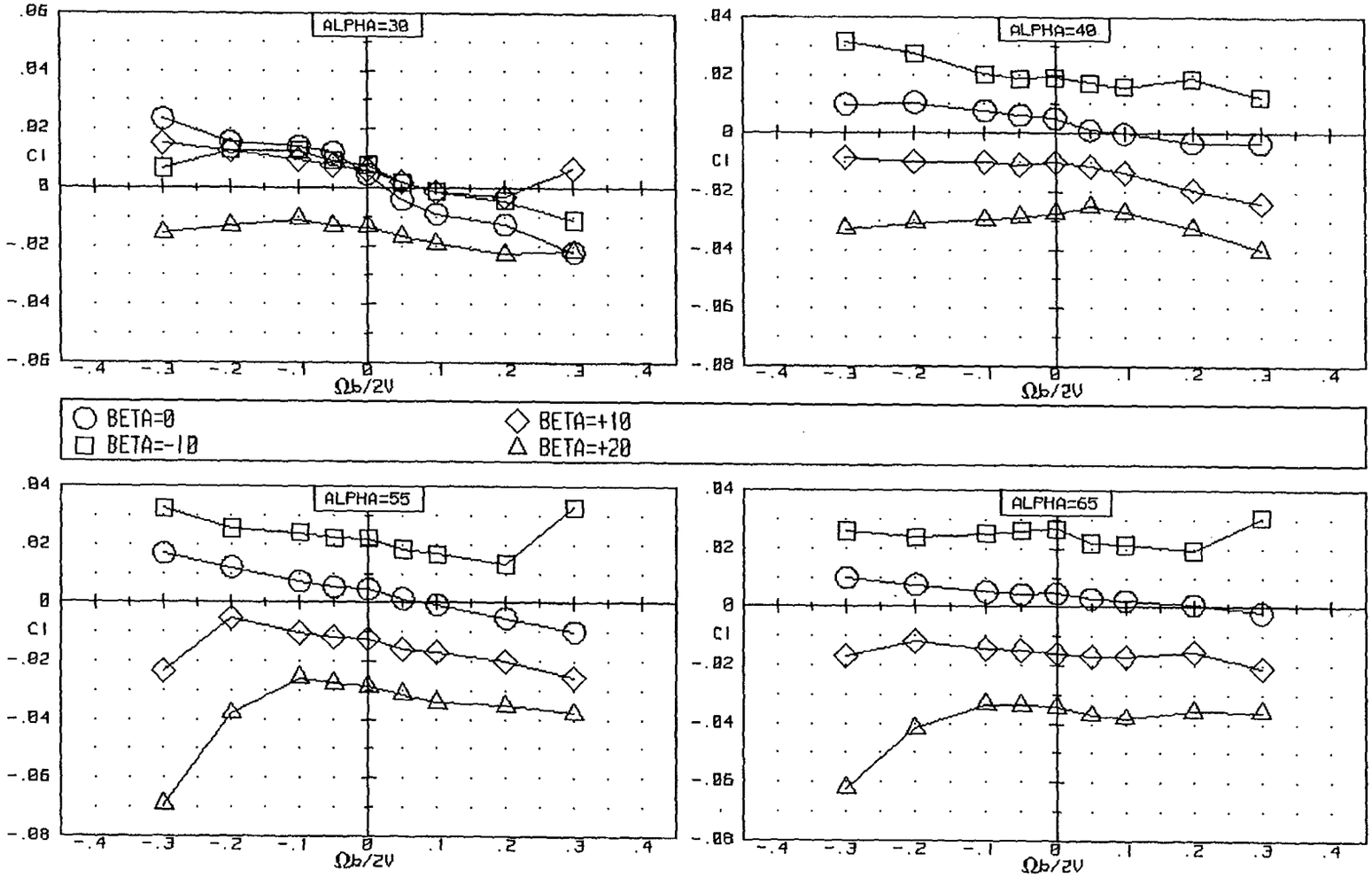

Figure 3-74. Continued.

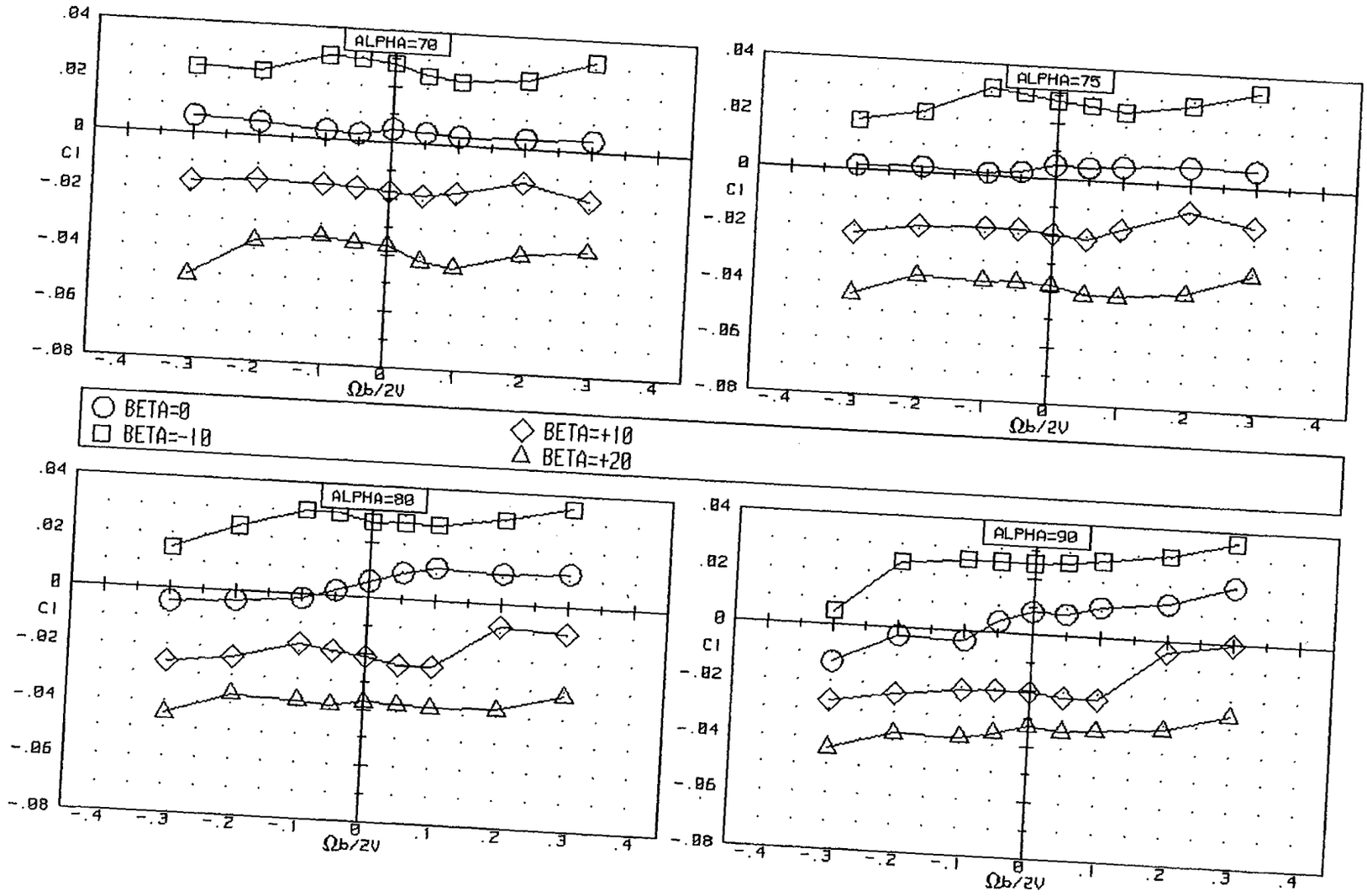

Figure 3-74. Concluded.

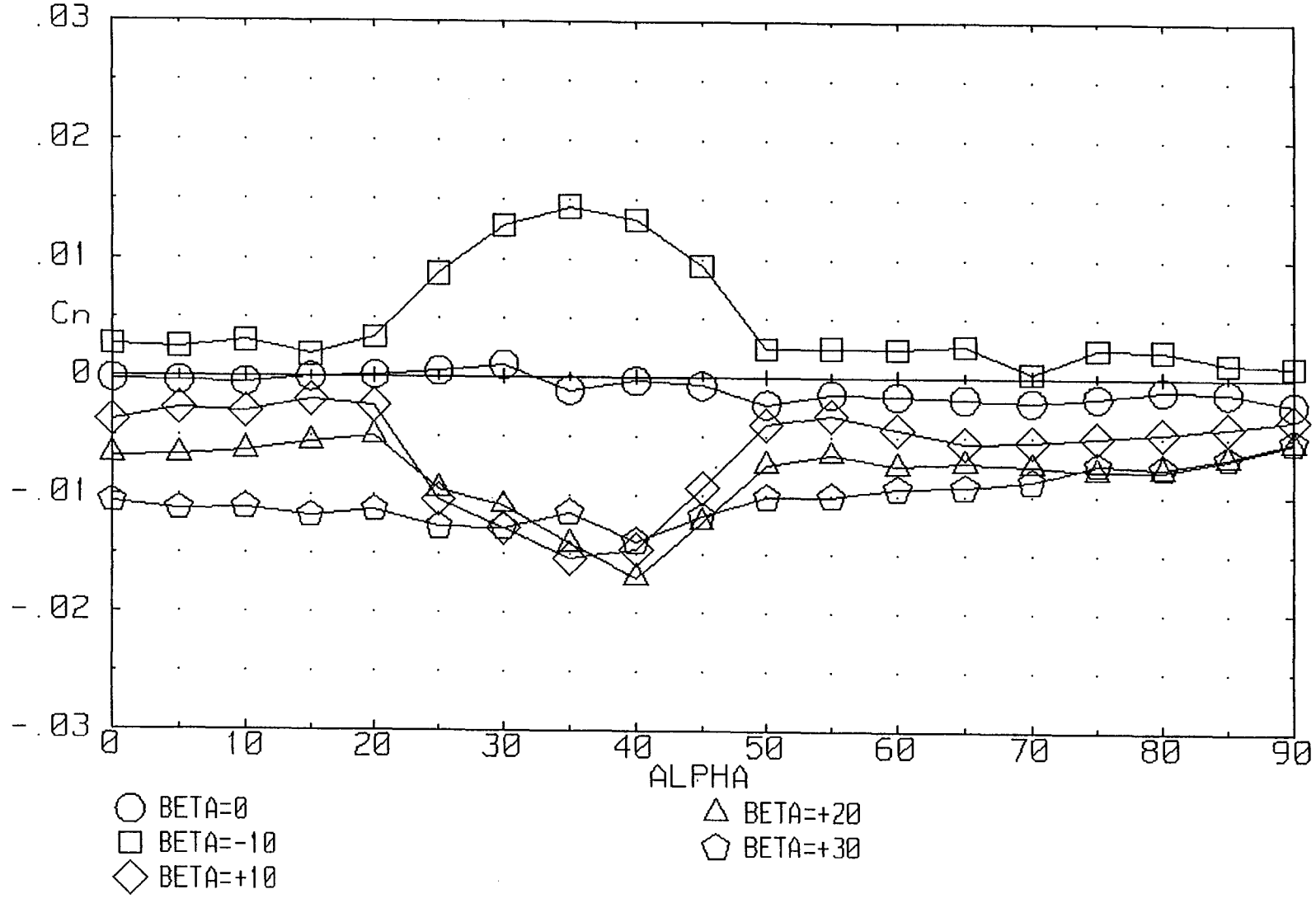

Figure 3-75. Effect of Sideslip Angle on Static Yawing Moment Characteristics for the ICE 101 (LEF=0).

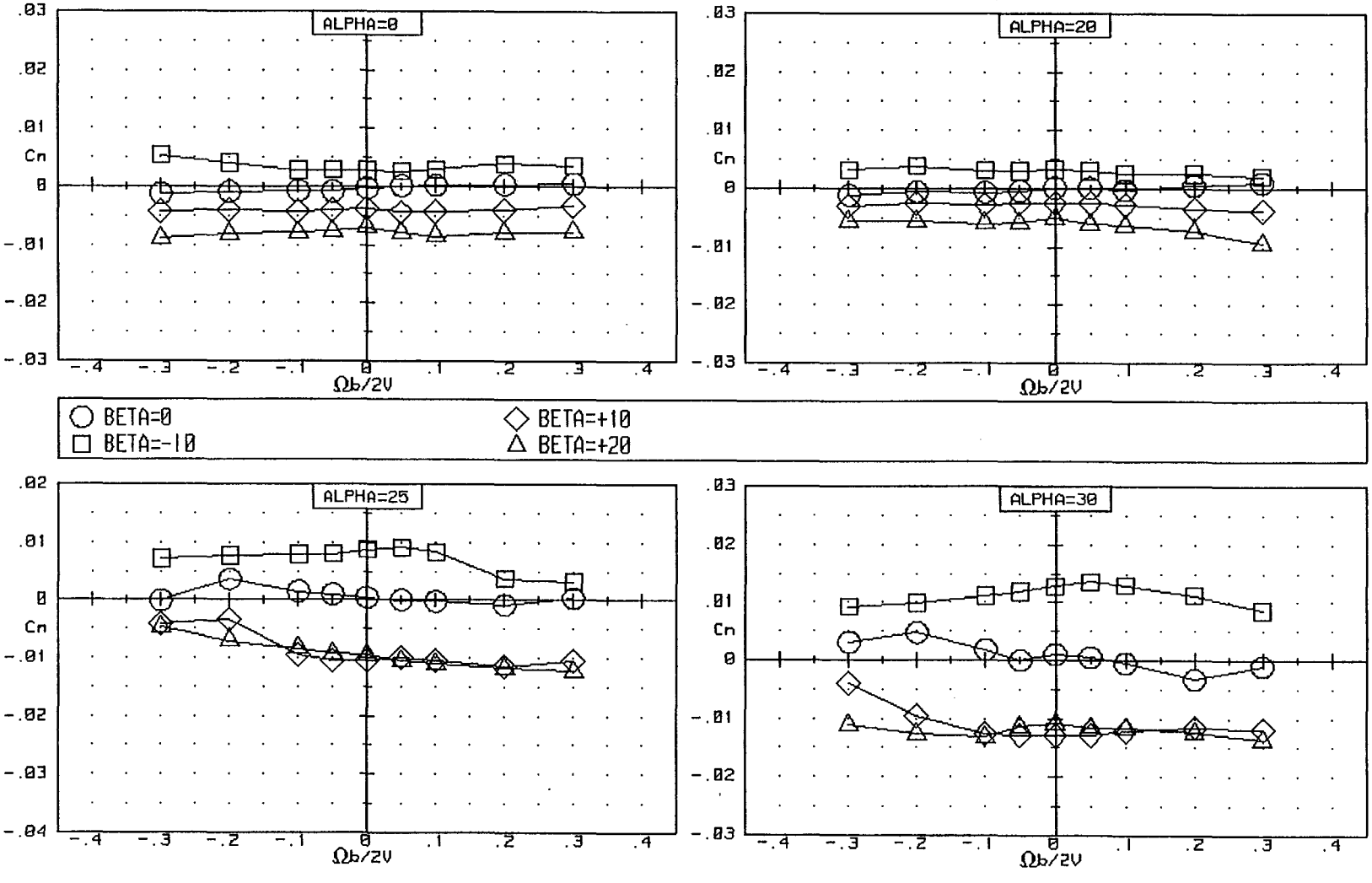

Figure 3-76. Effect of Rotation Rate and Sideslip Angle on Yawing Moment for the ICE 101 (LEF=0).

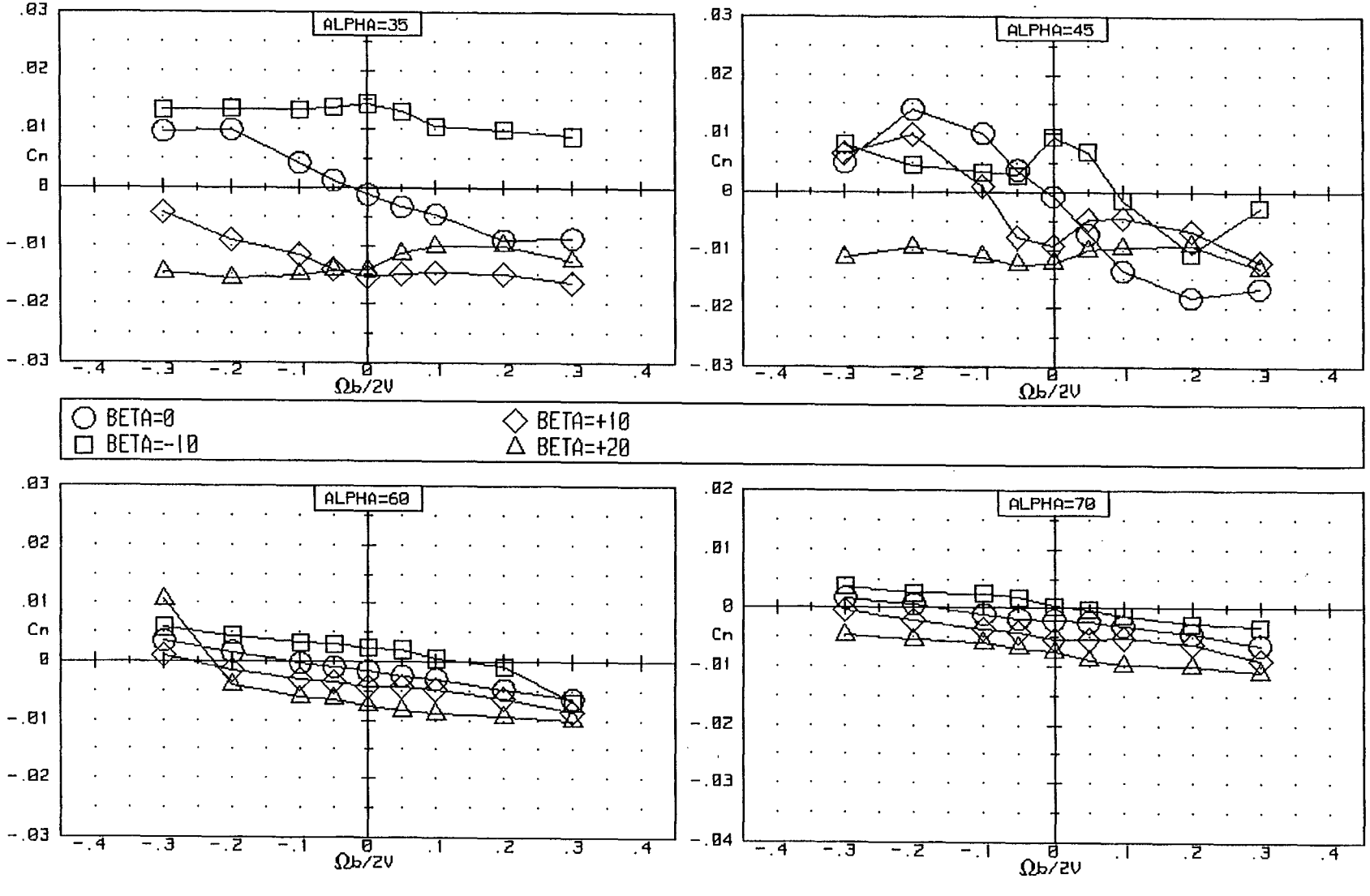

Figure 3-76. Continued.

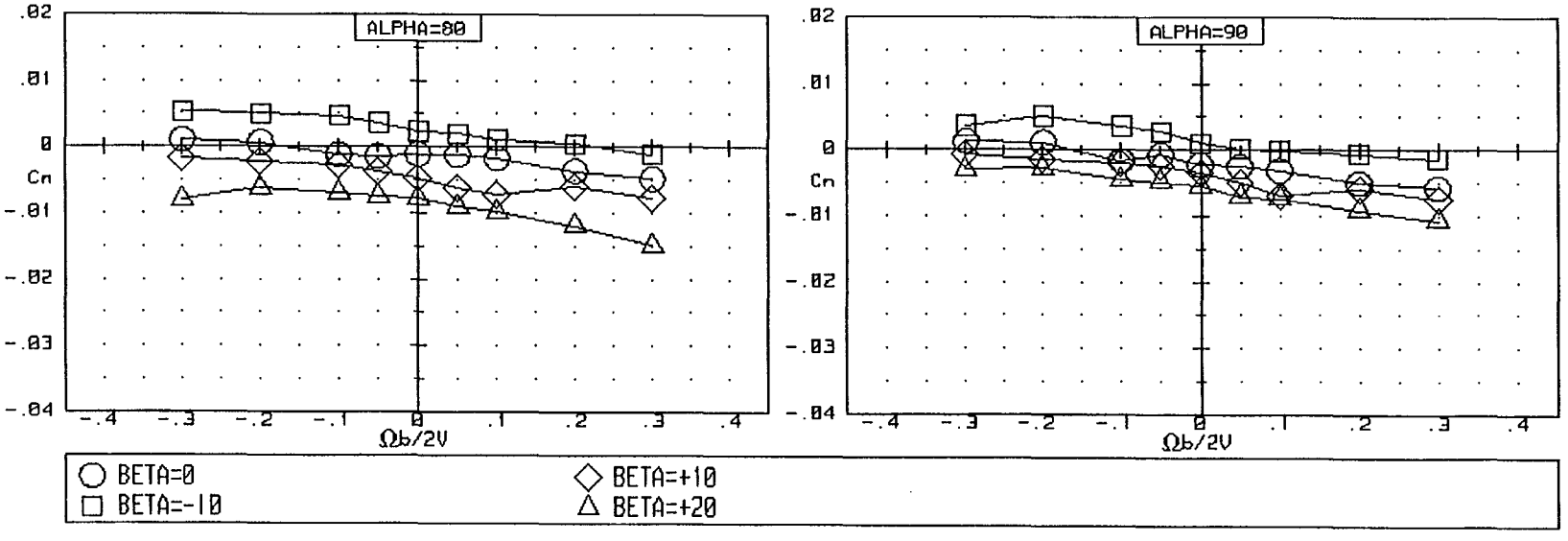

Figure 3-76. Concluded.

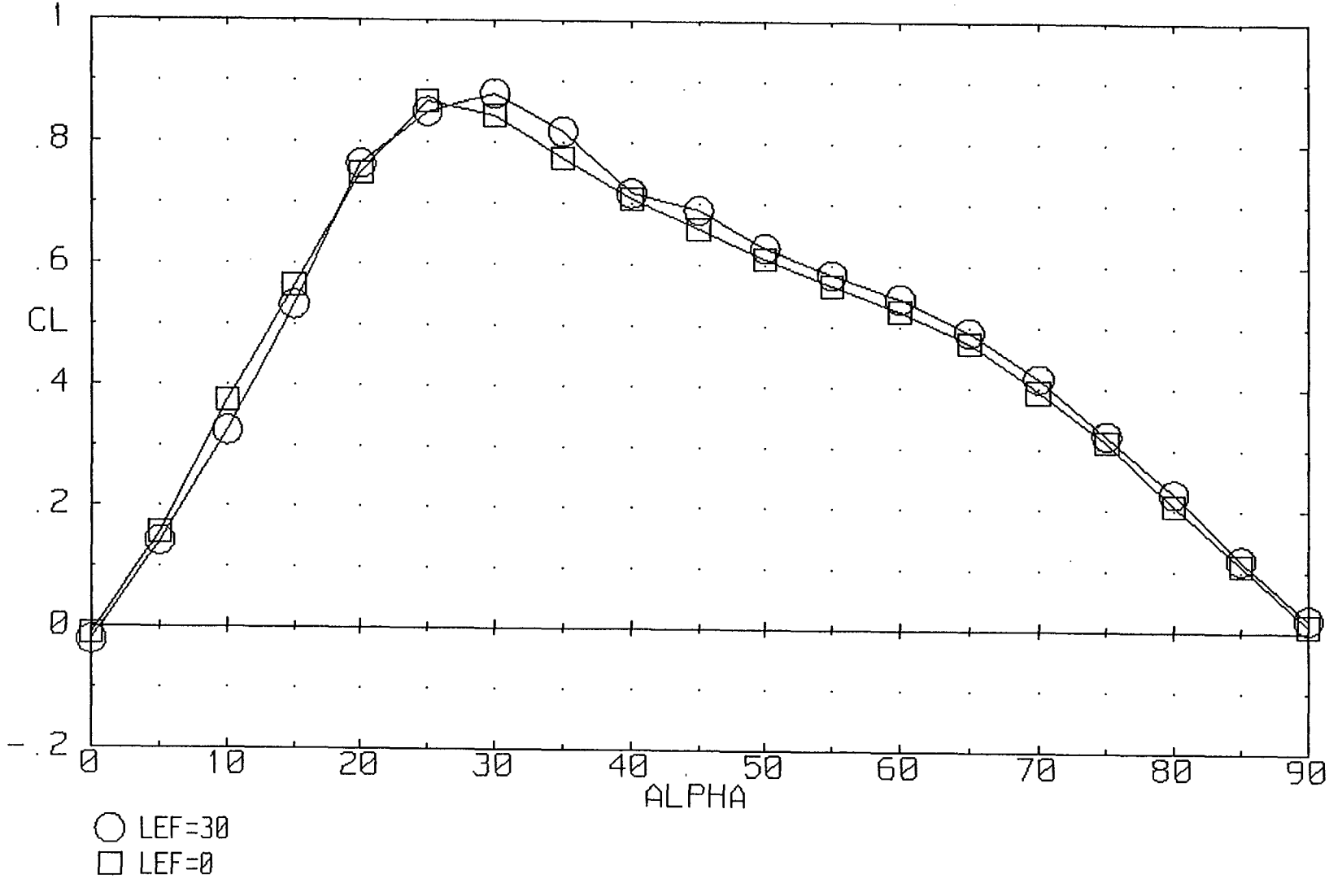

Figure 3-77. Effect of Leading Edge Flap Deflection on the Lift Coefficient for the ICE 101 (β=0°).

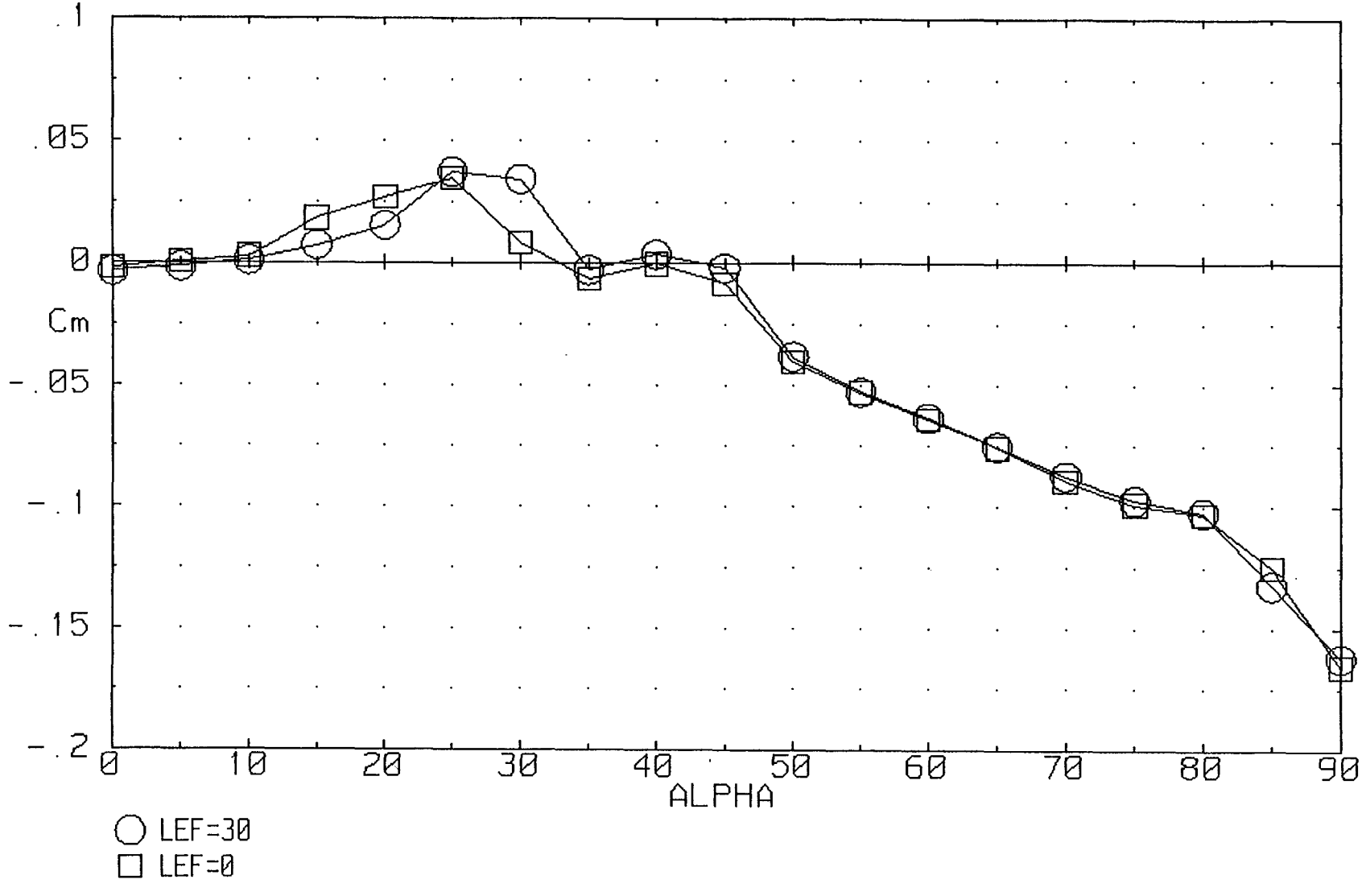

Figure 3-78. Effect of Leading Edge Flap Deflection on the Static Pitching Moment for the ICE 101 at β=0°.

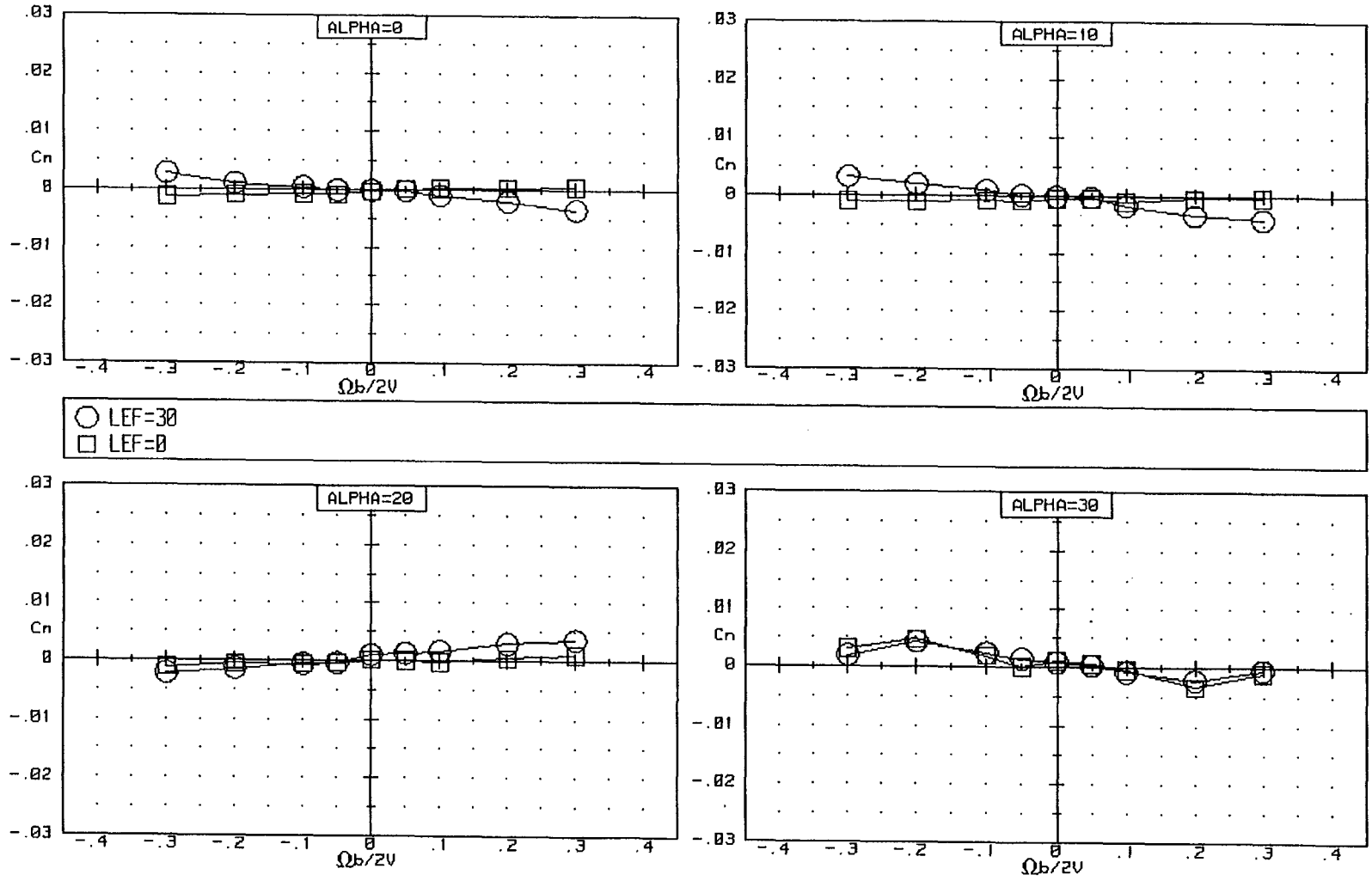

Figure 3-79. Effect of Rotation Rate and LEF Deflection on the Yawing Moment for the ICE 101 (β=0 °).

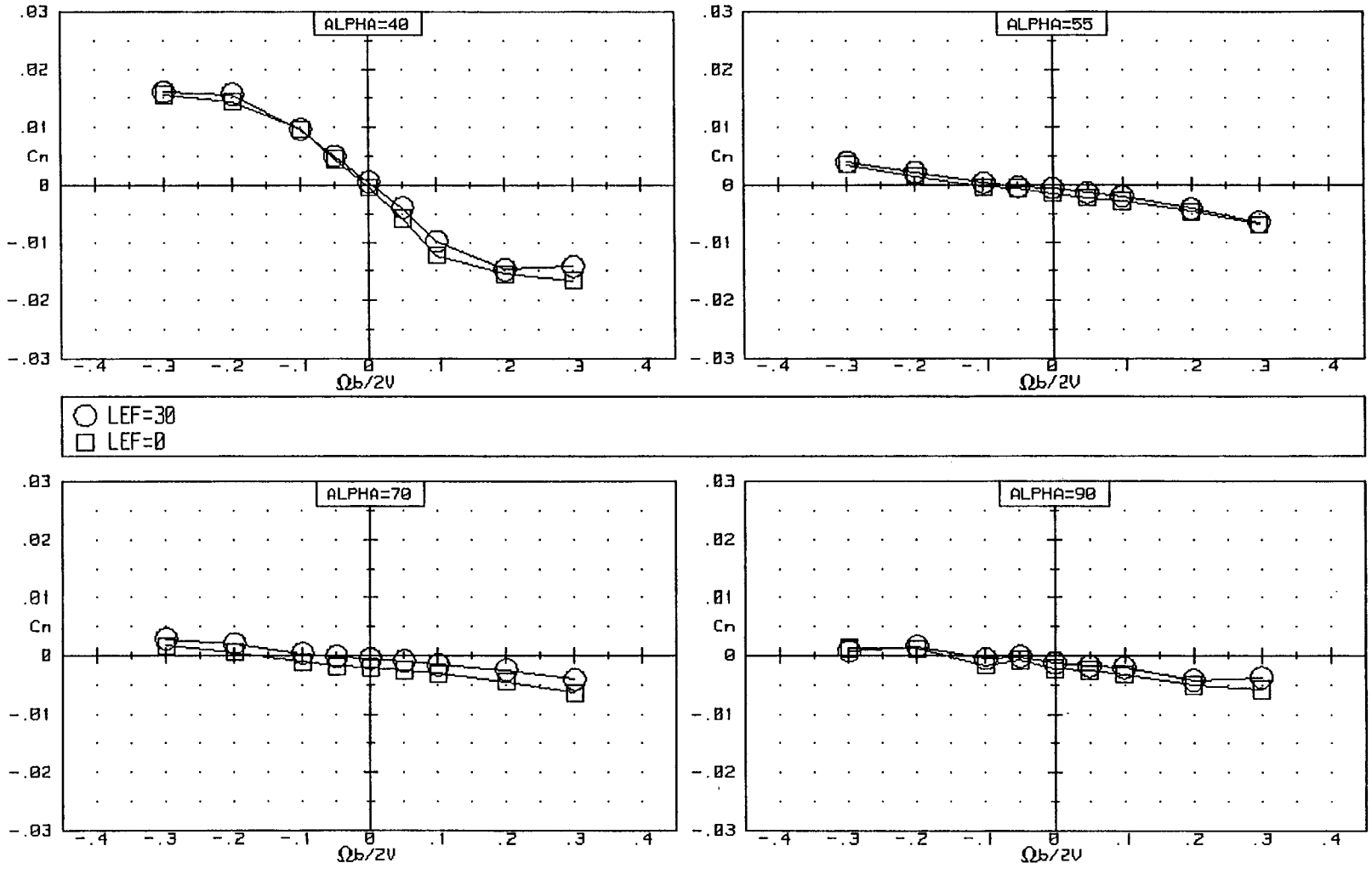

Figure 3-79. Concluded.

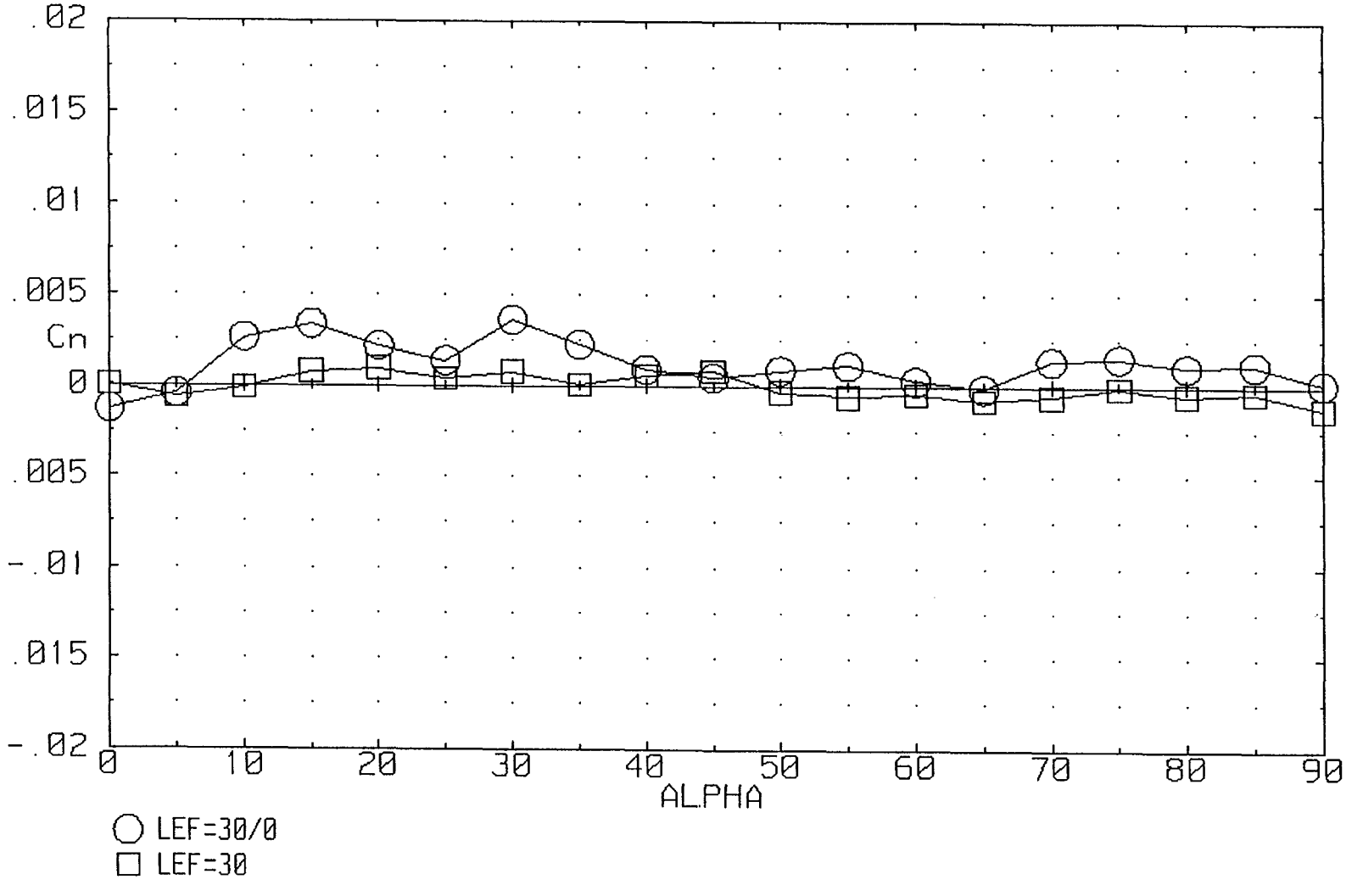

Figure 3-80. Effect of Differential LEF on Static Yawing Moment for the ICE 101 (β=0°).

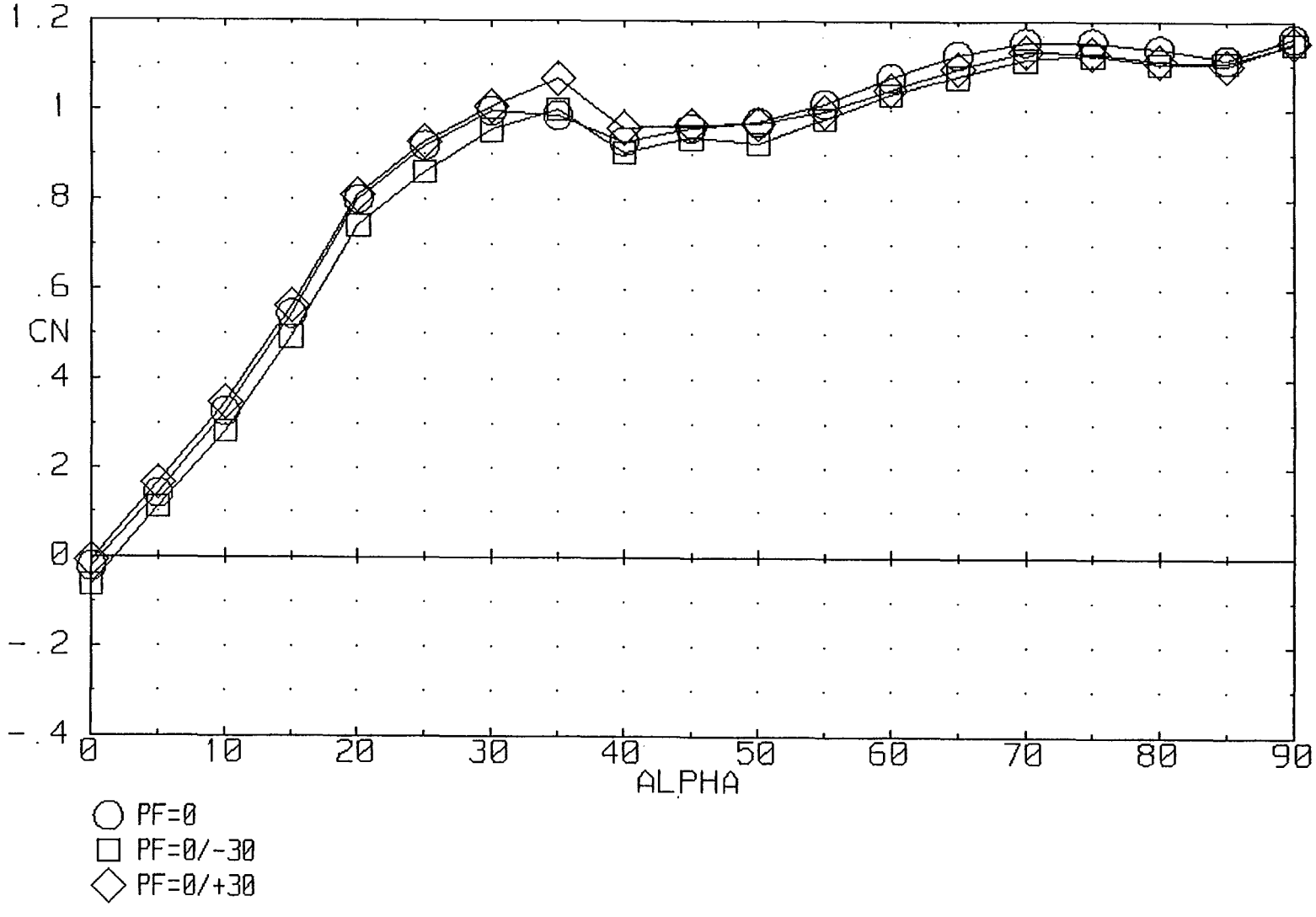

Figure 3-81. Effect of Pitch Flap Deflections on Normal Force for the ICE 101 (LEF=30, β=0°).

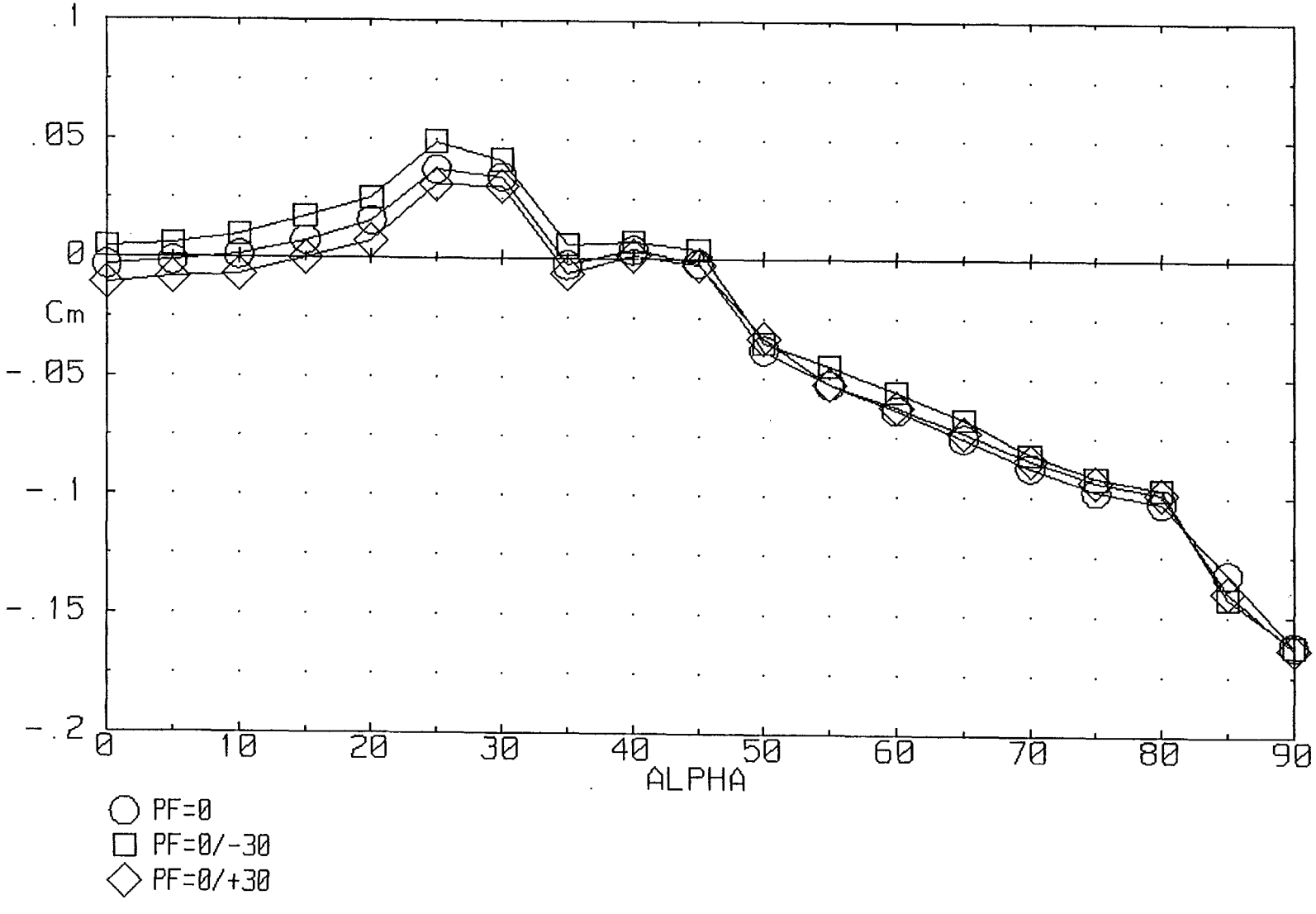

Figure 3-82. Pitching Moment due to Right-Hand Pitch Flap Deflections on the ICE 101 (LEF=30, β=0°).

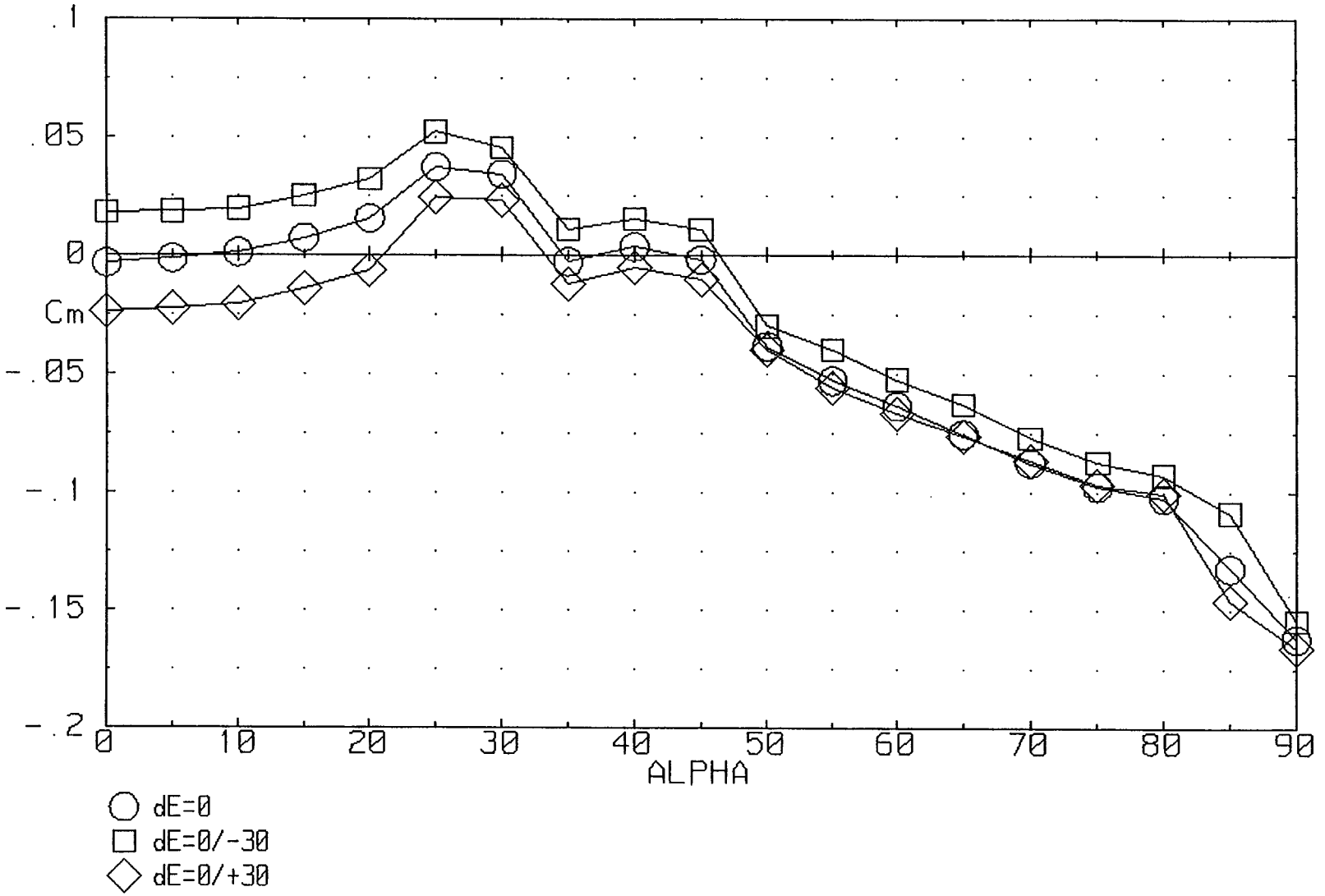

Figure 3-83. Pitching Moment due to Right-Hand Elevon Deflections on the ICE 101 (LEF=30, β=0°).

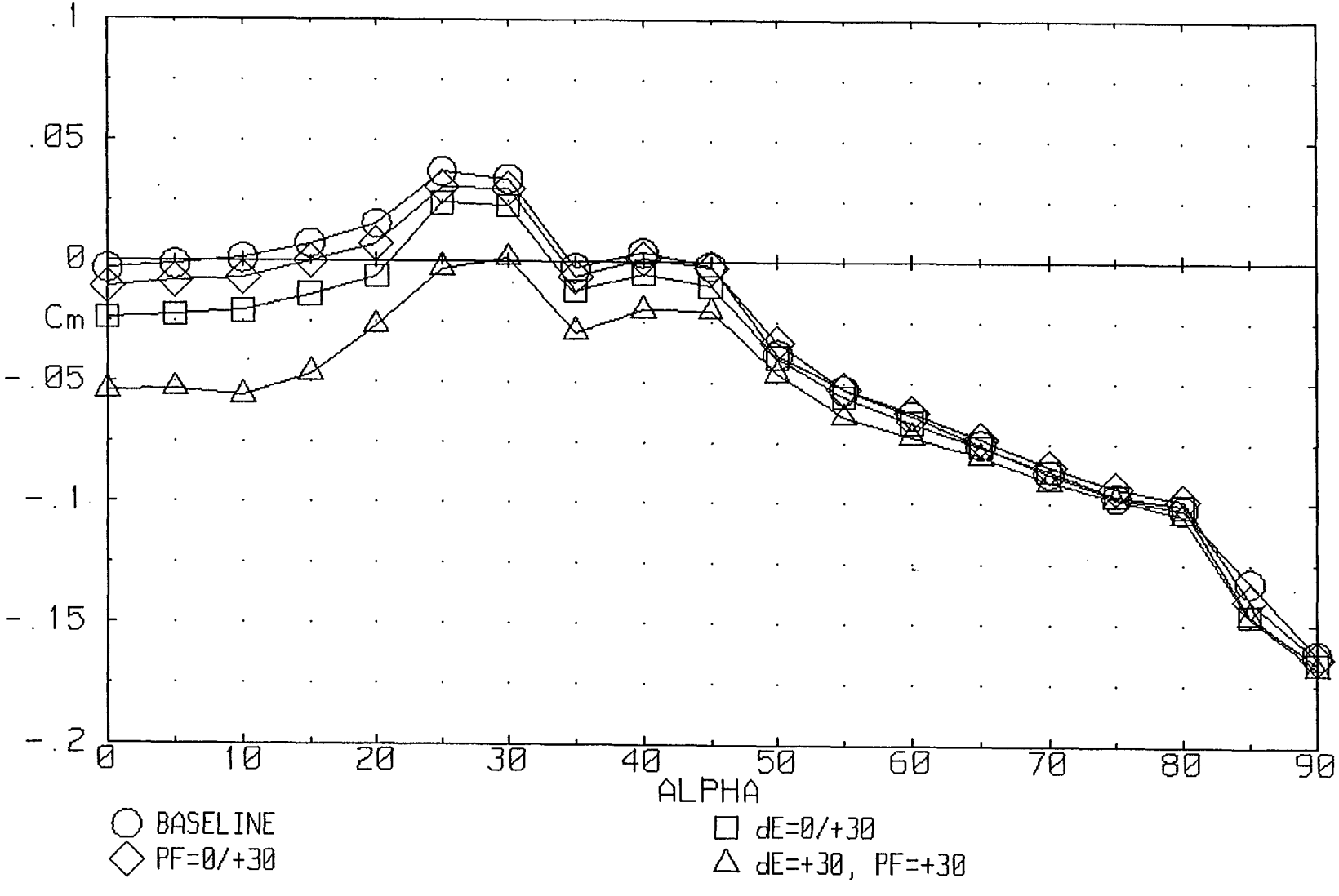

Figure 3-84. ICE 101 Maximum Nose Down Control Power for LEF=30.

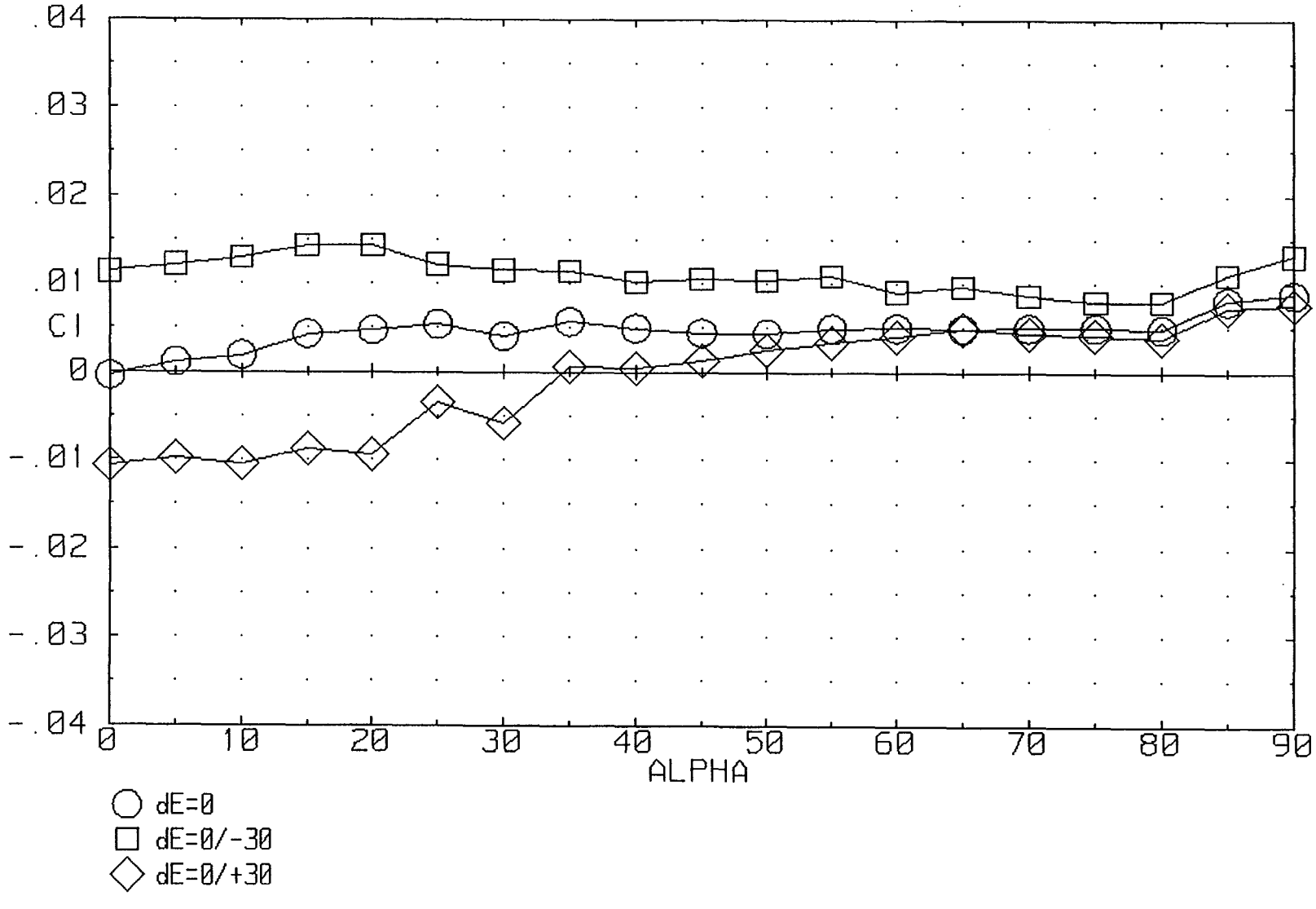

Figure 3-85. Rolling Moment due to Right-Hand Elevon Deflections on the ICE 101 (LEF=30, β=0°).

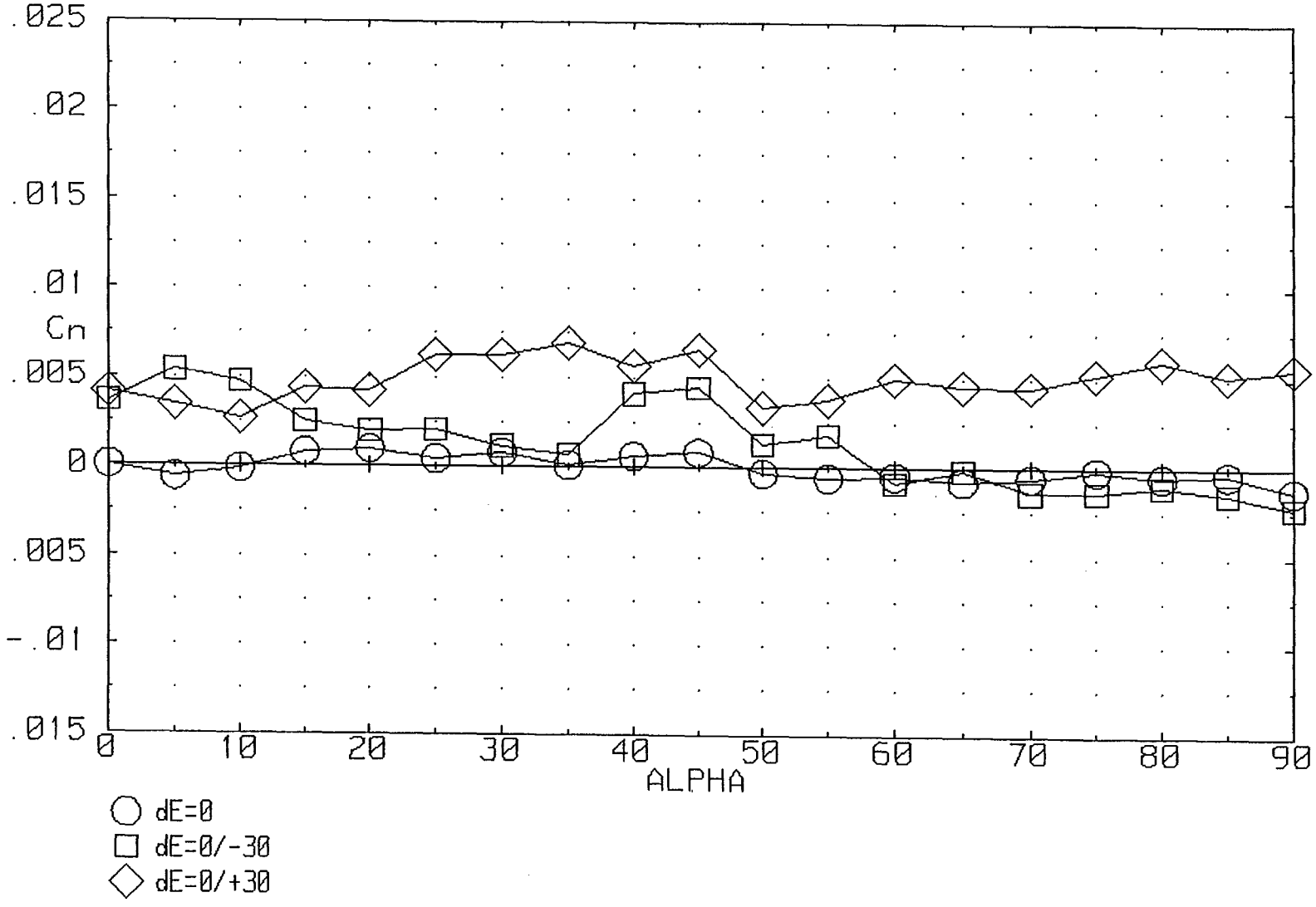

Figure 3-86. Yawing Moment due to Right-Hand Elevon Deflections on the ICE 101 (LEF=30, β=0°).

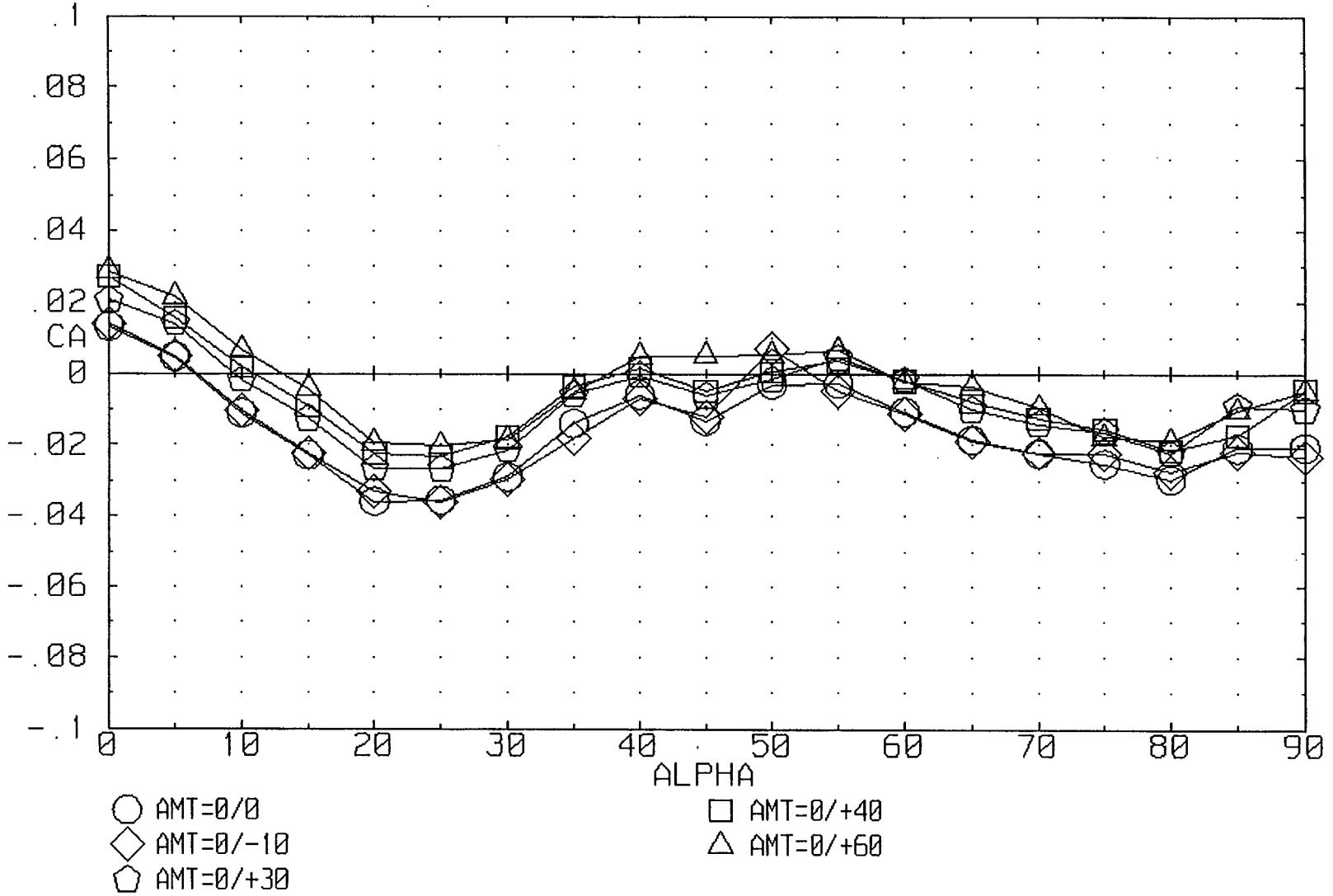

Figure 3-87. Axial Force due to AMT Deflection on the ICE 101 (LEF=30, β=0°).

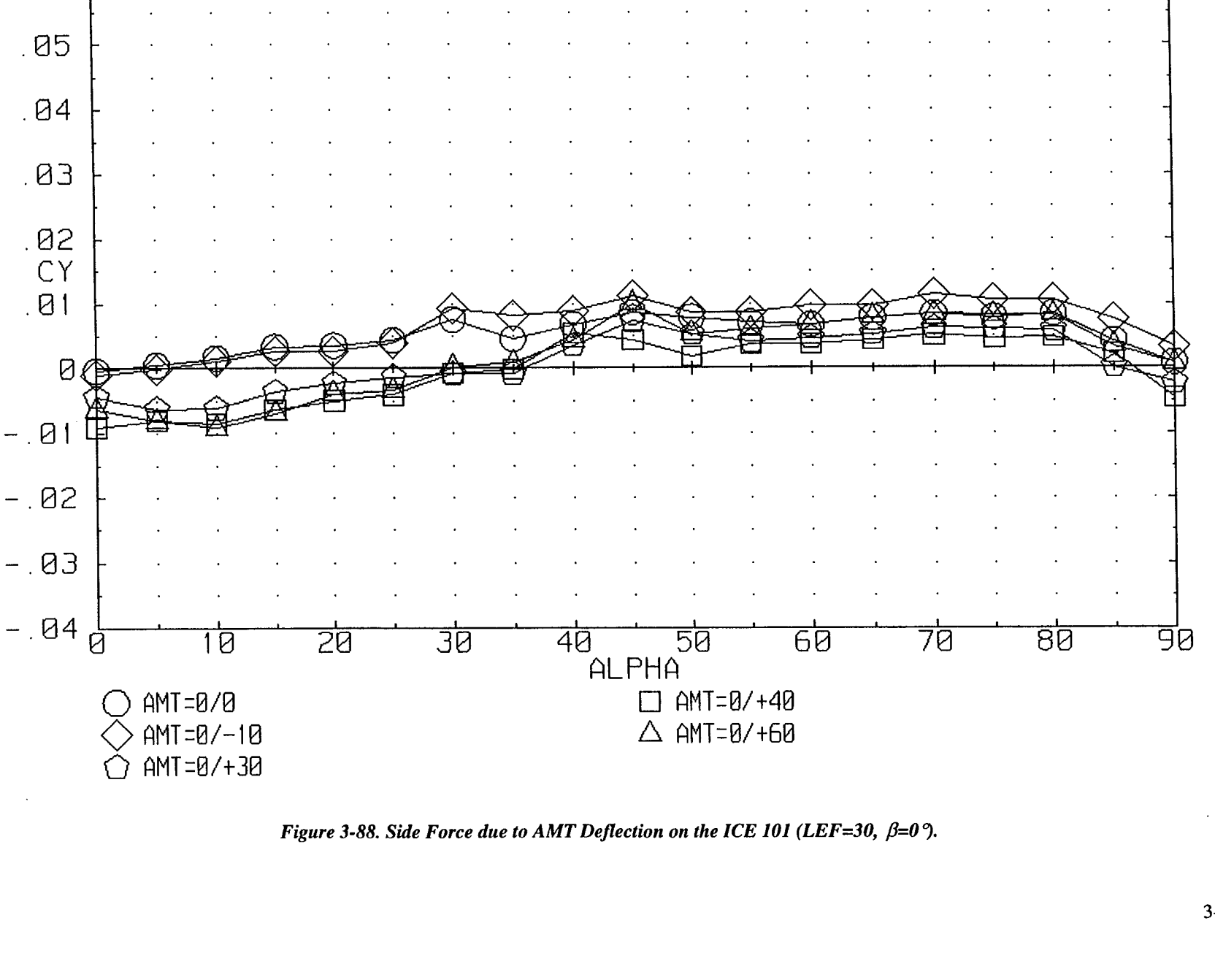

Figure 3-88. Side Force due to AMT Deflection on the ICE 101 (LEF=30, β=0°).

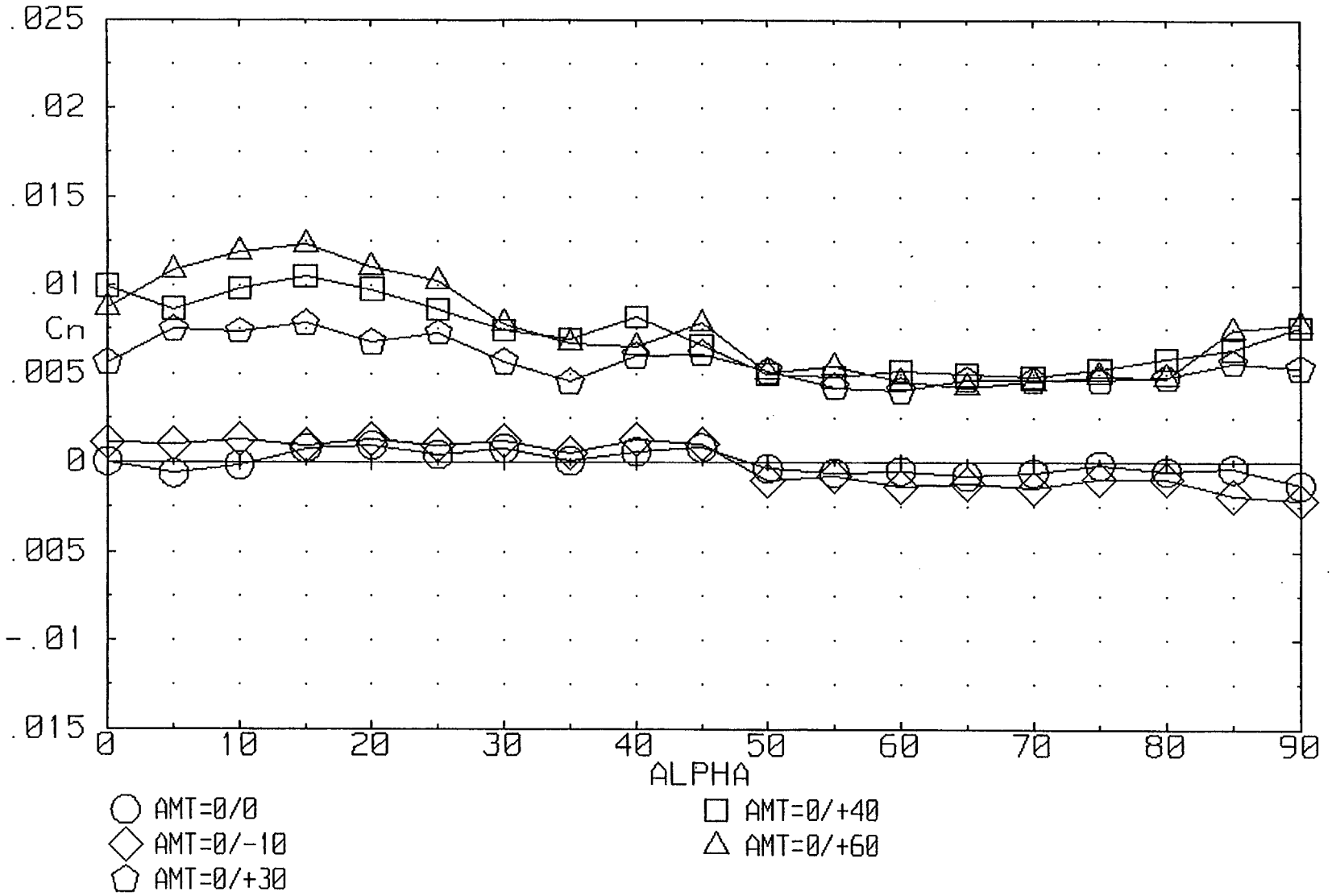

Figure 3-89. Effect of AMT Deflections on Yawing Moment for the ICE 101 (LEF=30, β=0°).

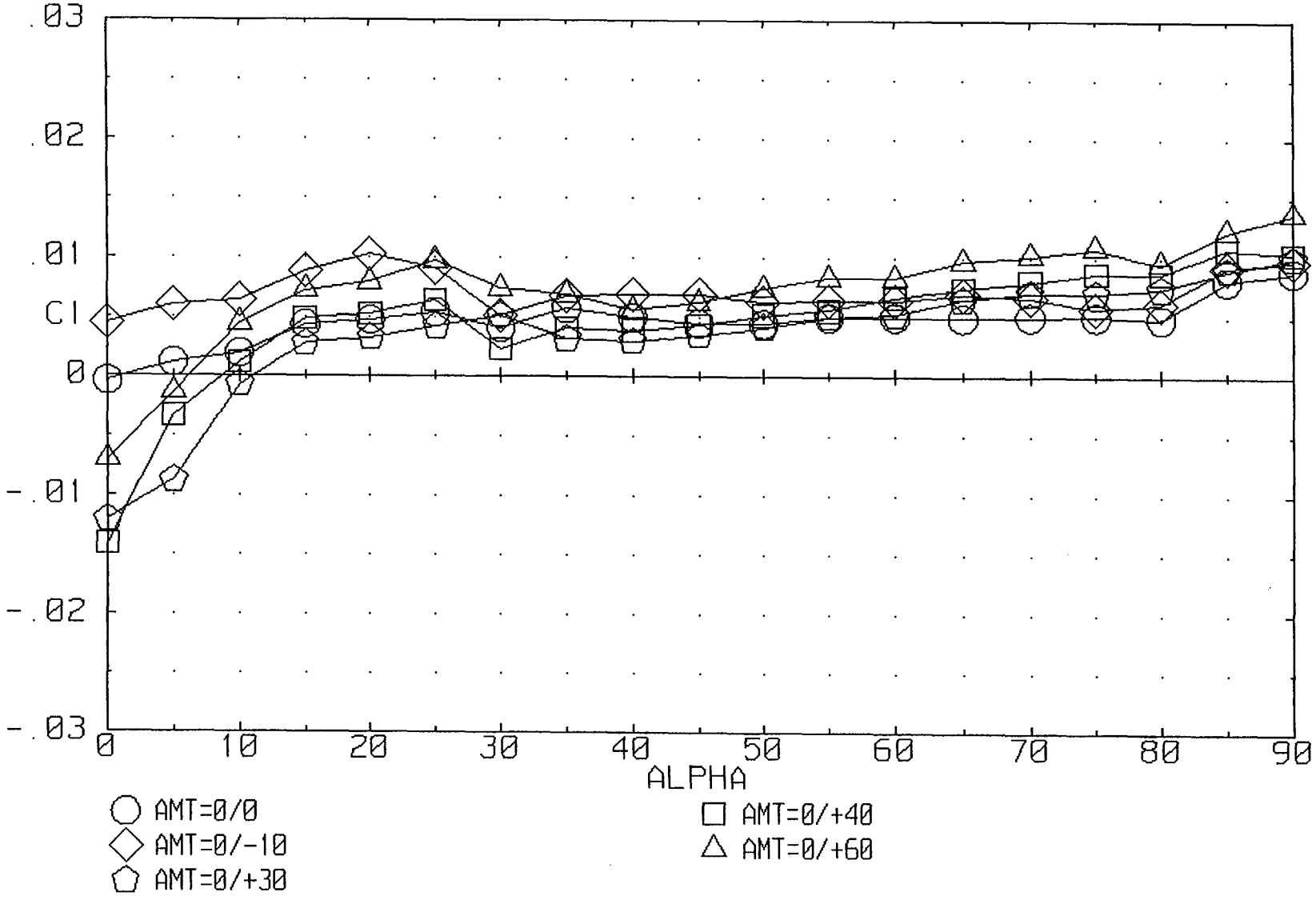

Figure 3-90. Effect of AMT Deflections on Rolling Moment for the ICE 101 (LEF=30, β=0°).

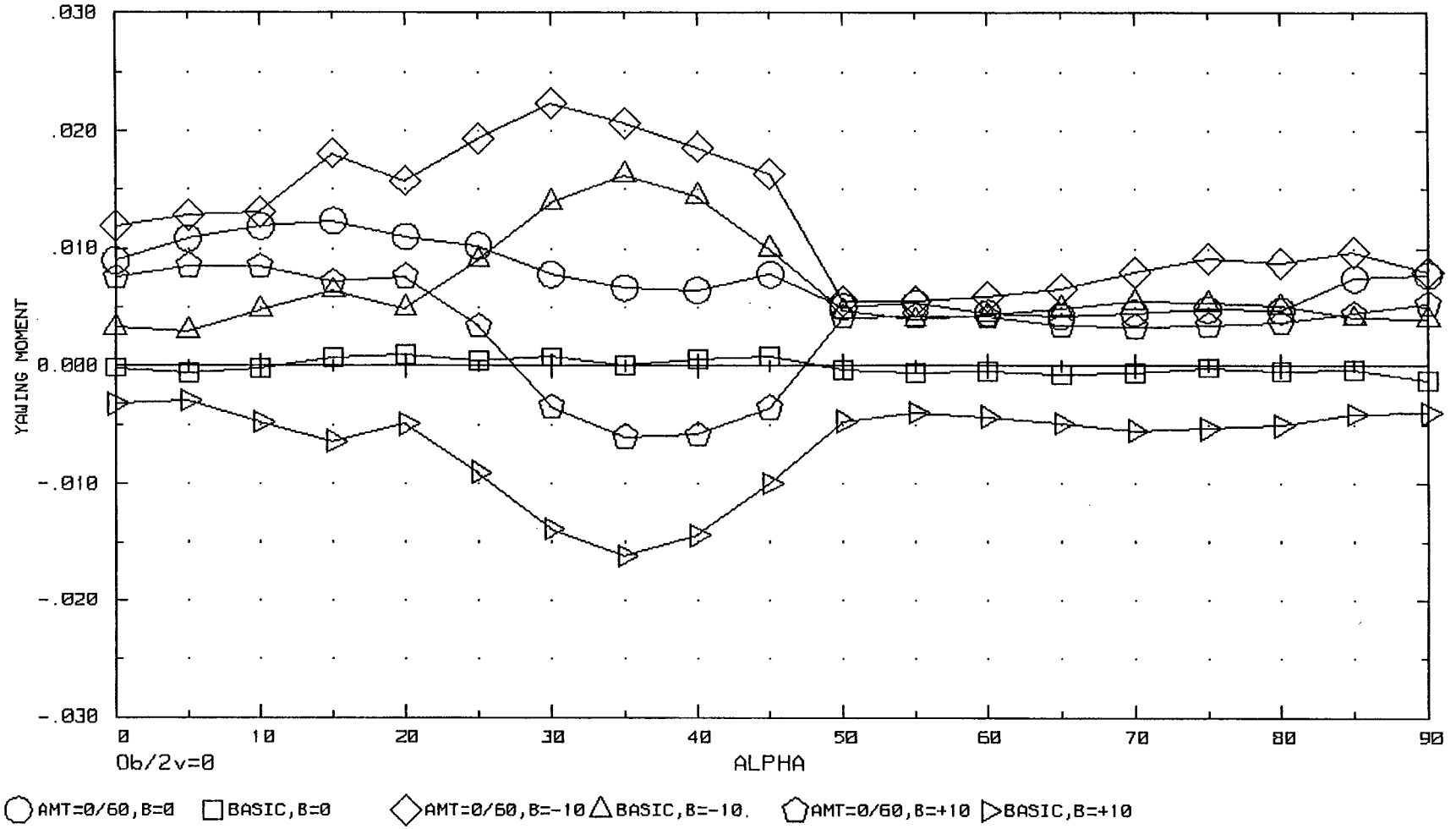

Figure 3-91. Effect of Sideslip on AMT Yaw Effectiveness for the ICE 101 (LEF=30, AMT=0/60).

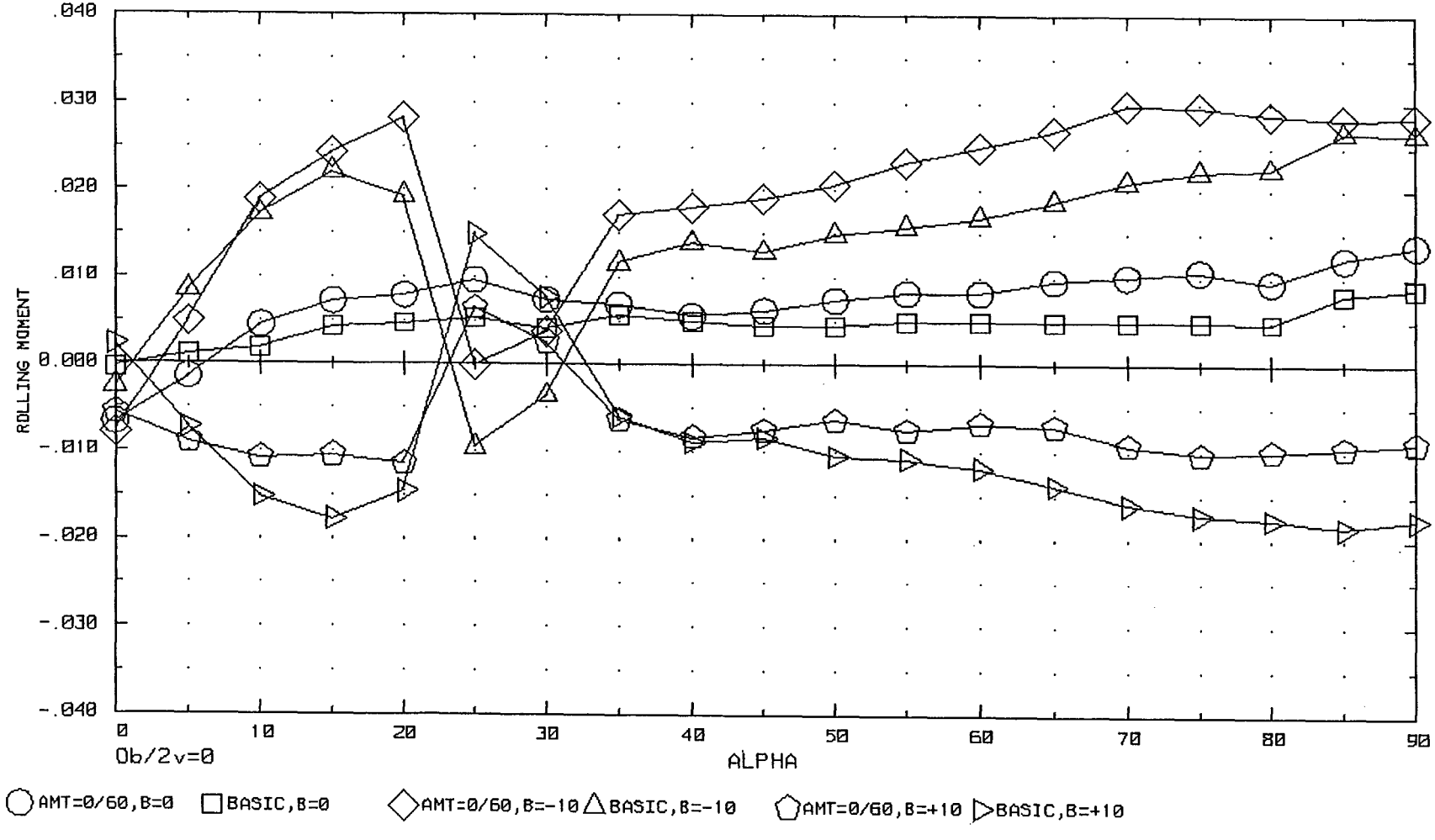

Figure 3-92. Effect of Sideslip on AMT Roll Effectiveness for the ICE 101 (LEF=30, AMT=0/60).

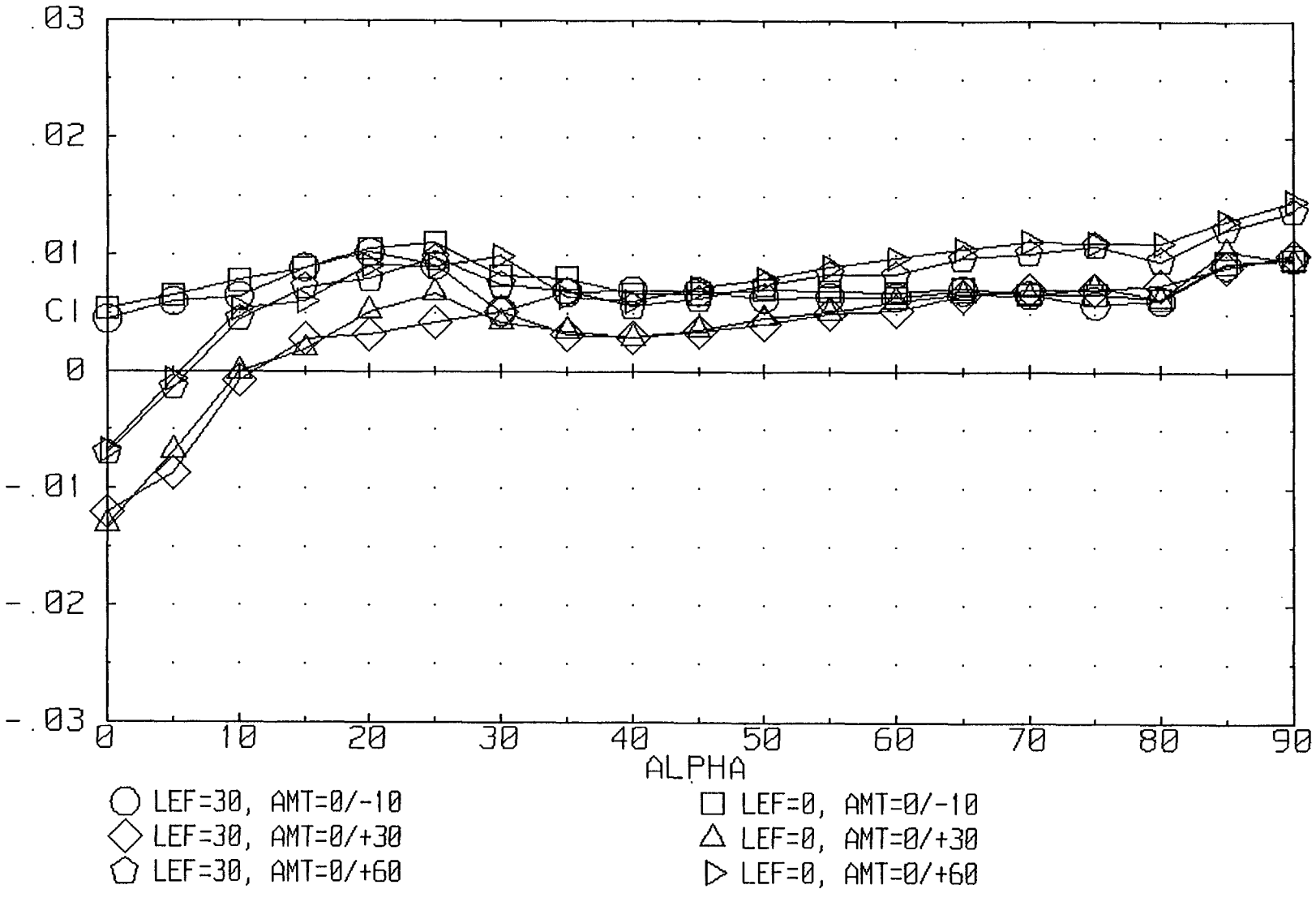

Figure 3-93. Effect of AMT/LEF Interactions on Rolling Moment for the ICE 101 (β=0°).

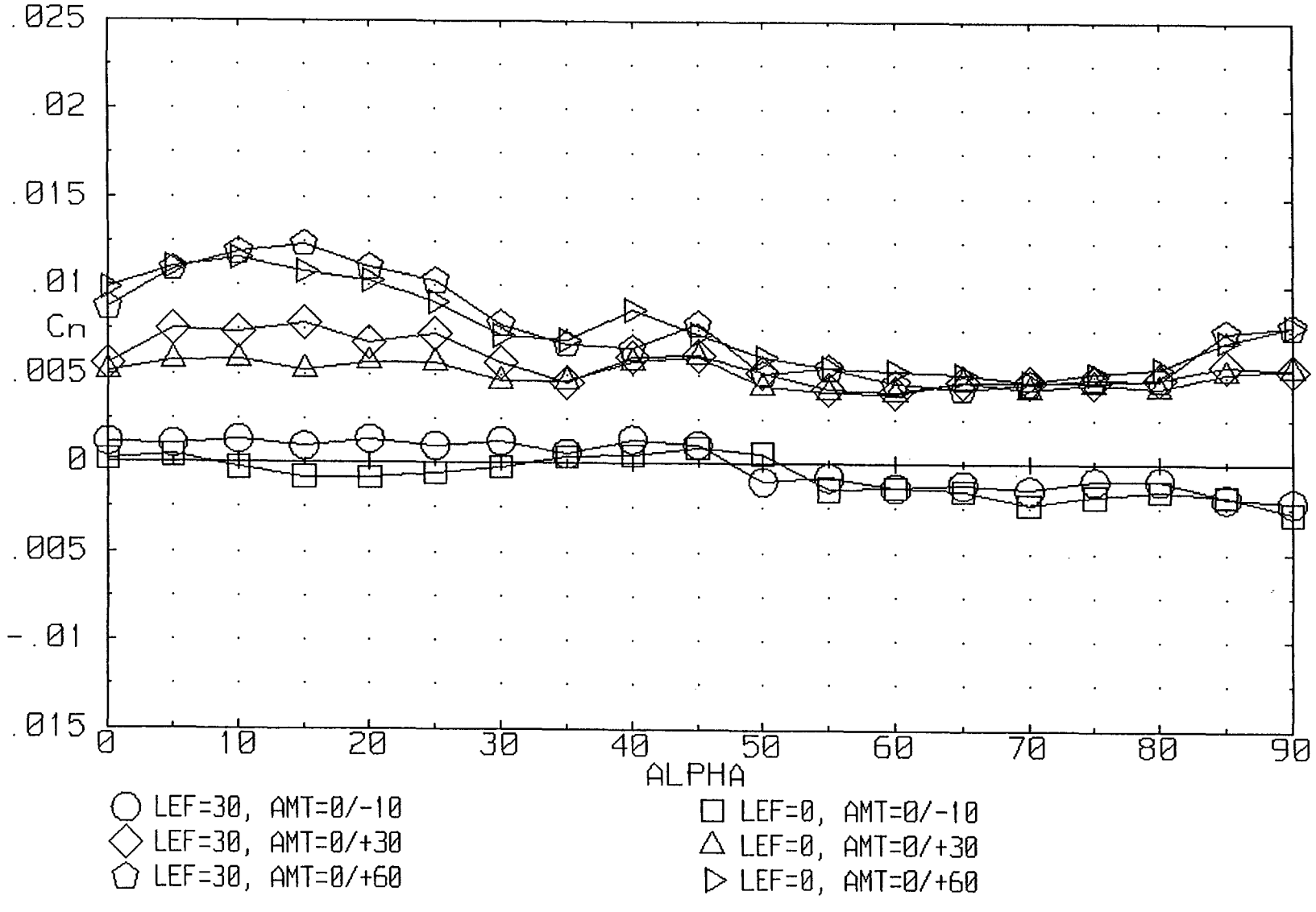

Figure 3-94. Effect of AMT/LEF Interactions on Yawing Moment for the ICE 101 (β=0°).

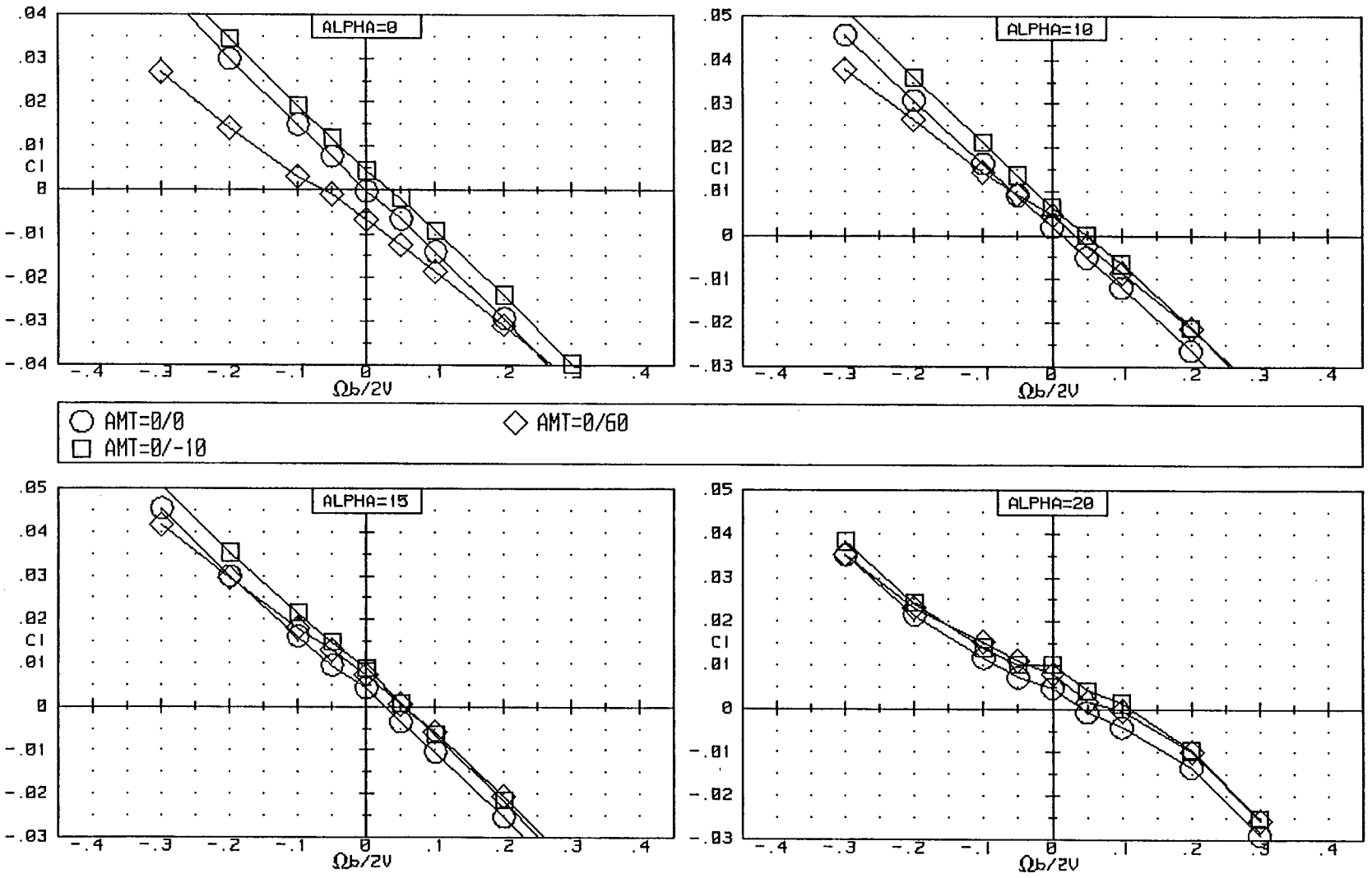

Figure 3-95. Effect of Rotation Rate and AMT Deflections on Rolling Moment for the ICE 101 (LEF=30, β=0°).

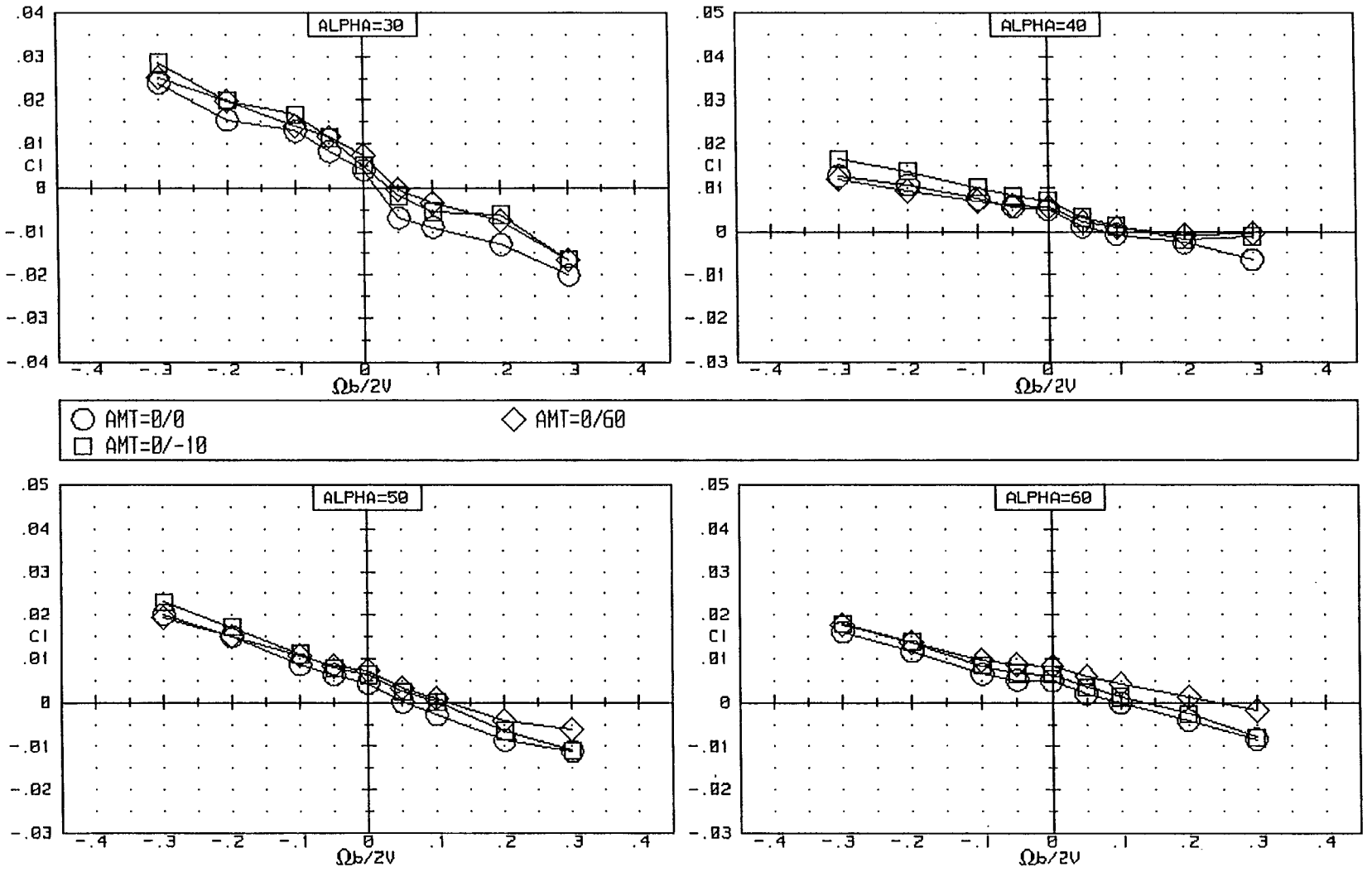

Figure 3-95. Continued.

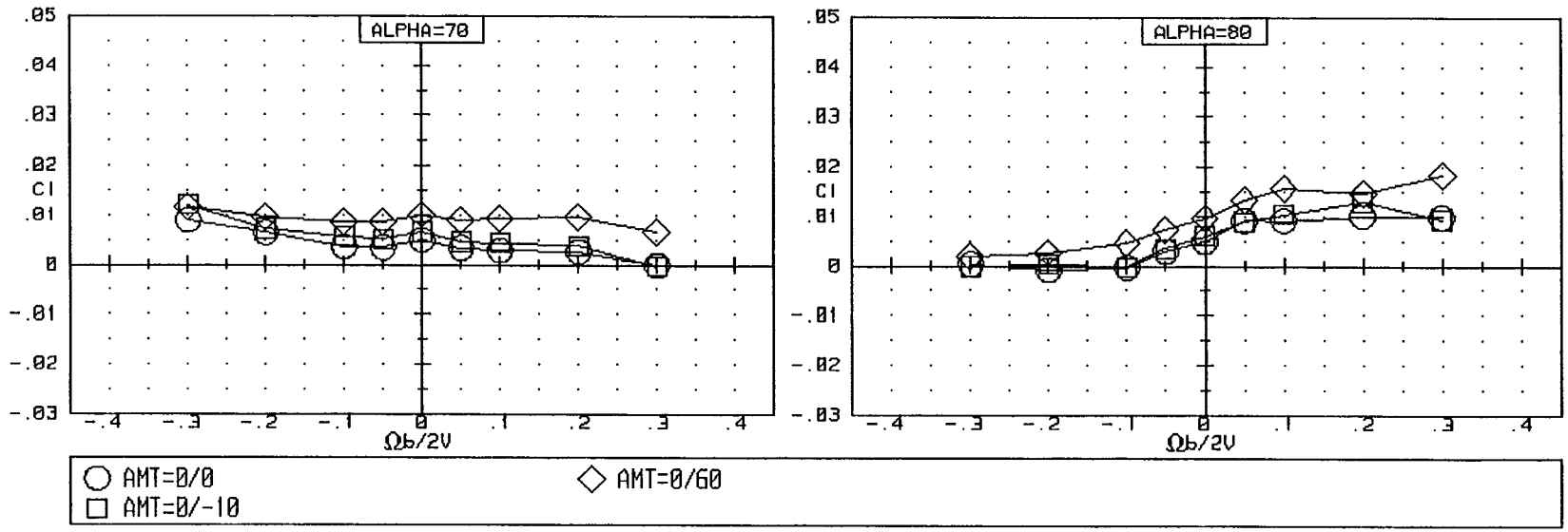

Figure 3-95. Concluded.

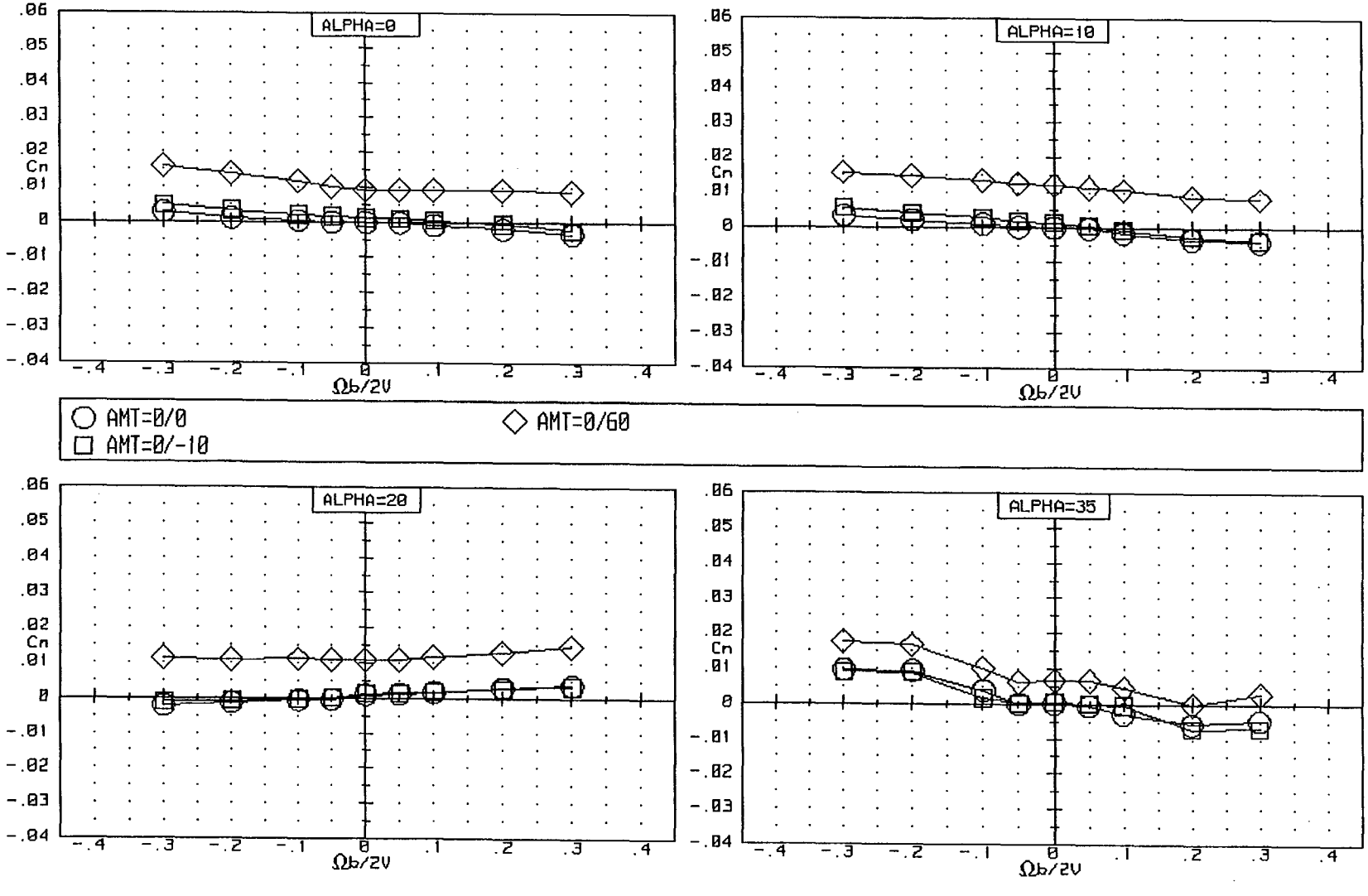

Figure 3-96. Effect of Rotation Rate and AMT Deflections on Yawing Moment for the ICE 101 (LEF=30, β=0°).

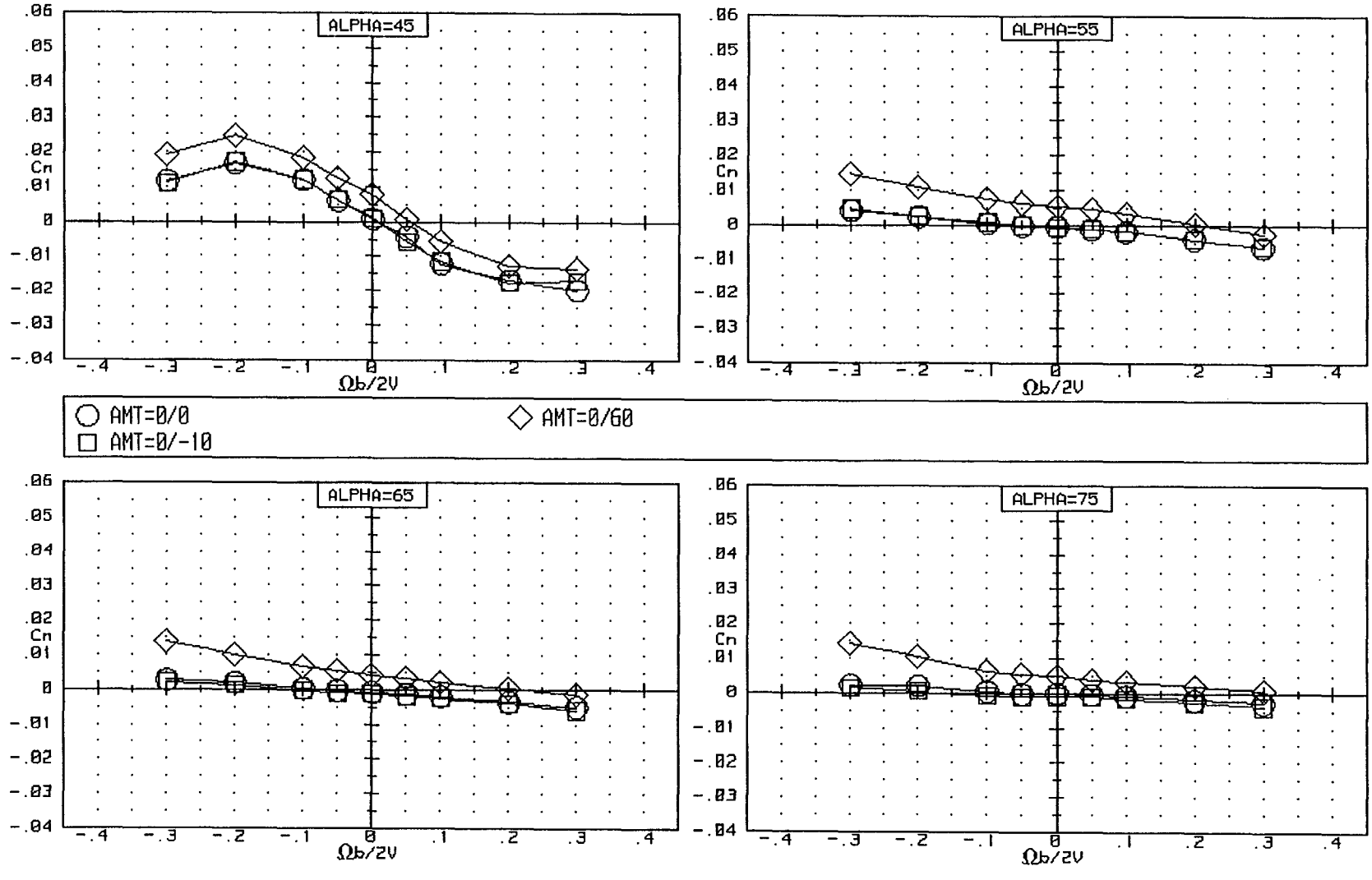

Figure 3-96. Continued.

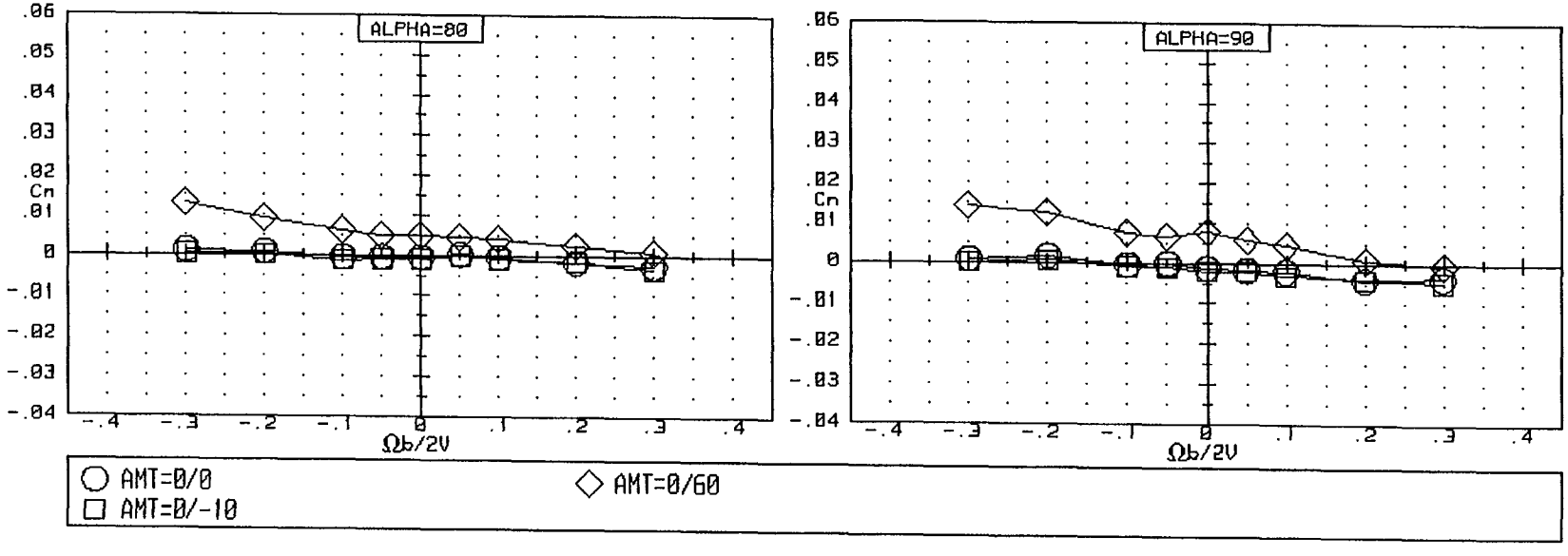

Figure 3-96. Concluded.

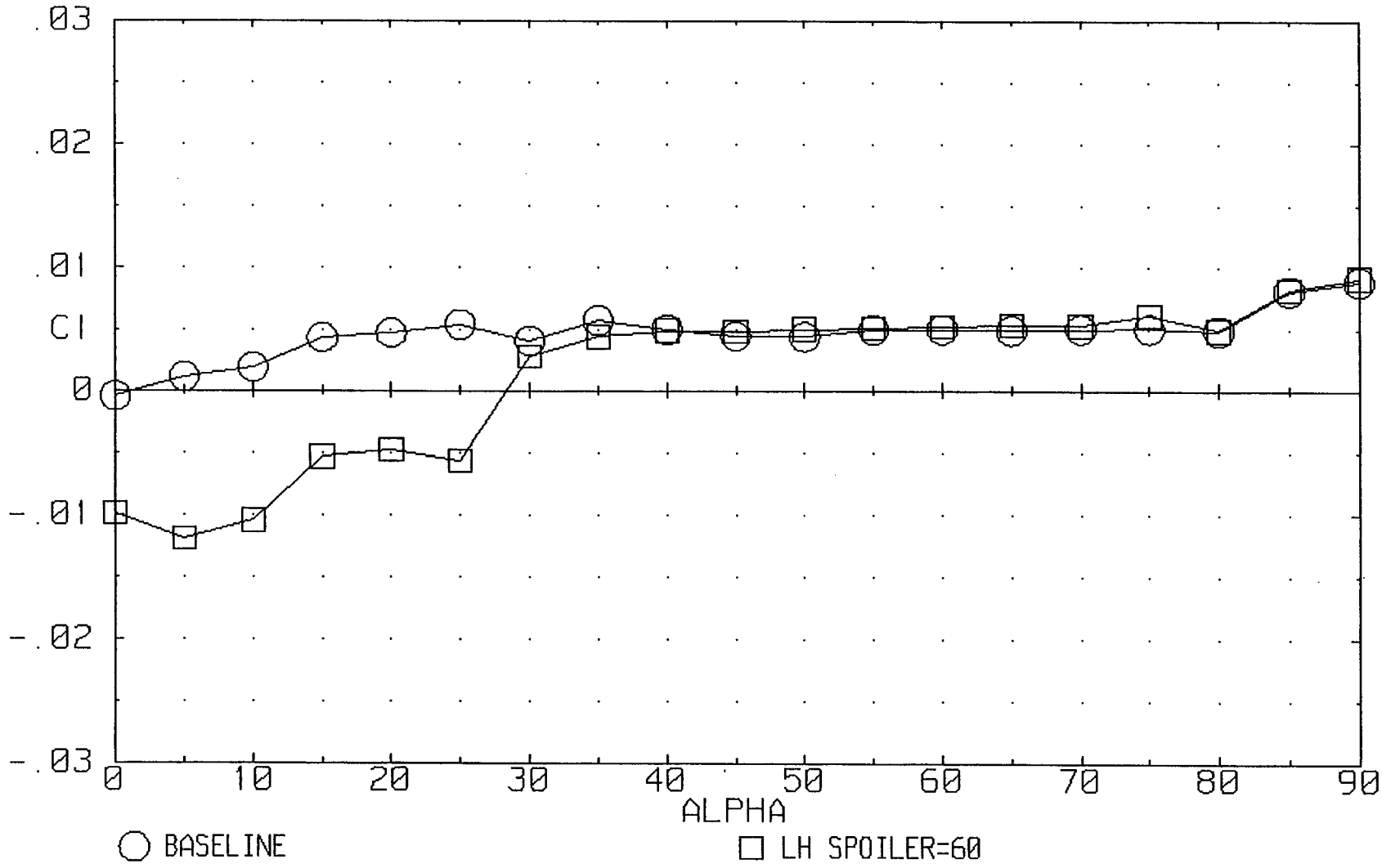

Figure 3-97. Rolling Moment due to Left-Hand Spoiler Deployment on the ICE 101 (LEF=30, β=0°).

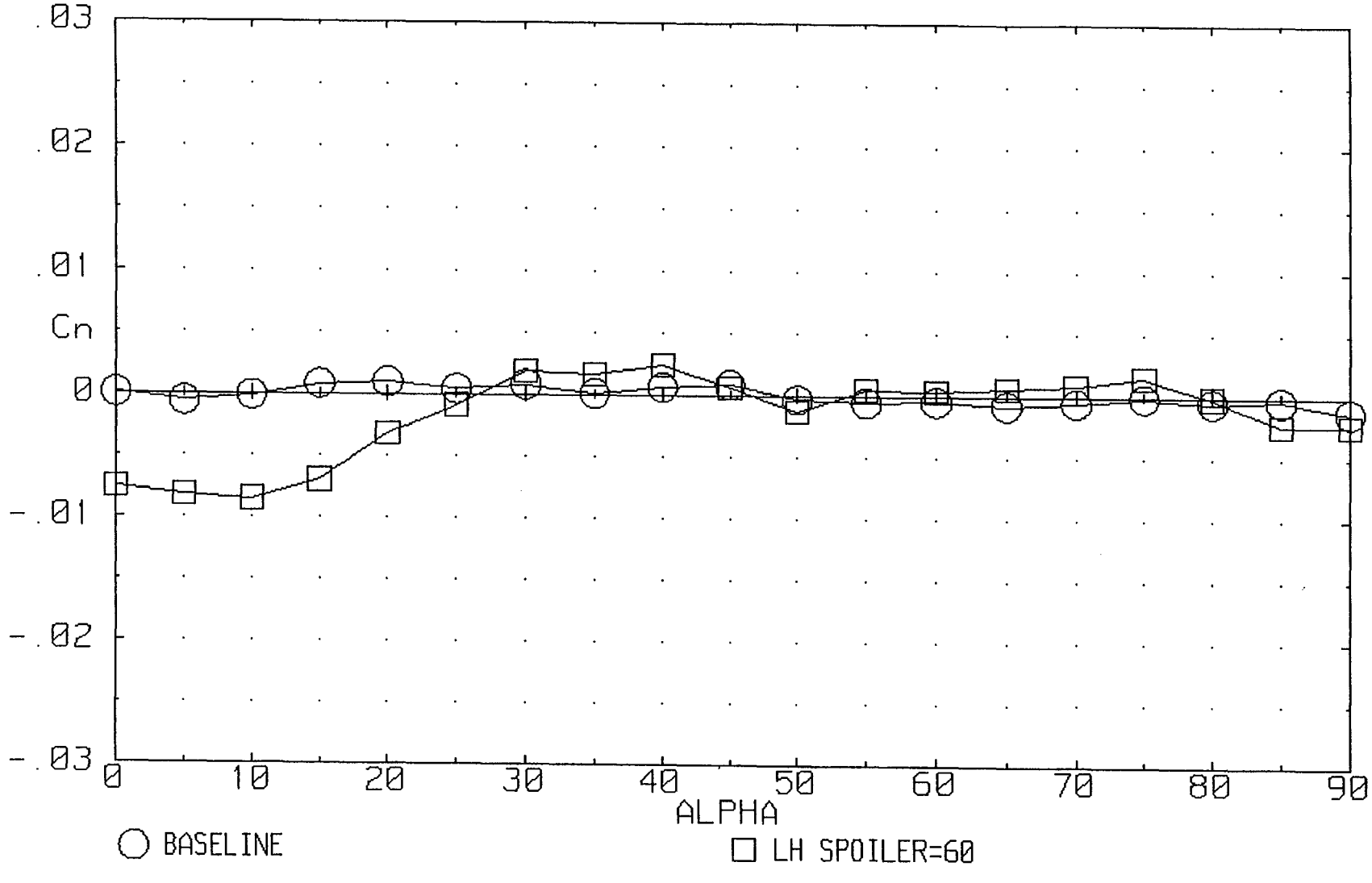

Figure 3-98. Yawing Moment due to Left-Hand Spoiler Deployment on the ICE 101 (LEF=30, β=0°).

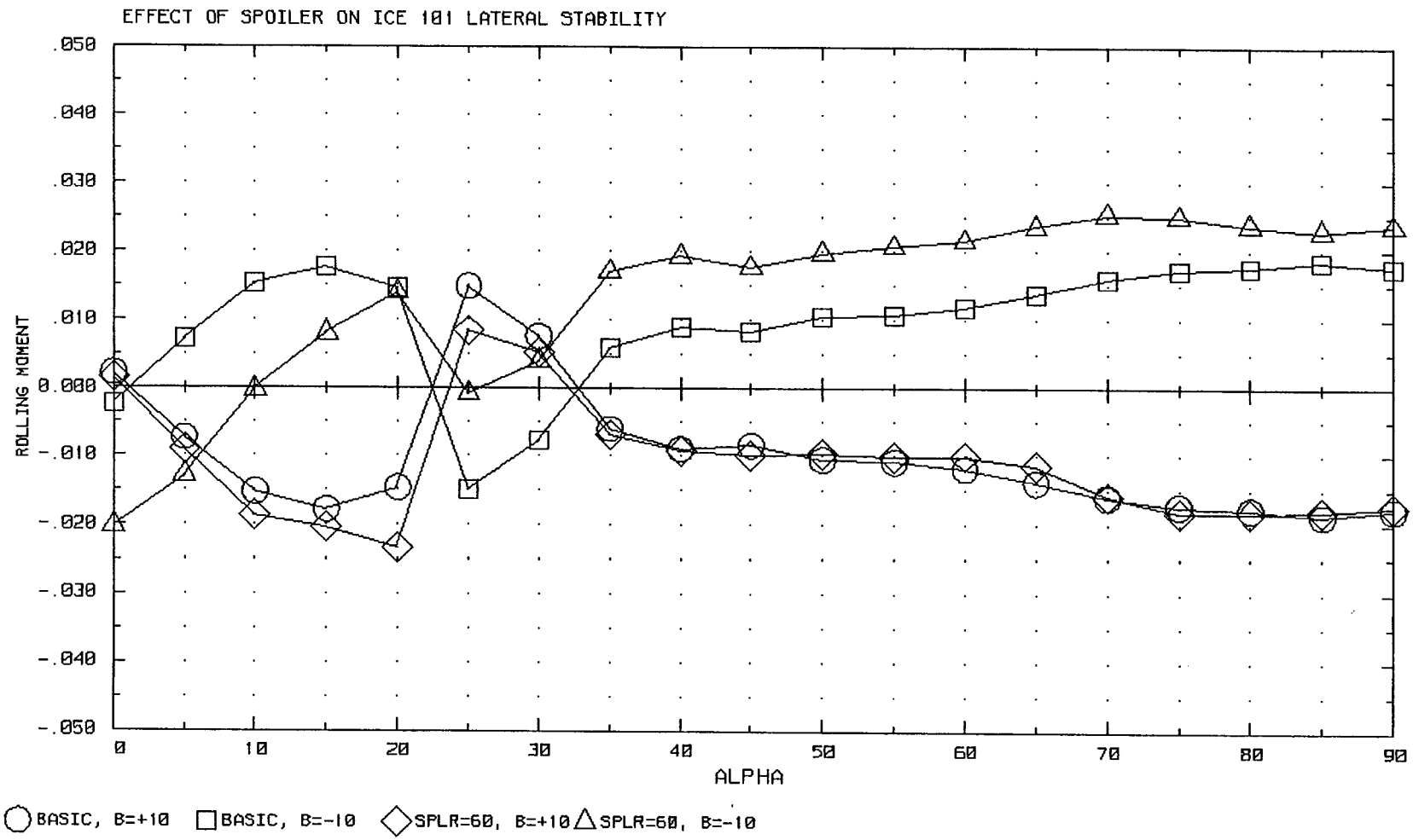

Figure 3-99. Effect of Left-Hand Spoiler on Lateral Stability for the ICE 101 (LEF=30).

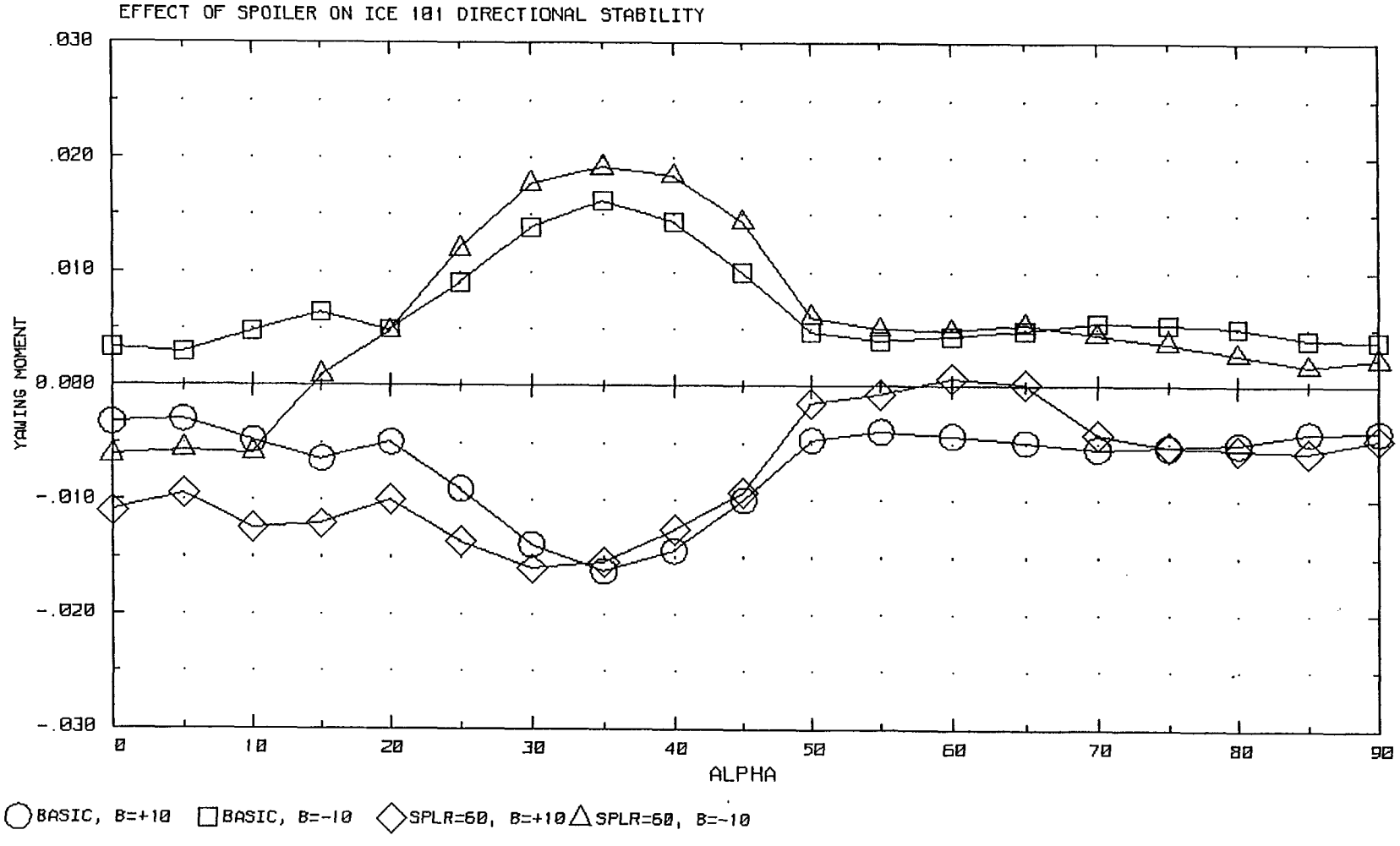

Figure 3-100. Effect of Left-Hand Spoiler on Directional Stability for the ICE 101 (LEF=30).

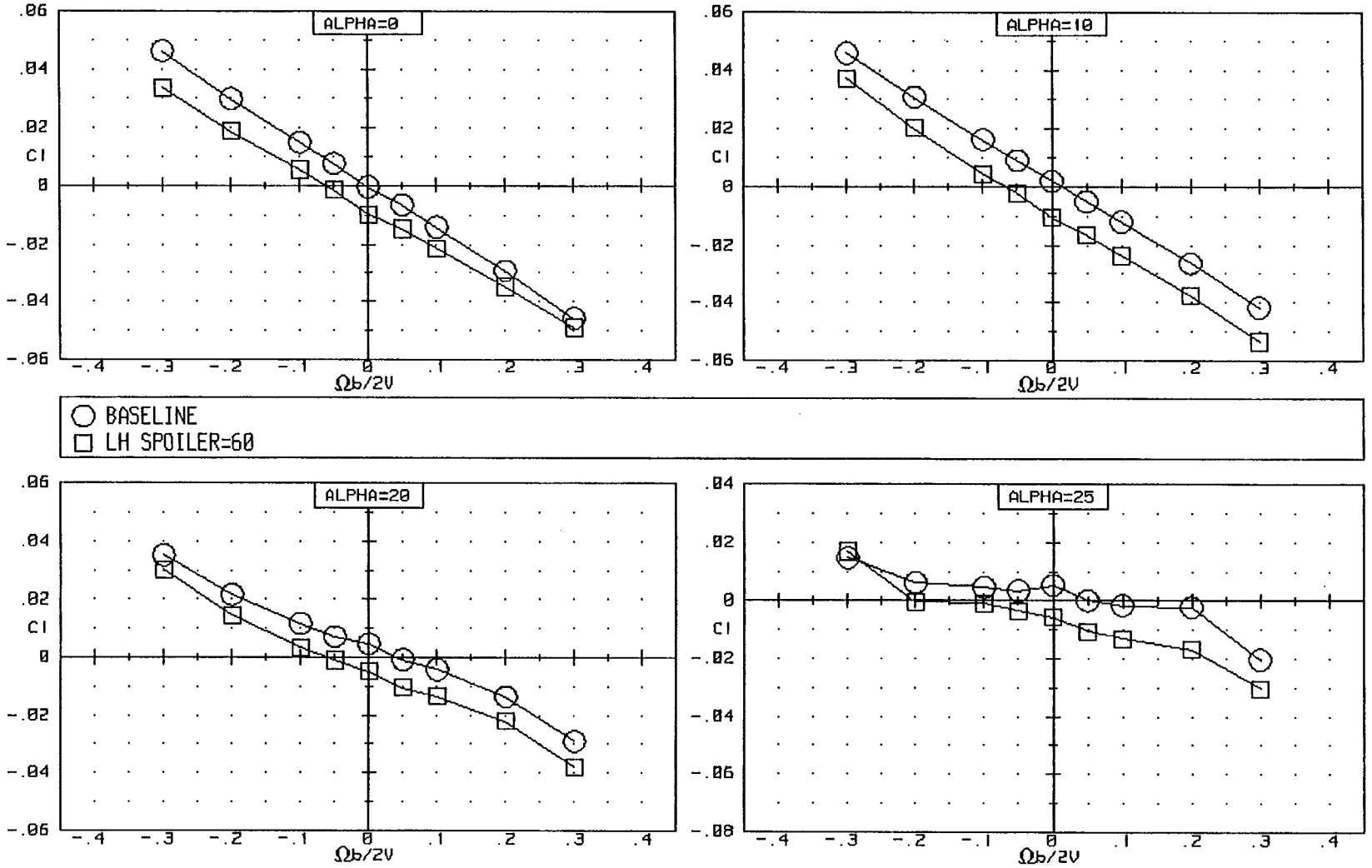

Figure 3-101. Effect of Rotation Rate and Left-Hand Spoiler on Rolling Moment for the ICE 101 (LEF=30, β=0°).

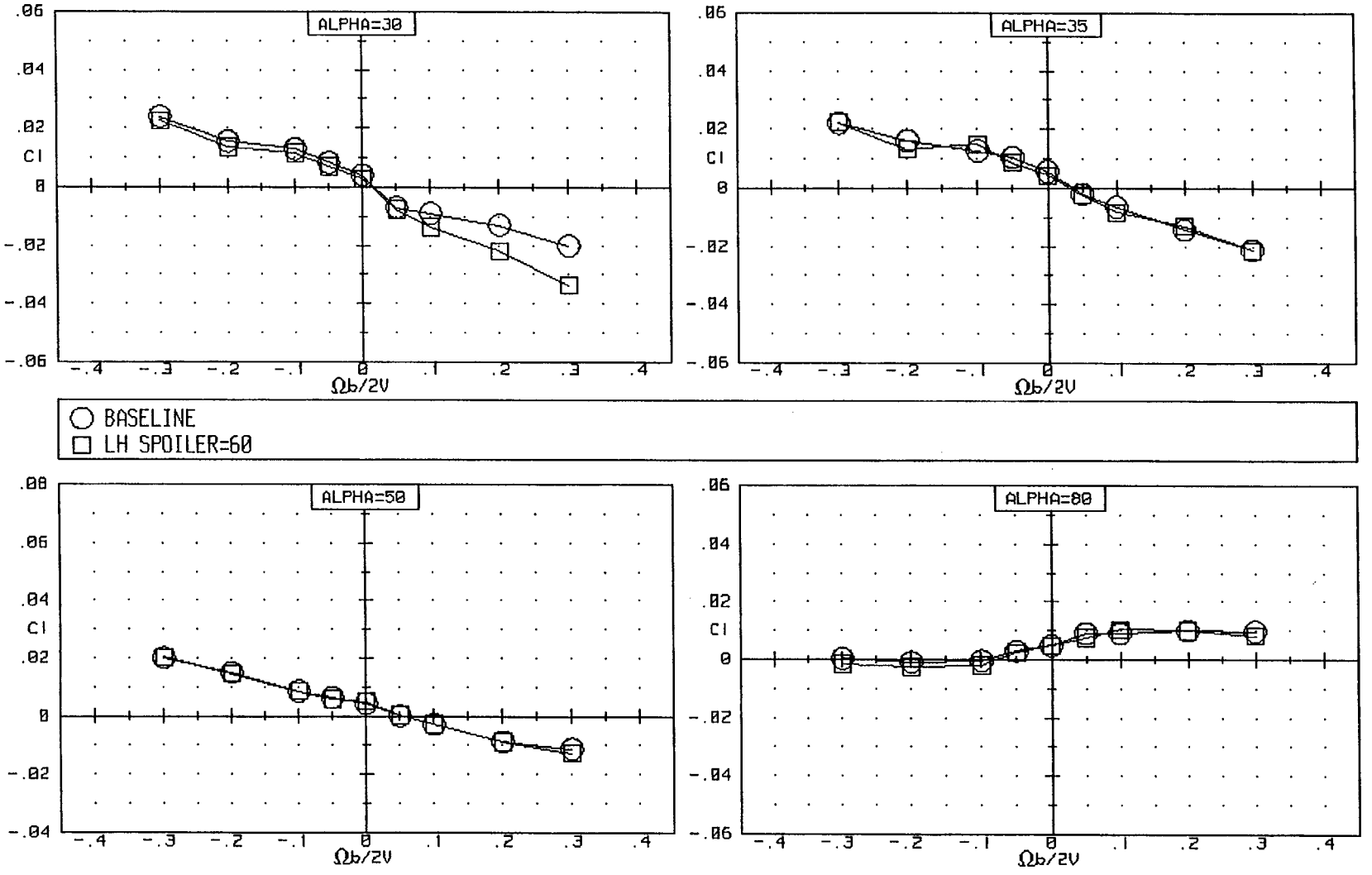

Figure 3-101. Concluded.

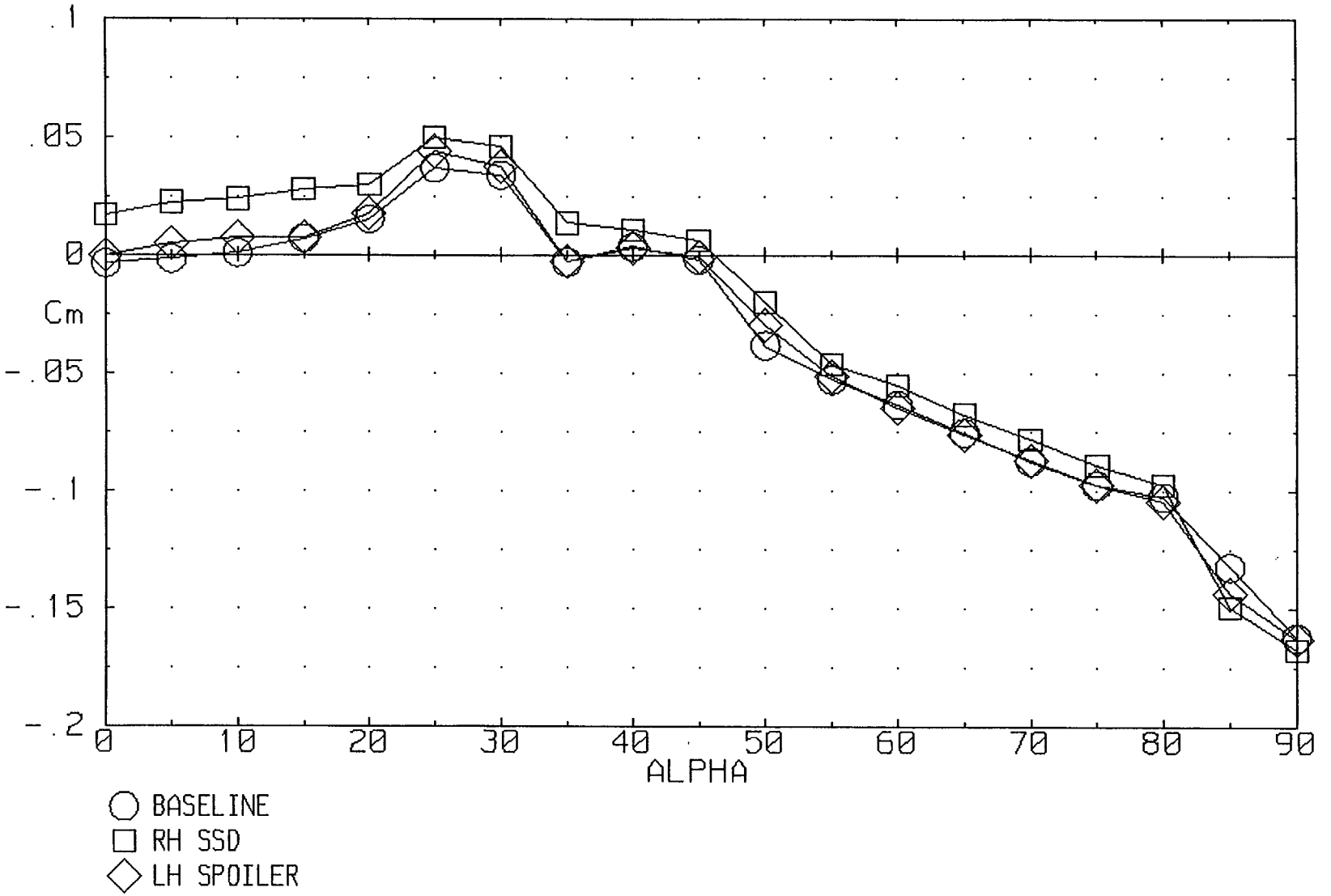

Figure 3-102. Pitching Moment due to Right-Hand SSD on the ICE 101 (LEF=30, β=0°).

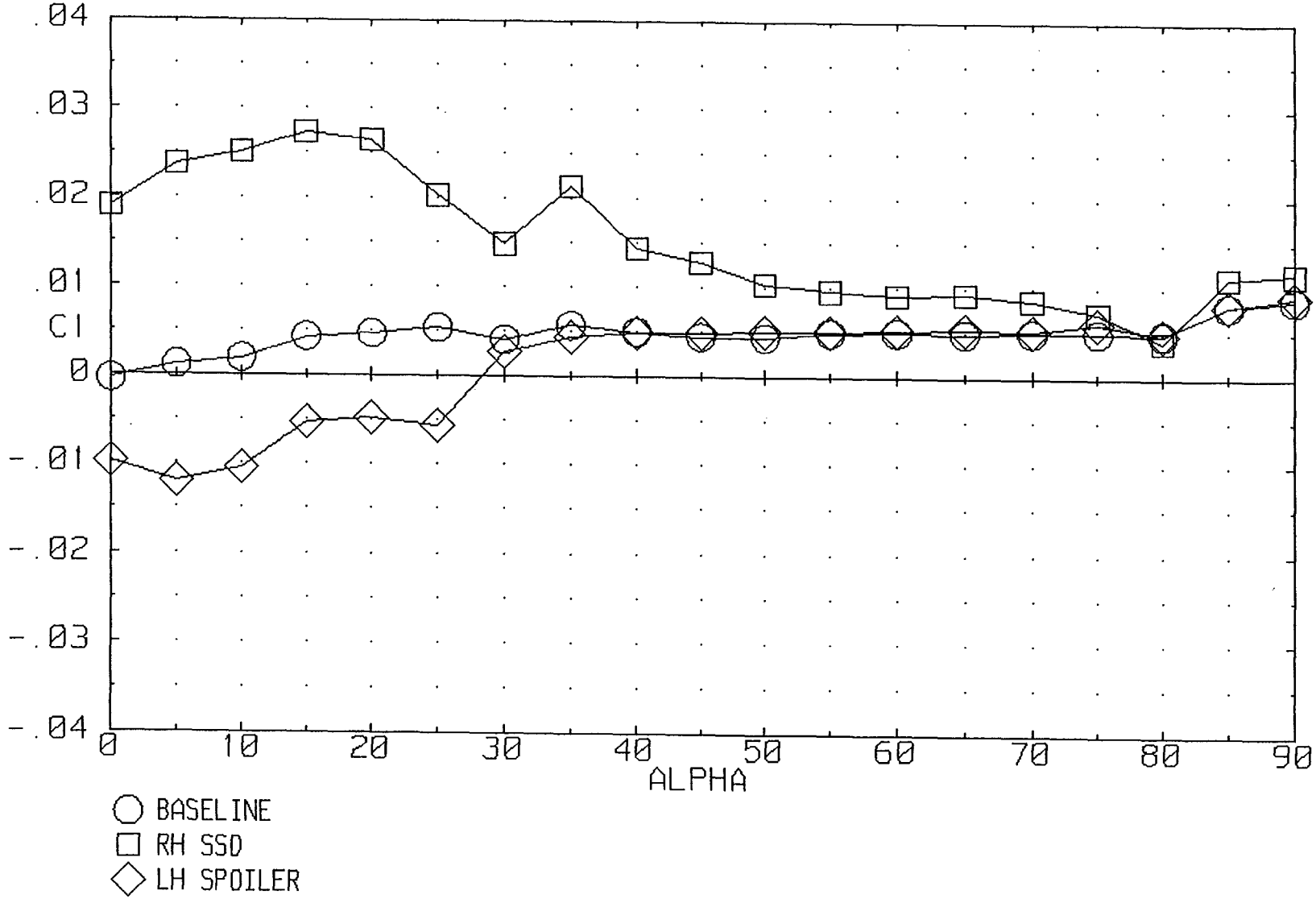

Figure 3-103. Effect of Right-Hand SSD on Rolling Moment for the ICE 101 (LEF=30, β=0°).

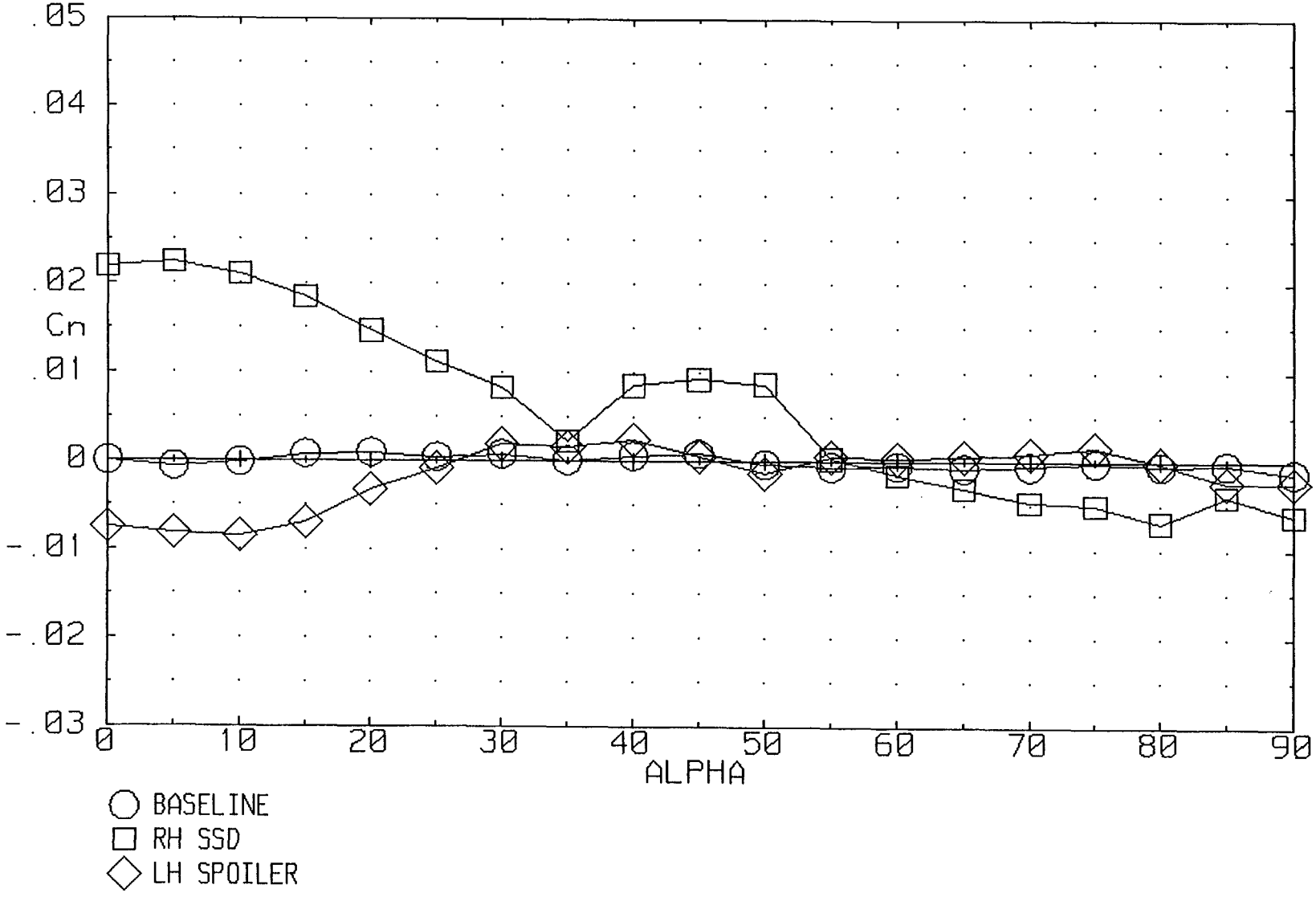

Figure 3-104. Effect of Right-Hand SSD on Yawing Moment for the ICE 101 (LEF=30, β=0°).

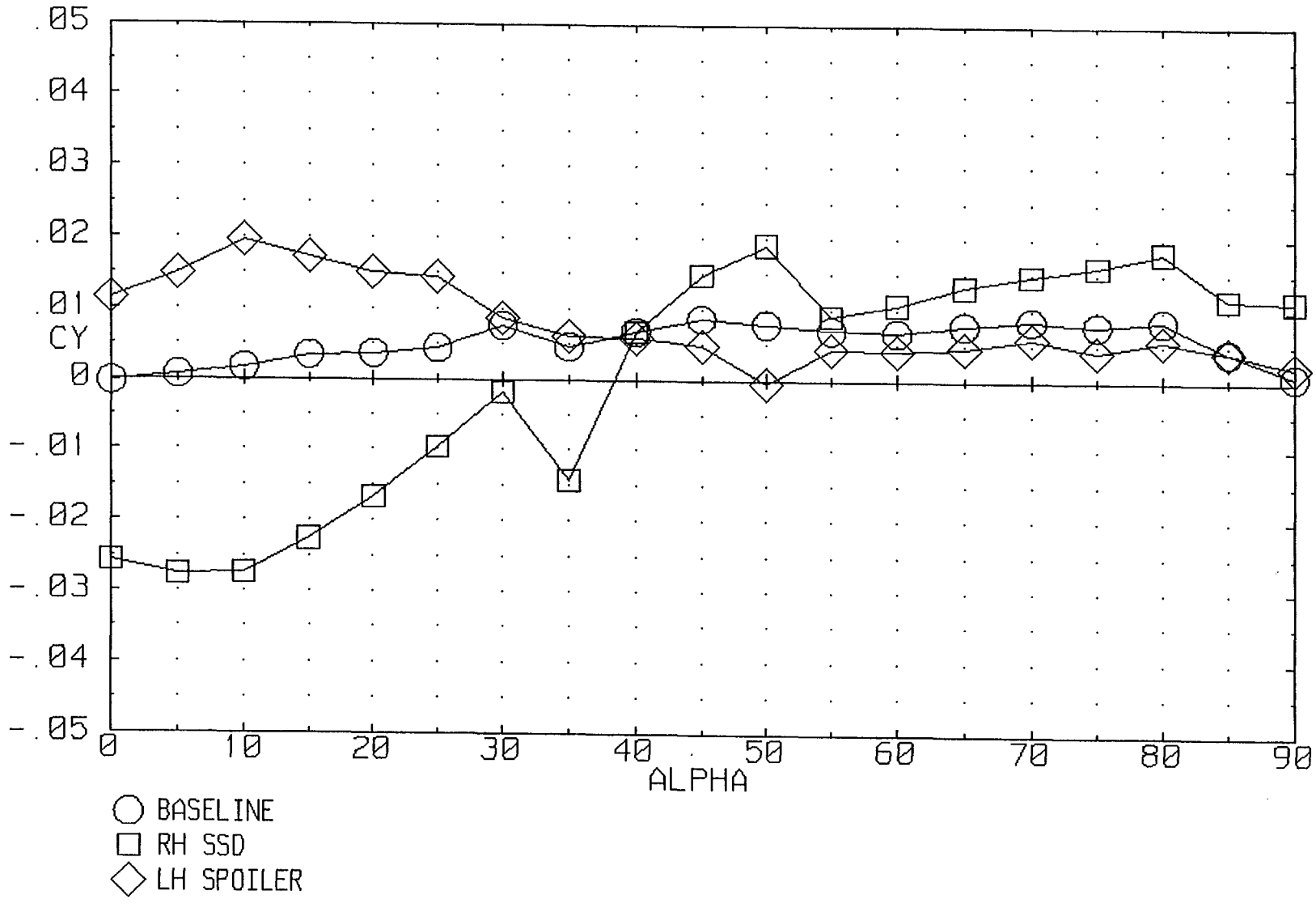

Figure 3-105. Effect of Right-Hand SSD on Side Force for the ICE 101 (LEF=30, β=0°).

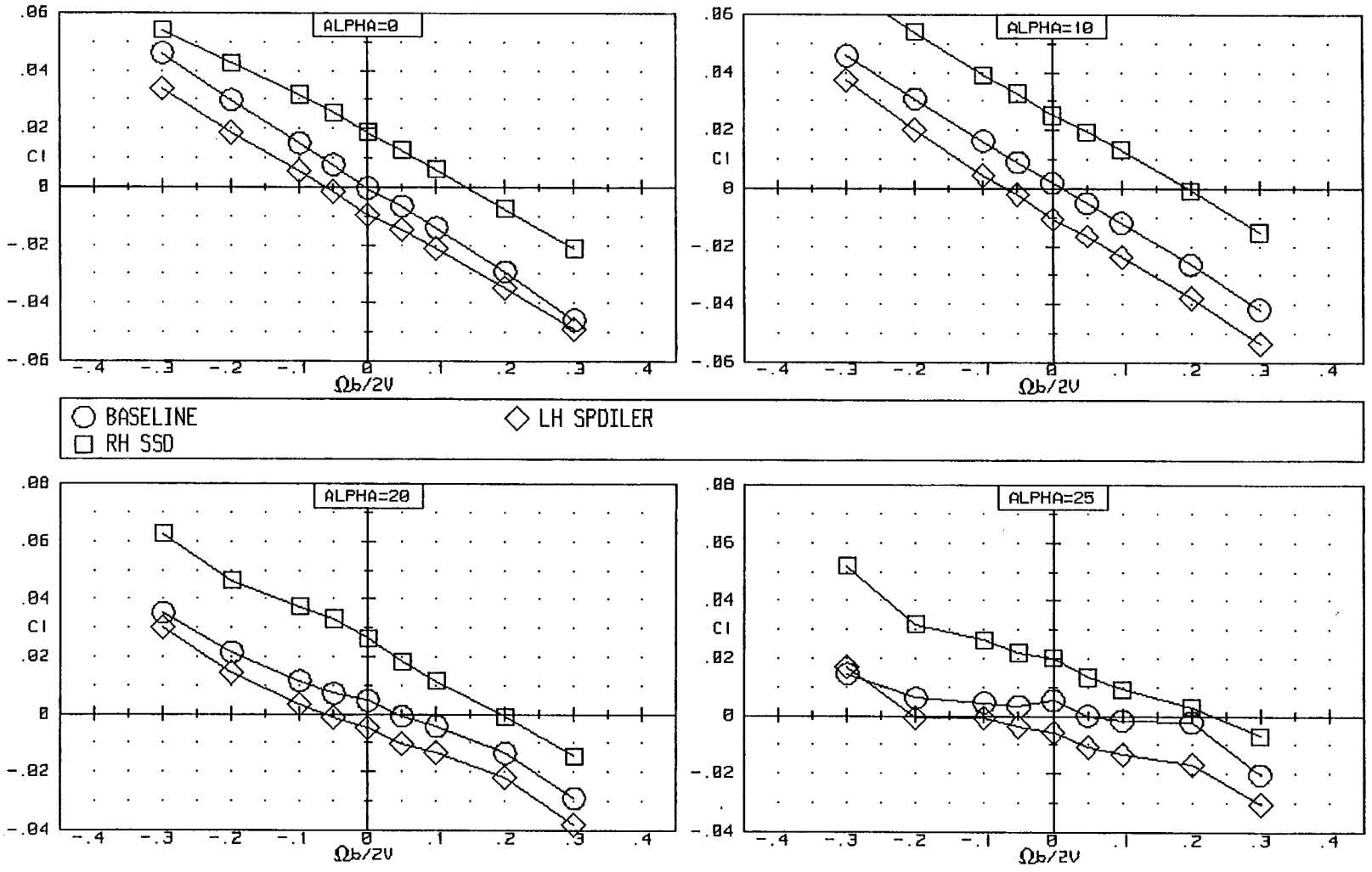

Figure 3-106. Effect of Rotation Rate and Right-Hand SSD on Rolling Moment for the ICE 101 (LEF=30, β=0°).

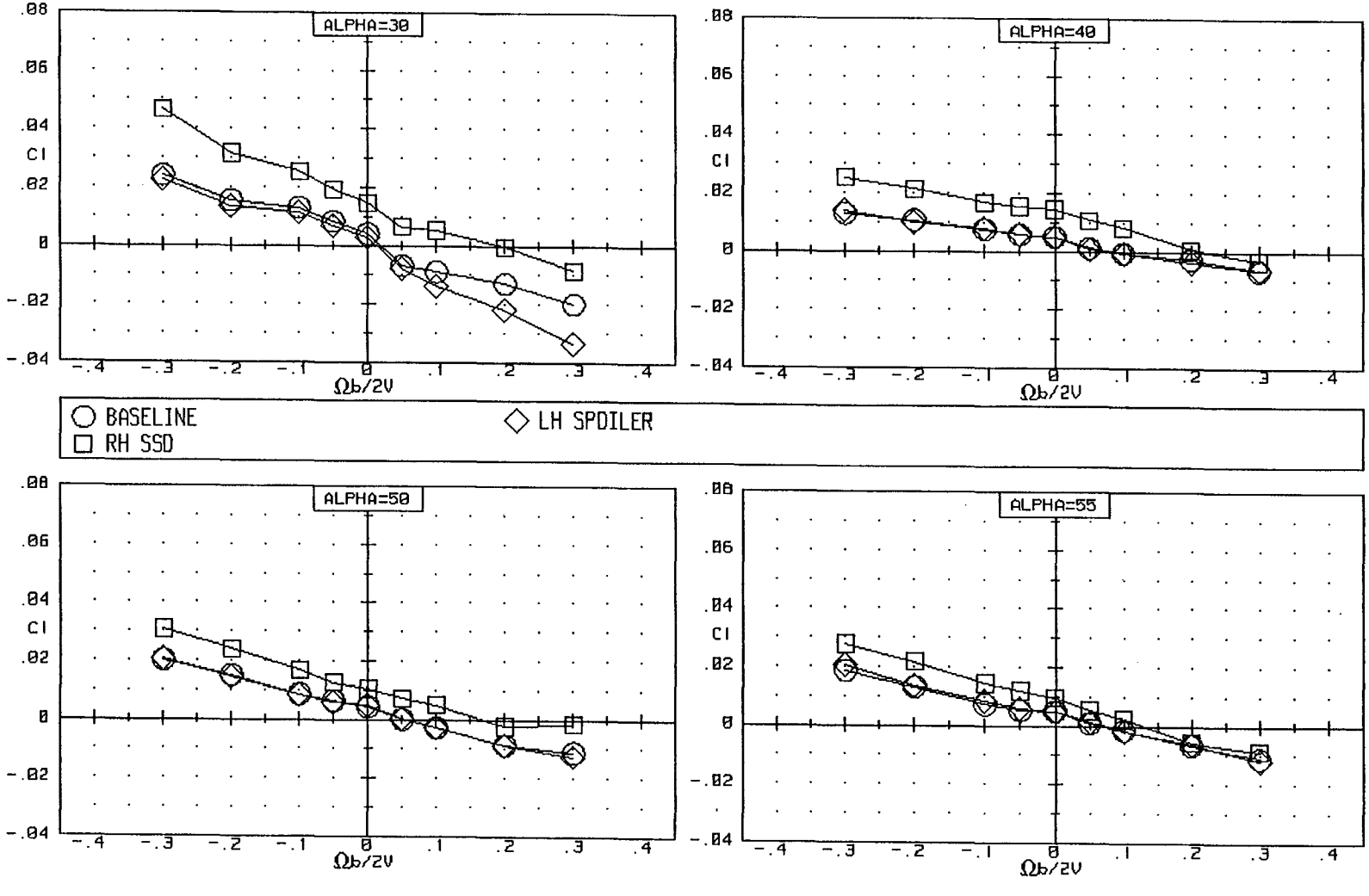

Figure 3-106. Continued.

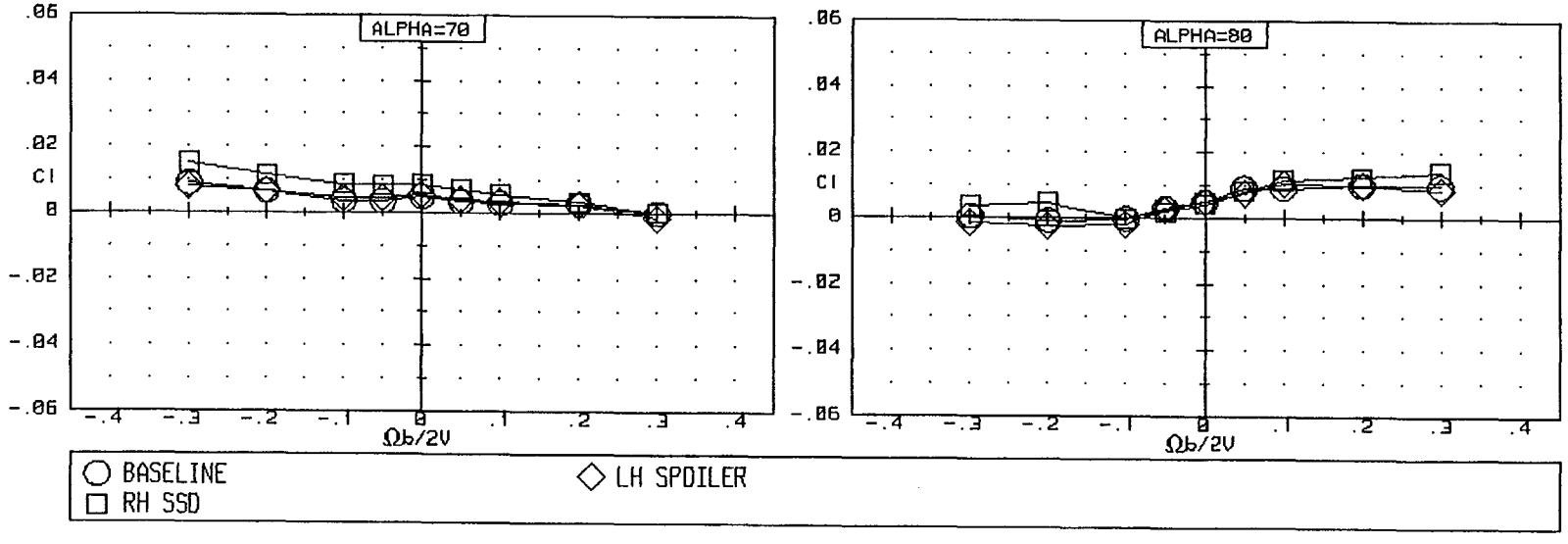

Figure 3-106. Concluded.

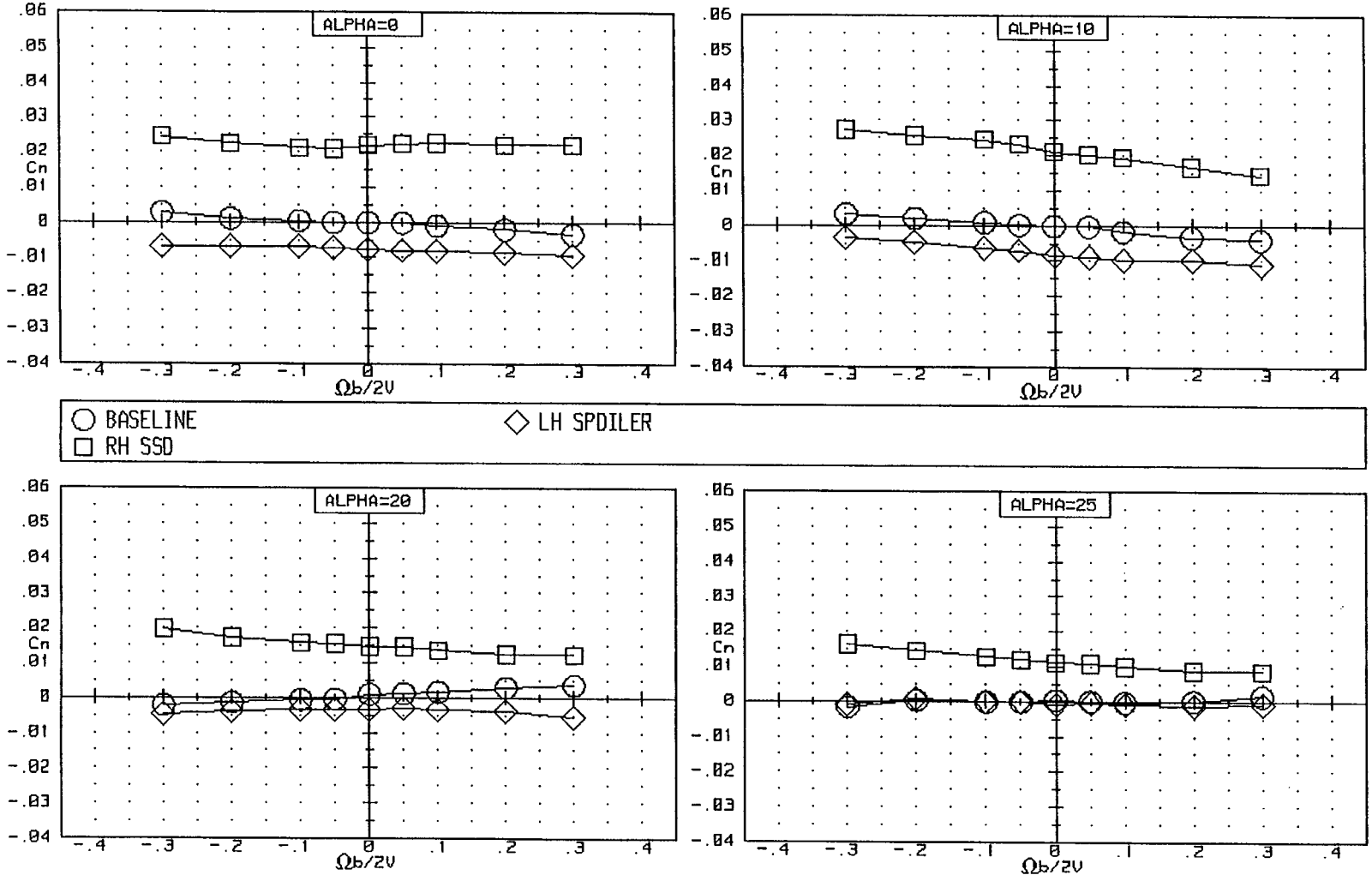

Figure 3-107. Effect of Rotation Rate and Right-Hand SSD on Yawing Moment for the ICE 101 (LEF=30, β=0°).

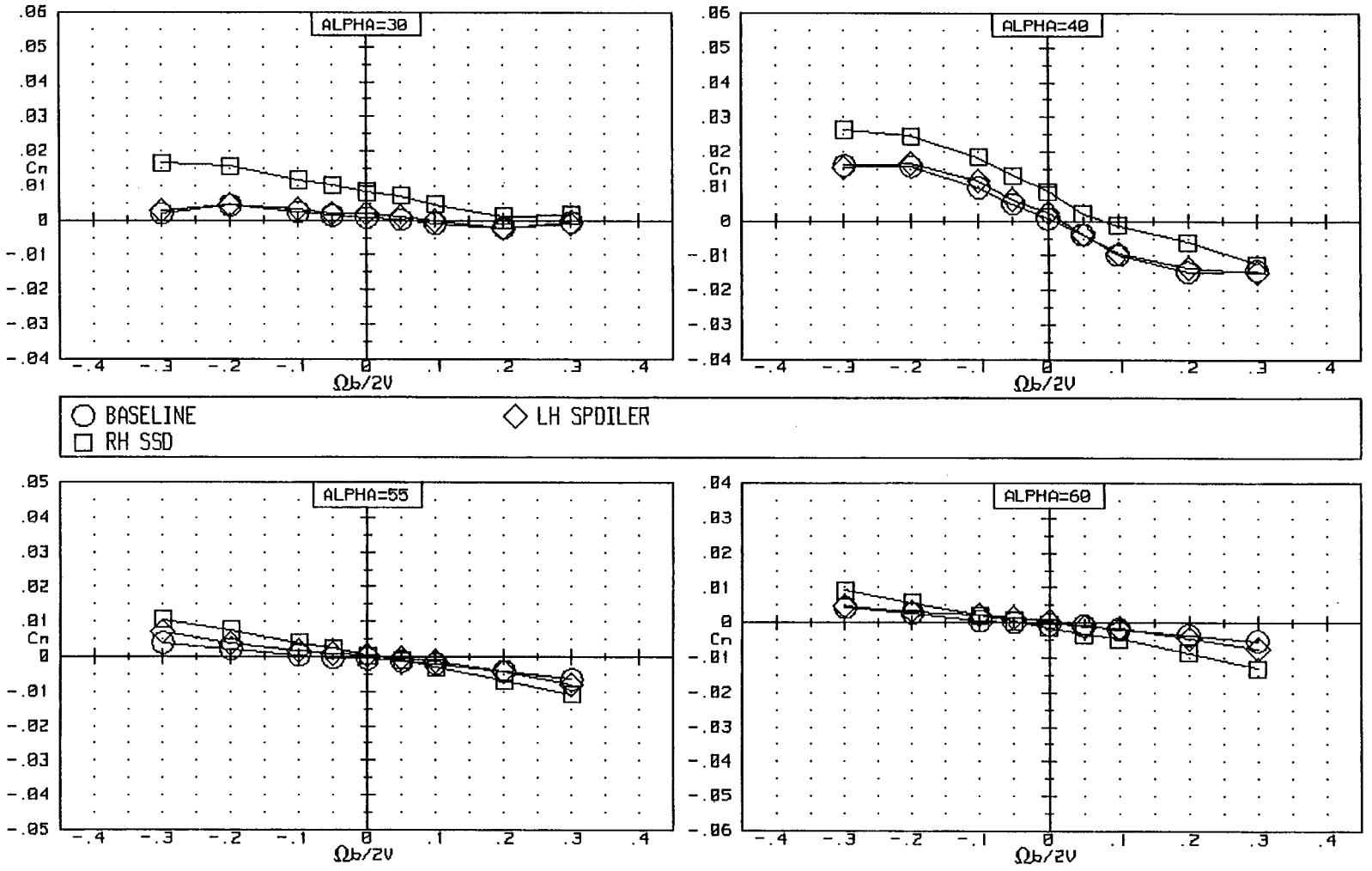

Figure 3-107. Continued.

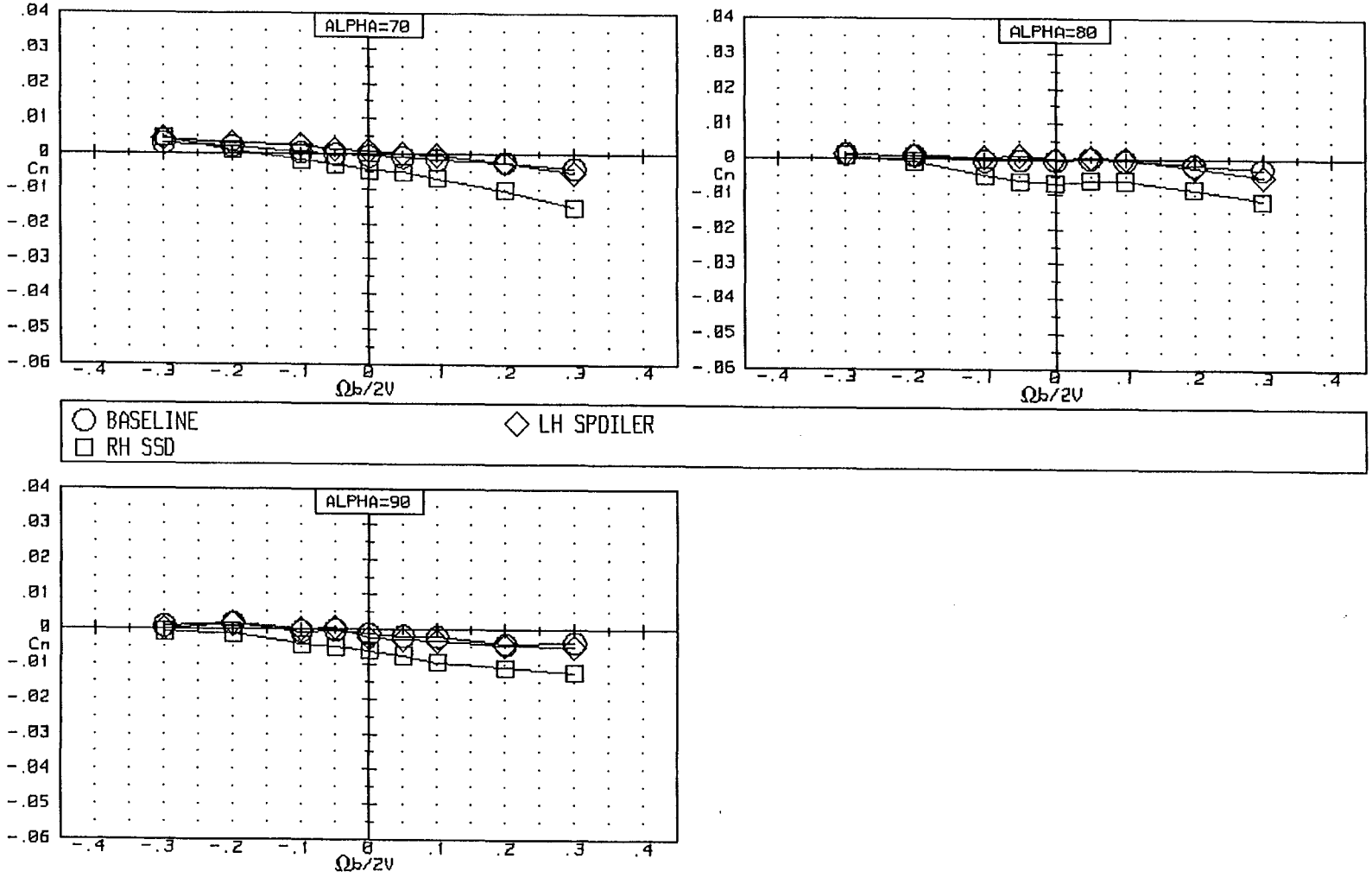

Figure 3-107. Concluded.

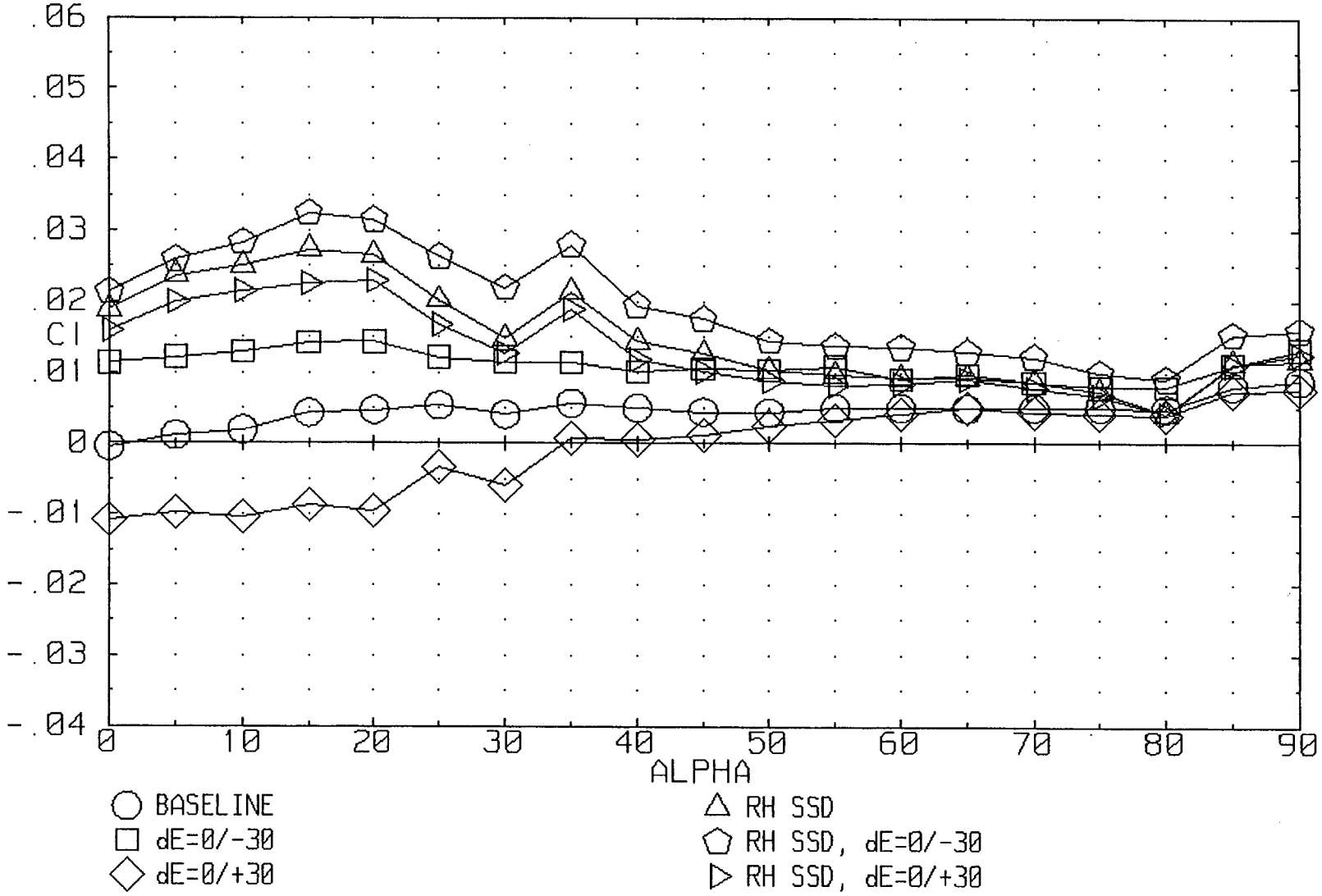

Figure 3-108. Effect of SSD/Elevon Interactions on Rolling Moment for the ICE 101 (LEF=30, β=0°).

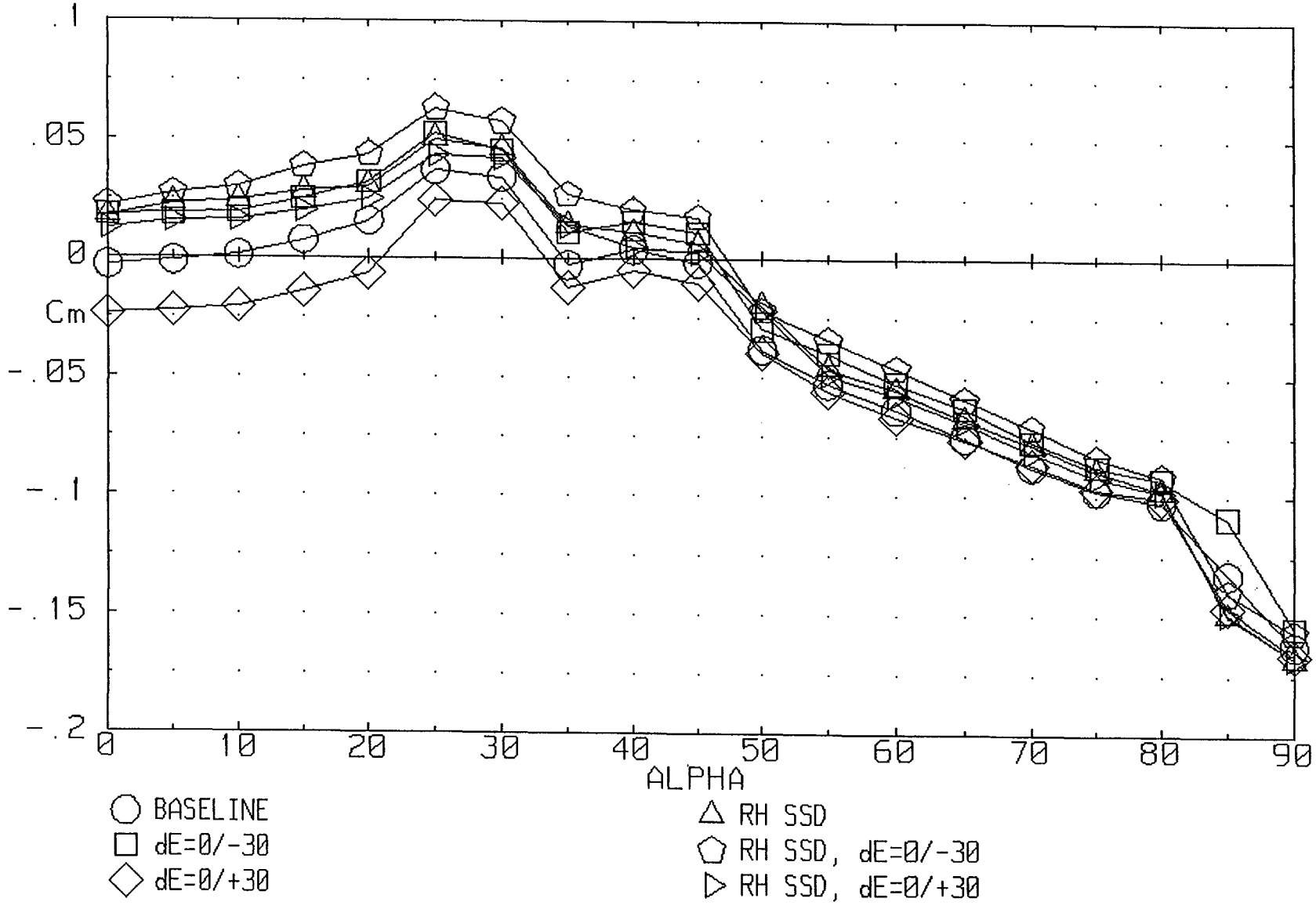

Figure 3-109. Effect of SSD/Elevon Interactions on Pitching Moment for the ICE 101 (LEF=30, β=0°).

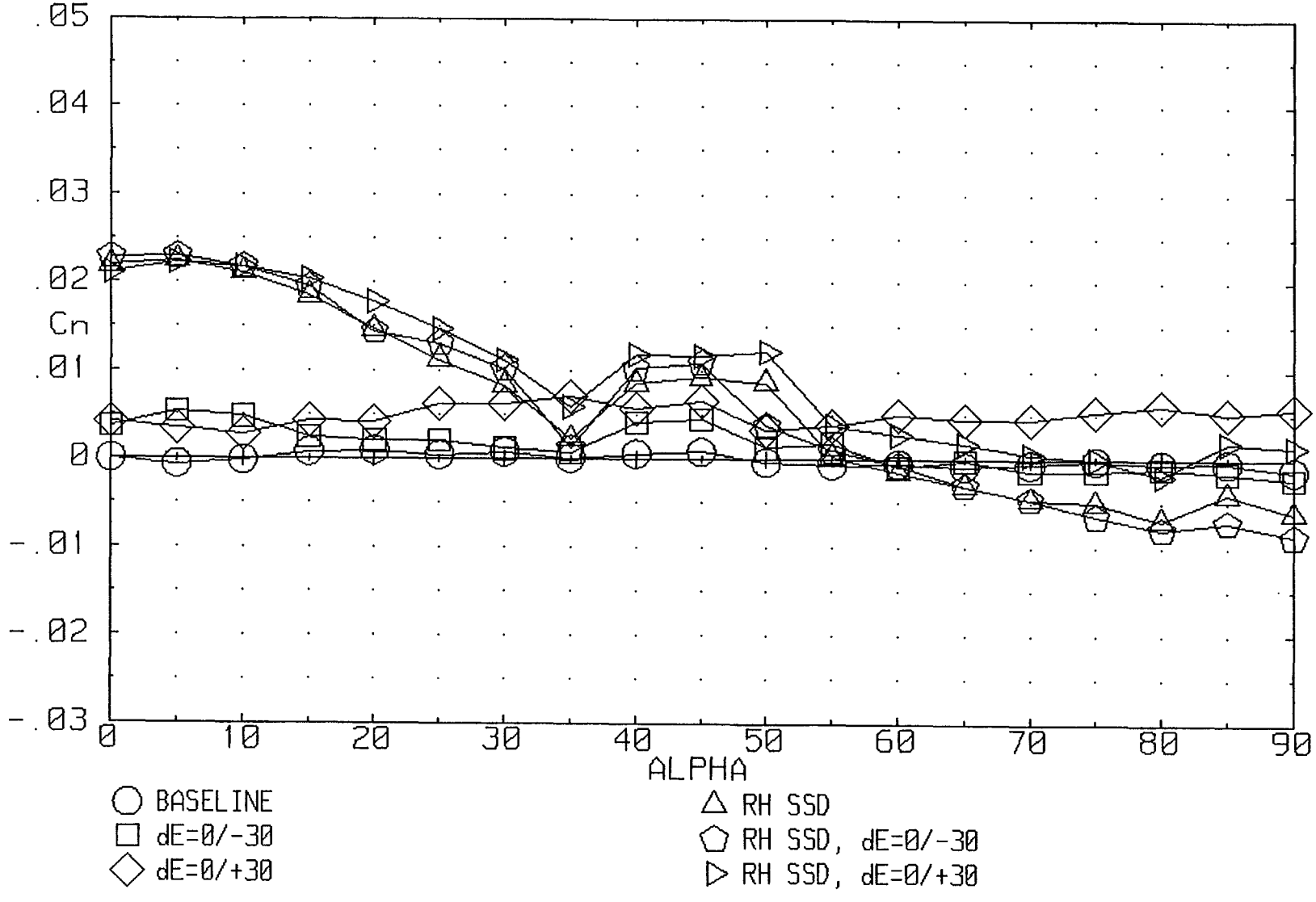

Figure 3-110. Effect of SSD/Elevon Interactions on Yawing Moment for the ICE 101 (LEF=30, β=0°).

4 SARL Wind Tunnel Test

4.1 Summary

A low-speed wind tunnel test (Mach 0.3) was conducted on a 1/18th scale flying wing model of a tailless fighter. The wing employed conical camber, a 65 deg leading edge sweep and a sawtooth trailing edge. The model was similar to the ICE 101 configuration previously described. The primary objective of the test was to investigate innovative aerodynamic control effector concepts for highly maneuverable tailless fighter aircraft. Two promising control concepts that had been previously researched, the all moving wing tip (AMT) and the spoiler-slot-deflector (SSD), were the focus of this test. The test results show that an AMT with a skewed pivot trunion provides improved yaw control power over one with a trunion oriented along a fuselage station. Conical wing camber degraded AMT yaw effectiveness at low AOA due to delayed flow separation over the deflected tip. Outboard locations of a spoiler-slot-deflector offer improved directional control compared to more inboard locations; furthermore, the adverse interactions with a trailing edge elevon are not as severe for the outboard-located SSD. Neither the AMT or SSD yaw control effectiveness was adversely affected by sideslip through high angles-of-attack. These results are all consistent with those observed during small-scale tests at the LMTAS ADF wind tunnel.

4.2 Introduction

The third wind tunnel test performed during the Innovative Control Effectors Phase 2 contract was a low-speed entry at the Subsonic Aerodynamic Research Laboratory (SARL) 7' X 10' wind tunnel located at WPAFB, Ohio. An existing 1/18th scale high-speed model of the LMTAS tailless fighter was modified under the ICE contract for this test. This model was representative of the 101-series of configurations investigated under Phase 1 of the ICE contract [Dorsett and Mehl, 1996]. An all new left wing was constructed incorporating two AMT and two SSD configurations.

The SARL test had four major objectives:

- Acquire high fidelity aerodynamic data for AMT and SSD controls.
- Validate results observed in previous tests.
- Evaluate slot geometry impacts on SSD effectiveness.
- Investigate methods to minimize adverse aerodynamic interactions between the SSD and elevon.

4.3 Model Description

A 1/18th scale high-speed wind tunnel model of the LMTAS tailless fighter concept was modified to incorporate all-moving wing tip and spoiler-slot-deflector controls. The original model incorporated inboard and outboard LEF, pitch flaps, elevons and an aileron/clamshell control surface on the trailing edge of the wing. In addition, upper and lower surface spoilers could be tested as well as a deployable rudder concept described by Dorsett and Mehl (1996). A photograph of the model is shown in Figure 4-1.

Integration of the SSD and AMT control surfaces required the manufacture of a new wing for the model. To keep model construction costs down, the SSD and AMT controls were only built into the left wing of the model. The new wing's external mold lines were made identical to the original model except for "actuator fairings" located on the bottom of the wing near the all moving tip. The model was designed to meet transonic and supersonic testing load criteria.

4.3.1 SSD Control Description

The new wing was constructed with a large slot, or vent located in front of the elevon, running from near the root to just outboard of the elevon. Five solid plugs were machined from Aluminum to fill the slot when testing zero deflection configurations. Individual plugs could be removed to vary the location and overall span of the hole and therefore the location of the SSD control surface. An inboard and outboard SSD location were provided, mimicking those tested during the small scale ADF test. (Figure 4-2 shows an assembly drawing for the new wing constructed for the SARL test.)

Three spoiler and deflector deflections were constructed (15, 45 and 60 deg) from bent Stainless Steel plate. The control surface hingelines were swept aft 25 deg to align with the sawtooth trailing edge of the wing. The aft hingeline sweep also provides increased spanwise moment arm from the control surface to the CG resulting in improved directional control effectiveness. The 60 deg spoiler and deflector parts were cut in half chordwise such that one-half of the control surface could be deflected at a time. This was done to simulate the segmented SSD control described for Configuration 101-1 during ICE Phase 1 [Dorsett and Mehl, 1996]. The spoiler was attached to the upper wing surface in a recessed land just forward of the large vent. The deflector attached directly to the lower wing surface and was not recessed into the wing contour. This resulted in an aft-facing step behind the deflector. Small filler pieces were required to smooth the upper surface of the wing when running with the SSD installed. Figure 4-2 includes a cross section of the SSD at 60 deg deflection. Figure 4-3 shows a drawing of various SSD configurations run during the test. Finally, Table 4-1 summarizes the SSD control combinations possible with this arrangement. Note that due to limitations on test time, the half-segments were not tested at the inboard location.

Table 4-1: Description of Possible SSD Combinations on the ICE High-Speed Model

Description	Area/Surface (in^2)	Centroid Location (2y/b)	Volume Ratio (One Surface Only)	Sketch
Outboard	9.6	0.558	0.0098	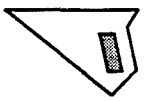
Outboard Outer Half	4.8	0.645	0.0055	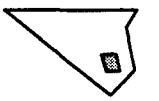
Outboard Inner Half	4.8	0.471	0.0043	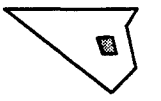
Inboard	9.6	0.469	0.0085	
Inboard Outer Half	4.8	0.557	0.0049	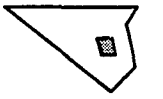
Inboard Inner Half	4.8	0.383	0.0036	

In addition to being able to vary spanwise location and control surface area, other variations on the SSD concept were investigated as well:

- Vents were added to the spoiler and deflector surfaces to try and reduce the aerodynamic interaction with the elevon.
- Fairings were placed inside the "slot" to smooth airflow.
- Simulated structural ribs were placed inside the slot to represent a more realistic structural integration.

Figure 4-3 illustrates each of these variations.

4.3.2 AMT

Two all-moving tip control concepts were integrated into the new left wing. A straight AMT (pivot trunion parallel to a fuselage station) was incorporated just outboard of the SSD and elevon. By removing the straight AMT and installing a filler piece, a skewed AMT (pivot trunion swept aft 25 deg) could also be fitted. The skewed AMT was identical in relative size and planform to that tested on both the ADF model and the rotary balance model. The straight AMT was sized to approximately the same area as the skewed tip; note that, it was not consistent with either of the straight AMTs tested during the ADF entry. Deflection blocks were used to set the AMT deflection angle by mating with a land machined into the integral AMT pivot shaft. The deflection blocks were held in place by two cap-head screws. Blocks were available for ±10, ±30 and ±60 deg deflections. Only ±10, +30 and +60 deg deflections were tested, however. Figure 4-2 shows the two AMT installations. AMT geometric characteristics are detailed in Table 4-2 below. Note that the moment arm used in the calculation of the control volume ratio accounts for the skewed pivot trunion, resulting in a greater arm to the CG.

Table 4-2: All Moving Wing Tip Geometric Paramters

Parameter (Model Scale)	Straight AMT	Skewed AMT
Area (in^2)	8.87	8.64
Arm to CG (in)	10.75	13.86
Volume Ratio	0.0106	0.0130
Sketch	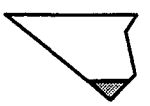	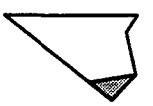

Figure 4-4 shows the two AMT planforms. Note the actuator fairing on the bottom surface (see also Figure 4-3). The fairings were required to house the AMT pivot shaft within the thin outboard wing section. A duplicate "bolt-on" fairing was constructed for the right wing so that the model contours would remain symmetric.

Integration of the AMT required modification of the outboard LEF. Small add-on LEF segments were machined so that the LEF matched up properly with either the straight or skewed AMT.

Comparison of Model with ADF and LAMP Models

Due to high-speed aerodynamic load considerations and differences in aft fuselage contour, the high-speed model control surface geometry was slightly different than that tested at ADF and LAMP. Figure 4-5 shows a comparison of the three wind tunnel model's planforms. The elevons, pitch flaps and skewed AMT were

identical for the three models. However, the SSD locations and sizes were slightly different between the three models as was the straight AMT planform.

One key difference between the various models was that the high-speed model incorporated conical camber in the wing. The previous two models had flat wings. The camber was built into the original LMTAS tailless fighter model; therefore, the new wing had to be manufactured to match the existing camber lines. As a consequence, the AMT leading edges were highly cambered resulting in poor low AOA AMT yaw control effectiveness (see results, below).

Finally, the LMTAS tailless fighter model did not incorporate inlets. Recall that the LAMP model had simple, non-flow through inlets. The ADF model did not incorporate inlets either; however, the forebody profile was slightly different from the high-speed model.

Model reference geometry is described in Table 4-3 below.

Table 4-3: SARL Test Model Reference Geometry

Data Reduction Constant	Value (Full Scale)
Model Scale	$1/18^{th}$
Reference Area (S, ft^2)	808.6
Reference Span (b, ft)	37.5
Mean Aerodynamic Chord (cbar, in)	345.0
Leading Edge MAC (FSLEMAC, in)	160.45
X-Moment Reference Center (MRC, % MAC)	38.0
Z-Moment Reference Center (WL MRC, in)	100.0

Control Surface Deflection Convention

Table 4-4 lists each control surface, the available deflections (left wing only) and its deflection convention. The controls on the right wing consisted of inboard and outboard LEF (not tested), elevons and pitch flaps.

Table 4-4: High Speed Model Control Surface Deflection Convention

Control Surface	Deflections Available (deg)	Positive Deflection Convention
Elevon	-30, -10, 0, 10, 30	TED
Pitch Flap	-30, -10, 0, 10, 30	TED
Inboard LEF	0, 40	LED
Outboard LEF	0, 20, 40	LED
Straight & Skewed AMT	0, ±10, ±30, ±60	TED
Inboard & Outboard Spoiler (No Vents)	15, 45, 60	TEU
Inboard & Outboard Deflector (Vented)	60	LED
Inboard & Outboard Half Spoiler	60	TEU
Inboard & Outboard Half Deflector	60	LED

Note: TED = Trailing Edge Down; LED = Leading Edge Down; TEU = Trailing Edge Up

4.4 Facility Description

The SARL wind tunnel is an open circuit wind tunnel with a 7' X 10' test section. The test section is oriented with the 10' dimension in the vertical plane. A 20,000 SHP motor drives an eighteen blade fan giving the tunnel a capability of reaching flow speeds in excess of Mach 0.6. An array of screens at the mouth of the tunnel provide a uniform flow through the test section.

The model was supported on an aft-sting capable of pitch angles up to 45 deg. The sting can be yawed ±10 deg in the test section; additionally, the sting can be rolled through 360 deg providing the capability of achieving large sideslip angles through 45 deg AOA. Only the roll and pitch capability were used during the current test to achieve the desired AOA and sideslip angles. Force and moment data were collected using a TASK Mk 40 1.5" diameter force balance.

4.5 Test Conditions

Flow conditions run during the test are summarized below:

- Mach Number: 0.2, 0.3, 0.5 (most runs at Mach 0.3)
- R_N (X 10^6 1/ft): 1.3, 1.9, 3.1 (varying with Mach)
- q (psf): 120 (at Mach 0.3)
- AOA Range (deg): -4 to 30 by 2, 35 to 45 by 5
- Sideslip Range (deg): -20, -15, -10, -8 to 8 by 2, 10, 15, 20

The run log is included as Table 4-5, below. Note that there were also fixed sideslip runs at varying AOA following the AOA schedule shown above.

Table 4-5: 1996 ICE SARL Run Log

ICE Phase II SARL Run Plan

Sref = 808.6 ft^2
MAC = 345.0 in
bref = 37.5 ft
X MRC = 38% MAC
WL MRC = 100 in
FS LEMAC = 160.45 in

A1 = Pitch Sweep -4 to 30 by 2 deg; 30 to 45 by 5 deg
B1 = Beta Sweep -20, -15, -10, -8 to 8 by 2 deg, 10, 15, 20

Configuration:
1: B1F1F2F3F4F5R1S1S2W1Y1

Note: All configurations are priority 1 unless noted.
All runs at Mach 0.3 unless noted.
Use sawtooth trailing edge for all configurations.
"Vents" describes both vented spoiler and deflector unless specified.

		Pitch Flaps		Elevons		OB LEF		Spoiler	Deflector	AMT	AOA=var; AOS=					AOS=var; AOA=									
No.	Configuration	L	R	L	R	L	R	L	L	L	-20	-10	0	10	20	0	15	20	25	27.5	30	32.5	35	37.5	40
1	1: Baseline w/ Old Wings	0	0	0	0	0	0	0	0	0	3	4	2	5	6	7		8							
2	2: Baseline w/ New Left Wing										43	44	32,42	45	46	48	49	50	51	52	53	54	55	56	57
3	Pitch Flap Series	-30	-30										58												
4		-10	-10										59												
5		10	10										60												
6		30	30										61												
7	Elevon Series	0	0	-30									62												
8				-10									63												
9				10									64												
10				30									65												
11	LEF Series	0	0	0		20							138												
12	(Skewed LEF)					40							143												
13	IB SSD (No Vents)					0		15	15		240	241	239	242	243										
14								45	45		246	245	244	247	248										
15								60	60				253			254	255	256	257	258	259	260	261	262	263
16	IB SSD/Elevon			-30				15	15				238												
17	(No Internal Struct.)			30									237												
18	(No Vents)							45	45				249												
19				-30									250												
20								60	60				251												
21				30									252												

		Pitch Flaps		Elevons		OB LEF		Spoiler	Deflector	AMT	AOA=var; AOS=					AOS=var; AOA=									
No.	Configuration	L	R	L	R	L	R	L	L	L	-20	-10	0	10	20	0	15	20	25	27.5	30	32.5	35	37.5	40
22	IB SSD/Pitch Flap	-30	-30	0	0	0	0	60	60	0			265												
23		30	30										264												
24	IB SSD+Vents/Pitch Flap												267												
25		-30	-30										266												
26	OB SSD (No Vents)	0	0					15	0				158												
27									15		163	164	162	165	166										
28									45				167												
29									60				168												
30								45					183												
31									45		187	188	186	189	190										
32									15				167												
33									0				157												
34								60					158												
35									15				168												
36									45				169												
37									60				170			171	172	173	174	175	176	177	178	179	180
38	OB SSD w/ Vents												191			192					193				
39	OB SSD No Vents w/ Fairings							60	60				216			217					218				
40	OB SSD No Vents w/ Struct.												225			226					227				
41								45	45				222												
42								15	15				221												
43	OB SSD/Elevon			-30									202												
44	(No Internal Struct.)			-10									210												
45	(No Vents)			10									211												
46				30									201												
47								45	45				200												
48				10									212												
49				-10									209												
50				-30									203												
51								60	60				204												
52				10									213												
53				-10									208												
54				30									199												
55	OB SSD+Vents/Elevon			-30									206												
56				30									197												
57	OB SSD+Fairings/Elevon												220												
58	(No Vents)			-30									219												

		Pitch Flaps		Elevons		OB LEF		Spoiler	Deflector	AMT	AOA=var; AOS=					AOS=var; AOA=									
No.	Configuration	L	R	L	R	L	R	L	L	L	-20	-10	0	10	20	0	15	20	25	27.5	30	32.5	35	37.5	40
59	OB SSD/Pitch Flap	-30	-30	0	0	0	0	60	60	0			215												
60		30	30										214												
61	Straight AMT	0	0					0	0	-10	67	68	66	69	70										
62										30	77	78	76	79	80										
63										60			81			82	83	84	85	86	87	88	89	90	91
64	Straight AMT/Elevon			-30									92												
65				30									93												
66	Skewed AMT			0						-10	127	128	126	129	130										
67										30	117	118	116	119	120										
68										60			103			104	105	106	107	108	109	110	111	112	113
69	Skewed AMT/Elevon			-30									133												
70				30									134												
71										30			136												
72				-30									132												
73										-10			131												
74				30									135												
75				0						10	122	123	121	124	125										
76	Straight AMT									10	72	73	71	74	75										
77	Skewed AMT/LEF					20				60			139												
78										30			137												
79						40							142												
80										60			140												
81	60 deg LEF					60				0	144	145	143	146	147										
82	OB SSD+Struct/Elevon			-30		0		60	60				224												
83				30									223												
84	Split OB SSD			0					IB 60			231	230	232											
85								OB 60	OB 60			160	159	161											
86	Baseline (Repeat)							0	0				9												
87	*												10												
88	w/o R-H Tip Fairing												41												
89	Baseline (Repeat)												94			95		96							
90	Baseline (M=0.5)												47												
91	OB SSD (M=0.2)							60	60				182												
92	OB SSD (M=0.5)												181												
93	OB SSD + Struct. (M=0.2)												228												
94	OB SSD + Struct. (M=0.5)												229												
95	Vented Spoiler/Solid Deflector												195												
96	Vented Deflector/Solid Spoiler												194												

		Knuckle Flaps	LEF	Pitch Flaps		Elevons		LEF		Spoiler	Deflector	AMT	AOA=var; AOS=					AOS=var; AOA=				
No.	Configuration		LOB/LIB/RIB/ROB	L	R	L	R	L	R	L	L	L	-20	-10	0	10	20	0	15	20	25	27.5
97	Vented Deflector/Solid Spoiler	OFF	0/0/0/0	0	0	30	0	0	0	60	60	0			198								
98	& Elevon					-30									207								
99	Vented Spoiler/Solid Deflector														205								
100	& Elevon					30									196								
101	1: Baseline (Old Wings) Inverted					0				0	0				11								
	LMTAS Proprietary Testing																						
111	Flow Angularity Checks	0													97			101					
112															98			102					
113															99								
114															100								
115	Baseline Repeat														149			150		151			
116	Split OB SSD/Elevon					-30				IB 60	IB 60				233								
117						-10									234								
118						10									235								
119						30									236								

4.6 Discussion of Results

A discussion of the SARL results follows. Unless otherwise specified, all data presented in this section are in the body axis coordinate system and referenced to 38% MAC. The force and moment coefficients are non-dimensionalized by the data shown in Table 4-3, above.

4.6.1 Data Tie-in and Repeatability

The model used for this test was previously tested at SARL in 1994 [Dorsett, 1994], the NASA LaRC 8' transonic wind tunnel and the NASA LaRC 4' Unitary supersonic wind tunnel, both in 1992 [Peters, 1995]. The model was first run with the original wings to tie in with the 1994 SARL wind tunnel data. After good agreement with the 1994 data was confirmed, the left wing that was developed for the ICE study was installed, and baseline comparisons made once again to determine the fidelity of the new installation. Figures 4-6 and 4-7 show the longitudinal and lateral-directional tie-in with the 1994 data, respectively. Excellent agreement in the longitudinal data was observed up to 35 deg AOA with small differences observed in the data at higher AOA. The lateral-directional differences were negligible. The most noticeable differences were found in the side force data (particularly at AOA = 20 deg). However, because of the tailless design, this configuration does not generate large side forces in the first place. The

differences are very small compared to the overall TASK balance side force capacity (e.g., 3 lbs out of 800 lbs maximum).

Figures 4-8 and 4-9 show the tie-in and repeatability between the new wing and the original wings. The only significant difference was observed in pitching moment in the form of a 30-count C_{mo} shift. The shift was attributed to the under-wing actuator fairings housing the AMT shafts. The right fairing was removed (the left was integral with the wing and could not be removed) and the C_{mo} shift was cut in half (Figure 4-10).

4.6.2 All Moving Wing Tip

Comparison of straight and skewed AMT control effectiveness is shown in Figure 4-11. Note that the skewed AMT is slightly smaller in area than the straight tip, yet it provides greater control power for a given deflection. The skewed hingeline generates significant side force increments that aid yawing moment. The control generates adverse rolling moments below 10 - 15 deg AOA (depending on deflection) and favorable rolling moments at higher AOA; these results are consistent with previous data (e.g., ADF and rotary balance results).

Yaw effectiveness is essentially constant for a given deflection above 10 deg AOA. However, yaw power drops off at low AOA. This is inconsistent with both the ADF and rotary balance results. Recall that the high speed model incorporates a considerable degree of conical camber. The AMT generates yawing moment primarily through increased drag on the deflected tip acting through a moment arm. The camber has the effect of keeping the flow attached over the wing tip to a higher local AOA (i.e., AOA + upwash + tip deflection) than an uncambered airfoil. ADF and rotary balance results as well as other previous AMT data published in Dorsett and Mehl (1996) indicated essentially constant yaw effectiveness with AOA for trailing edge down AMT deflections. The cambered wing on the current model resulted in poor AMT performance at low AOA.

This effect can be further illustrated by studying the axial force curves vs. AOA (Figure 4-12). The local slope change in C_A (e.g., a less negative slope) between 8 deg and 10 deg AOA is indicative of flow separation. The increasing ΔC_A between zero and tip-deflected cases corresponds with the increased yaw power above 10 deg AOA. Figure 4-13 shows a close-up of the AMT deflected -10 deg on the high-speed model. Note the camber at the leading edge of the tip.

Effect of Sideslip

Figures 4-14 and 4-15 show the effect of sideslip on straight and skewed AMT control power, respectively. Sideslip effects on yaw power are relatively benign at all AOA. Sideslip effects on rolling moment are nonlinear, but tend to be small or zero for windward sideslip angles greater than 10 deg (i.e., -10 deg β), increasingly negative between $\pm$10 deg β, and return to near zero at large leeward β (positive in this case). These results are consistent with those obtained in the ADF and rotary balance tests.

Interaction with Elevon

Figures 4-16 and 4-17 show the effect that the skewed AMT has on control effectiveness for both -30 deg and 30 deg elevon deflections, respectively. These curves represent elevon control power in the presence of various tip deflections.

For the -30 deg elevon case, TED AMT deflections slightly reduced nose-up elevon pitch power between 10 deg and 20 deg AOA. They also degraded roll power over an AOA range between 10 deg and 30 deg. Notice too that the 60 deg AMT deflection doubled the zero-α elevon yaw. The -10 deg AMT deflection had no significant interaction with elevon control power.

Similar results were observed in the 30 deg elevon case. Once again, TED AMT deflections reduced elevon nose-down pitch power and roll power at moderate AOA. They also significantly increased elevon adverse yaw up to 30 deg AOA.

Interaction with LEF

AMT interactions with the left-hand LEF are shown in Figures 4-18 and 4-19. These data represent AMT control power in the presence of various LEF deflections. In both figures, note that deflecting the LEF reduces the favorable roll in the range of 15 deg to 30 deg AOA. Also, AMT yaw power is increased about 20% in the presence of AMT deflections for AOA > 10 deg.

4.6.3 Spoiler-Slot Deflector

Discussion of SSD control effectiveness is broken up into two sections based on SSD control location: outboard and inboard.

Outboard SSD Location

SSD control effectiveness at the outboard location for three deflections is presented in Figure 4-20. At low AOA, the control generates nearly 1:1 roll to yaw in the favorable sense. Yaw power begins to fall off above 10 deg AOA with larger deflections retaining yaw effectiveness out to 40 deg AOA. Roll power is not as sensitive to AOA – significant roll effectiveness is retained beyond 42 deg AOA. Finally, outboard SSD deflections generate nose-up pitching moments. These results are all consistent with the ADF and rotary balance data.

The effect of sideslip on outboard SSD control power is illustrated in Figure 4-21. Yaw power is insensitive to sideslip below 25 deg AOA. Above 25 deg, windward sideslip has little effect on yaw power and actually improves yaw effectiveness at 40 deg AOA. Leeward sideslip angles generally degrade SSD control power above 25 deg AOA. Roll control power is affected in a nonlinear fashion by sideslip. Pitching moment becomes less nose up with increasingly leeward sideslip and more nose-up with increasing windward sideslip.

Figure 4-22 shows the effect of Mach and Reynolds number on SSD control power for a 60 deg deflection. There are no appreciable effects of Mach or Reynolds number over the range tested.

Interaction with Elevon and Pitch Flaps

Figures 4-23 through 4-26 summarize the aerodynamic interactions of the SSD with the elevon. SSD deflections reduce elevon pitch and roll effectiveness – the interaction is increasingly unfavorable with increasing SSD deflections. Large SSD deflections actually result in elevon control reversal at low AOA with the elevon deflected -30 deg. The degree of interaction decreases at higher AOA.

SSD aerodynamic interactions with the pitch flaps are not near as severe as those on the elevon (Figure 4-27). In fact, the outboard SSD results in a favorable interaction with the pitch flap creating greater pitch effectiveness for the control surface over a large AOA range. This effect was also observed in the ADF data for the outboard forward SSD location.

Effect of Venting the Outboard SSD

A set of 60 deg SSD deflections were constructed with 0.5" tall vents located at the base of the control surface along the hingeline (see Figure 4-3). It was hoped that the vents would help reduce the adverse interaction between the SSD and the elevons. Figure 4-28 shows the effect that the vents had on SSD control effectiveness. Each vented panel was tested individually, and then with both spoiler and deflector

vented. Venting the control surface resulted in essentially no change in yaw power. Roll power and nose-up pitch were reduced at low AOA. This effect was most pronounced with both the spoiler and deflector vented. Interaction of the vented SSD with the elevon is shown in Figures 4-29 and 4-30. Unfortunately, venting the SSD had little to no effect on the elevon interaction characteristics.

Internal Slot Variations

Two variations were made within the slot of the SSD. First, smooth fairings were attached to the front and rear walls of the slot cutout to smooth the airflow passing through the slot. Second, two small Aluminum pieces simulating wing rib structure were placed within the slot along a buttline. The "simulated structure" parts were located within the slot at buttlines 6.12 and 7.53 (model scale), respectively (reference figures 4-2 and 4-3). The effects of each of these variations on SSD control effectiveness are summarized in Figure 4-31. The fairings resulted in a small reduction in SSD roll power at all AOA. Nose-up pitch was also reduced slightly. Yaw effectiveness remained unchanged. The structural pieces had no effect on the SSD control characteristics.

It was hoped that some of the variations made to the SSD slot would reduce the interactions with the elevons. Figures 4-32 and 4-33 show that this was not the case. None of the modifications attempted had much affect on the adverse interaction with the elevon.

SSD Size Variation

Half-size 60 deg spoiler and deflector parts were tested to determine a size effect on SSD effectiveness and interaction with the elevon. The half-sized parts were made by cutting the full length SSD pieces in half. These parts were tested both at the inboard half and outboard half of the vent. The remainder of the vent was closed off with filler blocks. Figure 4-34 shows a photo of one of the half-size SSDs on the model.

Figure 4-35 shows the effectiveness of the half-size SSD controls compared with the baseline SSD at 60 deg. The smaller SSDs generate less than half the nose-up pitch of the full sized SSD. Low AOA roll power is similar between the inboard and outboard half segments generating less than half the roll power of the full-sized SSD. At high AOA, the inboard segment generates more roll effectiveness – nearly equaling the full-sized segment. The outboard segment generates slightly more yaw effectiveness at low AOA due to its increased moment arm with respect to the MRC. At AOA greater than 15 deg, the yaw effectiveness is similar for both half segments.

The half-segment interactions with the elevon are compared with the full-sized SSD interaction in Figures 4-36 through 4-39. Below 15 deg AOA, elevon pitch and roll power are not as affected by the half-sized segment as by the full-sized SSD. Above 15 deg AOA, the interactions are similar for both the half-sized and full SSD. Note that these data are presented only for the inboard half segment of the SSD. The outboard half-sized segment was not tested with the elevon. Data for ±10 deg elevon deflections show the interactions for both the full and half-sized SSD segments to be similar.

Inboard SSD Location

The SSD was moved inboard 1.1" model scale (2y/b = 0.088) by removing the inner-most filler block, and replacing the outer-most block (reference Figure 4-2). Inboard location control effectiveness curves are shown in Figure 4-40. Comparison of these data with those presented in Figure 4-20 show that at AOA = 0, control effectiveness is essentially unchanged by location. However, at higher AOA, the inboard location generated more nose-up pitch, greater roll power, and less yaw power than the outboard segment. These characteristics were also observed in the small scale ADF data.

Figures 4-41 and 4-42 show the aerodynamic interaction between the inboard SSD and the elevon. Figures 4-43 and 4-44 compare the IB SSD/elevon interactions with the outboard for -30 deg and 30 deg elevons, respectively. These data indicate that the inboard location creates a more adverse interaction than the

outboard location (i.e., less elevon pitch and roll control with the SSD open) for a given SSD deflection angle. This result was also observed during the ADF test.

Finally, Figure 4-45 shows the interaction between the IB SSD and the pitch flaps. Recall that the OB SSD interaction was slightly favorable to the pitch flap. The IB SSD location has an adverse interaction with the pitch flaps, particularly for nose-up control power. Note that these interactions are not as severe as those observed in the ADF test.

4.7 Control Power Variations with Control Volume

Data from all of the ICE Phase 2 wind tunnel tests (including both 101 and 201 configurations) were compiled to generate roll and yaw power relationships with control volume for both AMT and SSD controls. These data should be useful when making future aerodynamic effectiveness predictions for these types of control surfaces. Figures 4-46 and 4-47 show roll and yaw power variation with control volume for the AMT = 60 deg at AOA = 0, 15, 30, and 45 deg. Data from the various tests group well together at low AOA, but are more scattered at higher AOA, with the LAMP yawing moment data generally having lower magnitudes than either the SARL or ADF data.

The same type information is shown for the SSD in Figures 4-48 and 4-49. SSD roll power data are well grouped at AOA = 0 deg, becoming less organized as AOA increases and separated flow effects dominate. SSD yaw power data cluster together well for 0 deg and 15 deg AOA; trends are more difficult to pick out at higher AOA as the surface looses yaw effectiveness.

4.8 Conclusions

Overall, this test confirmed many of the results observed during the ADF small scale test (ADF 9605). Namely:

- The skewed AMT generates greater yaw power than the straight AMT due to favorable side forces contributing to the yawing moment.
- AMT yaw control power is generally unaffected by sideslip. Windward sideslip angles increase the AMT yaw effectiveness. Roll power is nonlinear with sideslip angle.
- The outboard SSD location is superior to the inboard location due to:
    1. Increased yaw power because of a greater moment arm with respect to the CG.
    2. Less nose-up pitching moment when deployed.
    3. Less severe SSD/elevon aerodynamic interactions.
    4. Slightly favorable SSD/pitch flap aerodynamic interactions.
- SSD yaw control power is generally unaffected by sideslip. Roll control effectiveness is nonlinear with sideslip.
- AMT and SSD control power trend linearly with control volume below 15 deg AOA. At higher AOA, control effectiveness does not increase as rapidly with increasing control volume as at low AOA.

New information learned during this test included:

- Conical camber has a detrimental effect on AMT yaw control power at low AOA due to delayed flow separation over the deflected tip. These control devices would be better suited to a wing with minimal or no conical camber.

- AMT/elevon control interactions are significant in the 10 deg to 30 deg AOA range – particularly with regard to reduction in elevon roll power. However, these interactions are not near as severe as the SSD/elevon interactions.

- The LEF provides a favorable interaction with AMT yaw power increasing its magnitude approximately 20% for AOA > 10 deg. AMT roll effectiveness is more adverse in the presence of LEF deflections.

- Internal structure seems to have no effect on SSD control performance so long as the slot area blocked by the structure is not too great.

- There were no Reynolds number effects observed in the SSD control data over a range of R_N = 1.3 to 3.1 x 10^6 1/ft. Note that Mach number varied between 0.2 and 0.5 during these runs.

- Smooth aerodynamic fairings inside the SSD slot provide no benefits with regard to control power or reduced SSD/elevon interaction. The fairings partially blocked the slot resulting in reduced SSD control effectiveness below 20 deg AOA. A similar reduction in SSD control power due to slot blockage was also observed during the ADF 9604 entry.

- Venting the lower portion of the spoiler and/or deflector along the hingeline did not provide any benefits with regard to control effectiveness or reduced SSD/elevon interaction.

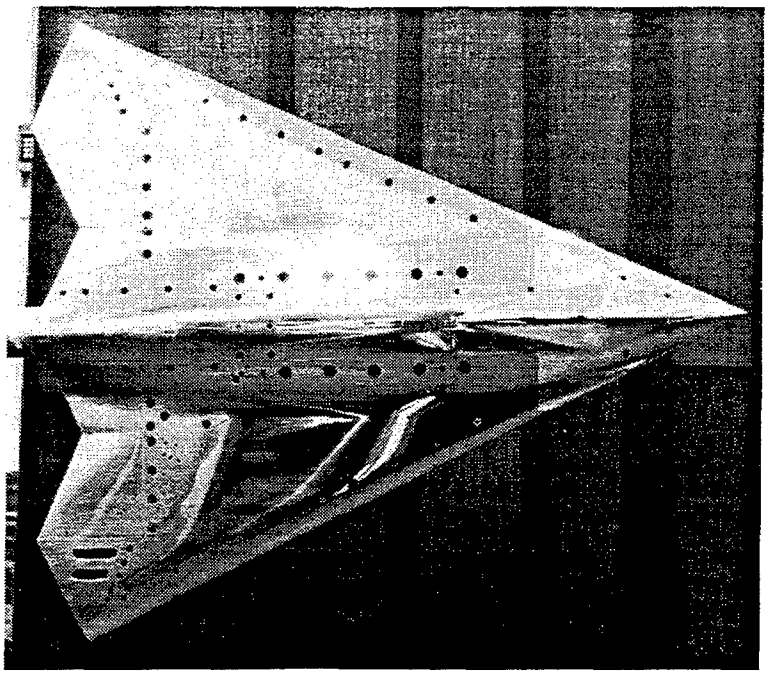

Figure 4-1: 1/18th Scale LMTAS Tailless Fighter Wind Tunnel Model

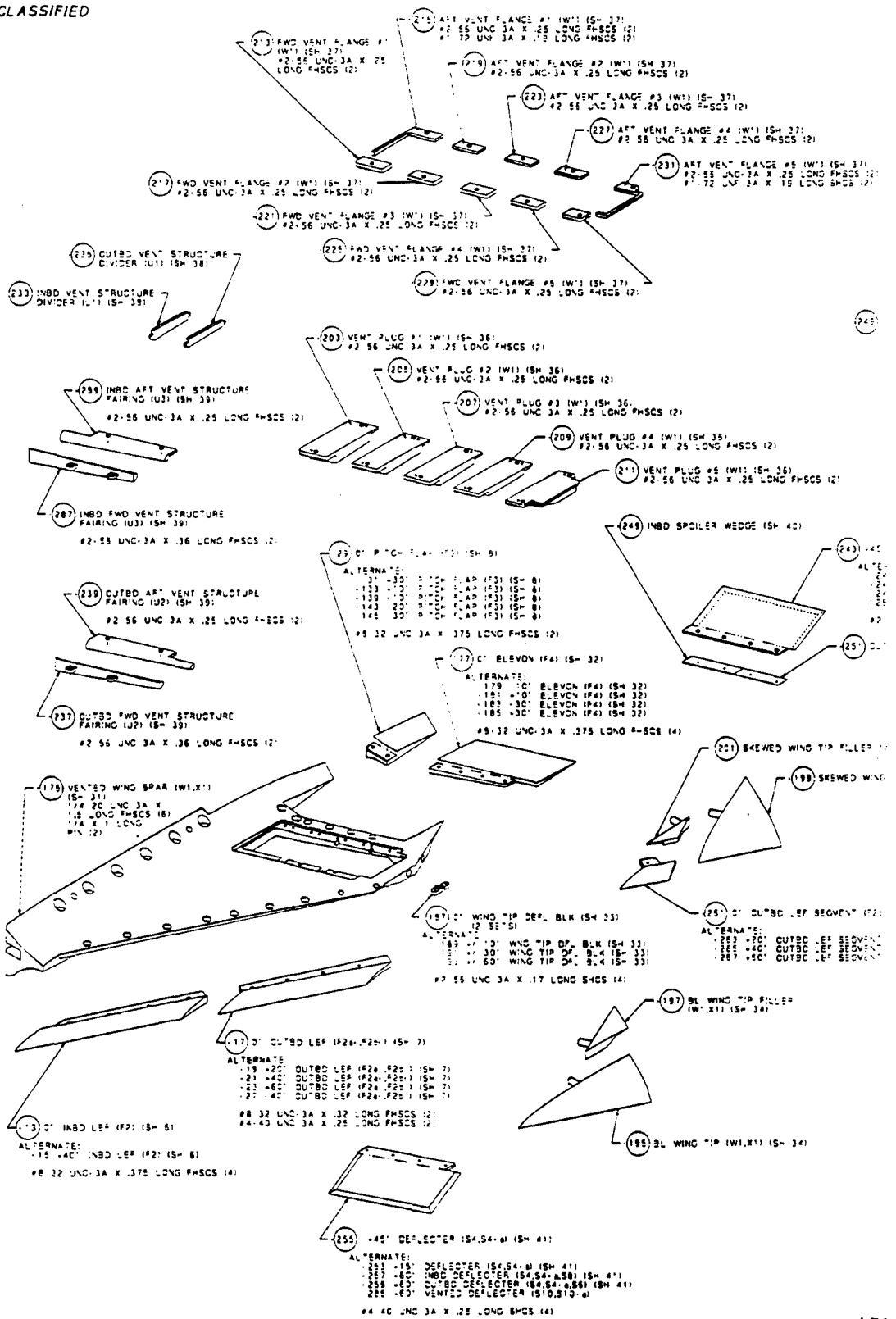

ISOMETRIC ASSY VIEW

SCALE 1/2

Figure 4-2: Assemi

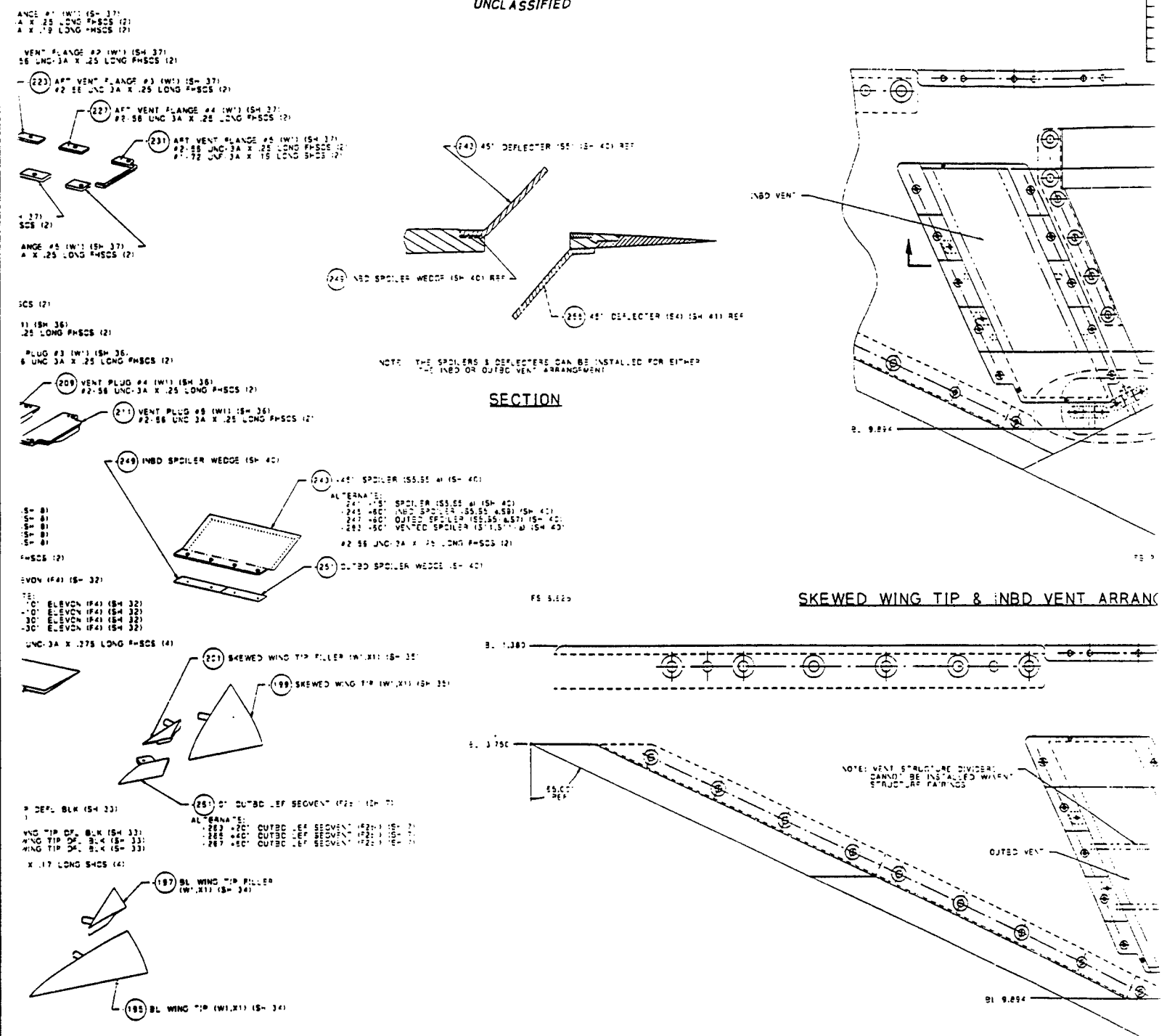

Figure 4-2: Assembly Drawing of New Wing Constructed for ICE SARL Test

IFIED

UNCLASSIFIED

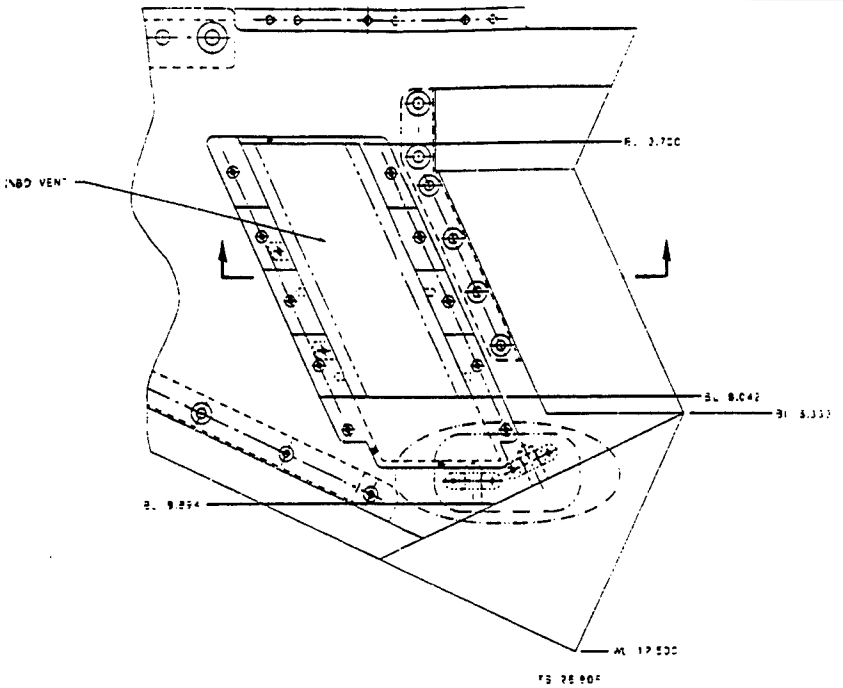

SKEWED WING TIP & INBD VENT ARRANGEMENT

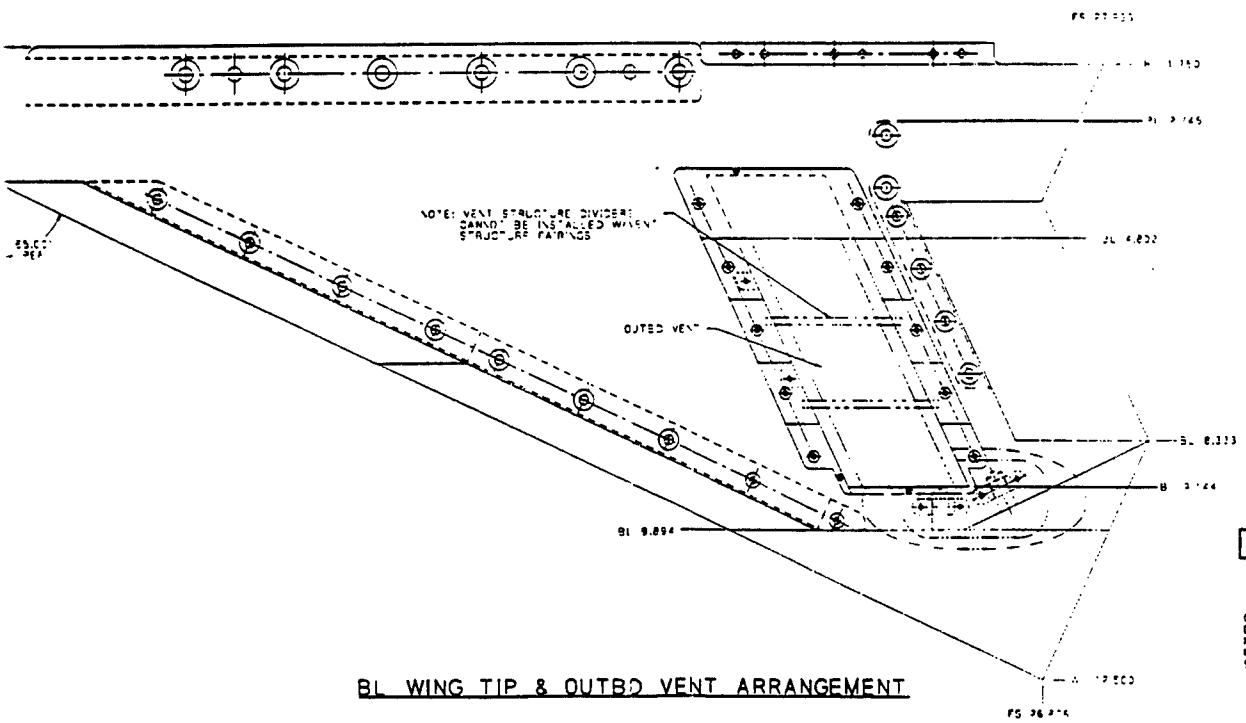

442ZW

SH 30

BL WING TIP & OUTBD VENT ARRANGEMENT

R ASSY

UNCLASSIFIED

FOR MODEL TEST USE ONLY

LOCKHEED MARTIN

FORT WORTH TEXAS

442ZW

ng Constructed for ICE SARL Test

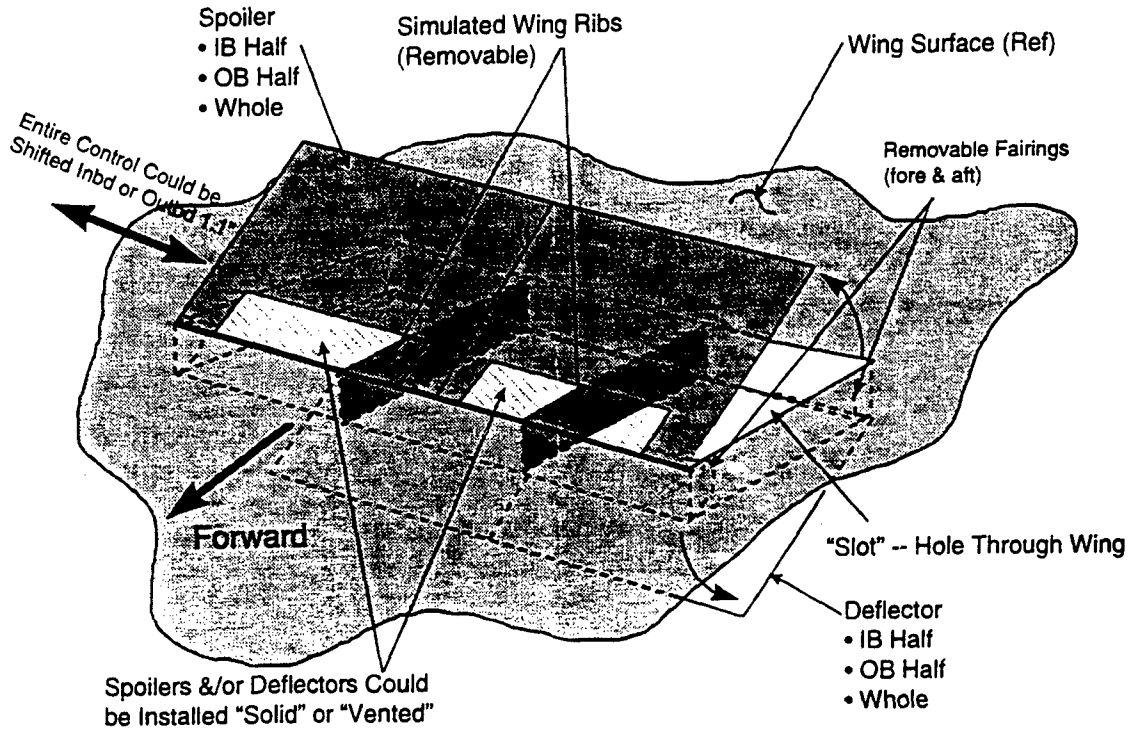

Figure 4-3: Various SSD Configurations Run During the SARL Test

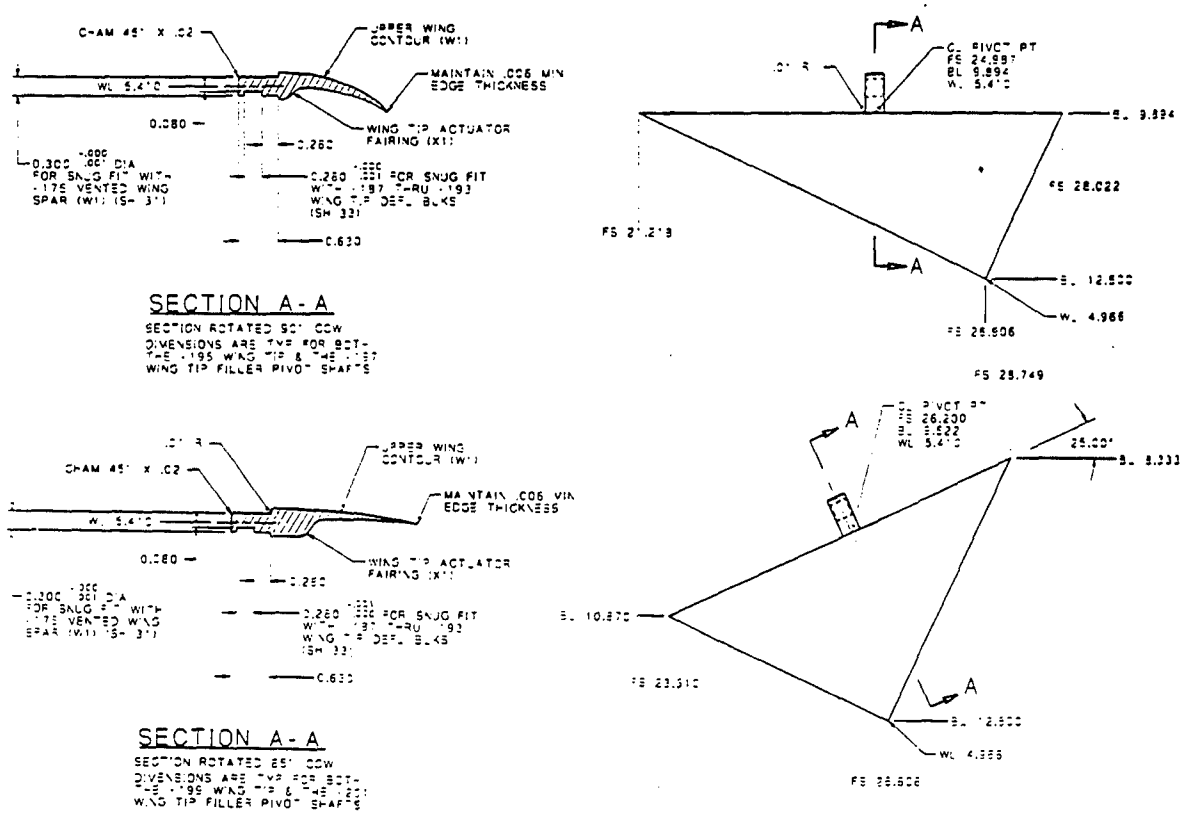

Figure 4-4: AMT Geometry

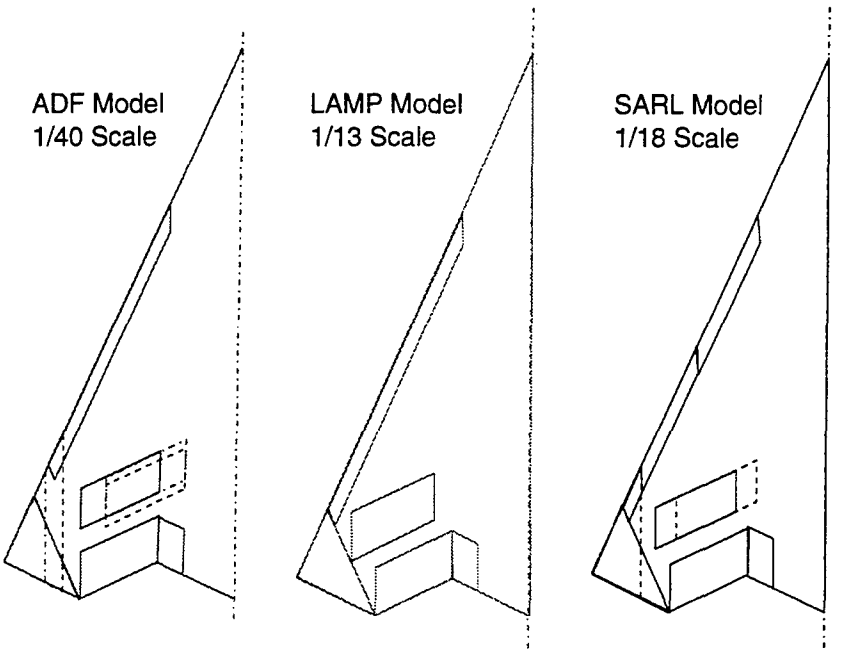

Figure 4-5: Comparison of ADF, LAMP and High-Speed Wind Tunnel Model Controls Geometry

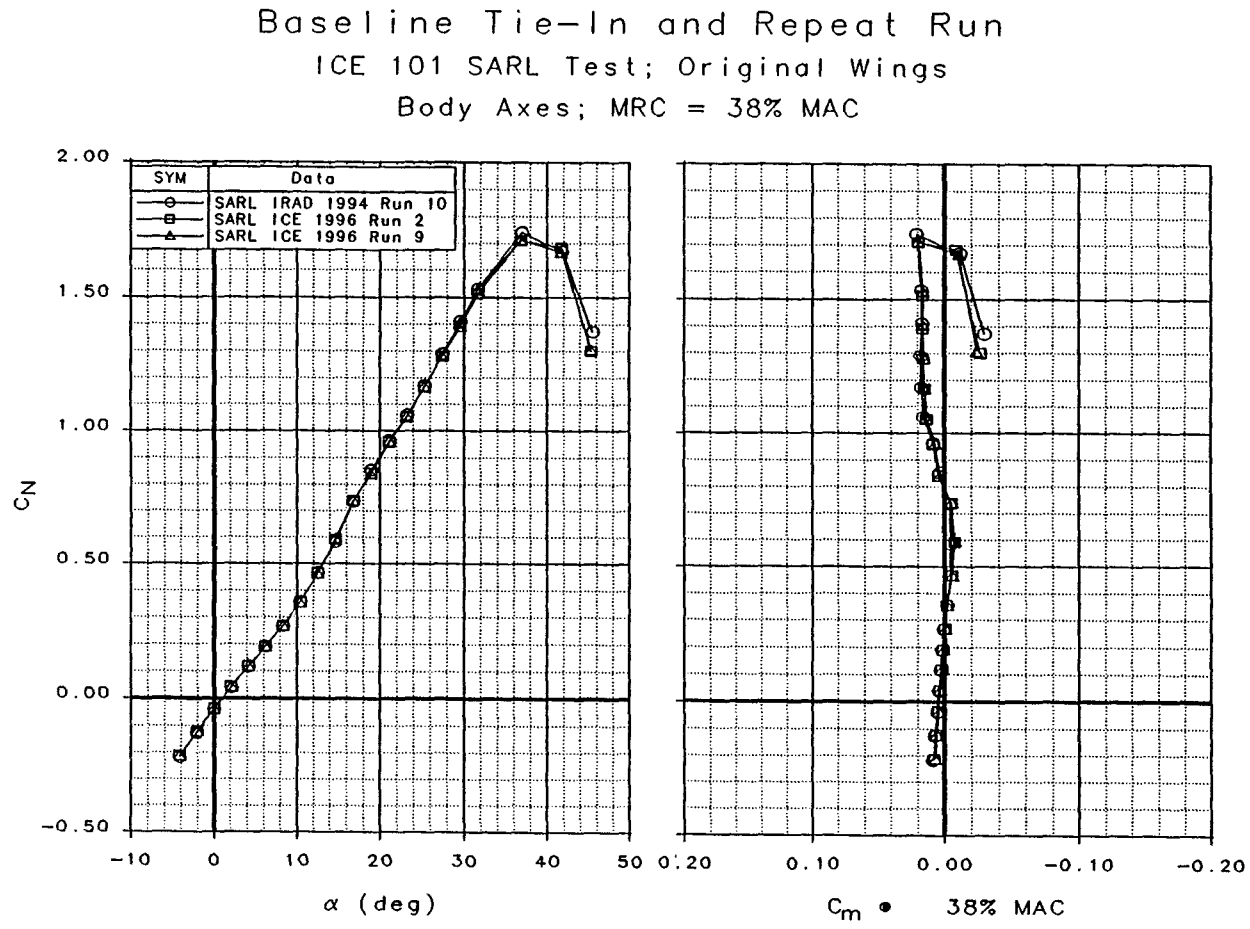

Figure 4-6: Longitudinal Data Tie-in with 1994 Test

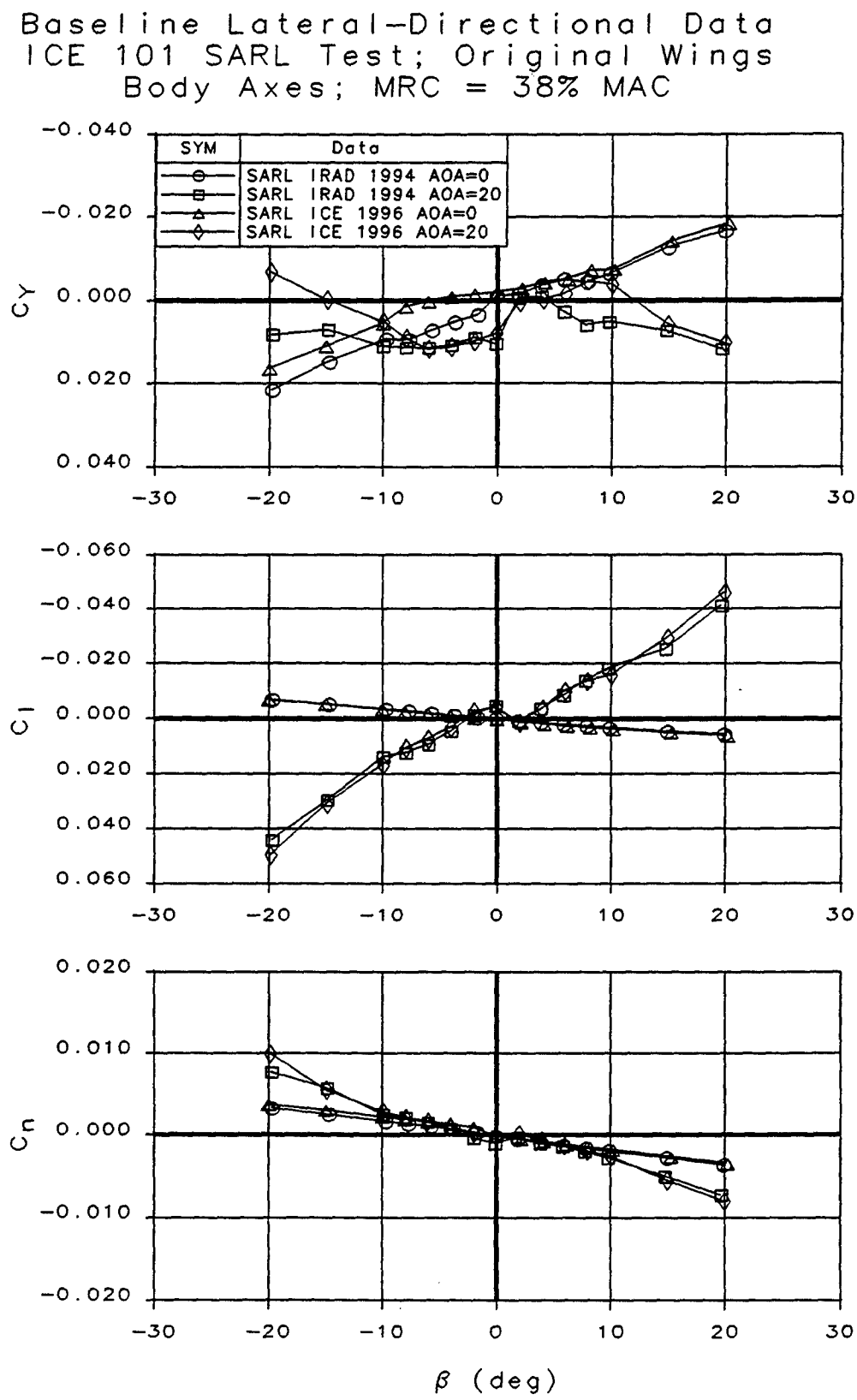

Figure 4-7: Lateral-Directional Data Tie-in with 1994 Test

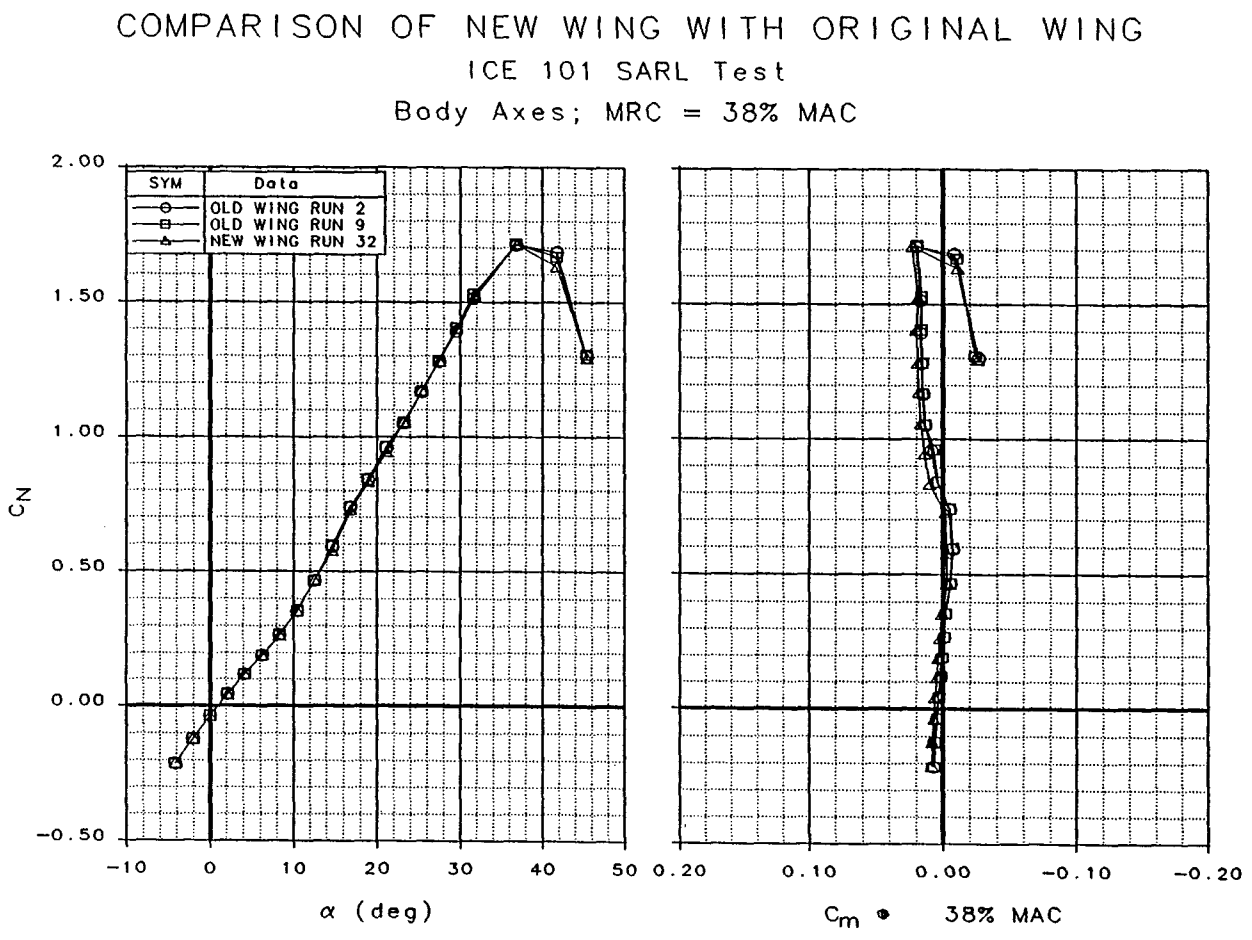

Figure 4-8: Longitudinal Data Tie-in Between New and Old Wings

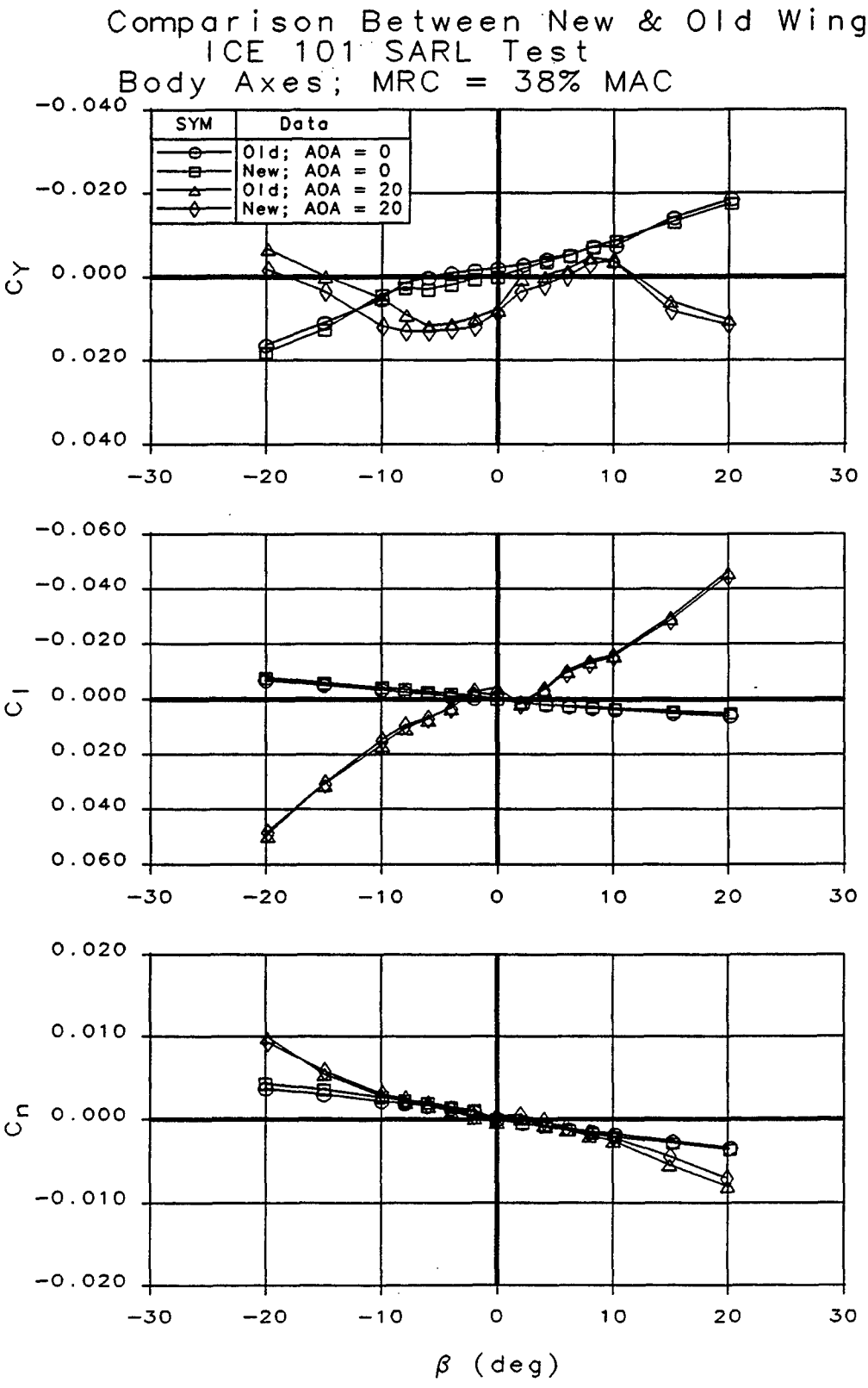

Figure 4-9: Lateral-Directional Data Tie-in Between New and Old Wings

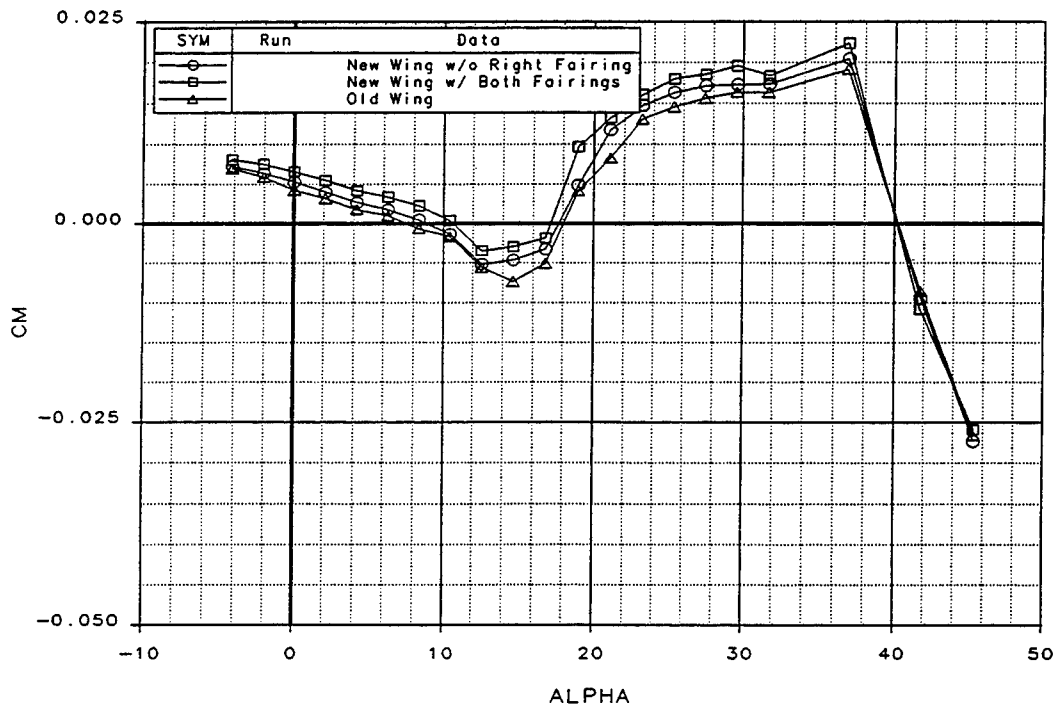

Figure 4-10: Pitching Moment Shift can be Explained by Presence of Actuator Fairings

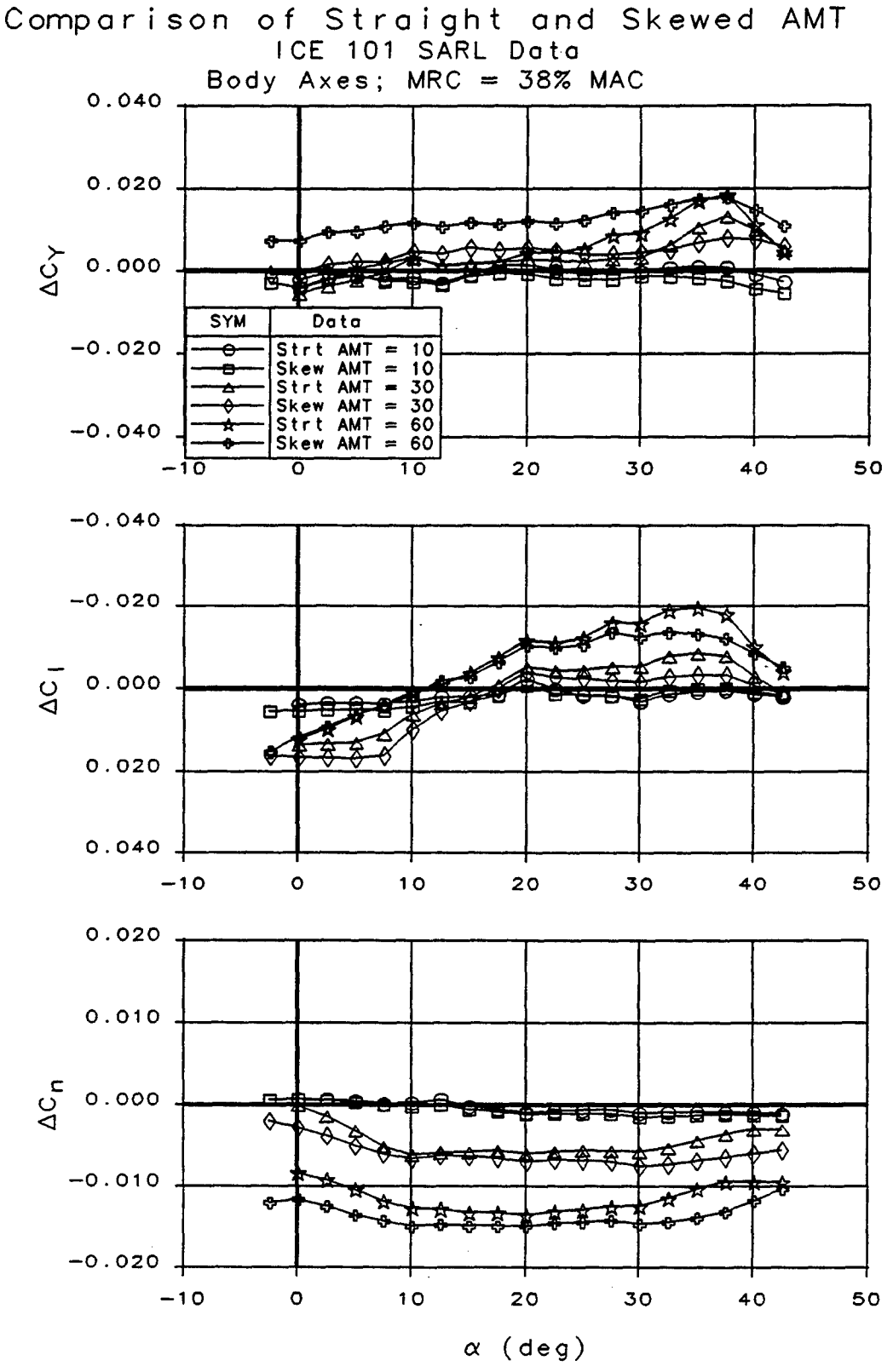

Figure 4-11: Straight and Skewed AMT Control Effectiveness

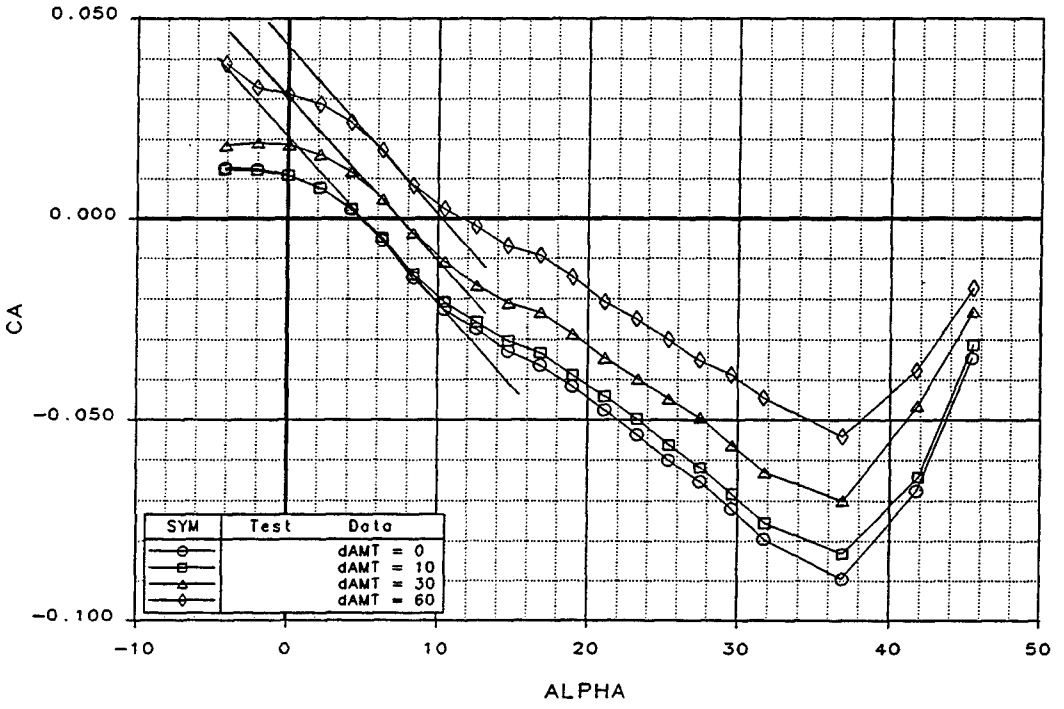

Figure 4-12: Axial Force Changes with AMT Deflection

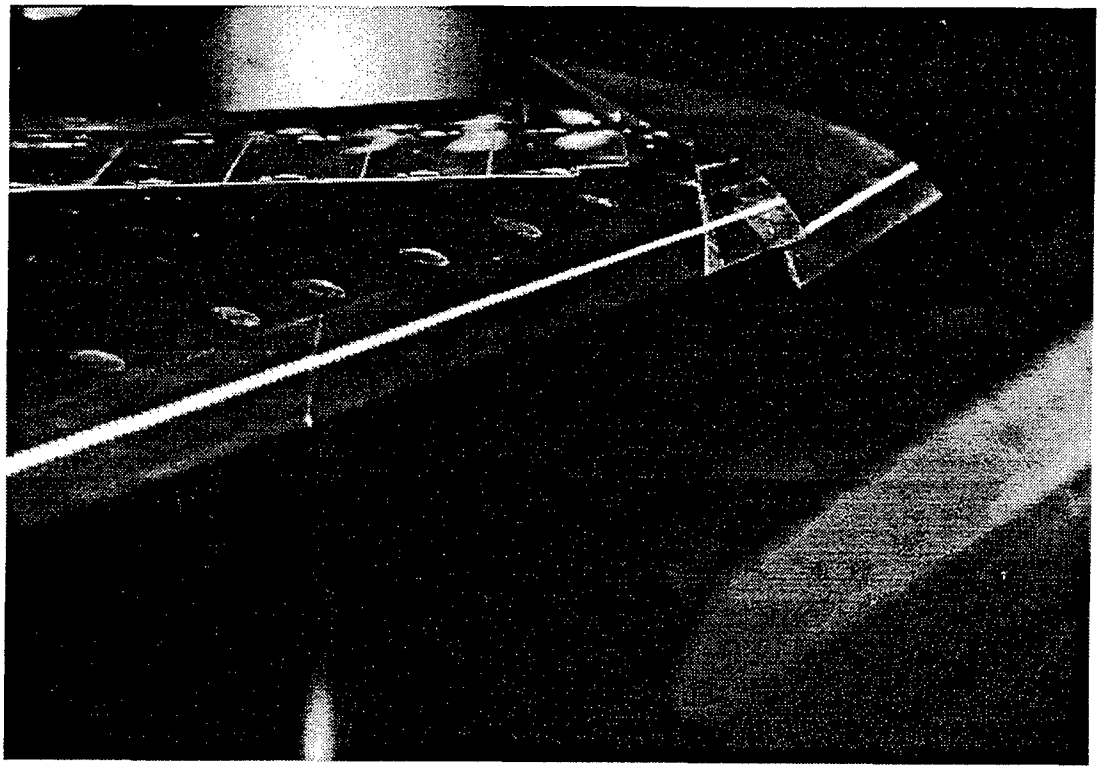

Figure 4-13: Deflected AMT Installed on the High Speed Model at SARL

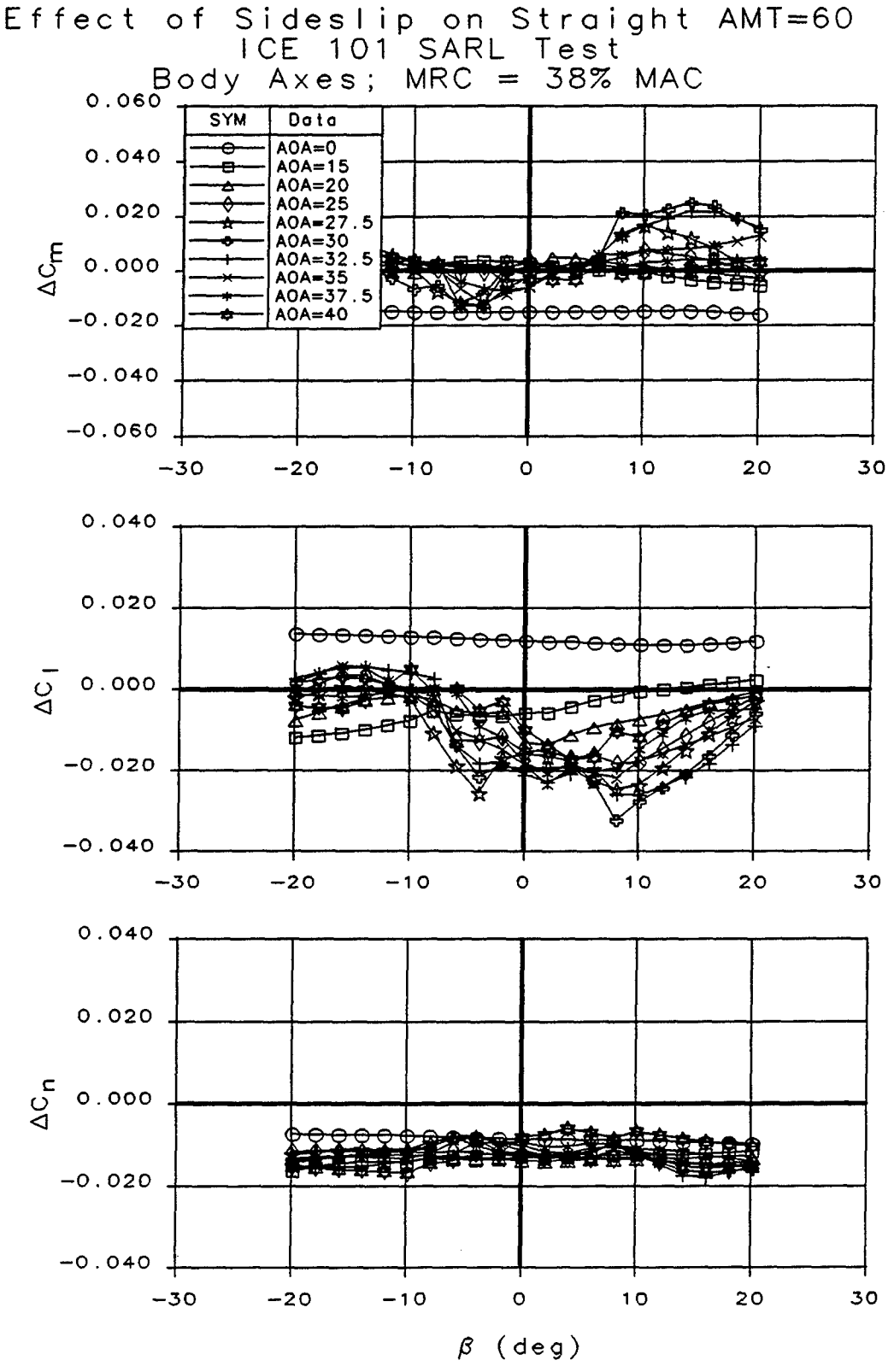

Figure 4-14: Sideslip Effects on Straight AMT Control Power

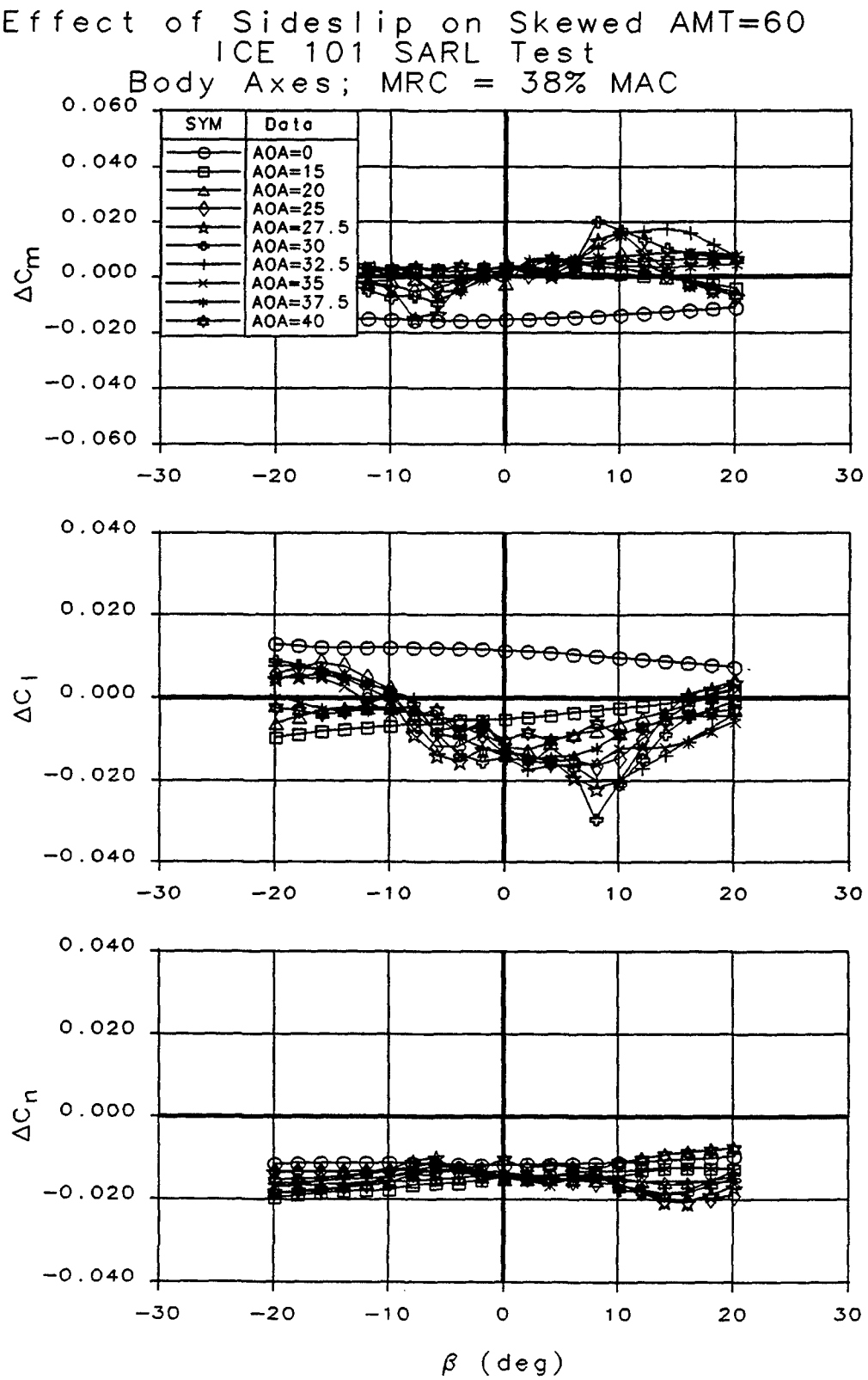

Figure 4-15: Sideslip Effects on Skewed AMT Control Power

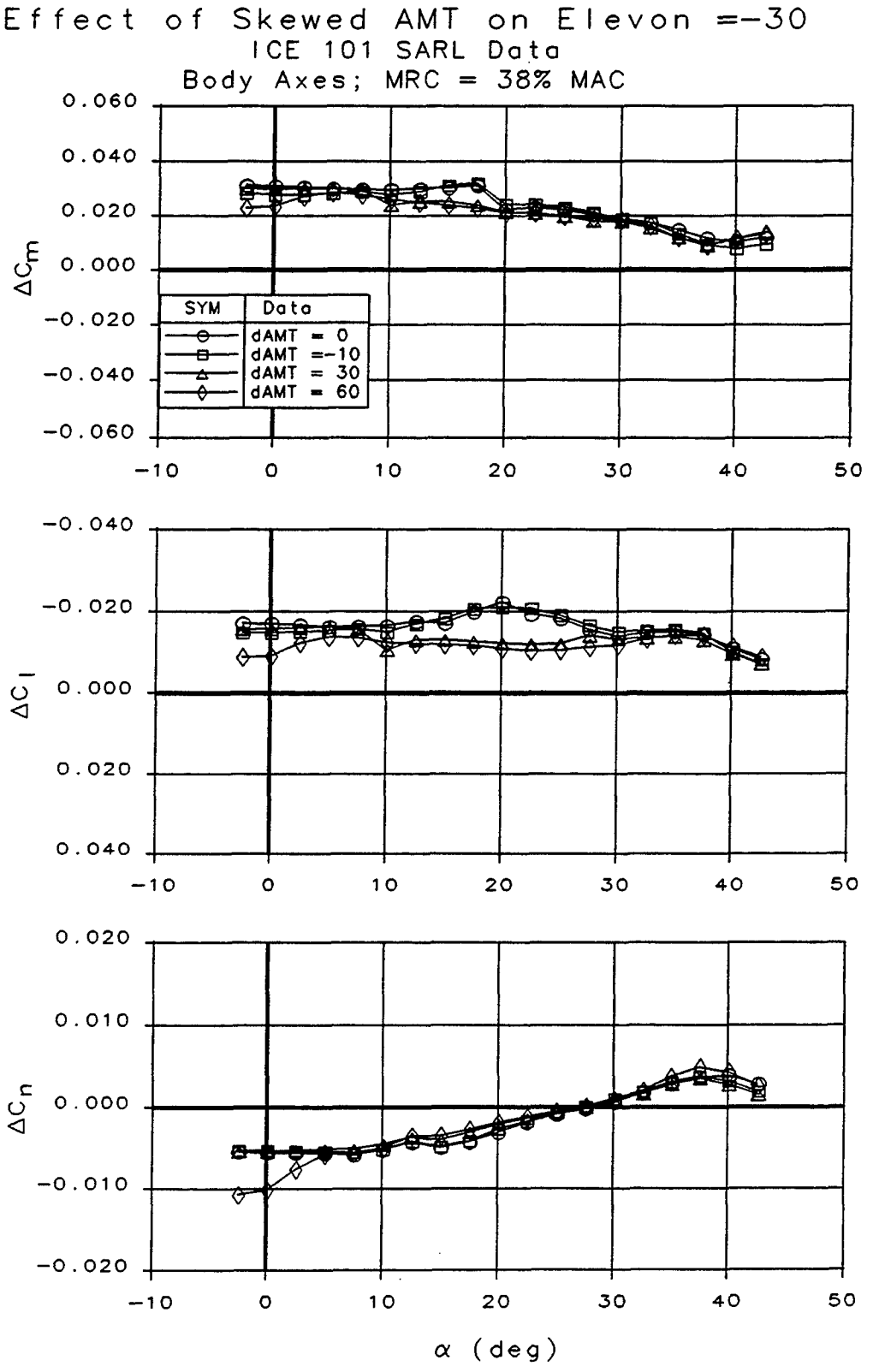

Figure 4-16: Skewed AMT Interaction with -30 deg Elevon

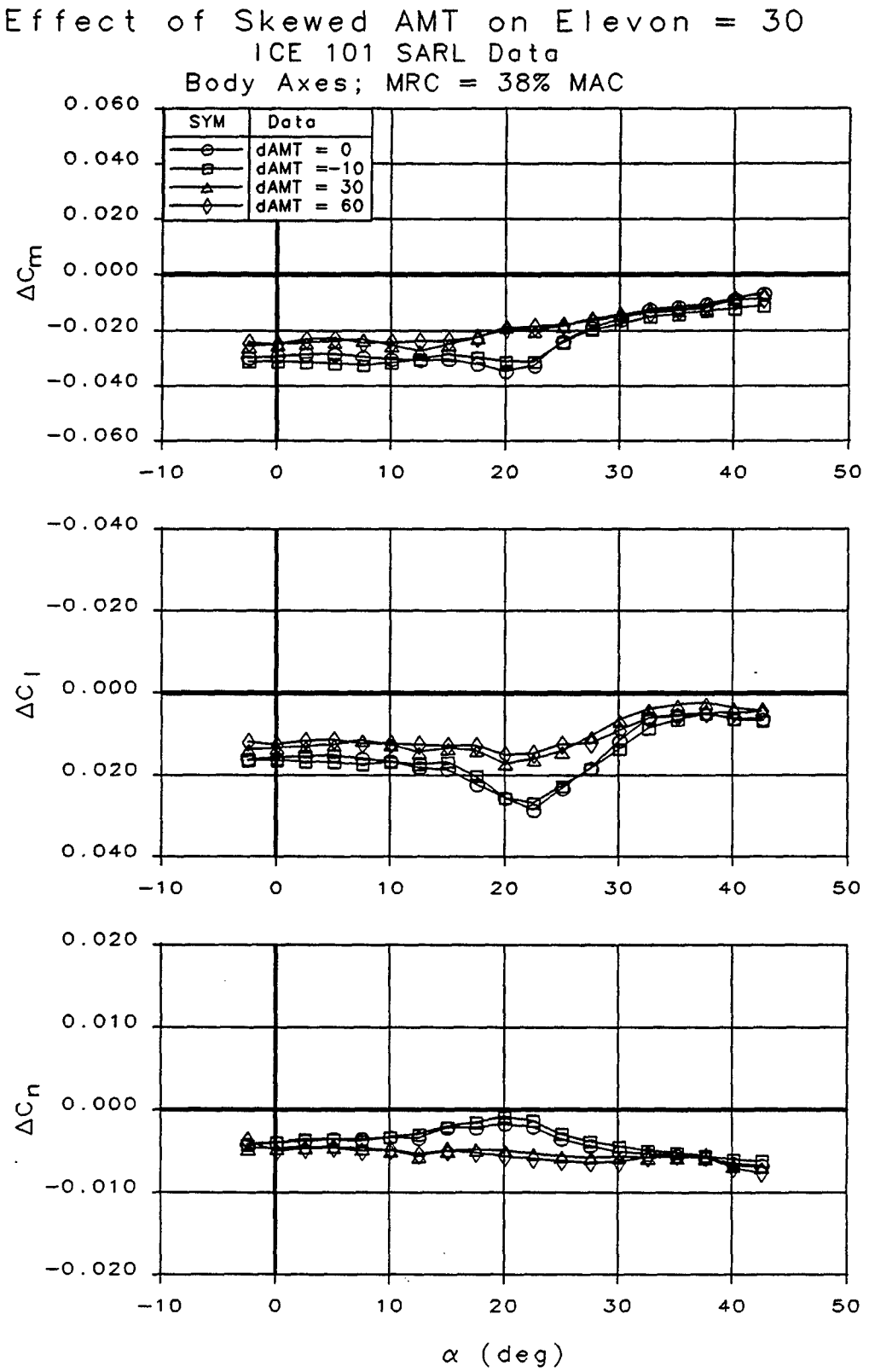

Figure 4-17: Skewed AMT Interaction with 30 deg Elevon

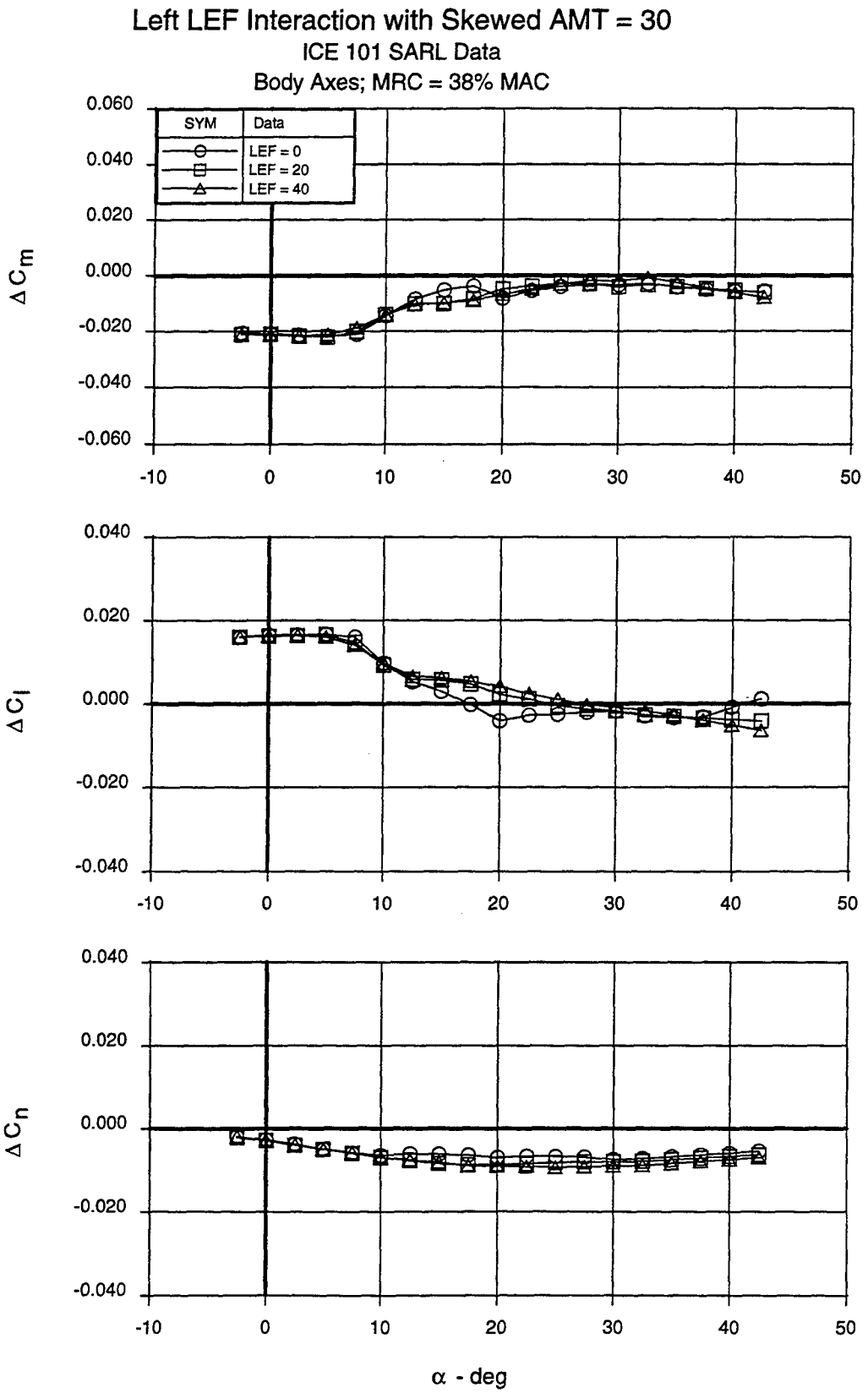

Figure 4-18: LEF Interaction with Skewed AMT = 30 deg

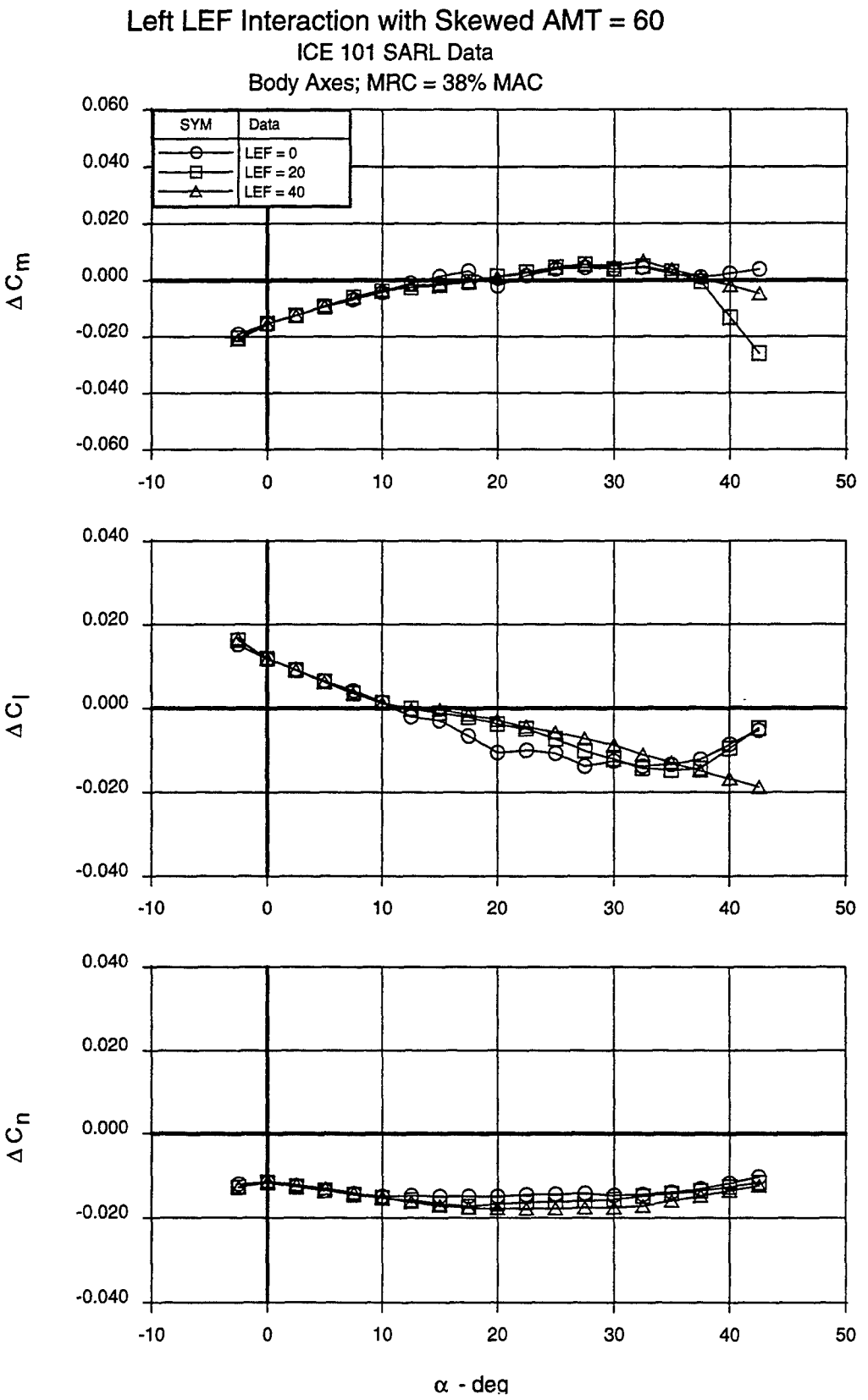

Figure 4-19: LEF Interaction with Skewed AMT = 60 deg

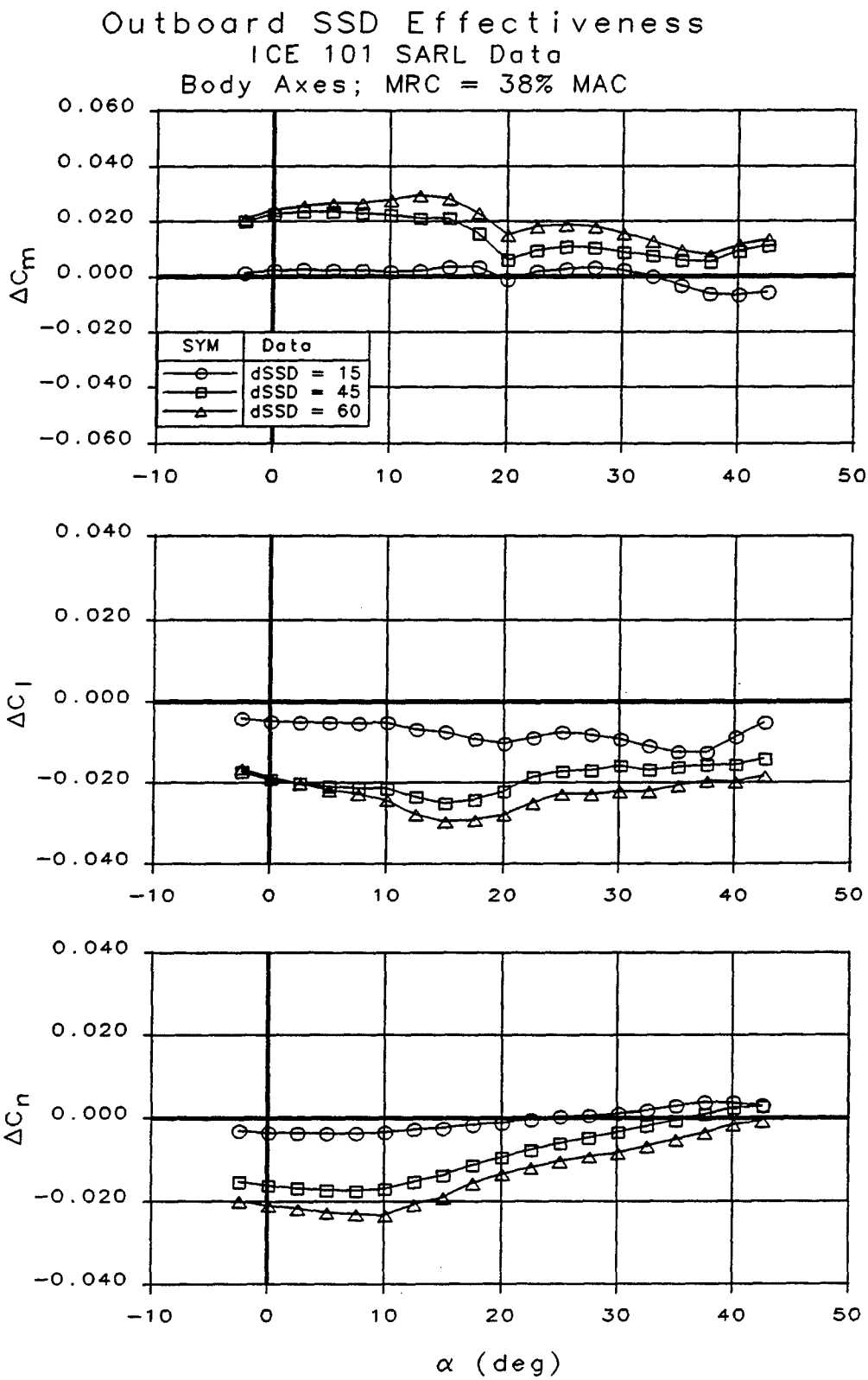

Figure 4-20: Outboard SSD Control Effectiveness

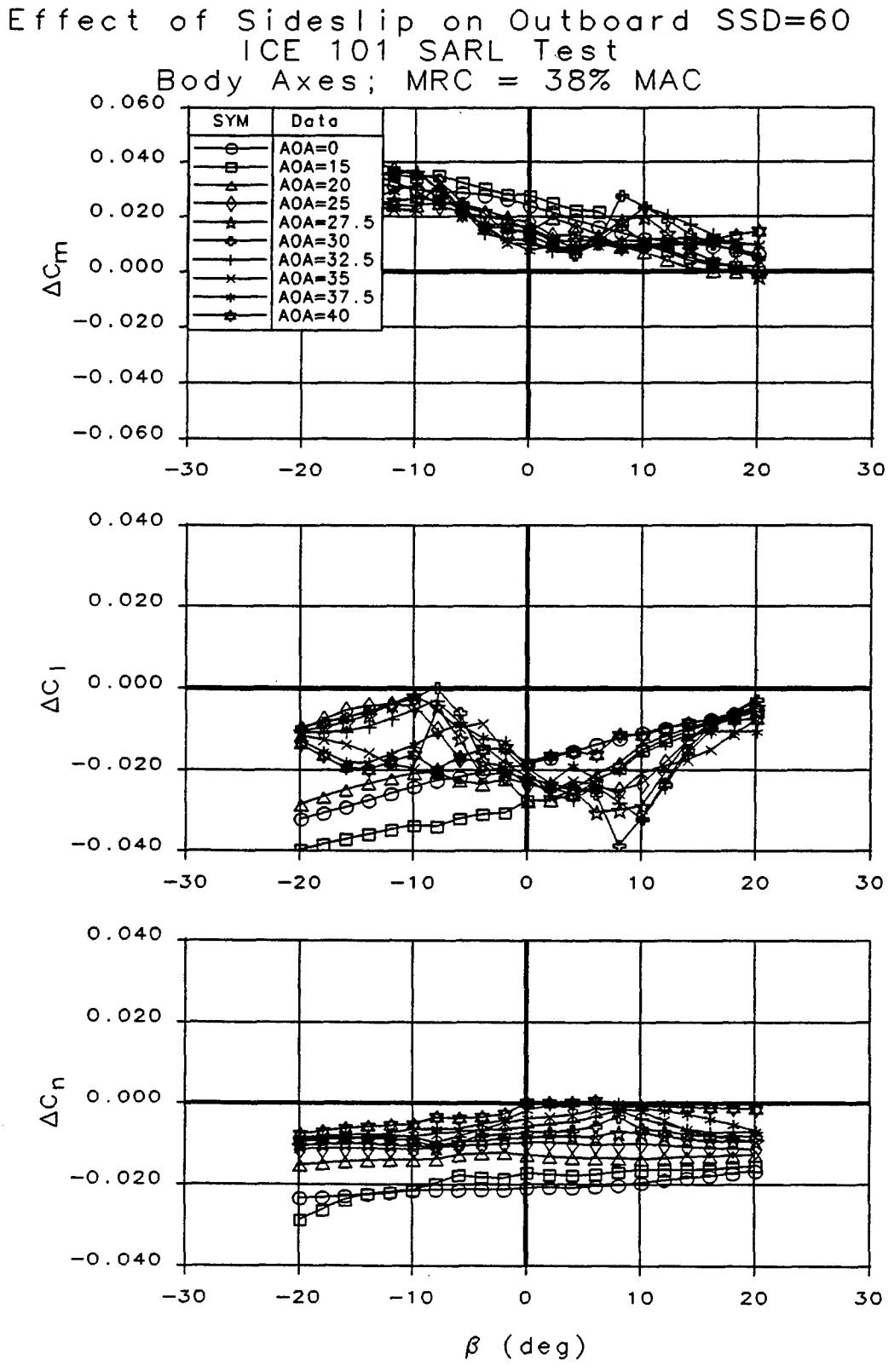

Figure 4-21: Summary of Sideslip Effects on Outboard SSD Control Power

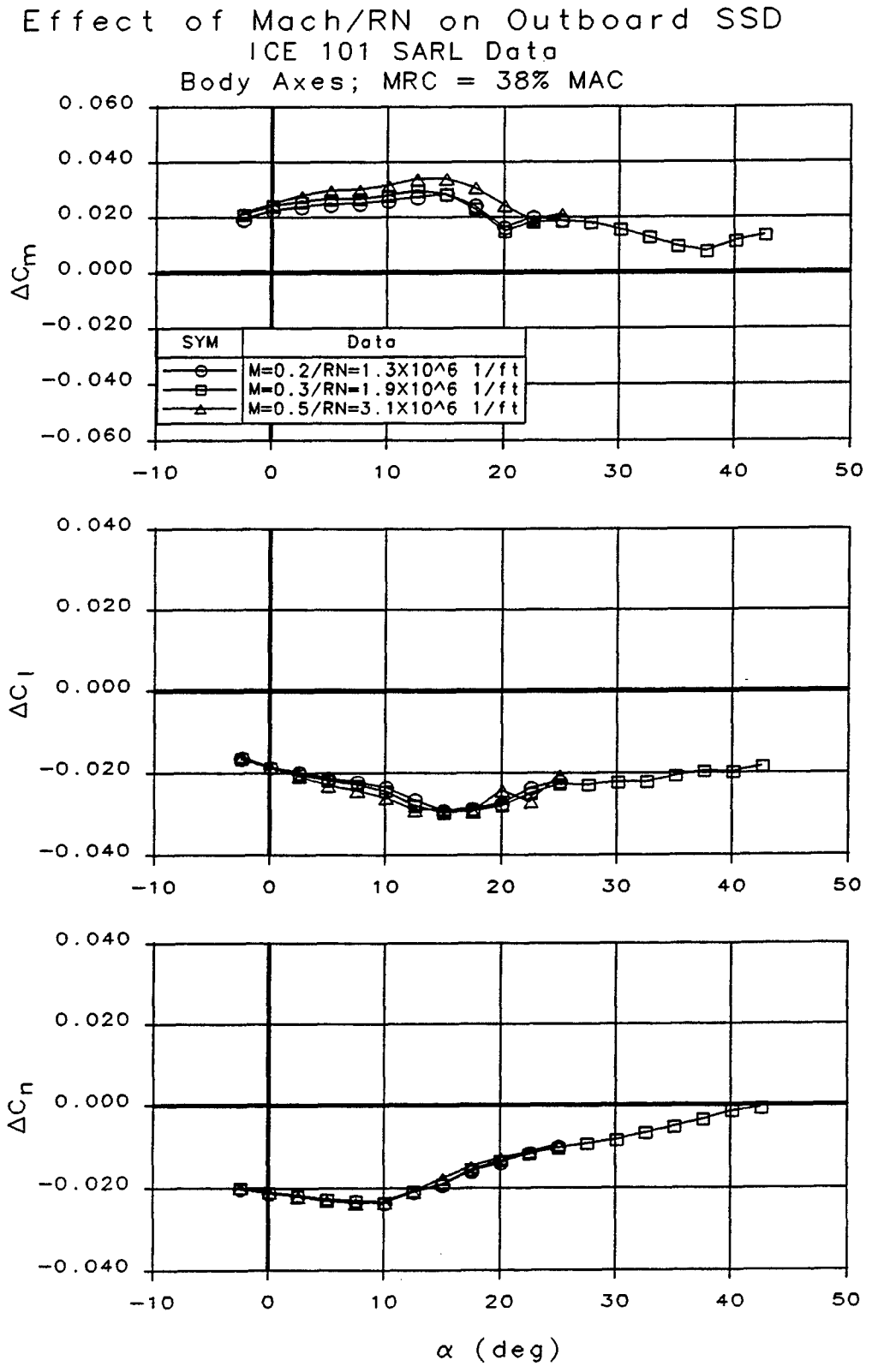

Figure 4-22: Effect of Mach and Reynolds Number Variation on SSD Control Power

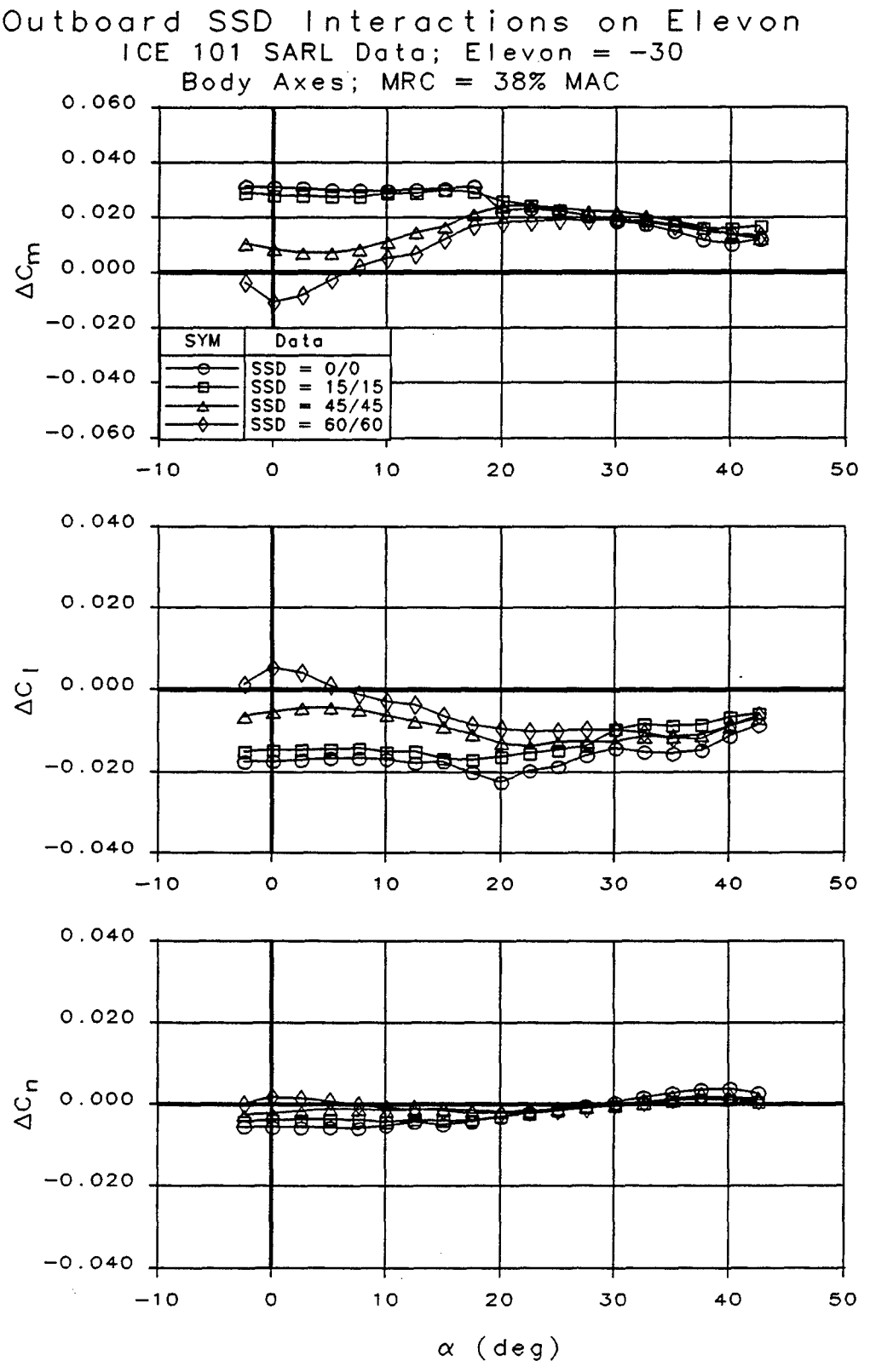

Figure 4-23: Outboard SSD Interaction with -30 deg Elevon

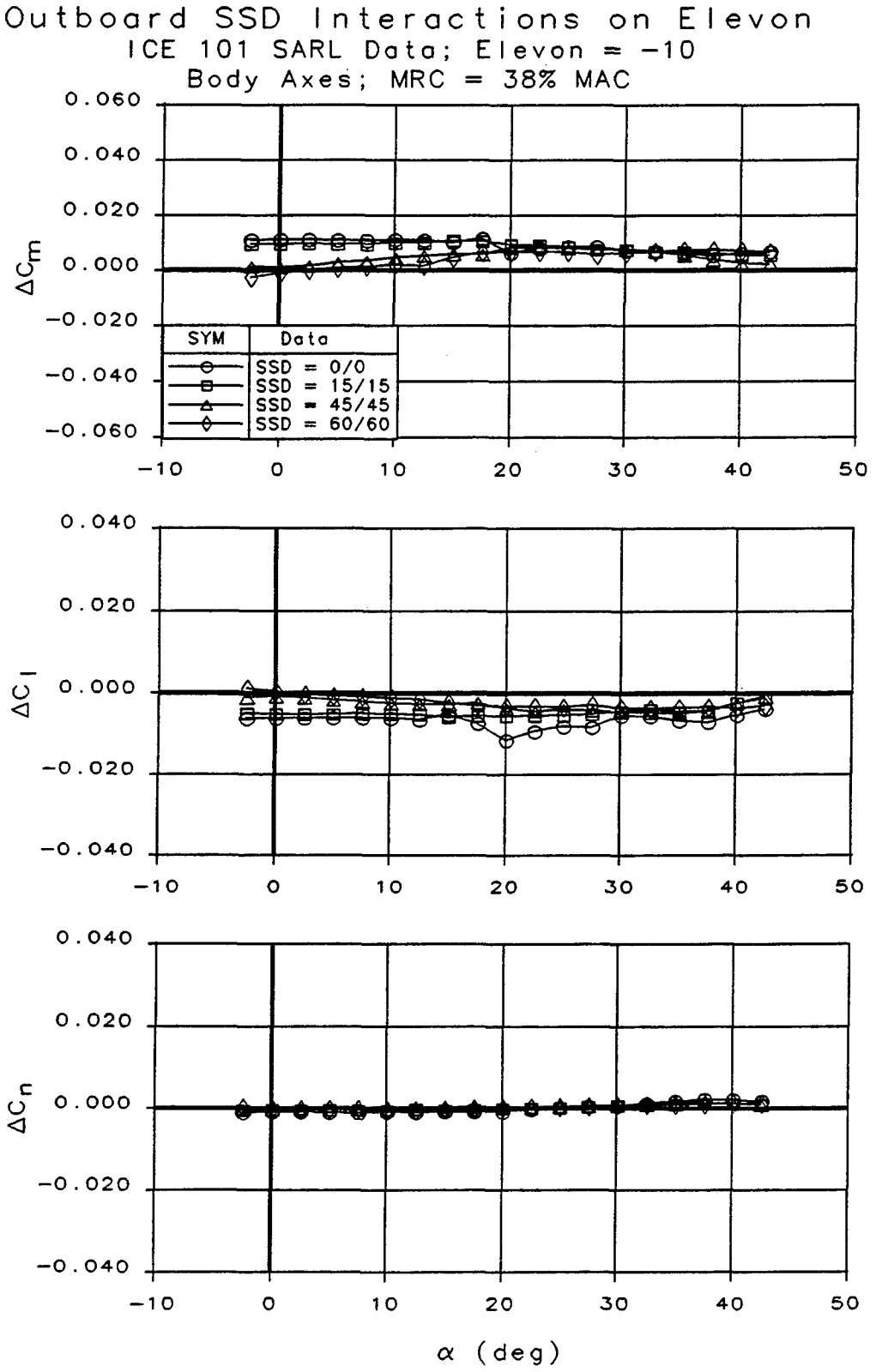

Figure 4-24: Outboard SSD Interaction with -10 deg Elevon

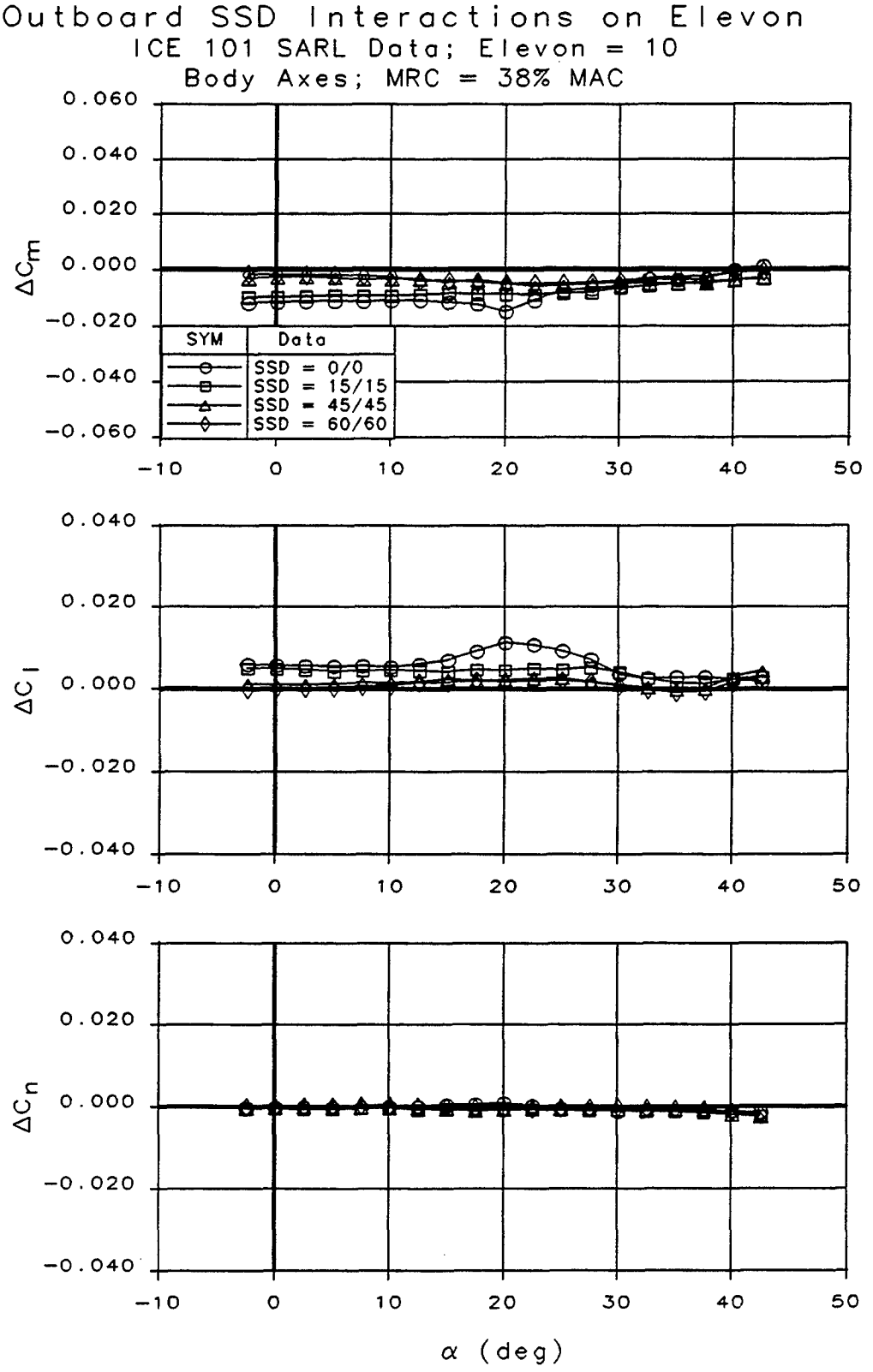

Figure 4-25: Outboard SSD Interaction with 10 deg Elevon

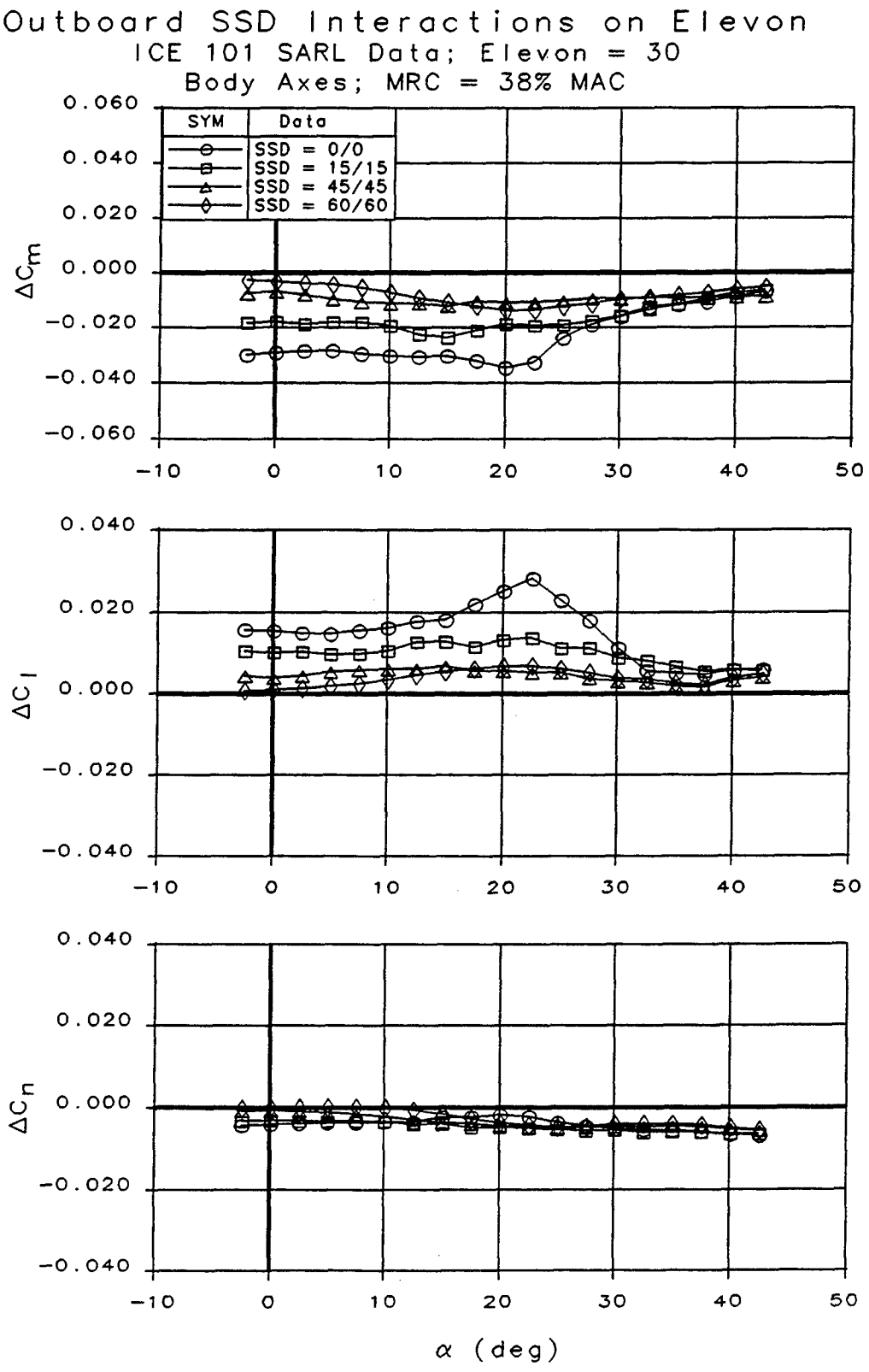

Figure 4-26: Outboard SSD Interaction with 30 deg Elevon

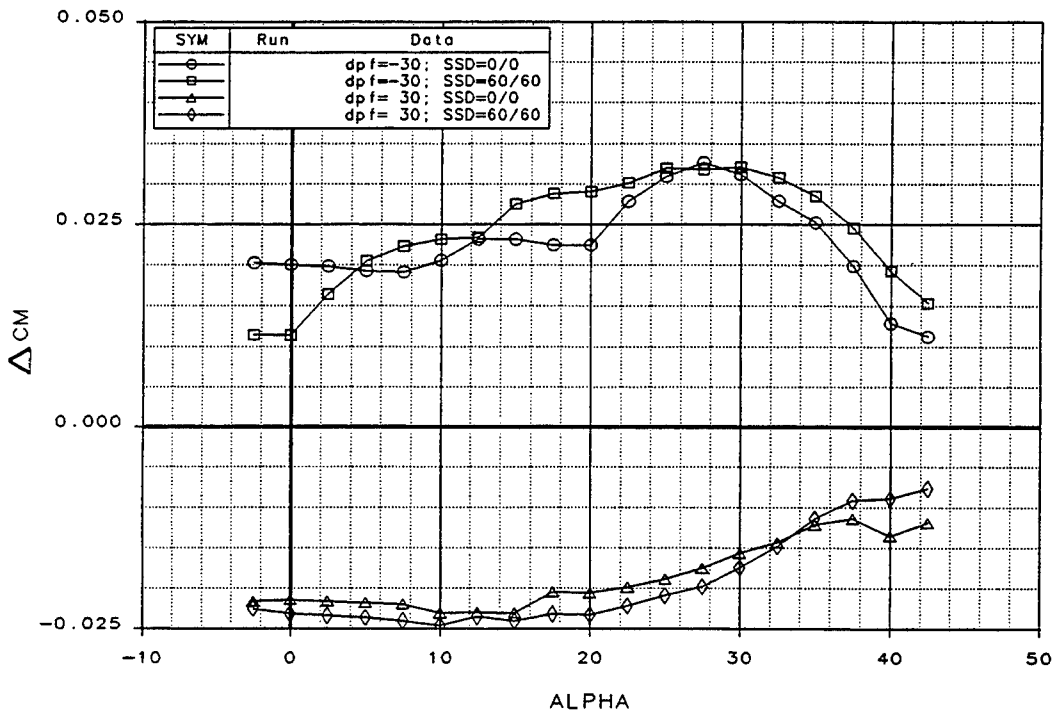

Figure 4-27: Outboard SSD Interaction with Pitch Flap Effectiveness

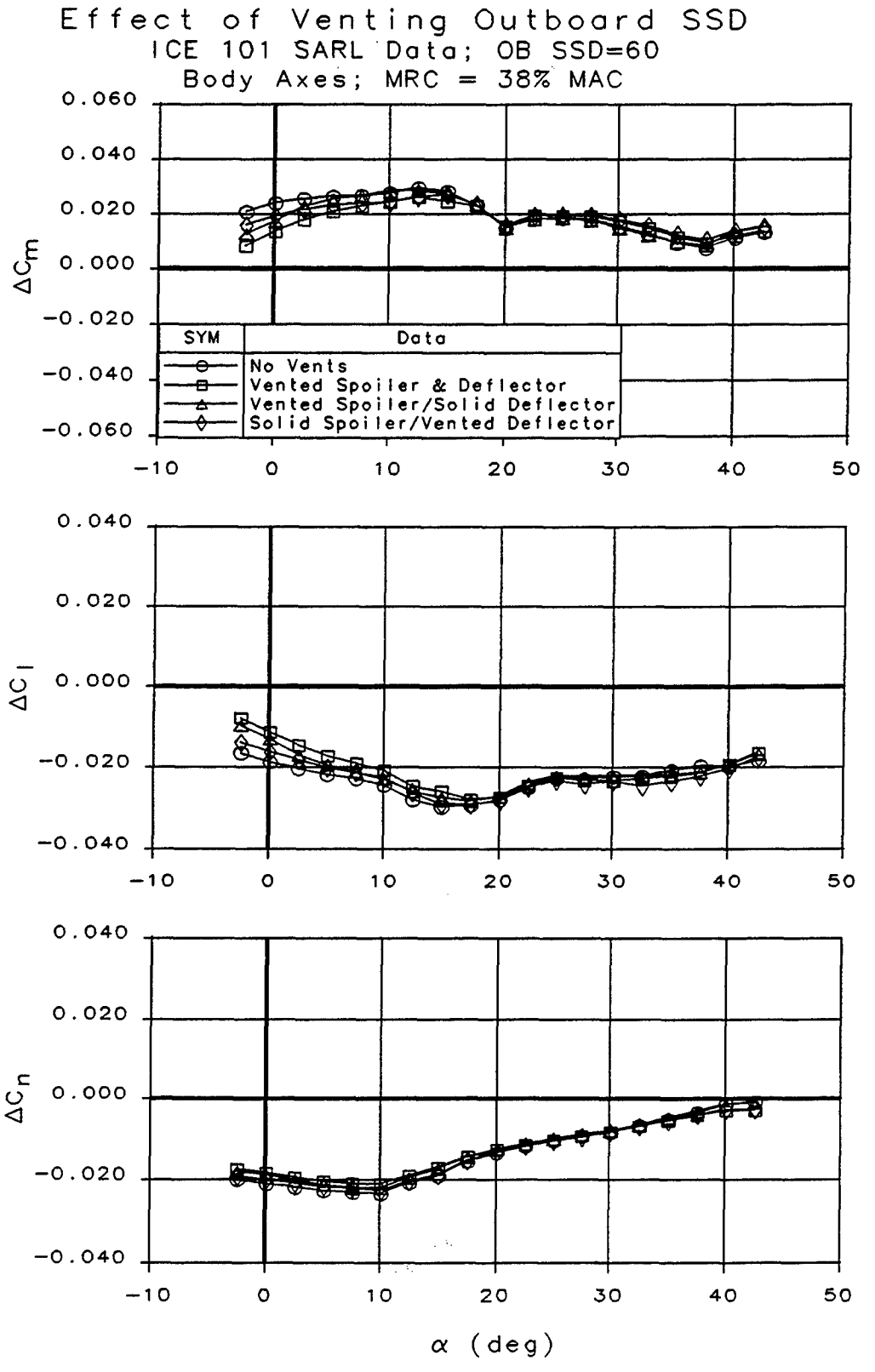

Figure 4-28: Effect of Venting the Spoiler and Deflector

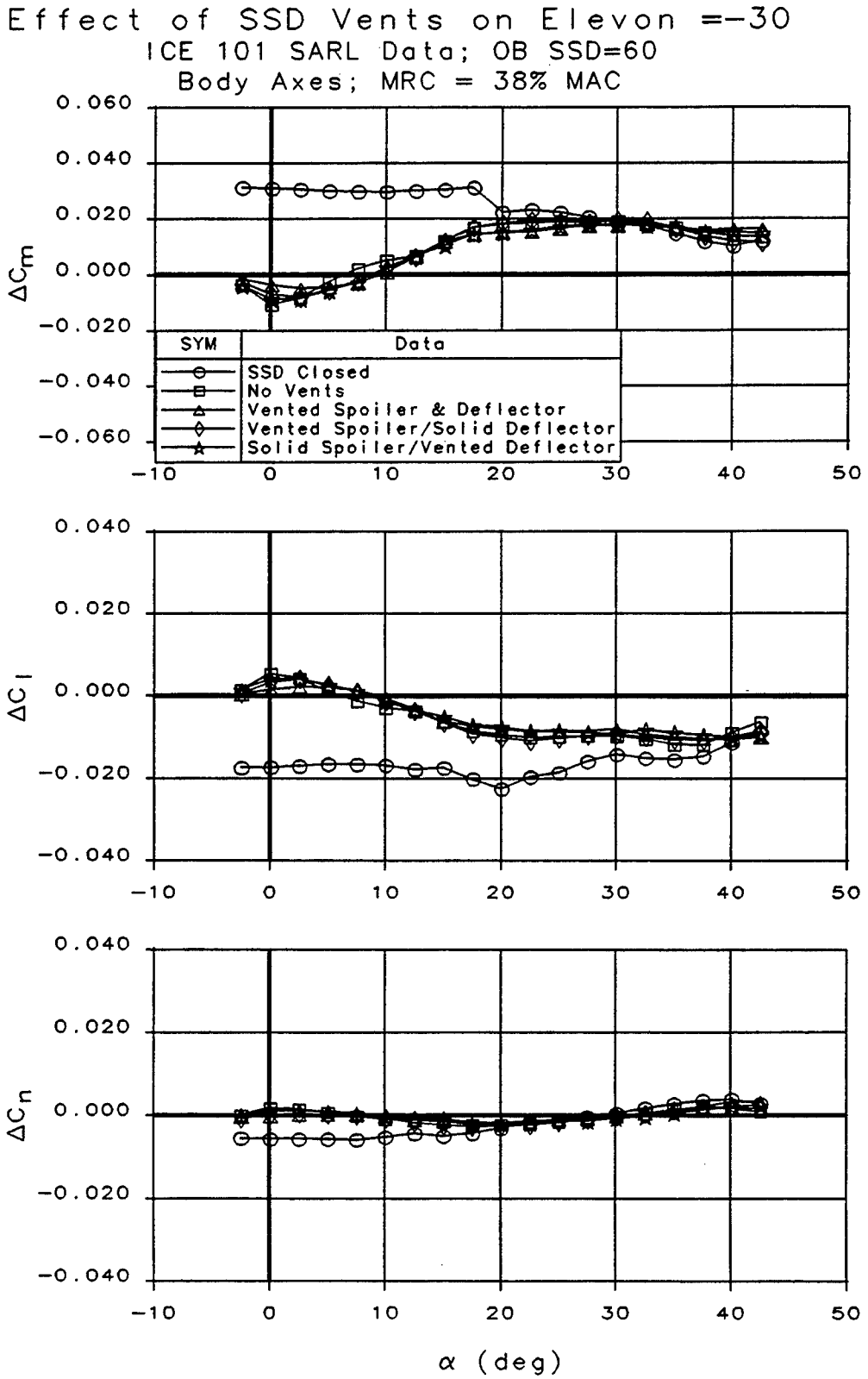

Figure 4-29: Interaction of Vented SSD with -30 deg Elevon

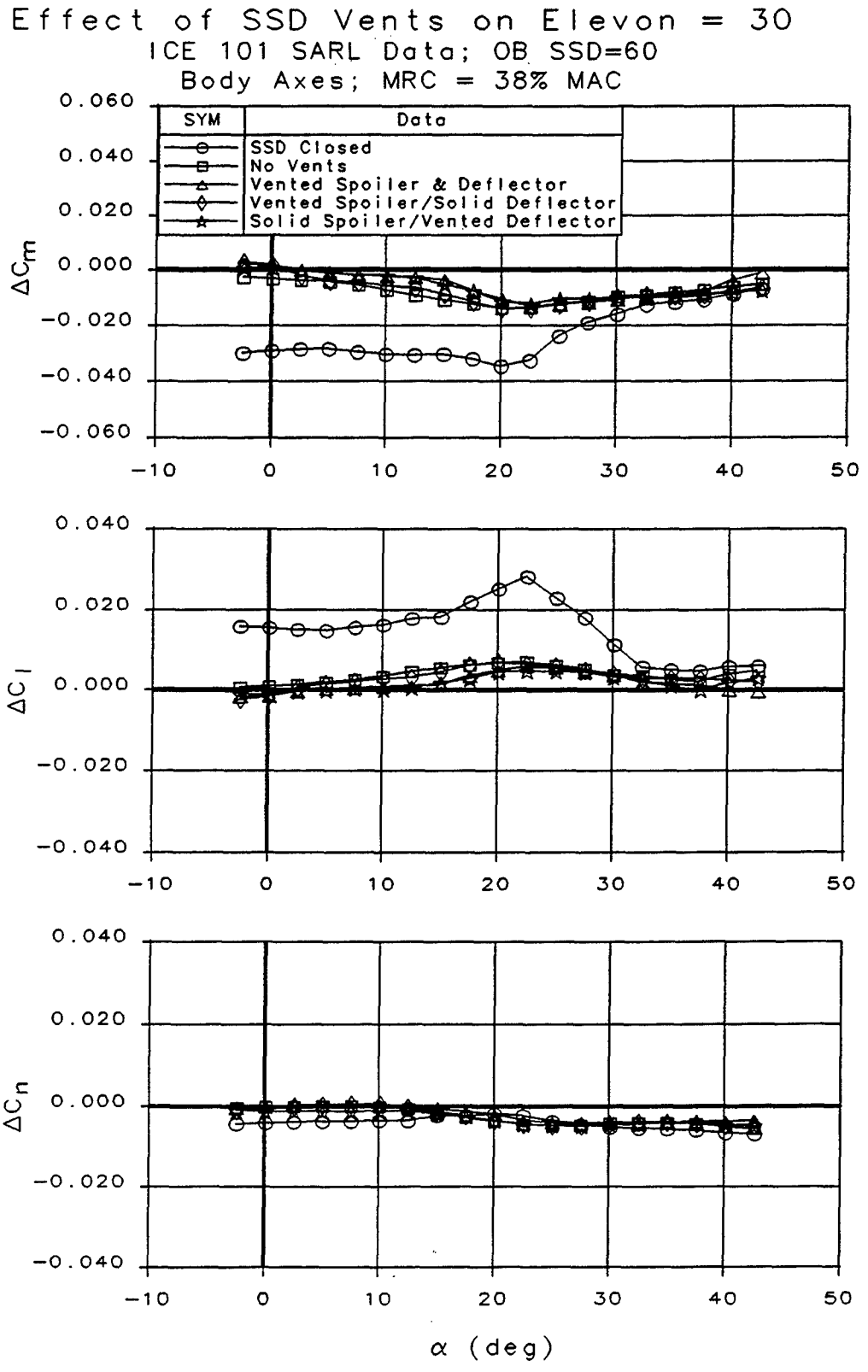

Figure 4-30: Effect of Vented SSD with 30 deg Elevon

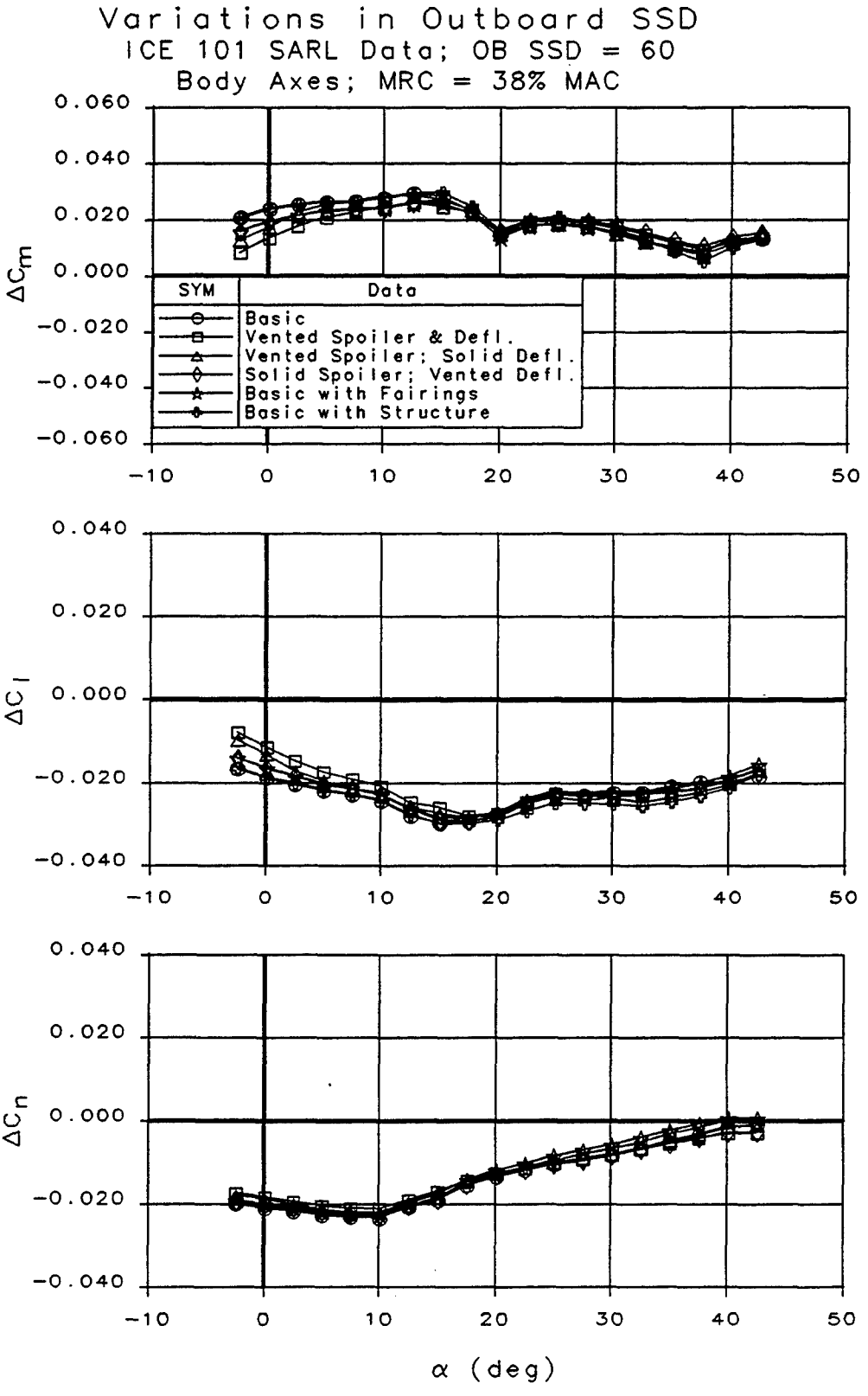

Figure 4-31: Effect of Slot Variations on SSD Control Power

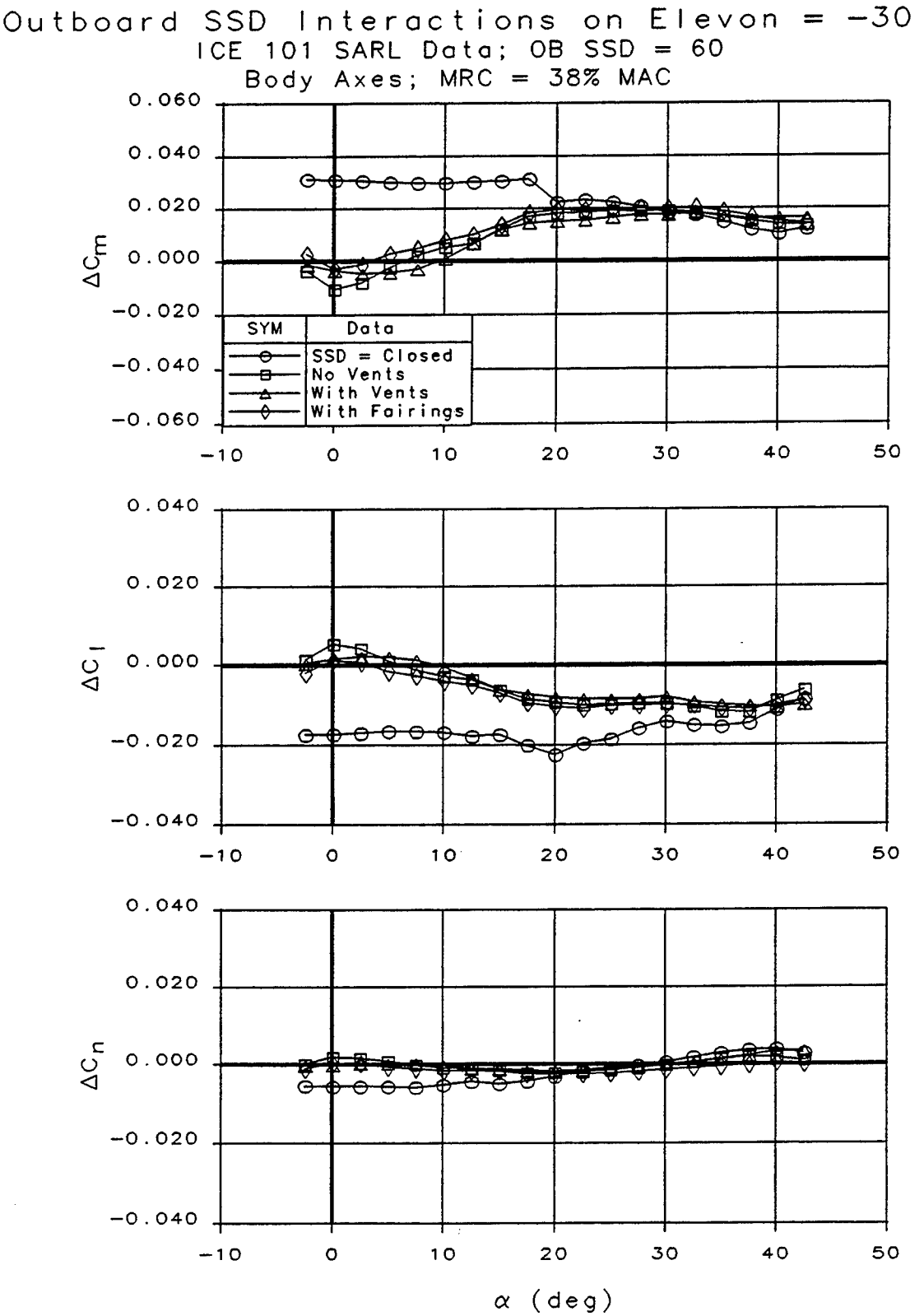

Figure 4-32: Effect of SSD Variations on Elevon = -30 Interaction

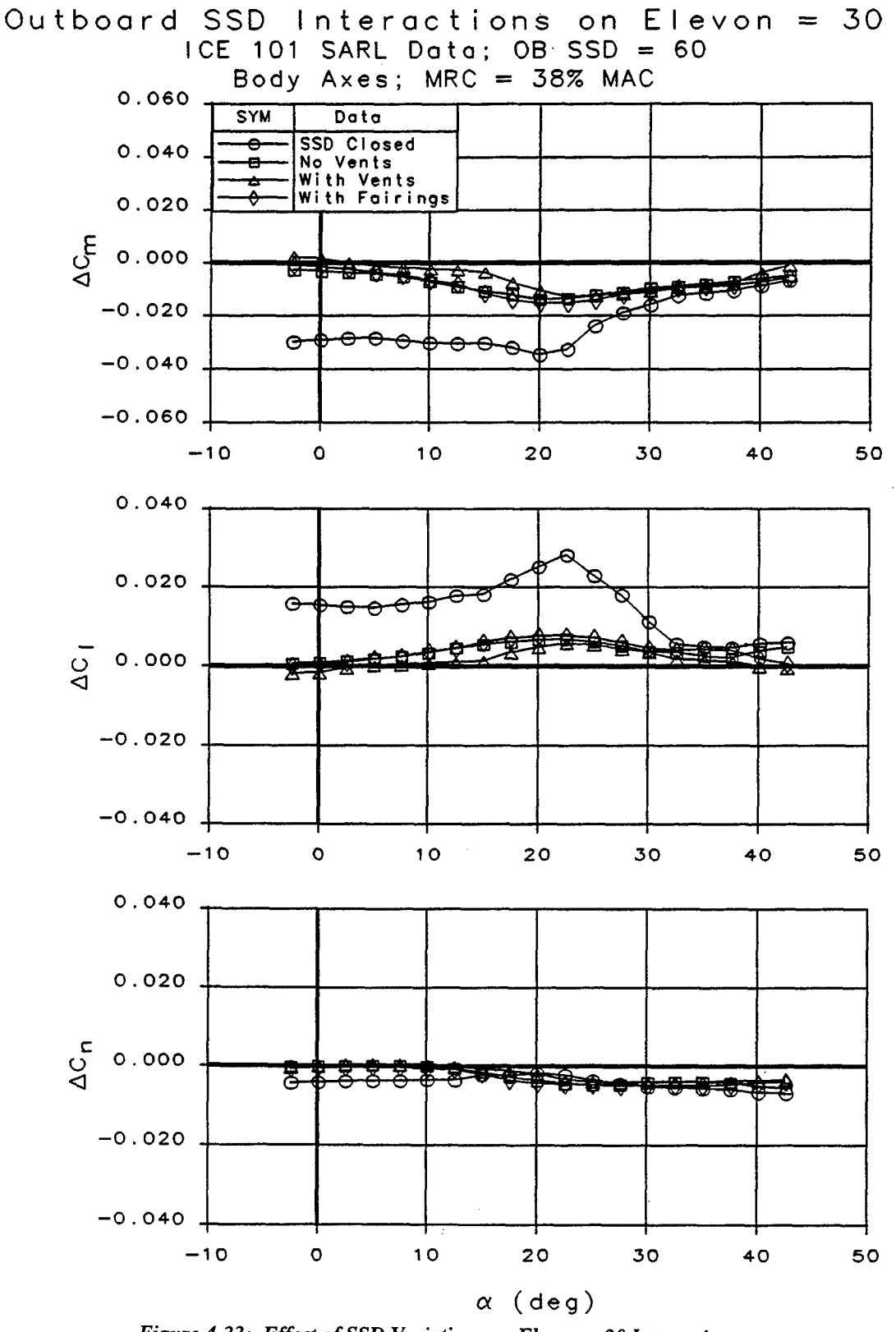

Figure 4-33: Effect of SSD Variations on Elevon = 30 Interaction

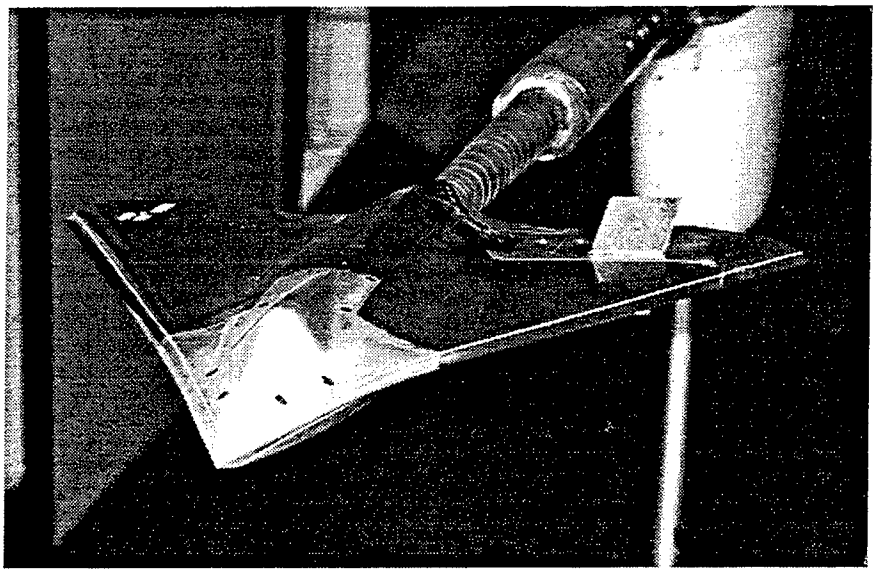

Figure 4-34: Half-Sized SSD

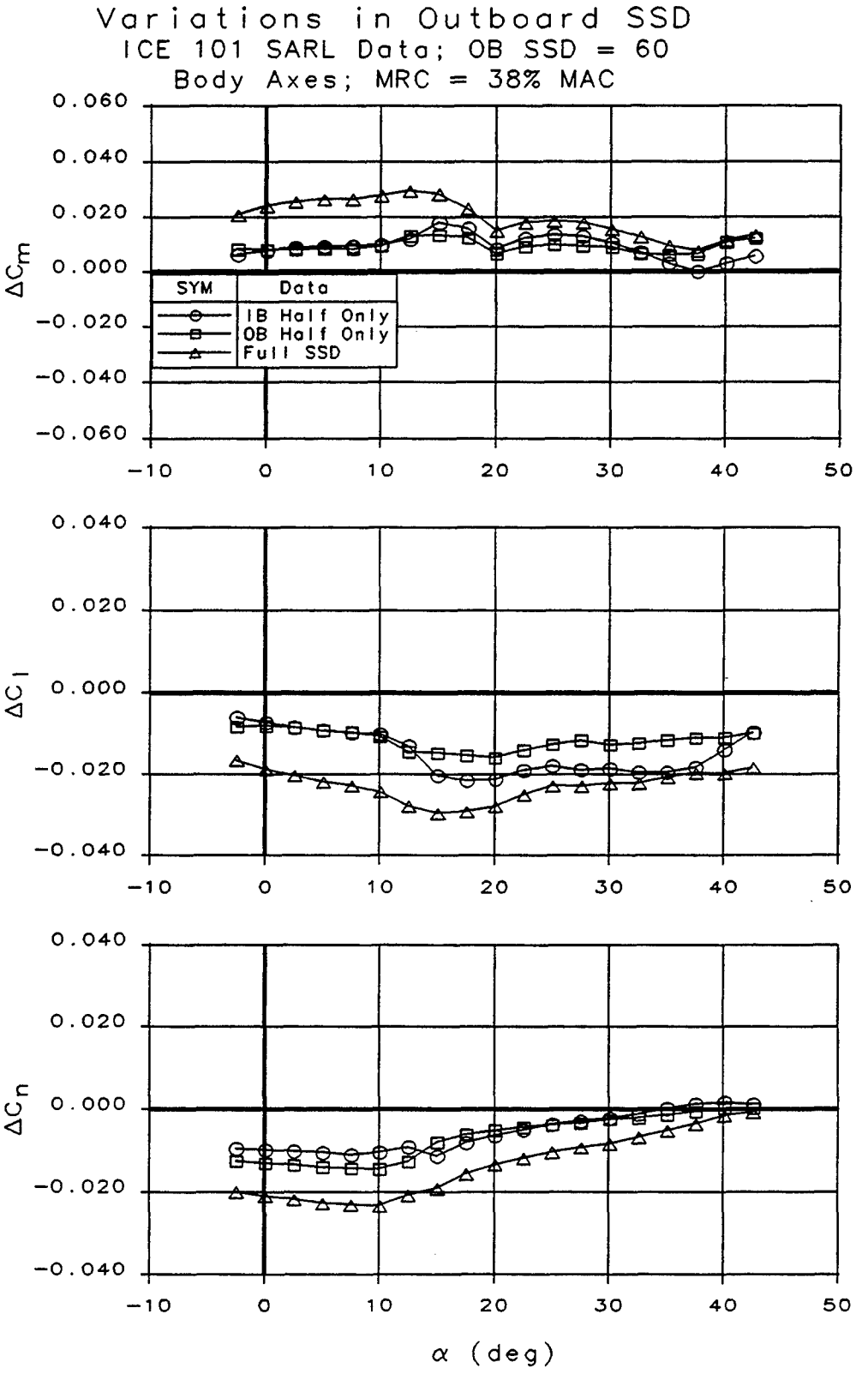

Figure 4-35: Segmented SSD Control Effectiveness

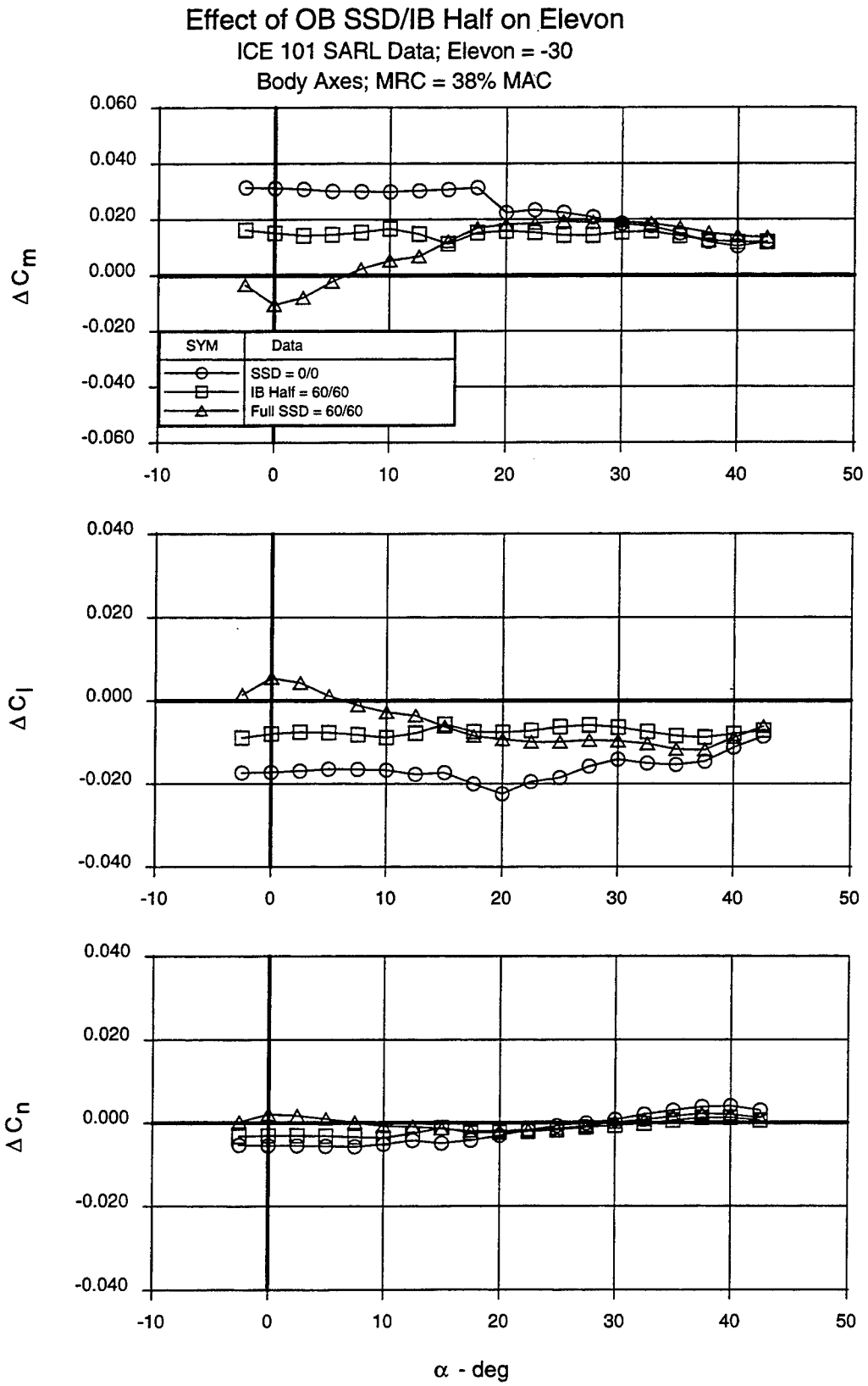

Figure 4-36: IB Half SSD Interaction with -30 deg Elevon

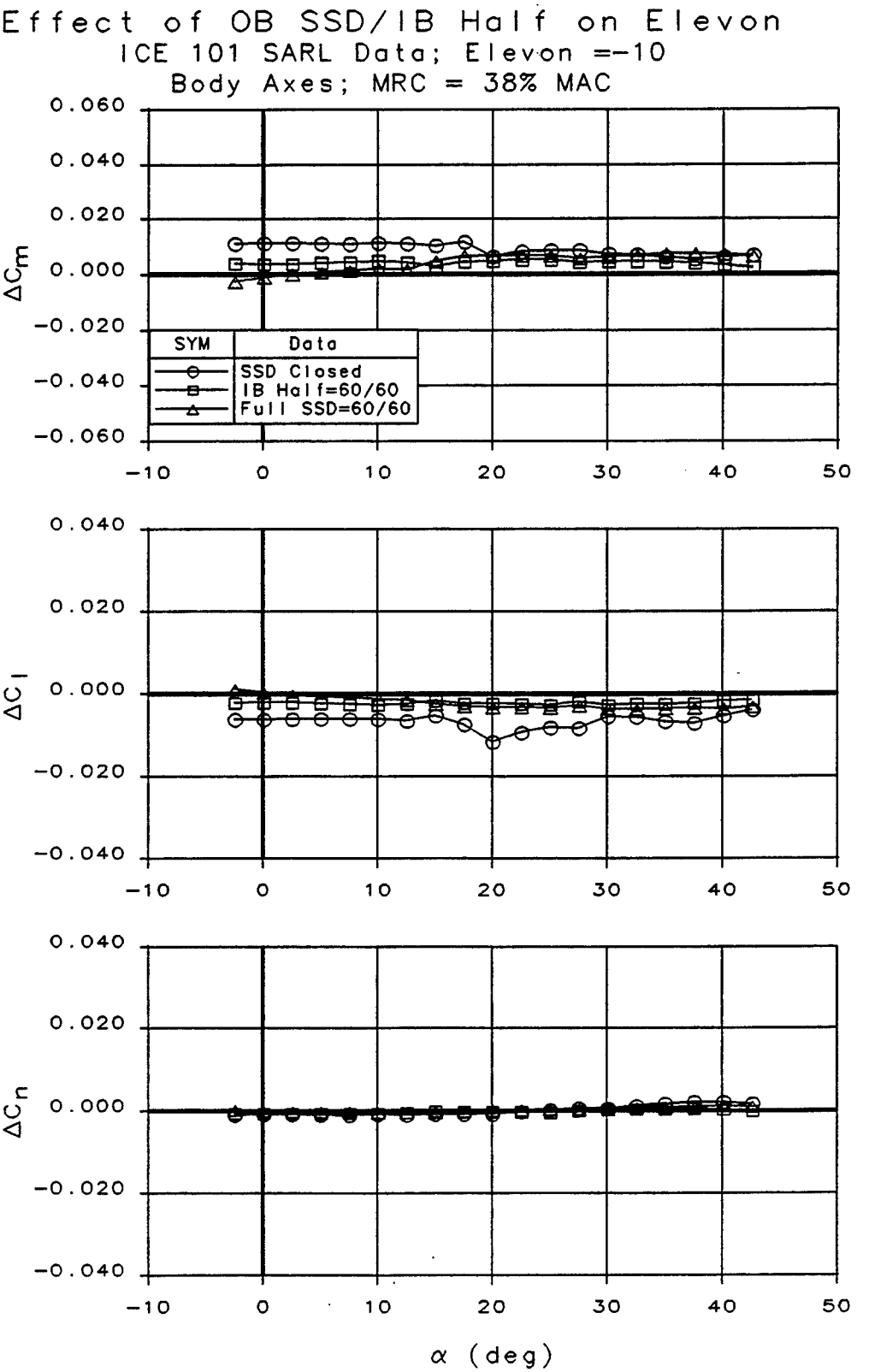

Figure 4-37: IB Half SSD Interaction with -10 deg Elevon

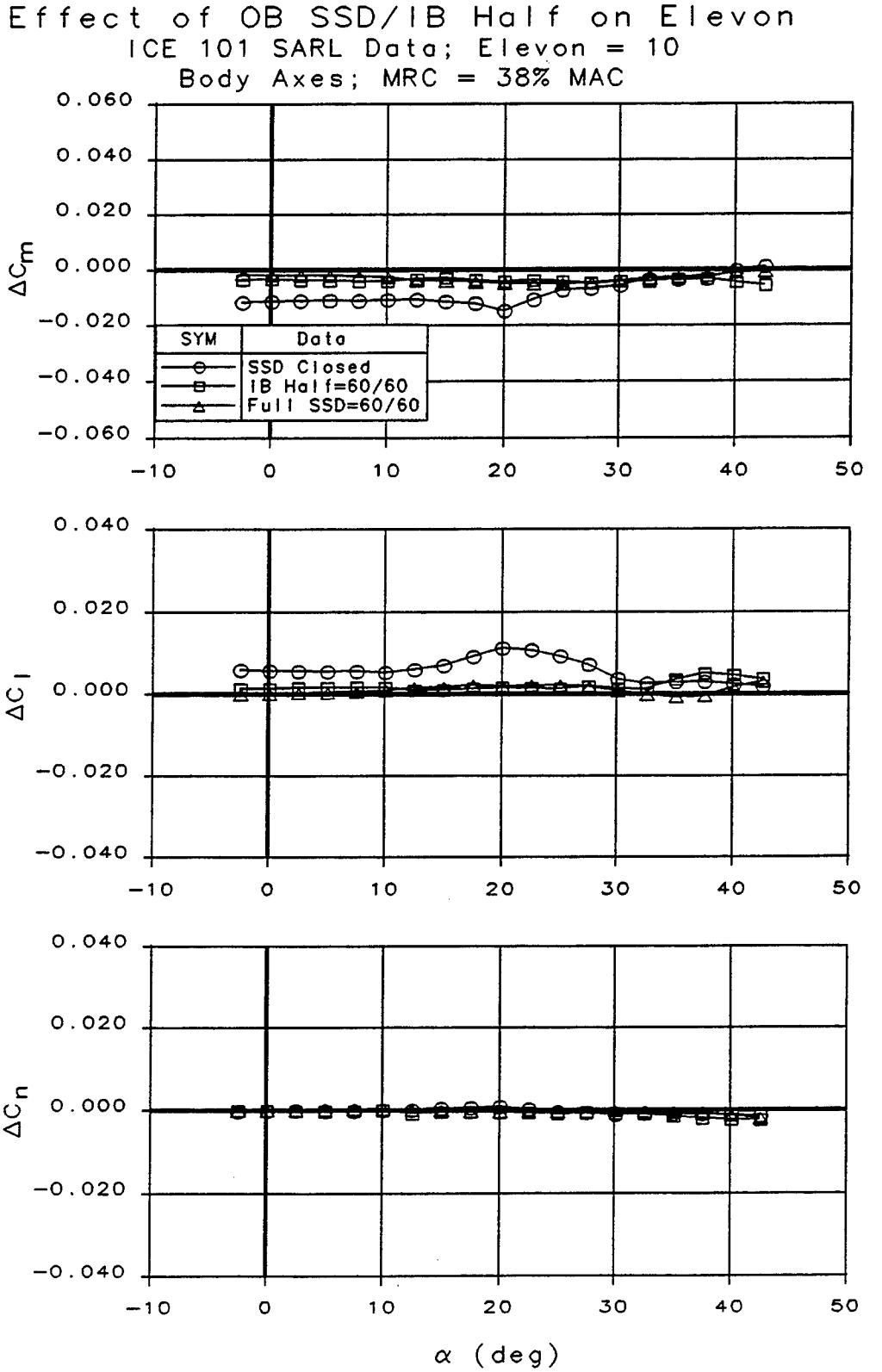

Figure 4-38: IB Half SSD Interaction with 10 deg Elevon

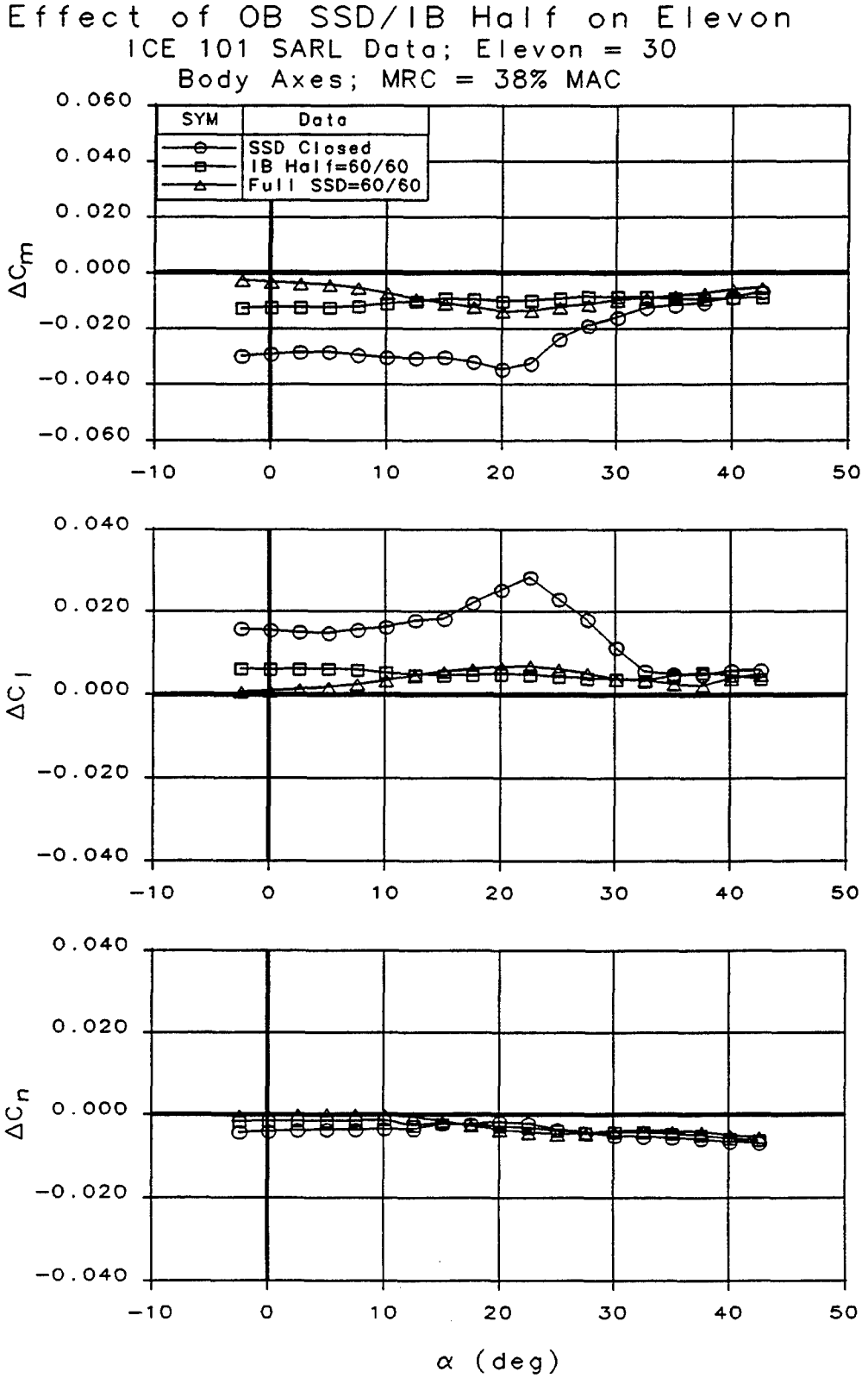

Figure 4-39: IB Half SSD Interaction with 30 deg Elevon

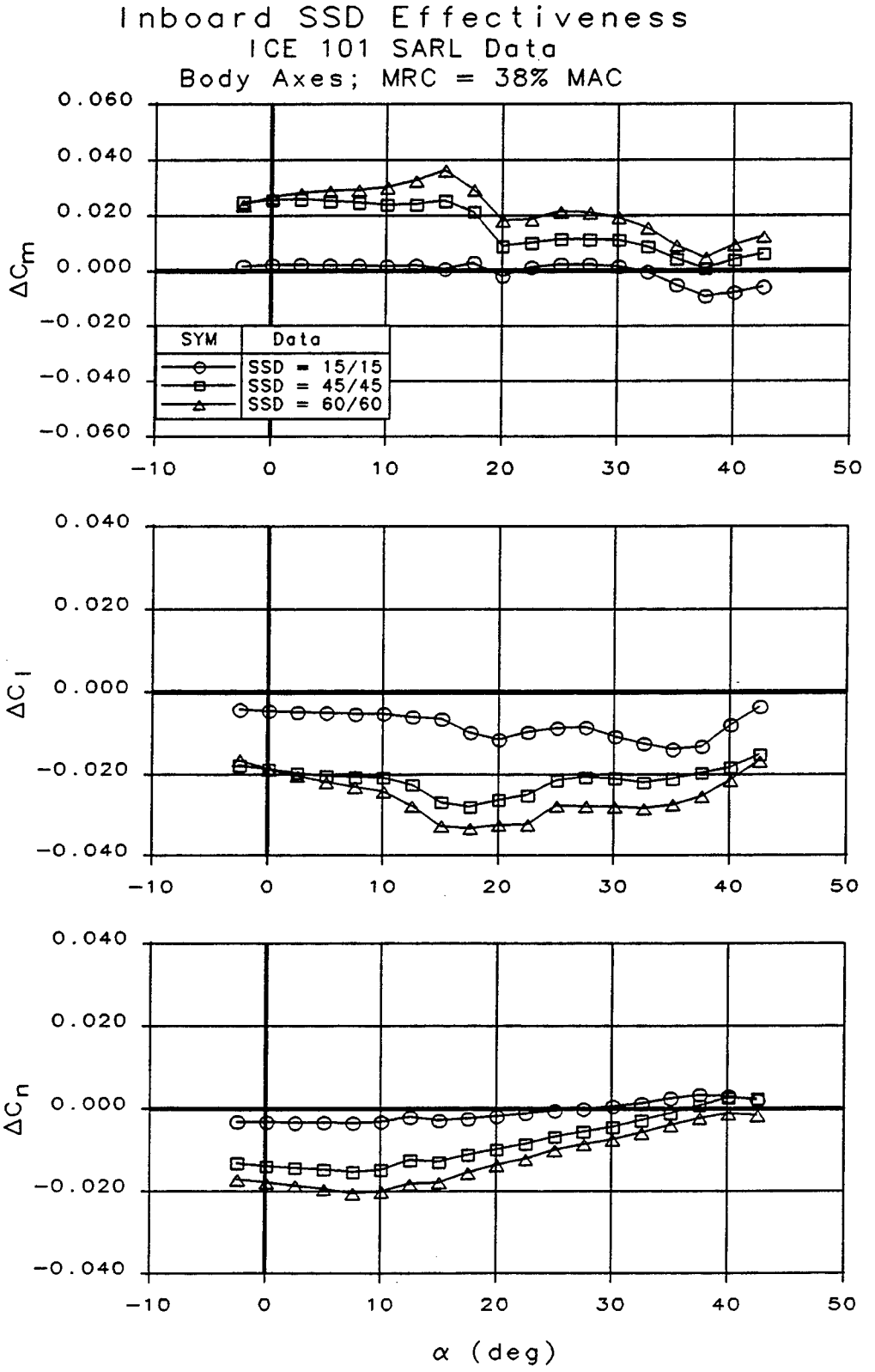

Figure 4-40: Inboard SSD Control Effectiveness

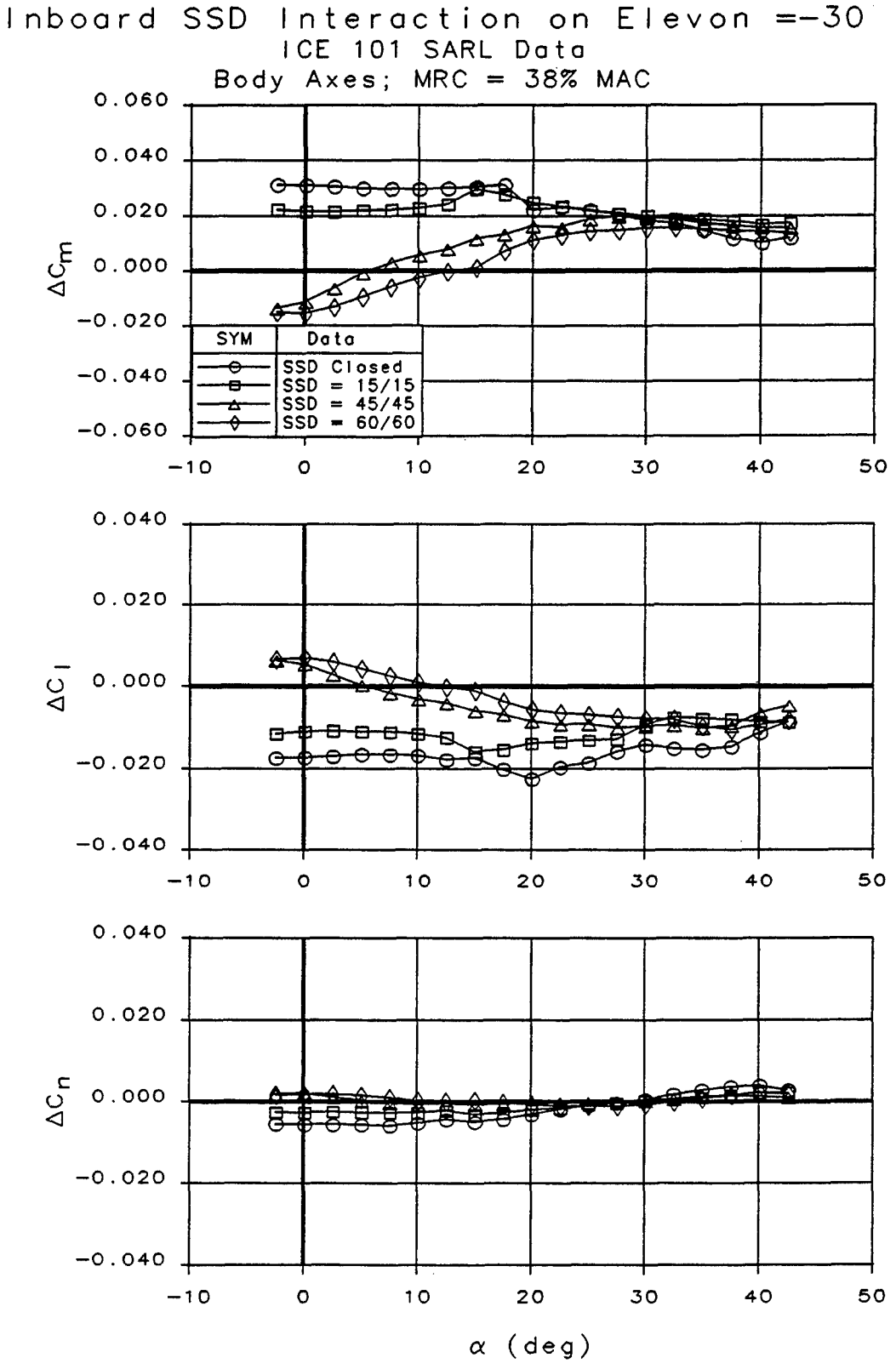

Figure 4-41: Inboard SSD Interaction with -30 deg Elevon

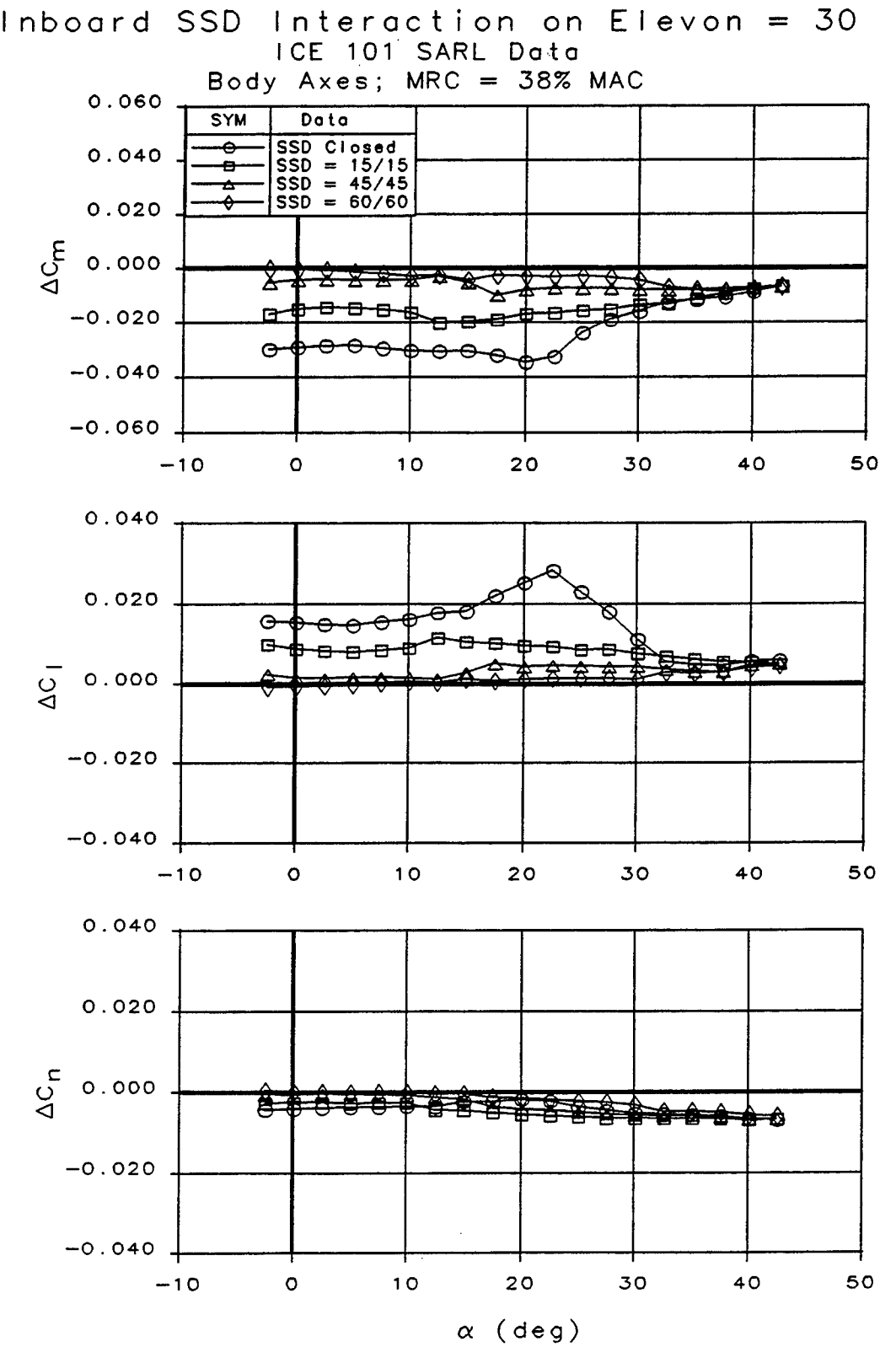

Figure 4-42: Inboard SSD Interaction with 30 deg Elevon

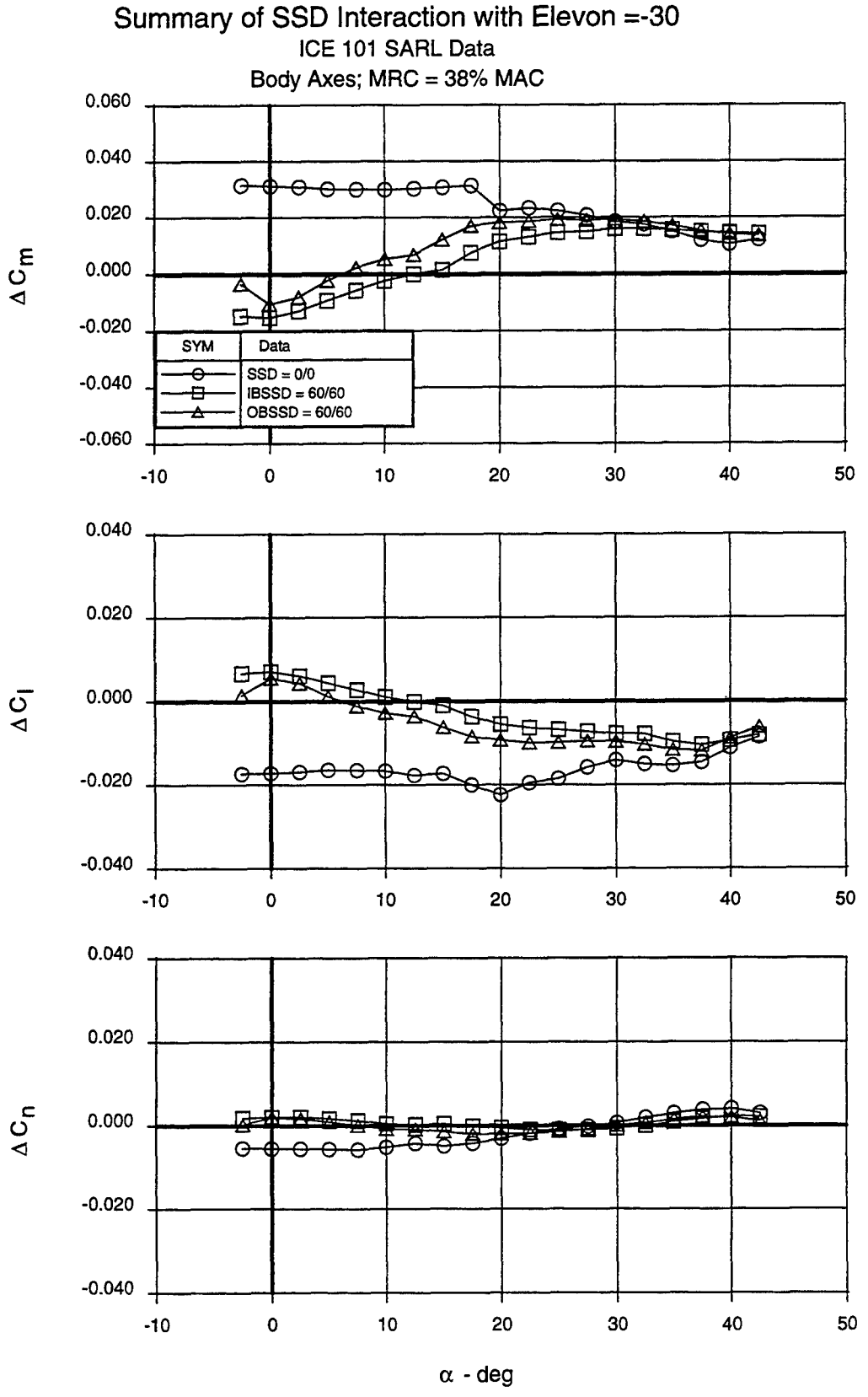

Figure 4-43: Effect of SSD Location on -30 deg Elevon Interaction

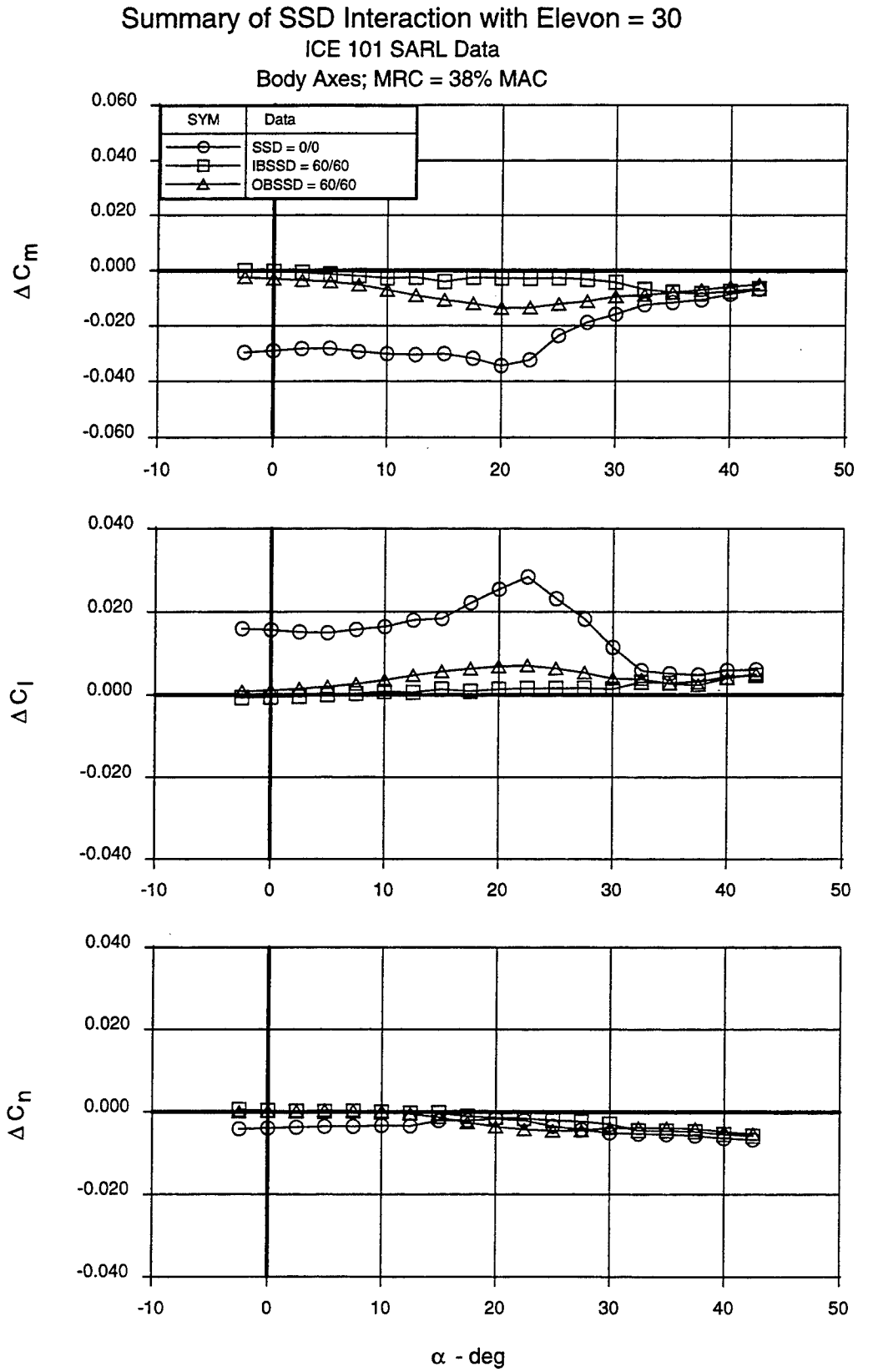

Figure 4-44: Effect of Location on 30 deg Elevon Interaction

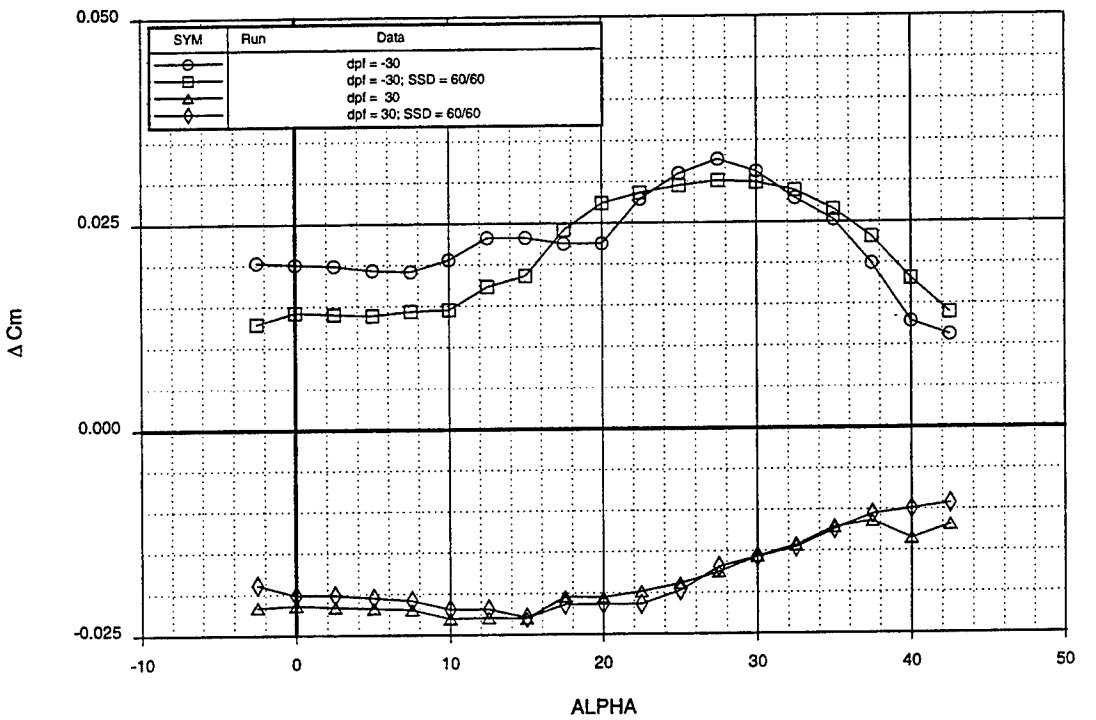

Figure 4-45: IB SSD Interactions with Pitch Flaps

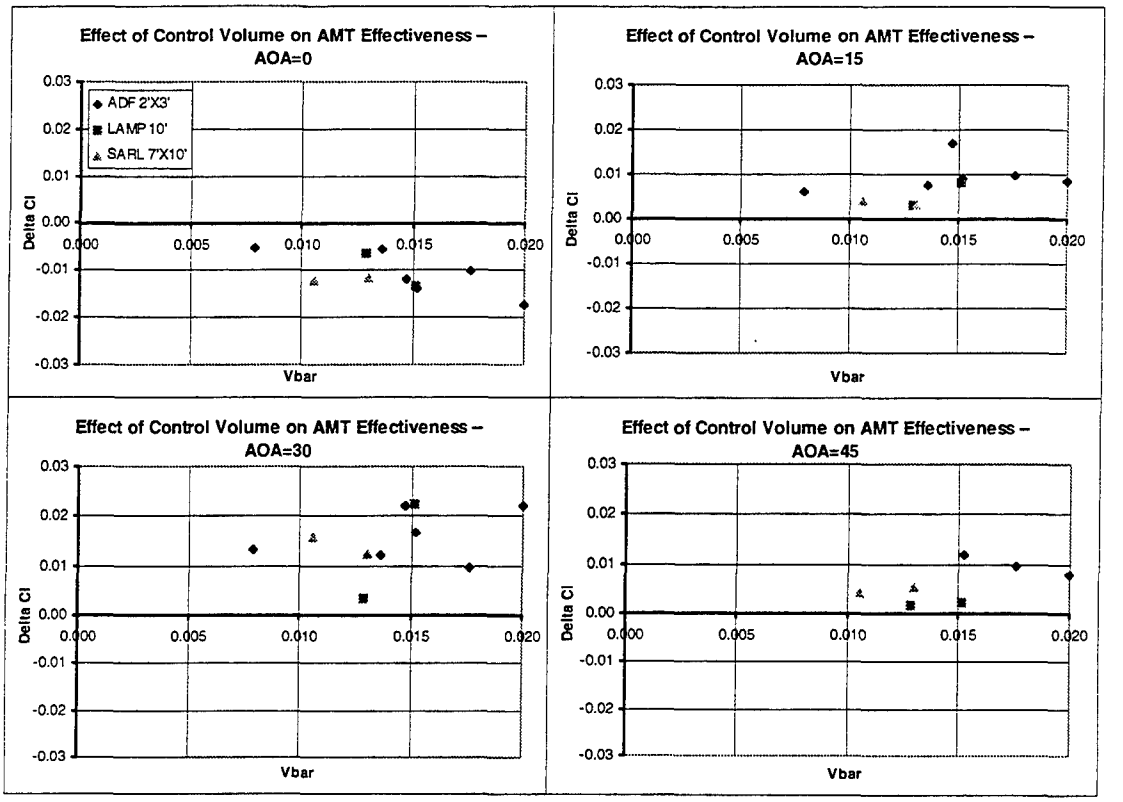

Figure 4-46: AMT Roll Power Variation with Control Volume (AMT = 60 deg)

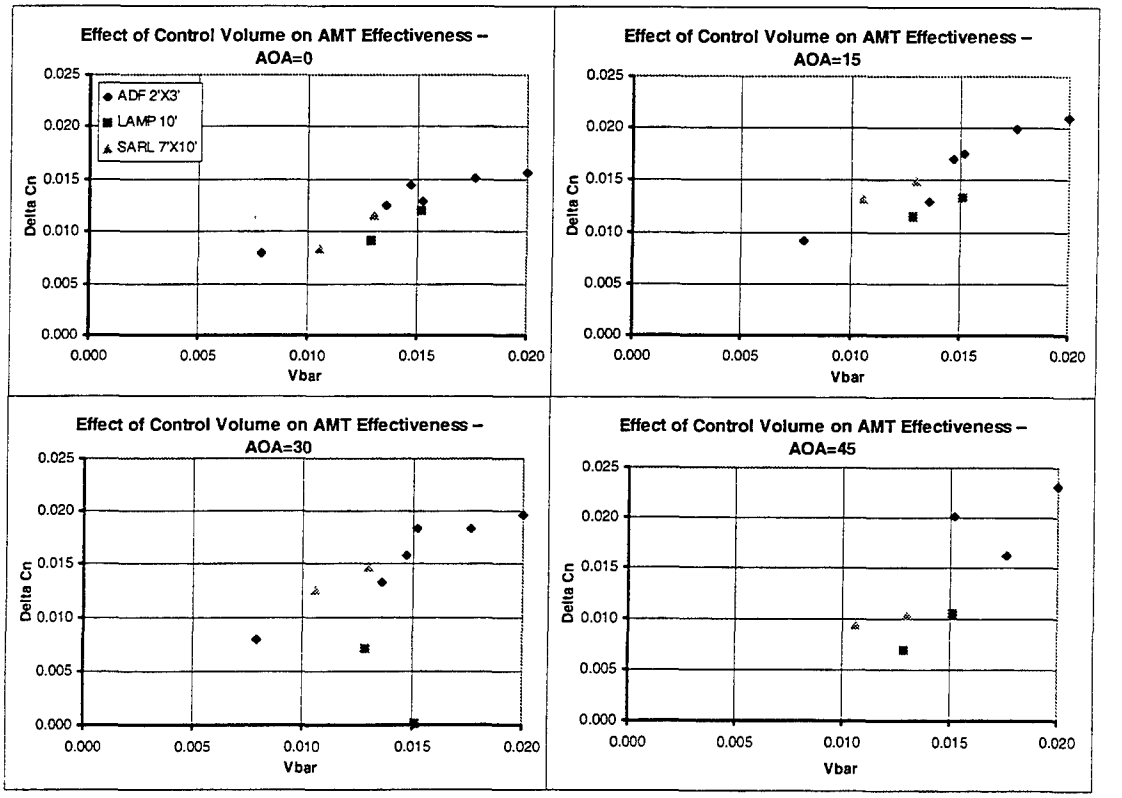

Figure 4-47: AMT Yaw Power Variation with Control Volume (AMT = 60 deg)

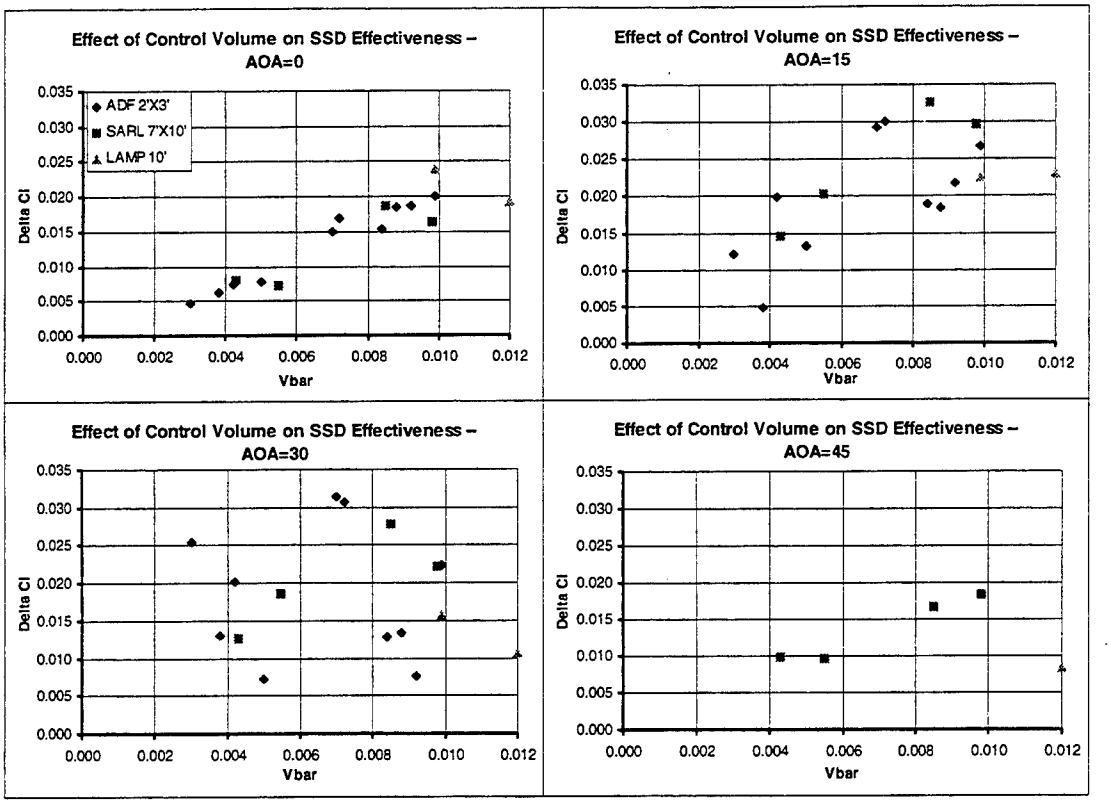

Figure 4-48: SSD Roll Power Variation with Control Volume (SSD = 60 deg)

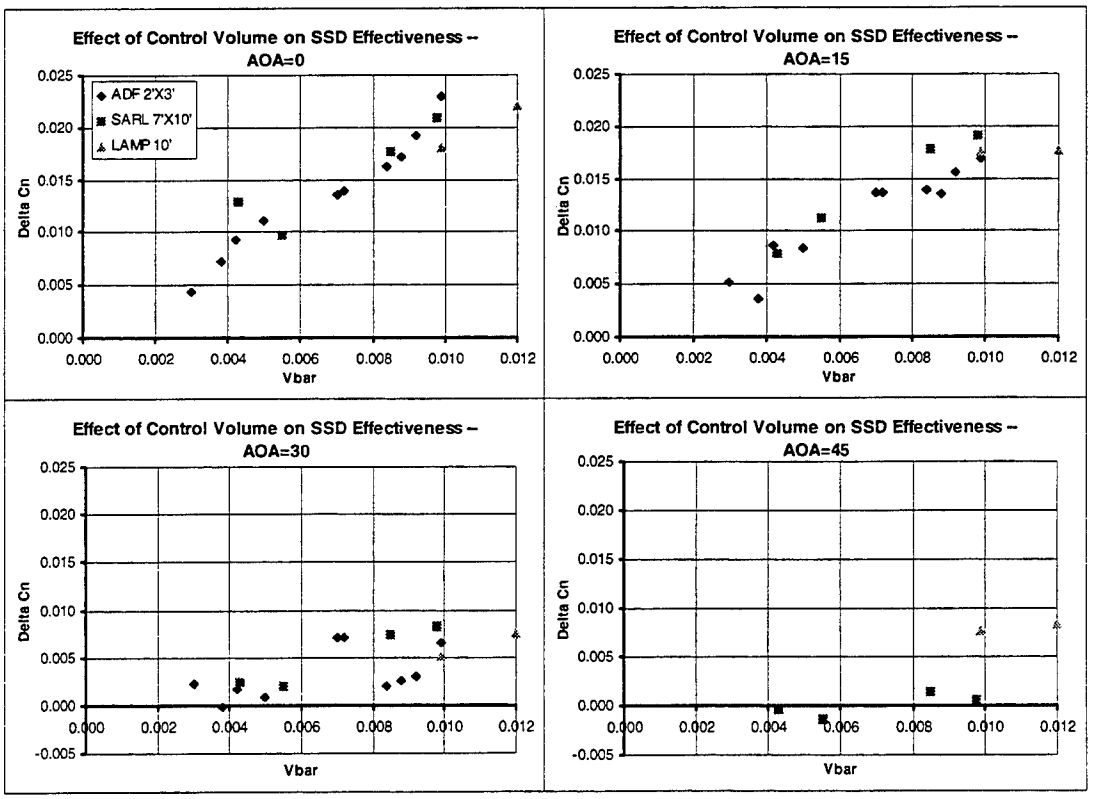

Figure 4-49: SSD Yaw Power Variation with Control Volume (SSD = 60 deg)

5 Simulation Database

The simulation databases for both the land-based (101 series) and the carrier-based (201 series) configurations were essentially completely reconstructed using new wind-tunnel data from the following tests that were conducted during ICE Phase 2: LMTAS ADF 9604 and 9605, LAMP 96, and SARL 96. Data from the ADF 9604 test was used to better document the carrier-based configurations by including finer control increments and interactions between some of the closely located wing-mounted control surfaces. The effects of steady rotation on both the 101 and 201 configurations were obtained during the LAMP 96 test. Because it was designed to primarily investigate spin characteristics, models may be tested to very large angles of attack and sideslips in the LAMP facility. For this reason, data were also obtained during this test that enabled the AOA range of many of the database components to be extended out to 90°, and the sideslip range was extended out to ±30° for many of the quantities that vary with sideslip. Because of the very low Reynolds number of the LAMP data, it was desired not to include the total coefficient values within the databases. For this reason, any LAMP data incorporated into the databases was in the form of an increment between a control deflected or rotating run and the corresponding controls neutral or static run. During the SARL 96 test, a larger scale and higher fidelity model of the land-based configurations was tested to obtain higher Reynolds number data than could be obtained in the LMTAS ADF tunnel. This data was used to describe the land-based configurations at AOAs below 45°. Similar to the ADF data for the 201 configurations, these data also included finer control increments and more control interactions than were previously available. Tables 5-1 and 5-2 respectively outline the database structure for the 101- and 201-series configurations by showing the database components, the independent variables and breakpoints, and the data source from which the component was constructed. When considered together, these new data sources were combined to replace or to expand all the database components for both configurations with the exception of the increments due to leading-edge flap deflection.

Both databases were constructed to be compatible with the LMTAS GEMD Version 2.3 software. This code requires a library format that contains both the data tables and the associated build-up equations. The user's simulation software passes the independent variable values to the GEMD library (AOA, sideslip, angular rates, control deflections, etc.), and the GEMD module returns the six total aerodynamic coefficients. All data in the simulation databases are in the body axis coordinate system, and they are referenced to the following geometric parameters.

	101	201
• S_{ref}, ft^2	808.60	705.60
• b_{ref}, ft	37.50	42.90
• MAC, in.	345.00	249.13
• FSLEMAC, in.	160.45	333.65
• MRC, %MAC	38.00	20.00
• WLMRC, in.	100.00	100.00

The starting point for the build-up equations for both databases is a basic coefficient that represents a neutral setting of all the controls undeflected. For the land-based configurations, this basic coefficient was a function of Mach number and AOA. No Mach variation was available for the carrier-based configurations, but their basic coefficients included a variation with canard and leading-edge flap deflection. Increments were added to these basic coefficients based on control deflection or angular rates to obtain the total aerodynamic coefficients. The effects of sideslip on the basic coefficients were also modeled as increments. These quantities were modeled in this way because they came from multiple data sources. By using this

method, the basic coefficient value could be obtained from the highest fidelity data, and the range of sideslip modeled could be made as large as possible by taking advantage of all the data from the multiple sources. During most of the wind-tunnel tests, the various control surfaces were tested on only one side of the configuration. The increments for the control surface on the opposite side were obtained by simply changing the sign of the rolling-moment, yawing-moment, and side-force components within either the data tables themselves or the build-up equations.

Table 5-1: Configuration 101-Series Simulation Database Description

Data Table	*Independent Variables*	*Mach Breakpoints*	*AOA Range deg*	*Sideslip Range deg*	*Additional Breakpoints*	*Control Interactions*	*Data Sources*
Basic Coefficients	Mach, AOA	0.30	-4.0 to 45.0	0	N/A	N/A	SARL 96
			45.0 to 90.0	"	"	"	LAMP 96
		0.60	1.0 to 29.0	"	"	"	LaRC 1035
		0.80	"	"	"	"	"
		0.90	1.0 to 26.0	"	"	"	"
		0.95	1.0 to 15.0	"	"	"	"
		1.20	1.0 to 29.0	"	"	"	"
		1.60	-2.0 to 17.0	"	"	"	LaRC 1734
		1.80	-2.0 to 20.0	"	"	"	"
		2.00	"	"	"	"	"
		2.16	"	"	"	"	"
Sideslip Increments	Mach, AOA, Beta	0.30	-2.5 to 45.0	-30 to 30	N/A	N/A	SARL 96 for $\beta \leq 20°$ LAMP 96 for $\beta \geq 20°$
			45.0 to 90.0	"	"	"	LAMP 96
		0.60	0.0 to 27.5	-8 to 8	"	"	LaRC 1035
		0.90	0.0 to 25.0	"	"	"	"
		1.20	"	"	"	"	"
		1.60	0.0 to 15.0	"	"	"	LaRC 1734
		1.80	0.0 to 10.0	"	"	"	"
		2.00	0.0 to 15.0	"	"	"	"
		2.16	"	"	"	"	"
Steady Rotation Increments	AOA, Beta, $\Omega b/2V$	N/A	0.0 to 90.0	-10 to 20	$\Omega b/2V$: ±0.05, ±0.1, ±0.2, ±0.3	N/A	LAMP 96
Inboard LEF Increments, Left & Right	AOA, Beta, $\delta_{LEF_{IB}}$	N/A	-2.5 to 45.0	-10 to 10	$\delta_{LEF_{IB}}$: 0, 40	N/A	SARL 94
Outboard LEF Increments, Left & Right	Mach, AOA, Beta, $\delta_{LEF_{OB}}$, $\delta_{LEF_{IB}}$	0.30	-2.5 to 45.0	-10 to 10	$\delta_{LEF_{OB}}$: -40, -20, 0, 20, 40	$\delta_{LEF_{IB}}$: 0, 40	SARL 94
		0.60	"	0	$\delta_{LEF_{OB}}$: 0, 40	None	LaRC 1035
		0.90	"	"	"	"	"
		1.20	"	"	"	"	"

Table 5-1 Continued.

Data Table	*Independent Variables*	*Mach Breakpoints*	*AOA Range deg*	*Sideslip Range deg*	*Additional Breakpoints*	*Control Interactions*	*Data Sources*
Elevon Increments, Left & Right	Mach, AOA, δ_e, δ_{SSD}	0.30	-2.5 to 45.0	0	δ_e: -30, -10, 0, 10, 30	δ_{SSD}: 0, 15, 45, 60	SARL 96
			45.0 to 90.0	"	δ_e: -30, 0, 30	None	LAMP 96
		0.60	-2.5 to 45.0	"		"	LaRC 1035
		0.90	"	"		"	"
		1.20	"	"		"	"
		1.60	"	"		"	LaRC 1734
		2.00	"	"		"	"
		2.16	"	"		"	"
Elevon/AMT Interaction, Left & Right	AOA, δ_e, δ_{AMT}	N/A	-2.5 to 42.5	0	δ_e: -30, 30	δ_{AMT}: 0, 30 ,60	SARL 96
Symmetric Pitch Flap Increments	Mach, AOA, δ_{pf}, δ_{SSD_L}, δ_{SSD_R}	0.30	-2.5 to 45.0	0	δ_{pf}: -30, -10, 0, 10, 30	δ_{SSD_L} & δ_{SSD_R}: 0, 15, 45, 60	SARL 96
			45.0 to 90.0	"	δ_{pf}: -30, 0, 30	None	LAMP 96
		0.60	0.0 to 30.0	"		"	LaRC 1035
		0.90	"	"		"	"
		1.20	"	"		"	"
		1.60	"	"		"	LaRC 1734
		2.00	"	"		"	"
		2.16	"	"		"	"
AMT Increments, Left & Right	AOA, Beta, δ_{AMT}	N/A	0.0 to 10.0	-30 to 30	δ_{AMT} = 0	None	SARL 96 for $\beta \leq 20°$ and LAMP 96 for $\beta = \pm 30°$
					δ_{AMT} = 10	"	ADF 9605 for $\beta \leq 20°$ and LAMP 96 for $\beta = \pm 30°$
					δ_{AMT} = 30	"	"
					δ_{AMT} = 40	"	SARL 96 for $\beta \leq 20°$ and LAMP 96 for $\beta = \pm 30°$
					δ_{AMT} = 60	"	"
			10.0 to 45.0	"		"	SARL 96
			45.0 to 90.0	"		"	LAMP 96

Table 5-1 Concluded.

Data Table	*Independent Variables*	*Mach Breakpoints*	*AOA Range deg*	*Sideslip Range deg*	*Additional Breakpoints*	*Control Interactions*	*Data Sources*
Mach Effects on AMT Increments	Mach	0.30, 0.60, 0.90, 1.04, 1.20, 1.60, 2.00, 2.16	N/A	N/A	N/A	N/A	
AMT/ OB LEF Interaction, Left & Right	AOA, δ_{AMT}, $\delta_{LEF_{OB}}$	N/A	-2.5 to 42.5	0	δ_{AMT}: 0, 30, 60	$\delta_{LEF_{OB}}$: 0, 20, 40	SARL 96
SSD Increments, Left & Right	AOA, Beta, δ_{SSD}	N/A	-2.5 to 45.0	-30 to 30	δ_{SSD}: 0, 15, 45, 60	None	SARL 96 for $\beta \leq 20°$ and LAMP 96 for $\beta = \pm 30°$
			45.0 to 90.0	"		"	LAMP 96
Mach Effects on SSD Increments	Mach	0.30, 0.60, 0.90, 1.20, 1.60, 2.00, 2.16	N/A	N/A	N/A	N/A	

Table 5-2: Configuration 201-Series Simulation Database Description

Data Table	Independent Variables	AOA Range deg	Sideslip Range deg	Additional Breakpoints	Control Interactions	Data Sources
Basic Coefficients	AOA, δ_C, δ_{LEF}	0.0 to 32.5	0	δ_C δ_{LEF} 10 0 10 10 0 0 0 25 -10 0 -10 20 -20 0 -20 20 -30 0 -30 30 -40 0 -40 30 -60 0 -60 30	None	ADF 9604
		32.5 to 45.0	"	δ_C δ_{LEF} 0 0 0 25 -20 20 -30 30 -40 0 -40 30 -60 0 -60 30	"	ADF 9604
		45.0 to 90.0	"	δ_C δ_{LEF} 0 0 0 25 -20 20 -40 30 -60 0 -60 30	"	LAMP 96

Table 5-2 Continued.

Data Table	*Independent Variables*	*AOA Range deg*	*Sideslip Range deg*	*Additional Breakpoints*	*Included Control Interactions*	*Data Sources*
Sideslip Increments	AOA, δ_C, δ_{LEF}	0.0 to 32.5	0 to 30 (reflected in build-up equations for negative sideslips)	δ_C δ_{LEF} 10 0 10 10 0 0 0 30 -10 0 -10 20 -20 0 -20 20 -30 0 -30 30 -40 0 -40 30 -60 0 -60 30	None	ADF 9604 for $\beta \leq 10°$, LAMP 96 for $\beta = \pm 20°$ and $\pm 30°$
		32.5 to 45.0	"	δ_C δ_{LEF} 0 0 0 30 -20 20 -30 30 -40 0 -40 30 -60 0 -60 30	"	ADF 9604 for $\beta \leq 10°$, LAMP 96 for $\beta = \pm 20°$ and $\pm 30°$
		45.0 to 90.0	"	δ_C δ_{LEF} 0 0 0 30 -20 20 -40 30 -60 0 -60 30	"	LAMP 96
Steady Rotation Increments	AOA, |Beta|, $\Omega b/2V$, δ_C, δ_{LEF}	0.0 to 90.0	0 to 20	$\Omega b/2V$: ± 0.05, ± 0.1, ± 0.2, ± 0.3	δ_C δ_{LEF} 0 0 0 30 -60 0 -60 30	LAMP 96

Table 5-2 Concluded.

Data Table	*Independent Variables*	*AOA Range deg*	*Sideslip Range deg*	*Additional Breakpoints*	*Included Control Interactions*	*Data Sources*
Elevon Increments, Left & Right	AOA, δ_e	0.0 to 45.0	0	δ_e: -30, -10, 0, 10, 30	None	ADF 9604
		45.0 to 90.0	"	δ_e: -30, 0, 30	"	LAMP 96
Symmetric Pitch Flap Increments	AOA, δ_{pf}	0.0 to 45.0	0	δ_{pf}: -30, -10, 0, 10, 30	None	ADF 9604
		45.0 to 90.0	"	δ_{pf}: -30, 0, 30	"	LAMP 96
Aileron Increments, Left & Right	AOA, δ_a, δ_{SSD}, δ_{AMT}	0.0 to 32.5	0	δ_a: -30, -10, 0, 10, 30	δ_{AMT}: -10, 0, 10, 30, 60 or δ_{SSD} = 0 and 60	ADF 9604
		45.0 to 90.0	"	δ_a: -30, 0, 30	None	LAMP 96
AMT Increments, Left & Right	AOA, Beta, δ_{AMT}	0.0 to 32.5	-30 to 30	δ_{AMT}: -10, 0, 10, 30, 60	None	ADF 9604 for $\beta \leq 10°$ and LAMP 96 for $\beta = \pm 20°$ and $\pm 30°$
		32.5 to 90.0	"	δ_{AMT}: -10, 0, 30, 60	"	LAMP 96
SSD Increments, Left & Right	AOA, Beta, δ_{SSD}	0.0 to 32.5	-30 to 30	δ_{SSD}: 0, 15, 30, 60	None	ADF 9604 for $\beta \leq 10°$ and LAMP 96 for $\beta = \pm 20°$ and $\pm 30°$
		32.5 to 90.0	"	δ_{SSD}: 0, 60	"	LAMP 96
SSD/LEF Interaction, Left & Right	AOA, δ_{SSD}, δ_{LEF}	0.0 to 32.5	0	δ_{SSD}: 0, 60	δ_{LEF}: 0, 30	ADF 9604
SSD/Canard Interaction, Left & Right	AOA, δ_{SSD}, δ_c	0.0 to 32.5	0	δ_{SSD}: 0, 60	δ_c: 10, 0, -10, -30	ADF 9604
Differential LEF Increments, Left & Right	AOA, Beta, $\delta_{LEF_{DIFF}}$, δ_c	0.0 to 45.0	-10 to 10	$\delta_{LEF_{DIFF}}$: 10, 20, 30,	δ_c: 10, 0, -20, -30, -40, -60	ADF 9604

6 Control Power Analysis

Existing LMTAS control power analysis tools were used to evaluate Configurations 101 and 201 with the latest updated wind-tunnel data obtained during the current study. These results were then compared with the original ICE Phase 1 predictions. The types of analysis that were performed included computations of the lateral-directional control power available from low to high AOA, evaluations of roll performance at critical flight conditions, and assessments of the power approach roll performance for the CV-based airplane. In addition, the roll agility metric (RAM) defined by the Fixed Wing Vehicle (FWV) initiative was computed for each configuration and compared with current F-16 and F-16 MATV data.

6.1 Methodology

Two primary software tools were used during this analysis: Control Power Available (CPA) and Control Power Required (CPR). These tools were developed by LMTAS using IR&D funds for the purposes of control suite sizing and preliminary evaluation of a given configuration's maneuver capabilities.

6.1.1 Control Power Available (CPA) Software

CPA is an aerodynamic database search tool that determines the maximum and minimum control moment capability obtainable from a given control suite. Before running CPA, an aerodynamic database is constructed from either aerodynamic predictions or wind-tunnel data. The level of complexity of this database is essentially unlimited by the software. Therefore, the control effectiveness increments for each surface may be made a function of any parameter, including sideslip or deflections of other control surfaces. If this type of construction is used, the effects of sideslip or control interactions on the total control power available may be evaluated.

To run CPA, the user designates the flight condition, the control surfaces to be evaluated, and the control deflection ranges and breakpoints (e.g., sweep the elevon from -30° to 30° by 10° increments). The routine initially computes the control moments corresponding to each possible combination of the specified control surface deflections. This dataset is then searched to determine the control surface deflection combinations that correspond to points on the boundary of the maximum control power available. The resulting data are stored in an output file that contains a map of the control "envelope" (roll vs. pitch vs. yaw) at each flight condition. These results are typically presented in the primed stability axis system [McRuer, et-al, 1973].

For configurations that have a large number of control surfaces, the total number of possible deflection combinations can become very large, even if relatively coarse breakpoints are used. Also, if one or more of these surfaces produces control moments about all three axes or interacts adversely with another surface, the appropriate combination to be used at a given flight condition may not be readily obvious. The ability of CPA to efficiently sort through the potential control combinations provides a powerful tool for determining which control surface combinations will maximize the control power potential at a given flight condition. This information can then be used to provide the control law designer with insight into how the control surface commands should be tailored throughout the flight envelope. During previous studies of tailless aircraft at high AOA, this task has proven not to be a trivial problem.

Figure 6-1 contains a typical CPA "envelope" that shows the functionality of lateral-directional control power available at various levels of pitch-control power. The top portion of the figure shows a contour map of roll power versus yaw power at varying levels of pitch power for a single angle of attack and Mach number. The lower portion shows the same data in 3-D format with nose-up pitch power plotted along the Z-Axis.

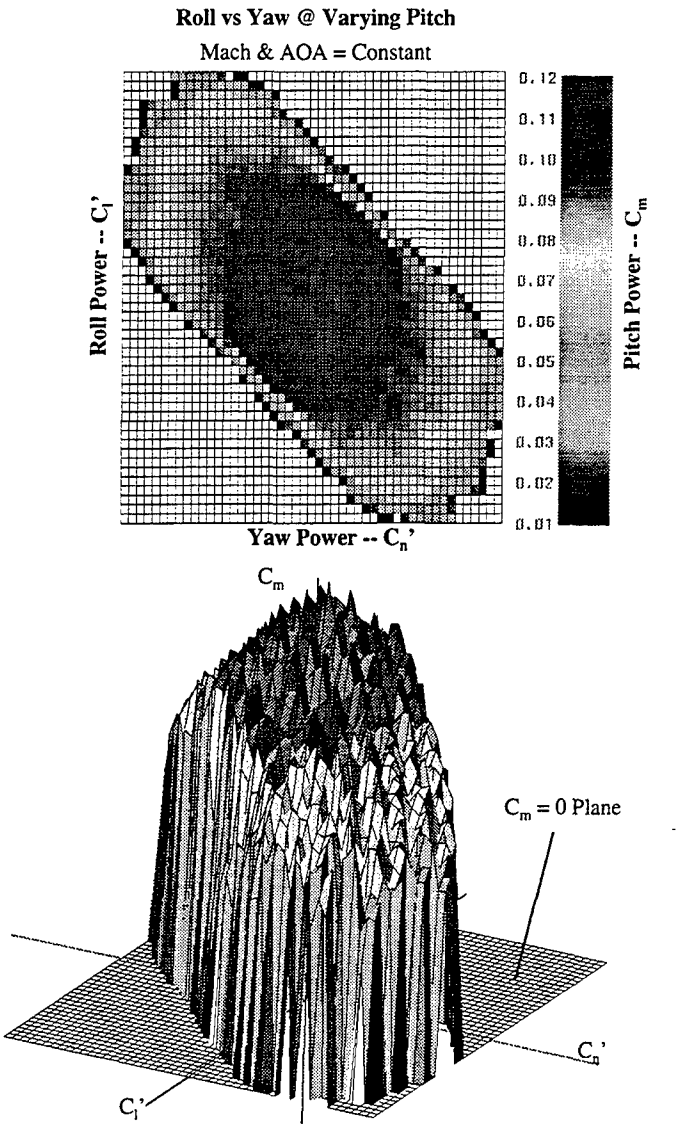

Figure 6-1: Example of Control Power Envelope Computed By CPA

An additional feature of the CPA software is the ability to determine the values of control power available about two of the axes for a fixed value of control moment about the third axis. This feature may be figuratively thought of as "cutting" the volume represented by the control power envelope to obtain cross sections. Figure 6-2 shows 2-D plots of these types of control envelope section cuts. The upper graph shows roll power versus yaw power when C_m=0. This type of graph shows the maximum levels of roll power that can be coordinated by the yaw control surfaces. It also shows the maximum level of coordinated yaw power. This value may be used with an assumed maximum sideslip angle to estimate the maximum level of augmented directional stability. The resulting computation will include the effects of sideslip on the effectiveness of the control surfaces that are being used for augmentation. The lower graph shows pitch power versus roll power when C_n'=0. This type of cut may be used to find the maximum coordinated roll-control power for varying levels of pitch-control power. When considered together, these cuts are useful for evaluating the roll/yaw/pitch control availability at various positions along the surface of the overall envelope. As alluded to previously, this consideration is both critical and difficult when analyzing a tailless aircraft with control surfaces that generate moments about all three axes where the control power available about any one axis is consequently a function of the control usage about the remaining axes.

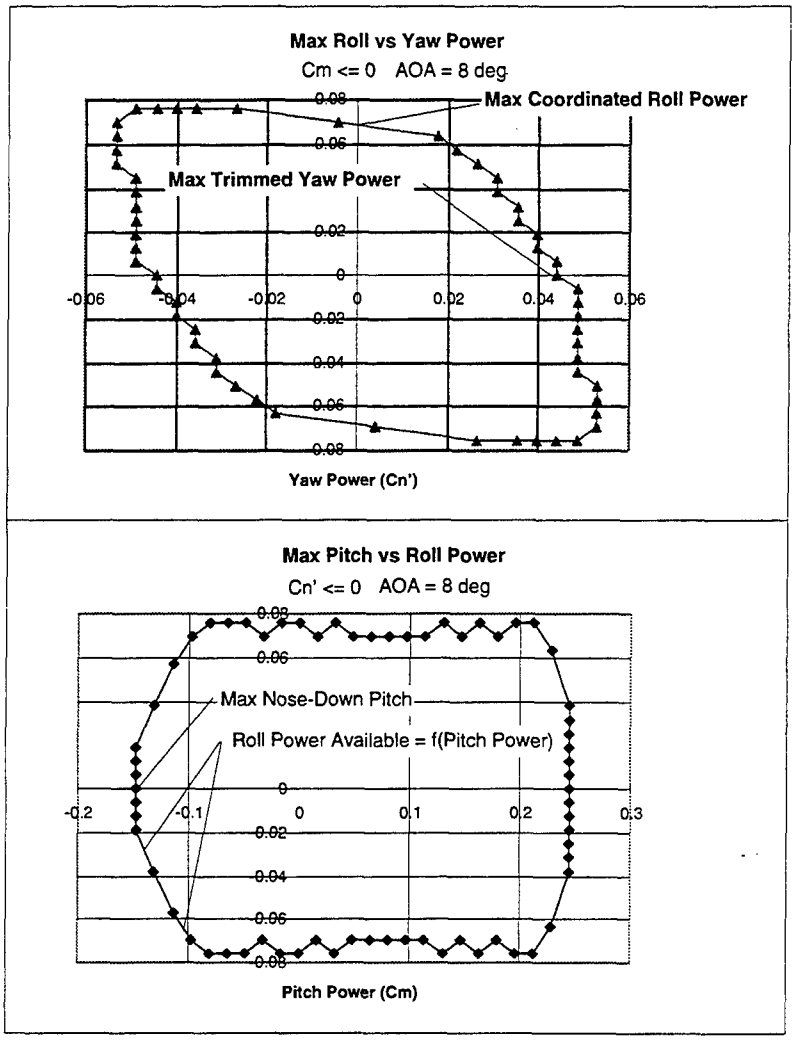

Figure 6-2: Example of Control Power Boundary Data Computed By CPA

In addition to these types of static evaluation, the control envelopes computed by CPA may also be used as inputs to the CPR simulation software that will be discussed in the following section. This option provides a very powerful tool with which to evaluate a given configuration's maneuver potential in a dynamic environment. If the analysis shows that the configuration's maneuvering performance requirements are not met, changes in control surface size may be quickly and easily evaluated. Also, the control envelope concept is very useful for evaluating preliminary designs for which the control blending scheme is not known during the conceptual design stage.

6.1.2 Control Power Required (CPR) Software

CPR is a six degree-of-freedom (6-DOF) simulation tool that is used to determine the amount of control power that a given aircraft requires to meet a maneuver specification. It may also be used to measure the maneuvering performance that the aircraft can achieve with its existing levels of control power (Figure 6-3). The idea for CPR was born from work documented in Thomas (1984) and Beaufrere (1987). In addition to the 6-DOF equations of motion, CPR contains a generic feedback flight control system (FCS) whose gains are computed on-line at each time step based on differences between the bare airframe characteristics and the desired closed-loop response.

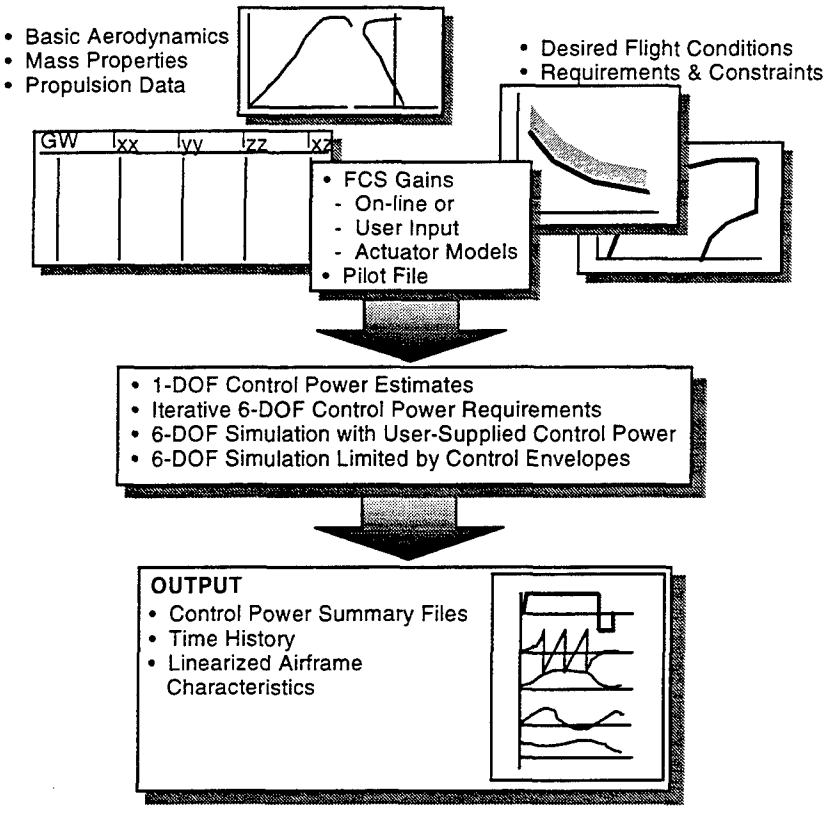

Figure 6-3: Illustration of CPR Software Utilization

CPR has four modes of operation: (1) static control power requirements, (2) iterative control power requirements, (3) basic simulation, and (4) simulation within CPA envelopes.

Option 1 is used to obtain an initial estimation of the total control moment requirements. It uses traditional, simplified, single-axis equations [Thomas, 1984]. Examples of the types of quantities that are computed within this option include the nose-down pitch power required to counteract inertial coupling or the roll power needed to achieve a given time-to-bank. To employ this option, the user is required to input the bare airframe characteristics (i.e., C_L, C_m, $C_{n\beta}$, etc. vs. α), the time-to-bank requirements, and the minimum required nose-down pitch acceleration.

Option 2 is used to obtain a more detailed estimation of the control power required than that obtained from the Option 1 computations. With input data similar to Option 1, Option 2 performs a simulation of a rolling maneuver using the full 6-DOF equations of motion. The control power available is treated as an unknown. An iterative process on control power is used to determine the level that is required to meet the maneuver performance specifications. By using this method, the effects of coupling between the different axes, the bare airframe stability level, and any control system nonlinearities can be properly evaluated. The computed control requirements are output in a summary file, and time histories of each iteration are also provided.

Option 3 is simply the basic 6-DOF simulation capability, and no control power estimation is performed. To use this option, the user must supply all the aerodynamic data, including the control power increments. This database may be as simple or complex as the user desires. Typically, this option is used to evaluate fairly conventional configurations. A pilot input file is used with this option to enable the modeling of selected maneuvers.

Option 4 provides a similar simulation capability to Option 3 except that the control power values are obtained from CPA envelope files instead of a traditional aerodynamic database. This method is useful for evaluating complex control suites that have significant interactions between surfaces or coupling about multiple axes. It also provides a method to analyze a configuration at the conceptual level when the details of the control surface blending scheme are not known.

The longitudinal axis FCS used in CPR (Figure 6-4) is an N_Z-command system that is very similar to the one described by Beaufrere (1987). It contains feedbacks of normal acceleration and pitch rate that are used to augment the short period dynamics. Pitch acceleration is fed back to cancel the first-order actuator pole. The product of body-axis roll rate and yaw rate is fed back to offset inertial pitch coupling during rolling maneuvers. For the specified closed-loop flying qualities (ω_{sp} or CAP and ζ_{sp}), the longitudinal FCS will emulate the desired short-period dynamics as long as either the longitudinal control surface rate or position limit is not encountered.

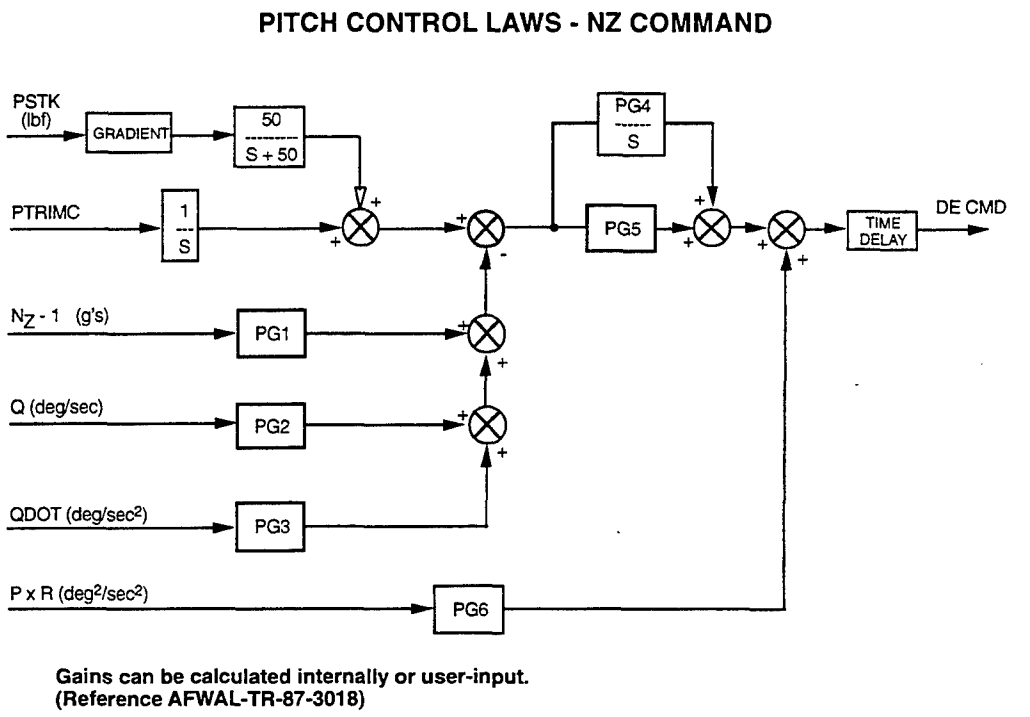

Figure 6-4: Longitudinal Axis Flight Control System Used In CPR

The lateral axis FCS is a stability-axis roll-rate-command system that includes the expected feedback of roll rate for computation of the error signal (Figure 6-5). Stability-axis yaw rate is also fed back to account for the effects of C_{l_r}. The gains are computed to enable the system to achieve the desired user-specified close-loop roll mode time constant (τ_r) as long as either the lateral control surface rate or position limit is not encountered.

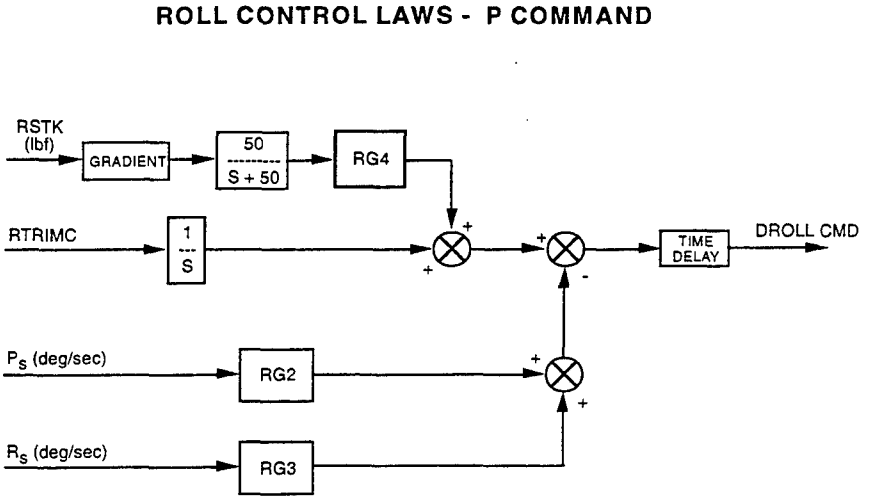

Figure 6-5 Lateral Axis Flight Control System Used In CPR

The directional axis FCS consists of a sideslip-command system that incorporates feedbacks of sideslip and sideslip rate (Figure 6-6). Stability-axis roll-rate feedback is included to account for the effects of C_{np}. Feedback of the product of roll rate and pitch rate is also included to counter inertial coupling. The gains are computed based on the bare airframe characteristics and the user-specified closed-loop Dutch roll frequency and damping.

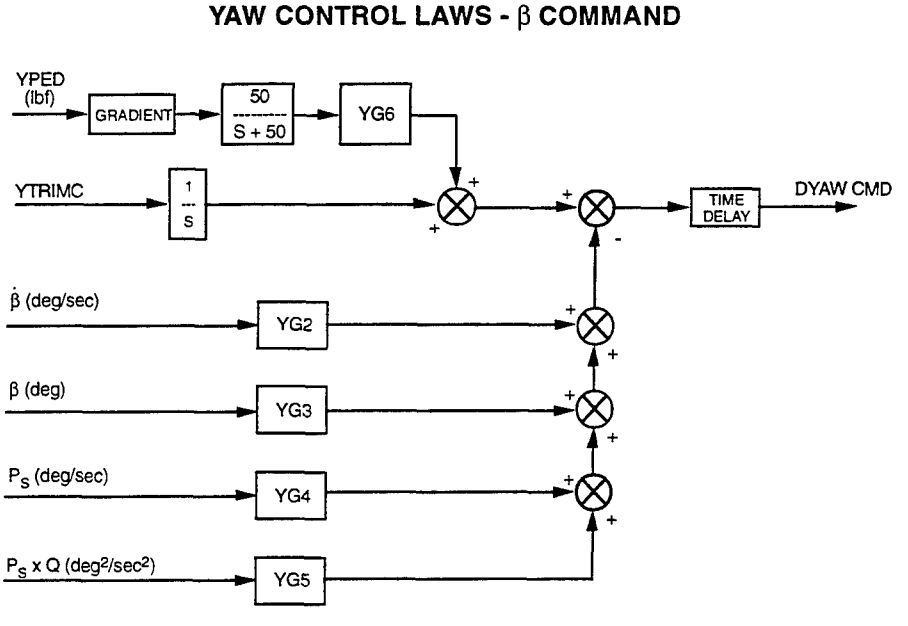

Figure 6-6 Directional Axis Flight Control System Used In CPR

The roll (DROLL) and yaw (DYAW) commands respectively obtained from the lateral axis and directional axis portions of the flight control system are mixed to obtain roll control surface (DELA) and yaw control surface (DELR) commands by using the logic shown in Figure 6-7. The gains YG1 and RG1 are computed based on the airframe roll-to-yaw characteristics to obtain decoupled primed stability-axis rotational accelerations. First-order actuator models are also included for each axis that contain rate and position limiting.

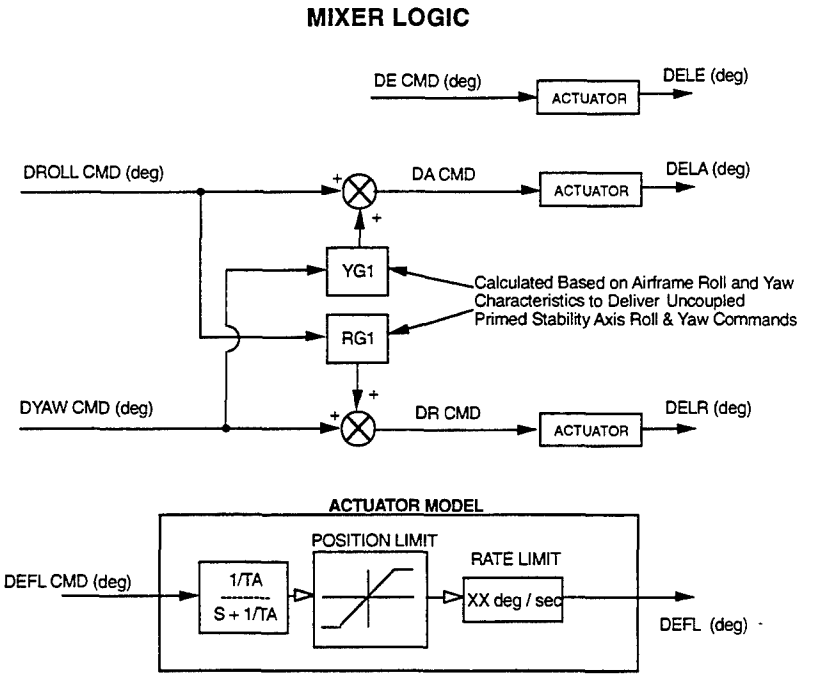

Figure 6-7: Lateral-Directional Command Mixer Used In CPR

6.1.3 Flight Conditions Investigated

During Phase 1 of the ICE study, three flight conditions were identified for use during the sizing of the lateral-directional control surfaces.

- Elevated g: 300 KCAS at 15K ft, AOA=20°, mil power and max A/B
- Low-speed/high AOA: 108 KCAS at 15K ft, AOA=30°, max A/B
- 1-g power approach: idle power and trim power

Rolls at these flight conditions are representative of the types of maneuvers that require the greatest amounts of lateral-directional control power within the operating environment of a typical military aircraft. These same conditions were analyzed again during the current study using the latest updated wind-tunnel data. The results were then compared to the ICE Phase 1 findings.

To provide an additional comparison, the lateral-directional flying qualities parameters of maximum coordinated roll power and maximum augmented directional stability were computed at 150 KCAS/15K ft for both the thrust vectoring on and off cases.

Finally, roll performance was predicted at AOAs of 0°, 15°, 25°, 35°, 50° and 75° at 194 KEAS/15K ft (equivalent to 100 m/s). These results were used to calculate the Roll Agility Metric (RAM) specified by

the DoD's Fixed Wing Vehicle (FWV) initiative. As shown below, RAM is a summation function of the times-to-bank 90° over the operational AOA range of the vehicle.

$$RAM = \sum_i \left[\frac{1}{\max(1.0, t_{\Delta\phi_{wind}=90} at \alpha_i)} \right]; \alpha_i = \left\{ [0,15,25,35,50,75]_{V=194\,KEAS}, [\alpha_{1-g}]_{V=583\,KEAS} \right\} \quad (6\text{-}1)$$

Throughout this study, multi-axis thrust vectoring (MATV) was modeled using a 15° maximum vector angle. This value was further limited to maintain less than 6,000 lbs. of off-axis force, which is consistent with the assumptions made during Phase 1 of the ICE program.

6.2 Land-Based: Configuration 101 Series

This section discusses the analysis of the two land-based configurations: 1) 101-1 which used the SSD as its primary yaw control surface and 2) 101-4 which used the AMT as its primary yaw control surface.

6.2.1 Basic Aerodynamic Effectiveness of Primary Yaw Control Surfaces

Figure 6-8 shows a comparison of the SSD effectiveness predicted during Phase 1 with the latest aerodynamic data obtained during the SARL wind-tunnel test. The Phase 1 SSD effectiveness curves were based on data from a 1/60th scale high-sweep research model that was tested in the LMTAS ADF wind tunnel. The figure reveals several differences between the measured and predicted data that are each beneficial. The current SSD arrangement produces more yaw-control effectiveness than was predicted for AOAs below 22.5°. They also produce considerably more favorable lateral control power than was originally forecast. Finally, the effects of SSD deflection on pitching moment were over-predicted during Phase 1. As a result, more of the total elevon deflection can be utilized for roll power instead of being used to trim out the nose-up moments generated by SSD deflections. Note that the current analysis uses the OB SSD location described in previous chapters.

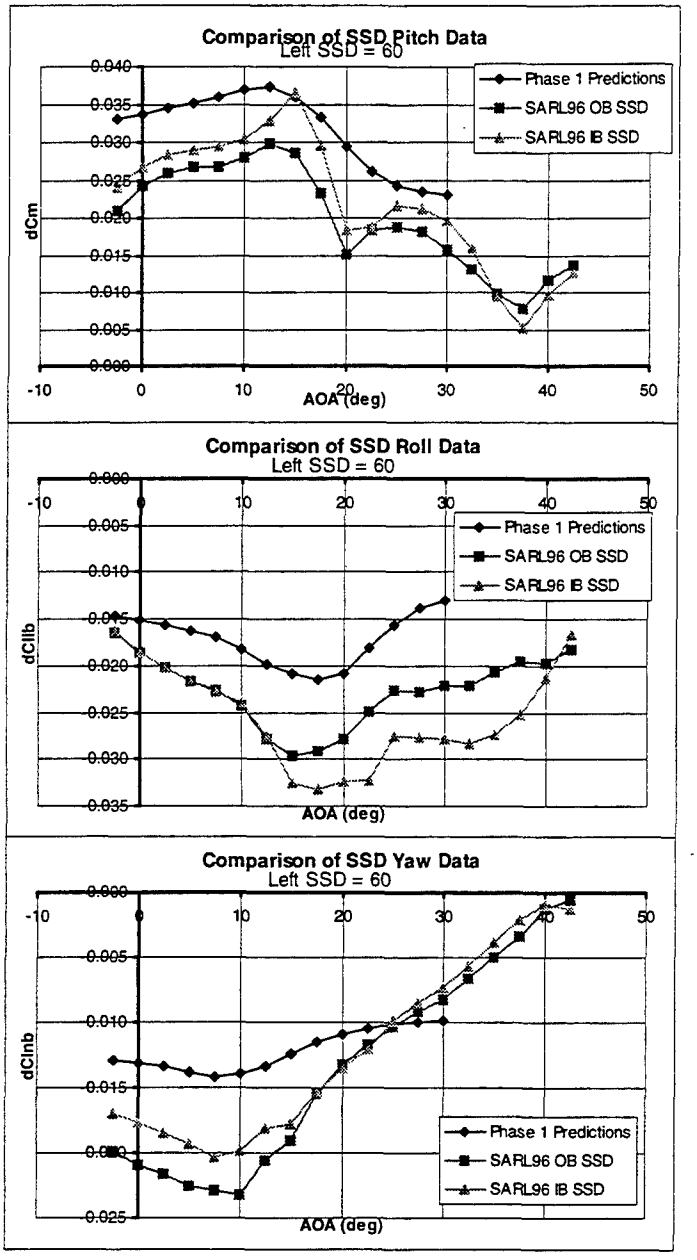

Figure 6-8: Comparison of SSD Effectiveness on Configuration 101-1 With Phase 1 Predictions

Figure 6-9 shows a similar comparison between the AMT effectiveness predicted during Phase 1 and the latest skewed AMT data obtained during the SARL wind-tunnel test. The Phase 1 data were obtained from an ADF wind-tunnel test of Configuration 201 [Dorsett & Mehl, 1996, App. C]. The predicted pitch and roll increments agreed better with the SARL data than did the corresponding values for the SSDs (Figure 6-8). The overall magnitudes of these increments were also smaller than those produced by the SSDs. This result indicated that the AMTs are more purely a yaw control device because they are less coupled about the longitudinal and lateral axes than the SSDs. The low-AOA yaw-control increments agreed very well with the predictions. At these AOAs, the AMTs were less effective than the SSDs. At AOAs above 10°, the yaw-control increments measured during the SARL test were significantly lower than the predictions. Despite this trend, the AMTs were considerably more effective than the SSDs at these higher AOAs. The discrepancies between the measured and predicted AMT yaw-control effectiveness were attributed to differences in the tested configurations from which the SARL data and Phase 1 predictions were obtained.

Analysis of the differences between the predicted and measured roll and yaw increments reveals that the measured data has a less favorable roll-to-yaw relationship than the original predicted data because either more adverse or less favorable rolling moment is produced at a given angle of attack. Furthermore, the difference in the measured and predicted pitching-moment increments was somewhat favorable in that the measured data generally showed a more nose-down increment than the predicted data.

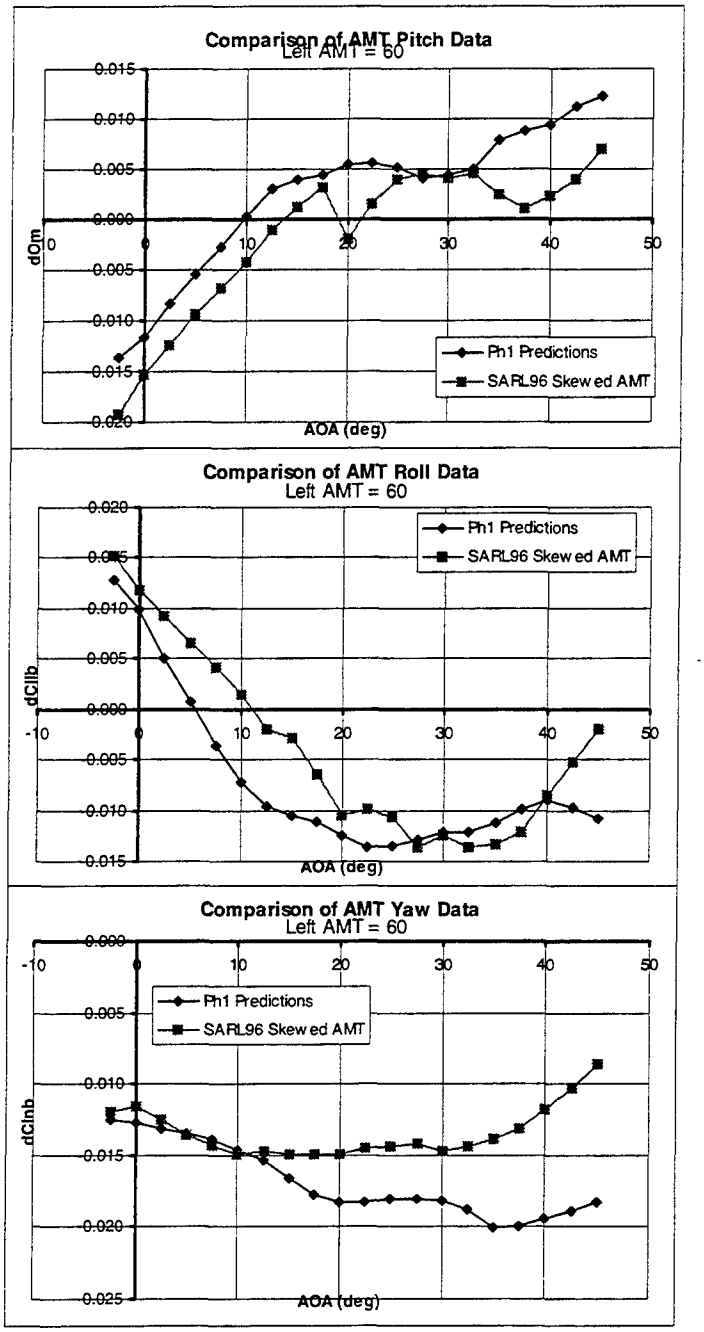

Figure 6-9: Comparison of AMT Effectiveness on Configuration 101-4 With Phase 1 Predictions

6.2.2 Control Power Envelopes

Using the CPA software, control power envelopes were computed for various AOAs around the three previously listed critical flight conditions that were originally used to size the control surfaces during Phase 1. The computed envelopes are shown in Figures 6-10 to 6-15. To properly account for the control power contribution obtained from thrust vectoring, representative throttle settings were used with each flight condition. Both mil power and max A/B were utilized at the 300 KCAS condition. At 108 KCAS, only max A/B was used. For power approach, the throttle was set at idle and the value for trim power. Although not shown, control power envelopes were also computed at various AOAs for the 150 KCAS condition. For these computations, the throttle was set at max A/B, and thrust vectoring was turned both off and on. These data were used to provide a comparison during the other forms of analysis that will be discussed subsequently.

The data shown in the figures represent maximum roll power vs. yaw power available for $C_m \leq 0$. These plots were created by slicing the 3-dimensional control envelope through the $C_m = 0$ station and plotting the resulting perimeter of the cross section. Control power data are presented in primed-stability-axis coefficient form as defined by the following equations in which the aerodynamic data and inertias are in the stability axis system. Use of the primed stability axis system allows the lateral and directional equations of motion to be decoupled. Evaluation of a configuration's lateral-directional flying qualities from static coefficients is then straight-forward. Parameters like coordinated roll power available can be readily assessed by looking for C_l' when $C_n' = 0$.

$$C_n' = \frac{C_n + \frac{I_{xz}}{I_{xx}} C_l}{1 - I_{xz}^2 / I_{xx} I_{zz}}$$

$$C_l' = \frac{C_l + \frac{I_{xz}}{I_{zz}} C_n}{1 - I_{xz}^2 / I_{xx} I_{zz}} \qquad (6\text{-}2)$$

The control power envelopes for Configurations 101-1 and 101-4 at the 300 KCAS flight condition are shown in Figures 6-10 and 6-11, respectively. For both configurations, increasing the throttle setting from mil power to max A/B resulted in only small increases in control power. This result highlights the reason that this flight condition was chosen for use during the control surface sizing task. At this higher speed and consequently increased dynamic pressure, the control moments available from MATV are not large when compared to the aerodynamic forces acting on the aircraft, and consequently the aircraft must rely heavily on aerodynamic control power. The intersection of each envelope with the y-axis indicates the amount of roll power that can be coordinated by the yaw control surfaces. For a given AOA, each configuration produced similar levels of coordinated roll power. In addition, each configuration was capable of producing larger amounts of roll control power that could not be coordinated, even with max A/B thrust. The 101-1 envelope shows more variability with AOA than the 101-4 envelope, and the 101-1 envelope becomes more adverse (rotated counter-clockwise) as AOA is increased. These results were attributed to decreases in the roll effectiveness of the SSDs that occur at the higher AOAs (Figure 6-8). They also indicated that the effectiveness of the AMTs is fairly constant throughout this range of AOAs (Figure 6-9).

The control power envelopes for the 108 KCAS flight condition are shown in figures 6-12 and 6-13 for Configurations 101-1 and 101-4, respectively. As stated previously, the throttle was set at max A/B for these cases. The figures show that both configurations have significant lateral-directional maneuvering potential at these relatively high AOAs with 101-1 having slightly higher coordinated roll power values than 101-4.

The control power envelopes for Configuration 101-1 at the power approach flight condition are shown in Figure 6-14. Data are shown for both the idle and trim power settings. When compared to the idle power case, the flatness of the trim power envelope across its top and bottom indicates that the yaw thrust vectoring provides sufficient coordination of all the aerodynamic roll power at each AOA that was tested. Similarly, sufficient aerodynamic yaw power is not available for coordination of all the aerodynamic roll power at the idle throttle setting.

The corresponding control power envelopes for Configuration 101-4 are shown in Figure 6-15. Comparing these results to the Configuration 101-1 data in Figure 6-14 indicates that 101-1 has more total roll power at a given AOA than 101-4, and 101-4 generally has slightly higher maximum levels of total yaw power. These results were attributed to the fact that the SSDs produce large body-axis rolling moments in addition to yawing moments in this AOA range, whereas the AMTs generate mostly yawing moments (Figures 6-8 and 6-9). These effects also cause the 101-4 envelope to be more adverse (rotated counter-clockwise) than the 101-1 envelope. As seen for Configuration 101-1, yaw thrust vectoring at the trim power setting is also able to coordinate all of the available aerodynamic roll power on Configuration 101-4.

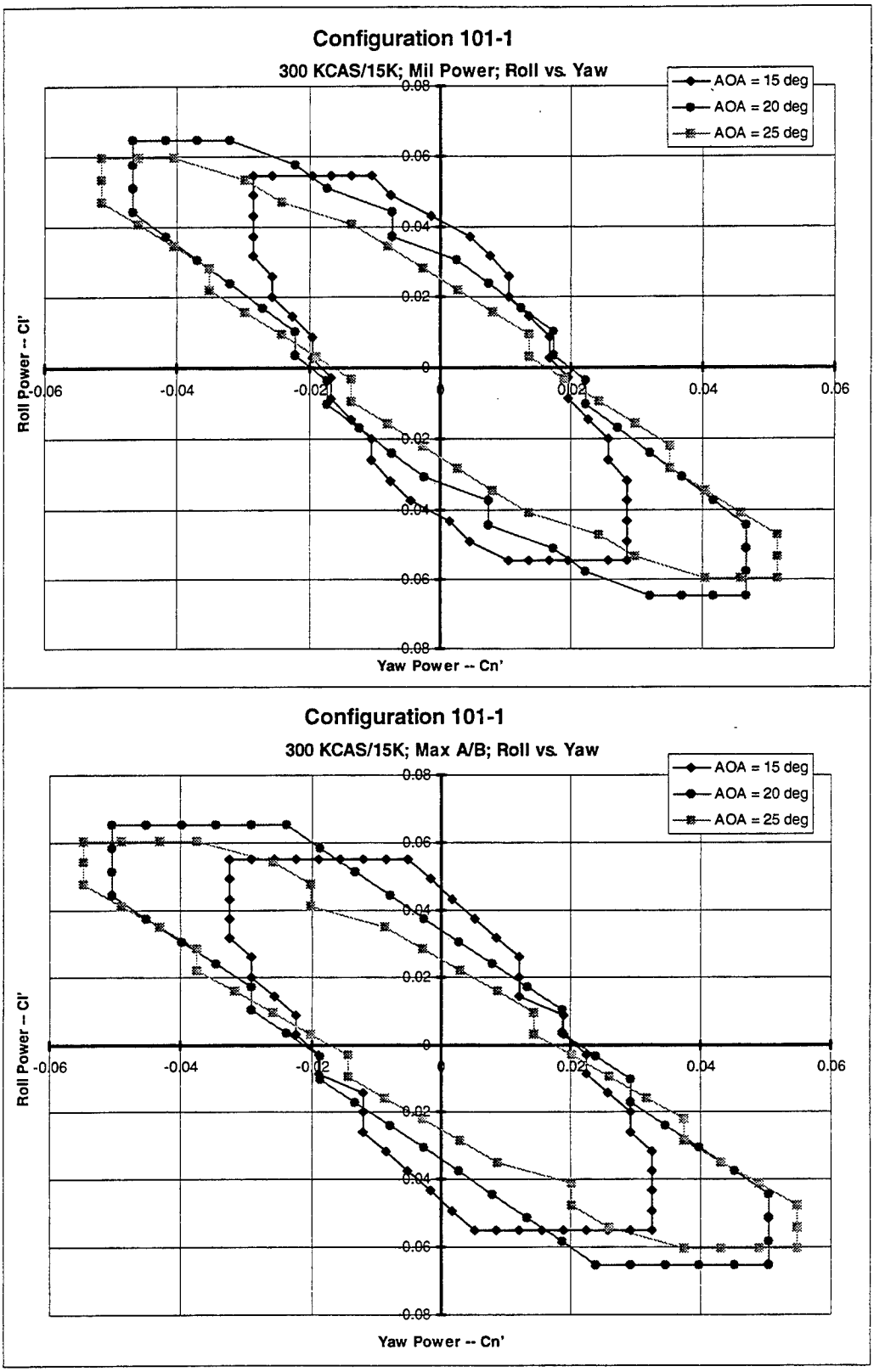

Figure 6-10: Configuration 101-1 Control Power Available at 300 KCAS/15K for Mil Power and Max A/B

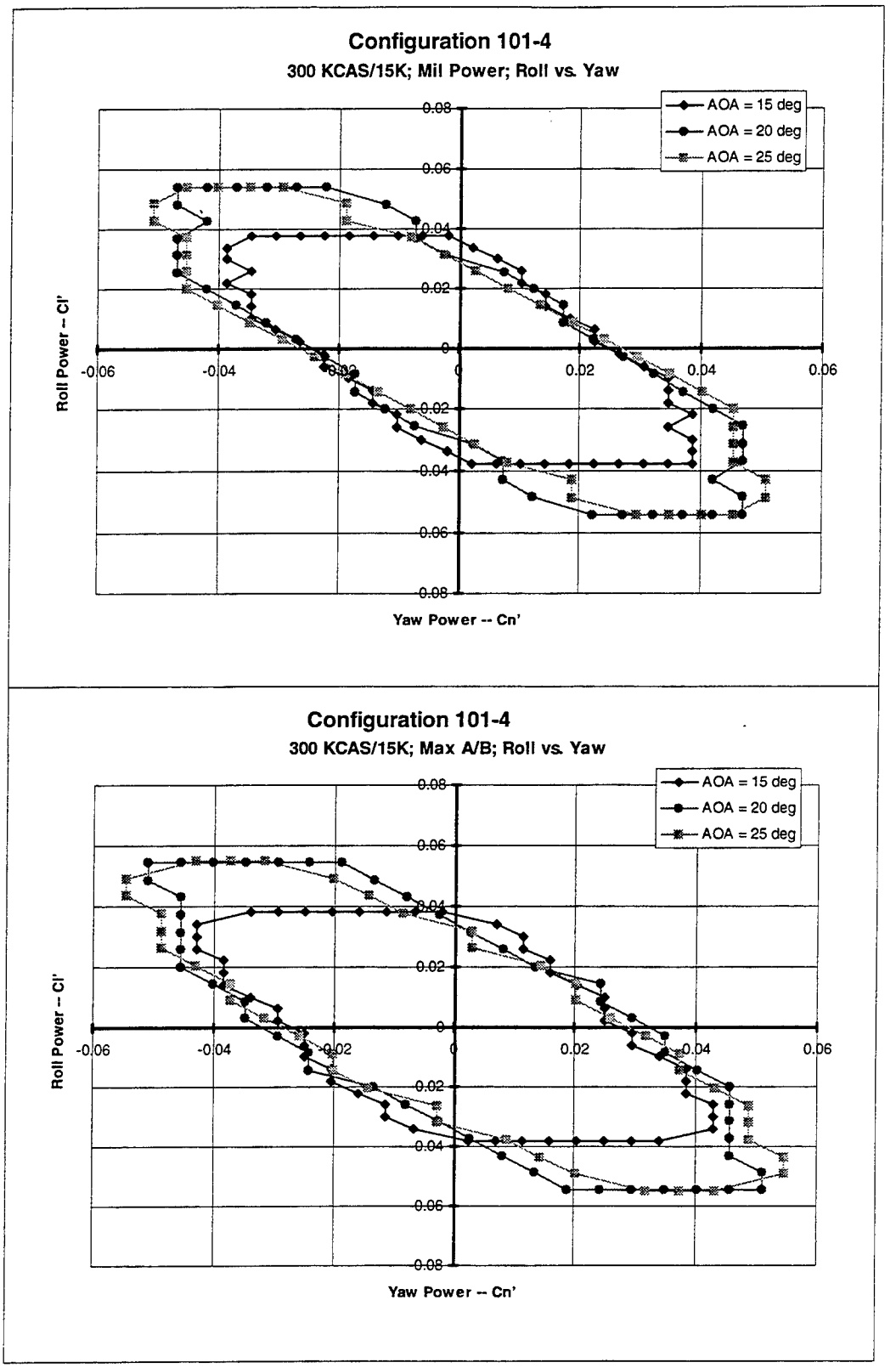

Figure 6-11: Configuration 101-4 Control Power Available at 300 KCAS/15K for Mil Power and Max A/B

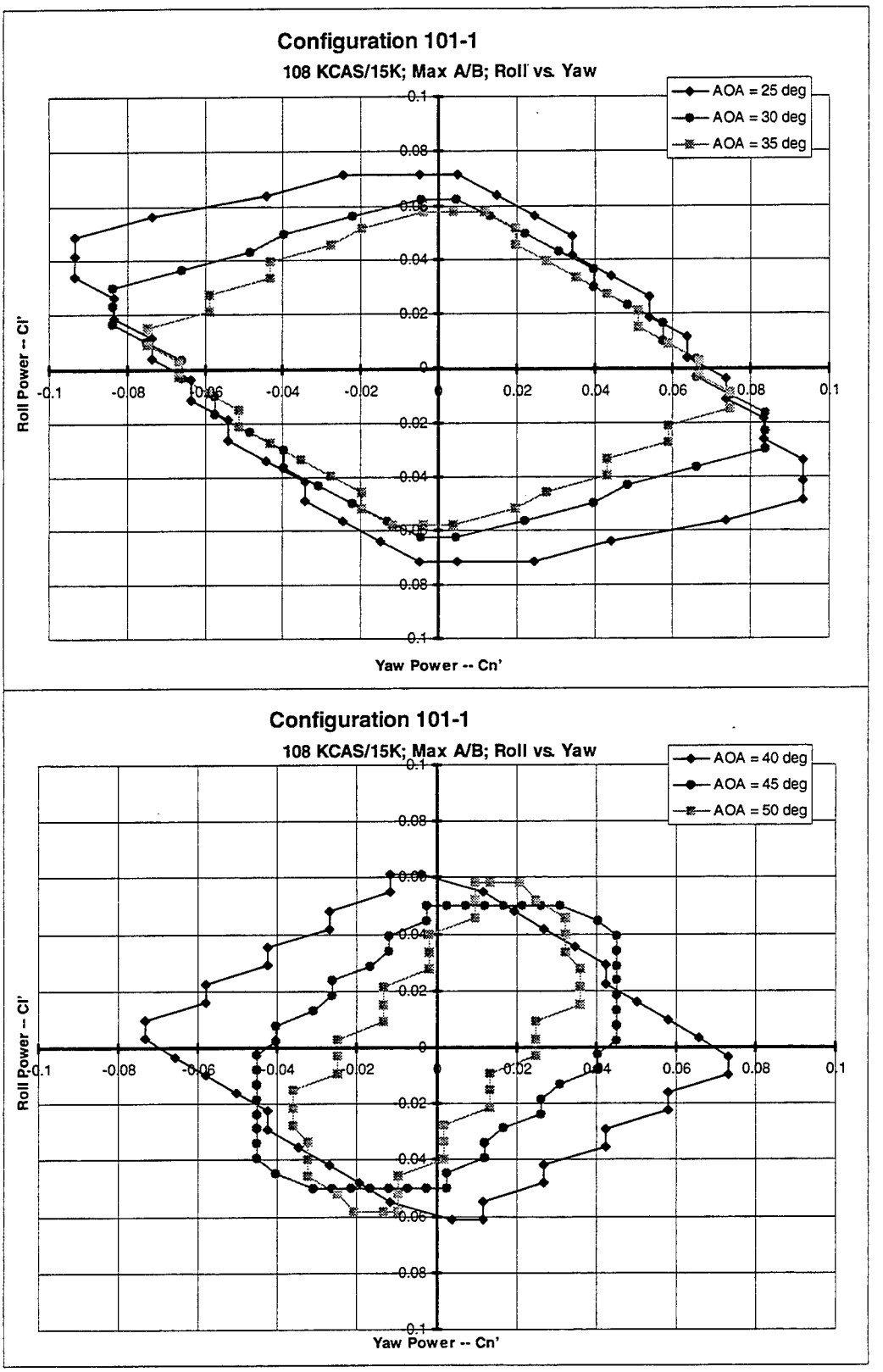

Figure 6-12: Configuration 101-1 Control Power Available at 108 KCAS/15K With Max A/B

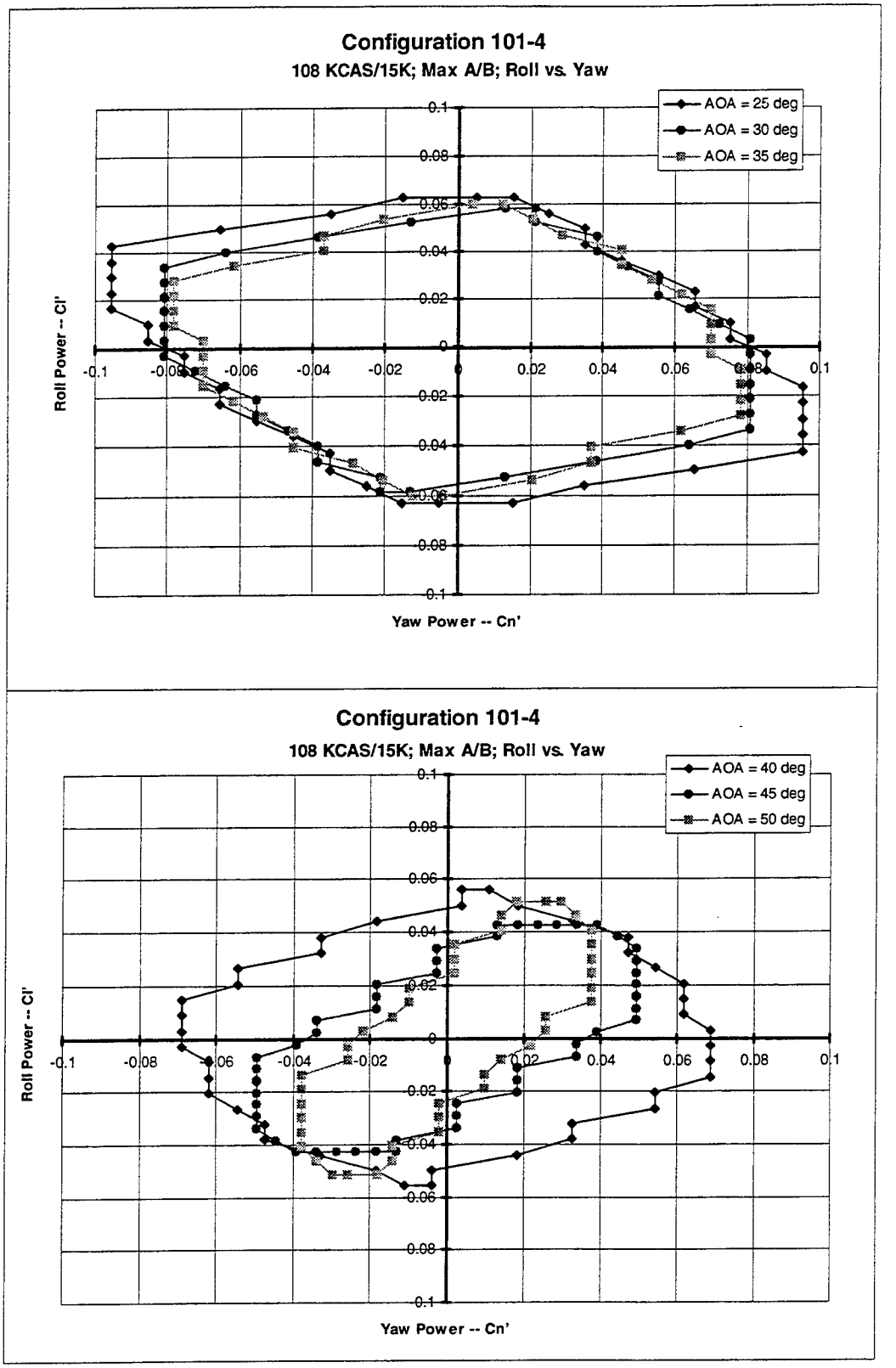

Figure 6-13: Configuration 101-4 Control Power Available at 108 KCAS/15K With Max A/B

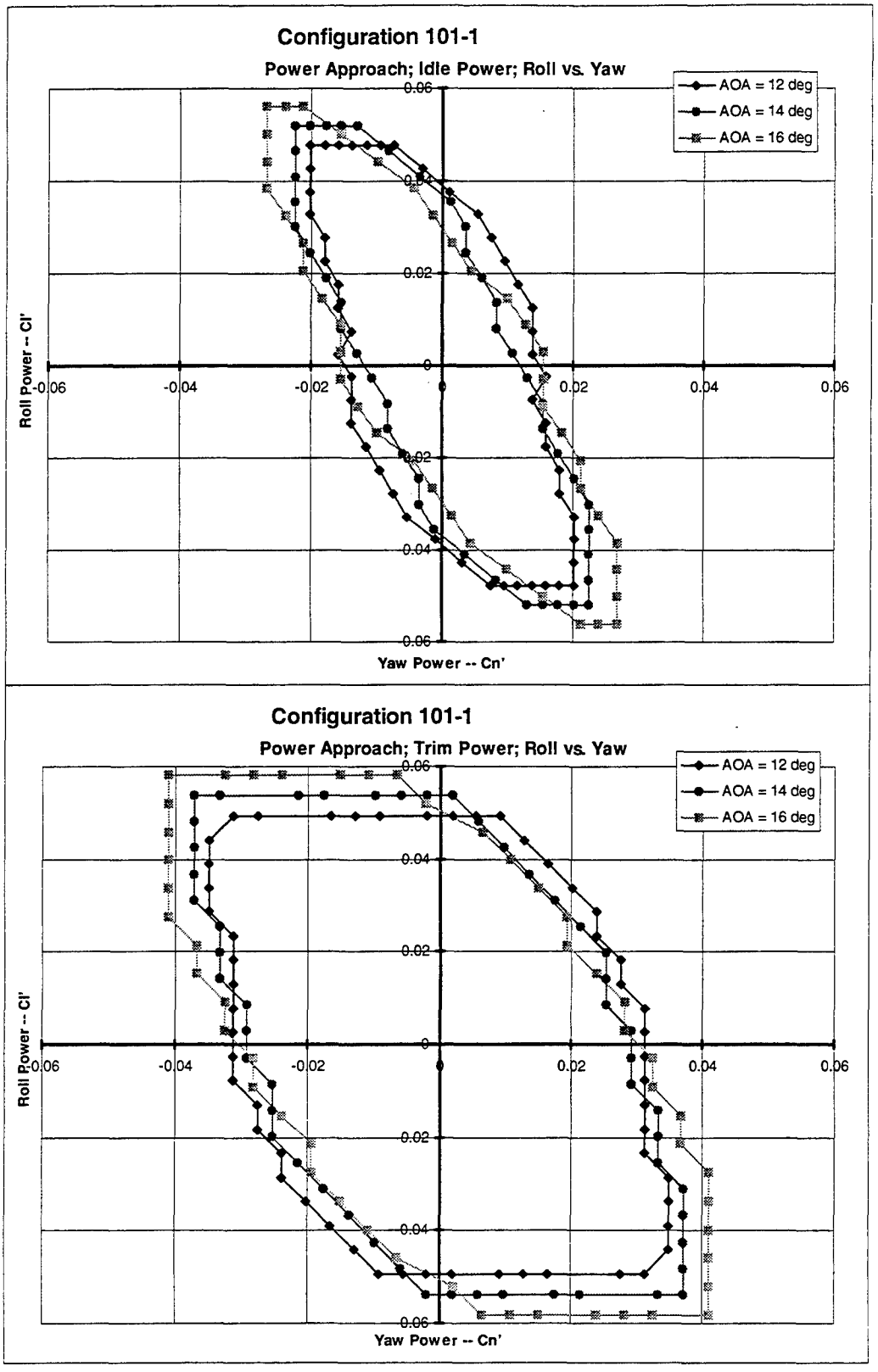

Figure 6-14: Configuration 101-1 Power Approach Control Power Available

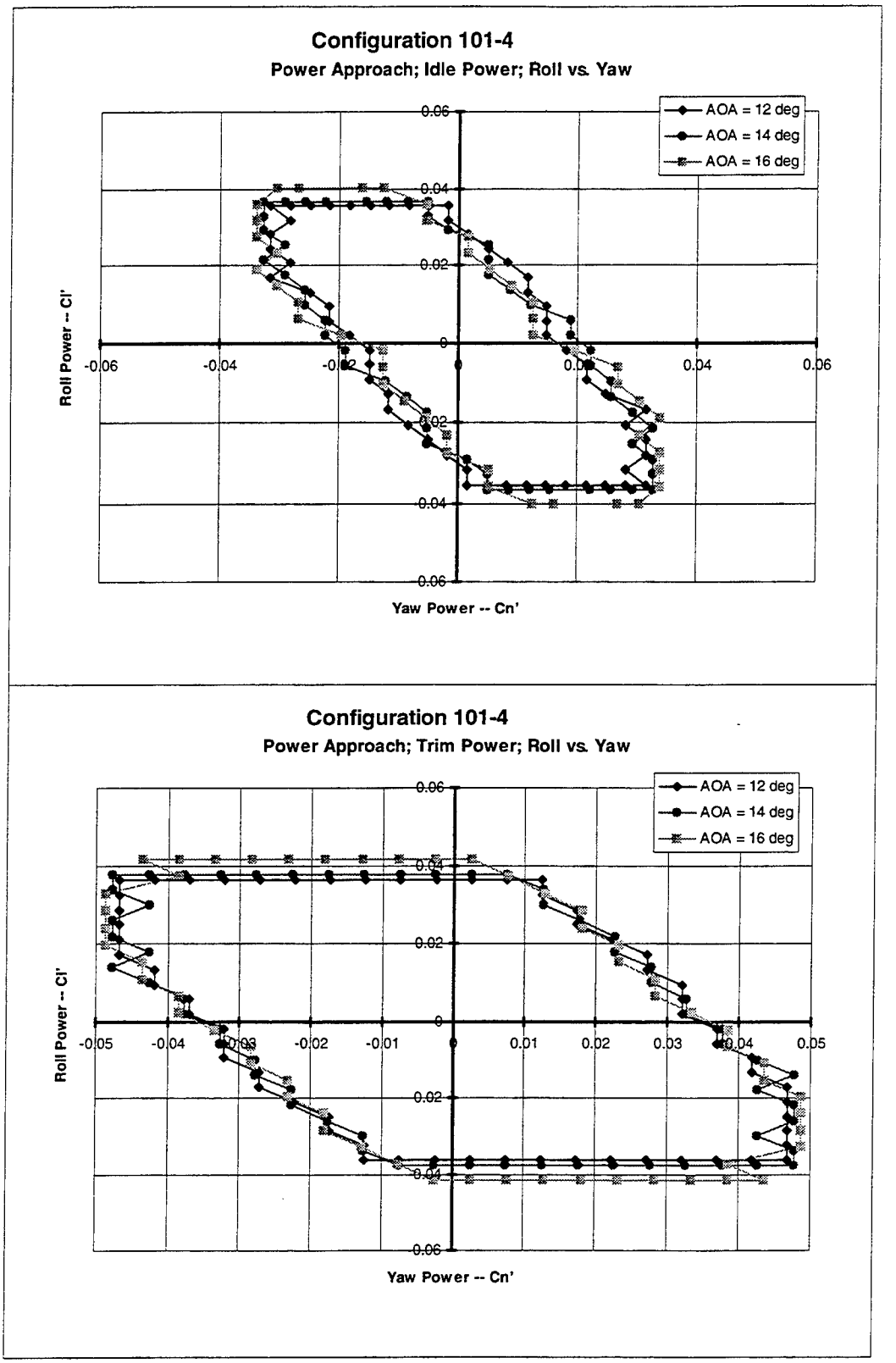

Figure 6-15: Configuration 101-4 Power Approach Control Power Available

6.2.3 Flying Qualities Analysis

This section discusses the following lateral-directional flying qualities parameters for both of the land-based configurations: 1) the maximum level of roll power that can be coordinated by the yaw control surfaces, 2) improvements in directional stability afforded by using the lateral-directional controls for augmentation, and 3) high-AOA roll performance results obtained by using the CPR 6-DOF simulation tool. As discussed previously, the 3-dimensional control power envelopes were used as input to CPR, and the control power values used to compute the responses were obtained from within these boundaries. Most of this analysis was performed for the 150 KCAS/15K flight condition. These data were obtained for a throttle setting of max A/B with the thrust vectoring both on and off. The thrust-vectoring-off case therefore described the capabilities that could be provided by using the aerodynamic controls only. Analysis was also performed for the 194 KEAS/15K flight condition at max A/B so that the FWV roll agility metric could be calculated.

Maximum Coordinated Roll Power

Figure 6-16 shows the maximum coordinated roll power ($C'_{l_{MAX}}$) values for both the 101-1 and 101-4 configurations. As indicated in the previous section, these data were obtained by noting the intersection of the C_l' axis with a control power envelope section cut at the C_m = 0 station. When only aerodynamic controls are used, Configuration 101-4 has considerably greater coordinated roll capability for AOAs below 45°. This result occurred because the AMTs produce higher coordinating yawing-moment increments at most of the AOAs investigated than those generated by the SSDs. These higher coordinating yawing moments enable more of the available roll power to be used. When both MATV and aerodynamic controls are applied, the two configurations have similar coordinated roll capabilities for AOAs below 40°. The combination of thrust vectoring and aerodynamic control provides ample coordinating yaw power so that most all the available roll power may be taken advantage of, and the resulting values of coordinated roll power are therefore much greater than the values obtained using aerodynamic controls only. At AOAs above 40°, 101-1 has higher rolling capability than 101-4 when thrust vectoring is included. At these higher AOAs, combinations of elevon and SSD deflections give Configuration 101-1 a greater amount of body-axis roll authority than Configuration 101-4. Despite the fact that the SSDs are not very effective in yaw at these higher AOAs (Figure 6-8), this higher available roll control power can be fully utilized in the presence of the coordinating yaw control afforded by MATV.

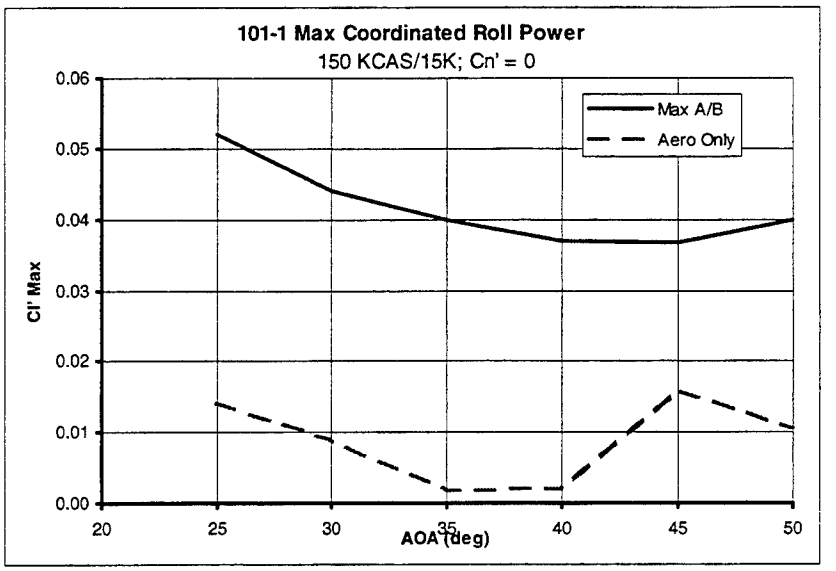

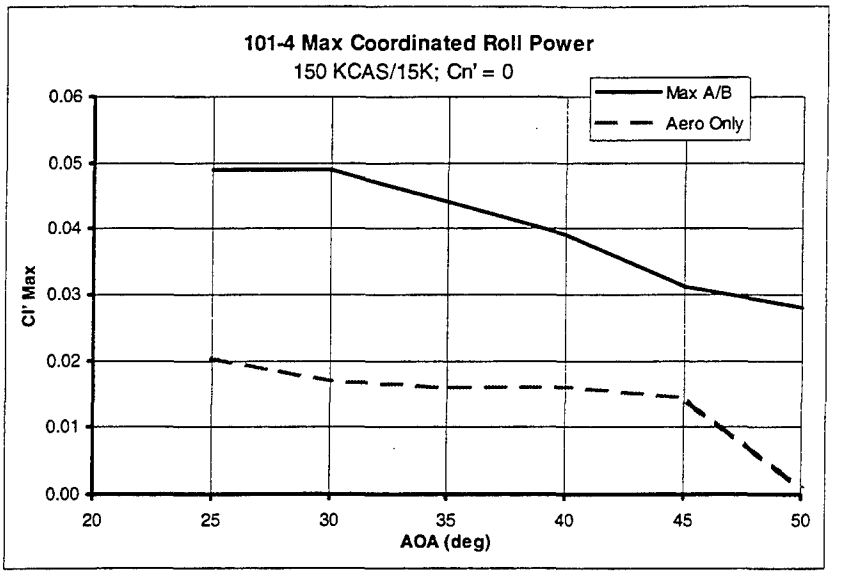

Figure 6-16: Maximum Coordinated Roll Power for Configurations 101-1 and 101-4 at 150 KCAS/15K

Lateral-Directional Stability Augmentation

The lateral-directional departure characteristics were computed using the familiar parameter $C_{n_{\beta DYN}}$, which was augmented out to the maximum sideslip angles for which data was available on a given configuration [Pelikan, 1983; Johnston & Heffley, 1981]. This quantity was computed by using equations 6-3. It should be noted that these computations include the effects of sideslip on the control power generated by the lateral-directional controls.

$$
\begin{aligned}
C_{n_{\beta_{AUG}}} &= \left(C_{n_\beta} + \frac{\Delta C_n(\beta)}{\beta_{MAX}} \right)_{StabilityAxis} \\
C_{l_{\beta_{AUG}}} &= \left(C_{l_\beta} + \frac{\Delta C_l(\beta)}{\beta_{MAX}} \right)_{StabilityAxis} \\
C'_{n_{\beta_{AUG}}} &= \left. \frac{C_{n_{\beta_{AUG}}} + \frac{I_{xz}}{I_{xx}} C_{l_{\beta_{AUG}}}}{1 - \frac{I_{xz}^2}{I_{xx} I_{zz}}} \right|_{StabilityAxis} \\
C'_{n_{\beta_{DYN}}}\ Augmented &= C'_{n_{\beta_{AUG}}} \frac{I_{zz_{Body}}}{I_{zz_{Stability}}}
\end{aligned}
\qquad (6\text{-}3)
$$

Figure 6-17 shows the augmented lateral-directional stability characteristics of Configuration 101-1 computed for various maximum sideslip angles. The curves without symbols represent the bare airframe characteristics. The figure shows that the bare airframe becomes completely stable at the larger sideslip angles throughout the AOA range investigated. As a result, the instabilities that occurred at a maximum sideslip angle of 10° make this condition the most critical case. Using the aerodynamic controls for augmentation made Configuration 101-1 stable for AOAs up to 30°, but instabilities still existed for AOAs between 30° and 40°. When adding the extra control power of thrust vectoring, Configuration 101-1 possessed stable values of $C_{n_{\beta DYN}}$ at all the AOAs and sideslip angles tested, and its maneuvering potential

is therefore not limited by departure concerns at these flight conditions when thrust vectoring is available for stability augmentation.

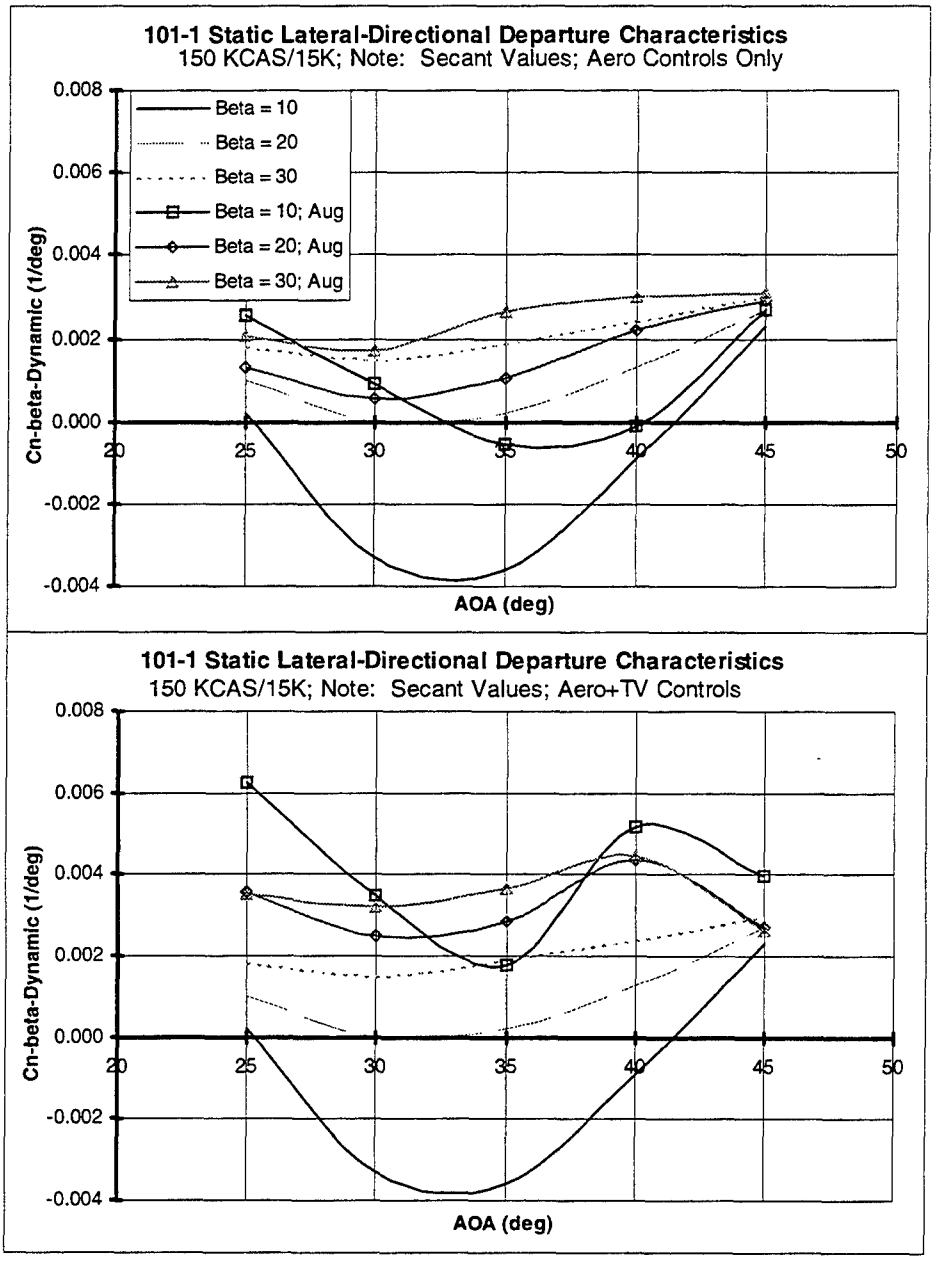

Figure 6-17: Configuration 101-1 High-AOA Lateral-Directional Departure Characteristics at 150 KCAS/15K

The corresponding values for Configuration 101-4 are shown in Figure 6-18. The control power generated by the AMTs was able to completely stabilize this configuration without the need for extra augmentation from thrust vectoring, which is a remarkable feat for a tailless fighter to accomplish.

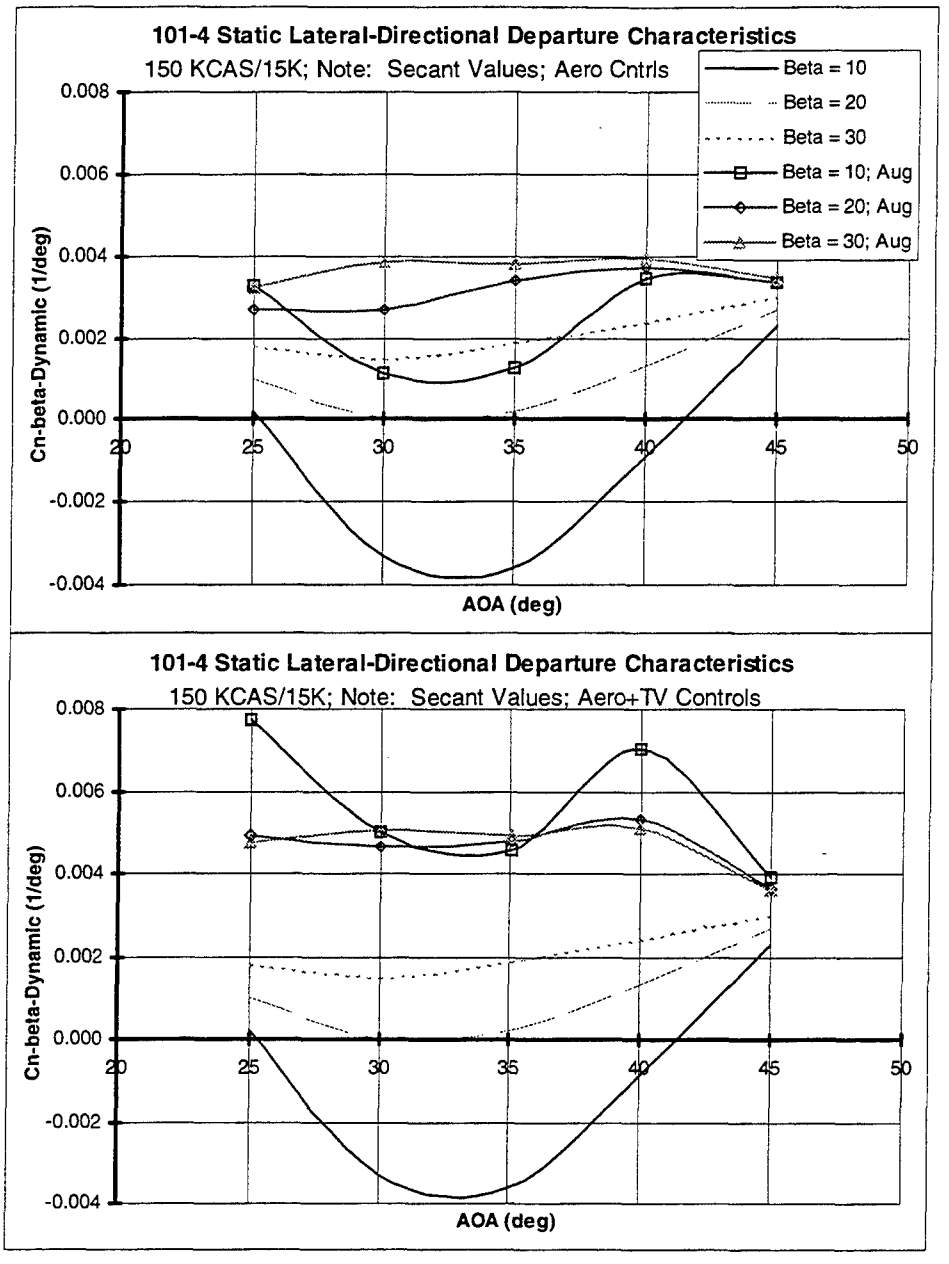

Figure 6-18: Configuration 101-4 High-AOA Lateral-Directional Departure Characteristics at 150 KCAS/15K

Roll Performance and Roll Agility Metric

The roll performance of both configurations was estimated by inputting the CPA control power envelopes into the 6-DOF CPR simulation tool and computing the time required to achieve specified changes in wind-axis bank angle. Sample time histories of the response to a full lateral stick step input at the 194 KEAS/15K flight condition are shown in Figure 6-19. The data shown are for Configuration 101-1 starting at initial AOAs of either 25° or 35°. Figure 6-20 contains a compilation of all the times-to-bank computed at 194 KEAS/15K. Also shown in this figure is the roll agility metric (RAM), which was computed using Equation 6-1. For comparison purposes, additional data are shown for both the baseline F-16 and the F-16 MATV. Both of the ICE configurations have lower times-to-bank and therefore superior roll agility when compared to the baseline F-16. They also demonstrate better performance than even the highly agile

F-16 MATV airplane. It should be noted at this point that both F-16 simulations are much higher fidelity than those used to compute the ICE configuration values, and they represent actual existing aircraft instead of a conceptual research design. If subsequent development work is performed to bring the ICE configurations closer to a production vehicle, additional real-world considerations and any associated restrictions on maneuvering performance or control system design may result in the ICE configuration values becoming closer to the F-16 results.

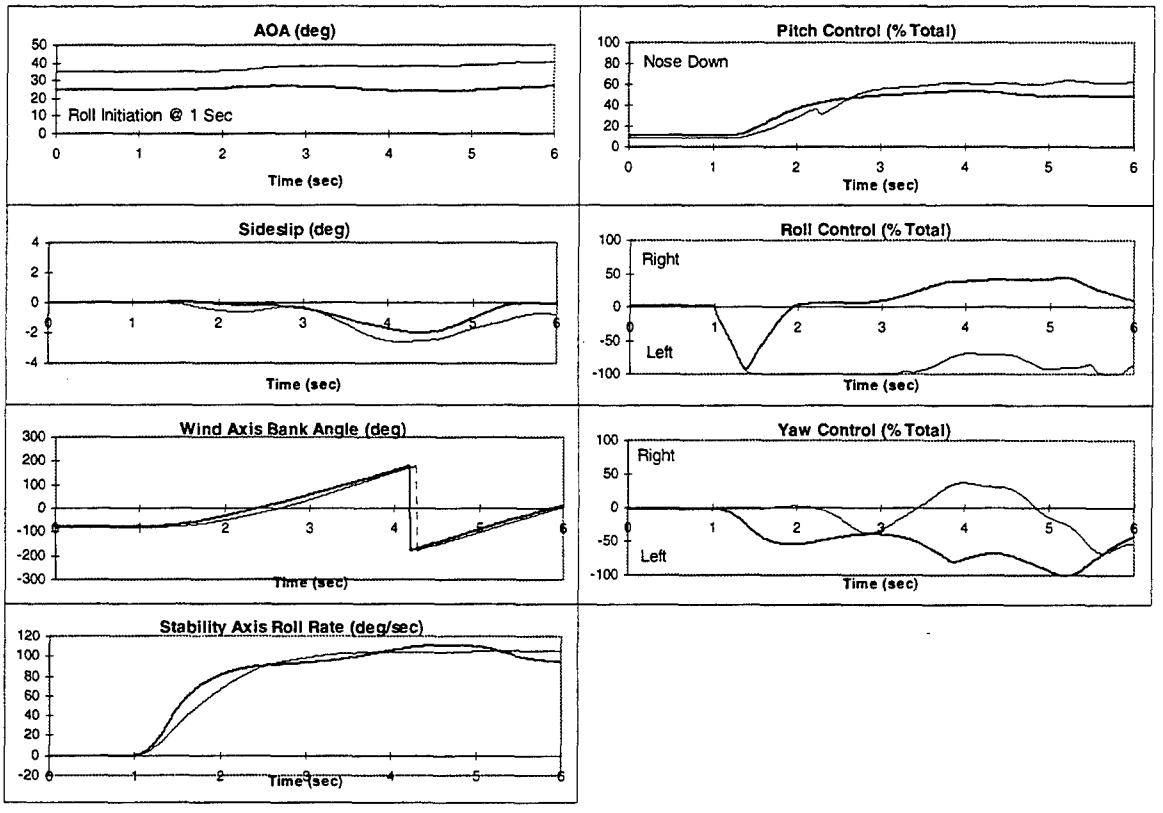

Figure 6-19: Time History of Configuration 101-1 Roll Performance at 194 KEAS/15K for Two Initial AOAs

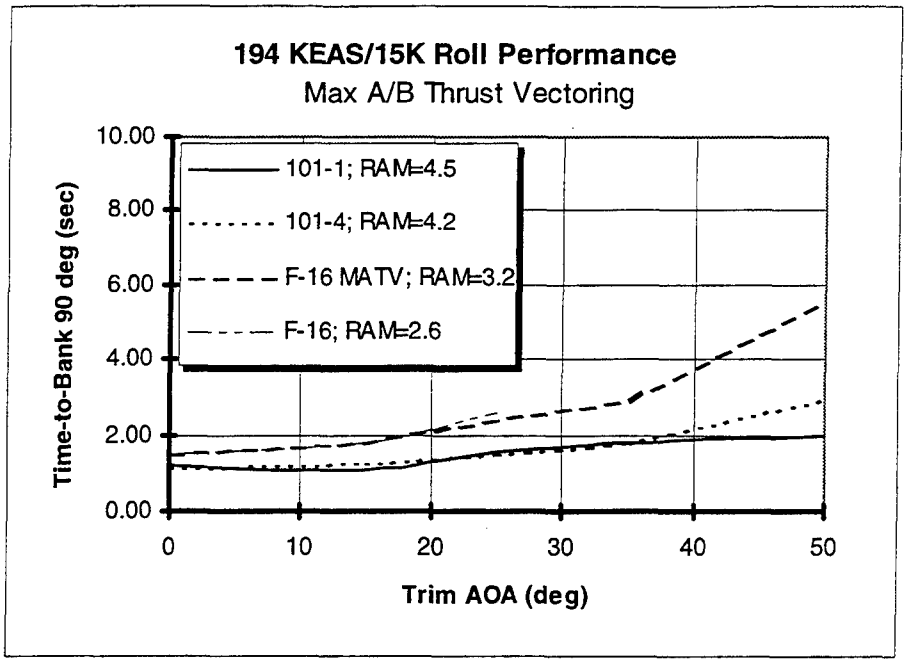

Figure 6-20: Configuration 101 Time-To-Bank 90° at 194 KEAS/15K and FWV Roll Agility Metric

Table 6-1 summarizes Configuration 101-series roll performance. Conditions that did not achieve the roll performance goals are highlighted.

Table 6-1: Configuration 101-Series Roll Performance Summary

Configuration	Flight Condition	Power Setting	Time-to-Bank $\Delta\phi$ ($\Delta\phi$ /sec)	Time-to-Bank $\Delta\phi$ Goal ($\Delta\phi$ /sec)
101-1	Power Approach/α=14 141 KCAS	Idle	30/1.1	30/1.1
"	"	Trim	30/0.9	"
"	**300 KCAS/α=20**	**Mil Power**	**90/1.3**	**90/1.1**
"	"	**Max A/B**	**90/1.2**	"
"	**108 KCAS/α=30**	"	**90/2.3**	**90/2.0**
"	108 KCAS/α=45	"	90/2.9	90/4.0
101-4	**Power Approach/α=14** 141 KCAS	**Idle**	**30/1.2**	**30/1.1**
"	"	Trim	30/1.0	"
"	300 KCAS/α=20	Mil Power	90/1.0	90/1.1
"	300 KCAS/α=20	Max A/B	90/0.9	"
"	**108 KCAS/α=30**	"	**90/2.5**	**90/2.0**
"	108 KCAS/α=45	"	90/3.2	90/4.0

Comparisons With Phase 1 Results

For conditions where Phase 1 data were available, each of the flying qualities parameters computed during this study was compared to its corresponding Phase 1 prediction. Figure 6-21 compares the maximum coordinated roll power and augmented lateral-directional stability values for Configuration 101-1 at the 150 KCAS/15K flight condition. These results are shown for aerodynamic controls. The Phase 2 results are more favorable across the board. Configuration 101-1 exhibits greater coordinated roll capability and higher augmented directional stability than were predicted. These results were a direct consequence of the more favorable SSD performance than was originally expected (Figure 6-8). As discussed previously, the SSDs generated considerably more roll control power throughout the AOA range tested than was originally forecast, and they produced greater yaw power for AOAs below 22.5°. In addition, the effects on pitching-moment of deflecting the SSDs were over-predicted during Phase 1. As a result, greater elevon roll authority could be used because they were not needed to trim the nose-up moments generated by SSD deflections. All these effects combined to yield the observed improvements in performance over the Phase 1 predictions.

Figure 6-22 compares the corresponding results for Configuration 101-4. Unlike Configuration 101-1, the 101-4 Phase 2 coordinated roll power and augmented stability values compared well with the Phase 1 predictions because the effectiveness of the AMTs (Figure 6-9) was more accurately predicted than the effectiveness of the SSDs (Figure 6-8). The Phase 2 coordinated roll power values were not as great above an AOA of 25° because the AMTs were less effective in yaw than originally predicted. At the lower AOAs,

the coordinated roll power was also somewhat over-predicted because the AMTs generated higher adverse rolling moments at these AOAs than were originally anticipated.

Phase 2 maximum coordinated roll power values and time-to-bank roll performance are compared in bar chart format to the Phase 1 predictions in Figure 6-23. Data are shown for the three critical flight conditions that were originally used to size the control surfaces. For both Configuration 101-1 and 101-4, the Phase 2 time-to-bank results agree well with the Phase 1 data for the power approach and 300 KCAS/20° AOA flight conditions, and both configurations achieved the associated roll performance requirements. For the 300 KCAS/20° AOA condition, Configuration 101-1 had significantly higher coordinated roll power than was originally predicted, but this increase in available roll power did not result in a notable increase in roll performance because inertial pitch coupling limited the amount of this additional roll power that could be utilized. At the 108 KCAS/30° AOA flight condition, the roll performance was significantly worse than that predicted during Phase 1, and the time-to-bank 90° requirement was not achieved by either configuration. These results were partially attributed to the lower than predicted coordinated roll power values. They were also influenced by a more nose-up bare airframe pitching-moment than that used to compute the Phase 1 results. Larger elevon deflections were required to trim out these moments, and therefore less elevon deflection was available for roll control.

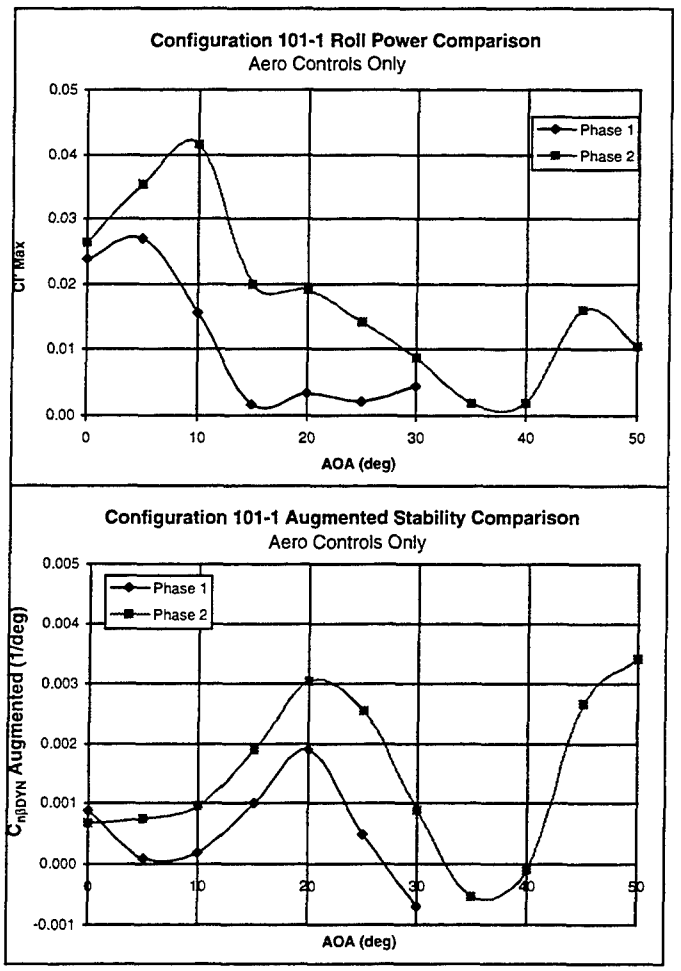

Figure 6-21: Comparison of Configuration 101-1 Lateral-Directional Flying Qualities With Phase 1 Results

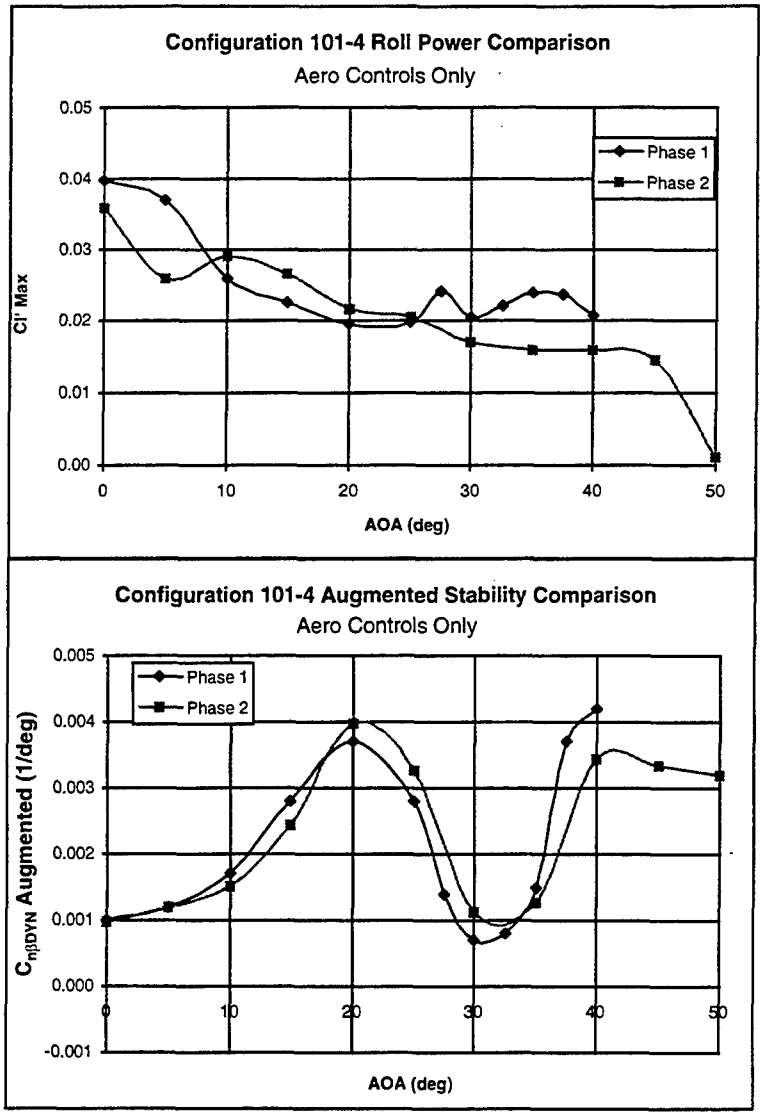

Figure 6-22: Comparison of Configuration 101-4 Lateral-Directional Flying Qualities With Phase 1 Results

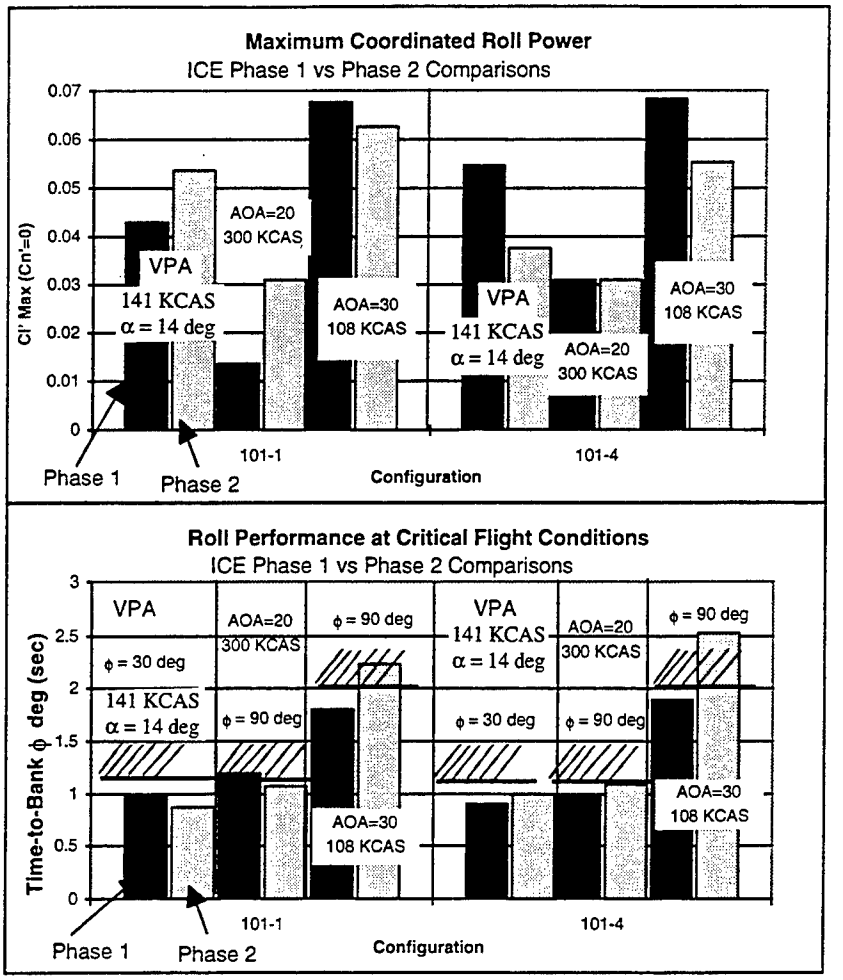

Figure 6-23: Comparison of Configuration 101 Roll Performance Predictions With Phase 1 Results

6.3 Carrier-Based: Configuration 201 Series

This section discusses the analysis of the two carrier-based configurations: 1) 201-1 which used the SSD as its primary yaw control surface and 2) 201-4 which used the AMT as its primary yaw control surface.

6.3.1 Basic Aerodynamic Effectiveness of Primary Yaw Control Surfaces

Figure 6-24 shows a comparison of the SSD effectiveness predicted during Phase 1 with the latest aerodynamic data obtained during the LAMP and the supplementary ADF wind-tunnel tests. The Phase 1 SSD effectiveness curves were based on data from the same ADF wind-tunnel test of a 1/60th scale high-sweep research model that was used for the Configuration 101-1 comparison. To better represent the 201-1 configuration, these data were scaled with the ratio of the Configuration 201-1 control volume to that of the ADF test configuration. Similar to the results obtained on 101-1 (Figure 6-8), the comparison reveals several differences between the measured and predicted data that are each beneficial. For AOAs below 20°, the SSDs produced considerably higher yaw-control effectiveness than was predicted, and these values were approximately twice as large as the predictions for the low AOAs below 10°. This variation was attributed to differences in the 201-1 and ADF test configurations. The primary difference was that the ICE Phase 2 SSDs were located farther outboard, and they therefore had a larger moment arm about the yaw axis, than did those on the ADF test configuration. The SSDs also generated slightly higher favorable rolling moments than were originally forecast for AOAs below 20°. Also similar to the land-based configuration

results, the effects of SSD deflection on pitching moment were over-predicted on the carrier-based configurations during Phase 1. Although these effects were fairly small, this result indicated that more of the total elevon deflection could be utilized for roll control instead of being required to trim out the nose-up pitching-moment increments resulting from SSD deflections.

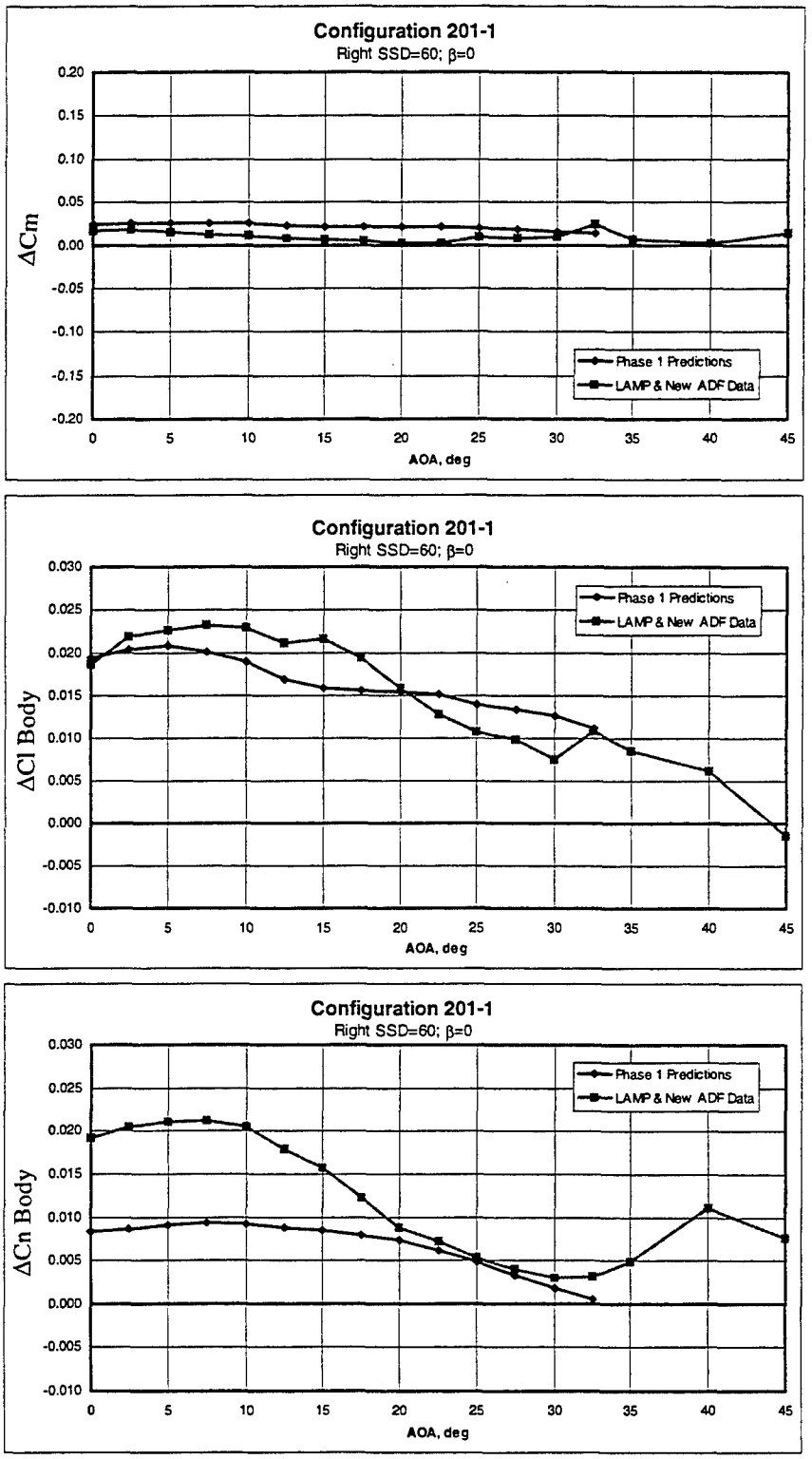

Figure 6-24: Comparison of SSD Effectiveness on Configuration 201-1 With Phase 1 Predictions

Figure 6-25 shows a similar comparison between the AMT effectiveness predicted during Phase 1 and the latest aerodynamic data obtained during the LAMP and the supplementary ADF wind-tunnel tests. As mentioned previously, the Phase 1 predictions were obtained from an earlier ADF test on the ICE 201 Configuration [Dorsett & Mehl, 1996, App. C]. Like the SSDs (Figures 6-8 and 6-24), the comparison of AMT effectiveness was also similar to that obtained for the land-based configurations (Figure 6-9). The predicted pitch and roll increments agreed better with the SARL and LAMP data than did the corresponding values for the SSDs (Figure 6-24), but slightly smaller favorable rolling moments were generated than were originally predicted. At the lower AOAs, the yaw-control increments agreed very well with the predictions, and the AMTs are slightly less effective than the SSDs. At AOAs above 15°, the yaw-control increments measured during the SARL and LAMP tests were significantly lower than the predictions. But despite this trend, the AMTs were considerably more effective than the SSDs at these higher AOAs. One possible reason for the differences in the Phase 2 data and the predictions was that a multiplier was applied to the original ADF data to account for increased control volume that was anticipated to be needed to meet the power approach requirements at an AOA of approximately 11°. This process accurately predicted the low-AOA AMT effectiveness. Additional testing of AMTs has shown that the variation in their effectiveness with changes in control volume generally decreases as AOA is increased. For this reason, using a constant multiplier for the whole AOA range most likely caused the AMT effectiveness values at the higher AOAs to be over-predicted.

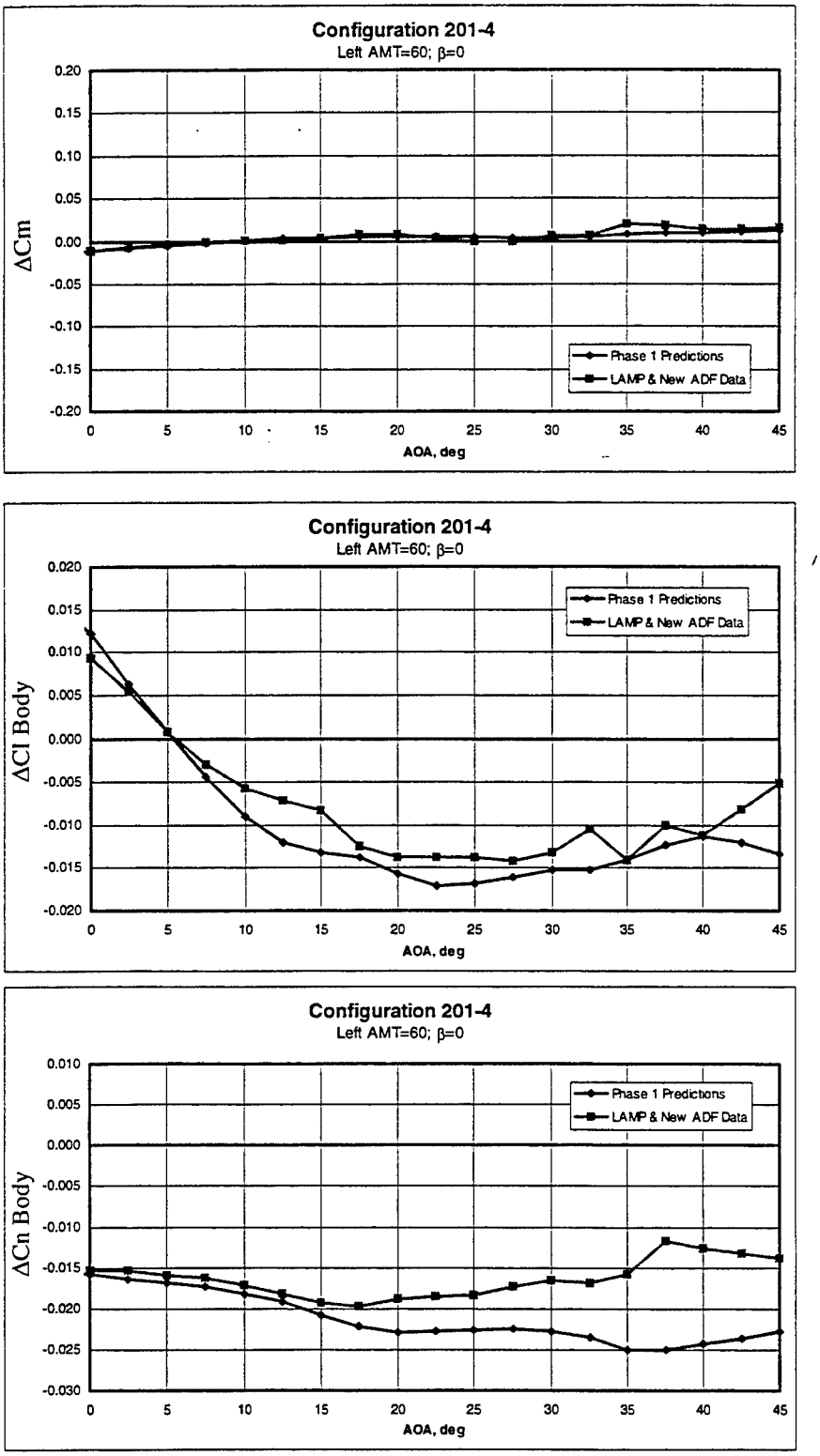

Figure 6-25: Comparison of AMT Effectiveness on Configuration 201-4 With Phase 1 Predictions

6.3.2 Control Power Envelopes

Using the CPA software, control power envelopes were computed in the same manner and at the same conditions as those that were used for analysis of the land-based configurations. The computed envelopes for the 300 KCAS/15K and 108 KCAS/15K flight conditions are shown in Figures 6-26 to 6-29. The envelopes computed for the power approach condition will be presented and discussed in a following section on carrier suitability.

The control power envelopes for Configurations 201-1 and 201-4 at the 300 KCAS flight condition are shown in Figures 6-26 and 6-27, respectively. As seen for the land-based configurations (Figures 6-10 and 6-11), increasing the throttle setting from mil power to max A/B resulted in only small increases in control power on both the carrier-based configurations. As outlined previously, this result occurred because the control moments available from MATV are not large when compared to the aerodynamic forces acting on the aircraft at this higher speed and consequently higher dynamic pressure. When in max A/B, each configuration generated similar levels of coordinated roll power for a given AOA. When in mil power, Configuration 201-4 generally produced slightly higher values. At most of the AOAs, both configurations were capable of producing larger amounts of roll control power than could be coordinated, even when using thrust vectoring at a max A/B throttle setting. The 201-1 envelope becomes more adverse (rotated counter-clockwise) than the 101-4 envelope as AOA is increased, and the 201-4 envelope is generally larger than that of the 201-1 configuration. These results were attributed primarily to the greater yaw-control effectiveness of the AMTs (Figure 6-25) over that of the SSDs (Figure 6-24) at the investigated AOAs.

The control power envelopes for the 108 KCAS flight condition are shown in figures 6-28 and 6-29 for Configurations 201-1 and 201-4, respectively. The figures show that, like the land-based configurations (Figures 6-12 and 6-13), both carrier-based configurations have significant lateral-directional maneuvering potential at these relatively high AOAs with 201-4 having slightly higher values than 201-1. The figures also show an effect that was not seen on the land-based configurations. At AOAs of 40° and 45°, the envelopes are much less symmetric about the origin than the envelopes for the other AOAs. This effect was attributed to differences in aerodynamic asymmetries that occurred as the canard deflection was varied. The data in these control envelopes represent increments away from a neutral controls setting of all the surfaces undeflected. Because symmetric deflection of the canards was one of the control surface variations that was used to compute the control envelopes, any changes in aerodynamic asymmetry resulting from canard deflection were included in the control envelopes. Variation in these asymmetries effectively changes the condition about which the increments from the other surfaces are applied, which results in a shift of the control envelope away from the origin.

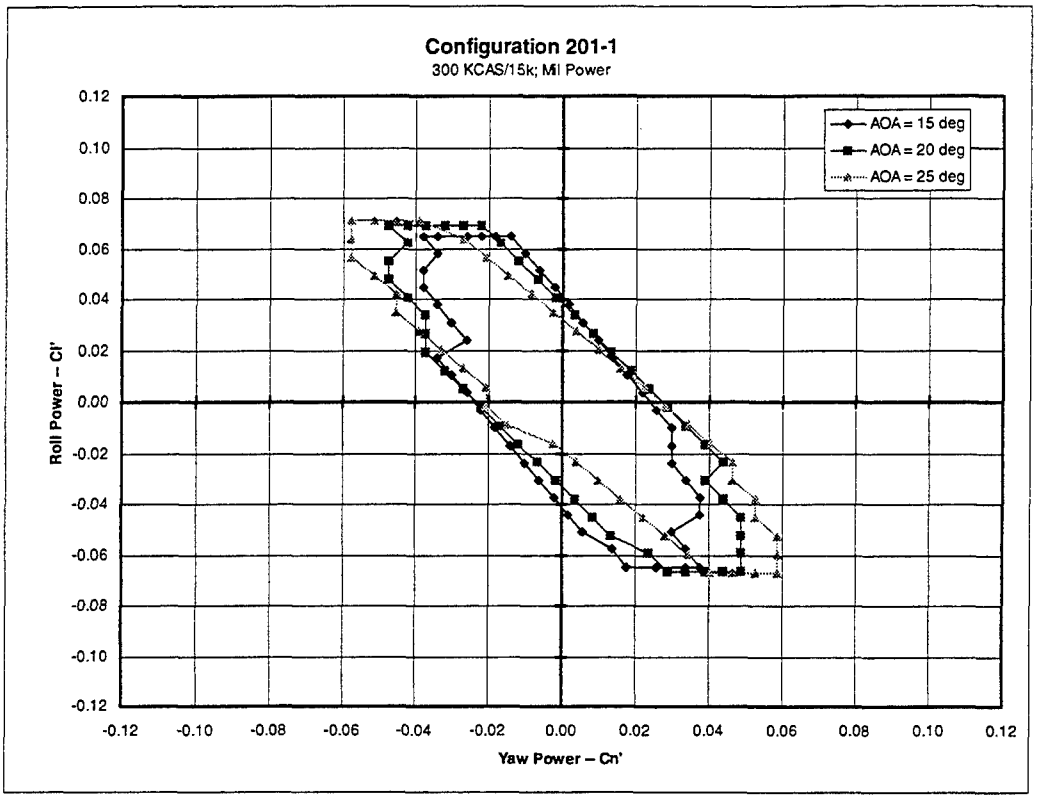

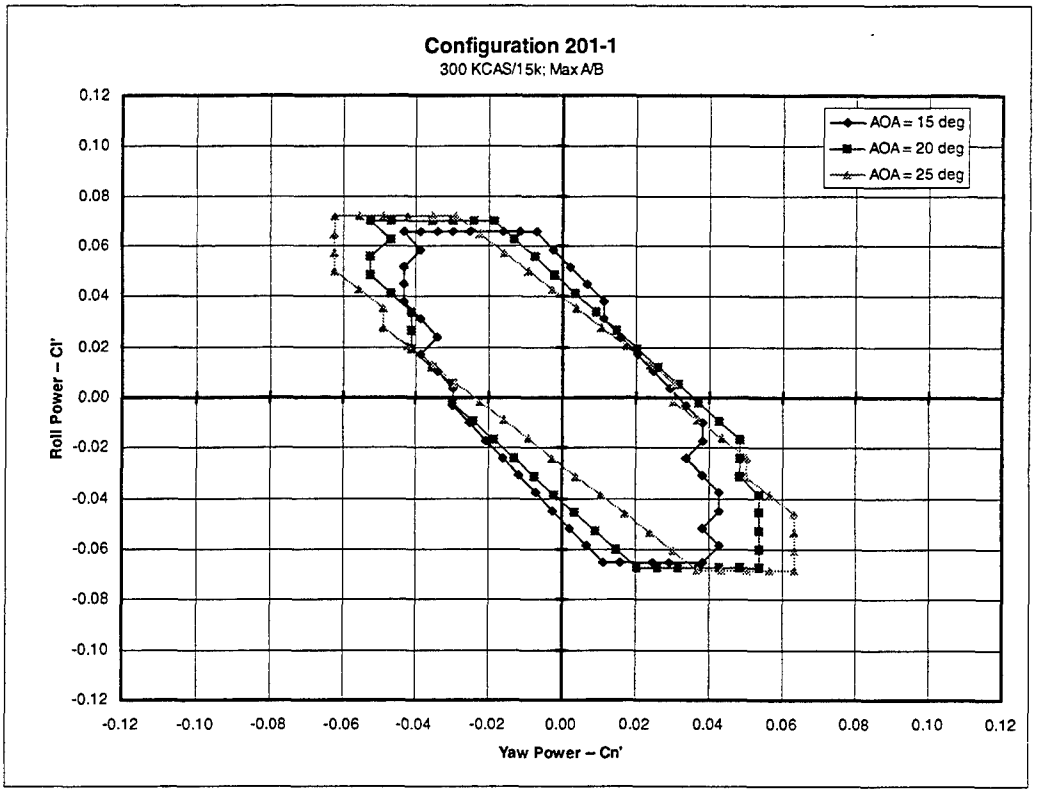

Figure 6-26: Configuration 201-1 Control Power Available at 300 KCAS/15K for Mil Power and Max A/B

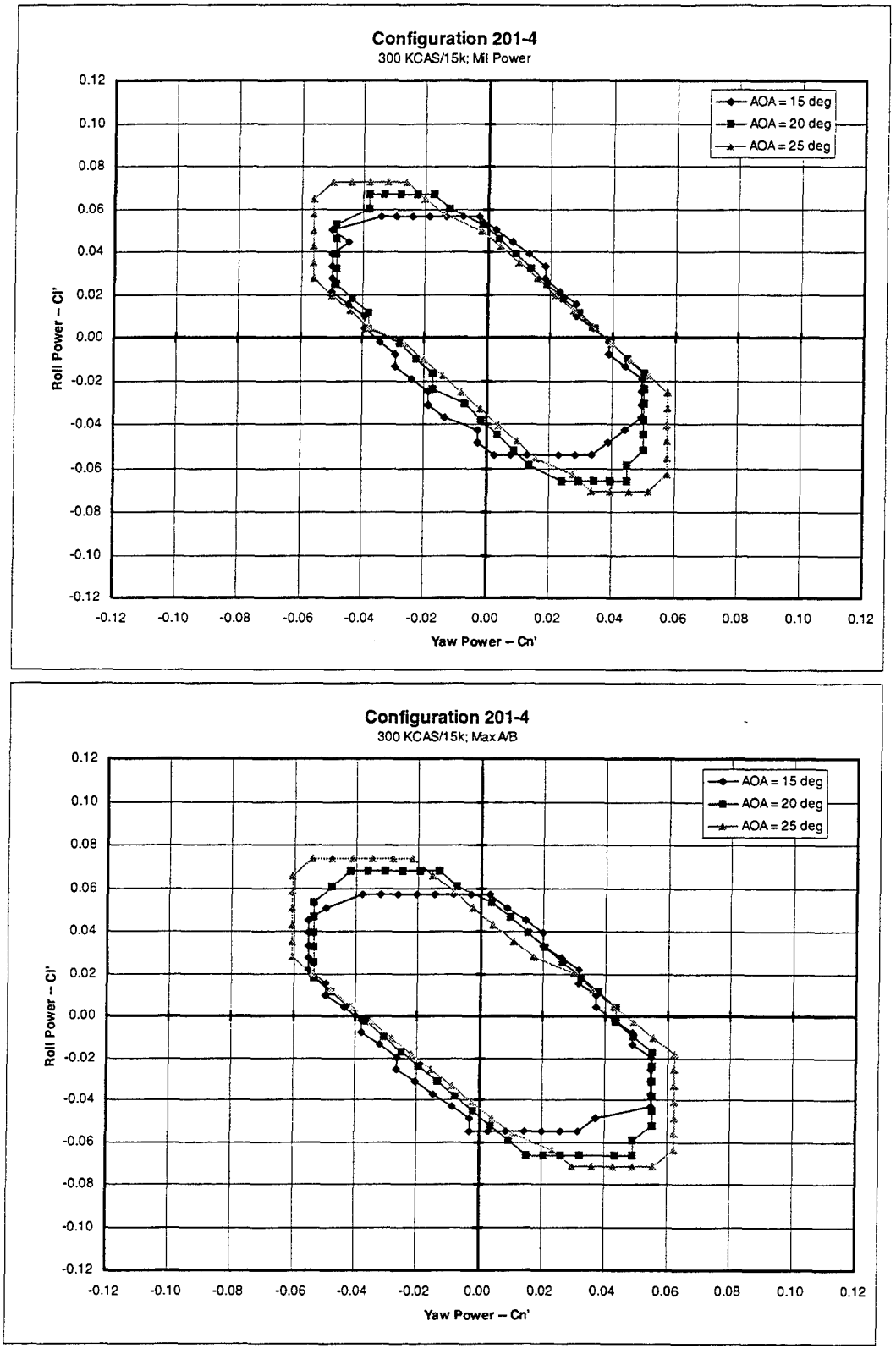

Figure 6-27: Configuration 201-4 Control Power Available at 300 KCAS/15K for Mil Power and Max A/B

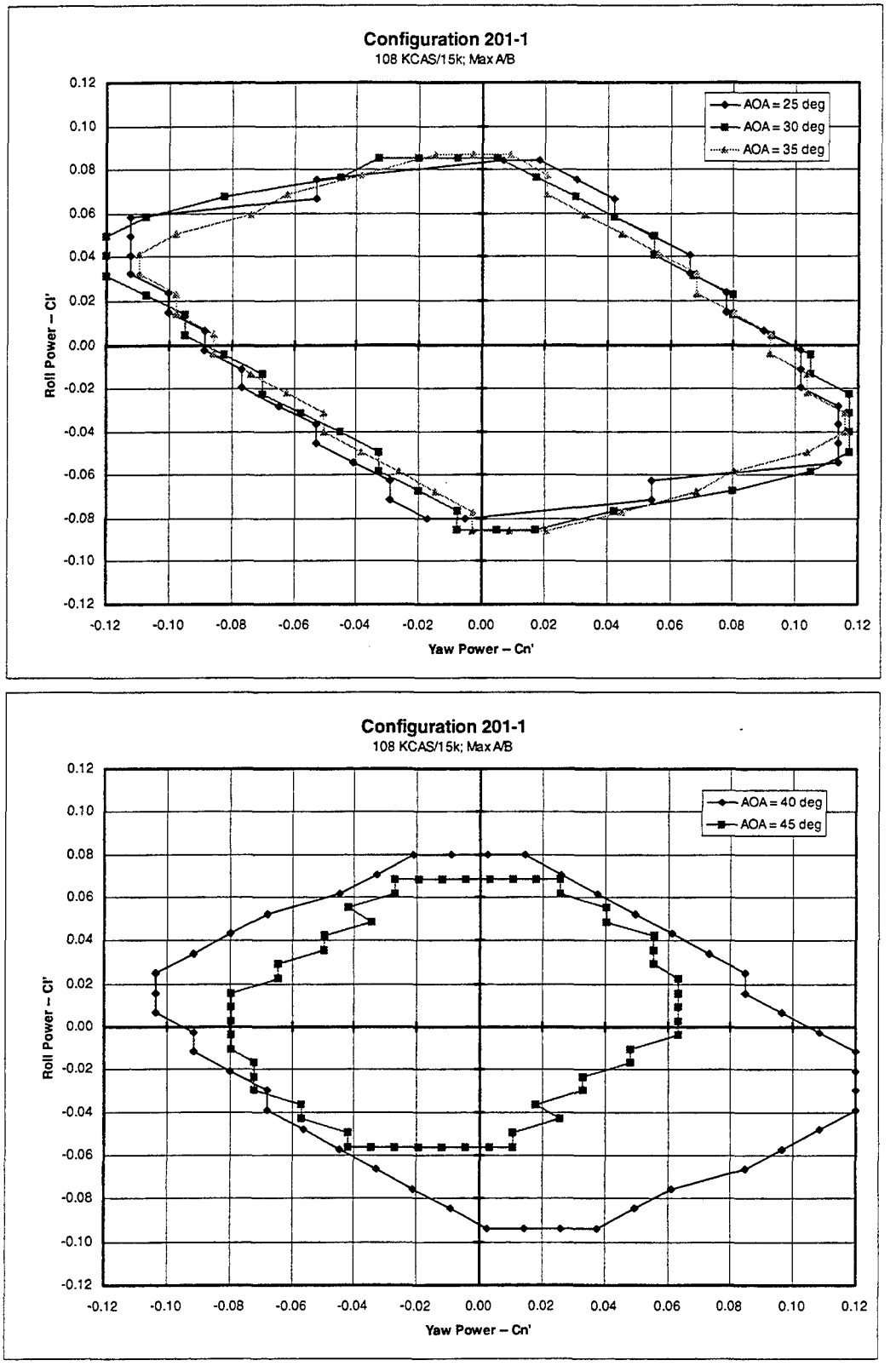

Figure 6-28: Configuration 201-1 Control Power Available at 108 KCAS/15K With Max A/B

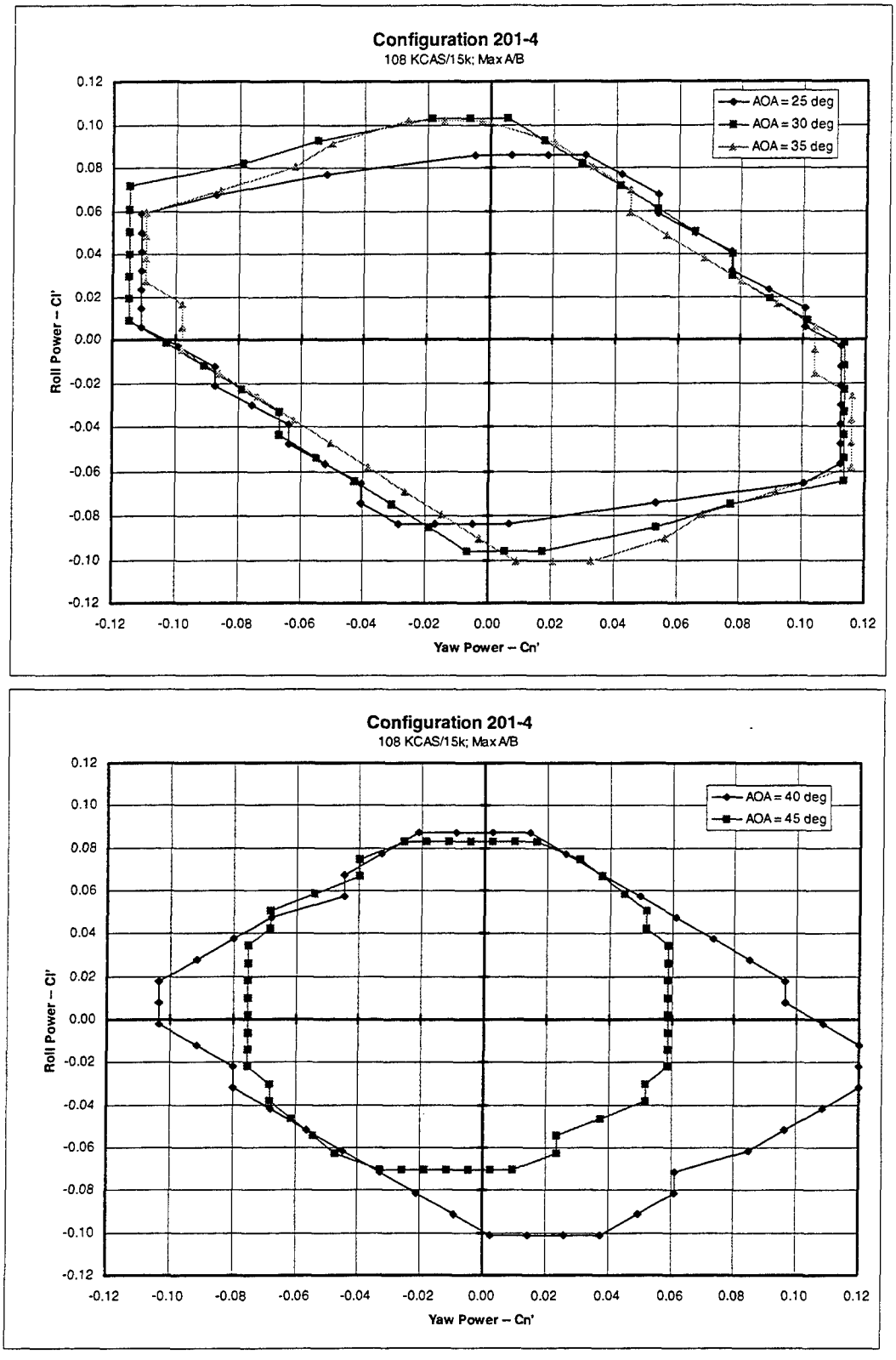

Figure 6-29: Configuration 201-4 Control Power Available at 108 KCAS/15K With Max A/B

6.3.3 Flying Qualities Analysis

This section discusses the following lateral-directional flying qualities parameters for both of the carrier-based configurations: 1) the maximum level of roll power that can be coordinated by the yaw control surfaces, 2) improvements in directional stability afforded by using the lateral-directional controls for augmentation, and 3) power approach and high-AOA roll performance results obtained by using the CPR 6-DOF simulation tool. These parameters were computed in the same fashion and at the same conditions as for the land-based configurations.

Maximum Coordinated Roll Power

Figure 6-30 shows the maximum coordinated roll power ($C'_{l_{MAX}}$) values for both the 201-1 and 201-4 configurations at the 150 KCAS/15K flight condition. When using aerodynamic controls only, Configuration 201-4 has higher coordinated roll capability than Configuration 201-1 throughout the AOA range investigated. This result was attributed primarily to the fact that the AMTs generate higher coordinating yawing moments than the SSDs throughout this AOA range, which enable Configuration 201-4 to utilize more of the available roll control power. When both MATV and aerodynamic controls are applied, the additional coordinating yaw power available from thrust vectoring enables both configurations to take advantage of more of the available roll power, and the resulting values of coordinated roll power are therefore much greater than the values obtained when using aerodynamic controls only. Similar to the aerodynamic controls only case, Configuration 201-4 has more coordinated roll power than 201-1 when thrust vectoring is included for most of the AOAs investigated.

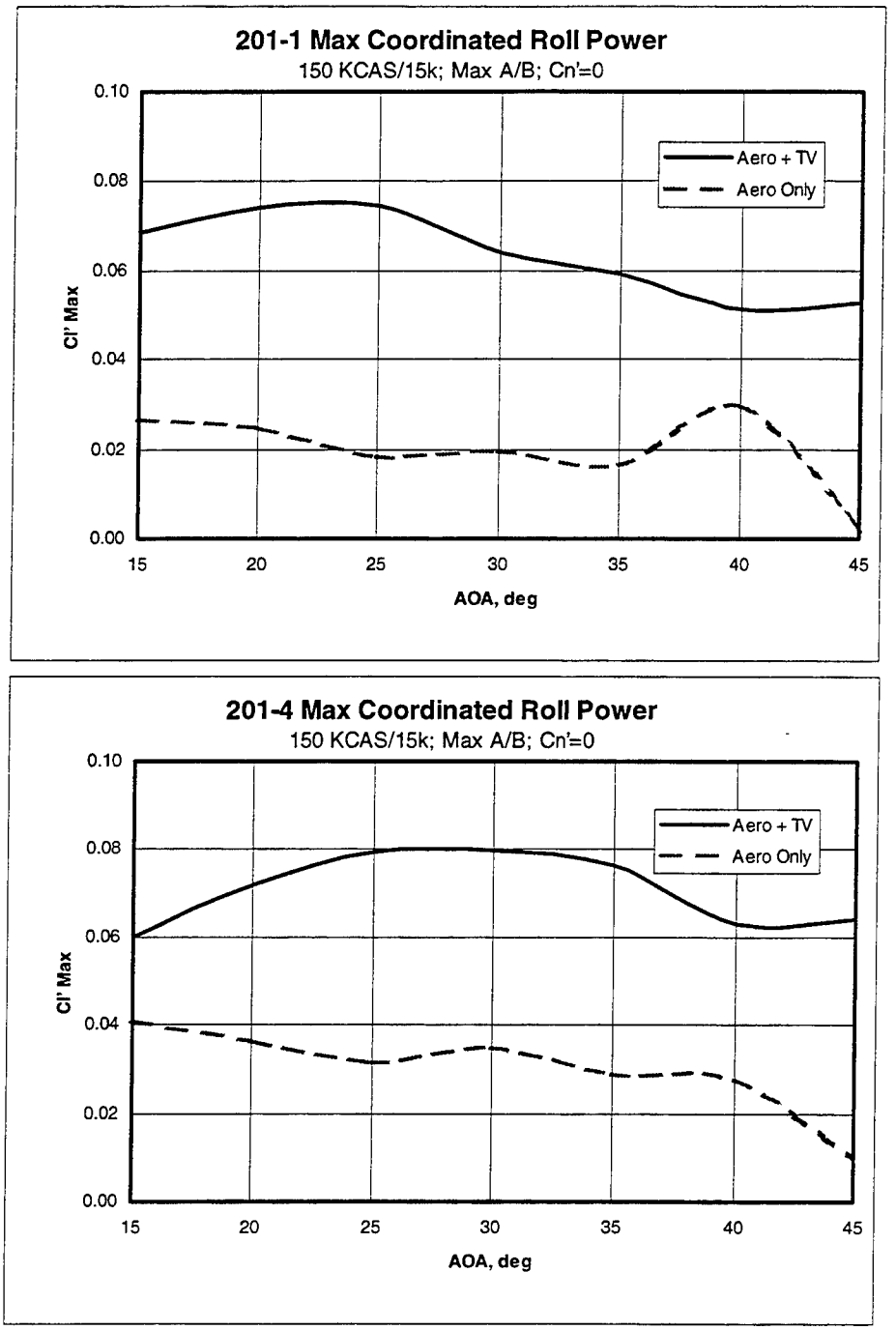

Figure 6-30: Maximum Coordinated Roll Power for Configurations 201-1 and 201-4 at 150 KCAS/15K

Lateral-Directional Stability Augmentation

The lateral-directional departure characteristics were computed using the familiar parameter $C_{n_{\beta DYN}}$, which was augmented out to a maximum sideslip angle of 10°. Figure 6-31 shows the augmented lateral-

directional stability characteristics of Configuration 201-1 at the 150 KCAS/15K flight condition. The figure shows that the bare airframe possesses reasonably good characteristics on its own in that it is stable at all the AOAs investigated except 30° and 45°. Using aerodynamic controls only for augmentation stabilized the configuration at an AOA of 30°, but it was unable to affect the 45° AOA point because lower control power was available at this relatively high AOA. Applying the aerodynamic controls for augmentation caused a reduction in $C_{n_{\beta DYN}}$ from the bare airframe values at an AOA of 35°. As discussed previously in the control envelope section, this result appeared to be caused by the effects of changes in the aerodynamic asymmetries resulting from canard deflections. The introduction of asymmetries tended to skew the control envelope away from the origin, which meant that more control power was available in one direction than the other. This destabilization may also have been partially caused by an adverse effect of sideslip on the effectiveness of the lateral-directional control surfaces. When adding the extra control power of thrust vectoring, Configuration 201-1 possessed stable values of $C_{n_{\beta DYN}}$ at all the AOAs investigated, and its maneuvering potential would therefore not be limited by departure concerns at these flight conditions when thrust vectoring is available for stability augmentation.

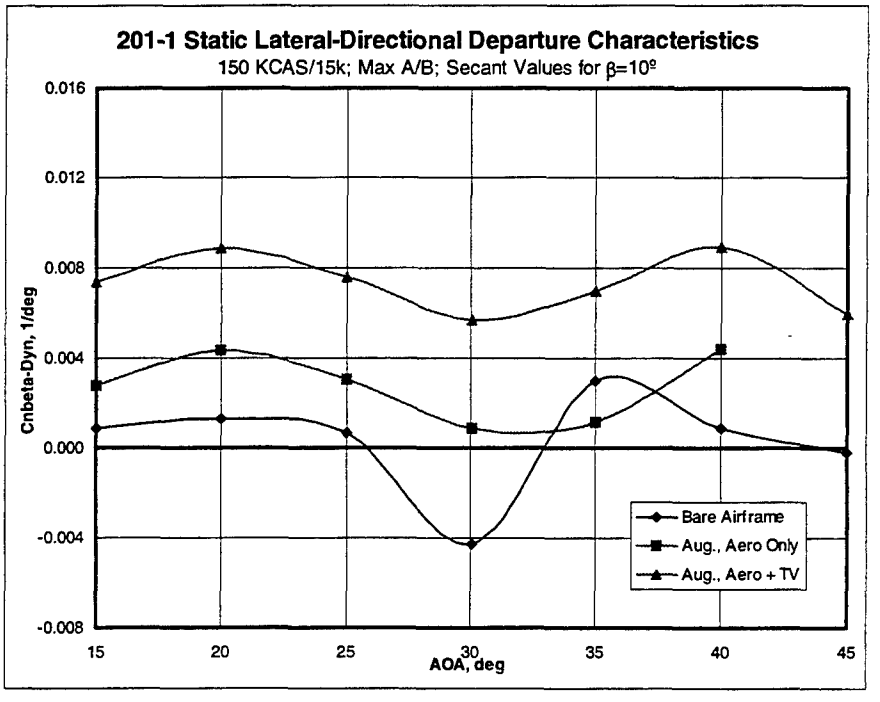

Figure 6-31: Configuration 201-1 High-AOA Lateral-Directional Departure Characteristics at 150 KCAS/15K

The corresponding values for Configuration 201-4 are shown in Figure 6-32. Similar to the results for the land-based configuration (Figure 6-18), the control power generated by the AMTs was able to completely stabilize the carrier-based configuration without needing the extra augmentation afforded by thrust vectoring. As stated in the land-based configuration section, this outcome is a remarkable achievement for a tailless fighter design to accomplish.

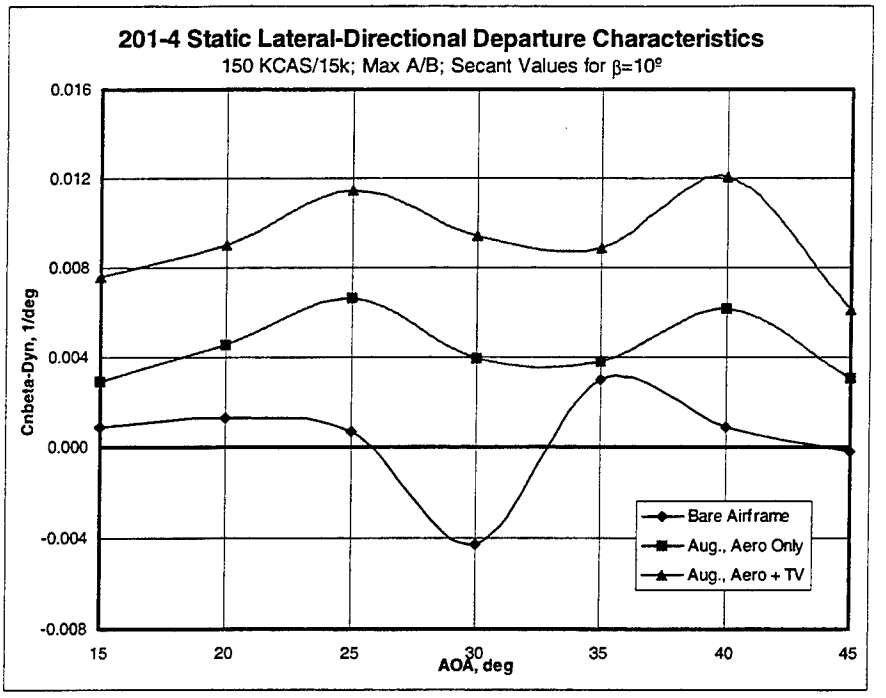

Figure 6-32: Configuration 201-4 High-AOA Lateral-Directional Departure Characteristics at 150 KCAS/15K

Up & Away Roll Performance and Roll Agility Metric

The roll performance of both configurations was estimated by inputting the CPA control power envelopes into the 6-DOF CPR simulation tool and computing the time required to achieve 90° of wind-axis bank angle change. Sample time histories of the response to a full lateral stick step input at the 194 KEAS/15K flight condition and an initial AOA of 30° are shown in Figure 6-33 for both Configuration 201-1 and 201-4. Figure 6-34 contains a compilation of all the times-to-bank computed at 194 KEAS/15K. Also shown in this figure is the roll agility metric (RAM), which was computed using Equation 6-1. For comparison purposes, data are shown for both the baseline F-16 and the F-16 MATV. Similar to the land-based configurations (Figure 6-20), both of the carrier-based configurations have lower times-to-bank and therefore superior roll agility when compared to the baseline F-16, and they also demonstrate better performance than even the highly agile F-16 MATV airplane. As alluded to previously, both of the F-16 simulations are much higher fidelity than those used to compute the ICE configuration values, and they represent existing aircraft instead of a conceptual research design. If subsequent development work is performed to bring the ICE configurations closer to a production vehicle, additional real-world considerations and any associated restrictions on maneuvering performance or control system design may result in the ICE configuration values becoming closer to the F-16 results.

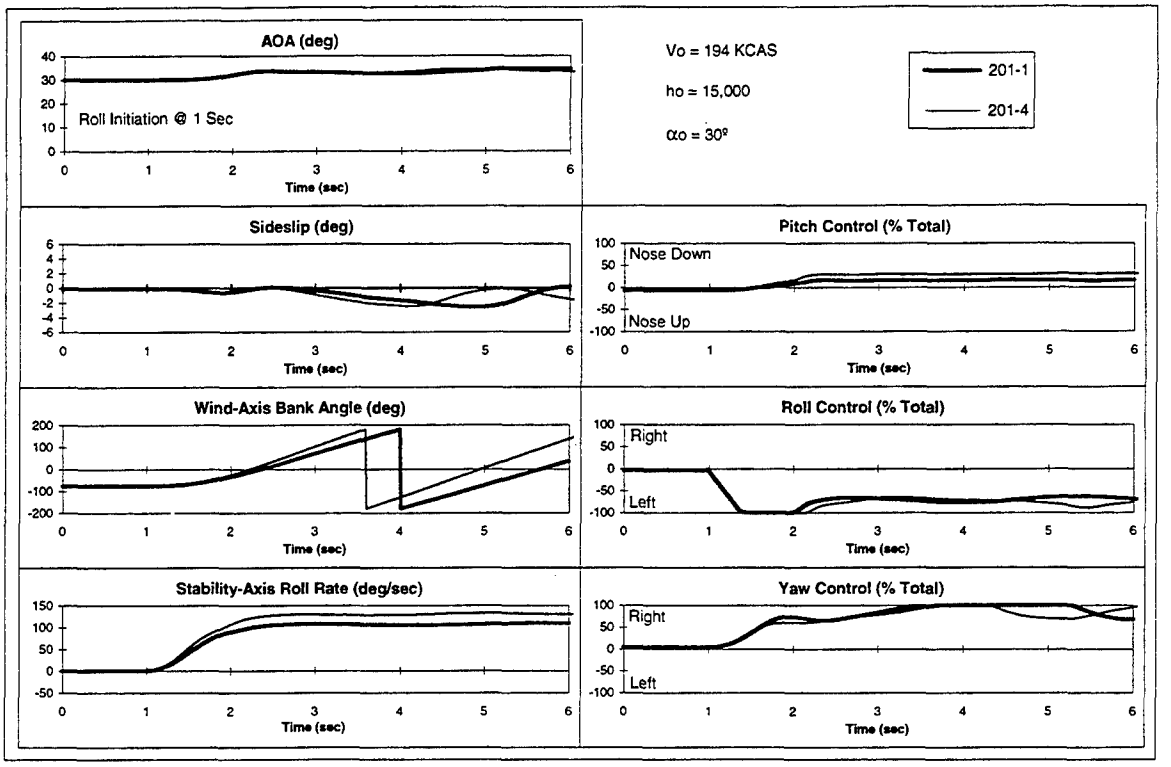

Figure 6-33: Comparison of Configurations 201-1 and 201-4 Roll Performance at 194 KCAS/15K

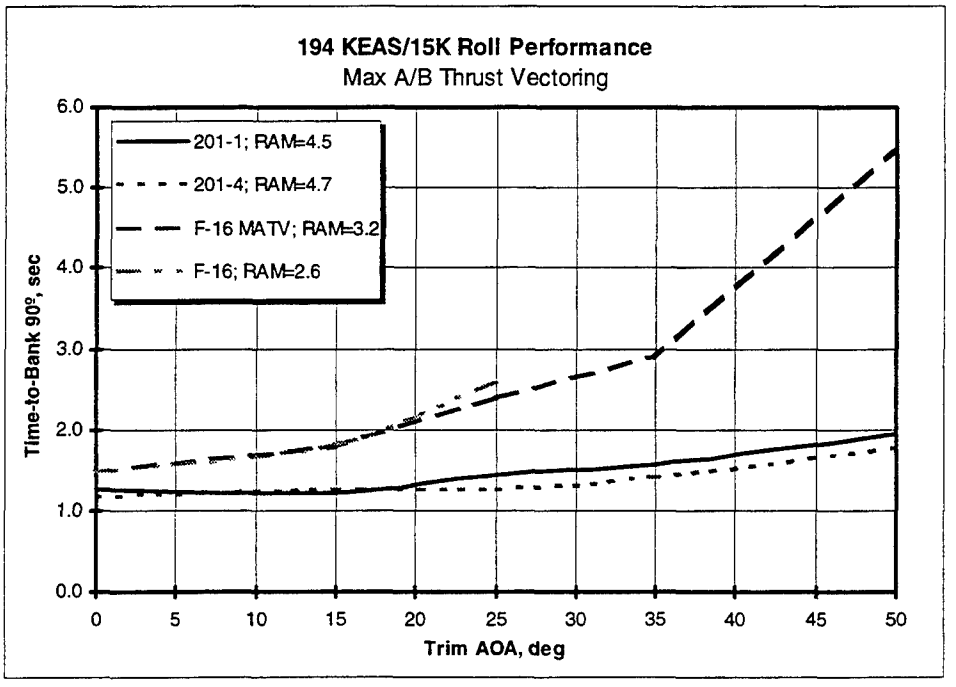

Figure 6-34: Configuration 201-Series Time-To-Bank 90° at 194 KEAS/15K and FWV Roll Agility Metric

Table 6-2 summarizes up and away roll performance data for the Configuration 201-series airplanes. Power approach roll performance is discussed in a separate section. Conditions that did not achieve the roll performance goals are highlighted.

Table 6-2: Configuration 201-Series Up & Away Roll Performance Summary

Configuration	Flight Condition	Power Setting	Time-to-Bank $\Delta\phi$ ($\Delta\phi$ /sec)	Time-to-Bank $\Delta\phi$ Goal ($\Delta\phi$ /sec)
201-1	**300 KCAS/α=20**	**Mil Power**	**90/1.2**	**90/1.1**
"	"	Max A/B	90/1.1	"
"	108 KCAS/α=30	"	90/2.0	90/2.0
"	108 KCAS/α=45	"	90/3.3	90/4.0
201-4	300 KCAS/α=20	Mil Power	90/1.0	90/1.1
"	300 KCAS/α=20	Max A/B	90/0.9	"
"	108 KCAS/α=30	"	90/2.0	90/2.0
"	108 KCAS/α=45	"	90/3.2	90/4.0

Power Approach Roll Performance For Carrier Suitability

During Phase 1 of the ICE study, power approach roll performance at minimum flying weight was shown to be a critical control sizing condition for the 201-series of airplanes [Dorsett & Mehl, 1996]. This analysis was performed again during Phase 2 with the latest updated wind-tunnel data.

Because power approach is a relatively low-AOA flight condition, the ADF 9604 wind tunnel data was used exclusively during this analysis instead of LAMP data. New trimmed lift curves were generated. Figure 6-35 shows a comparison of these curves with the Phase 1 predictions along with the associated canard, LEF, and trailing-edge control surface deflections. At low AOAs below 10°, the canard was fixed at 10° LEU to maximize lift. At higher AOAs, it was scheduled more LED so that the trailing-edge control deflections would not be required to exceed 15° TED to trim the aircraft. This method ensured that both longitudinal and lateral control margins were retained for gust alleviation or use during rolling maneuvers. The current data predict higher levels of trimmed lift for AOAs up to 17°, which is above the vision limit approach AOA of 11.2° that was computed during Phase 1. The Phase 2 data also show a lower trimmed $C_{L_{MAX}}$. The primary reason for these trimmed lift discrepancies is that the latest data includes a greater number of control deflection breakpoints than were available during the Phase 1 study, which improved the fidelity of the Phase 2 trimmed lift computations.

The higher trimmed lift values available within the range of possible approach AOAs allow the configuration to approach at slower speeds for a given weight and AOA combination. Slowing the approach speed degrades roll performance because of the associated reduction in dynamic pressure, which makes this flight condition even more critical than before. For this reason, the Phase 2 power approach roll analysis was performed using both sets of trimmed lift data for comparison with the Phase 1 results.

Figure 6-36 shows a comparison between the Configuration 201-1 Phase 1 and Phase 2 roll vs. yaw control envelopes at AOAs of 8°, 10° and 12°. It should be noted that the Phase 1 control envelopes were computed

for trim power, but the Phase 2 envelopes represent an idle power throttle setting. Despite this difference, the Phase 2 idle power data show nearly as much coordinated roll power as the Phase 1 trim power data. This result is due to the current SSD data showing greater effectiveness than the Phase 1 predictions (Figure 6-24).

Figure 6-37 shows the power approach roll performance at varying wind-over-deck (WOD) speeds and bring back weights for Configuration 201-1. The critical case is zero bring back weight (minimum flying weight) because this condition represents the slowest speed at which the aircraft will fly for a given AOA. WOD is defined as $1.05*V_{PA} - V_{ENGAGE}$, where V_{ENGAGE} is set by the aircraft carrier's arresting gear capabilities. For airplanes in the weight class of Configuration 201, the maximum engagement speed for the Mk 7 Mod 3 (CV71, USS Roosevelt) arresting gear is 145 KTAS. The figure shows that Configuration 201-1 has considerably better power approach roll performance than was originally predicted during Phase 1, but it still falls somewhat short of the required 30° bank angle change in 1.0 sec criterion. Roll performance is better when the Phase 1 lift data are used because the approach speeds are somewhat faster.

Power approach control power envelopes for Configuration 201-4 are shown in Figure 6-38. Both data sets include the effects of thrust vectoring at an idle throttle setting. The Phase 1 data represent an AMT with an area of 32.7 ft^2 and a chordwise hinge line. The Phase 2 data represent a smaller AMT (area of 25.8 ft^2) with a skewed hinge line. The Phase 2 data compare very favorably with the Phase 1 results. Slightly less coordinated roll power occurred than was predicted at an AOA of 8°, and slightly more coordinated roll power was generated at an AOA of 12° than was originally forecast. These results clearly show the benefit of the skewed AMT concept in that roughly the same coordinated roll power was obtained from a skewed AMT that was 21% smaller than the original unskewed AMT. The power approach roll performance data for Configuration 201-4 are shown in Figure 6-39. When comparing these results with the same trimmed lift values (i.e., Phase 1 data), the roll performance is very similar to the Phase 1 predictions. When using the higher Phase 2 trimmed lift values, the roll performance is reduced because of the resulting slower approach speeds.

Table 6-3 shows coordinated roll power and roll performance comparisons for Configurations 201-1 and 201-4 in both idle and trim power. These results represent zero bring back weight, and they were run with the Phase 2 lift data – the lowest airspeed condition. The trim power results indicate that neither configuration meets the Level 1 roll performance criteria of 30° of bank angle change in 1 second at the vision limit speed. Note that they will achieve the MIL-F-8785C requirement of 30° in 1.1 second (equivalent to about 25° in 1.0 second) at these conditions. Furthermore, both configurations have very similar power approach roll performance. Since trim power thrust vectoring together with aerodynamic controls coordinates all of the available roll power, additional roll power (i.e., slightly larger aileron, SSD, elevon, etc.) will probably be required to make these configurations achieve the desired roll performance at the necessary approach speeds. Additional analysis with more refined mass properties data should be conducted prior to revising the control surface sizes.

Table 6-3: Effect of Power Setting on PA Roll Performance

Configuration	Power Setting	$C_l'_{max}$ Coordinated	ϕ @ 1 sec (deg; Goal = 30)
201-1	Idle	0.0413	24.3
201-1	Trim	0.0623	28.9
201-4	Idle	0.0443	23.6
201-4	Trim	0.04768	27.7

Note: Phase 2 lift data at minimum flying weight vision limit speed (α = 11.2 deg; 125.7 KTAS)

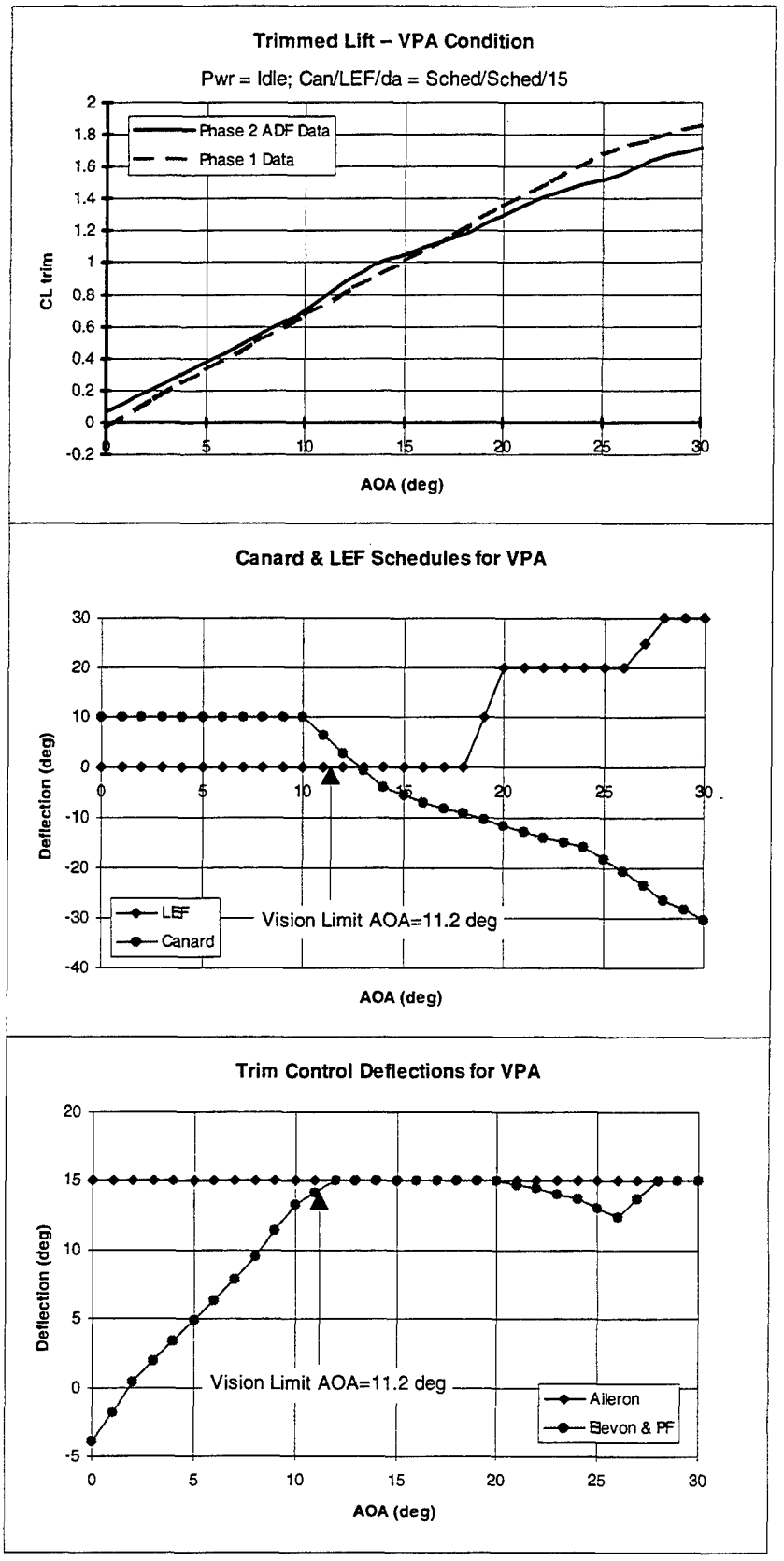

Figure 6-35: Configuration 201 Power Approach Trim Conditions

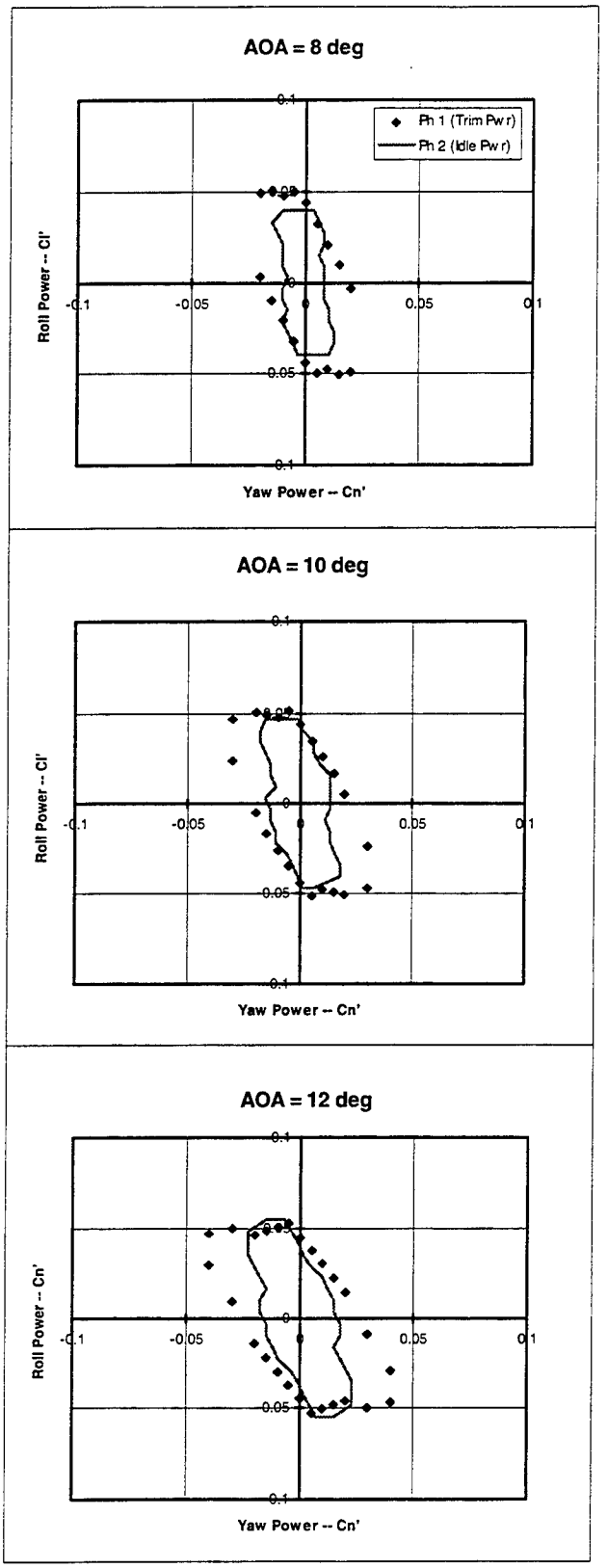

Figure 6-36: Comparison of Configuration 201-1 PA Control Power Available With Phase 1 Results

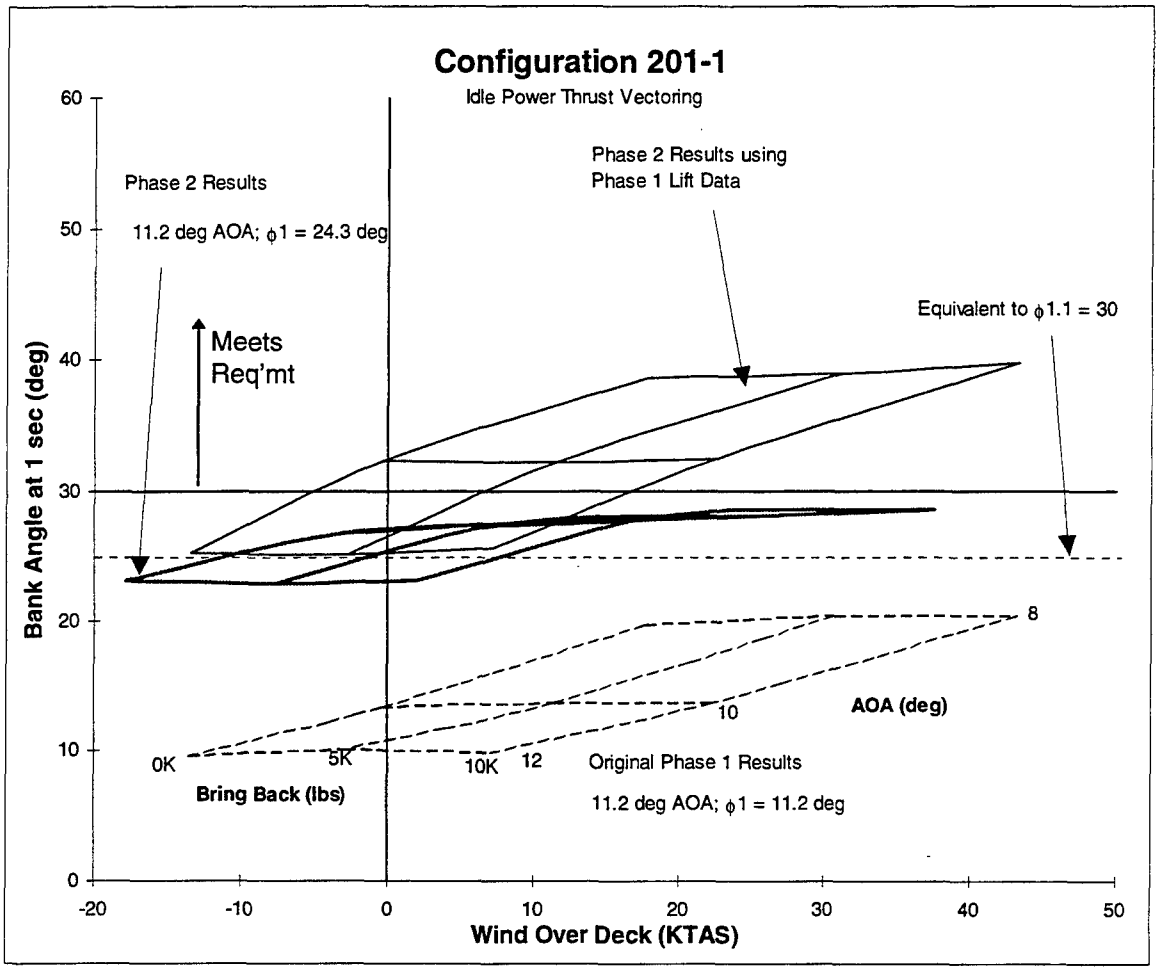

Figure 6-37: Comparison of Configuration 201-1 Power Approach Roll Performance With Phase 1 Results

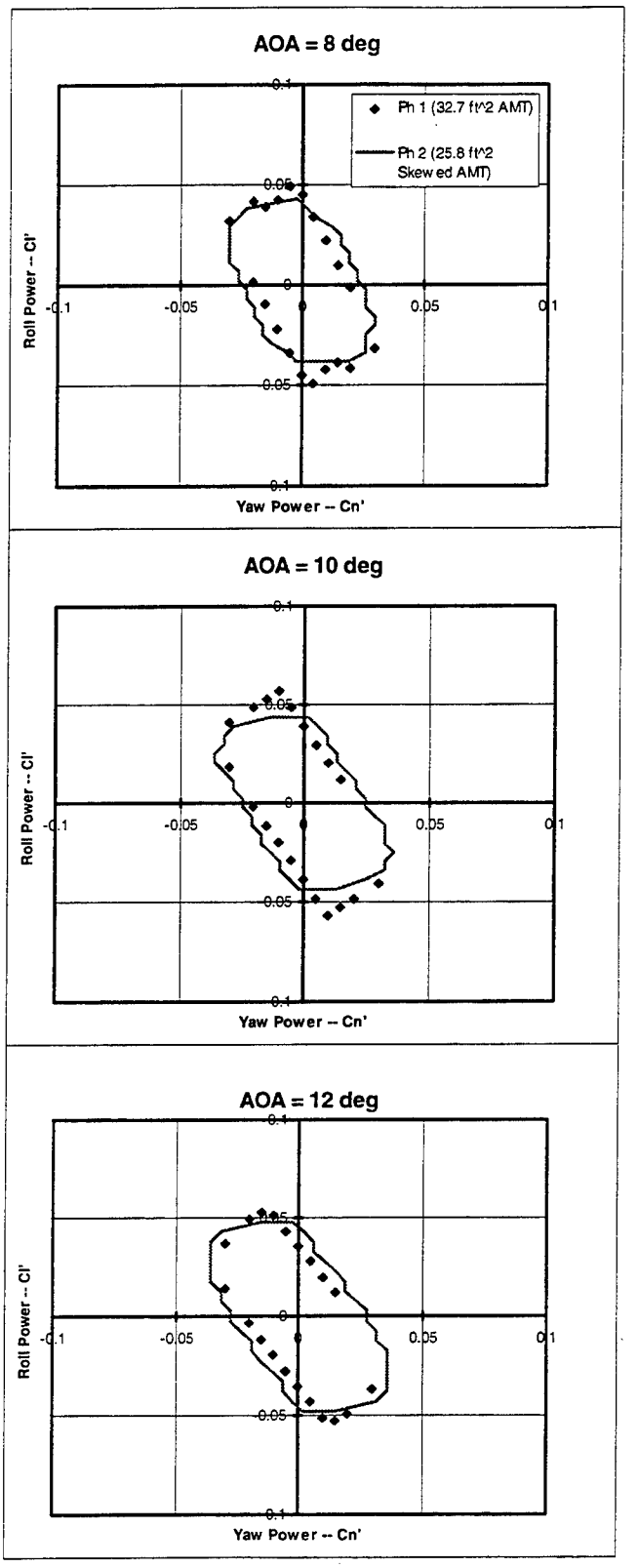

Figure 6-38: Comparison of Configuration 201-4 PA Control Power Available With Phase 1 Results

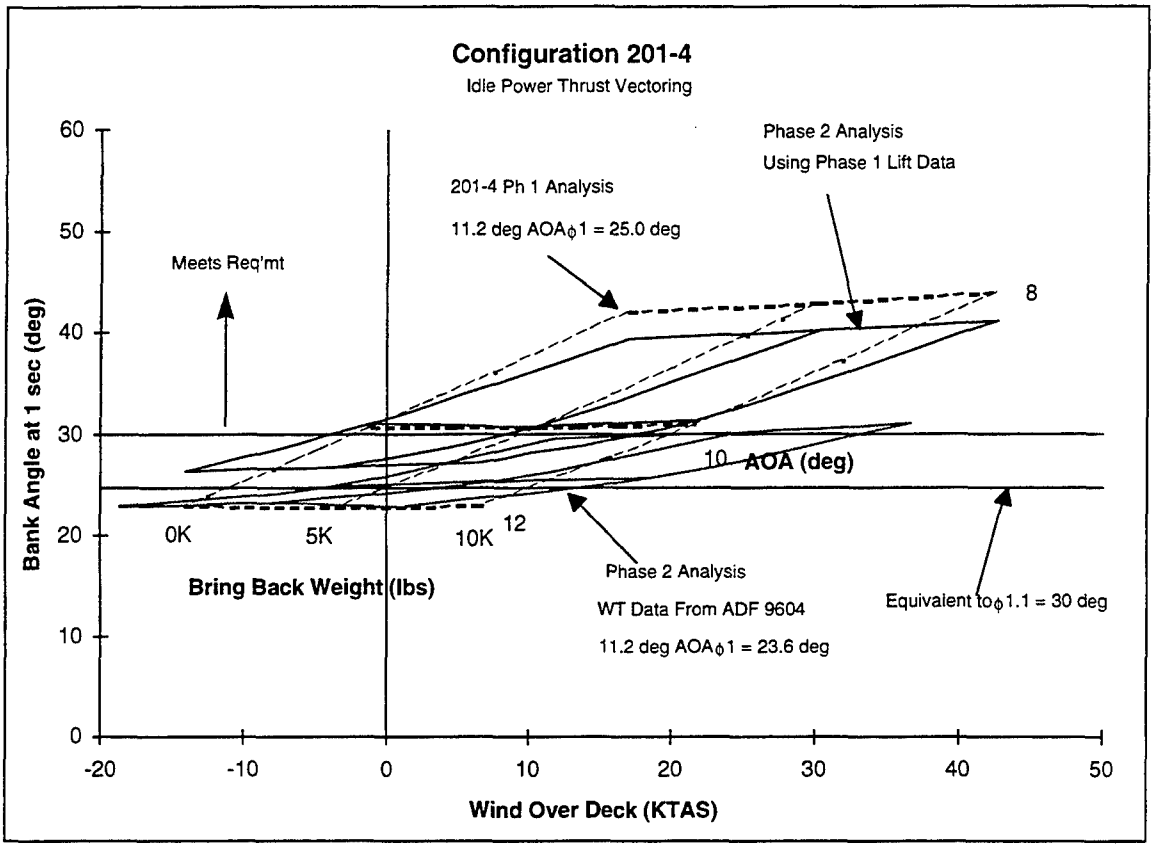

Figure 6-39: Comparison of Configuration 201-4 Power Approach Roll Performance With Phase 1 Results

Comparisons With Phase 1 Results

Each of the flying qualities parameters computed during this study was compared to its corresponding Phase 1 prediction at the conditions where Phase 1 data was available. Figure 6-40 compares the maximum coordinated roll power and augmented lateral-directional stability values for Configuration 201-1 at the 150 KCAS/15K flight condition. The Phase 2 results are more favorable across the board for both the aerodynamic controls only and aerodynamic controls plus thrust vectoring cases. Configuration 201-1 exhibits greater coordinated roll capability and higher augmented directional stability than were predicted during Phase 1. These results are partially a consequence of the more favorable SSD performance than was originally expected (Figure 6-24). As discussed previously, the SSDs generated considerably more yaw control power and higher favorable rolling moments for AOAs below 20° than was originally forecast. In addition, the effects on pitching-moment of deflecting the SSDs were over-predicted during Phase 1. As a result, more of the elevons could be used for roll power because they were not needed to trim the nose-up moments generated by SSD deflections. All these effects contributed to the observed improvements in performance over the Phase 1 predictions.

Figure 6-41 compares the corresponding results for Configuration 201-4. The 201-4 Phase 2 coordinated roll power and augmented stability values compare more closely to the Phase 1 predictions than did the 201-1 results (Figure 6-40) because the effectiveness of the AMTs (Figure 6-25) was more accurately predicted than the effectiveness of the SSDs (Figure 6-24). With the exception of coordinated roll power below an AOA of 20°, the Phase 2 data show improvements over the Phase 1 predictions for both quantities. These improvements were partially attributed to the higher fidelity of the Phase 2 database, which enabled finer control deflection increments to be used during the construction of the control power envelopes.

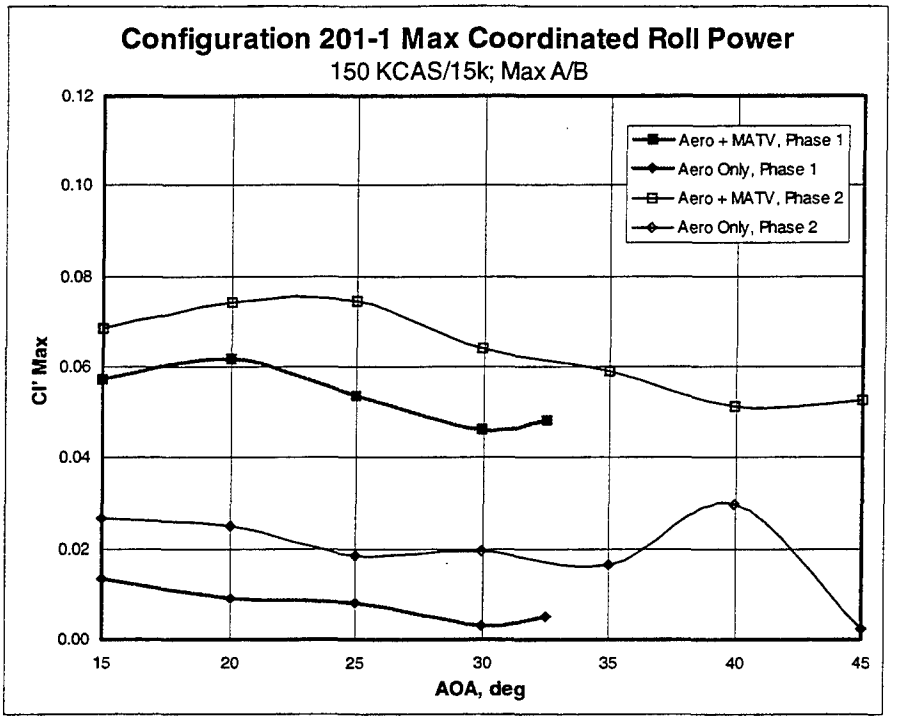

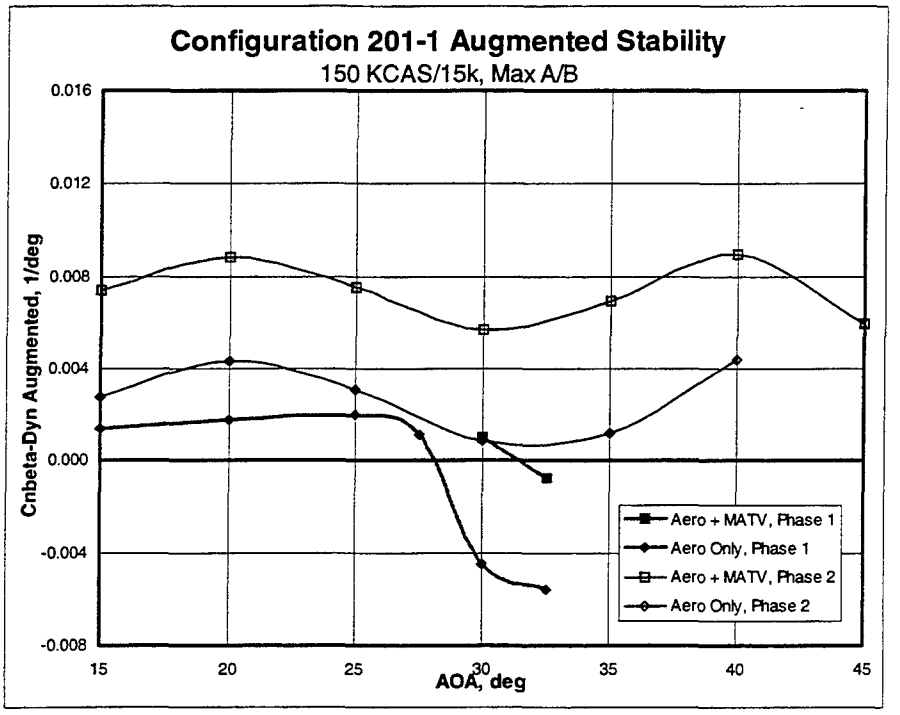

Figure 6-40: Comparison of Configuration 201-1 Lateral-Directional Flying Qualities With Phase 1 Results

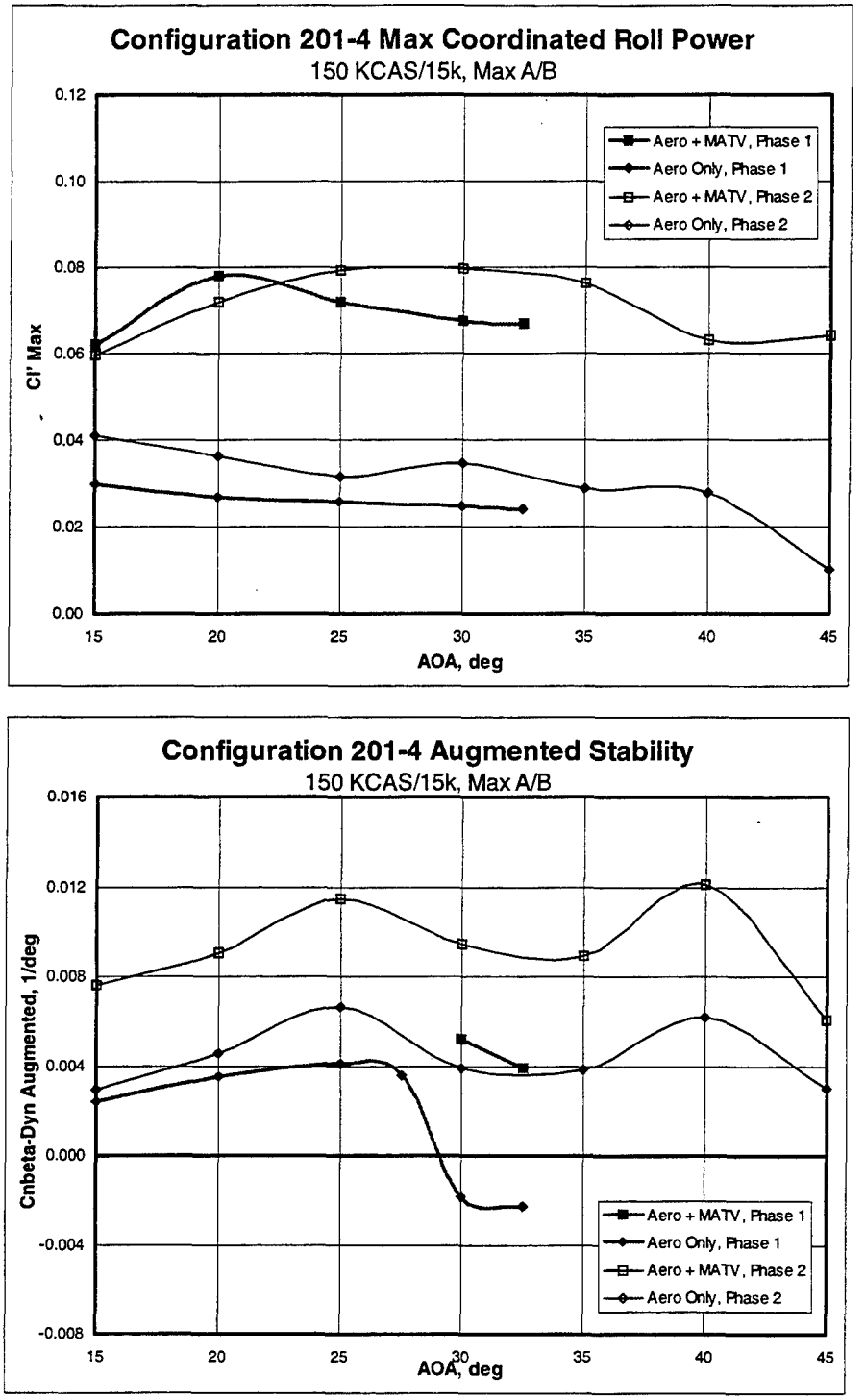

Figure 6-41: Comparison of Configuration 201-4 Lateral-Directional Flying Qualities With Phase 1 Results

The Phase 2 time-to-bank 90° roll performance values are compared in bar chart format to the Phase 1 predictions in Figure 6-42. Data are shown for the 108 KCAS/15K flight condition at an AOA of 30°. Phase 1 data were not available at the other flight conditions. The roll performance of both configurations was improved over the Phase 1 predictions due to the increased coordinated roll power available from both

the SSDs and AMTs, and both configurations met the performance requirement of 90° of bank angle change in 2.0 seconds.

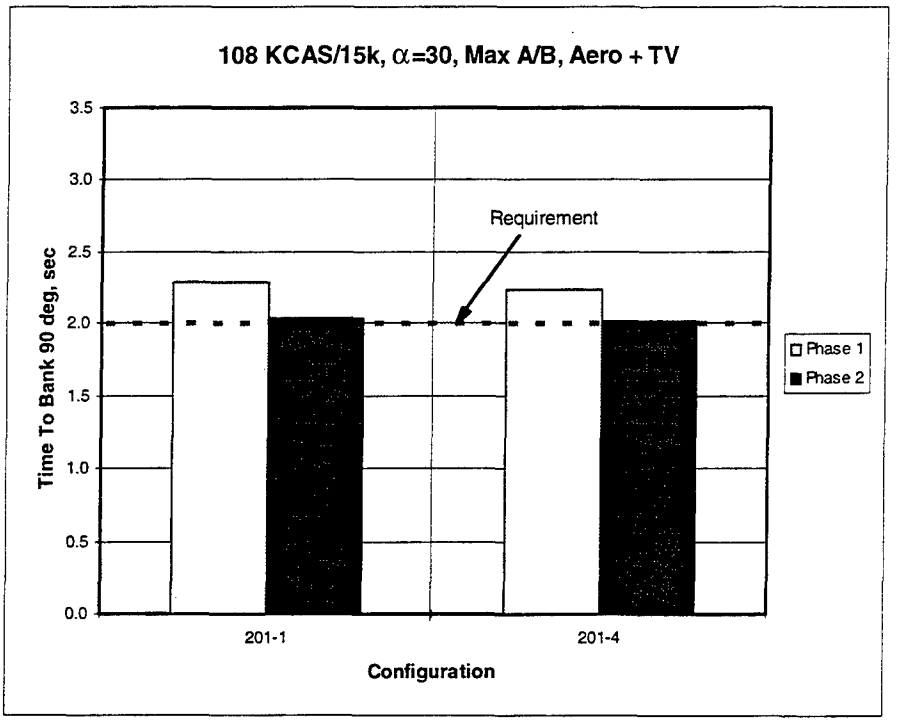

Figure 6-42: Comparison of Configuration 201 Roll Performance Predictions With Phase 1 Results

7 Conclusions

The conclusions reached during Phase 2 of the ICE program are summarized below.

7.1 All Moving Wing Tip

- Of all the concepts investigated during the ICE program, the AMT is the best overall effector for full-envelope directional control of a highly maneuverable tailless fighter.

- The AMT produced nearly constant body-axis yaw power for AOAs below 40°. And although less than the low-AOA values, significant yaw power was retained for AOAs up to 90°. Yaw control power was insensitive to rotation rate. In addition, yaw-control effectiveness improved with windward sideslip, which increased the viability of using the AMT for directional stability augmentation.

- AMT deflection generated adverse body-axis rolling moments at AOAs below 10°. But for AOAs between 10° and 90°, favorable rolling moments were produced. This result indicated that the AMT would be capable of providing good high-AOA roll coordination capability. AMT roll power was nonlinear with sideslip and rotation rate.

- Small nose-down pitching-moment increments were generated by trailing-edge-down AMT deflections. This beneficial secondary result indicated that symmetric AMT deflections could be used to provide additional high-AOA nose-down recovery. Furthermore, this characteristic frees up more of the deflection range of the other control surfaces (i.e., elevons and pitch flaps) to be used for roll control because they are not required to counter the adverse nose-up pitching moments that are created by some of the other types of control concepts (i.e., the SSD).

- Sweeping the hingeline of the AMT aft improved the directional control effectiveness by generating favorable side-force increments that increased the overall yaw power produced by the deflection.

- AMT lateral-directional control power scaled well with control volume ratio for AOAs up to 20°. But above AOAs of 20°, scaling AMT effectiveness with control volume should be used with caution.

- Configurations that incorporated the AMT (101-4 and 201-4) achieved impressive high-AOA maneuvering performance, even without using thrust vectoring. The AMTs alone provided sufficient augmenting yaw power to stabilize both land-based and carrier-based configurations at all the AOAs investigated.

- The AMT had sufficient control power to provide anti-spin and spin recovery control when deflected 60° trailing-edge down on the advancing wing. This result was observed for both the land-based flying-wing and carrier-based canard-delta configurations.

7.2 Spoiler-Slot-Deflector

- The SSDs generated large body-axis yawing moments for AOAs below 20° that were larger than those that were produced by the AMTs at these same AOAs. The yaw power of the SSDs was retained for AOAs up to 40°, but the AMTs were more effective at these higher AOAs.

- Favorable rolling moments were produced by SSD deflection for most of the AOAs investigated.

- Similar to the AMTs, SSD yaw power was insensitive to windward sideslip, and it therefore provided significant yaw-augmentation capabilities throughout the AOA range investigated. In contrast, the SSD was more affected by rotation rate than the AMT.

- SSD control power was found to be sensitive to slot blockage, but the amount of blockage representative of simulated wing structure did not have an appreciable impact on SSD control effectiveness. The optimum slot area was consistent with that of the individual spoiler or deflector flaps.

- The control power produced by trailing-edge surfaces which were mounted aft of the SSDs was found to be severely curtailed by even small SSD deflections. This effect could complicate the control law design process. Moving the SSD as far forward and as far outboard of the affected trailing-edge control as possible minimized the adverse interaction. Outboard and forward locations for the SSD also improved their yaw-control effectiveness for AOAs below 20° because of the increased spanwise moment arm. Similarly, sweeping the hingeline of the SSDs aft would further increase its moment arm and thereby increase its effectiveness.

- Similar to the AMTs, SSD lateral-directional control power scaled well with control volume ratio for AOAs below 20°. But for AOAs above 20°, scaling SSD effectiveness with control volume should be used with caution.

- The SSD yaw-control effectiveness measured during Phase 2 was considerably better than that predicted during Phase 1. As a result, the maneuvering performance calculated during Phase 2 for the SSD-configured airplanes (101-1 and 201-1) was also superior to the Phase 1 predictions. Unlike the AMT-configured aircraft (Configuration 101-4), Configuration 101-1 did not have sufficient aerodynamic yaw authority to stabilize the airplane at AOAs above 30° in the absence of thrust vectoring.

- Similar to the AMTs, the SSDs had sufficient control power to provide anti-spin and spin recovery control when deflected 60° on the advancing wing for both the land-based flying-wing and carrier-based canard-delta configurations. Pro-spin elevon deflections used in conjunction with anti-spin SSD deflections were required for spin recovery on the land-based configuration.

7.3 Control Power Analysis

- Configurations 101-4, 201-1 and 201-4 have unlimited AOA capability when using aerodynamic control power alone. Configuration 101-1 runs out of augmenting directional control power for AOAs above 30°, but it has unlimited AOA potential when yaw thrust vectoring is added. All four configurations have substantial high-AOA maneuvering potential when control power from aerodynamic and propulsion effectors is used together.

- Configurations 101-1, 201-1, and 201-4 had overall better roll performance and high-AOA characteristics than those predicted during Phase 1, and the corresponding values for Configuration 101-4 were very similar to the Phase 1 predictions. Neither of the land-based configurations achieved the goal of 90° bank angle change in 2.0 seconds when at an AOA of 30° and an airspeed of 108 KCAS, but they both exceeded the corresponding goal of 4.0 seconds when at an initial AOA of 45°. Both carrier-based configurations achieved or exceeded the high-AOA roll performance goals specified during Phase 1. This result was attributed to the fact that the carrier-based control power was set by carrier suitability considerations (notably, power approach roll performance), whereas the land-based configurations control power sizing conditions were more balanced across the flight conditions that were investigated.

- The carrier-based configurations both have similar power approach roll performance. Both nearly achieve the Level 1 requirement of 30° bank angle change in 1 second at minimum flying weight (the critical flying qualities condition) with trim power thrust vectoring. Because the combination of trim power thrust vectoring and aerodynamic controls coordinates all of the available roll power, additional

yaw power will not appreciably improve roll performance. Additional roll power will probably be required (i.e., larger elevon and/or aileron, etc.) to improve power approach roll performance.

- The four ICE configurations manifested values of the FWV roll agility metric that were 30% to 40% larger than those for the highly agile F-16 MATV.

7.4 Recommendations

Based on the wind-tunnel testing to date, ICE technology is rated at a technology readiness level (TRL) of 4. To achieve a TRL of 5, transonic wind tunnel data must be collected to validate high-speed control effectiveness and to ensure that the AMT and SSD are viable across the full flight envelope as was predicted during ICE Phase 1. Additional studies that need to be conducted include:

- Development of aeroelastic effects on AMT and SSD control power.

- Refinement of transonic hinge moment data. This task may be accomplished by using either wind tunnel or CFD analyses.

- Revisit structural, hydraulic and weight estimates generated during ICE Phase 1 using new aeroelastic and hinge moment data.

- Conduct a detailed RCS integration study to determine the effects of hingeline and actuation details on RCS performance. Investigate potential treatment suites to minimize RCS. This study should involve both computational and range testing using component and/or subscale models.

8 References

Beaufrere, H.L., et al, "Control Power Requirements for Statically Unstable Aircraft", AFWAL-TR-87-3018, June 1987.

Behrbohm, H., "Basic Low Speed Aerodynamics of the Short-Coupled Canard Configuration of Small Aspect Ratio", SAAB TN 60, July 1965.

Bihrle, W., Jr., "Prediction of High Alpha Flight Characteristics Utilizing Rotary Balance Data", 13th ICAS Congress/AIAA Aircraft Systems & Technology Conference Proceedings, August 1981.

Bihrle, W., Jr., "Spin Prediction Techniques", *Journal of Aircraft*, Vol. 20, No. 2, Feb. 1983.

Das, A., Longo, J.M.A., "Numerical Analysis of the Vortical Flow Around a Delta Wing-Canard Configuration", *Journal of Aircraft*, Vol. 32, No. 4, 1995, pp. 716-725.

Dickes, E.G., "Rotary Balance Data and Analysis of the T-45A Update Airplane from -90 deg to +180 deg Angle-of-Attack", Bihrle Applied Research Report No. 91-3, July 1991.

Doane, P.M., et al, "Multi System Integrated Control (MuSIC) Program", WRDC-TR-90-6001, Wright Reseach and Development Center, WPAFB, OH, June 1990.

Dorsett, K.M., Mehl, D.R., "Innovative Control Effectors (ICE)", WL-TR-96-3043, January 1996.

Dorsett, K.M. "Low-Speed Wind Tunnel Data Analysis of a 1/18th Scale Tailless Fighter", ERR-FW-4323, Lockheed Martin Tactical Aircraft Systems, December 1994.

Heoijmakers, H.W.M., "Modeling and Numerical Simulation of Vortex Flow in Aerodynamics", *AGARD Fluid Dyamics Panel Symposium on Vortex Flow Aerodynamics*, 1990, Paper No. 1, (AGARD-CP-494).

Houlden, H.P., "Analysis of F-18E/F Rotary Balance Force and Moment and Surface Pressure Data", Bihrle Applied Research Report No, 95-10, November 1995.

Hummel, D., Oelker, H.-Chr., "Low-Speed Characteristics of the Wing-Canard Configuration of the International Vortex Flow Experiment", *Journal of Aircraft*, Vol. 31, No. 4, 1994, pp. 868-878.

Johnson, J.L., Grafton, S.B., and Yip, L.P., "Exploratory Investigation of the Effects of Vortex Bursting on the High Angle-of-Attack Lateral-Directional Stability Characteristics of Highly Swept Wings", AIAA-80-0463, 1980.

Kay, J., Ralston, J.N., "F-15E High Angle-of-Attack Study, Including Data, Analysis, Aerodynamic Math Modeling and Simulation", Bihrle Applied Research Report No. 95-2, March 1995.

McRuer, D., Ashkenas, I., Graham, D., Aircraft Dynamics and Automatic Control, Princeton University Press, Princeton, NJ, 1973, p. 257.

Peters, S.E., "Wind Tunnel Data Analysis of an Advanced Concept Fighter Aircraft", Lockheed Martin Tactical Aircraft Systems, SCTR 95-003, April 1995.

Stoll, F., Koenig, D.G., "Large Scale Wind Tunnel Investigation of a Close-Coupled Canard-Delta-Wing Fighter Model Through High Angles-of-Attack", AIAA 83-2554, Oct. 1983.

Thomas, R.W., "Analysis of Aircraft Stability and Control Design Methods", AFWAL-TR-84-3038, May 1984.